

NOVEMBER 2022

AJNR

VOLUME 43 • PP 1549-1685

AJNR

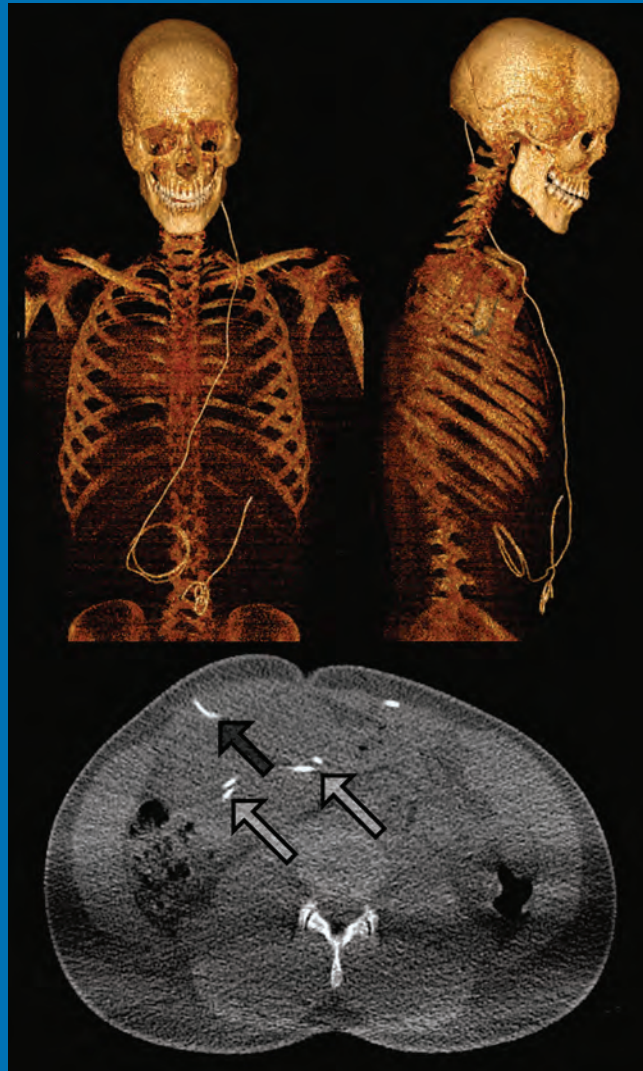
AMERICAN JOURNAL OF NEURORADIOLOGY

NOVEMBER 2022
VOLUME 43
NUMBER 11
WWW.AJNR.ORG

THE JOURNAL OF DIAGNOSTIC AND
INTERVENTIONAL NEURORADIOLOGY

7T SWI for diagnosis of astrocytic and oligodendroglial tumors
Whole-body ultra-low-dose CT for ventriculoperitoneal shunt complications
Dual-energy CT for risk stratification of intracranial hemorrhage in stroke
MR imaging findings of carcinoma ex pleomorphic adenoma

Official Journal ASNR • ASFNR • ASHNR • ASPNR • ASSR



FRED™ X™

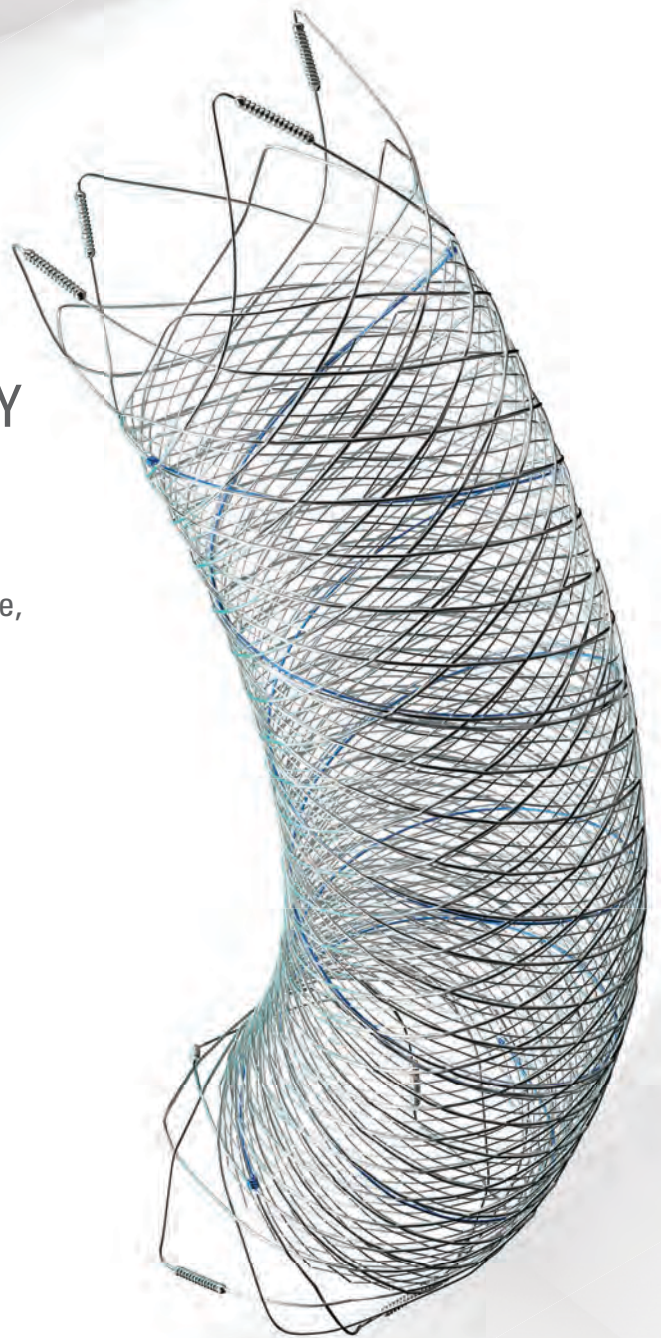
Flow Diverter Stent

THE NEXT ADVANCEMENT IN FLOW DIVERSION TECHNOLOGY

The FRED™ X Flow Diverter features the same precise placement and immediate opening of the FRED™ Device, now with X Technology. X Technology is a covalently bonded, nanoscale surface treatment, designed to:

- **REDUCE MATERIAL THROMBOGENICITY¹**
- **MAINTAIN NATURAL VESSEL HEALING RESPONSE^{2,3,4}**
- **IMPROVE DEVICE DELIVERABILITY AND RESHEATHING¹**

The only FDA PMA approved portfolio with a 0.021" delivery system for smaller device sizes, and no distal lead wire.



For more information, contact your local MicroVention sales representative or visit our website. www.microvention.com

 **MicroVention™**
TERUMO

¹ Data is derived from in vivo and ex vitro testing and may not be representative of clinical performance.

¹ Data on file

² Tanaka M et al. Design of biocompatible and biodegradable polymers based on intermediate water concept. *Polymer Journal*. 2015;47:114-121.

³ Tanaka M et al. Blood compatible aspects of poly(2-methoxyethylacrylate) (PMEA) – relationship between protein adsorption and platelet adhesion on PMEAs surface. *Biomaterials*. 2000;21:1471-1481.

⁴ Schiel L et al. X Coating™: A new biopassive polymer coating. *Canadian Perfusion Canadienne*. June 2001;11(2):9.

Indications for Use: The FRED X System is indicated for use in the internal carotid artery from the petrous segment to the terminus for the endovascular treatment of adult patients (22 years of age or older) with wide-necked (neck width 4 mm or dome-to-neck ratio < 2) saccular or fusiform intracranial aneurysms arising from a parent vessel with a diameter 2.0 mm and 5.0 mm.

Rx Only: Federal (United States) law restricts this device to sale by or on the order of a physician. For Healthcare professionals intended use only.

MICROVENTION, FRED and HEADWAY are registered trademarks of MicroVention, Inc. in the United States and other jurisdictions. Stylized X is a trademark of MicroVention, Inc. © 2022 MicroVention, Inc. MM1222 US 03/22

WEB™ 17

Aneurysm Embolization System

LOWER PROFILE



NEW SIZES



MORE ACCESS OPTIONS



INDICATIONS FOR USE:

The WEB Aneurysm Embolization System is intended for the endovascular embolization of ruptured and unruptured intracranial aneurysms and other neurovascular abnormalities such as arteriovenous fistulae (AVF). The WEB Aneurysm Embolization System is also intended for vascular occlusion of blood vessels within the neurovascular system to permanently obstruct blood flow to an aneurysm or other vascular malformation.

POTENTIAL COMPLICATIONS:

Potential complications include but are not limited to the following: hematoma at the site of entry, aneurysm rupture, emboli, vessel perforation, parent artery occlusion, hemorrhage, ischemia, vasospasm, clot formation, device migration or misplacement, premature or difficult device detachment, non-detachment, incomplete aneurysm filling, revascularization, post-embolization syndrome, and neurological deficits including stroke and death. For complete indications, potential complications, warnings, precautions, and instructions, see instructions for use (IFU provided with the device).

VIA 21, 27, 33 - The VIA Microcatheter is intended for the introduction of interventional devices (such as the WEB device/stents/flow diverters) and infusion of diagnostic agents (such as contrast media) into the neuro, peripheral, and coronary vasculature.

VIA 17,17 Preshaped - The VIA Microcatheter is intended for the introduction of interventional devices (such as the WEB device/stents/flow diverters) and infusion of diagnostic agents (such as contrast media) into the neuro, peripheral, and coronary vasculature.

The VIA Microcatheter is contraindicated for use with liquid embolic materials, such as n-butyl 2-cyanoacrylate or ethylene vinyl alcohol & DMSO (dimethyl sulfoxide).

The device should only be used by physicians who have undergone training in all aspects of the WEB Aneurysm Embolization System procedure as prescribed by the manufacturer.

RX Only: Federal law restricts this device to sale by or on the order of a physician.

For healthcare professional intended use only.



MicroVention Worldwide
Innovation Center PH +1.714.247.8000

35 Enterprise
Aliso Viejo, CA 92656 USA
MicroVention UK Limited PH +44 (0) 191 258 6777
MicroVention Europe, S.A.R.L. PH +33 (1) 39 21 77 46
MicroVention Deutschland GmbH PH +49 211 210 798-0
Website microvention.com



WEB™ and VIA™ are registered trademarks
of Sequent Medical, Inc. in the United States.

©2021 MicroVention, Inc. MM1184 WW 11/2021

multihance[®]
(gadobenate dimeglumine)
injection, 529 mg/mL

What does seeing better with MultiHance[®] mean?^{1-4*}

MultiHance[®] demonstrated superiority in both qualitative and quantitative enhancement of brain lesions compared with Dotarem[®] at 0.1 mmol/kg dose.^{1†}

- The 0.1 mmol/kg dose of MultiHance demonstrated consistently better visualization for all readers for all visualization endpoints vs non-contrast MRI.
- 3 blinded and independent readers reported superiority ($P < 0.002$) of 0.1-mmol/kg MultiHance for all endpoints in Arm 1.
- 3 blinded independent readers also reported the mean percentage signal enhancement of lesions on the TISE images was significantly ($P < .0006$) higher for MultiHance compared with Dotarem in patients given 0.1-mmol/kg doses of both agents. Similar results were obtained for determination of LBR. LBR findings on TIGRE images were similar.

The individuals who appear are for illustrative purposes. All persons depicted are models and not real patients.

Please see Brief Summary of Prescribing Information including Boxed Warning on adjacent page.

*MRI imaging of the CNS in adult and pediatric patients to visualize lesions with abnormal BBB or abnormal vascularity of the brain, spine and associated tissues or to evaluate adults with known or suspected renal or aorto-ilio-femoral occlusive vascular disease.

†Multicenter, multinational, double-blind randomized, intraindividual crossover study design of 177 patients with known or suspected brain tumors. Each patient received 0.1-mmol/kg doses of MultiHance and Dotarem in two identical MR imaging examinations. For Arm 1, the contrast agents for patients were administered by IV using manual bolus injection ($n=83$) or power a power injector ($n=13$). The agents were administered at 0.1mmol/kg of body weight, corresponding to 0.2 mL/kg for MultiHance and for Dotarem. For Arm 2, Administration of agents were IV using manual bolus injection ($n=83$) or power a power injector ($n=24$). The agents were administered 0.05 mmol/kg of body weight, corresponding to 0.1 mL/kg for MultiHance and at 0.1mmol/kg of body weight, corresponding to 0.2 mL/kg for Dotarem. All injections were followed by a saline flush of up to 30 mL. The interval between the 2 MR imaging examinations was > 48 hours to avoid carryover effects but < 14 days to minimize the chance of disease progression. All images were evaluated by 3 blinded, independent experienced radiologists who were unaffiliated with the study centers. Each reader evaluated the patient images separately and independently. Images were evaluated qualitatively for diagnostic and quality and scored for: 1) lesion border delineation, 2) disease extent, 3) visualization of lesion internal morphology, and 4) lesion contrast enhancement compared with surrounding normal tissue. All assessments used a 3-point scales from 1 (examination 1 better) through 0 (examinations equal) to 1 (examination 2 better).

Dotarem[®] (Gadoterate) is a registered trademark of Guebert, Aulnay-sous-Bois, France. **Reference:** Vaneckova M, Herman M, Smith MP, et al. The benefits of high relaxivity for brain tumor imaging: results of a multicenter intraindividual crossover comparison of gadobenate dimeglumine with gadoterate meglumine (The BENEFIT Study). *AJNR Am J Neuroradiol.* 2015 Sep;36(9):1589-1598.

MultiHance[®] (gadobenate dimeglumine) injection, 529 mg/mL and MultiHance[®] Multipack[™] (gadobenate dimeglumine) injection, 529 mg/mL

Indications and Usage:

MultiHance[®] (gadobenate dimeglumine) injection, 529 mg/mL is a gadolinium-based contrast agent indicated for intravenous use in:

- Magnetic resonance imaging (MRI) of the central nervous system (CNS) in adults and pediatric patients (including term neonates) to visualize lesions with abnormal blood-brain barrier or abnormal vascularity of the brain, spine, and associated tissues and
- Magnetic resonance angiography (MRA) to evaluate adults with known or suspected renal or aorto-ilio-femoral occlusive vascular disease

IMPORTANT SAFETY INFORMATION:

WARNING: NEPHROGENIC SYSTEMIC FIBROSIS

Gadolinium-based contrast agents (GBCAs) increase the risk for NSF among patients with impaired elimination of the drugs. Avoid use of GBCAs in these patients unless the diagnostic information is essential and not available with non-contrasted MRI or other modalities. NSF may result in fatal or debilitating systemic fibrosis affecting the skin, muscle and internal organs.

- **The risk for NSF appears highest among patients with:**
 - chronic, severe kidney disease ($GFR < 30 \text{ mL/min/1.73m}^2$), or
 - acute kidney injury.
- **Screen patients for acute kidney injury and other conditions that may reduce renal function. For patients at risk for chronically reduced renal function (e.g. age > 60 years, hypertension or diabetes), estimate the glomerular filtration rate (GFR) through laboratory testing.**
- **For patients at highest risk for NSF, do not exceed the recommended MultiHance dose and allow a sufficient period of time for elimination of the drug from the body prior to re-administration.**

CONTRAINDICATIONS

MultiHance is contraindicated in patients with known allergic or hypersensitivity reactions to gadolinium-based contrast agents.

WARNINGS AND PRECAUTIONS

Nephrogenic Systemic Fibrosis: NSF has occurred in patients with impaired elimination of GBCAs. Higher than recommended dosing or repeated dosing appears to increase risk.

Hypersensitivity Reactions: Anaphylactic and anaphylactoid reactions have been reported, involving cardiovascular, respiratory, and/or cutaneous manifestations. Some patients experienced circulatory collapse and died. In most cases, initial symptoms occurred within minutes of MultiHance administration and resolved with prompt emergency treatment. Consider the risk for hypersensitivity reactions, especially in patients with a history of hypersensitivity reactions or a history of asthma or other allergic disorders.

Gadolinium Retention: Gadolinium is retained for months or years in several organs. The highest concentrations have been identified in the bone, followed by brain, skin, kidney, liver, and spleen. At equivalent doses, retention varies among the linear agents. Retention is lowest and similar among the macrocyclic GBCAs. Consequences of gadolinium retention in the brain have not been established, but they have been established in the skin and other organs in patients with impaired renal function. Minimize repetitive GBCA imaging studies, particularly closely spaced studies when possible.

Acute Renal Failure: In patients with renal insufficiency, acute renal failure requiring dialysis or worsening renal function have occurred with the use of GBCAs. The risk of renal failure may increase with increasing dose of the contrast agent. Screen all patients for renal dysfunction by obtaining a history and/or laboratory tests.

Extravasation and Injection Site Reactions: Extravasation of MultiHance may lead to injection site reactions, characterized by local pain or burning sensation, swelling, blistering, and necrosis. Exercise caution to avoid local extravasation during intravenous administration of MultiHance.

Cardiac Arrhythmias: Cardiac arrhythmias have been observed in patients receiving MultiHance in clinical trials. Assess patients for underlying conditions



MR Suite



or medications that predispose to arrhythmias. The effects on QTc by MultiHance dose, other drugs, and medical conditions were not systematically studied.

Interference with Visualization of Certain Lesions: Certain lesions seen on non-contrast images may not be seen on contrast images. Exercise caution when interpreting contrast MR images in the absence of companion non-contrast MR images.

ADVERSE REACTIONS

The most commonly reported adverse reactions are nausea (1.3%) and headache (1.2%).

USE IN SPECIFIC POPULATIONS

Pregnancy: GBCAs cross the human placenta and result in fetal exposure and gadolinium retention. Use only if imaging is essential during pregnancy and cannot be delayed.

Lactation: There is no information on the effects of the drug on the breastfed infant or the effects of the drug on milk production. However, limited literature reports that breastfeeding after MultiHance administration to the mother would result in the infant receiving an oral dose of 0.001%–0.04% of the maternal dose.

Pediatric Use: MultiHance is approved for intravenous use for MRI of the CNS to visualize lesions with abnormal blood brain barrier or abnormal vascularity of the brain, spine, and associated tissues in pediatric patients from birth, including term neonates, to less than 17 years of age. Adverse reactions in pediatric patients were similar to those reported in adults. No dose adjustment according to age is necessary in pediatric patients two years of age and older. For pediatric patients, less than 2 years of age, the recommended dosage range is 0.1 to 0.2 mL/kg. The safety of MultiHance has not been established in preterm neonates.

You are encouraged to report negative side effects of prescription drugs to the FDA. Visit www.fda.gov/medwatch or call 1-800-FDA-1088.

Please see full Prescribing Information and Patient Medication Guide for additional important safety information for/regarding

MultiHance (gadobenate dimeglumine) injection, 529 mg/mL at https://imaging.bracco.com/sites/braccoimaging.com/files/technica_sheet_pdf/us-en-2019-01-16-spc-medication-guide-multihance.pdf

MultiHance is manufactured for Bracco Diagnostics Inc. by BIPSO GmbH – 78224 Singen (Germany) and by Patheon Italia S.p.A., Ferentino, Italy. MultiHance is a registered trademark of Bracco International B.V. MultiHance Multipack is a trademark of Bracco International B.V. All other trademarks and registered trademarks are the property of their respective owners.

References: **1.** Vaneckova M, Herman M, Smith MP, et al. The benefits of high relaxivity for brain tumor imaging: results of a multicenter intraindividual crossover comparison of gadobenate dimeglumine with gadoterate meglumine (The BENEFIT Study). *AJNR Am J Neuroradiol.* 2015 Sep;36(9):1589–1598. **2.** Seidl Z, Vymazal J, Mechi M, et al. Does higher gadolinium concentration play a role in the morphologic assessment of brain tumors? Results of a multicenter intraindividual crossover comparison of gadobutrol versus gadobenate dimeglumine (the MERIT Study). *AJNR Am J Neuroradiol.* 2012 Jun-Jul;33(6):1050–1058. **3.** Maravilla KR, Maldjian JA, Schmalfluss IM, et al. Contrast enhancement of central nervous system lesions: multicenter intraindividual crossover comparative study of two MR contrast agents. *Radiology.* 2006 Aug;240(2):389–400. **4.** Rowley HA, Scialfa G, Gao PY, et al. Contrast-enhanced MR imaging of brain lesions: a large-scale intraindividual crossover comparison of gadobenate dimeglumine versus gadodiamide. *AJNR Am J Neuroradiol.* 2008 Jul;29(9):1684–1691.

Bracco Diagnostics Inc.
259 Prospect Plains Road, Building H
Monroe Township, NJ 08831 USA
Phone: 609-514-2200
Toll Free: 1-877-272-2269 (U.S. only)
Fax: 609-514-2446

© 2022 Bracco Diagnostics Inc. All Rights Reserved. US-MH-2100020 04/22

WARNING: NEPHROGENIC SYSTEMIC FIBROSIS
Gadolinium-based contrast agents (GBCAs) increase the risk for NSF among patients with impaired elimination of the drugs.
Avoid use of GBCAs in these patients unless the diagnostic information is essential and not available with non-contrast MRI or other modalities. NSF may result in fatal or debilitating systemic fibrosis affecting the skin, muscle and internal organs.

- The risk for NSF appears highest among patients with:
 - chronic, severe kidney disease (GFR <30 mL/min/1.73m²), or
 - acute kidney injury.
- Screen patients for acute kidney injury and other conditions that may reduce renal function. For patients at risk for chronically reduced renal function (e.g., age > 60 years, hypertension or diabetes), estimate the glomerular filtration rate (GFR) through laboratory testing.
- For patients at highest risk for NSF, do not exceed the recommended MultiHance dose and allow a sufficient period of time for elimination of the drug from the body prior to re-administration. [see **Warnings and Precautions (5.1)**]

1 INDICATIONS AND USAGE

1.1 MRI of the Central Nervous System (CNS)

MultiHance is indicated for intravenous use in magnetic resonance imaging (MRI) of the central nervous system (CNS) in adults and pediatric patients (including term neonates), to visualize lesions with abnormal blood-brain barrier or abnormal vascularity of the brain, spine, and associated tissues.

1.2 MRA of Renal and Aorto-ilio-femoral Vessels

MultiHance is indicated for use in magnetic resonance angiography (MRA) to evaluate adults with known or suspected renal or aorto-ilio-femoral occlusive vascular disease.

4 CONTRAINDICATIONS MultiHance is contraindicated in patients with known allergic or hypersensitivity reactions to gadolinium-based contrast agents [see **Warnings and Precautions (5.2)**].

5 WARNINGS AND PRECAUTIONS

5.1 Nephrogenic Systemic Fibrosis (NSF) Gadolinium-based contrast agents (GBCAs) increase the risk for nephrogenic systemic fibrosis (NSF) among patients with impaired elimination of the drugs. Avoid use of GBCAs among these patients unless the diagnostic information is essential and not available with non-contrast enhanced MRI or other modalities. The GBCA-associated NSF risk appears highest for patients with chronic, severe kidney disease (GFR <30 mL/min/1.73m²) as well as patients with acute kidney injury. The risk appears lower for patients with chronic, moderate kidney disease (GFR 30-59 mL/min/1.73m²) and little, if any, for patients with chronic, mild kidney disease (GFR 60-89 mL/min/1.73m²). NSF may result in fatal or debilitating fibrosis affecting the skin, muscle and internal organs. Report any diagnosis of NSF following MultiHance administration to Bracco Diagnostics (1-800-257-5161) or FDA (1-800-FDA-1088 or www.fda.gov/medwatch).

Screen patients for acute kidney injury and other conditions that may reduce renal function. Features of acute kidney injury consist of rapid (over hours to days) and usually reversible decrease in kidney function, commonly in the setting of surgery, severe infection, injury or drug-induced kidney toxicity. Serum creatinine levels and estimated GFR may not reliably assess renal function in the setting of acute kidney injury. For patients at risk for chronically reduced renal function (e.g., age > 60 years, diabetes mellitus or chronic hypertension), estimate the GFR through laboratory testing.

Among the factors that may increase the risk for NSF are repeated or higher than recommended doses of a GBCA and the degree of renal impairment at the time of exposure. Record the specific GBCA and the dose administered to a patient. For patients at highest risk for NSF, do not exceed the recommended MultiHance dose and allow a sufficient period of time for elimination of the drug prior to re-administration. For patients receiving hemodialysis, physicians may consider the prompt initiation of hemodialysis following the administration of a GBCA in order to enhance the contrast agent's elimination. The usefulness of hemodialysis in the prevention of NSF is unknown [see **Dosage and Administration (2) and Clinical Pharmacology (12)**].

5.2 Hypersensitivity Reactions Anaphylactic and anaphylactoid reactions have been reported, involving cardiovascular, respiratory, and/or cutaneous manifestations. Some patients experienced circulatory collapse and died. In most cases, initial symptoms occurred within minutes of MultiHance administration and resolved with prompt emergency treatment. Prior to MultiHance administration, ensure the availability of personnel, training and medications to treat hypersensitivity reactions. If such a reaction occurs stop MultiHance and immediately begin appropriate therapy. Additionally, consider the risk for hypersensitivity reactions, especially in patients with a history of hypersensitivity reactions or a history of asthma or other allergic disorders. Observe patients for signs and symptoms of a hypersensitivity reaction during and for up to 2 hours after MultiHance administration.

5.3 Gadolinium Retention Gadolinium is retained for months or years in several organs. The highest concentrations (nanomoles per gram of tissue) have been identified in the bone, followed by other organs (e.g., brain, skin, kidney, liver, and spleen). The duration of retention also varies by tissue and is longest in bone. Linear GBCAs cause more retention than macrocyclic GBCAs. At equivalent doses, gadolinium retention varies among the linear agents with Omniscan (gadoterate meglumine) and Optmark (gadoversetamide) causing greater retention than other linear agents [Eovist (gadoterate sodium), Magnevist (gadopentetate dimeglumine), MultiHance (gadobenate dimeglumine)]. Retention is lowest and similar among the macrocyclic GBCAs [Dotarem (gadoterate meglumine), Gadavist (gadobutrol), ProHance (gadoteridol)].

Consequences of gadolinium retention in the brain have not been established. Pathologic and clinical consequences of GBCA administration and retention in skin and other organs have been established in patients with impaired renal function [see **Warnings and Precautions (5.1)**]. There are rare reports of pathologic skin changes in patients with normal renal function. Adverse events involving multiple organ systems have been reported in patients with normal renal function without an established causal link to gadolinium retention [see **Adverse Reactions (6.2)**]. While clinical consequences of gadolinium retention have not been established in patients with normal renal function, certain patients might be at higher risk. These include patients requiring multiple lifetime doses, pregnant and pediatric patients, and patients with inflammatory conditions. Consider the retention characteristics of the agent when choosing a GBCA for these patients. Minimize repetitive GBCA imaging studies, particularly closely spaced studies when possible.

5.4 Acute Renal Failure In patients with renal insufficiency, acute renal failure requiring dialysis or worsening renal function have occurred with the use of gadolinium-based contrast agents. The risk of renal failure may increase with increasing dose of the contrast agent. Screen all patients for renal dysfunction by obtaining a history and/or laboratory tests. Consider follow-up renal function assessments for patients with a history of renal dysfunction.

5.5 Extravasation and Injection Site Reactions Extravasation of MultiHance may lead to injection site reactions, characterized by local pain or burning sensation, swelling, blistering, and necrosis. In animal experiments, local reactions including eschar and necrosis were noted even on Day 8 post-intravenous injection of MultiHance. Exercise caution to avoid local extravasation during intravenous administration of MultiHance. If extravasation occurs, evaluate and treat as necessary if local reactions develop.

5.6 Cardiac Arrhythmias Cardiac arrhythmias have been observed in patients receiving MultiHance in clinical trials [see **Adverse Reactions (6.1)**]. Assess patients for underlying conditions or medications that predispose to arrhythmias.

A double-blind, placebo-controlled, 24-hour post dose continuous monitoring, crossover study in 47 subjects evaluated the effect of 0.2 mmol/kg MultiHance on ECG intervals including QTc. The average changes in QTc values compared with placebo were minimal (<5 msec). QTc prolongation between 30 and 60 msec were noted in 20 subjects who received MultiHance vs. 11 subjects who received placebo. Prolongations > 61 msec were noted in 6 subjects who received MultiHance and in 3 subjects who received placebo. None of these subjects had associated malignant arrhythmias. The effects on QTc by MultiHance dose, other drugs, and medical conditions were not systematically studied.

5.7 Interference with Visualization of Certain Lesions Certain lesions seen on non-contrast images may not be seen on contrast-images. Exercise caution when interpreting contrast MRI images in the absence of companion non-contrast MRI images.

6 ADVERSE REACTIONS

The following adverse reactions are discussed in greater detail in other sections of the label.

- Nephrogenic systemic fibrosis [see **Warnings and Precautions (5.1)**]

• Hypersensitivity reactions [see **Warnings and Precautions (5.2)**]

6.1 Clinical Trials Experience

Because clinical trials are conducted under widely varying conditions, adverse reaction rates observed in the clinical trials of a drug cannot be directly compared to rates in the clinical trials of another drug and may not reflect the rates observed in practice.

Adult In clinical trials with MultiHance, a total of 4967 adult subjects (137 healthy volunteers and 4830 patients) received MultiHance at doses ranging from 0.005 to 0.4 mmol/kg. There were 2838 (57%) men and 2129 (43%) women with a mean age of 56.5 years (range 18 to 93 years). A total of 4403 (89%) subjects were Caucasian, 134 (3%) Black, 275 (6%) Asian, 40 (1%) Hispanic, 70 (1%) in other racial groups, and for 45 (1%) subjects, race was not reported.

The most commonly reported adverse reactions in adult subjects who received MultiHance were nausea (1.3%) and headache (1.2%). Most adverse reactions were mild to moderate in intensity. One subject experienced a serious anaphylactoid reaction with laryngeal spasm and dyspnea [see **Warnings and Precautions (5.2)**]. Serious adverse reactions consisting of convulsions, pulmonary edema, acute necrotizing pancreatitis, and anaphylactoid reactions were reported in 0.1% of subjects in clinical trials. Adverse reactions that occurred in at least 0.5% of 4967 adult subjects who received MultiHance are listed below (Table 2), in decreasing order of occurrence within each system.

Number of subjects dosed	4967
Number of subjects with any adverse reaction	517 (10.4%)
Gastrointestinal Disorders	67 (1.3%)
Nausea	67 (1.3%)
General Disorders and Administration Site Disorders	
Injection Site Reaction	54 (1.1%)
Fatigue	49 (1.0%)
Nervous System Disorders	
Headache	60 (1.2%)
Dysgeusia	33 (0.7%)
Paresthesia	24 (0.5%)
Dizziness	24 (0.5%)

The following adverse reactions occurred in less than 0.5% of the 4967 adult subjects who received MultiHance. Serious adverse reactions described above are not repeated below.

Blood and Lymphatic System Disorders: Basophilia; **Cardiac Disorders:** Atrioventricular block first degree; **Eye Disorders:** Eye pruritus, eye swelling, ocular hyperemia, visual disturbance; **Gastrointestinal Disorders:** Abdominal pain or discomfort, diarrhea, dry mouth, lip swelling, parosmia, oral tongue edema, vomiting; **General Disorders and Administration Site Conditions:** Chest pain or discomfort, chills, malaise; **Immune System Disorders:** Hypersensitivity; **Investigations:** Nonspecific changes in laboratory tests (including hematology, blood chemistry, liver enzymes and urinalysis), blood pressure and electrocardiogram parameters (including PR, QRS and QT intervals and ST-T segment changes); **Musculoskeletal and Connective Tissue Disorders:** Myalgia; **Nervous System Disorders:** Parosmia, tremor; **Respiratory, Thoracic and Mediastinal Disorders:** Dyspnea, laryngospasm, nasal congestion, sneezing, wheezing; **Skin and Subcutaneous Tissue Disorders:** Hyperhidrosis, pruritus, rash, swelling face, urticaria.

Pediatric In clinical trials of MultiHance in MRI of the CNS, 217 pediatric subjects received MultiHance at a dose of 0.1 mmol/kg. A total of 112 (52%) subjects were male and the overall mean age was 8.3 years (range 4 days to 17 years). A total of 168 (77%) subjects were Caucasian, 12 (6%) Black, 12 (6%) Asian, 24 (11%), Hispanic, and 1 (<1%) in other racial groups. Adverse reactions were reported for 14 (6.5%) of the subjects. The frequency and the nature of the adverse reactions were similar to those seen in the adult patients. The most commonly reported adverse reactions were vomiting (1.4%), pyrexia (0.9%), and hyperhidrosis (0.9%). No subject died during study participation. A serious adverse reaction of worsening of vomiting was reported for one (0.5%) patient with a brain tumor (glioma) for which a causal relationship to MultiHance could not be excluded.

Pediatric Patients In clinical trials of MultiHance in MRI of the CNS, 307 pediatric subjects received MultiHance at a dose of 0.1 mmol/kg. A total of 160 (52%) subjects were male and the overall mean age was 6.0 years (range, 2 days to 17 years). A total of 211 (65%) subjects were Caucasian, 24 (8%) Black, 15 (6%) Asian, 39 (13%), Hispanic, 2 (<1%) in other racial groups, and for 16 (5%), race was not reported. Adverse reactions were reported for 14 (4.6%) of the subjects. The frequency and the nature of the adverse reactions were similar to those seen in the adult patients. The most commonly reported adverse reactions were vomiting (1.0%), pyrexia (0.7%), and hyperhidrosis (0.7%). No subject died during study participation.

6.2 Post-marketing Experience

The following adverse reactions have been identified during post approval use of MultiHance. Because these reactions are reported voluntarily from a population of uncertain size, it is not always possible to reliably estimate their frequency or establish a causal relationship to drug exposure.

Immune System Disorders: Anaphylactic, anaphylactoid and hypersensitivity reactions manifested with various degrees of severity up to anaphylactic shock, loss of consciousness and death. The reactions generally involved signs or symptoms of respiratory, cardiovascular, and/or mucocutaneous abnormalities.

General Disorders and Administration Site Conditions: Extravasation of MultiHance may lead to injection site reactions, characterized by local pain or burning sensation, swelling, blistering, and necrosis [see **Warnings and Precautions (5.4)**]. Adverse events with variable onset and duration have been reported after GBCA administration [see **Warnings and Precautions (5.5)**]. These include fatigue, asthenia, pain syndromes, and heterogeneous clusters of symptoms in the neurological, cutaneous, and musculoskeletal systems. **Skin:** Gadolinium associated plaques.

7 DRUG INTERACTIONS

7.1 Transporter-Based Drug-Drug Interactions MultiHance and other drugs may compete for the canalicular multi-specific organic anion transporter (MOAT) also referred to as MRP2 or ABC2). Therefore MultiHance may prolong the systemic exposure of drugs such as cisplatin, antitriacyclines (e.g. doxorubicin, daunorubicin), vinca alkaloids (e.g. vincristine), methotrexate, etoposide, tamoxifen, and paclitaxel. In particular, consider the potential for prolonged drug exposure in patients with decreased MOAT activity (e.g. Dubin Johnson syndrome).

8 USE IN SPECIFIC POPULATIONS

8.1 Pregnancy Risk Summary GBCAs cross the placenta and result in fetal exposure and gadolinium retention. The human data on the association between GBCAs and adverse fetal outcomes are limited and inconclusive (see Data). In animal reproduction studies, gadobenate dimeglumine has been shown to be teratogenic in rabbits following repeated intravenous administration during organogenesis at doses up to 6 times the recommended human dose. There were no adverse developmental effects observed in rats with intravenous administration of gadobenate dimeglumine during organogenesis at doses up to three times the recommended human dose (see Data). Because of the potential risks of gadolinium to the fetus, use MultiHance only if imaging is essential during pregnancy and cannot be delayed. The estimated background risk of major birth defects and miscarriage for the indicated population is unknown. All pregnancies have a background risk of birth defect, loss, or other adverse outcomes. In the U.S. general population, the estimated background risk of major birth defects and miscarriage in clinically recognized pregnancies is 2 to 4% and is 15 to 20%, respectively. **Data Human Data** Contrast enhancement is visualized in the human placenta and fetal tissues after maternal GBCA administration. Cohort studies and case reports on exposure to GBCAs during pregnancy have not reported a clear association between GBCAs and adverse effects in the exposed neonates. However, a retrospective cohort study, comparing pregnant women who had a GBCA MRI to pregnant women who did not have an MRI, reported a higher occurrence of stillbirths and neonatal deaths in the group receiving GBCA MRI. Limitations of this study include a lack of comparison with non-contrast MRI and lack of information about the maternal indication for MRI. Overall, these data preclude a reliable evaluation of the potential risk of adverse fetal outcomes with the use of GBCAs in pregnancy. **Animal Data** Gadolinium Retention GBCAs administered to pregnant non-human primates (0.1 mmol/kg on gestational days 85 and 135) result in measurable gadolinium concentration in the offspring in bone, brain, skin, liver, kidney, and spleen for at least 7 months. GBCAs administered to pregnant mice (2 mmol/kg daily on gestational days 16 through 19) result in measurable gadolinium concentrations in the pups in bone, brain, kidney, liver, blood, muscle, and spleen at one month postnatal age.

Reproductive Toxicology Gadobenate dimeglumine has been shown to be teratogenic in rabbits when administered intravenously at 2 mmol/kg/day (6 times the recommended human dose based on body surface area) during organogenesis (day 6 to 18) inducing microphthalmia/small eye and/or focal retinal fold in 3 fetuses from 3 separate litters. In addition, MultiHance intravenously administered at 3 mmol/kg/day (10 times the

recommended human dose based on body surface area) has been shown to increase intrauterine deaths in rabbits. There was no evidence that MultiHance induced teratogenic effects in rats at doses up to 2 mmol/kg/day (3 times the recommended human dose based on body surface area), however, rat dams exhibited no systemic toxicity at this dose. There were no adverse effects on the birth, survival, growth, development and fertility of the F1 generation at doses up to 2 mmol/kg in a rat peri- and post-natal (Segment III) study.

10 OVERDOSAGE

Clinical consequences of overdose with MultiHance have not been reported. Treatment of an overdose should be directed toward support of vital functions and prompt institution of symptomatic therapy. In a Phase I clinical study, doses up to 0.4 mmol/kg were administered to patients. MultiHance has been shown to be dialyzable [see **Clinical Pharmacology (12.3)**].

12 CLINICAL PHARMACOLOGY

12.1 Mechanism of Action Gadobenate dimeglumine is a paramagnetic agent and, as such, develops a magnetic moment when placed in a magnetic field. The large magnetic moment produced by the paramagnetic agent results in a large local magnetic field, which can enhance the relaxation rates of water protons in its vicinity leading to an increase of signal intensity (brightness) of tissue.

In magnetic resonance imaging (MRI), visualization of normal and pathological tissue depends in part on variations in the radiofrequency signal intensity that occur with (1) differences in proton density; (2) differences of the spin-lattice or longitudinal relaxation times (T1); and (3) differences in the spin-spin or transverse relaxation time (T2). When placed in a magnetic field, gadobenate dimeglumine increases the T1 and T2 relaxation time in target tissues. At recommended doses, the effect is observed with greatest sensitivity in the T1-weighted sequences.

12.2 Pharmacodynamics Unlike other tested paramagnetic contrast agents (See Table 3), MultiHance demonstrates weak and transient interactions with serum proteins that causes slowing in the molecular tumbling dynamics, resulting in strong increases in relaxivity in solutions containing serum proteins. The improved relaxation effect can contribute to increased contrast-to-noise ratio and lesion-to-brain ratio, which may improve visualization.

	Human plasma	
	r ₁	r ₂
Gadobenate	9.7 ^a	12.5 ^a
Gadopentetate	4.9 ^b	6.3 ^b
Gadodiamide (Gadoteridol)	5.4 ^c	—

r₁ and r₂ relaxivities indicate the efficiency in shortening T1 and T2 relaxation times, respectively. ^a In hyperhydrated human plasma, at 39°C. ^b In citrated human plasma, at 37°C. ^c Not available.

Disruption of the blood-brain barrier or abnormal vascularity allows enhancement by MultiHance of lesions such as neoplasms, abscesses, and infarcts. Uptake of MultiHance into hepatocytes has been demonstrated.

12.3 Pharmacokinetics Three single-dose intravenous studies were conducted in 32 healthy male subjects to assess the pharmacokinetics of gadobenate dimeglumine. The doses administered in these studies ranged from 0.005 to 0.4 mmol/kg. Upon injection, the meglumine salt is completely dissociated from the gadobenate dimeglumine complex. Thus, the pharmacokinetics is based on the assay of gadobenate ion. The MRI contrast effective ion is gadobenate dimeglumine. Data for plasma concentration and area under the curve demonstrated linear dependence on the administered dose. The pharmacokinetics of gadobenate ion following intravenous administration can be best described using a two-compartment model.

Distribution Gadobenate ion has a rapid distribution half-life (reported as mean ± SD) of 0.084 ± 0.012 to 0.025 ± 0.072 hours. Volume of distribution of the central compartment ranged from 0.074 ± 0.017 to 0.158 ± 0.038 L/kg, and estimates of volume of distribution by area ranged from 0.170 ± 0.016 to 0.282 ± 0.079 L/kg. These latter estimates are approximately equivalent to the average volume of extracellular body water in man. *In vitro* studies showed no appreciable binding of gadobenate ion to human serum proteins.

Elimination Gadobenate ion is eliminated predominantly via the kidneys, with 78% to 96% of an administered dose recovered in the urine. Total plasma clearance and renal clearance estimates of gadobenate ion were similar, ranging from 0.093 ± 0.010 to 0.133 ± 0.020 L/hr/kg and 0.082 ± 0.007 to 0.104 ± 0.039 L/hr/kg, respectively. The clearance is similar to that of substances that are subject to glomerular filtration. The mean elimination half-life ranged from 1.17 ± 0.26 to 2.02 ± 0.60 hours. A small percentage of the administered dose (0.6% to 4%) is eliminated via the biliary route and recovered in feces.

Metabolism There was no detectable biotransformation of gadobenate ion. Dissociation of gadobenate ion *in vivo* has been shown to be minimal, with less than 1% of the free chelating agent being recovered alone in feces.

Pharmacokinetics in Special Populations

Renal Impairment A single intravenous dose of 0.2 mmol/kg of MultiHance was administered to 20 subjects with impaired renal function (6 men and 14 women) with moderate renal impairment [urine creatinine clearance >30 to <60 mL/min] and 5 men and 6 women with severe renal impairment [urine creatinine clearance >10 to <30 mL/min]. Mean estimates of the elimination half-life were 6.1 ± 3.0 and 9.5 ± 3.1 hours for the moderate and severe renal impairment groups, respectively as compared with 1.0 to 2.0 hours in healthy volunteers.

Hemodialysis: A single intravenous dose of 0.2 mmol/kg of MultiHance was administered to 11 subjects (5 males and 6 females) with end-stage renal disease requiring hemodialysis to determine the pharmacokinetics and dialyzability of gadobenate. Approximately 72% of the dose was recovered by hemodialysis over a 4-hour period. The mean elimination half-life on dialysis was 1.21 ± 0.29 hours as compared with 42.4 ± 2.4 hours when off dialysis. **Hepatic Impairment:** A single intravenous dose of 0.1 mmol/kg of MultiHance was administered to 11 subjects (8 males and 3 females) with impaired liver function (Class B or C modified Child-Pugh Classification). Hepatic impairment had little effect on the pharmacokinetics of MultiHance with the parameters being similar to those calculated for healthy subjects. **Gender, Age, Race:** A multiple regression analysis performed using pooled data from several pharmacokinetic studies found no significant effect of sex upon the pharmacokinetics of gadobenate. Clearance appeared to decrease slightly with increasing age. Since variations due to age appeared marginal, dosage adjustment for geriatric population is not recommended. Pharmacokinetic differences due to race have not been systematically studied.

Pediatric: A population pharmacokinetic analysis incorporated data from 25 healthy subjects (14 males and 11 females) and 15 subjects undergoing MRI imaging of the central nervous system (7 males and 8 females) between ages of 2 and 16 years. The subjects received a single intravenous dose of 0.1 mmol/kg of MultiHance. The geometric mean C_{max} was 62.3 µg/mL (n=16) in children 2 to 5 years of age, and 64.2 µg/mL (n=24) in children older than 5 years. The geometric mean AUC_{0-∞} was 77.9 µg·h/mL in children 2-5 years of age (n=16) and 82.6 µg·h/mL in children older than 5 years (n=24). The geometric mean half-life was 1.2 hours in children 2 to 5 years of age and 0.93 hours in children older than 5 years. There was no significant gender-related difference in the pharmacokinetic parameters in the pediatric patients. Over 80% of the dose was recovered in urine after 24 hours. Pharmacokinetic simulations indicate similar AUC and C_{max} values for MultiHance in pediatric subjects less than 2 years when compared to those reported for adults; no age-based dose adjustment is necessary for this pediatric population.

17 PATIENT COUNSELING INFORMATION

17.1 Nephrogenic Systemic Fibrosis Instruct patients to inform their physician if they: • have a history of kidney and/or liver disease, or • have recently received a GBCA. GBCAs increase the risk for NSF among patients with impaired elimination of the drugs. To counsel patients at risk for NSF: • Describe the clinical manifestations of NSF • Describe procedures to screen for the detection of renal impairment.

Instruct the patients to contact their physician if they develop signs or symptoms of NSF following MultiHance administration, such as burning, itching, swelling, scaling, hardening and tightening of the skin; red or dark patches on the skin; stiffness in joints with trouble moving, bending or straightening the arms, hands, legs or feet; pain in the hip bones or ribs; or muscle weakness.

17.2 Common Adverse Reactions

Inform patients that they may experience:

- reactions along the venous injection site, such as mild and transient burning or pain or feeling of warmth or coldness at the injection site
- side effects of feeling hot, nausea, and headache.

17.3 General Precautions

Instruct patients scheduled to receive MultiHance to inform their physician if they: • are pregnant or breast feeding • have a history of renal disease, heart disease, seizure, asthma or allergic respiratory diseases • are taking any medications • have any allergies to any of the ingredients of MultiHance.

CALL FOR AJNR EDITORIAL FELLOWSHIP CANDIDATES

ASNR and AJNR are pleased once again to join efforts with other imaging-related journals that have training programs on editorial aspects of publishing for trainees or junior staff (<5 years on staff), including Radiology (Olmsted fellowship), AJR (Figley and Rogers fellowships), JACR (Bruce J. Hillman fellowship), and Radiologia.

2023 Candidate Information and Requirements

GOALS

- Increase interest in editorial and publication-related activities in younger individuals.
- Increase understanding and participation in the AJNR review process.
- Incorporate into AJNR's Editorial Board younger individuals who have previous experience in the review and publication process.
- Fill a specific need in neuroradiology not offered by other similar fellowships.
- Increase the relationship between "new" generation of neuroradiologists and more established individuals.
- Increase visibility of AJNR among younger neuroradiologists.

ACTIVITIES OF THE FELLOWSHIP

- Serve as Editorial Fellow for one year. This individual will be listed on the masthead as such.
- Review at least one manuscript per month for 12 months. Evaluate all review articles submitted to AJNR.
- Learn how electronic manuscript review systems work.
- Be involved in the final decision of selected manuscripts together with the Editor-in-Chief.
- Participate in all monthly Senior Editor telephone conference calls.
- Participate in 2 virtual meetings of the Editorial Board.
- Evaluate progress and adjust program to specific needs in annual meeting or telephone conference with the Editor-in-Chief.
- Embark on an editorial scientific or bibliometric project that will lead to the submission of an article to AJNR or another appropriate journal as determined by the Editor-in-Chief. This project will be presented by the Editorial Fellow at the ASNR annual meeting. The Foundation of the ASNR will provide \$2000 funding for this activity.
- Recruit trainees as reviewers as determined by the Editor-in-Chief.
- Serve as Guest Editor for an issue of AJNR's News Digest with a timely topic.

QUALIFICATIONS

- Be a fellow in neuroradiology from North America, including Canada (this may be extended to include other countries).
- Be a junior faculty neuroradiology member (< 5 years) in either an academic or private environment.
- Be an "in-training" or member of ASNR in any other category.

APPLICATION

- Include a short letter of intent with statement of goals and desired research project. CV must be included.
- Include a letter of recommendation from the Division Chief or fellowship program director. A statement of protected time to perform the functions outlined is desirable.
- Applications will be evaluated by AJNR's Senior Editors prior to the ASNR annual meeting. The name of the selected individual will be announced at the meeting.
- Applications should be received by March 1, 2023 and sent to Ms. Karen Halm, AJNR Managing Editor, electronically at khalm@asnr.org.



The next generation GBCA from Guerbet is here



To learn more,
scan QR code or visit
www.guerbet-us.com

I am a global citizen.
I am patient-centered care.
I am committed to health equity.
I am a teacher.
I am a life-long learner.
I am determined.
I am curious.
I am a collaborative team player.
I am a volunteer.
I am ASNR.

Don't miss out on the tools, resources and relationships you've come to rely on. Log in and renew your ASNR membership today! www.asnr.org

ASNR
American Society of Neuroradiology

AJNR

AMERICAN JOURNAL OF NEURORADIOLOGY

NOVEMBER 2022
VOLUME 43
NUMBER 11
WWW.AJNR.ORG

Publication Preview at www.ajnr.org features articles released in advance of print. Visit www.ajnrblog.org to comment on AJNR content and chat with colleagues and AJNR's News Digest at <http://ajnrdigest.org> to read the stories behind the latest research in neuroimaging.

1549 **PERSPECTIVES** *M. Hauben*

REVIEW ARTICLE

-   1550 **Radiologic Evaluation Criteria for Chronic Subdural Hematomas: Recommendations for Clinical Trials** *R. McDonough, et al.* **ADULT BRAIN**

GENERAL CONTENTS

-     1559 **Cluster Analysis of DSC MRI, Dynamic Contrast-Enhanced MRI, and DWI Parameters Associated with Prognosis in Patients with Glioblastoma after Removal of the Contrast-Enhancing Component: A Preliminary Study** *H. Chung, et al.* **ADULT BRAIN FUNCTIONAL**
-  1567 **Diffuse Large B-Cell Epstein-Barr Virus-Positive Primary CNS Lymphoma in Non-AIDS Patients: High Diagnostic Accuracy of DSC Perfusion Metrics** *A. Pons-Escoda, et al.* **ADULT BRAIN FUNCTIONAL**
-    1575 **SWI by 7T MR Imaging for the Microscopic Imaging Diagnosis of Astrocytic and Oligodendroglial Tumors** *M. Natsumeda, et al.* **ADULT BRAIN FUNCTIONAL**
-  1582 **The Value of Preoperative Phase-Contrast MRI in Predicting the Clinical Outcome of Moyamoya Disease after Encephalo-Duro-Arterial Synangiosis Surgery** *S. Liu, et al.* **ADULT BRAIN**
-   1589 **Quantitative Intracerebral Iodine Extravasation in Risk Stratification for Intracranial Hemorrhage in Patients with Acute Ischemic Stroke** *C. Ma, et al.* **ADULT BRAIN**
-  1597 **Diagnostic Performance of Whole-Body Ultra-Low-Dose CT for Detection of Mechanical Ventriculoperitoneal Shunt Complications: A Retrospective Analysis** *S. Afat, et al.* **ADULT BRAIN**
-  1603 **Schizencephaly in Hereditary Hemorrhagic Telangiectasia** *J.J. Gaines, et al.* **ADULT BRAIN**
-  1608 **Delayed CTP-Derived Deep Venous Outflow: A Novel Predictor of Striatocapsular Infarction after MI Thrombectomy** *S. Peretz, et al.* **ADULT BRAIN**
-  1615 **Learning Curve for Flow Diversion of Posterior Circulation Aneurysms: A Long-Term International Multicenter Cohort Study** *N. Adeeb, et al.* **INTERVENTIONAL**
- 1621 **Effective Dose Measurements of the Latest-Generation Angiographic System in Patients with Acute Stroke: A Comparison with the Newest Multidetector CT Generation** *A. Brehm, et al.* **INTERVENTIONAL**

AJNR (Am J Neuroradiol ISSN 0195-6108) is a journal published monthly, owned and published by the American Society of Neuroradiology (ASNR), 820 Jorie Boulevard, Oak Brook, IL 60523. Annual dues for the ASNR include approximately 21% for a journal subscription. The journal is printed by Intellicor Communications, 330 Eden Road, Lancaster, PA 17601; Periodicals postage paid at Oak Brook, IL and additional mailing offices. Printed in the U.S.A. POSTMASTER: Please send address changes to American Journal of Neuroradiology, P.O. Box 3000, Denville, NJ 07834, U.S.A. Subscription rates: nonmember \$430 (\$505 foreign) print and online, \$320 online only; institutions \$495 (\$565 foreign) print and basic online, \$980 (\$1050 foreign) print and extended online, \$380 online only (basic), \$825 online only (extended); single copies are \$35 each (\$40 foreign). Indexed by PubMed/MEDLINE, BIOSIS Previews, Current Contents (Clinical Medicine and Life Sciences), EMBASE, Google Scholar, HighWire Press, Q-Sensei, RefSeek, Science Citation Index, SCI Expanded, ReadCube, and Semantic Scholar. Copyright © American Society of Neuroradiology.

EDITOR-IN-CHIEF

Jeffrey S. Ross, MD

Professor of Radiology, Department of Radiology,
Mayo Clinic College of Medicine, Phoenix, AZ

SENIOR EDITORS

Harry J. Cloft, MD, PhD

Professor of Radiology and Neurosurgery,
Department of Radiology, Mayo Clinic College of
Medicine, Rochester, MN

Christopher G. Filippi, MD

Professor and Alice Ettinger-Jack R. Dreyfuss
Chair of Radiology,
Tufts University School of Medicine,
Radiologist-in-Chief
Tufts University Medical Center, Boston, MA

Thierry A.G.M. Huisman, MD, PD, FICIS, FACR

Radiologist-in-Chief and Chair of Radiology, Texas
Children's Hospital,
Professor of Radiology, Pediatrics, Neurosurgery,
and OBGYN, Baylor College of Medicine,
Houston, TX

Yvonne W. Lui, MD

Associate Professor of Radiology,
Chief of Neuroradiology,
New York University School of Medicine,
New York, NY

C.D. Phillips, MD, FACR

Professor of Radiology, Weill Cornell Medical
College, Director of Head and Neck Imaging,
New York-Presbyterian Hospital, New York, NY

Lubdha M. Shah, MD, MS

Professor of Radiology and Director of Spine
Imaging, University of Utah Department of
Radiology and Imaging Sciences, Salt Lake City, UT

STATISTICAL SENIOR EDITOR

Bryan A. Comstock, MS

Senior Biostatistician,
Department of Biostatistics,
University of Washington, Seattle, WA

ARTIFICIAL INTELLIGENCE DEPUTY EDITOR

Peter D. Chang, MD

Assistant Professor-in-Residence,
Departments of Radiological Sciences,
Computer Sciences, and Pathology,
Director, Center for Artificial Intelligence in
Diagnostic Medicine (CAIDM),
University of California, Irvine, Irvine, CA

EDITORIAL BOARD

Ashley H. Aiken, *Atlanta, GA*

Matthew D. Alexander, *Salt Lake City, UT*

Lea M. Alhilali, *Phoenix, AZ*

Jason W. Allen, *Atlanta, GA*

Mohammed A. Almekhlafi, *Calgary, Alberta, Canada*

Niranjan Balu, *Seattle, WA*

Matthew J. Barkovich, *San Francisco, CA*

Joachim Berkefeld, *Frankfurt, Germany*

Karen Buch, *Boston, MA*

Judah Burns, *New York, NY*

Danielle Byrne, *Dublin, Ireland*

Federico Cagnazzo, *Montpellier, France*

Gloria C. Chiang, *New York, NY*

Daniel Chow, *Irvine, CA*

Kars C.J. Compagne, *Rotterdam, The Netherlands*

Yonghong Ding, *Rochester, MN*

Birgit Ertl-Wagner, *Toronto, Ontario, Canada*

Aaron Field, *Madison, WI*

Nils D. Forkert, *Calgary, Alberta, Canada*

Frank Gaillard, *Melbourne, Australia*

Joseph J. Gemmete, *Ann Arbor, Michigan*

Brent Griffith, *Detroit, MI*

Michael J. Hoch, *Philadelphia, PA*

Joseph M. Hoxworth, *Phoenix, AZ*

Raymond Y. Huang, *Boston, MA*

Susie Y. Huang, *Boston, MA*

Ferdinand K. Hui, *Honolulu, HI*

Christof Karmonik, *Houston, TX*

Gregor Kasprian, *Vienna, Austria*

Timothy J. Kaufmann, *Rochester, MN*

Hillary R. Kelly, *Boston, MA*

Toshibumi Kinoshita, *Akita, Japan*

Ioannis Koktzoglou, *Evanston, IL*

Stephen F. Kralik, *Houston, TX*

Luke Ledbetter, *Los Angeles, CA*

Franklin A. Marden, *Chicago, IL*

Markus A. Möhlenbruch, *Heidelberg, Germany*

Mahmud Mossa-Basha, *Morrisville, NC*

Renato Hoffmann Nunes, *Sao Paulo, Brazil*

Sam Payabvash, *New Haven, CT*

Johannes A.R. Pfaff, *Salzburg, Austria*

Eike I. Piechowiak, *Bern, Switzerland*

Laurent Pierot, *Reims, France*

Alexander R. Podgorsak, *Chicago, IL*

Eytan Raz, *New York, NY*

Jeff Rudie, *San Diego, CA*

Paul M. Ruggieri, *Cleveland, OH*

Fatih Seker, *Heidelberg, Germany*

Maksim Shapiro, *New York, NY*

Timothy Shepherd, *New York, NY*

Mark S. Shiroishi, *Los Angeles, CA*

Neetu Soni, *Rochester, NY*

Ashok Srinivasan, *Ann Arbor, MI*

Jason F. Talbott, *San Francisco, CA*

Anderanik Tomasian, *Los Angeles, CA*

Fabio Triulzi, *Milan, Italy*

Arastoo Vossough, *Philadelphia, PA*

Richard Watts, *New Haven, CT*

Elysa Widjaja, *Toronto, Ontario, Canada*

Ronald Wolf, *Philadelphia, Pennsylvania*

Shuang Xia, *Tianjin, China*

Leonard Yeo, *Singapore*

Woong Yoon, *Gwangju, South Korea*

David M. Yousem, *Evergreen, CO*

Carlos Zamora, *Chapel Hill, NC*

Chengcheng Zhu, *Seattle, WA*

EDITORIAL FELLOW

Alexandre Boutet, *Toronto, Ontario, Canada*

SPECIAL CONSULTANTS TO THE EDITOR

AJNR Blog Editor

Neil Lall, *Denver, CO*

Case of the Month Editor

Nicholas Stence, *Aurora, CO*

Case of the Week Editors

Matylda Machnowska, *Toronto, Ontario, Canada*

Anvita Pauranik, *Calgary, Alberta, Canada*

Vinil Shah, *San Francisco, CA*

Classic Case Editor

Sandy Cheng-Yu Chen, *Taipei, Taiwan*

Health Care and Socioeconomics Editor

Pina C. Sanelli, *New York, NY*

Physics Editor

Greg Zaharchuk, *Stanford, CA*

Podcast Editor

Kevin Hiatt, *Winston-Salem, NC*

Twitter Editor

Jacob Ormsby, *Albuquerque, NM*

Official Journal:

American Society of Neuroradiology

American Society of Functional Neuroradiology

American Society of Head and Neck Radiology

American Society of Pediatric Neuroradiology

American Society of Spine Radiology

Founding Editor

Juan M. Taveras

Editors Emeriti

Mauricio Castillo, Robert I. Grossman,

Michael S. Huckman, Robert M. Quencer

Managing Editor

Karen Halm

Assistant Managing Editor

Laura Wilhelm

Executive Director, ASNR



Mary Beth Hepp



Title: Central Park Lake. With its ample supply of rowboats, rowers and their passive companions can tour the many sites bordering the 220 acres of water (all accessible to pedestrians as well) including the Central Park West skyline, which includes some of the most iconic New York City architecture. From this vantage point, which looks north-northwest, we are treated to 2 classically inspired New York City buildings designed by famed architect Emery Roth. First, on the left, is the San Remo (completed 1930), the city's first twin tower, capped by circular colonnades inspired by the Choragic Monument of Lysicrates. Right of center is the massive but less lofty Beresford (completed 1929), with its 3 massive octagonal, copper-capped towers. As with much of the city's skyline, zoning laws influenced design. The 1916 zoning law required setbacks for high rises to preserve sunlight and air flow at street level, and influenced the Beresford, while the Multiple Dwelling Law of 1929 only accommodated a massive and towering residential complex like the San Remo conditional on a split tower, for similar reasons. If one walks or sails slightly to the left, a third Emery Roth building, the El Dorado, comes into view to the north.

Manfred Hauben, MD, MPH, Pfizer Inc and NYU Langone Health, New York City

Radiologic Evaluation Criteria for Chronic Subdural Hematomas: Recommendations for Clinical Trials

 R. McDonough,  M. Bechstein,  J. Fiehler,  U. Zanolini,  H. Rai,  A. Siddiqui,  E. Shotar,  A. Rouchaud,  K. Kallmes,  M. Goyal, and  S. Gellissen



ABSTRACT

SUMMARY: Embolization of the middle meningeal artery has gained substantial interest as a therapy for chronic subdural hematomas. For the results of the currently running chronic subdural hematoma trials to inform clinical practice, sufficient accuracy and matching definitions are necessary. We summarized the current practice in chronic subdural hematoma evaluation and derived suggestions on reporting standards using the (Nested) Knowledge AutoLit living review platform. On the basis of the most commonly reported data elements, we suggested a set of standardized image-based study end points for chronic subdural hematoma evaluation for future trials. The measurement methods and reporting standards as proposed in this article have been derived from published best practices and are endorsed by the European Society of Minimally Invasive Neurological Therapy's research committee. The standardization of radiologic outcome measures and measurement techniques in chronic subdural hematoma embolization trials would increase the impact and implication of each trial as well as facilitate data pooling for increased statistical power and, therefore, translation to clinical practice.

ABBREVIATIONS: cSDH = chronic subdural hematoma; MLS = midline-shift; MLS-M = MLS versus midline or displacement perpendicular to the midline; MLS-T = MLS transverse; MMA = middle meningeal artery; NK = (Nested) Knowledge; SDH = subdural hematoma

Chronic subdural hematoma (cSDH) is a frequently occurring pathology in daily neurosurgical practice, with increasing frequency as the population ages.¹ However, there is still a relative lack of high-quality evidence at many decision points in the treatment algorithm of the typical patient with cSDH, which is far from optimized.² Despite numerous studies investigating the management of cSDH, questions about the choice of surgical technique, adjuvant therapies, and postoperative care remain unanswered. Many of the studies published in the literature report heterogeneous baseline data, using variable terminology and definitions of operative technique, and evaluate disparate outcome measures.³ Even cSDH lacks a universally accepted definition.⁴


In recent years, middle meningeal artery (MMA) embolization has emerged as a new and promising therapy option for cSDH.⁵⁻⁷ Numerous clinical trials evaluating the safety and efficacy of this new treatment method have recently been initiated, and some have already published their results.⁷ A systematic review of 96 studies examining clinical outcomes in patients with cSDH revealed that 39% of the studies used a radiologic outcome measure generally based on a postoperative CT scan. However, these radiologic outcome measures were highly heterogeneous, as was the timing of the scans.³ Furthermore, there seems to be a lack of consensus on how to determine a specific radiologic outcome measure. For example, various techniques on how to measure subdural hematoma (SDH) thickness and volume or even midline shift (MLS) exist.⁸⁻¹⁰ These techniques pose a significant barrier to establishing an evidence-based approach for the management of cSDH, as stated in published meta-analyses that have sought to elucidate the optimal treatment options for cSDH.^{3,6,11} To overcome these barriers and enable cross-study evaluation of the efficacy of MMA embolization, and other cSDH treatments, the development of standardized outcome measures is needed, which should subsequently be reported by all clinical studies and trials concerning a specific disease state.

In this article, we describe and discuss the heterogeneity of radiologic outcome measures for clinical trials on MMA embolization for cSDH. To emphasize the relevance of a common definition and selection of radiographically defined parameters, we completed a review of radiologic outcomes and inclusion/exclusion

Received November 23, 2021; accepted after revision February 8, 2022.

From the Department of Diagnostic and Interventional Neuroradiology (R.M., M.B., J.F., U.Z., S.G.), University Medical Center Hamburg-Eppendorf, Hamburg, Germany; Research Committee (M.B., J.F., U.Z., E.S., A.R.), European Society of Minimally Invasive Neurological Therapy, Zürich, Switzerland; Department of Neurosurgery (H.R., A.S.), University at Buffalo, Buffalo, New York; Neuroradiology Department (E.S.), Pitié-Salpêtrière Hospital, Paris, France; Department of Neuroradiology (A.R.), Dupuytren University Hospital of Limoges, Limoges Cedex, France; Nested Knowledge, Inc (K.K.), St. Paul, Minnesota; and Department of Radiology (R.M., M.G.), University of Calgary Cumming School of Medicine, Calgary, Alberta, Canada.

Please address correspondence to Susanne Gellissen, MD, University Medical Center Hamburg-Eppendorf, Department of Diagnostic and Interventional Neuroradiology, Martinistr 52, 20246 Hamburg, Germany; e-mail: s.siemonsen@uke.de; @rosevmcd; @mayankG0

 Indicates open access to non-subscribers at www.ajnr.org

 Indicates article with online supplemental data.

<http://dx.doi.org/10.3174/ajnr.A7503>

criteria in active cSDH trials. Furthermore, we propose a potential standardized methodology for defining and measuring radiologic outcomes of cSDH, as well as how and when to report them. Because published research on the evaluation of the accuracy and reliability of specific radiologic outcome measures such as cSDH volume, width, and MLS specifically in cSDH is sparse, the measurement methods and reporting standards as proposed in this article have been derived from the best published practices and are endorsed by European Society of Minimally Invasive Neurological Therapy's research committee.

MATERIALS AND METHODS

Clinical Trials of cSDH Embolization

We performed a literature search of ClinicalTrials.gov to identify currently active or complete and unpublished trials on MMA embolization in patients with cSDH. ClinicalTrials.gov was searched for the terms Chronic AND Subdural AND (hematoma OR haematoma OR hemorrhage OR haemorrhage OR bleeding) AND (embolization OR embolization) on August 7, 2021. The review of these clinical trials was then conducted through the AutoLit platform (Nested Knowledge [NK]; <https://nested-knowledge.com>).¹²

All interventions used and radiologic outcome data elements as well as image-based inclusion or exclusion criteria were tagged by using the AutoLit tagging feature. Included studies were scanned for the predetermined radiologic outcomes with the related definitions and follow-up time points, and a unique tag was created for each data element found on the basis of a full-protocol review, as relevant. All tagging was completed by 1 author and quality-controlled by an independent author.

Qualitative synthesis on the frequency of study design types and data elements was graphically presented in the form of a sunburst diagram on the Synthesis feature (NK) after the completion of tagging different studies. Each section represented a tag that was applied across trials, and frequency could be determined by the platform on the basis of the number of studies that had that tag (Fig 1; for interactive version, see <https://nested-knowledge.com/nest/qualitative/461>). After quantitative summary data were extracted from the NK Qualitative Synthesis feature, the appropriate tables and figures were created using Microsoft-based data presentation software (Microsoft Excel and PowerPoint).

RESULTS

Study Characteristics

As of August 7, 2021, fifteen studies, of these 12 randomized controlled trials, relating to embolization of the MMA of cSDH had been identified on clinicaltrials.gov. All of these 15 studies used image-based measures as end points. The main imaging-based outcome data elements and inclusion/exclusion criteria were based on measures of the following: cSDH size, MLS, radiographic resolution, radiographic recurrence, and radiographic progression. The most frequent radiologic outcome measures identified were cSDH size (11/15, 73.3%) and cSDH recurrence (9/15, 60%).

Five of 15 (33.3%) trials also reported radiologic measurements as inclusion or exclusion criteria. The most frequently

identified in-/exclusion criterion was cSDH width > 10 mm (in 4 of 5). However, some of these criteria may evolve as discussions among the trial investigators continue. Details on the radiologic measures are listed in the Online Supplemental Data.

In addition, the planned follow-up periods and intervals of the trials were highly heterogeneous: Periods of follow-up ranged from 6 weeks to 12 months, with intervals between visits ranging from 2 weeks to 6 months.

SDH Width and Volume Measurement

As in Online Supplemental Data the determination of cSDH width and volume is an essential factor for cSDH treatment monitoring and the definition of radiologic recurrence or progression.

However, for both variables, a number of different measurement techniques have been published and compared. For cSDH volume estimation, manual computer-assisted volumetric analysis is considered the gold standard. To facilitate volume measurement in cSDH, a simple bedside estimation method, known as the ABC/2 method, was proposed and validated for use in the measurement of acute and cSDH volume.¹³⁻¹⁵ This method is based on the mathematic formula for the volume of an ellipsoid, $4/3\pi \times (A/2) \times (B/2) \times (C/2)$, where A, B, and C represent the 3 diameters of the ellipsoid commonly measured on the axial plane. If π is estimated to be 3, the formula simplifies to ABC/2.¹⁶⁻¹⁸ To our knowledge, only 3 published studies explicitly evaluated this volumetric measurement technique specifically in patients with cSDH.^{14,15,19} In addition, the study by Gebel et al¹³ involved patients with acute subdural hematomas as well as chronic ones.

Overall, the assessed volume measurement techniques showed a high correlation with the criterion standard in patients with acute as well as cSDH.¹³⁻¹⁵ Sucu et al¹⁵ compared 5 different ABC/2-based volume measurement formulas to identify the formula that provided the most accurate estimation of hematoma volume compared with the criterion standard. Although all 5 formulas showed excellent correlation with the criterion standard, the ABC/2 method with the measurement of maximum width and length, which are not necessarily on the same section, achieved the highest correlation coefficient. Won et al¹⁴ found a correlation between ABC/2 and computer-assisted values with an R^2 of 0.93 when evaluating 100 cSDHs in 82 patients. This group used the section with the maximum length to determine maximum width (taken perpendicular to the length). For determination of hematoma depth, the number of slices with visible hematoma multiplied by section thickness was performed in all 3 studies.¹³⁻¹⁵

To elucidate some of the shortcomings and problems arising from the above-mentioned techniques, we applied some of these width-measurement methods to specific patients with unevenly shaped hematomas (Fig 2C). These cases illustrate that accurately following the given measurement techniques may lead to measurements that do not seem to correspond to hematoma width as we would define it according to the underlying formula of the radius of an ellipsoid-shaped body. As demonstrated in Fig 2, inaccurate width measurements are particularly likely to occur in hematomas that are close to the vertex and those that are irregularly (ie, not crescent) shaped. Indeed, the further removed the cSDH collection is from an ellipsoid shape, the less accurate the



FIG 1. Sunburst diagram of data elements in the NK nest for this study. Clicking on each data element outputs a frequency of the tag associated with it, as well as frequently co-occurring tags. See <https://nested-knowledge.com/nest/qualitative/461> for an interactive version of this figure.

ABC/2 formula is.²⁰ According to a study by Manickam et al¹⁹ that measured the proximity to an ellipsoid shape using 3D simulations, most cSDHs demonstrated highly irregular morphology, and only a very few (9%) remotely conformed to ellipsoid geometric morphology.

Above the superior temporal line, axial CT slices are no longer perpendicular to the cranium or cSDH (Fig 2C, patient 1); rather, they run obliquely because of the curvature of the cranial vault. Therefore, the width of the cSDH measured on a section close to vertex is greater than it actually is. Furthermore, because of their

chronic nature and traction of developing membranes, cSDHs are not always symmetrically crescent-shaped; they may appear as asymmetric shapes, such as a comma, pear, or lens on axial CT slices (Fig 2C, patients 2 and 3). As a result, whenever possible, computer-assisted volumetric analysis should be applied, especially in studies in which longitudinal analyses are performed. Most CT scanners today can produce axial slices of 0.625-mm thickness, generating relatively isometric voxels of $0.625 \times 0.5 \times 0.5$ mm. These can be reconstructed in the coronal plane for improved accuracy of measurement.

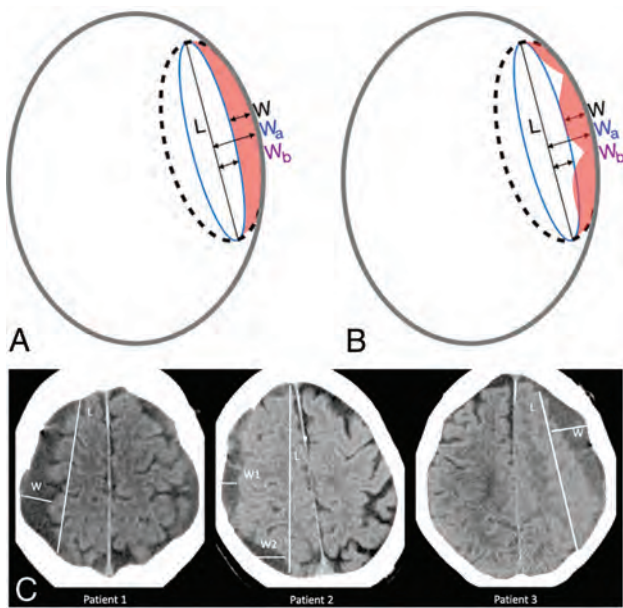


FIG 2. The effect of SDH morphology on volume calculation using the ABC/2. The formula is derived by assuming a crescent shape (the difference between a large ellipsoid and a small ellipsoid, both of which are cut in half). A and B, L = length; W = width, difference between ellipsoids = W_a , W_b ; C, Thickness (not shown) (L and C are the same for both ellipsoids). The formula thus reduces to volume of crescent-shaped cSDH = $(4/3 \pi L W_a C - 4/3 \pi L W_b C) / 2 = (L W_a C - L W_b C) / 2 = L W C / 2 (= ABC/2)$. A, The assumed crescent shape allows accurate calculation due to the way the ABC/2 formula is derived (right panel). B, When the SDH is irregular, however, the ABC/2 loses accuracy and can lead to overestimation of the true volume. C, cSDH maximum width perpendicular to the maximum length marked in specific patients with unevenly shaped hematomas. Patient 1: width of the subdural hematoma measured on a section close to vertex (W) is greater than it actually is. Patient 2: inhomogeneous convex- and concave-shaped hematomas. Maximum width (W_2) measurement is diagonal and not accurate. W_1 would be more accurate in this case. Patient 3: maximum width measured perpendicular to length but slices hematoma diagonally.

Selection of radiologic measurement techniques requires both high accuracy and harmonization across studies to provide meaningful comparative data. Thus, even though most ABC/2 volume measurement techniques show a high correlation with the criterion standard,¹³⁻¹⁵ a designated standard measurement technique needs to be defined to ensure comparability among clinical studies.

Another problem lies in the lack of validation of certain methodologies with respect to specific situations. For example, the question of the cSDH width-measurement technique most suitable to reliably detect changes in cSDH size, especially after therapy, remains currently unanswered. However, if cSDH width is reported, details on the assessment technique should be described and measurements should be reported in combination with cSDH volume.

Only a few studies address problems regarding cSDH segmentation. Sucu et al,¹⁵ for example, excluded 6 of 28 patients with cSDH because it was not possible to differentiate the isodense hematoma from the brain parenchyma on CT scans. Certainly, the frequency of this problem may also be dependent on the image contrast/

quality produced by a particular CT protocol on a particular model. Therefore, in such scenarios, signs of mass effect, such as MLS and local cortical flattening, can be evaluated to compare cSDH sizes. However, how to include these cases in trials or studies in which accurate measurements of hematoma size and volume are compared pre- and postoperatively remains unclear. Nevertheless, such scenarios should be reported and described.

MLS

Another frequent outcome measure in cSDH studies is MLS, a sign of a space-occupying effect. Besides cisternal compression and sulcal flattening, MLS is an important indicator of mass effect and can help determine the need for surgical intervention.⁹

Different measurement techniques for the estimation of MLS have been published.^{8,9,21} There are 2 possible measurement techniques (MLS transverse: displacement relative to the tabula interna in relation to the width of the intracranial space [MLS-T] and MLS versus midline or displacement perpendicular to ideal midline [MLS-M]) that can each be combined with either a specific predefined anatomic measurement location (which also indirectly predefines the section and location of the measurement) or the identification of the location with the estimated largest MLS (which can be a different section and location in each patient). MLS estimation in cSDH according to these techniques can lead to very different measurements.²¹ Overall, the septum pellucidum seems to be the structure that is more sensitive to the space-occupying effect of intracranial masses. Variations, especially when longitudinal studies are analyzed, might also be dependent on section thickness and patient position or image reconstruction. Measurement of MLS-M might be a more reliable estimate and has shown high interobserver agreement.²² Moreover, determining the midline is easier than determining the width of the intracranial space, especially if the patient is not perfectly aligned during CT examination or if the skull is asymmetric, deformed, or has been removed by surgery or trauma, which is also of high relevance in studies including pre- and postoperative scans of patients with cSDH. So far, no study has systematically compared MLS estimations using the aforementioned measurement techniques in patients with cSDH and their specific intrarater and interrater variability.

On the basis of the currently available information, we propose the following MLS measurements in future cSDH therapy studies:

- As MLS-M, ie, perpendicular to the midline joining the most anterior and posterior visible points on the falx, especially in studies including patients undergoing an operation (to increase pre- and postoperative comparability and decrease the effects of asymmetry of the skull)
- If available, measurements should be conducted on axial and coronal slices
- On axial slices, measurements of the maximum at the level and location of the foramen of Monro and as the maximum displacement of the septum pellucidum relative to the midline should be taken (to increase sensitivity for hematomas located at the convexity)
- On coronal slices, measurements of the maximum MLS of the septum pellucidum at the level of the highest point of the septum should be taken (to decrease the effects of slice thickness and patient position or image reconstruction)

- Overall, MLS should then be determined as the mean of these 3 measurements (or 2 in cases in which coronal reconstructions are missing).

Examples of the described MLS measurements are shown in Fig 3.

Patient presentation may also impact the level to which MLS indicates cSDH size and mass effect. Most notably, bilateral cSDH is common. When it occurs, the midline is pushed back to its normal position, making the MLS less useful in such patients. Atrophy is another factor influencing the degree of MLS. Therefore, other imaging features and clinical information must be taken into account to adequately evaluate the mass effect.¹⁰

Measuring postoperative MLS alone probably plays a smaller role in cSDH because clinical improvement can be achieved with partial evacuation, which could result in residual cSDH and MLS.^{10,23} Therefore, the MLS should always be assessed in conjunction with other parameters such as clinical information and cSDH volume. Nonetheless, we strongly encourage authors to provide a detailed description of the algorithms/measurement techniques used when reporting cSDH width, volume, MLS, or other quantitative radiologic measures. A summary of expert suggestions for measurement performance in cSDH is provided in Table 1.

Follow-up Image Evaluation

Postoperative image findings and characteristics differ from those of preoperative examinations. Intracranial air collections, removal or deformation of the skull, and changes in hematoma shape and

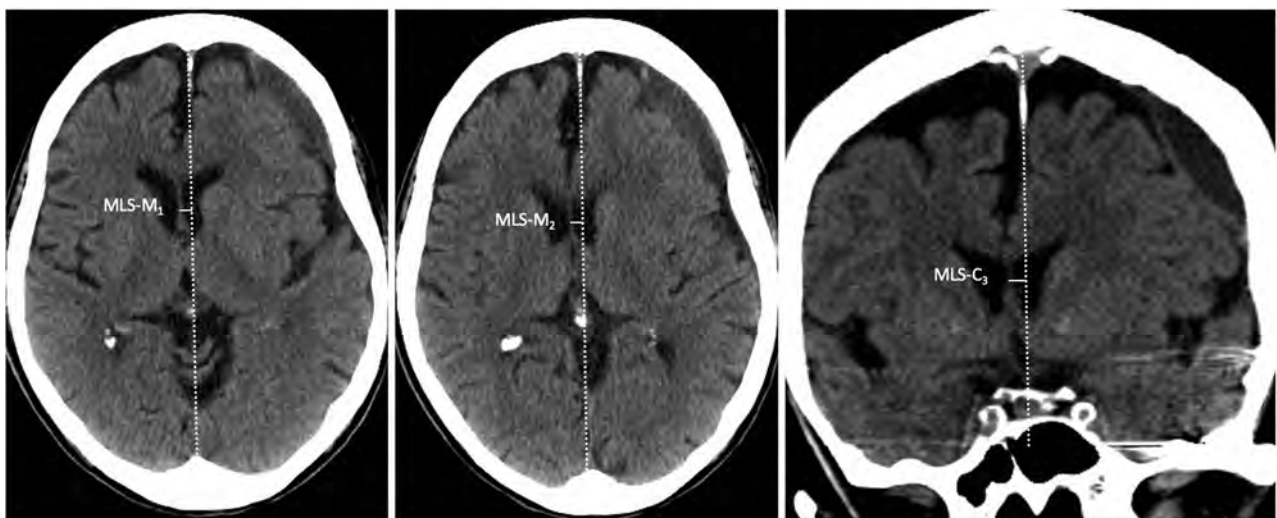
composition represent some of the issues that can complicate comparison of pre- and postoperative radiologic measurements.

Embolization of the meningeal artery is currently performed either as a primary therapeutic option in patients with cSDH or as a secondary measure when persistent or recurrent hematoma occurs following an operation. Therefore, these differences may also be relevant for a number of radiologic features obtained in the current embolization trials⁷ and should be carefully addressed, particularly with respect to longitudinal observations and treatment monitoring. Most studies include radiologic hematoma recurrence or progression as their primary or secondary end points (Table 1).

Hence, strict definitions and standardization of image analyses should be mandatory. However, to our knowledge, there are currently no studies specifically evaluating the applicability and accuracy of the above-mentioned measurement techniques in patients with cSDH after an operation, when early postoperative changes are still visible and the brain has not yet recovered and unfolded to its full extent. Therefore, in such cases, authors should provide detailed reports on whether air collections were included in volumetric measurements or how they obtained measurements if the skull had been removed or deformed.

Follow-up Period and Intervals for cSDH Embolization Studies

Standardization of follow-up periods and intervals of the cSDH embolization trials would be advantageous in that it would increase the overall value, validity, and significance of each individual clinical trial and enable joint analyses.



MLS-M₁ (axial)
level of the Foramina Monroi

MLS-M₂ (axial)
level of the maximum displacement of the septum pellucidum

MLS-C₃ (coronal)
level of the highest point of the septum pellucidum

$$MLS = \frac{MLS.M_1 + MLS.M_2 + MLS.C_3}{3}$$

FIG 3. Proposed MLS measurement as the mean of maximum at the level and location of the foramen of Monroi (MLS-M₁), the maximum displacement of the septum pellucidum relative to the midline (MLS-M₂), and the maximum MLS of the septum pellucidum at the level of the highest point of the septum on coronal slices (MLS-C₃). Overall MLS is determined as the mean of these 3 measurements (or 2 in cases in which coronal reconstructions are missing). MLS-M indicates axial MLS perpendicular to the midline; MLS-C, coronal MLS perpendicular to the midline.

Table 1. Expert suggestions for radiologic measurements of cSDH for volume, width, MLS, and reporting

cSDH Volume/Width	MLS	Reporting
<ul style="list-style-type: none"> • Preferably use computer-assisted volumetric analysis • In case width is measured, report detailed methodology 	<ul style="list-style-type: none"> • Measured perpendicular to the midline joining the most anterior and posterior visible points on the falx • Measurements should be conducted on axial and coronal slices • On axial slices measured at the level and location of the foramen of Monro and as the maximum displacement of the septum pellucidum relative to the midline • On coronal slices as the maximum MLS of the septum pellucidum at the level of the highest point of the septum • Overall MLS should then be determined as mean of these 3 (or 2 in case no coronal slices are available) measurements 	<ul style="list-style-type: none"> • cSDH width should always be evaluated and reported in context with cSDH volume measurements, MLS, and clinical information • MLS should always be assessed together with other parameters such as clinical information and cSDH volume • Detailed description of the used algorithms when reporting cSDH width, volume, MLS, or other quantitative radiologic measures should be provided

After surgical evacuation, routine follow-up CTs do not seem to provide any benefit over CTs performed only in patients with clinical deterioration or persisting neurologic deficits with respect to good clinical outcome.²⁴ In addition, patients who were followed clinically without routine follow-up CT had fewer repeat surgeries—and this link may be causative, meaning that differential radiologic follow-up strategies are, in fact, influencing the data on reoperation and rendering studies yet more noncomparable in methods and outcomes.

Thus, in cSDH embolization studies, possible complications may occur during the postoperative period, such as infarction or new intracranial hemorrhage, for which the window of occurrence is not well-defined. In addition, radiologic progression is often stated as a primary or secondary outcome measure, and dictates whether additional surgical evacuation is performed.²⁵ Furthermore, cSDH embolization might also be performed in combination with surgical evacuation therapy and is sometimes even performed in asymptomatic patients.²⁶ Therefore, only performing posttreatment follow-up in case of clinical deterioration would be ineffective. However, currently, there are no studies explicitly evaluating the benefit of repeat and early follow-up CTs and the use of radiologic progression as the outcome parameter in cSDH embolization studies.

We, therefore, suggest a common imaging and clinical evaluation protocol for the application in cSDH embolization trials with a follow-up of 180 days (6 months).

To detect possible treatment-related complications such as ischemic infarction or new intracranial hemorrhage and to provide a postoperative reference for further comparisons, we suggest an early follow-up scan after 24 hours (1 day).

In addition, we suggest performing 2 additional CT scans because in contrast to surgical evacuation, embolization therapy does not result in an immediate reduction of hematoma size. Furthermore, repeat scans might allow the identification of possible early predictors of successful cSDH volume reduction or resolution after 6 months.²⁷

To monitor treatment effect and hematoma evolution across time, 2 more scans at 14–28 days (2–4 weeks) and 60–90 days (2–3 months) are also suggested.

Parameters of Radiographic Progression

It is unclear which radiographic parameter is the most relevant for the definition of progression; a postoperative increase in cSDH volume might not necessarily correspond to a progression in MLS or SDH width due to brain atrophy. However, a progression in MLS will more likely correspond to an increase in cSDH volume. In contrast, cSDH width might increase on the basis of hematoma organization and shape alterations, but the overall volume could remain the same. The application of different thresholds for each of these parameters to define progression also affects the sensitivity and specificity across these radiologic measures.

It is, therefore, vital that the reproducibility and comparability of longitudinal measurements be taken into account for each parameter. Volume changes corresponding to a few voxels that might have been segmented differently at the edge of the hematoma might already lead to an increase or decrease in volume. Here, automatic artificial intelligence–based segmentation algorithms are likely more accurate and could increase reproducibility, but further development and diagnostic accuracy studies are needed to confirm this possibility. Neural networks can be used to automatically segment cSDH to obtain more accurate volume measurements closer to the criterion standard. However, to our knowledge, only 1 study has applied this automatic segmentation technique specifically to patients with cSDH so far.²⁸ In their study, Kellogg et al²⁸ used a convolutional neural network to segment cSDH on CT scans, achieving an average DICE score of 0.806. However, this technique might be limited when it comes to the segmentation of isodense cSDH, and so far, there is no broader availability of this technique.

Furthermore, width measurements in longitudinal studies might be dependent on hematoma-shape changes and, therefore, are not directly comparable. However, any form of measurable recurrence might indicate a later progression with concurrent clinical symptoms. Therefore, radiographic parameters should always be evaluated and reported in the context of clinical information and, as much as possible, at similar time points with similar sets of related outcome measures.

Advantages and disadvantages of all parameters to indicate radiographic progression are shown in Table 2.

Table 2. Advantages and disadvantages of singular and combinations of radiographic measurements to evaluate cSDH progression

	Advantage	Disadvantage
Width	Simple, practical, good external applicability, sensitivity easy to adjust (2 vs 5 mm, and so forth)	Too dependent on measurement technique and location, sensitivity might be low
Volume	Intuitively the right choice, presumably most accurate	Labor intensive, unlikely to be used in day-to-day practice
Volume + width	Raises the bar for specificity	More challenging to interpret, 2 thresholds to define Less sensitive
Volume + width + MLS	Raises the bar for specificity even further	Even more challenging to interpret, definition issues, 2 <i>df</i> (>2 mm and > 2 mm and > 20 mL) Low sensitivity

Recurrence and Progression as Study End Points in cSDH Embolization Trials

Recurrence and progression are frequently included as either primary or secondary end points in the cSDH embolization trials.²⁹ However, as shown in the Online Supplemental Data, there is no official standardized definition of radiographic hematoma recurrence or progression.

Furthermore, the application of thresholds and various definitions of primary and secondary radiologic end points also leads to altered sensitivities and specificities for the detection of recurrence and progression. Using radiographic progression as a study end point, therefore, poses some challenges, especially when considering the individual clinical relevance. However, due to the nature of the Onyx embolization agent (Covidien), we believe that a combination of both clinical and radiologic outcome measures is vital to the integrity of the trials and their ability to potentially change clinical practice. First, the addition of micronized tantalum powder to Onyx results in it being radiopaque.³⁰ This means that a surgeon viewing the posttreatment CT or angiography scans cannot be blinded to the assignment of the patient to the control or treatment arm, which could lead to substantial bias with regard to further decision-making.

Furthermore, while clinical outcomes are generally of more value due to the above-provided reasons, no validated clinical measurement tool for cSDH exists, leaving room for imprecision and further bias. For example, it is difficult to say whether a patient with dementia who presented with mild headache and confusion and is now less confused following treatment constitutes a clinical improvement. This is in contrast to stroke trials, in which the National Institutes of Health Stroke Scale and modified Rankin Scale allow consistent, validated reporting of clinical outcomes. As a result, a trial that reports differing rates of recurrence requiring repeat surgery between the 2 arms on the basis of clinical assessment (a “soft” measure) would need to corroborate this outcome with concurrent radiographic evidence of cSDH volume reduction (a “hard” measure). It is critical, therefore, that the volumetric measurements are as accurate as possible. Due to the previously mentioned variations in hematoma size, morphology, density, and location, the only way to consistently achieve this accuracy is to perform section-by-section computer-assisted delineation of volumes followed by summation (ie, the criterion standard). The commonly applied ABC/2 methodology and its derivations are subject to too much variation and are, thus, insufficient as an outcome measure.

DISCUSSION

Recommendations for Standardizing Outcome Reporting

On the basis of these factors, we propose the standardized reporting of a clinical outcome (ie, rate of recurrence requiring surgery) and radiographic change as measured by manual computer-assisted volumetric analysis as outcome measures for the cSDH embolization trials. While such a measurement may seem cumbersome for the clinical routine, it provides the greatest potential to gain quality evidence. If the trial results should prove positive, adjustment for increased ease of implementation could be addressed at a later time point in conjunction with ongoing communication about the most clinically meaningful radiologic measures and best practices for using them (eg, manual versus automated) to maximize specificity, sensitivity, and replicability.

In addition, following completion of the trials, the standardization of the measurement technique, as well as the follow-up intervals, would facilitate meta-analysis of the results, boosting the quality of evidence for otherwise underrepresented subgroups, and provide more concrete guidance to the study design in future trials. Also, while there are likely to be differences in techniques and software when implementing a standard methodology, every center will have, for example, a standard axial CT scan of 5 mm. This would be particularly important if the trials were to report conflicting results or if results of a few are not positive. To this end, it will be critical to demonstrate that the radiographic outcome is in line with the clinical outcome, be it symptomatic improvement or reduction of necessary repeat interventions.

Because radiologic parameters seem to play a minor role when it comes to the definition of in- or exclusion criteria for clinical trials and because the selection of in- or exclusion criteria is very dependent on the scope and design of the trial, providing recommendations is outside the scope of this article. However, when radiologic criteria are applied, we suggest the same methods as we defined for radiologic outcome parameters and strongly encourage detailed documentation of methodology, while also emphasizing the need for the homogenization of measurement techniques.

Acceptable Variations

After initial training on the specific study standards, a constant quality control is required to guarantee a low interobserver variability, both for imaging core lab readers and for the core lab readers with the radiologists at the clinical sites. On the basis of

our own unpublished observations, the deviation of MLS in individual patients among core lab readers and between local readings and the core lab should be <2 mm in at least 80% of the cases. The deviation of cSDH thickness measurements in individual patients should be <2 mm among core lab readers and <3 mm between local readings and those of the core lab (in at least 80% of the cases).

Limitations

Our common-data-elements review of existing cSDH trials has several limitations: First and most important, we based our analysis on reported protocols for collection of end points based on clinicaltrials.gov and other public-facing documentation of these studies and, therefore, may not have captured all study practices. However, this issue is yet another important part of study reporting—full and transparent outcome reporting from the stage of protocol drafting through to publication is necessary for replicable and transparent research. As we described throughout this article, there are very few published studies addressing the methodologic validity of imaging-based outcome measures specifically in cSDH. The here-proposed radiologic outcome parameters and measurement techniques are, therefore, based on current practice, practicability, and basic knowledge endorsed by the European Society of Minimally Invasive Neurological Therapy consortium. Furthermore, our recommendations reflect the research and experience of a limited group of experts, and further open dialogue is necessary to confirm the appropriateness of our recommended outcome set for cSDH trials. In addition, we would like to emphasize the need for further research addressing the reliability of measurement techniques defining radiologic outcome parameters in clinical trials of cSDH embolization. However, with this work, we aimed to highlight the need for homogenization and clear definition of outcome measures and hope to initiate further discussion and elucidate research concerning this topic.

CONCLUSIONS

Moving toward the standardization of radiologic outcome measures and measurement techniques in cSDH would increase the impact and significance of each embolization trial. Many open questions remain, especially with regard to the evaluation of the applicability and validity of radiologic outcome measures such as volume, width, and MLS in postoperative scans and as treatment-monitoring options. Currently, it seems as though manual computer-assisted measurements of cSDH volume represent the only viable option for sufficient accuracy. Furthermore, the definition of the optimal trial end point remains unclear and is highly dependent on the hypothesis to be tested. However, in order for the results of the currently running cSDH embolization trials to change clinical practice, we believe a combination of radiologic and clinical outcome measures is necessary. It is possible and reasonable that once the role of embolization for cSDH is well-established, a more simplified user-friendly version of hematoma measurement that has been adequately validated against the criterion standard of manual computer-assisted volume measurements may be used in day-to-day practice. However, the major findings here—that radiologic outcome reporting in currently

active cSDH trials is highly heterogeneous and noncomparable—require open, rapid, and ongoing communication about study design among neurointerventionalists to ensure that these trials contribute to larger-scale, comparable outcomes research in support of evidence-based practice.

Disclosure forms provided by the authors are available with the full text and PDF of this article at www.ajnr.org.

REFERENCES

1. Balsaer D, Farooq S, Mehmood T, et al. **Actual and projected incidence rates for chronic subdural hematomas in United States Veterans Administration and civilian populations.** *J Neurosurg* 2015;123:1209–15 CrossRef Medline
2. Iorio-Morin C, Touchette C, Lévesque M, et al. **Chronic subdural hematoma: toward a new management paradigm for an increasingly complex population.** *J Neurotrauma* 2018;35:1882–85 CrossRef Medline
3. Chari A, Hocking KC, Broughton E, et al. **Core outcomes and common data elements in chronic subdural hematoma: a systematic review of the literature focusing on reported outcomes.** *J Neurotrauma* 2016;33:1212–19 CrossRef Medline
4. Poulsen FR, Halle B, Pottegård A, et al. **Subdural hematoma cases identified through a Danish patient register: diagnosis validity, clinical characteristics, and preadmission antithrombotic drug use.** *Pharmacoepidemiol Drug Saf* 2016;25:1253–62 CrossRef Medline
5. Link TW, Boddu S, Paine SM, et al. **Middle meningeal artery embolization for chronic subdural hematoma: a series of 60 cases.** *Neurosurgery* 2019;85:801–07 CrossRef Medline
6. Gilligan J, Gologorsky Y. **Middle meningeal artery embolization for chronic subdural hematoma: current state and future directions.** *World Neurosurg* 2020;139:622–23 CrossRef Medline
7. Haldrup M, Ketharanathan B, Debrabant B, et al. **Embolization of the middle meningeal artery in patients with chronic subdural hematoma: a systematic review and meta-analysis.** *Acta Neurochir (Wien)* 2020;162:777–84 CrossRef Medline
8. Vande Vyvere T, Wilms G, Claes L, et al; Collaborative European NeuroTrauma Effectiveness Research in Traumatic Brain Injury (CENTER-TBI) Investigators and Participants. **Central versus local radiological reading of acute computed tomography characteristics in multi-center traumatic brain injury research.** *J Neurotrauma* 2019;36:1080–92 CrossRef Medline
9. Bullock MR, Chesnut R, Ghajar J, et al. **Guidelines for the surgical management of traumatic brain injury author group.** *Neurosurgery* 2006;58:S2–vi CrossRef
10. Liao CC, Chen YF, Xiao F. **Brain midline shift measurement and its automation: a review of techniques and algorithms.** *Int J Biomed Imaging* 2018;2018:4303161 CrossRef Medline
11. Edlmann E, Holl DC, Lingsma HF, et al; International Collaborative Research Initiative on Chronic Subdural Haematoma (iCORIC) study group. **Systematic review of current randomised control trials in chronic subdural haematoma and proposal for an international collaborative approach.** *Acta Neurochir (Wien)* 2020;162:763–76 CrossRef Medline
12. {NESTED} KNOWLEDGE. **Bringing systematic review to life: AutoLit & Synthesis.** 2021 <https://nested-knowledge.com/>. Accessed January 28, 2022
13. Gebel JM, Sila CA, Sloan MA, et al. **Comparison of the ABC/2 estimation technique to computer-assisted volumetric analysis of intraparenchymal and subdural hematomas complicating the GUSTO-1 trial.** *Stroke* 1998;29:1799–1801 CrossRef Medline
14. Won SY, Zagorci A, Dubinski D, et al. **Excellent accuracy of ABC/2 volume formula compared to computer-assisted volumetric analysis of subdural hematomas.** *PLoS One* 2018;13:e0199809 CrossRef Medline
15. Sucu HK, Gokmen M, Gelal F. **The value of XYZ/2 technique compared with computer-assisted volumetric analysis to estimate the**

- volume of chronic subdural hematoma.** *Stroke* 2005;36:998–1000 CrossRef Medline
16. Sachs J, Sachs E. **A simple formula for calculating the volume of subdural hematomas.** *Neurosurgery* 1977;1:60–61 CrossRef Medline
 17. Kasner SE. **Geometry and subdural hematoma volume.** *Stroke* 1999;30:188 CrossRef Medline
 18. Kothari RU, Brott T, Broderick JP, et al. **The ABCs of measuring intracerebral hemorrhage volumes.** *Stroke* 1996;27:1304–05 CrossRef Medline
 19. Manickam A, Marshman LAG, Johnston R, et al. **Mathematical formulae to estimate chronic subdural haematoma volume: flawed assumption regarding ellipsoid morphology.** *J Clin Neurosci* 2017;40:39–43 CrossRef Medline
 20. Barras CD, Asadi H, Phal PM, et al. **Audit of CT reporting standards in cases of intracerebral haemorrhage at a comprehensive stroke centre in Australia.** *J Med Imaging Radiat Oncol* 2016;60:720–27 CrossRef Medline
 21. Sucu HK, Gelal F, Gökmen M, et al. **Can midline brain shift be used as a prognostic factor to predict postoperative restoration of consciousness in patients with chronic subdural hematoma?** *Surg Neurol* 2006;66:178–82 CrossRef Medline
 22. Bhattathiri PS, Gregson B, Manjunath Prasad KS, et al. **Reliability assessment of computerized tomography scanning measurements in intracerebral hematoma.** *Neurosurg Focus* 2003;15:e6 CrossRef Medline
 23. Tabaddor K, Shulmon K. **Definitive treatment of chronic subdural hematoma by twist-drill craniostomy and closed-system drainage.** *J Neurosurg* 1977;46:220–26 CrossRef Medline
 24. Schucht P, Fischer U, Fung C, et al. **Follow-up computed tomography after evacuation of chronic subdural hematoma.** *N Engl J Med* 2019;380:1186–87 CrossRef Medline
 25. Srivatsan A, Mohanty A, Nascimento FA, et al. **Middle meningeal artery embolization for chronic subdural hematoma: meta-analysis and systematic review.** *World Neurosurg* 2019;122:613–19 CrossRef Medline
 26. Ban SP, Hwang G, Byoun HS, et al. **Middle meningeal artery embolization for chronic subdural hematoma.** *Radiology* 2018;286:992–99 CrossRef Medline
 27. Stanišić M, Hald J, Rasmussen IA, et al. **Volume and densities of chronic subdural haematoma obtained from CT imaging as predictors of postoperative recurrence: a prospective study of 107 operated patients.** *Acta Neurochir (Wien)* 2013;155:323–33 CrossRef Medline
 28. Kellogg RT, Vargas J, Barros G, et al. **Segmentation of chronic subdural hematomas using 3D convolutional neural networks.** *World Neurosurg* 2021;148:e58–65 CrossRef Medline
 29. Court J, Touchette CJ, Iorio-Morin C, et al. **Embolization of the middle meningeal artery in chronic subdural hematoma: a systematic review.** *Clin Neurol Neurosurg* 2019;186:105464 CrossRef Medline
 30. Van Rooij WJ, Sluzewski M, Beute GN. **Brain AVM embolization with Onyx.** *AJNR Am J Neuroradiol* 2007;28:172–77 Medline

Cluster Analysis of DSC MRI, Dynamic Contrast-Enhanced MRI, and DWI Parameters Associated with Prognosis in Patients with Glioblastoma after Removal of the Contrast-Enhancing Component: A Preliminary Study

H. Chung, H. Seo, S.H. Choi, C.-K. Park, T.M. Kim, S.-H. Park, J.K. Won, J.H. Lee, S.-T. Lee, J.Y. Lee, I. Hwang, K.M. Kang, and T.J. Yun



ABSTRACT

BACKGROUND AND PURPOSE: No report has been published on the use of DSC MR imaging, DCE MR imaging, and DWI parameters in combination to create a prognostic prediction model in glioblastoma patients. The aim of this study was to develop a machine learning–based model to find preoperative multiparametric MR imaging parameters associated with prognosis in patients with glioblastoma. Normalized CBV, volume transfer constant, and ADC of the nonenhancing T2 high-signal-intensity lesions were evaluated using K-means clustering.

MATERIALS AND METHODS: A total of 142 patients with glioblastoma who underwent preoperative MR imaging and total resection were included in this retrospective study. From the normalized CBV, volume transfer constant, and ADC maps, the parametric data were sorted using the K-means clustering method. Patients were divided into training and test sets (ratio, 1:1), and the optimal number of clusters was determined using receiver operating characteristic analysis. Kaplan-Meier survival analysis and log-rank tests were performed to identify potential parametric predictors. A multivariate Cox proportional hazard model was conducted to adjust for clinical predictors.

RESULTS: The nonenhancing T2 high-signal-intensity lesions were divided into 6 clusters. The cluster (class 4) with the relatively low normalized CBV and volume transfer constant value and the lowest ADC values was most associated with predicting glioblastoma prognosis. The optimal cutoff of the class 4 volume fraction of nonenhancing T2 high-signal-intensity lesions predicting 1-year progression-free survival was 9.70%, below which the cutoff was associated with longer progression-free survival. Two Kaplan-Meier curves based on the cutoff value showed a statistically significant difference ($P = .037$). When we adjusted for all clinical predictors, the cluster with the relatively low normalized CBV and volume transfer constant values and the lowest ADC value was an independent prognostic marker (hazard ratio, 3.04; $P = .048$). The multivariate Cox proportional hazard model showed a concordance index of 0.699 for progression-free survival.

CONCLUSIONS: Our model showed that nonenhancing T2 high-signal-intensity lesions with the relatively low normalized CBV, low volume transfer constant values, and the lowest ADC values could serve as useful prognostic imaging markers for predicting survival outcomes in patients with glioblastoma.

ABBREVIATIONS: CE = contrast-enhancing; CEL = contrast-enhancing lesion; DCE = dynamic contrast-enhanced; GBM = glioblastoma; GTR = gross total resection; K^{trans} = volume transfer constant; MGMT = O6-methylguanine-DNA methyltransferase; ML = machine learning; nCBV = normalized CBV; NE-T2HSIL = nonenhancing T2 high-signal-intensity lesion; PFS = progression-free survival

Glioblastoma (GBM) is the most common and most aggressive malignant tumor of the CNS.¹⁻³ Because the gross total resection (GTR) of the contrast-enhancing lesion (CEL)

component of GBM is associated with longer survival,⁴ the current standard treatment of GBM consists of a maximally safe GTR of the CEL, followed by adjuvant concurrent chemoradiation

Received April 17, 2022; accepted after revision August 21.

From the Seoul National University College of Medicine (H.C., H.S.), Seoul, Korea; Department of Radiology (S.H.C., J.Y.L., I.H., K.M.K., T.J.Y.), Seoul National University Hospital, Seoul National University College of Medicine, Seoul, Korea; Center for Nanoparticle Research (S.H.C.), Institute for Basic Science, Seoul, Korea; School of Chemical and Biological Engineering (S.H.C.), Seoul National University, Seoul, Korea; and Department of Neurosurgery (C.-K.P.), Internal Medicine and Cancer Research Institute (T.M.K.), Departments of Pathology (S.-H.P., J.K.W.), Radiation Oncology and Cancer Research Institute (J.H.L.), and Neurology (S.-T.L.), Seoul National University Hospital, Seoul, Korea.

H. Chung and H. Seo contributed equally to this work.

This study was supported by a grant from the Korea Healthcare Technology R&D Projects, Ministry for Health, Welfare & Family Affairs (HI16C111), by the Brain Research Program through the National Research Foundation of Korea funded by the Ministry of Science, Information and Communication Technology and Future Planning (NRF-2016M3C7A1914002), by the Basic Science Research Program through the National

Research Foundation of Korea funded by the Ministry of Science, Information and Communication Technology & Future Planning (NRF-2020RIA2C2008949 and NRF-2020RIA4A1018714), by the Creative-Pioneering Researchers Program through Seoul National University, by the Institute for Basic Science (IBS-R006-A1), and by the Basic Science Research Program through the National Research Foundation of Korea by the Ministry of Education (2017RID1A1B04034838). Otherwise, we have no conflicts of interest.

Please address correspondence to Seung Hong Choi, MD, PhD, Department of Radiology, Seoul National University Hospital, 101 Daehak-ro, Jongno-gu, Seoul, 03080, Korea; e-mail: verocay@snuh.org

Indicates open access to non-subscribers at www.ajnr.org

Indicates article with online supplemental data.

Indicates article with supplemental online video.

<http://dx.doi.org/10.3174/ajnr.A7655>

therapy.⁵ However, GBM frequently recurs as tumor cells infiltrate beyond the CEL components, leading to a dismal prognosis with an average overall survival rate of approximately 16 months.⁶ Tumor cells that infiltrate past the CEL margin are visualized as hyperintense lesions on T2WI and are known as nonenhancing T2 high-signal-intensity lesions (NE-T2HSILs).⁷ It is known that the preoperative T2-hyperintensity lesions that surround the CEL components of GBM are mainly composed of NE-T2HSILs and vasogenic edema.⁷ The importance of the residual NE-T2HSIL has recently been recognized, and studies have found that NE-T2HSIL affects the prognosis of patients with GBM.⁷⁻⁹ The preoperative prognosis of GBM in terms of the NE-T2HSIL, therefore, enables more aggressive management of the tumor if necessary, which could lead to survival benefits.⁷

Advanced MR imaging detects various aspects of tumor pathophysiology and enables noninvasive visualization of the tumor. Because the survival and proliferation of tumor cells are highly related to angiogenesis and an increase in vascular permeability,¹⁰ perfusion and diffusion imaging is expected to provide additional useful information about the NE-T2HSILs of GBM. Dynamic contrast-enhanced (DCE) MR imaging is a standard technique used to assess the integrity of the BBB on the basis of T1 enhancement. An important perfusion-related parameter measured in DCE MR imaging studies is the volume transfer constant (K^{trans}). K^{trans} is defined as the rate at which the contrast agent leaks into the extravascular extracellular space per volume of tissue.¹¹ DSC MR imaging, another perfusion-weighted MR imaging technique, measures capillary perfusion on the basis of the susceptibility effect in T2*-weighted images. Normalized CBV (nCBV), the most common perfusion parameter used in DSC MR imaging studies, reflects the presence of blood vessels in each individual voxel.¹² Last, DWI evaluates the random motion of water molecules. Quantitative analysis of the DWI enables the calculation of the ADC, which is known to have an inverse correlation with tissue cellularity.¹³

Extracting and combining MR imaging features from multiple modalities is labor-intensive, and achieving satisfactory diagnostic accuracy remains a major challenge. With recent developments in artificial intelligence, machine learning (ML) techniques have been steadily applied in glioma imaging studies and are revealing ways to solve these problems. ML techniques can efficiently process complex imaging data, identify meaningful disease patterns, and thus help radiologists make precise predictions about the progression of the disease.¹⁴ Therefore, the application of ML techniques in imaging analysis will enable the effective integration of complementary imaging information obtained from using multiple MR imaging modalities.

Although previous studies have been conducted to combine several MR imaging modalities for the improvement of the prognosis of GBM, no report has been published on the use of DSC MR imaging, DCE MR imaging, and DWI parameters in combination to create a prognostic model.^{15,16} Our study specifically focused on the NE-T2HSILs of GBM because of their importance as a site of recurrence and their relationship to prognosis, especially in patients with GBM who underwent GTR of the contrast-enhancing (CE) components. Our aim was, therefore, to find

nCBV, K^{trans} , and ADC parameters associated with prognosis in NE-T2HSIL on T2-FLAIR after GTR of the contrast-enhancing components in patients with GBM using ML-based cluster analysis.

MATERIALS AND METHODS

Patients

This retrospective study was approved by the institutional review board of the Seoul National University Hospital (IRB No. 1811-164-992), and the requirement for informed consent was waived. In this study, a total of 273 patients who were diagnosed with GBM from April 2010 to December 2019 were initially reviewed. Among the 273 patients, patients were selected according to the selection criteria outlined below.

The inclusion criteria were as follows: 1) patients older than 18 years of age, 2) diagnosed with GBM according to the 2016 World Health Organization Classification of Tumors of the Central Nervous System,³ 3) who had preoperative conventional MR imaging including 3D CE-T1WI and T2-weighted FLAIR imaging, 4) who had preoperative advanced MR imaging, including DCE MR imaging, DSC MR imaging, and DWI, and 5) who underwent standard treatment, which includes GTR followed by concurrent chemoradiation therapy with 6 cycles of adjuvant temozolomide. The exclusion criteria were as follows: 1) patients with loss of raw data ($n = 22$), 2) lost to follow-up ($n = 41$), 3) who had undergone partial resection ($n = 12$), 4) who had undergone biopsy only ($n = 14$), 5) who did not complete standard treatment ($n = 12$), 6) who had unreadable data ($n = 28$), and 7) a loss of clinical information ($n = 2$). Under these inclusion and exclusion criteria, a total of 142 patients (85 men and 57 women; age range, 22–84 years) were ultimately enrolled in this study (Online Supplemental Data).

All included patients were divided into the progression group ($n = 113$) or the nonprogression group ($n = 29$) 1 year after the operation. The patients periodically underwent clinicoradiologic follow-up after completion of the standard treatment and were diagnosed with disease progression if they met at least 1 criterion of the Response Assessment in Neuro-Oncology (RANO) criteria. The RANO criteria are as follows: 1) $\geq 25\%$ increase in the sum of the products of perpendicular diameters of enhancing lesions with the smallest tumor measurement, 2) any new lesion, 3) clear clinical deterioration not attributable to cause other than the tumor, and 4) clear progression of nonmeasurable disease.¹⁷

Mask Segmentation and Advanced Image Processing

The 3D CE-T1WIs of all patients were registered and resliced into isometric voxels of $1 \times 1 \times 1 \text{ mm}^3$ to achieve spatial alignment and correct motion artifacts across consecutive images. The T2 FLAIR, nCBV, K^{trans} , and ADC maps were then coregistered and resliced to the isovoxel CE-T1WI using rigid transformations with 6 *df* in the SPM package (Version 12; www.fil.ion.ucl.ac.uk/spm/).

A 3D U-Net-based deep learning model was created using the open data set and images from several organizations, and the tumor segmentation masks were generated on the basis of 3D CE-T1WI and FLAIR images. Using the tumor masks, we analyzed nCBV, K^{trans} , and ADC values in the NE-T2HSILs, and the segmentation

Table 1: Clinical characteristics of the study population

Characteristics	Mean (SD) or No. (%)
Age (yr)	56.0 (13.2)
Sex	
Male	85 (59.9%)
Female	57 (40.1%)
IDH1	
Wild-type	133 (93.4%)
Mutant	9 (6.3%)
MGMT promoter	
Unmethylated	68 (47.9%)
Methylated	74 (52.1%)

of the NE-T2HSIL was validated by an experienced neuroradiologist (with 19 years of experience in neuro-oncologic imaging). The process of mask segmentation and image processing is shown in the Online Supplemental Data.

K-Means Clustering Analysis and Optimization of the Number of Clusters

Using the tumor-segmentation masks, we performed voxelwise K-means clustering in the NE-T2HSILs based on nCBV, K^{trans} , and ADC maps. The K-means clustering module in the scikit-learn Python package (<https://scikit-learn.org/stable/index.html>) was used. K-means clustering is an iterative analysis that partitions a data set into K clusters, optimizing the similarities among data in a group while maintaining the greatest possible separation between different groups. K initial means are randomly selected, and each time new data are added to the program, they are assigned to the cluster with the closest mean. In the next step, the mean of the selected cluster is recalculated, and this process is repeated until all the data have been added to the program.¹⁸ All voxels from all segmented masks in the training set were first combined and then divided into multiple clusters based on the similarities across data points in the same cluster and the differences across data points in different clusters. To determine the optimal number of clusters, we ran the program several times from 3 to 6 clusters. Finally, the best cluster number was chosen, which best discriminates the 1-year progression-free survival (PFS) in the training set on the basis of a univariate analysis.

Patient Population: Training and Test Sets

We randomly assigned all patients to a training or test set to prevent overfitting in the K-means clustering analysis. We divided the training set and test set at a ratio of 1:1. Each training set consisted of 71 patients, and the test set consisted of 71 patients. The patients in the training and the test sets were equally balanced with respect to the 2 prognosis groups. Next, the K-means clustering performance was evaluated using the parametric data of all patients in the test set.

Clinical Predictors and Outcome Definition

Clinical predictors were obtained from all patients' medical records, including sex, age, isocitrate dehydrogenase isozyme 1 (IDH1) mutation status, and *O*⁶-methylguanine-DNA methyltransferase (MGMT) promoter methylation status. The primary end point of this study was PFS. For those patients who were diagnosed with tumor progression according to the RANO criteria,

PFS was calculated from the day of the operation until the day of progression. For those patients who showed no progression during the follow-up period, PFS was monitored at the time of the last follow-up MR imaging examination, and PFS was estimated by survival analysis.

Variable Selection

The selection of variables that are significantly relevant to the patient's survival outcome is extremely important in developing a prognostic model. The variables we analyzed in this study included the volume fractions of each parametric cluster in the NE-T2HSIL and several clinical predictors, including sex, age, IDH1 mutation status, and MGMT promoter methylation status. We first applied these variables in the univariate analysis and then included the variables that were found to be statistically significant in the multivariate analysis.

MR imaging protocol, imaging processing, and statistical analysis are summarized in the Online Supplemental Data.

RESULTS

Demographic Data of the Study Population

A total of 142 patients who were diagnosed with GBM were enrolled in our study. The demographic data of all enrolled patients are summarized in Table 1. During the follow-up period, 113 (79.6%) patients experienced progression, and 29 (20.4%) patients did not experience progression 1 year after the operation. Patient demographics in the training and test sets are summarized in the Online Supplemental Data.

Optimization of the Number of Clusters Using the Training and Test Sets

To determine the optimal number of clusters, we randomly divided all enrolled patients into a training set and a test set at a ratio of 1:1. The initial K-means clustering was performed on the parametric data of all patients in the training set. All voxels from the segmented NE-T2HSIL masks were divided into clusters on the basis of the nCBV, K^{trans} , and ADC maps. A range of cluster numbers was entered, and finally, the cluster number of 6 ($k = 6$) was chosen because it best discriminated the 1-year PFS in the training set on the basis of univariate analysis (Online Supplemental Data). Receiver operating characteristic analysis was performed for both the training and test sets, and the areas under the curve were 0.69 and 0.67, respectively. The area under the curve values suggest that the division into 6 clusters is an acceptable distinction (Online Supplemental Data).

Class 4r Correlated with PFS in All Patients

After we validated the number of clusters, the training and test sets were combined for survival analysis. The 2D clustering plots based on the nCBV, K^{trans} , and ADC values are demonstrated in the Online Supplemental Data. The average percentages of voxels in each of the 6 clusters were 4.99%, 18.42%, 8.41%, 27.34%, 29.24%, and 19.60% in numeric order. The parametric information for each cluster is shown in the Online Supplemental Data. Among the 6 clusters, "class 4" was the cluster with the relatively low nCBV and K^{trans} values and the lowest ADC values in the segmented NE-T2HSIL mask. We found that a higher class 4

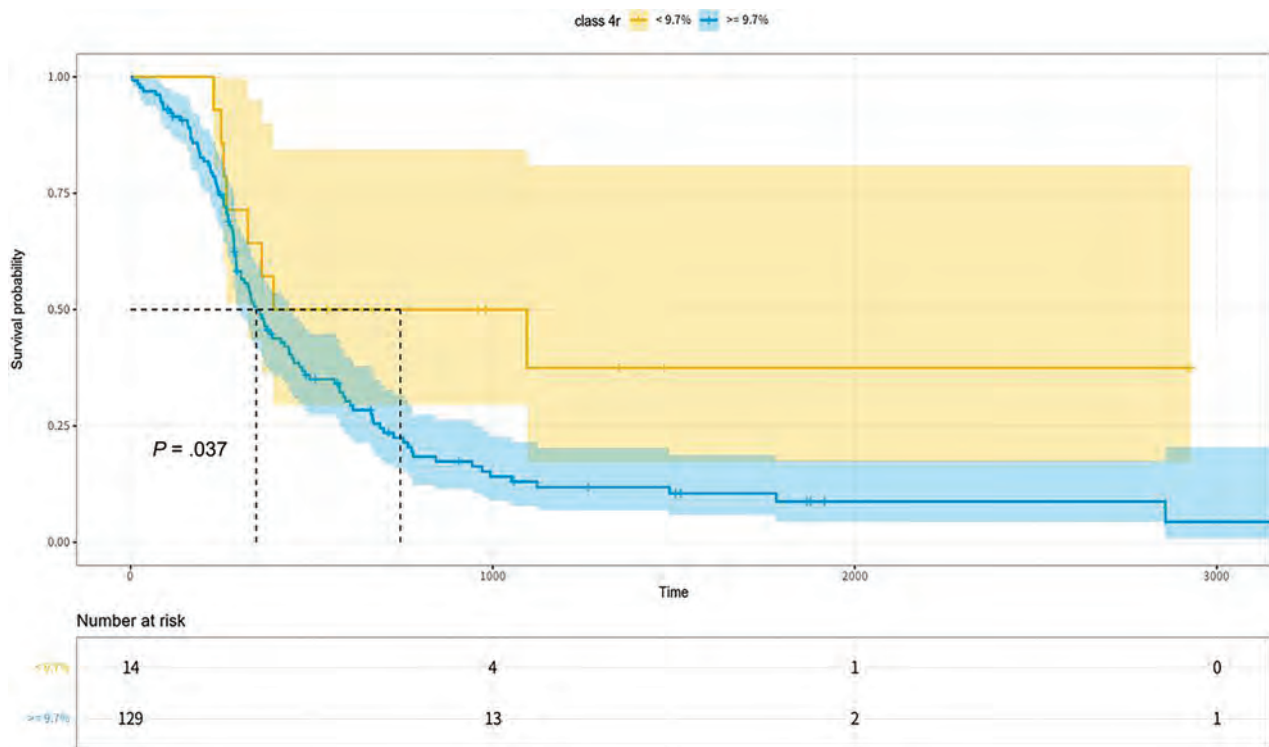


FIG 1. Kaplan-Meier survival curves stratified on the basis of the optimal class 4r cut-point value (9.70%) for PFS and the number at risk table (blue). Kaplan-Meier curve with class 4r \geq 9.70% (yellow). Kaplan-Meier curve with class 4r $<$ 9.70%. Two KM curves showed a statistically significant difference ($P = .037$).

Table 2: Univariate Cox proportional hazard analysis of the potential prognostic factors for 1-year PFS

Variables	Hazard Ratio	Wald	P Value
Age	1.02	3.90	.047
Sex			
Female	0.70	3.40	.066
Preoperative KPS	0.98	3.74	.054
<i>IDH1</i> mutation			
Mutant	0.21	7.10	.008
<i>MGMT</i> promoter			
Methylated	0.31	35	<.001
NE-T2HSIL volume			
Class 1	1.00	0.08	.78
Class 2	1.00	0.32	.57
Class 3	1.00	0.00	.98
Class 4	1.00	2.30	.13
Class 5	1.00	0.01	.92
Class 6	1.00	0.59	.44
NE-T2HSIL VF			
Class 1r	0.84	0.02	.89
Class 2r	0.66	0.46	.50
Class 3r	2.69	0.02	.90
Class 4r	3.04	3.90	.048
Class 5r	0.59	0.51	.47
Class 6r	0.64	0.46	.50

Note:—KPS, karnofsky performance status; VF, volume fraction.

volume fraction was associated with a shorter PFS in patients with GBM. We defined the term “class 4r” as the volume fraction of cluster 4 in the total NE-T2HSIL of each patient. A video clip with a 3D clustering plot can be accessed in the Online Supplemental Data.

Stratification Based on Class 4r and Survival Analysis in All Patients

Our study suggested that class 4r in the NE-T2HSIL was associated with 1-year PFS prediction in GBM. The optimal cutoff of class 4r for stratifying the shorter and longer PFS groups was 9.70% of the NE-T2HSIL volume fraction. The cutoff value distinguished the 2 PFS groups with a significant difference in the log-rank test ($P = .037$). Thus, our results showed that patients with GBM with a class 4r of $<$ 9.7% had a significantly longer PFS time than patients with a class 4r of \geq 9.7%. The Kaplan-Meier survival curves and a table with the “numbers at risk” are shown in Fig 1.

Univariate and Multivariate Analysis in All Patients

The univariate Cox proportional hazard analysis showed that clinical variables such as age, *IDH1* mutation status, and *MGMT* promoter methylation status were independent predictors of 1-year PFS in patients with GBM. In addition, among the MR imaging parametric variables, only an increase in class 4r was identified as an adverse predictor of PFS (Table 2).

In the multivariate Cox proportional hazard analysis, a statistically significant difference in PFS between patients with low and high class 4r values (hazard ratio, 3.04; 95% CI, 1.00–9.10; P value = .048) was observed, which was independent of prognostic genetic factors, including *IDH1* mutation status and *MGMT* promoter methylation status (Table 3). The concordance index value for PFS was 0.699 (standard error, 0.025), indicating that the volume fraction of regions with the relatively low nCBV and K^{trans} values and the lowest ADC value is a moderately good

predictor of 1-year PFS. Two representative cases of a patient with a PFS of <1 year and a patient with a PFS of >1 year are shown in Figs 2 and 3.

DISCUSSION

In this study, we developed a multiparametric prognostic model for patients with GBM who received GTR of the CEL mass. We found that a higher volume fraction of voxels with relatively low nCBV and K^{trans} values and the lowest ADC value in NE-T2HSIL showed a significant association with worse GBM prognosis: A low K^{trans} value indicates preserved vascular permeability due to subtle BBB damage,¹⁹ a low nCBV value implies a lack of tumor

angiogenesis,²⁰ and a low ADC value reflects an increase in tumor cellularity.¹³ Thus, regions of relatively low nCBV and K^{trans} values and the lowest ADC value represent the hypoxic hypercellular regions within the NE-T2HSIL. We believe that a high content of these regions in the NE-T2HSIL can be a significant prognostic factor in predicting the survival outcomes of GBM.

Few studies have used DSC MR imaging, DCE MR imaging, or DWI to evaluate MR imaging-derived parameters in the NE-T2HSIL to predict the prognosis of GBM. Derived from DWI, a low ADC value can be used as a marker indicating regions with a high content of microscopic tumor cells.¹³ On T2WI, however, these microscopic tumor cells are in a mixture of vasogenic edema, where high ADC values are present.²¹ Hence, the low ADC level helps locate the regions with high microscopic tumor cell content from the vasogenic edema mixture.^{21,22} Consistent with our finding, Lee et al²¹ also suggested that the minimum ADC value of NE-T2HSIL may indicate the infiltration of neoplastic cells in peritumoral edema.

Derived from DCE and DSC MR imaging, K^{trans} and nCBV values reflect the extent of perfusion and tissue vascularity. Our finding of low K^{trans} and low nCBV levels can be interpreted as hypoxic tumor regions, which are key to the highly infiltrative

Table 3: Multivariate Cox proportional hazard analysis to analyze significant independent predictors of 1-year PFS

Variables	Hazard Ratio	95% CI	P Value
NE-T2HSIL VF			
Class 4r	3.36	1.17–9.63	.024
Age	1.02	1.00–1.04	.014
IDH1	0.44	0.13–1.45	.178
MGMT promoter	0.27	0.17–0.41	<.001

Note:—VF indicates volume fraction.

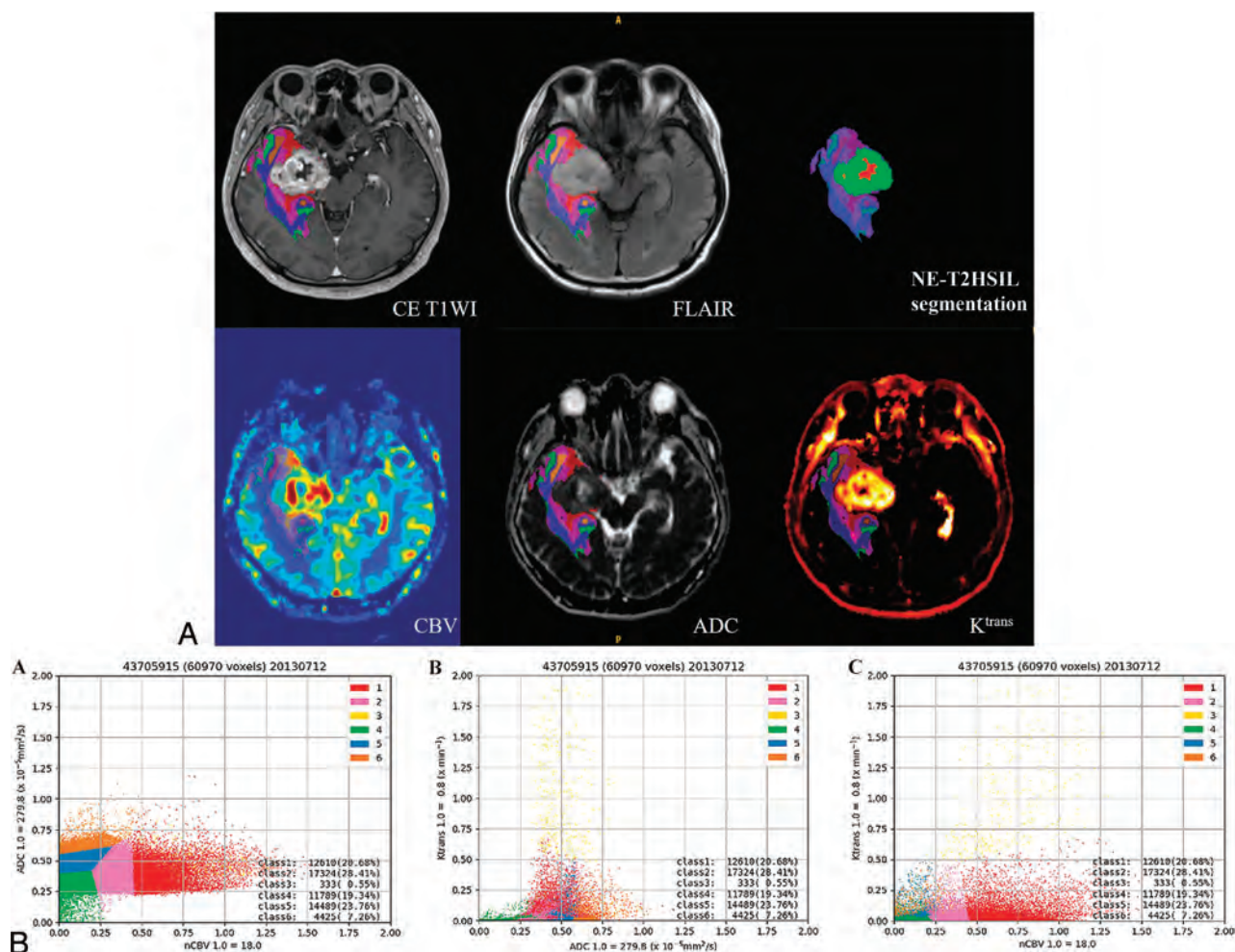


FIG 2. A representative case of a patient with a PFS < 1 year (PFS = 6.73 months) after the operation. A, Depiction of the preoperative 3D CE-T1WI and FLAIR images, segmentation of the NE-T2HSIL, and nCBV, ADC, K^{trans} maps derived from DSC MR imaging, DWI, and DCE MR imaging, respectively. B, 2D plots defined by the clustered voxels within the NE-T2HSIL based on the nCBV, ADC, and K^{trans} maps.

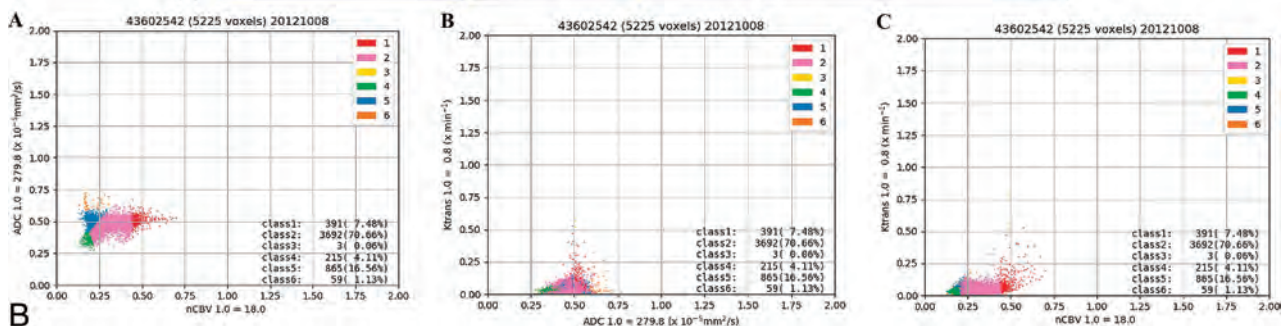
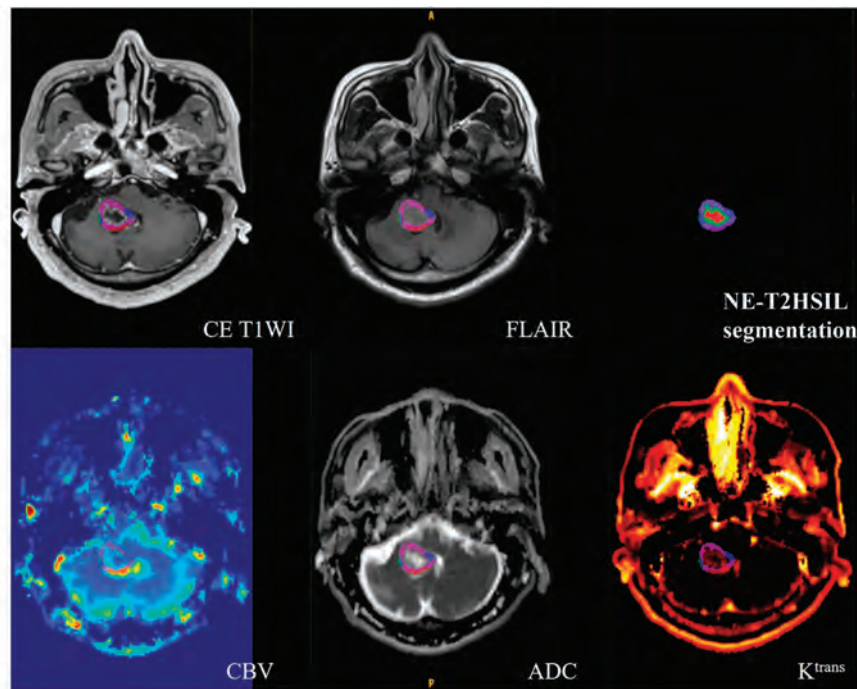


FIG 3. A representative case of a patient with a PFS of >1 year (PFS = 7.97 years) after the operation. A, Depiction of the preoperative 3D CE-T1WI and FLAIR images, segmentation of the NE-T2HSIL, and nCBV, ADC, K^{trans} maps derived from DSC MR imaging, DWI, and DCE MR imaging, respectively. B, 2D plots defined by the clustered voxels within the NE-T2HSIL based on the nCBV, ADC, and K^{trans} maps.

nature of GBM.²³⁻²⁵ Local hypoxic tumor conditions prompt the activation of hypoxia-inducible factor 1, leading to vascular endothelial growth factor production. The vascular endothelial growth factor then promotes angiogenesis and invasion of the normal brain parenchyma, which ultimately lead to tumor progression.^{25,26} However, our results contradict those of previous studies. For example, Kim et al²⁷ recently suggested the potential of a high K^{trans} value within the NE-T2HSIL in predicting the prognosis of GBM. According to that study, patients with GBM with higher K^{trans} values in the 99th percentile had a worse prognosis. With respect to rCBV, Jain et al⁹ reported that higher mean rCBV values in NE-T2HSIL are associated with a worse prognosis in GBM. The reason for the discrepancies between our current data and these 2 previous studies is that these 2 reports did not include the ADC parameter, a tissue cellularity imaging marker. We believe that in the NE-T2HSIL, a low ADC value resulting from hypercellularity is more important than hypervascularity or hyperpermeability for the prognosis; additionally, hypoxic hypercellular areas seem to have an aggressive potential.

We believe that this discrepancy is caused by the following 2 factors: First, while the previous studies used only 1 or 2 MR imaging parameters, our study included 3 MR imaging parameters (ADC, K^{trans} , and nCBV) at the same time to create a prognostic model of GBM. Therefore, we detected the most prognostic components reflecting tumor cellularity, angiogenesis, and vascular permeability in patients with GBM. Second, in previous studies, the NE-T2HSILs were analyzed as a whole, with a representative parametric value being determined independent of their composition. Our study, however, divided the NE-T2HSILs into edematous parts and microscopic tumor cells on the basis of DSC MR imaging, DCE MR imaging, and DWI, taking into account the different components that make up the NE-T2HSILs in GBM.

Despite the discrepancy between our results and previous studies, we suggest that regions with low parametric values within the NE-T2HSILs may relate to the early stages of pseudopalisade development. Pseudopalisades are unique pathologic features that differentiate GBM from low-grade gliomas.²⁸ Although the detailed mechanism for the formation of pseudopalisades remains unclear, a new model proposed by Rong et al²⁶ may provide

insight into our results. According to this model, the high incidence of intravascular thrombosis in patients with GBM can directly trigger or spread hypoxia within the tumor. After vascular insult, however, the BBB and vascular structure remain intact to some extent. This feature keeps permeability relatively low until pseudopalisading cells migrate away from the vascular occlusion site, secrete proangiogenic factors, and develop central necrosis.²⁶ Therefore, tumor voxels with relatively low nCBV and K^{trans} values and the lowest ADC value could represent NE-T2HSILs with large numbers of pseudopalisading cells in the early stages of development.

Our study has several limitations. First, it is based on a retrospective design that is inevitably prone to selection bias. However, we tried to minimize the selection bias by collecting most of the data from April 2010 to December 2019 in the Seoul National University Hospital. Second, all patient data were collected from a single medical center. Future studies with multicenter data could help validate and generalize our results. Third, the size of our study population was relatively small, especially the number of samples in the nonprogression groups, so a future study is warranted in a large population for the validation of our results. Last, although we have suggested a plausible correlation between pathologic features and imaging features, this study lacks pathologic validation because the NE-T2HSILs are not the usual target of GBM.

CONCLUSIONS

The multiparametric model showed that the NE-T2HSILs with the relatively low nCBV and K^{trans} values and the lowest ADC value could serve as useful imaging markers in predicting survival outcomes in patients with GBM. Our investigation could help radiologists locate hypoxic, hypercellular regions of the NE-T2HSIL, consider more aggressive treatment to prevent early tumor recurrence, and ultimately improve the overall survival of patients with GBM.

Disclosure forms provided by the authors are available with the full text and PDF of this article at www.ajnr.org.

REFERENCES

- Silantyev AS, Falzone L, Libra M, et al. **Current and future trends on diagnosis and prognosis of glioblastoma: from molecular biology to proteomics.** *Cells* 2019;8:863 CrossRef Medline
- Thakkar JP, Dolecek TA, Horbinski C, et al. **Epidemiologic and molecular prognostic review of glioblastoma.** *Cancer Epidemiol Biomarkers Prev* 2014;23:1985–96 CrossRef Medline
- Louis DN, Perry A, Reifenberger G, et al. **The 2016 World Health Organization Classification of Tumors of the Central Nervous System: a summary.** *Acta Neuropathol* 2016;131:803–20 CrossRef Medline
- Hardesty DA, Sanai N. **The value of glioma extent of resection in the modern neurosurgical era.** *Front Neurol* 2012;3:140 CrossRef Medline
- Weller M, van den Bent M, Tonn JC, et al; European Association for Neuro-Oncology (EANO) Task Force on Gliomas. **European Association for Neuro-Oncology (EANO) guideline on the diagnosis and treatment of adult astrocytic and oligodendroglial gliomas.** *Lancet Oncol* 2017;18:e315–29 CrossRef Medline
- Omuro A, DeAngelis LM. **Glioblastoma and other malignant gliomas: a clinical review.** *JAMA* 2013;310:1842–50 CrossRef Medline

- Lasocki A, Gaillard F. **Non-contrast-enhancing tumor: a new frontier in glioblastoma research.** *AJNR Am J Neuroradiol* 2019;40:758–65 CrossRef Medline
- Grabowski MM, Recinos PF, Nowacki AS, et al. **Residual tumor volume versus extent of resection: predictors of survival after surgery for glioblastoma.** *J Neurosurg* 2014;121:1115–23 CrossRef Medline
- Jain R, Poisson LM, Gutman D, et al. **Outcome prediction in patients with glioblastoma by using imaging, clinical, and genomic biomarkers: focus on the nonenhancing component of the tumor.** *Radiology* 2014;272:484–93 CrossRef Medline
- Jain R. **Measurements of tumor vascular leakiness using DCE in brain tumors: clinical applications.** *NMR Biomed* 2013;26:1042–49 CrossRef Medline
- Heye AK, Culling RD, Valdes HM, et al. **Assessment of blood-brain barrier disruption using dynamic contrast-enhanced MRI: a systematic review.** *Neuroimage Clin* 2014;6:262–74 CrossRef Medline
- Thompson G, Mills SJ, Coope DJ, et al. **Imaging biomarkers of angiogenesis and the microvascular environment in cerebral tumours.** *Br J Radiol* 2011;84(Spec No 2):S127–44 CrossRef Medline
- Koh DM, Collins DJ. **Diffusion-weighted MRI in the body: applications and challenges in oncology.** *AJR Am J Roentgenol* 2007;188:1622–35 CrossRef Medline
- Kourou K, Exarchos TP, Exarchos KP, et al. **Machine learning applications in cancer prognosis and prediction.** *Comput Struct Biotechnol J* 2015;13:8–17 CrossRef Medline
- Heiss WD, Raab P, Lanfermann H. **Multimodality assessment of brain tumors and tumor recurrence.** *J Nucl Med* 2011;52:1585–1600 CrossRef Medline
- Macyszyn L, Akbari H, Pisapia JM, et al. **Imaging patterns predict patient survival and molecular subtype in glioblastoma via machine learning techniques.** *Neuro Oncol* 2016;18:417–25 CrossRef Medline
- Kang Y, Hong EK, Rhim JH, et al. **Prognostic value of dynamic contrast-enhanced MRI-derived pharmacokinetic variables in glioblastoma patients: analysis of contrast-enhancing lesions and non-enhancing T2 high-signal intensity lesions.** *Korean J Radiol* 2020;21:707–16 CrossRef Medline
- Ashabi A, Sahibuddin SB, Haghghi MS. **The systematic review of K-means clustering algorithm.** In: *Proceedings of the 9th International Conference on Networks, Communication and Computing*, Tokyo, Japan. December 18–20, 2020:13–18 CrossRef
- Barnes SR, Ng TS, Montagne A, et al. **Optimal acquisition and modeling parameters for accurate assessment of low K^{trans} blood-brain barrier permeability using dynamic contrast-enhanced MRI.** *Magn Reson Med* 2016;75:1967–77 CrossRef Medline
- Jain R, Griffith B, Alotaibi F, et al. **Glioma angiogenesis and perfusion imaging: understanding the relationship between tumor blood volume and leakiness with increasing glioma grade.** *AJNR Am J Neuroradiol* 2015;36:2030–35 CrossRef Medline
- Lee EJ, terBrugge K, Mikulis D, et al. **Diagnostic value of peritumoral minimum apparent diffusion coefficient for differentiation of glioblastoma multiforme from solitary metastatic lesions.** *AJR Am J Roentgenol* 2011;196:71–76 CrossRef Medline
- Chiang IC, Kuo YT, Lu CY, et al. **Distinction between high-grade gliomas and solitary metastases using peritumoral 3-T magnetic resonance spectroscopy, diffusion, and perfusion imagings.** *Neuroradiology* 2004;46:619–27 CrossRef Medline
- Yang L, Lin C, Wang L, et al. **Hypoxia and hypoxia-inducible factors in glioblastoma multiforme progression and therapeutic implications.** *Exp Cell Res* 2012;318:2417–26 CrossRef Medline
- Kaur B, Khwaja FW, Severson EA, et al. **Hypoxia and the hypoxia-inducible-factor pathway in glioma growth and angiogenesis.** *Neuro Oncol* 2005;7:134–53 CrossRef Medline
- Monteiro AR, Hill R, Pilkington GJ, et al. **The role of hypoxia in glioblastoma invasion.** *Cells* 2017;6:45 CrossRef Medline

26. Rong Y, Durden DL, Van Meir EG, et al. **“Pseudopalisading” necrosis in glioblastoma: a familiar morphologic feature that links vascular pathology, hypoxia, and angiogenesis.** *J Neuropathol Exp Neurol* 2006;65:529–39 CrossRef Medline
27. Kim R, Choi SH, Yun TJ, et al. **Prognosis prediction of non-enhancing T2 high signal intensity lesions in glioblastoma patients after standard treatment: application of dynamic contrast-enhanced MR imaging.** *Eur Radiol* 2017;27:1176–85 CrossRef Medline
28. Brat DJ, Castellano-Sanchez AA, Hunter SB, et al. **Pseudopalisades in glioblastoma are hypoxic, express extracellular matrix proteases, and are formed by an actively migrating cell population.** *Cancer Res* 2004;64:920–27 CrossRef Medline

Diffuse Large B-Cell Epstein-Barr Virus–Positive Primary CNS Lymphoma in Non-AIDS Patients: High Diagnostic Accuracy of DSC Perfusion Metrics

A. Pons-Escoda, A. García-Ruiz, P. Naval-Baudin, F. Grussu, M. Viveros, N. Vidal, J. Bruna, G. Plans, M. Cos, R. Perez-Lopez, and C. Majós



ABSTRACT

BACKGROUND AND PURPOSE: Immunodeficiency-associated CNS lymphoma may occur in different clinical scenarios beyond AIDS. This subtype of CNS lymphoma is diffuse large B-cell and Epstein-Barr virus–positive. Its accurate presurgical diagnosis is often unfeasible because it appears as ring-enhancing lesions mimicking glioblastoma or metastasis. In this article, we describe clinicoradiologic features and test the performance of DSC-PWI metrics for presurgical identification.

MATERIALS AND METHODS: Patients without AIDS with histologically confirmed diffuse large B-cell Epstein-Barr virus–positive primary CNS lymphoma (December 2010 to January 2022) and diagnostic MR imaging without onco-specific treatment were retrospectively studied. Clinical, demographic, and conventional imaging data were reviewed. Previously published DSC-PWI time-intensity curve analysis methodology, to presurgically identify primary CNS lymphoma, was used in this particular lymphoma subtype and compared with a prior cohort of 33 patients with Epstein-Barr virus–negative CNS lymphoma, 35 with glioblastoma, and 36 with metastasis data. Normalized curves were analyzed and compared on a point-by-point basis, and previously published classifiers were tested. The standard percentage of signal recovery and CBV values were also evaluated.

RESULTS: Seven patients with Epstein-Barr virus–positive primary CNS lymphoma were included in the study. DSC-PWI normalized time-intensity curve analysis performed the best for presurgical identification of Epstein-Barr virus–positive CNS lymphoma (area under the receiver operating characteristic curve of 0.984 for glioblastoma and 0.898 for metastasis), followed by the percentage of signal recovery (0.833 and 0.873) and CBV (0.855 and 0.687).

CONCLUSIONS: When a necrotic tumor is found in a potentially immunocompromised host, neuroradiologists should consider Epstein-Barr virus–positive CNS lymphoma. DSC-PWI could be very useful for presurgical characterization, with especially strong performance of normalized time-intensity curves.

ABBREVIATIONS: AUC = area under the receiving operating characteristic curve; CE = contrast-enhanced; DLBC = diffuse large B-cell; EBV = Epstein-Barr virus; GE = gradient-echo; nTIC = normalized time-intensity curve; PCNSL = primary CNS lymphoma; PSR = percentage of signal recovery; rCBV = relative CBV; TIC = time-intensity curve; WHO = World Health Organization

Presurgical suspicion of CNS lymphoma is crucial for patient management. When it is suspected, initial corticosteroids

should be avoided, and biopsy instead of surgical resection is recommended.^{1,2}

Conventional imaging features of CNS lymphoma are widely described,^{3–7} but they mainly refer to primary CNS lymphoma

Received April 27, 2022; accepted after revision September 2.

From the Departments of Radiology (A.P.-E., P.N.-B., M.V., M.C., C.M.), Pathology (N.V.), and Neurosurgery (G.P.), Hospital Universitari de Bellvitge, Barcelona, Spain; Neurooncology Unit (A.P.-E., N.V., J.B., G.P., C.M.), Institut d'Investigació Biomèdica de Bellvitge-IDIBELL, Barcelona, Spain; Radiomics Group (A.G.-R., F.G., R.P.-L.), Vall d'Hebron Institut d'Oncologia, Barcelona, Spain; and Department of Radiology (R.P.-L.), Hospital Universitari Vall d'Hebron, Barcelona, Spain.

A.P.-E. and A.G.-R. are co-first authors of the manuscript. A.P.-E., P.N.-B., and C.M. created the experimental design. A.P.-E. led the investigation. A.P.-E. did the data collection. A.G.-R., F.G., and R.P.-L. led the data processing and statistical analysis in direct collaboration with A.P.-E., P.N.-B., and C.M. A.P.-E., P.N.-B., and C.M. wrote the manuscript and chose the best images. J.B. made important contributions to the final manuscript. A.P.-E. did the bibliographic research. M.V., M.C., N.V., G.P., and J.B. played an important role in imaging, patient data, or pathology sample acquisitions. All the authors have participated in the realization, review, and correction of the manuscript and its images, and all the authors have read and approved its submission to this journal.

This work was partially supported by a grant from the Instituto de Salud Carlos III (PI20/00360) to Carles Majós and Albert Pons-Escoda. Francesco Grussu has received funding from the postdoctoral fellowships program Beatriu de Pinós (2020 BP 00117), funded by the Secretary of Universities and Research (Government of Catalonia). Raquel Perez-Lopez is supported by a Prostate Cancer Foundation Young Investigator Award, CRIS Foundation Talent Award (TALENT-05), Fero Foundation, and the Instituto de Salud Carlos III.

Please address correspondence to Albert Pons-Escoda, MD, Radiology Department, Institut de Diagnòstic per la Imatge (IDI), Hospital Universitari de Bellvitge, C/Feixa Llarga SN, L'Hospitalet de Llobregat, 08907 Barcelona, Spain; e-mail: albert.pons.idi@gencat.cat; @PonsEscoda

Indicates article with online supplemental data.

<http://dx.doi.org/10.3174/ajnr.A7668>

(PCNSL), which specifically is Epstein-Barr virus (EBV)-negative and occurs in immunocompetent patients.⁸ However, less frequent subtypes of CNS lymphoma do not follow this imaging pattern. This is the case of immunodeficiency-associated CNS lymphoma, which usually appears as ring-enhancing lesions with central necrosis complicating accurate presurgical diagnosis.⁹⁻¹⁴

The World Health Organization (WHO) Classification of Tumors of the CNS includes B-cell and EBV-positivity as essential criteria for immunodeficiency-associated CNS lymphoma. Diffuse large B-cell (DLBC) EBV positive^{8,15} lymphoma is considered a distinct immunobiologic entity and represents nearly 10% of all CNS lymphomas.¹⁶ In the scientific literature, DLBC EBV-positive CNS lymphoma is mainly described in the context of AIDS. However, while the AIDS incidence is decreasing, other causes of immunodeficiency are increasing. This is the case for iatrogenesis (treatment-induced immunosuppression) in the context of post-transplantation or for other causes such as autoimmune diseases, or even for other situations such as immunosenescence and chronic inflammation.¹⁷⁻²¹

DSC-PWI is a quantitative MR imaging technique that has shown promising results for presurgical identification of PCNSL. This tumor shows a characteristic time-intensity curve (TIC), which can be precisely evaluated with a new methodology that renders normalized TICs (nTICs)^{22,23} as well as by a lower relative CBV (rCBV) and a higher percentage of signal recovery (PSR) than glioblastoma or metastasis.^{22,24-30} However, to the best of our knowledge, there is very little literature regarding DSC-PWI features specific to DLBC EBV-positive CNS lymphoma.¹⁰

In summary, DLBC EBV-positive CNS lymphoma constitutes a unique clinical immunobiologic entity with particular imaging features that challenge its presurgical diagnosis. Conventional imaging is usually misleading, and comprehensive analysis of the full potential of DSC-PWI in this scenario is lacking.

In this article, the clinical and radiologic features of a homogeneous data set of patients with DLBC EBV-positive CNS lymphoma without AIDS are comprehensively described. The main objective of the study was to test the performance of DSC-PWI metrics (nTIC, PSR, CBV) for the presurgical differentiation of this entity from glioblastoma and metastasis.

MATERIALS AND METHODS

The research ethics committee of the Hospital Universitari de Bellvitge tertiary center approved this retrospective study and issued a waiver for a specific informed consent. Patient data were protected and anonymized in accordance with European Union General Data Protection Regulation legislation.

Patients

Records of patients with confirmed primary DLBC EBV-positive CNS lymphoma (December 2010 to January 2022) were retrieved from our center's database. Inclusion criteria were the following: 1) confirmed tumor diagnosis by histology (2016 WHO lymphoid neoplasm¹⁵ and 2021 WHO CNS tumor⁸ classification); 2) extension study without evidence of systemic lymphoma; and 3) available diagnostic MR imaging examination without onco-specific treatment.

Relevant clinical and demographic data were retrieved from the hospital records, including age, sex, underlying conditions, radiologic diagnosis, histopathologic diagnosis, and initial diagnostic-therapeutic patient management.

For comparison of the obtained perfusion metrics, we retrieved DSC-PWI data from previously published²² cases of EBV-negative PCNSL, glioblastoma, and metastasis, which are balanced by technique and demographic characteristics, as well as quality-filtered.

Imaging

The MR images included in the study were acquired in a single center with 1 of 2 scanners, either an Ingenia 1.5T or an Intera 1.5T (Philips Healthcare), both using a 16-channel head coil. MR imaging examinations included T1WI, contrast-enhanced (CE) T1WI, TSE-T2WI, gradient-echo (GE) T2*WI, DWI, and DSC-PWI.

Conventional Imaging. Two experienced neuroradiologists from our tertiary reference center neuro-oncology unit, A.P.-E. and C.M., with >8 and 25 years of experience in neuro-oncologic radiology, respectively, visually assessed T1WI, CE-T1WI, TSE-T2WI, GE-T2*WI, and DWI sequences. The assessment was done independently and included the number of lesions, location, ring enhancement, TSE-T2WI signal intensity, GE-T2*WI hemorrhagic components, and diffusion restriction. Discrepancies were resolved by consensus.

Perfusion Imaging Acquisition. Two GE DSC-PWI sequences were used. The first (2 cases) included 40 dynamic volumes with a temporal resolution of 1.9 seconds with the following parameters: flip angle = 7°, TE = 25–30 ms, TR = 16–20 ms, in-plane resolution = 1.72 mm, and section-thickness = 1.5 mm. The second (5 cases) included 60 dynamic volumes with a temporal resolution of 1.6 seconds with flip angle = 75°, TE = 40 ms, TR = 1522–1771 ms, pixel spacing = 1.75 mm, and section thickness = 5 mm. The intravenous contrast was gadobutrol, 1 mmol/mL, 0.1 mmol/kg. No contrast preload administered. Baseline acquisition was on the order of 10 points. The start of the automatic injection (4–5 mL/s) was by a manual setting.

Postprocessing. The segmentations of enhancing tumor and contralateral normal-appearing WM were performed on CE-T1WI semiautomatically (histogram intensity thresholding) and coregistered with DSC-PWI. Necrosis was not included in the segmentations. Segmentations were performed on 3D Slicer, Version 4.10 (<http://www.slicer.org>), and coregistration was with the BRAINSFit module (3D Slicer). TICs were preprocessed using the method proposed by Pons-Escoda et al,^{22,23} which renders nTICs: Signal-intensity values of the enhancing tumor TIC were normalized by dividing by the maximal signal intensity drop of the normal-appearing WM, and time values were normalized as relative to the period of the descending curve on normal-appearing WM. The resultant nTICs are time- and intensity-normalized, making them comparable among patients. The TICs were processed using Python 3.6 software (<https://www.python.org/downloads/release/python-360/>).

Visual evaluation of the average curves and point-by-point statistical comparison (Mann-Whitney *U* test) were performed.

Table 1: Clinical overview of the included patients with pathology-confirmed DLBC EBV-positive CNS lymphoma

	Age (yr)	Sex	Underlying Conditions	Radiologic Diagnosis ^a	Diagnostic-Therapeutic Initial Management
P 1	66	Male	Kidney transplant	Multiple metastases ^b	Biopsy: reason, multiple lesions
P 2	76	Male	Chronic myeloproliferative disorder; essential thrombocythemia	Glioblastoma	Biopsy: reason, patient basal clinical status
P 3	74	Male	Liver transplant	Single metastasis ^c	Biopsy: reason, second-look radiologic opinion
P 4	62	Female	Systemic sclerosis and discoid cutaneous lupus	Glioblastoma	Maximal safe surgical resection
P 5	70	Female	Immunosenescence	Multiple metastases or multifocal glioblastoma	Biopsy: reason, multiple lesions
P 6	63	Male	Autoimmune hepatitis	Metastasis or glioblastoma	Maximal safe surgical resection
P 7	78	Female	Kidney transplant	Single metastasis	Maximal safe surgical resection

Note:—P indicates patient.

^a Based on a radiologic report from our neuro-oncology reference tertiary university hospital.

^b Atypical infection was considered, but as an unlikely option.

^c A second-look opinion raised the possibility of atypical lymphoma.

Table 2: Radiologic overview of the included patients with pathology-confirmed large B-cell EBV-positive primary CNS lymphoma

	No.	Location	Necrosis	CE-T1WI Ring	T2WI Solid Parts	T2*WI Hemorrhage	DWI Solid Parts
P 1	Multiple	Bilateral basal ganglia and cortico-subcortical	Yes	Irregular thick and nodular	Heterogeneous hyperintense	Moderate	Heterogeneous restricted
P 2	Single	Parietal corticosubcortical	Yes	Irregular thick	Heterogeneous intermediate	Subtle	Heterogeneous intermediate
P 3	Single	Frontal cortico-subcortical	Yes	Irregular thick	Heterogeneous hypointense	Moderate	Heterogeneous restricted
P 4	Single	Parietal cortico-subcortical	Yes	Irregular thick	Heterogeneous hyperintense	Prominent	Heterogeneous restricted
P 5	Multiple	Cortico-subcortical unilateral	Yes	Irregular thin	Heterogeneous hypointense	Prominent	Heterogeneous intermediate
P 6	Single	Basal ganglia	Yes	Irregular thick	Homogenous hypointense	Prominent	Heterogeneous restricted
P 7	Single	Frontal subcortical	Yes	Regular thin	Homogenous hypointense	Moderate	Homogeneous restricted

Two previously published classifiers to differentiate PCNSL from glioblastoma and metastasis through nTICs were used to assess the performance in the particular group of DLBC EBV-positive CNS lymphomas.²² Also, we assessed the performance of mean rCBV and PSR. rCBV was obtained after leakage correction and normalized to the contralateral normal-appearing WM³¹ with 3D Slicer, Version 4.10, and PSR was obtained as described by Cha et al.³²

Additionally, replicating the same prior methodology²² (logistic binary regression on the 5 most discriminatory points of the curve), we trained a 1-way nTIC model to differentiate PCNSL and glioblastoma/metastasis as a single group and tested it for DLBC EBV-positive CNS lymphoma.

RESULTS

Patients

Seven patients fulfilled the inclusion criteria and were included in the study (4 men; mean age, 70 years; range, 62–78 years). The underlying conditions were the following: 3 iatrogenic in the context of posttransplant, 2 iatrogenic in the context of autoimmune disease, 1 chronic inflammation, and 1, elderly, related to immunosenescence.^{15,17,19–21} The original radiologic diagnosis

was metastasis or glioblastoma in all patients. Initial biopsy was recommended in 4 cases, while the remaining patients were candidates for initial maximal safe resection. Patient characteristics are specified in Table 1. Four patients with DLBC EBV-positive CNS lymphoma were on corticosteroids at the time of MR imaging.

For perfusion metrics comparisons, DSC-PWI data from 33 patients with EBV-negative primary CNS lymphomas, 35 with glioblastomas, and 36 patients with metastases (total, 104; fifty-five men; mean age, 60 years; range, 18–82 years) were included. These data were previously acquired in the same center, with same technical parameters,²² and there were no significant differences in their distributions with the currently analyzed cohort (χ^2 test, $P = .108$).

Imaging

Conventional Imaging. Conventional imaging findings are shown in Table 2. The most relevant findings on MR imaging were the following: single lesions and peripheral cortico-subcortical location; necrotic lesions with ring enhancement and different degrees of hemorrhage; and heterogeneous signal on DWI (Table 2 and Fig 1). An unexpected TSE-T2 heterogeneously iso-/hypointense signal of the central nonenhancing content of lesions was also described.

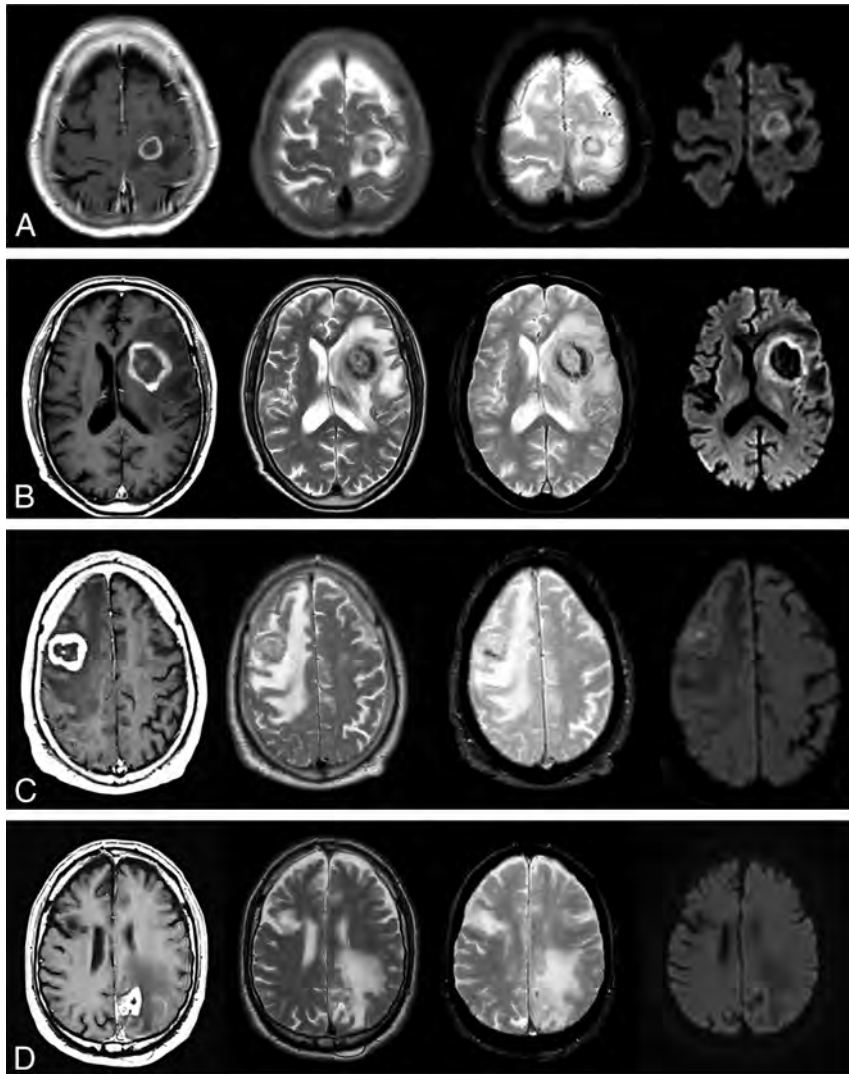


FIG 1. Visual summary of MR imaging features in 4 patients with pathology-confirmed DLBC EBV-positive CNS lymphoma. One patient in each row: CE-T1WI, TSE-T2WI, GE-T2*WI, and DWI at $b = 1000$. Regular thin ring enhancement of a subcortical lesion in A, irregular thick ring enhancement of a basal-ganglia lesion in B. The solid walls of lesions show homogeneous TSE-T2WI low signal and restricted diffusion. Incidental right frontal chronic infarct in D. Irregular thick ring enhancement in cortico-subcortical lesions: frontal in C, parietal in D. Heterogeneous signal on TSE-T2WI: hypointense in C, iso- to hyperintense in D. Intermediate heterogeneous signal on DWI. Different amounts of hemorrhage in all cases are depicted by the GE-T2*WI. Note the TSE-T2WI heterogeneous iso- to hypointense signal of the nonenhancing central content of tumors in A–C, especially in B and C.

Perfusion Imaging. Figure 2 overlays the average nTIC for DLBC EBV-positive CNS lymphoma, PCNSL (EBV-negative), metastasis, and glioblastoma. Few differences were detected between DLBC EBV-positive CNS lymphoma and PCNSL. The most relevant visual differences with metastasis or glioblastoma were seen around the maximal-signal-intensity drop and signal-recovery segments of the curves. The Mann-Whitney *U* test found significant differences between DLBC EBV-positive CNS lymphoma and glioblastoma or metastasis at almost all time points of the curve, with the greatest level around the maximal-signal-intensity drop and signal-recovery segments, reinforcing the visual assessment.

Results of the 2 previously published classifier algorithms,²² along with the classification potential of PSR and rCBV, can be

found in Table 3, Fig 3, and the Online Supplemental Data. The 2 nTIC algorithms showed the most significant differences ($P < .001$ for glioblastoma and metastasis) and the best classification results. For glioblastoma, they yielded an area under the receiver operating curve (AUC) of 0.984, accuracy of 0.93, sensitivity of 1.0, and specificity of 0.91, while for metastasis, they yielded an AUC of 0.898, accuracy of 0.82, sensitivity of 1.0, and specificity of 0.78. Additionally, PSR was also significant for both comparisons, albeit slightly less so ($P < .01$ for both, AUC = 0.833 and 0.873). Finally, rCBV yielded significant differences for DLBC EBV-positive CNS lymphoma against glioblastoma ($P = .003$, AUC = 0.855), but not against metastasis ($P = .122$, AUC = 0.687).

Furthermore, when we compared DLBC EBV-positive CNS lymphoma and PCNSL, visual assessment of average nTICs showed very similar morphology, and statistical comparison confirmed no significant differences between them in the Mann-Whitney *U* test. Moreover, no significant differences were found in PSR, while rCBV showed a barely significant difference ($P = .05$). All results are summarized in Table 3, Fig 3, and the Online Supplemental Data.

Last, the 1-way adapted classifier results can be found in the Online Supplemental Data. The nTIC algorithm (Online Supplemental Data) discriminated between DLBC EBV-positive CNS lymphoma and glioblastoma/metastasis as a whole, with AUC = 0.90, while the AUC was 0.85 for PSR and 0.77 for rCBV.

No significant differences were found in all time points of nTICs, CBV, or PSR values among the different DSC-PWI

techniques (Mann-Whitney *U* test, P values = .245–1), neither among patients with nor without corticosteroids at the time of MR imaging (Mann-Whitney *U* test, P values = .157–.724).

DISCUSSION

In this study, we present a unique cohort of 7 patients with DLBC EBV-positive CNS lymphoma without AIDS in whom DSC-PWI was performed and compare them with those with PCNSL (EBV-negative), glioblastoma, and metastasis. While conventional imaging was misleading due to the strong similarity between DLBC EBV-positive CNS lymphoma and glioblastoma or metastasis, DSC-PWI metrics provided promising results, the best determined by nTIC analysis. Moreover, this is the first study to describe and

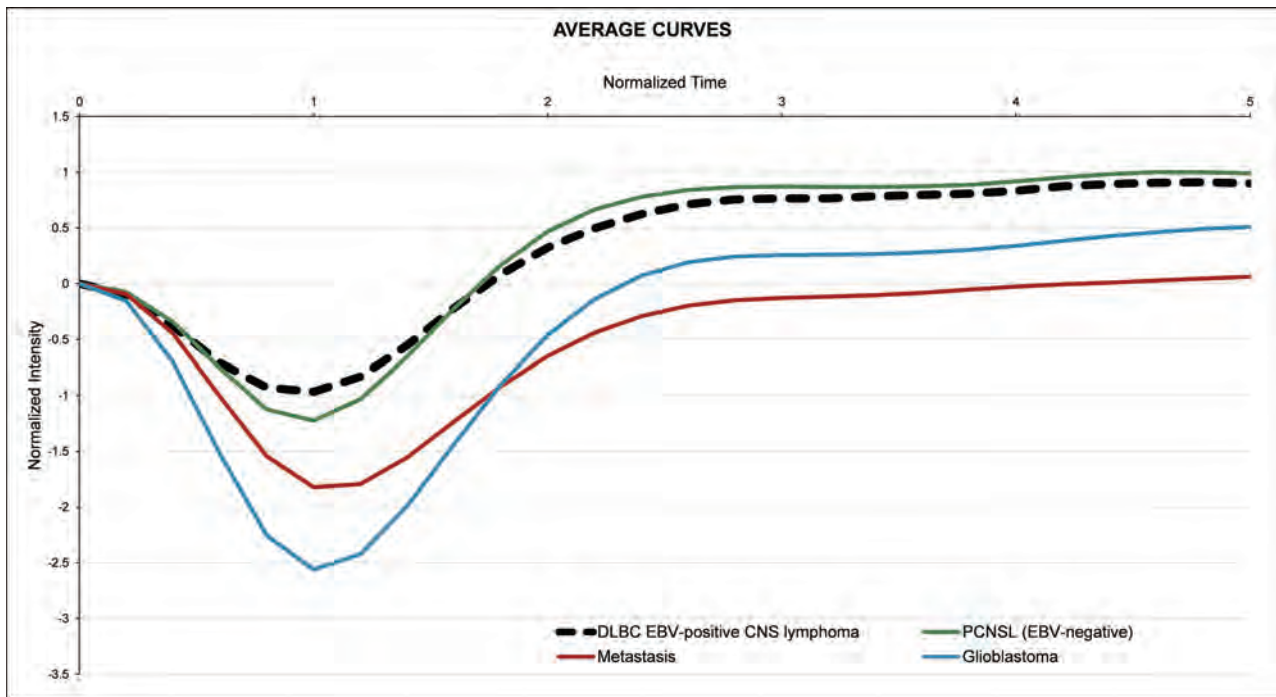


FIG 2. Average nTIC of DLBC EBV-positive CNS lymphoma, PCNSL (EBV-negative), metastasis, and glioblastoma. Few differences may be seen between DLBC EBV-positive CNS lymphoma and PCNSL. The most relevant visual differences between DLBC EBV-positive CNS lymphoma and metastasis or glioblastoma are seen around the maximal-signal-intensity drop and the signal-recovery segments of the curves.

Table 3: Summary of results

	P^a	AUC
nTIC algorithms		
vs glioblastoma	<.001	0.984
vs metastasis	<.001	0.898
PSR		
vs glioblastoma	.006	0.833
vs metastasis	.002	0.873
rCBV		
vs glioblastoma	.003	0.855
vs metastasis	.122	0.687

^aStatistical significance, Mann-Whitney *U* test.

analyze DLBC EBV-positive CNS lymphoma nTIC features and PSR values, to the best of our knowledge.

Currently, it is recognized that DLBC EBV-positive CNS lymphoma is a specific subtype of CNS lymphoma associated with immunodeficiency.^{8,15,16} AIDS-related CNS lymphoma appeared to become one of the most frequent brain tumors in the 1990s due to the explosion of the AIDS pandemic.³³ However, with the advent of antiretroviral therapies, AIDS-related CNS lymphoma has gradually decreased in the 2000s.^{34,35} Inherent to medical advances, other non-AIDS immunodeficiencies such as iatrogenic (posttransplantation and others), immunosenescence, and chronic inflammation have increased and probably overtaken AIDS as a cause of immunodeficiency-related CNS lymphoma.^{17-21,36} Also, due to the differing underlying physiopathologies of these conditions, strict monitoring of patients, and the improvement in imaging techniques, necrotic tumors have become the main radiologic differentials.^{14,37-39}

In the authors' opinion, radiology literature regarding DLBC EBV-positive CNS lymphoma without AIDS is scarce, probably due to the constantly evolving epidemiologic scenario and the relative rarity of the disease, making it difficult to pool these patients accurately.^{14,16-21,33-35,37-39} However, DLBC EBV-positive CNS lymphoma without AIDS is a clear and specific clinical immunobiologic entity that is challenging to diagnose because of the uncommon signatures for the much more frequent PCNSL and its great similarity to glioblastoma and metastasis on conventional imaging.^{14,37-39} Last, its identification before any surgical approach is crucial for optimal management because prompt biopsy without corticosteroids is the best choice, while surgical resection is not recommended.¹

In reference to the role of DSC-PWI, our literature search identified only 1 article that specifically assessed DSC-PWI of patients with DLBC EBV-positive CNS lymphoma without AIDS.¹⁰ Another article¹⁴ analyzed a subgroup of CNS lymphomas under the term "atypical PCNSL" in patients without AIDS. Lee et al¹⁰ specifically assessed rCBV values of patients with DLBC EBV-positive CNS lymphoma and compared them with those in patients who were EBV-negative. They did not find differences between EBV-positive and EBV-negative CNS lymphomas, while we found a slightly significant difference. On the other hand, Suh et al¹⁴ reported relevant differences in rCBV values between their patients with atypical PCNSL and glioblastoma, congruent with our results. Nevertheless, in both articles the DSC-PWI analysis remained limited to rCBV, and the absence of AIDS is considered enough to rule out immunodeficiency, which raises the question of whether CNS lymphomas included in these articles could actually be "other

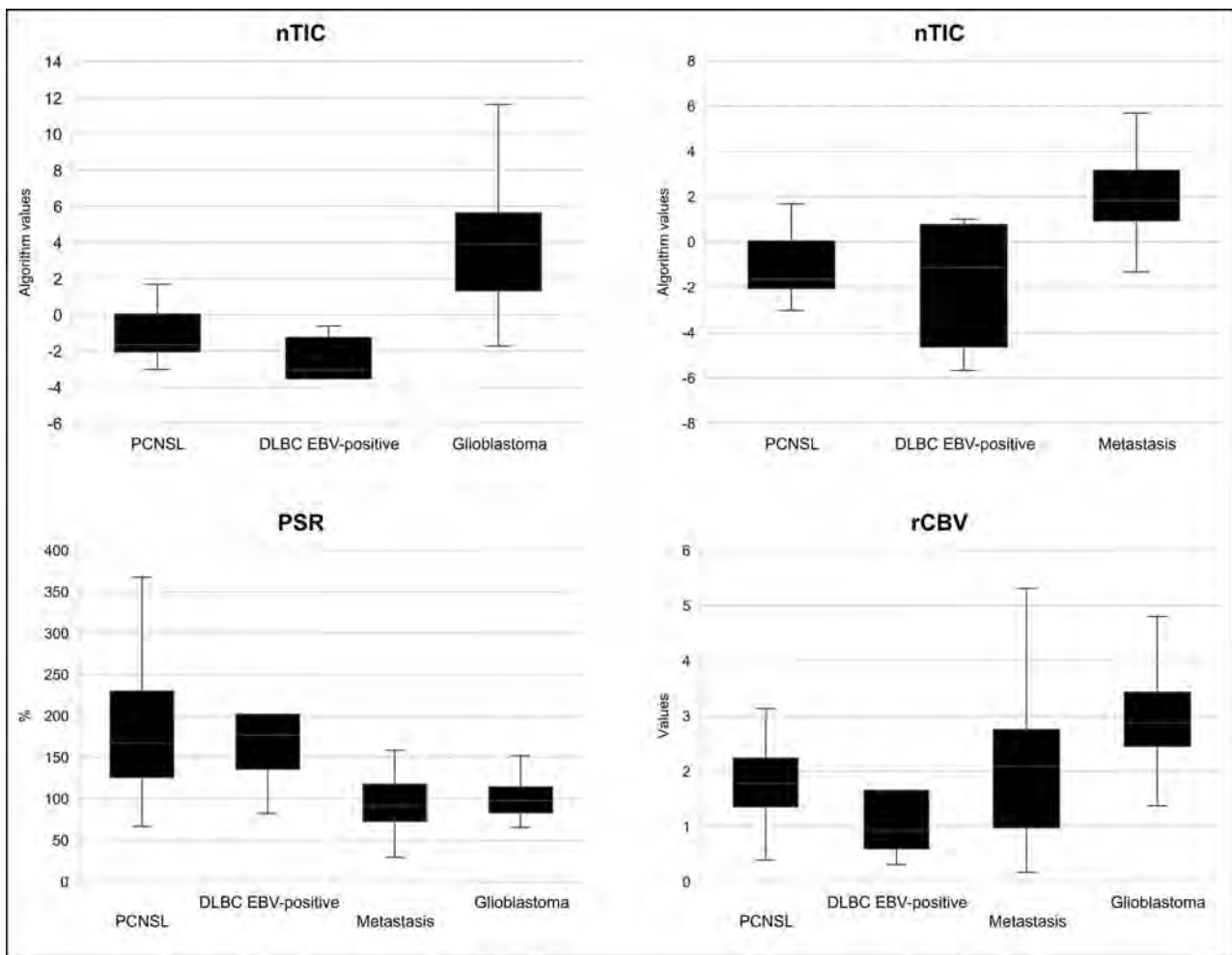


FIG 3. Boxplots depicting the results of the nTIC algorithms to differentiate PCNSL versus glioblastoma (*upper left*) and PCNSL versus metastasis (*upper right*) for each tumor subtype. *Lower row:* Boxplots depicting PSR and rCBV values for each tumor subtype.

immunodeficiency-associated,” such as ours. Finally, the mere comparison of EBV-positive and EBV-negative CNS lymphoma¹⁰ and the noninclusion of metastasis in the differential¹⁴ may condition the lack of clinically relevant information from our point of view and experience. To overcome these issues, we present a unique cohort with comprehensive clinical and demographic information and pathologic diagnosis according to the 2016 WHO lymphoid neoplasm¹⁵ and the 2021 WHO CNS tumor⁸ classifications, and we systematically describe conventional imaging and analyze the full potential of DSC-PWI to presurgically identify DLBC EBV-positive CNS lymphoma.

In this study, standard DSC-PWI metrics of PSR and rCBV achieved good or acceptable results in pair-wise discrimination of DLBC EBV-positive CNS lymphoma and glioblastoma or metastasis. Nonetheless, the application of previously reported nTICs analysis methodology²² yielded improved diagnostic performance. We mainly applied the previously published PCNSL presurgical classifier algorithms²² to our data set; but as a secondary analysis, we generated a dedicated algorithm to differentiate PCNSL and glioblastoma/metastasis as a whole group, also obtaining excellent results. Additionally, the curve-normalization process allows overlaying the averaged nTICs of relevant differential diagnoses

(Fig 2), which offers radiologist-friendly visual evaluation of curve differences. An additional advantage of the nTIC classifier results is the high-sensitivity levels provided, which is ideal in this scenario in which the most relevant goal is to raise suspicion of CNS lymphoma to avoid prebiopsy corticosteroids and potentially harmful tumor resection.²

DSC-PWI pulse-sequence parameters are known to influence CBV and PSR values, often paradoxically (ie, those sequences optimized for CBV calculations may be suboptimal for PSR and vice versa).⁴⁰ In this respect, we believe that the use of nTICs could be an alternative, especially in heterogeneous samples with nonstandardized technical acquisitions, which could be the situation among many neuroradiology departments worldwide such as ours because in this scenario, the evaluation of the whole normalized curve could surpass standard approaches such as CBV and PSR calculations.^{22,23}

On the other hand, in our experience, conventional imaging findings were insufficient to raise suspicion of CNS lymphoma because these tumors appear almost consistently as ring-enhancing necrotic lesions, with differing amounts of hemorrhage, mimicking glioblastoma or metastasis.⁹⁻¹⁴ We noted a prevalent heterogeneous low TSE-T2 signal from the central nonenhancing content of lesions,

not attributable to hemorrhage or calcification and, to the best of our knowledge, not usually seen in glioblastoma or metastasis.

Several considerations should be taken into account concerning this study. The single-site and retrospective character of the study may affect reproducibility. Nevertheless, they may also have conferred useful homogeneity to the study. Also, the limited number of cases of DLBC EBV-positive CNS lymphoma included may raise objections. However, this is a rare condition that needs to be detected presurgically, and the DSC-PWI characteristics have hardly been evaluated in the literature. At any rate, the data set suffices for a proof-of-concept demonstration, and our results warrant further multicentric prospective studies for validation. Furthermore, heterogeneous DSC-PWI technique acquisition parameters may compromise the generalizability of our concrete results. However, nTIC methodology is applicable elsewhere, and thresholds could be adapted in technically different cohorts.

Moreover, in our data set, no significant differences were found in nTICs among different DSC-PWI techniques, and indeed the nTIC method was created itself to hypothetically attenuate the impact of technical and physiologic variability on isolated parameter evaluation. Some of the data used in this investigation were part of previously published studies,^{22,23} but the aims of the study were clearly differentiated, and prior data were used for comparisons and differential diagnoses. Moreover, the use of previously published algorithms conferred a certain robustness on the study. Additionally, the reliability of data is ensured because they are available, well-balanced, curated, and filtered for prior publication. Finally, the absence of infection and brain abscess in the differential is a limitation. However, in our clinical experience with this data set of patients, glioblastoma and metastasis were the main differential diagnoses considered.

CONCLUSIONS

DSC-PWI could be very useful to presurgically differentiate DLBC EBV-positive CNS lymphoma and glioblastoma or metastasis. Among DSC-PWI metrics, nTIC curvology assessment could surpass the performance of standard PSR and rCBV measures. Neuroradiologists should be aware of any risk factors for immunodeficiency when facing a necrotic tumor in the brain. In the event of potential immunodeficiency, careful assessment of DSC-PWI may raise the suspicion of DLBC EBV-positive CNS lymphoma, which would drastically alter patient management.

ACKNOWLEDGMENTS

We thank CERCA Programme/Generalitat de Catalunya for institutional support.

Disclosure forms provided by the authors are available with the full text and PDF of this article at www.ajnr.org.

REFERENCES

- Chiavazza C, Pellerino A, Ferrio F, et al. **Primary CNS lymphomas: challenges in diagnosis and monitoring.** *Biomed Res Int* 2018;2018:3606970 CrossRef Medline
- Qian L, Tomuleasa C, Florian I-A, et al. **Advances in the treatment of newly diagnosed primary central nervous system lymphomas.** *Blood Res* 2017;52:159–66 CrossRef Medline
- Bühning U, Herrlinger U, Krings T, et al. **MRI features of primary central nervous system lymphomas at presentation.** *Neurology* 2001;57:393–96 CrossRef Medline
- Malikova H, Koubska E, Weichert J, et al. **Can morphological MRI differentiate between primary central nervous system lymphoma and glioblastoma?** *Cancer Imaging* 2016;16:40 CrossRef Medline
- Mansour A, Qandeel M, Abdel-Razeq H, et al. **MR imaging features of intracranial primary CNS lymphoma in immune competent patients.** *Cancer Imaging* 2014;14:22 CrossRef Medline
- Haldorsen IS, Espeland A, Larsson EM. **Central nervous system lymphoma: characteristic findings on traditional and advanced imaging.** *AJNR Am J Neuroradiol* 2011;32:984–92 CrossRef Medline
- Tang YZ, Booth TC, Bhogal P, et al. **Imaging of primary central nervous system lymphoma.** *Clin Radiol* 2011;66:768–77 CrossRef Medline
- WHO Classification of Tumours Editorial Board. *World Health Organization Classification of Tumours of the Central Nervous System.* 5th ed. International Agency for Research on Cancer; 2021
- Sauter A, Faul C, Bitzer M, et al. **Imaging findings in immunosuppressed patients with Epstein Barr virus-related B cell malignant lymphoma.** *AJR Am J Roentgenol* 2010;194:141–49 CrossRef Medline
- Lee HY, Kim HS, Park JW, et al. **Atypical imaging features of Epstein-Barr virus-positive primary central nervous system lymphomas in patients without AIDS.** *AJNR Am J Neuroradiol* 2013;34:1562–67 CrossRef Medline
- Jiménez de la Peña M del M, Vicente LG, Alonso RC, et al. **The multiple faces of nervous system lymphoma. Atypical magnetic resonance imaging features and contribution of the advanced imaging.** *Curr Probl Diagn Radiol* 2017;46:136–45 CrossRef Medline
- Lin X, Khan IRA, Seet YH, et al. **Atypical radiological findings of primary central nervous system lymphoma.** *Neuroradiology* 2020;62:669–76 CrossRef Medline
- Shin DJ, Lee EJ, Lee JE, et al. **Common and uncommon features of central nervous system lymphoma on traditional and advanced imaging modalities.** *Neurographics* 2017;7:437–49 CrossRef
- Suh CH, Kim HS, Lee SS, et al. **Atypical imaging features of primary central nervous system lymphoma that mimics glioblastoma: utility of intravoxel incoherent motion MR imaging.** *Radiology* 2014;272:504–13 CrossRef Medline
- Swerdlow SH, Campo E, Pileri SA, et al. **The 2016 revision of the World Health Organization classification of lymphoid neoplasms.** *Blood* 2016;127:2375–90 CrossRef Medline
- Gandhi MK, Hoang T, Law SC, et al. **EBV-associated primary CNS lymphoma occurring after immunosuppression is a distinct immunobiological entity.** *Blood* 2021;137:1468–77 CrossRef Medline
- Mahale P, Shiels MS, Lynch CF, et al. **Incidence and outcomes of primary central nervous system lymphoma in solid organ transplant recipients.** *Am J Transplant* 2018;18:453–61 CrossRef Medline
- Verdu-Bou M, Tapia G, Hernandez-Rodriguez A, et al. **Clinical and therapeutic implications of Epstein-Barr virus in HIV-related lymphomas.** *Cancers (Basel)* 2021;13:5534 CrossRef Medline
- Kaulen LD, Karschnia P, Dietrich J, et al. **Autoimmune disease-related primary CNS lymphoma: systematic review and meta-analysis.** *J Neurooncol* 2020;149:153–59 CrossRef Medline
- Mancuso S, Carlisi M, Santoro M, et al. **Immunosenescence and lymphomagenesis.** *Immun Ageing* 2018;15:22 CrossRef Medline
- Barosi G. **An immune dysregulation in MPN.** *Curr Hematol Malig Rep* 2014;9:331–39 CrossRef Medline
- Pons-Escoda A, Garcia-Ruiz A, Naval-Baudin P, et al. **Presurgical identification of primary central nervous system lymphoma with normalized time-intensity curve: a pilot study of a new method to analyze DSC-PWI.** *AJNR Am J Neuroradiol* 2020;41:1816–24 CrossRef Medline
- Pons-Escoda A, Garcia-Ruiz A, Naval-Baudin P, et al. **Voxel-level analysis of normalized DSC-PWI time-intensity curves: a potential generalizable approach and its proof of concept in discriminating glioblastoma and metastasis.** *Eur Radiol* 2022;32:3705–15 CrossRef Medline

24. Lee MD, Baird GL, Bell LC, et al. **Utility of percentage signal recovery and baseline signal in DSC-MRI optimized for relative CBV measurement for differentiating glioblastoma, lymphoma, metastasis, and meningioma.** *AJNR Am J Neuroradiol* 2019;40:1445–50 CrossRef Medline
25. Xing Z, You RX, Li J, et al. **Differentiation of primary central nervous system lymphomas from high-grade gliomas by rCBV and percentage of signal intensity recovery derived from dynamic susceptibility-weighted contrast-enhanced perfusion MR imaging.** *Clin Neuroradiol* 2014;24:329–36 CrossRef Medline
26. Neska-Matuszewska M, Bładowska J, Saósiadek M, et al. **Differentiation of glioblastoma multiforme, metastases and primary central nervous system lymphomas using multiparametric perfusion and diffusion MR imaging of a tumor core and a peritumoral zone: searching for a practical approach.** *PLoS One* 2018;13:e0191341 CrossRef Medline
27. Wang S, Kim S, Chawla S, et al. **Differentiation between glioblastomas, solitary brain metastases, and primary cerebral lymphomas using diffusion tensor and dynamic susceptibility contrast-enhanced MR imaging.** *AJNR Am J Neuroradiol* 2011;32:507–14 CrossRef Medline
28. Lee IH, Kim ST, Kim HJ, et al. **Analysis of perfusion weighted image of CNS lymphoma.** *Eur J Radiol* 2010;76:48–51 CrossRef Medline
29. Calli C, Kitis O, Yuntun N, et al. **Perfusion and diffusion MR imaging in enhancing malignant cerebral tumors.** *Eur J Radiol* 2006;58:394–403 CrossRef Medline
30. Mangla R, Kolar B, Zhu T, et al. **Percentage signal recovery derived from MR dynamic susceptibility contrast imaging is useful to differentiate common enhancing malignant lesions of the brain.** *AJNR Am J Neuroradiol* 2011;32:1004–10 CrossRef Medline
31. Boxerman JL, Schmainda KM, Weisskoff RM. **Relative cerebral blood volume maps corrected for contrast agent extravasation significantly correlate with glioma tumor grade, whereas uncorrected maps do not.** *AJNR Am J Neuroradiol* 2006;27:859–67 Medline
32. Cha S, Lupo JM, Chen MH, et al. **Differentiation of glioblastoma multiforme and single brain metastasis by peak height and percentage of signal intensity recovery derived from dynamic susceptibility-weighted contrast-enhanced perfusion MR imaging.** *AJNR Am J Neuroradiol* 2007;28:1078–84 CrossRef Medline
33. Corn BW, Marcus SM, Topham A, et al. **Will primary central nervous system lymphoma be the most frequent brain tumor diagnosed in the year 2000?** *Cancer* 1997;79:2409–13 Medline
34. Kadan-Lottick NS, Skluzacek MC, Gurney JG. **Decreasing incidence rates of primary central nervous system lymphoma.** *Cancer* 2002;95:193–202 CrossRef Medline
35. De Robles P, Fiest KM, Frolkis AD, et al. **The worldwide incidence and prevalence of primary brain tumors: a systematic review and meta-analysis.** *Neuro Oncol* 2015;17:776–83 CrossRef Medline
36. Adachi K, Yamaguchi F, Node Y, et al. **Neuroimaging of primary central nervous system lymphoma in immunocompetent patients: comparison of recent and previous findings.** *J Nippon Med Sch* 2013;80:174–83 CrossRef Medline
37. Wang ZD, Liu HH, Ma ZX, et al. **Toxoplasma gondii infection in immunocompromised patients: a systematic review and meta-analysis.** *Front Microbiol* 2017;8:1–12 CrossRef Medline
38. Arendt G, Maschke M. **Update: opportunistic infections of the central nervous system in patients with iatrogenic immunosuppression: an update.** *Neurology International Open* 2017;1:E316–25 CrossRef
39. Morollón N, Rodríguez F, Duarte J, et al. **Brain lesions in a long-term kidney transplant recipient: primary cerebral lymphoma or cerebral toxoplasmosis?** *Neurologia* 2017;32:268–70 CrossRef Medline
40. Cindil E, Sendur HN, Cerit MN, et al. **Validation of combined use of DWI and percentage signal recovery-optimized protocol of DSC-MRI in differentiation of high-grade glioma, metastasis, and lymphoma.** *Neuroradiology* 2021;63:331–42 CrossRef Medline

SWI by 7T MR Imaging for the Microscopic Imaging Diagnosis of Astrocytic and Oligodendroglial Tumors

M. Natsumeda, H. Matsuzawa, M. Watanabe, K. Motohashi, R. Gabdulkhaev, Y. Tsukamoto, Y. Kanemaru, J. Watanabe, R. Ogura, M. Okada, S. Kurabe, K. Okamoto, A. Kakita, H. Igarashi, and Y. Fujii



ABSTRACT

BACKGROUND AND PURPOSE: Despite advances in molecular imaging, preoperative diagnosis of astrocytomas and oligodendrogliomas can be challenging. In the present study, we assessed whether 7T SWI can be used to distinguish astrocytomas and oligodendrogliomas and whether malignant grading of gliomas is possible.

MATERIALS AND METHODS: 7T SWI was performed on 21 patients with gliomas before surgery with optimization for sharp visualization of the corticomedullary junction. Scoring for cortical thickening and displacement of medullary vessels, characteristic of oligodendroglial tumors, and cortical tapering, characteristic of astrocytic tumors, was performed. Additionally, characteristics of malignancy, including thickening of the medullary veins, the presence of microbleeds, and/or necrosis were scored.

RESULTS: Scoring for oligodendroglial (highest possible score, +3) and astrocytic (lowest score possible, -3) characteristics yielded a significant difference between astrocytomas and oligodendrogliomas (mean, -1.93 versus +1.71, $P < .01$). Scoring for malignancy was significantly different among the World Health Organization grade II ($n = 10$), grade III ($n = 4$), and grade IV ($n = 7$) tumors (mean, 0.20 versus 1.38 versus 2.79). Cortical thickening was observed significantly more frequently in oligodendrogliomas ($P < .02$), with a sensitivity of 71.4% and specificity of 85.7%; observation of tapering of the cortex was higher in astrocytomas ($P < .01$) with a sensitivity of 85.7% and specificity of 100%.

CONCLUSIONS: Visualization of the corticomedullary junction by 7T SWI was useful in distinguishing astrocytomas and oligodendrogliomas. Observation of tapering of the cortex was most sensitive and specific for diagnosing astrocytomas. Reliably predicting malignant grade was also possible by 7T SWI.

ABBREVIATIONS: GRE = gradient recalled-echo; LIV = local image variance; WHO = World Health Organization; *IDH* = isocitrate dehydrogenase

Recent molecular analyses have greatly advanced our ability to pathologically diagnose gliomas. Isocitrate dehydrogenase (*IDH*) mutation in the absence of 1p/19q codeletion is diagnostic for astrocytomas, and *IDH* mutation with 1p/19q codeletion, for oligodendrogliomas.¹

However, radiographically distinguishing astrocytomas and oligodendrogliomas remains challenging by conventional MR

imaging. Features such as calcification and lower homogeneous signal on T2WI are characteristic for 1p/19q-codeleted oligodendrogliomas, whereas the presence of T2 FLAIR mismatch and subventricular zone invasion is characteristic of 1p/19q-noncodeleted, *IDH*-mutant astrocytomas.^{2,3} MR perfusion studies have suggested that higher maximum relative CBV⁴ and lower extravascular extracellular distribution volume (V_e) values, especially in conjunction with calcification and high cortical involvement, are suggestive of oligodendroglioma.⁵ MR spectroscopy studies revealed that the metabolites mIns-to-Cr ratio was significantly higher in astrocytomas compared with oligodendrogliomas.⁶ Furthermore, MR imaging texture analysis⁷ and radiomics⁸ were applied to reliably distinguish astrocytomas and oligodendrogliomas. Molecular imaging of gliomas has also entered the era of clinical application. The detection of the oncometabolite 2-hydroxyglutarate by MR spectroscopy has made accurate, presurgical diagnosis of *IDH*-mutant gliomas possible.⁹⁻¹¹ A recent MR spectroscopy study suggested that cystathionine is a marker for oligodendrogliomas with 1p/19q codeletion,¹² though more robust methods are desired.

Received October 14, 2021; accepted after revision August 21, 2022.

From the Department of Neurosurgery (M.N., K.M., Y.T., Y.K., J.W., R.O., M.O., S.K., Y.F.), Center for Integrated Human Brain Science (H.M., M.W., H.I.), Department of Pathology (R.G., A.K.), and Department of Translational Research (K.O.), Brain Research Institute, Niigata University, Niigata, Japan.

M. Natsumeda and H. Matsuzawa contributed equally to this work.

This work was partially funded by grants from Japan Society for Promotion of Science to Y. Fujii (17K10888, 21H03042).

Please address correspondence to Yukihiko Fujii, MD, PhD, Department of Neurosurgery, Brain Research Institute, Niigata University, 1-757 Asahimachidori, Chuo-ku, Niigata, Japan 951-8585; e-mail: yfujii@bri.niigata-u.ac.jp

Indicates open access to non-subscribers at www.ajnr.org

Indicates article with online supplemental data.

<http://dx.doi.org/10.3174/ajnr.A7666>

Marked improvements in the contrast-to-noise ratio by 7T MR imaging has enabled visualization of high-resolution images. Seminal work by Duyn et al¹³ used gradient recalled-echo (GRE) MR imaging and a multichannel detector to achieve a nominal voxel size of $0.24 \times 0.24 \times 1.0 \text{ mm}^3$ (58 nL). We have previously described the microscopic application of 7T MR imaging by post-processing of T2* GRE images to depict senile plaquelike structures in Alzheimer disease.¹⁴ By means of this method, visualization of the corticomedullary junction,¹⁵ medullary vessels, and microbleeds was possible, aiding in the diagnosis of gliomas. Especially, the visualization of the corticomedullary junction and fine medullary vessels is not possible by 3T MR imaging. Here, we report for the first time, the usefulness of 7T SWI for the preoperative diagnosis of astrocytomas and oligodendrogliomas, as well as malignant grading.

MATERIALS AND METHODS

Patients

Twenty-one adult patients with World Health Organization (WHO) grade II–IV gliomas, including 13 (61.9%) patients with relatively small (diameter of <3 cm) gliomas localized to the cortical and/or subcortical area, undergoing 7T MR imaging evaluation at the Center for Integrated Brain Science, Niigata University before surgical treatment at the Department of Neurosurgery, Niigata University between April 2009 and December 2015 were included in the study. Written informed consent was obtained from all participants in accordance with the human research guidelines of the internal review board of Niigata University (approval # H16-263).

7T MR Imaging. SWI studies were performed using a 7T Signa Horizon LX (GE Healthcare) MR imaging system. Details of the clinical microscopic imaging techniques used were previously described.^{16–18}

High-resolution T2*-weighted 2D GRE images were obtained with TR = 220 ms, TE = 21.4 ms, flip angle = 20°, FOV = 80 × 80 mm, and matrix size = 512 × 512 with 3-mm thickness ($0.156 \times 0.156 \times 3 \text{ mm}$ in spatial resolution) (Online Supplemental Data). SWIs were obtained by postprocessing of T2*-weighted 2D GRE images, adhering to methods originally introduced by Reichenbach et al¹⁹ using in-house software written in MATLAB (MathWorks) on a Windows-based computer (Online Supplemental Data).²⁰

To determine the optimal postprocessing parameters for assessment of gliomas, we altered the kernel size of the filter sequentially from 4 to 255 (Online Supplemental Data) and the number of phase mask multiplications from 0 to 54 (Online Supplemental Data). A kernel size filter of 64 was determined to be optimal for phase unwrapping (Online Supplemental Data) and the number of phase mask multiplications to optimize the contrast-to-noise ratio 9 times (Online Supplemental Data) for the visualization of veins running inside the tumor. Thus, the optimal parameters to visualize gliomas were the same as those previously reported for microscopic imaging of senile plaquelike structures in patients with Alzheimer disease.¹⁴

Pathologic Diagnosis

Surgical specimens were independently analyzed by 2 pathologists (R.G. and A.K.) and diagnosed according to the WHO 2016 classification.²¹ Differences in diagnosis (mainly judgments between

WHO grades II and III) in a couple of cases were resolved by delimitation. IDH1 R132H (H09 clone, Dianova, 1:100), ATRX (polyclonal, SIGMA-Aldrich; 1:1000), and P53 (clone DO-7; Dako Omnis; 1:50) immunohistochemical analysis was performed in formalin-fixed, paraffin-embedded sections using the avidin-biotin-peroxidase method (Vectorlabs) with diaminobenzidine as the chromogen and counterstained with hematoxylin.²²

For cases showing negative staining for IDH1 R132H, DNA sequencing for *IDH1* and *IDH2* was analyzed. Methods for sequencing are specified in the Online Supplemental Data.

Assessment of 1p/19q Codeletion

Methods for assessment of 1p/19q codeletion are detailed in the Online Supplemental Data.

Assessment of 7T Imaging

One experienced neuroradiologist (K.O.) and a neurosurgeon (M.N.) independently assessed 7T SWIs, blinded to the clinical information. Thickening of the cortex, assessed by an increase of the distance from the cortical surface to the corticomedullary junction by $\geq 50\%$ (scored +1 present/–1 absent) and displacement of medullary vessels (scored +1 present/–1 absent) were considered characteristic of oligodendrogliomas. The tapering or thinning of the corticomedullary junction was considered characteristic of astrocytomas (scored –1 present/+1 absent). Therefore, a minimum score of –3 (astrocytoma-like) and maximum score of +3 (oligodendroglioma-like) were assessed. Findings for malignancy were also scored. The thickening of the medullary veins and the presence of microbleeds and/or necrosis were each scored as +1 when present, zero when absent. Thus, a minimum score of zero and a maximum score of +3 were possible. Scores were presented as means (SD). To calculate the sensitivity and specificity of specific categories, the 2 scorers resolved interobserver variability by thorough discussion.

Statistical Analyses

Differences between 2 groups were assessed by an unpaired *t* test, differences among 3 groups were assessed by the 1-way ANOVA test with the post hoc Tukey multiple comparison test, and contingency tables were assessed by the Fisher exact test using GraphPad Prism 9 software (GraphPad Software). Error bars represent standard error of the mean unless otherwise specified. *P* < .05 was considered statistically significant.

RESULTS

Optimization of SWI

After optimization, the visualization of the corticomedullary junction, seen as a hypointense band (triangles), and elongation of the medullary vessels running perpendicular to the cortical surface (brackets) were clearly depicted by 7T SWI (Fig 1A). This detail cannot be achieved by SWI (Fig 1B), T1-weighted (Fig 1C), or FLAIR imaging (Fig 1D) using a conventional 3T machine. Additionally, 7T SWIs appeared to show higher resolution than 3T SWIs (Online Supplemental Data), though specific parameters differed.

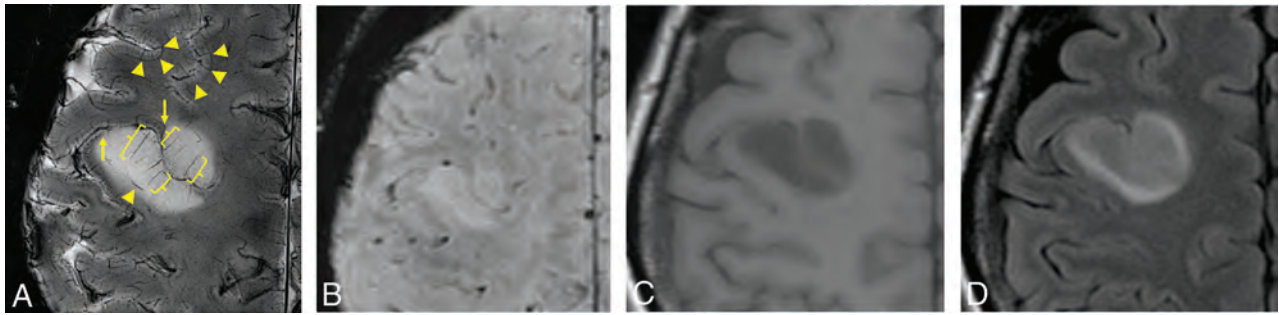


FIG 1. Comparison of 7T SWI and 3T MR imaging. Displacement of the corticomедullary junction, seen as a hypointense band (*triangles*), and elongation of medullary veins running perpendicular to the cortical surface (*brackets*) can be observed on 7T SWI (spatial resolution, $0.156 \times 0.156 \times 3$ mm; total scan time, 3 minutes and 48 seconds; number of slices, 5) (A), which cannot be appreciated on 3T SWI ($0.653 \times 0.653 \times 2$ mm; 4 minutes and 12 seconds; 64 slices) (B), 3T T1-weighted images (C), or 3T FLAIR images (D) obtained on a 3T clinical scanner. Apparent cortical thickening was observed in this diffuse astrocytoma, giving the impression of an oligodendroglioma. However, on close inspection, tapering of the cortex is observed at the edges of the lesion (A, *arrows*).

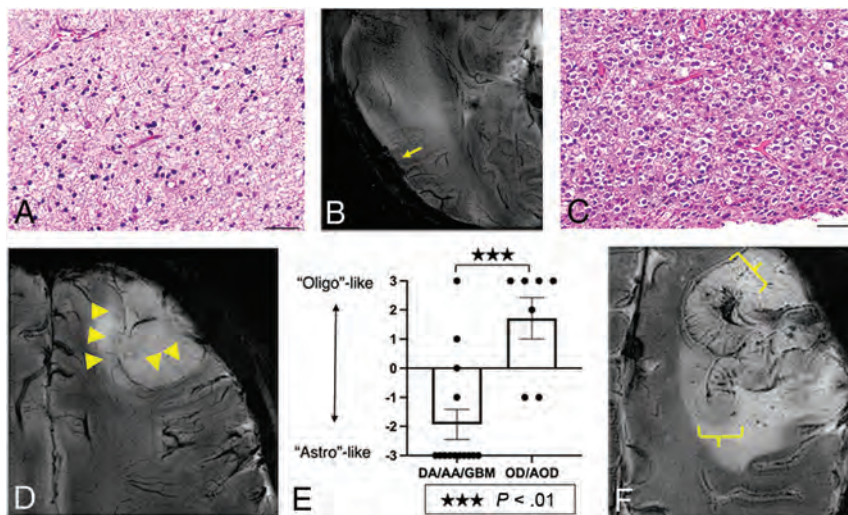


FIG 2. 7T SWI characteristics of astrocytic and oligodendroglial lesions. Astrocytic lesions (A) were predominantly located in the WM and displayed infiltrative growth and focal obscuring of the corticomедullary junction (*arrow*) without displacing medullary vessels and other normal structures on 7T SWI (B). An oligodendroglioma (WHO grade II) with classic perinuclear halos and chicken wire-like vessels (C) shows thickening of the cortex (*triangles*), elongation but not thickening of the medullary vessels of the cortex, and expansive growth, displacing the medullary vessels on 7T-SWI (D). Scoring yielded a significant difference between astrocytomas and oligodendrogliomas (mean -1.93 versus $+1.71$, $P < .01$) (E). In a case of anaplastic oligodendroglioma, *IDH*-mutant and 1p/19q-codeleted, diffuse thickening of the cortex without tapering, thickening of medullary vessels, and microbleeds were observed (F). Scale bars = $50 \mu\text{m}$. DA/AA/GBM indicates diffuse astrocytoma/anaplastic astrocytoma/glioblastoma; OD/AOD, oligodendroglioma/anaplastic oligodendroglioma.

Pathologic Diagnosis

Demographics, pathologic diagnoses, and molecular profiles of the 21 patients with gliomas are summarized in the Online Supplemental Data. The age of patients ranged from 29 to 81 years (median, 50 years); 10 female patients and 11 male patients were recruited. Tumors in 7 of 21 (33%) patients were pathologically diagnosed as WHO grade IV; 4 (19%), as WHO grade III; and 10 (48%), as grade II. The *IDH1* R132H mutation was detected in 12 (57%) tumors; *IDH2* R172W, in 1 (5%) tumor; and the rest (38%) were *IDH1/2* wild-type. The 1p/19q codeletion was detected by fluorescence in situ hybridization in 7 (33%) cases and thus these were diagnosed as

oligodendroglioma. In 1 diffuse astrocytoma, an *IDH*-mutant case, 1p was intact but 19q loss was detected (Online Supplemental Data).

Scoring for Astrocytic and Oligodendroglial Characteristics

A representative astrocytic tumor (Fig 2A) showed predominant WM invasion without massive cortical involvement and focal disappearance of the corticomедullary junction (Fig 2B, *arrow*). Hypointensities reflecting normal vascular structures were not displaced and/or became less obvious, reflecting the invasive nature of astrocytomas. Oligodendrogliomas (Fig 2C), on the other hand, showed cortical involvement with likely cortical thickening, elongation of cortical medullary vessels, and displacement of vascular structures, evidence of expansive growth (Fig 2D). Scoring for these characteristics yielded a significant difference between astrocytomas and oligodendrogliomas (mean -1.93 [SD, 0.10] versus $+1.71$ [SD, 0.20], $P < .001$, Fig 2E).

We next looked at the sensitivity and specificity of each characteristic to

diagnose oligodendrogliomas and astrocytomas. Cortical thickening was found in 5 of 7 (71.4%) oligodendrogliomas, whereas only 2 of 14 (14.3%) astrocytomas showed this feature ($P < .02$). Therefore, observation of cortical thickening yielded a sensitivity of 71.4% and specificity of 85.7% for diagnosing oligodendrogliomas. Likewise, displacement of medullary vessels was found in 4 of 7 (57.1%) oligodendrogliomas but in only 3 of 14 (21.4%) astrocytomas ($P = .16$), thus yielding a sensitivity of 57.1% and specificity of 78.6% for diagnosing oligodendrogliomas. Finally, observation of tapering of the cortex, suggesting invasion of the tumor from the WM into the cortex, was found in 12 of 14

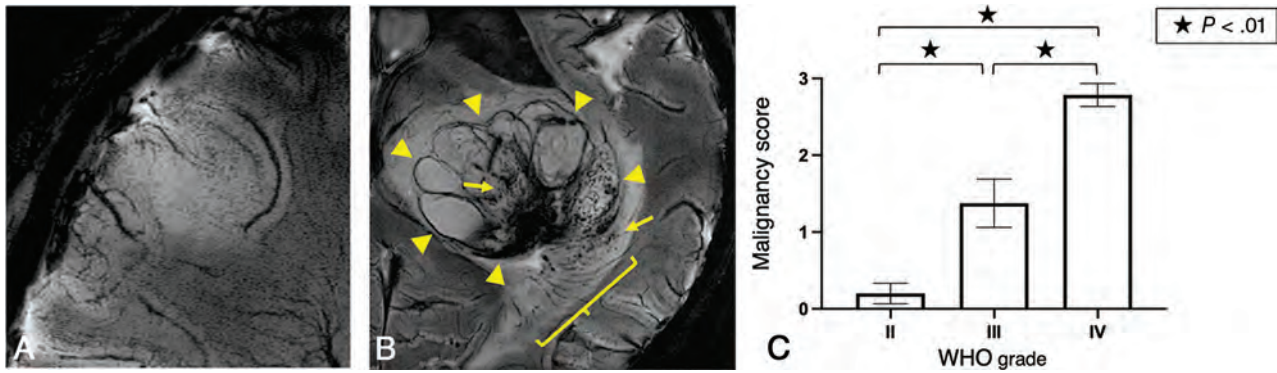


FIG 3. Malignancy scoring of gliomas. A diffuse astrocytoma, *IDH* mutant (WHO grade II) with a malignancy score of 0 (A), and a glioblastoma, *IDH* wild-type (WHO grade IV) with a malignancy score of 3, with evidence of thickening of medullary vessels (bracket), microbleeds (arrows) and necrosis (surrounded by triangles) (B). Malignancy scoring was significantly elevated in WHO grade III tumors compared with grade II (mean, 1.38 versus 0.20, $P < .01$), and grade IV tumors compared with grade III (mean, 2.79 versus 1.38, $P < .01$) and grade II ($P < .01$) (C).

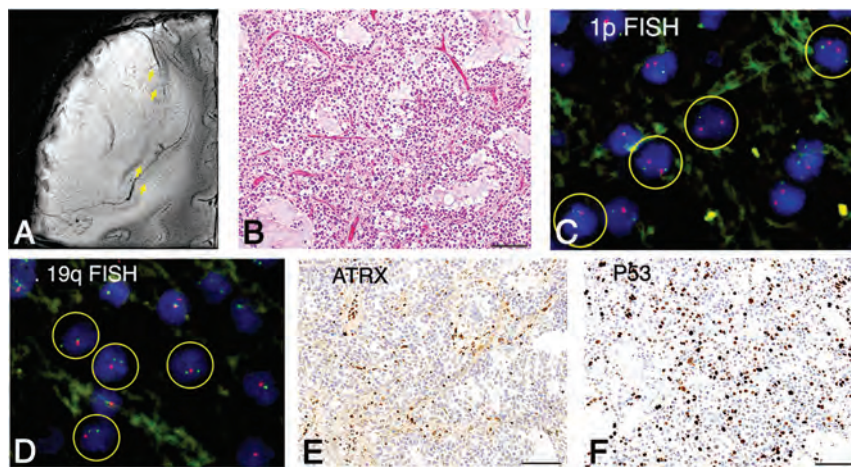


FIG 4. A diffuse astrocytoma, *IDH*-mutant, displaying thickening of the cortex with elongation of medullary vessels (arrows) and expansive growth on 7T MR imaging, mimicking an oligodendroglioma (A). Morphologically, the tumor displayed predominantly oligodendroglia-like pathology (B). Fluorescence in situ hybridization (FISH) revealed 1p-intact (C), 19q-loss (D). ATRX staining was lost in tumor cells (E), and P53 was immunopositive (>10% positive) (F), suggesting astrocytic lineage. Scale bars = 100 μm . Circles indicate individual tumor cells.

(85.7%) astrocytomas, but in none of the 7 (0%) oligodendrogliomas ($P < .01$) that showed diffuse thickening of the cortex. Therefore, this observation yielded a sensitivity of 85.7% and specificity of 100% in diagnosing astrocytomas. In a case of a relatively small cortical-subcortical tumor, elongation of medullary vessels in the cortex and distinct borders were observed, giving the impression of an oligodendroglioma (Fig 1A). However, observation of the corticomедullary junction demonstrated tapering of the cortex at the edges (Fig 1A, arrows), suggesting invasion of a subcortical tumor into the cortex, and pathologic diagnosis was diffuse astrocytoma, *IDH*-mutant. In a pathologically confirmed anaplastic oligodendroglioma, *IDH*-mutant and 1p/19q-codeleted, diffuse cortical thickening without tapering was observed (Fig 2F, brackets).

Scoring for Malignancy

Scoring for malignancy was performed by detection of microbleeds, thickening of medullary veins, and/or necrosis. An oligodendroglioma, *IDH*-mutant and 1p/19q-codeleted (WHO grade

II) assessed as zero points (Fig 3A) and a glioblastoma, *IDH* wild-type (WHO grade IV) scored as 3 points (Fig 3B) for malignancy are presented. Scoring was significantly different among WHO grade II (diffuse astrocytomas and oligodendrogliomas, $n = 10$), grade III (anaplastic astrocytoma and anaplastic oligodendrogliomas, $n = 4$), and grade IV (glioblastomas, $n = 7$) tumors (mean, 0.20 [SD, 0.0] versus 1.38 [SD, 0.18] versus 2.79 [SD, 0.10], Fig 4C) (II versus III $P < .01$; III versus IV $P < .01$; and II versus IV $P < .01$). Most interesting, all 4 WHO grade II oligodendrogliomas had a malignancy score of zero, whereas WHO grade III anaplastic oligodendrogliomas were scored as 1.5 or 2 (mean, 1.67, $P < .03$) (Online Supplemental Data). Notably, thickening of medullary vessels was observed in all WHO grade III anaplastic oligodendrogliomas (Fig 2F), but in none of the WHO grade II oligodendrogliomas (Fig 2D) ($P < .03$).

Diffuse Astrocytoma Displaying Radiographic and Pathologic Features of Oligodendroglioma

One astrocytoma had radiographic characteristics of cortical thickening without tapering and displacement of medullary vessels, characteristic of oligodendrogliomas (Fig 4A). Hence, the scoring was +3. Close pathologic examination revealed that the tumor itself had predominant, morphologic characteristics of oligodendroglioma (Fig 4B). The 1p/19q analysis revealed 19q loss, but 1p was intact (Fig 4C, -D). Most interesting, ATRX immunostaining was lost (Fig 4E) and P53 staining was positive (Fig 4F) in tumor cells, suggestive of *IDH*-mutant astrocytoma.

DISCUSSION

In the present report, we show, for the first time, that 7T SWI is useful in distinguishing astrocytic and oligodendroglial tumors.

Very fine details such as thickening and displacement of medullary vessels and disruption and displacement of the corticomedullary junction, which are not readily detected by 3T SWI, were observed by 7T MR microscopy. This method was especially useful in the diagnosis of small gliomas located in cortical/subcortical areas. We found that thickening of the cortex and elongation of corticomedullary vessels and displacement of medullary vessels and other normal structures were suggestive of oligodendroglial tumors, with a few exceptions. On the other hand, tapering of the cortex and latency of medullary vessels were characteristic of astrocytic tumors.

Astrocytomas with Oligodendrogloma-like Characteristics

We found 1 case showing cortical involvement and expansive growth on 7T SWI (Fig 4A) and displaying a predominant oligodendrogloma-like morphology (Fig 4B). However, surrogate markers including ATRX loss and P53 immunopositivity suggested astrocytic tumor, and 1p/19q fluorescence in situ hybridization indicated that 1p was intact, though 19q was lost. Otani et al²³ reported 7 cases of *IDH*-mutant and 1p-intact/19q-loss anaplastic astrocytomas, containing areas of oligodendrogloma-like morphology with longer survival compared with 19q-intact anaplastic astrocytomas. Radiographic features of these tumors were not mentioned in the report. The presence of such cases that would be diagnosed as *IDH*-mutant, 1p/19q-noncodeleted astrocytomas but possessing oligodendrogloma-like features may confound the radiographic diagnosis of astrocytic-versus-oligodendroglial tumors.

7T SWI for Determination of Malignant Grade. Furthermore, we found that detection of microbleeds, thickened medullary vessels, and/or necrosis was suggestive of malignant tumors. Massive necrosis can often be observed by 1.5 or 3T MR imaging, but microbleeds can be difficult to distinguish from blood vessels or small necrosis, and medullary vessels cannot readily be observed even on postcontrast images. Medullary vessels were clearly depicted on 7T SWI without the use of contrast media. Most interesting, all 4 WHO grade II oligodendroglomas had a malignancy score of zero, whereas none of the 3 WHO grade III anaplastic oligodendroglomas had a malignancy score of zero. Notably, thickening of the medullary vessels was observed in all WHO grade III oligodendroglomas, whereas none of the WHO grade II oligodendroglomas showed thickening ($P < .03$). A recent article suggests the difficulty of differentiating WHO grade II and III oligodendroglomas by conventional T1 contrast-enhanced and FLAIR images.²⁴ Di Ciantis et al²⁵ showed that in 6 of 21 (29%) patients with intractable epilepsy with conventional MRIs with unrevealing findings, structural lesions were found by 7T 2D GRE. Further investigation is needed, but 7T SWI may detect vessel changes and small microbleeds not observed on conventional MR imaging.

Interpreting the Findings on 7T SWI in Gliomas

In the present report, we found 7T SWI to be useful in distinguishing oligodendroglomas and astrocytomas and high susceptibility correlated with malignancy. Susceptibility is most likely affected by venous structures within the tumor, microbleeds, as well as iron and calcium deposition. When one pathologically

diagnoses gliomas, not much attention is given to venous structures within the tumor. Detailed assessment of venous structures within gliomas may lead to a better understanding of the intensities found on 7T SWI microscopy.

Application of 7T SWI in Assessment of Brain Tumors and Other Diseases

Reports of 7T SWI for radiographic assessment of brain tumors have largely been restricted to small reports.²⁶ An important study by Grabner et al²⁷ showed that local image variance (LIV) or quantification of hypointensities on 7T SWI was higher in 21 high-grade gliomas compared with 9 low-grade gliomas and that significantly higher values were found in *IDH1*-R132H-negative gliomas compared with *IDH1*-R132H-positive ones. Evidently, the results of LIV SWI correspond with malignancy scores in the present article, being higher in higher-grade gliomas. Correlation of LIV SWI and *IDH* mutation can be interpreted as follows: A high percentage of lower-grade gliomas exist in *IDH*-mutant cases, whereas *IDH* wild-type gliomas are likely to be glioblastomas. Di Ieva et al²⁸ reported the usefulness of fact-based quantification as a robust method of assessing signal heterogeneity on 7T SWI to analyze tumor grade in gliomas, in agreement with results of the malignancy score in the present study.

Other 7T SWI reports exist of visualization of vascular anomalies such as cavernous malformations with associated developmental venous anomalies,^{29,30} radiation-induced microbleeds,³¹⁻³³ iron deposition in multiple sclerosis lesions,³⁴⁻³⁶ substantia nigra in Parkinson disease,³⁷ other degenerative diseases,³⁸ and senile plaquelike lesions in patients with Alzheimer disease.¹⁴ In the present study, we found that the same postprocessing methods were optimal for visualization of the corticomedullary junction and the small vasculature of gliomas.

Limitations

Study limitations include the small sample size, selection bias restricting eligible patients to those demonstrating mild or no symptoms to eliminate motion artifacts during long imaging times, lack of direct comparison between 7T SWI and 3T SWI in this series, the use of a semiquantitative scoring system that requires subjective judgment, difficulty of generalizing to clinical practice because of limited accessibility to 7T scanners, the use of a deliberately tailored protocol using 7T SWI with limited brain coverage, and the unavailability of multiparametric 7T data such as enhancement and diffusion restriction due to time constraints.

CONCLUSIONS

Despite recent advances, the preoperative diagnosis of gliomas remains challenging. In the present report, we performed 7T SWI in a series of 21 patients with gliomas and found a close correlation between findings of cortical thickening and displacement of medullary vessels on 7T SWI with oligodendroglomas, whereas cortical tapering and infiltrative expansion in the WM was found in astrocytomas. Tapering of the cortex was associated with the highest sensitivity and specificity in distinguishing astrocytomas from oligodendroglomas. Additionally, observations of thickening of medullary vessels, microbleeds, and necrosis were associated with a higher WHO grade. 7T SWI is a useful tool to distinguish

astrocytomas and oligodendrogliomas and to determine malignancy in these tumors.

ACKNOWLEDGMENTS

Professor Tsutomu Nakada died on July 1, 2018, before the acceptance of this manuscript. We acknowledge his many contributions to this research and manuscript including, but not limited to, acquisition of funding, conceptualization of study, optimization of imaging, and study supervision. The authors would also like to acknowledge all those who helped with imaging of patients, Dr Kenichi Yamada for providing 3T SWIs, Mr Hiroaki Saito for clinical 3T SWI, and Mr Shingo Nigorikawa for help with genetic analyses.

Disclosure forms provided by the authors are available with the full text and PDF of this article at www.ajnr.org.

REFERENCES

- Ohgaki H, Kleihues P. Genetic profile of astrocytic and oligodendroglial gliomas. *Brain Tumor Pathol* 2011;28:177–83 CrossRef Medline
- Zhao K, Sun G, Wang Q, et al. The diagnostic value of conventional MRI and CT features in the identification of the IDH1-mutant and 1p/19q co-deletion in WHO grade II gliomas. *Acad Radiol* 2021;28:e189–98 CrossRef Medline
- Broen MP, Smits M, Wijnenga MM, et al. The T2-FLAIR mismatch sign as an imaging marker for non-enhancing IDH-mutant, 1p/19q-intact lower-grade glioma: a validation study. *Neuro Oncol* 2018;20:1393–99 CrossRef Medline
- Cha S, Tihan T, Crawford F, et al. Differentiation of low-grade astrocytomas by using quantitative blood-volume measurements derived from dynamic susceptibility contrast-enhanced MR imaging. *AJNR Am J Neuroradiol* 2005;26:266–73 Medline
- Yoon HJ, Ahn KJ, Lee S, et al. Differential diagnosis of oligodendroglial and astrocytic tumors using imaging results: the added value of perfusion MR imaging. *Neuroradiology* 2017;59:665–75 CrossRef Medline
- Chawla S, Oleaga L, Wang S, et al. Role of proton magnetic resonance spectroscopy in differentiating oligodendrogliomas from astrocytomas. *J Neuroimaging* 2010;20:3–8 CrossRef Medline
- Zhang S, Chiang GC, Magge RS, et al. MRI based texture analysis to classify low grade gliomas into astrocytoma and 1p/19q codeleted oligodendrogloma. *Magn Reson Imaging* 2019;57:254–58 CrossRef Medline
- Shofty B, Artzi M, Ben Bashat D, et al. MRI radiomics analysis of molecular alterations in low-grade gliomas. *Int J Comput Assist Radiol Surg* 2018;13:563–71 CrossRef Medline
- Choi C, Ganji SK, DeBerardinis RJ, et al. 2-hydroxyglutarate detection by magnetic resonance spectroscopy in IDH-mutated patients with gliomas. *Nat Med* 2012;18:624–29 CrossRef Medline
- Natsumeda M, Igarashi H, Nomura T, et al. Accumulation of 2-hydroxyglutarate in gliomas correlates with survival: a study by 3.0-Tesla magnetic resonance spectroscopy. *Acta Neuropathol Commun* 2014;2:158 CrossRef Medline
- Natsumeda M, Motohashi K, Igarashi H, et al. Reliable diagnosis of IDH-mutant glioblastoma by 2-hydroxyglutarate detection: a study by 3-T magnetic resonance spectroscopy. *Neurosurg Rev* 2018;41:641–47 CrossRef Medline
- Branzoli F, Pontoizeau C, Tchara L, et al. Cystathionine as a marker for 1p/19q codeleted gliomas by in vivo magnetic resonance spectroscopy. *Neuro Oncol* 2019;21:765–74 CrossRef Medline
- Duyn JH, van Gelderen P, Li TQ, et al. High-field MRI of brain cortical substructure based on signal phase. *Proc Natl Acad Sci U S A* 2007;104:11796–801 CrossRef Medline
- Nakada T, Matsuzawa H, Igarashi H, et al. In vivo visualization of senile-plaque-like pathology in Alzheimer's disease patients by MR microscopy on a 7T system. *J Neuroimaging* 2008;18:125–29 CrossRef Medline
- Nakada T, Matsuzawa H, Igarashi H, et al. Expansion of corticomedullary junction high-susceptibility region (CMJ-HSR) with aging: a clue in the pathogenesis of Alzheimer's disease? *J Neuroimaging* 2012;22:379–83 CrossRef Medline
- Kabasawa H, Nabetani A, Matsuzawa H, et al. Imaging optimization for in-vivo human micro imaging at 7T. In: *Proceedings of the International Society for Magnetic Resonance in Medicine*, Vancouver, British Columbia, Canada. April 12–18, 2006
- Nakada T, Nabetani A, Kabasawa H, et al. The passage to human MR microscopy. *Magn Reson Med Sci* 2005;4:83–87 CrossRef Medline
- Nakada T. Clinical application of high and ultra-high-field MRI. *Brain Dev* 2007;29:325–35 CrossRef Medline
- Reichenbach JR, Barth M, Haacke EM, et al. High-resolution MR venography at 3.0 Tesla. *J Comput Assist Tomogr* 2000;24:949–57 Medline
- Haacke EM, Xu Y, Cheng YC, et al. Susceptibility weighted imaging (SWI). *Magn Reson Med* 2004;52:612–18 CrossRef Medline
- Louis DN, Ohgaki H, Wiestler OD, et al. WHO Classification of Tumors of the Central Nervous System. International Agency for Research on Cancer; 2016
- Ogura R, Tsukamoto Y, Natsumeda M, et al. Immunohistochemical profiles of IDH1, MGMT and P53: practical significance for prognostication of patients with diffuse gliomas. *Neuropathology* 2015;35:324–35 CrossRef Medline
- Otani R, Uzuka T, Higuchi F, et al. IDH-mutated astrocytomas with 19q-loss constitute a subgroup that confers better prognosis. *Cancer Sci* 2018;109:2327–35 CrossRef Medline
- Zhao SS, Feng XL, Hu YC, et al. Better efficacy in differentiating WHO grade II from III oligodendrogliomas with machine-learning than radiologist's reading from conventional T1 contrast-enhanced and fluid attenuated inversion recovery images. *BMC Neurol* 2020;20:48 CrossRef Medline
- De Ciantis A, Barba C, Tassi L, et al. 7T MRI in focal epilepsy with unrevealing conventional field strength imaging. *Epilepsia* 2016;57:445–54 CrossRef Medline
- Moeninghoff C, Kraff O, Schlamann M, et al. Assessing a dysplastic cerebellar gangliocytoma (Lhermitte-Duclos disease) with 7T MR imaging. *Korean J Radiol* 2010;11:244–48 CrossRef Medline
- Grabner G, Kiesel B, Wohrer A, et al. Local image variance of 7 Tesla SWI is a new technique for preoperative characterization of diffusely infiltrating gliomas: correlation with tumour grade and IDH1 mutational status. *Eur Radiol* 2017;27:1556–67 CrossRef Medline
- Di Ieva A, God S, Grabner G, et al. Three-dimensional susceptibility-weighted imaging at 7 T using fractal-based quantitative analysis to grade gliomas. *Neuroradiology* 2013;55:35–40 CrossRef Medline
- Frischer JM, God S, Gruber A, et al. Susceptibility-weighted imaging at 7 T: improved diagnosis of cerebral cavernous malformations and associated developmental venous anomalies. *Neuroimage Clin* 2012;1:116–20 CrossRef Medline
- Dammann P, Wrede KH, Maderwald S, et al. The venous angioarchitecture of sporadic cerebral cavernous malformations: a susceptibility weighted imaging study at 7 T MRI. *J Neurol Neurosurg Psychiatry* 2013;84:194–200 CrossRef Medline
- Lupo JM, Chuang CF, Chang SM, et al. 7-Tesla susceptibility-weighted imaging to assess the effects of radiotherapy on normal-appearing brain in patients with glioma. *Int J Radiat Oncol Biol Phys* 2012;82:e493–500 CrossRef Medline
- Bian W, Banerjee S, Kelly DA, et al. Simultaneous imaging of radiation-induced cerebral microbleeds, arteries and veins, using a multiple gradient echo sequence at 7 Tesla. *J Magn Reson Imaging* 2015;42:269–79 CrossRef Medline

33. Morrison MA, Mueller S, Felton E, et al. **Rate of radiation-induced microbleed formation on 7T MRI relates to cognitive impairment in young patients treated with radiation therapy for a brain tumor.** *Radiother Oncol* 2021;154:145–53 CrossRef Medline
34. Haacke EM, Makki M, Ge Y, et al. **Characterizing iron deposition in multiple sclerosis lesions using susceptibility weighted imaging.** *J Magn Reson Imaging* 2009;29:537–44 CrossRef Medline
35. Louapre C, Treaba CA, Barletta V, et al. **Ultra-high field 7 T imaging in multiple sclerosis.** *Curr Opin Neurol* 2020;33:422–29 CrossRef Medline
36. Filippi M, Evangelou N, Kangarlu A, et al. **Ultra-high-field MR imaging in multiple sclerosis.** *J Neurol Neurosurg Psychiatry* 2014;85:60–66 CrossRef Medline
37. Cosottini M, Frosini D, Pesaresi I, et al. **MR imaging of the substantia nigra at 7 T enables diagnosis of Parkinson disease.** *Radiology* 2014;271:831–38 CrossRef Medline
38. Johns SLM, Ishaque A, Khan M, et al. **Quantifying changes on susceptibility weighted images in amyotrophic lateral sclerosis using MRI texture analysis.** *Amyotroph Lateral Scler Frontotemporal Degener* 2019;20:396–403 CrossRef Medline

The Value of Preoperative Phase-Contrast MRI in Predicting the Clinical Outcome of Moyamoya Disease after Encephalo-Duro-Arterial Synangiosis Surgery

S. Liu, M. Lu, C. Han, F. Hao, F. Sheng, Y. Liu, L. Zhang, D. Liu, R. Xie, H. Zhang, and J. Cai



ABSTRACT

BACKGROUND AND PURPOSE: In patients with Moyamoya disease, the relationship between preoperative hemodynamic status and prognosis after encephalo-duro-arterial synangiosis (EDAS) surgery was unclear. We aimed to explore the value of the preoperative hemodynamic status acquired by cine phase-contrast MR imaging in predicting collateral formation and clinical outcomes after EDAS surgery in patients with Moyamoya disease.

MATERIALS AND METHODS: Participants with Moyamoya disease were prospectively recruited and underwent preoperative phase-contrast MR imaging. All participants were classified into good and poor groups according to the collateral formation after EDAS surgery. On the basis of the change in the mRS system, participants were classified into the improved mRS group and the poor response group. Hemodynamic status including mean velocity, peak velocity, and blood volume flow of the superficial temporal artery was compared between groups. Logistic regression was performed to relate the phase-contrast MR imaging parameters to collateral formation and clinical outcomes.

RESULTS: A total of 45 patients with Moyamoya disease with unilateral EDAS surgery were finally included. Mean velocity, peak velocity, and blood volume flow of the ipsilateral superficial temporal artery were significantly greater in patients with good collateral formation compared with those with poor collateral formation ($P = .011$, $.004$, and $.013$, respectively). The mean velocity, peak velocity, and blood volume flow were independently associated with postoperative collateral formation after adjusting for confounding factors. Furthermore, the peak velocity of the ipsilateral superficial temporal artery was also significantly associated with improvement of the mRS score.

CONCLUSIONS: Good hemodynamic status of the ipsilateral superficial temporal artery as a donor artery evaluated by phase-contrast MR imaging was significantly associated with better collateral formation and improved mRS after EDAS surgery in patients with Moyamoya disease.

ABBREVIATIONS: BVF = blood volume flow; EDAS = encephalo-duro-arterial synangiosis; MMA = middle meningeal artery; MMD = Moyamoya disease; PC-MRI = phase-contrast MRI; rCBF = relative CBF; rCBV = relative CBV; rTTP = relative TTP; STA = superficial temporal artery; Vmean = mean velocity; Vpeak = peak velocity

Moyamoya disease (MMD) is a type of cerebrovascular disease characterized by progressive stenosis and even occlusive

changes in the bilateral terminal part of the ICA and the middle and anterior cerebral arteries.^{1,2} Encephalo-duro-arterial synangiosis (EDAS) is one of the most commonly used indirect surgical procedures.³⁻⁵ It reroutes a branch of the external carotid artery to the surface of the brain and relies on neovascularization via angiogenic mechanisms from pedicle-based grafts. Generally, the superficial temporal artery (STA) and its branches are the donor arteries. Therefore, identification of information about the STA as a donor artery may be beneficial in the prediction of surgical prognosis.

Received May 2, 2022; accepted after revision August 12.

From the Medical School of Chinese People's Liberation Army (S.L., L.Z.), Beijing, China; Department of Radiology (S.L., F.S., Y.L., L.Z., D.L., R.X., H.Z., J.C.), the Fifth Medical Center, and Department of Neurosurgery (C.H., F.H.), Chinese People's Liberation Army General Hospital, Beijing, China; and Department of Radiology (M.L.), Pingjin Hospital, Characteristic Medical Center of Chinese People's Armed Police Force, Tianjin, China.

Shitong Liu and Mingming Lu are co-first authors and contributed equally to this article.

Jianming Cai and Hongtao Zhang are co-senior authors and contributed equally to this article.

This study was supported by the grants of National Natural Science Foundation of China (82001774), Beijing Natural Science Foundation (7212100), Tianjin Science and Technology Project (TJWJ2021MS043), and Beijing Science and Technology Project (Z161100000516194).

Please address correspondence to Jianming Cai, MD, Department of Radiology, the Fifth Medical Center, Chinese PLA General Hospital, Beijing, 100853, China; e-mail: beili12345@sina.cn

Indicates open access to non-subscribers at www.ajnr.org

<http://dx.doi.org/10.3174/ajnr.A7667>

Previous studies proved that an increased caliber of the STA was associated with good prognosis of EDAS surgery.^{6,7} However, morphologic features of the STA could provide only indirect information. Functional characteristics, in particular the hemodynamic status, might provide more direct information about the role of the STA as the donor artery. To date, the relationship between the preoperative hemodynamic status of the STA and clinical outcome after surgery was unknown.

Phase-contrast MR imaging (PC-MR imaging) is a nonradioactive detection method for quantitatively analyzing the hemodynamic status of targeted vessels. The reliability and reproducibility of PC-MR imaging have been validated by several studies.^{8,9} PC-MR imaging has been performed in patients with MMD in several studies and could provide similar quantitative data of the targeted vessels.¹⁰⁻¹² Therefore, we hypothesized that the preoperative hemodynamic status of the STA is closely related to the development of collateral vasculature and the change of symptoms after the operation, aiming to explore the relationship between the hemodynamic status of the STA and postoperative outcomes in patients with MMD using PC-MR imaging.

MATERIALS AND METHODS

Study Population

This prospective study was approved by the institutional review board of Chinese PLA General Hospital. All participants provided written informed consent to participate in the study. From October 2020 to November 2021, consecutive participants who underwent their first EDAS surgery were recruited. Previously, PC-MR imaging examinations were performed in participants within 1 week before the operation. From the 59 participants, 14 were excluded for the following reasons: 1) poor image quality of the postoperative DSA or PC-MR imaging ($n = 3$); and 2) unavailable postoperative DSA ($n = 11$). Finally, 45 participants were recruited.

MR Imaging Examination

All participants underwent MR imaging examinations using a 3T whole-body MR imaging scanner (Magnetom Skyra; Siemens) with a head-neck coil. All participants were instructed to remain still during the examination.

The parameters of PC-MR images were as follows: TR = 20.36 ms; TE = 2.8 ms; section thickness = 5 mm; number of slices = 20; FOV = 233 × 340 mm; matrix = 176 × 256; flip angle = 20°; number of acquisitions = 3. Reconstructed MIP images of TOF, obtained previously, were used to position the PC-MR imaging sequence. The scan planes were placed where the targeted vessels were straight and perpendicular to the vessels on the basis of the coronal and sagittal projection images. Because the velocity of the vessels varied from one patient to another, prescans were performed to acquire the best velocity-encoding (the brightest sequence without any regurgitation). The prescan velocity-encoding of the STA was 15~45 cm/s.

The parameters of DSC images were as follows: TR = 1360 ms; TE = 30 ms; section thickness = 5 mm; number of slices = 20; FOV read = 229 mm; matrix = 144 × 144; flip angle = 90°; number of acquisitions = 60. Gadolinium contrast medium (Magnevist; Bayer HealthCare Pharmaceuticals) was intravenously injected using a high-pressure injector (Medrad Spectris Solaris EP MR

injection system; Bayer HealthCare) at the fifth acquisition (0.2 mL/kg, 4.5–5 mL/s) and followed immediately by a 30-mL physiologic saline flush.

Surgical Treatment

There is a standard procedure for the EDAS in our institution that is similar to that described previously in the literature.¹³ Generally, the STA and accompanying cuff of the galea connective tissue were exposed and then covered and sutured onto the surface of brain.

Angiography

All participants underwent DSA (Allura Xper FD20 angio system; Philips Healthcare) >3 months after the operation because the development of donor arteries was observed 3 months after indirect surgery.¹⁴ As selective catheterization and intra-arterial injection of nonionic monomeric iodine contrast medium were performed, anterior-posterior and lateral projection images of the bilateral ICAs, external carotid arteries, and dominant-side vertebral artery were obtained.

Data Analysis

MR Imaging Examination. Images of PC-MR imaging and DSC were transmitted to the syngo via (Siemens) postprocessing workstation. Hemodynamic information acquired by PC-MR imaging was obtained by drawing ROIs on the phase images, which contained the lumen of the vessel as much as possible without exceeding the vessel contour. To determine the boundary of the STA, the window width of magnitude images could be narrowed and the junction of hyperintensity (signal of blood flow) and isointensity (signal of soft tissue) was the boundary of the STA. Measurements of mean velocity (V_{mean}), peak velocity (V_{peak}), and blood volume flow (BVF) of the bilateral STA were performed and documented by 2 of the authors (H. Zhang and S. Liu), who had >5 years' experience and were blinded to the clinical symptoms.

DSC data were analyzed by MR perfusion software. Maps of DSC were generated using the local arterial input function mode. ROIs were manually drawn at the lateral MCA territories and cerebellum. The great cerebral vessels and ischemic or hemorrhage lesions were avoided. Relative TTP (rTTP) was calculated by subtracting the value of the MCA territories from the value of the cerebellum. Relative CBF (rCBF) and CBV (rCBV) were calculated by dividing the value of the MCA territories by the value of the cerebellum.¹⁵

DSA Examination. DSA data were independently evaluated by 2 neuroradiologists (H. Zhang and S. Liu) who were blinded to the radiologic findings. We modified the classification proposed by Matsushima et al,¹⁶ and collateral formation after surgery was divided into 4 grades, which included grade III, in which the area supplied by the surgical bypass covered more than two-thirds of the MCA distribution; grade II, in which between two-thirds and one-third of the MCA distribution was covered; grade I, in which less than one-third of the cortical branch of the MCA was covered; and grade 0, in which no collateral circulation was covered. Grades II and III were regarded as good collateral formation, and the others were poor collateral formation. In addition, morphologic

Table 1: Demographic and clinical characteristics

	Patients with MMD, Mean (SD) or No. (%)		P
	Good Collateral Formation (n = 23)	Poor Collateral Formation (n = 22)	
Sex, male	10 (43%)	12 (55%)	.458
Age (yr)	30.87 (SD, 18.36)	37.05 (SD, 17.57)	.256
Hypertension	8 (35%)	9 (41%)	.672
Hyperlipidemia	9 (39%)	11 (50%)	.463
CHD	1 (4%)	0 (0%)	1.000
Diabetes	3 (13%)	2 (10%)	1.000
Smoking	0 (0%)	3 (14%)	.217
DSA interval (mo)	7.11 (SD, 1.69)	7.73 (SD, 1.91)	.256
PCA involvement	4 (17%)	2 (9%)	.704
Diameter of MMA (mm)			
Ipsilateral	2.49 (SD, 0.51)	2.42 (SD, 0.4)	.674
Contralateral	2.30 (SD, 0.45)	2.19 (SD, 0.46)	.417
Preoperative DSC			
Ipsilateral rTTP (sec)	3.36 (SD, 2.07)	1.40 (SD, 1.57)	.002
Contralateral rTTP (sec)	1.72 (SD, 2.10)	1.07 (SD, 2.18)	.353
Ipsilateral CBF (mL/100 g/min)	1.04 (SD, 0.31)	1.31 (SD, 0.44)	.021
Contralateral CBF (mL/100 g/min)	1.18 (SD, 0.34)	1.24 (SD, 0.31)	.540
Ipsilateral CBV (mL/100 g)	1.77 (SD, 0.62)	2.23 (SD, 0.65)	.019
Contralateral CBV (mL/100 g)	1.89 (SD, 0.48)	2.12 (SD, 0.54)	.138
Suzuki stage			.775
I–II	4	2	
III–IV	13	17	
V–VI	6	3	

Note:—CHD indicates coronary heart disease; DSA interval, interval from surgery to DSA examination; PCA, posterior cerebral artery.

features of the ipsilateral STA, which included straightness of the bilateral STA and location of the bifurcation, were also evaluated. The STA with no more than 3 turns was regarded as straight. The high bifurcation position defined as the STA trunk accounted for more than half of the full length of the STA. Furthermore, the diameters of the bilateral middle meningeal artery (MMA) after EDAS surgery were measured on DSA images.

Clinical Follow-up. On the basis of the mRS system, preoperative and postoperative symptoms of patients were evaluated. Postoperative mRS was evaluated at the time of DSA examinations, which were performed at least 3 months after the operation. Participants were assigned to the improved group if their mRS scores improved by at least 1 grade. Patients with no change or worsening of symptoms after EDAS surgery were classified in the poor response group.

Statistical Analysis

Continuous variables were documented as mean (SD). Categorical variables were presented as frequencies. The independent Student *t* test was used if the continuous data adhered to a normal distribution and variance homogeneity. The Mann-Whitney *U* test was used to compare the difference in the Suzuki stage between the 2 groups. Categorical data were compared using the χ^2 test. The sensitivity, specificity, and cutoff values were calculated, respectively. Univariate and multivariable logistic regression models were used to calculate the OR and the corresponding 95% CI of PC-MR imaging in discriminating the collateral foundation and mRS. Interreader and intrareader reliability were determined via intraclass correlation coefficients and 95% CIs or κ values. Results with *P* < .05 were regarded as statistically significant. SPSS 23.0 software (Version 23.0; IBM) was used for statistical analysis.

RESULTS

Patient Characteristics

Among the 45 participants (23 women and 22 men; mean age, 33.89 [SD, 18.04] years), 17 had hypertension (38%), 20 had hyperlipidemia (44%), 5 had diabetes (11%), and 1 (2%) had coronary heart disease. Three (7%) participants had a history of smoking, and the posterior cerebral arteries in 6 (13%) participants were involved. The average time interval from EDAS surgery to the postoperative DSA examination was 7.41 (SD, 1.81) months. The number of participants in Suzuki stages I–II, III–IV, and V–VI was 6 (13%), 30 (67%), and 9 (20%), respectively.

On the basis of the neoangiogenesis after revascularization, 23 participants (grade II revascularization, *n* = 22; grade III, *n* = 1) were observed to have good collateral formation on DSA during follow-up and 22 (grade 0, *n* = 3; grade I, *n* = 19) had poor collateral formation. Preoperative perfusion status including rTTP, rCBF, and rCBV in the ipsilateral hemispheres with good collateral formation was significantly worse than that in those with poor collateral formation (all, *P* value < .05; Table 1). No statistically significant difference was found in other clinical features between the participants with good and poor collateral formation (Tables 1 and 2; Figs 1 and 2).

Association of Hemodynamic Features of STA and Postoperative Collateral Formation

The *V*_{mean} (6.69 [SD, 2.02] cm/s versus 5.30 [SD, 1.41] cm/s, *P* = .011), mean *V*_{peak} (22.62 [SD, 5.79] cm/s versus 17.00 [SD, 6.62] cm/s, *P* = .004), and mean BVF (0.70 [SD, 0.32] mL/s versus 0.50 [SD, 0.17] mL/s, *P* = .013) of the ipsilateral STA in participants with good collateral formation were significantly greater compared with those with poor collateral formation (Table 2 and Fig 3A).

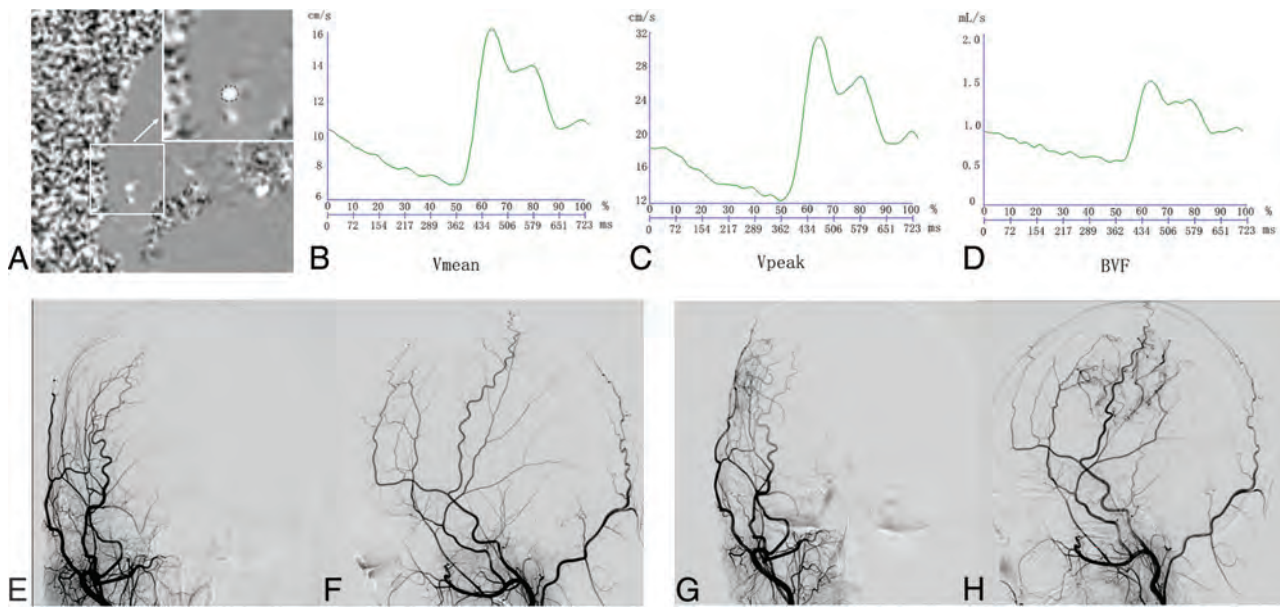


FIG 1. PC-MR imaging and DSA examination in a patient with good collateral formation. Images in a female patient diagnosed with MMD who had right EDAS surgery. She underwent PC-MRI and DSA before and 6 months after the operation. A, Phase image shows the ROI of the right STA. A, the *arrow* represents the enlarged view of the small white square. Modulation of the Vmean (B), Vpeak (C), and BVF (D) of the right STA acquired by PC-MRI. Anterior-posterior and lateral projections of preoperative (E and F) and postoperative (G and H) DSAs of the right external carotid artery show large areas of revascularization (more than one-third but less than two-thirds of MCA territory).

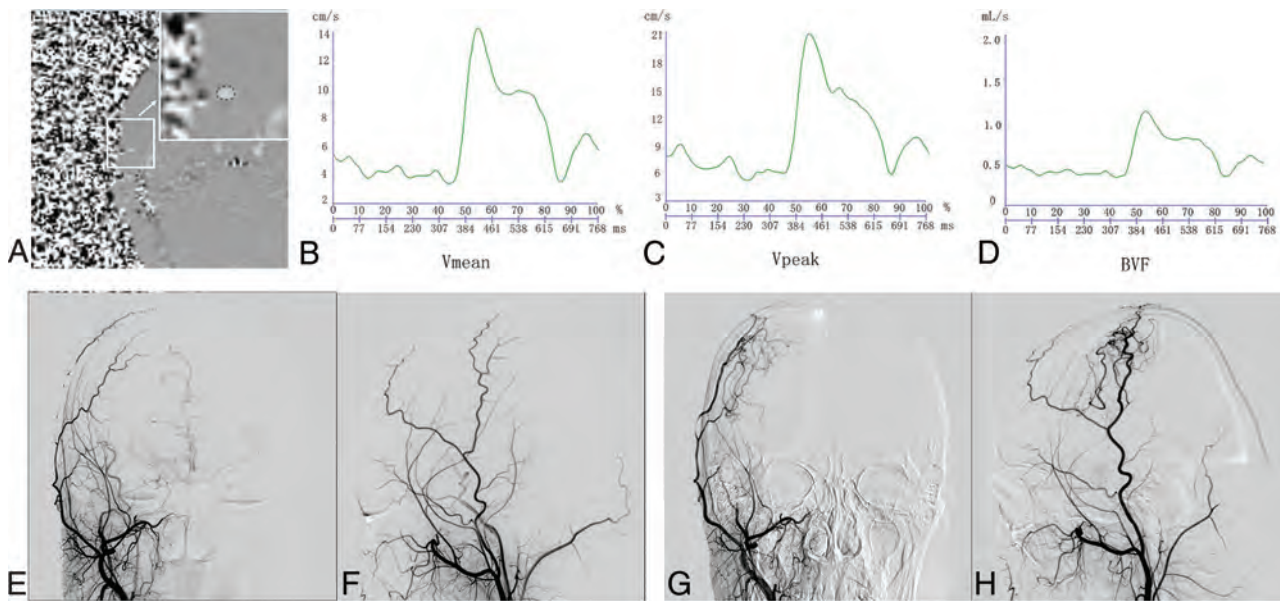


FIG 2. PC-MR imaging and DSA examination in a patient with poor collateral formation. Images in a male patient diagnosed with MMD who had right EDAS surgery. He underwent PC-MRI and DSA before and 7 months after the operation. A, Phase image shows the ROI of the right STA. A, the *arrow* represents the enlarged view of the small white square. Modulation of Vmean (B), Vpeak (C), and BVF (D) of the right STA acquired by PC-MRI. Anterior-posterior and lateral projections of preoperative (E and F) and postoperative (G and H) DSAs of right external carotid artery show small areas of revascularization (less than one-third of the MCA territory).

When the Vmean = 6.020 cm/s was taken as the cutoff value, the sensitivity and specificity of Vmean in predicting good collateral formation were 0.696 and 0.727, respectively. The sensitivity and specificity of Vpeak in predicting good collateral formation were 0.826 and 0.591, respectively, when Vpeak = 18.315 cm/s was taken as the cutoff value. Moreover, the cutoff value of BVF was 0.585 mL/s with a sensitivity of 0.652 and specificity of 0.818.

Univariate logistic analysis showed that greater Vmean (OR = 1.66; 95% CI, 1.08–2.53; $P = .020$), Vpeak (OR = 1.16; 95% CI, 1.04–1.30; $P = .009$), and BVF (OR = 1.04; 95% CI, 1.01–1.07; $P = .024$) of the ipsilateral STA were significantly associated with good collateral formation. Multivariate logistic analysis showed that the association of greater Vmean (OR = 2.28; 95% CI, 1.23–4.25; $P = .009$), Vpeak (OR = 1.18; 95% CI, 1.04–

Table 2: Comparison of measurements of the STA between participants with good and poor collateral formation

	Patients with MMD, Mean (SD) or No. (%)		P
	Good Collateral Formation (n = 23)	Poor Collateral Formation (n = 22)	
Morphologic features of ipsilateral STA			
Cross-sectional area (mm ²)	0.10 (SD, 0.03)	0.09 (SD, 0.02)	.258
Straightness	11 (48%)	13 (59%)	.449
High bifurcation position	10 (43%)	10 (46%)	.894
Morphologic features of contralateral STA			
Cross-sectional area (mm ²)	0.11 (SD, 0.02)	0.12 (SD, 0.04)	.095
Straightness	12 (52%)	2 (55%)	.873
High bifurcation position	14 (61%)	9 (41%)	.181
PC-MR imaging of ipsilateral STA			
Vmean (cm/s)	6.69 (SD, 2.02)	5.30 (SD, 1.41)	.011
Vpeak (cm/s)	22.62 (SD, 5.79)	17.00 (SD, 6.62)	.004
BVF (mL/s)	0.70 (SD, 0.32)	0.50 (SD, 0.17)	.013
PC-MR imaging of contralateral STA			
Vmean (cm/s)	7.08 (SD, 2.92)	6.03 (SD, 1.53)	.141
Vpeak (cm/s)	23.06 (SD, 6.37)	18.75 (SD, 6.07)	.025
BVF (mL/s)	0.74 (SD, 0.35)	0.61 (SD, 0.26)	.166

Note:—Ipsilateral STA indicates superficial temporal artery on the operative side; Contralateral STA, superficial temporal artery on the nonoperative side.

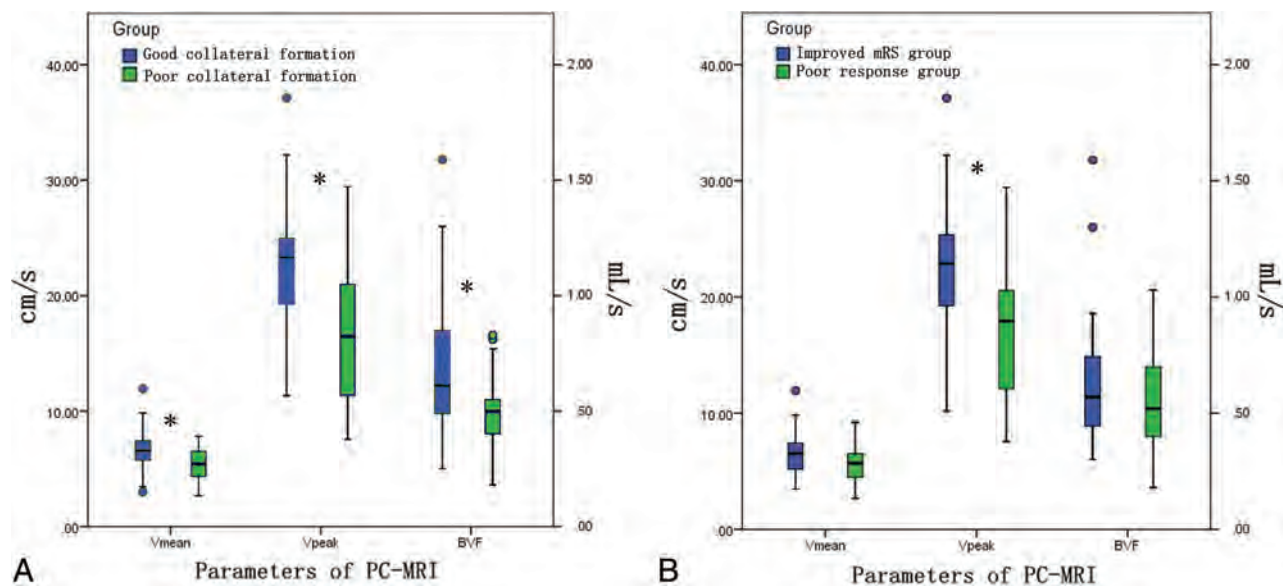


FIG 3. Comparison of PC-MR imaging parameters between patients with good and poor collateral formation (A) and between patients with improved mRS and poor response (B). The asterisk indicates $P < .05$.

1.34; $P = .010$), and BVF (OR = 1.73; 95% CI, 1.02–2.94; $P = .043$) of the ipsilateral STA and good collateral formation remained statistically significant after adjustment of patients' clinical characteristics (age, sex, hypertension, hyperlipidemia, diabetes, smoking, and the interval from the operation to the latest DSA examination), morphologic features of the ipsilateral STA (cross-sectional area, straightness, and high bifurcation position of STA), preoperative perfusion status (rCBV), and diameter of the ipsilateral MMA after EDAS (Table 3).

Association of Hemodynamic Information and Change of mRS

The mean Vpeak (22.13 [SD, 6.59] cm/s versus 17.30 [SD, 6.13] cm/s, $P = .015$) of the ipsilateral STA in participants with an improved

mRS was significantly greater compared with those with a poor response (Table 4 and Fig 3B).

Univariate logistic analysis showed that greater Vpeak (OR = 1.13; 95% CI, 1.02–1.26; $P = .022$) of the ipsilateral STA was significantly associated with improved mRS scores. Multivariate logistic analysis showed that the association of greater Vpeak (OR = 1.18; 95% CI, 1.03–1.34; $P = .014$) of the ipsilateral STA and improved mRS remained statistically significant after adjustment of participants' clinical characteristics (age, sex, hypertension, hyperlipidemia, diabetes, smoking, and the interval from the operation to latest DSA examination), morphologic features of ipsilateral STA (cross-sectional area, straightness, and high bifurcation position of the STA), preoperative rCBV, and diameter of the ipsilateral MMA.

Interaction of Age, Sex, and Preoperative rCBV

In predicting the collateral formation, no interactive effect was found between age and sex or between age and preoperative rCBV or between sex and preoperative rCBV (Table 5).

Reproducibility

κ values for the intrareader agreement in measurement of V_{mean} , V_{peak} , and BVF were 0.83, 0.92 and 0.85, respectively. For inter-reader agreement, the κ values were 0.80, 0.91, and 0.77 in the measurement of V_{mean} , V_{peak} , and BVF. The intrareader agreement in evaluating collateral formation was 0.82.

DISCUSSION

To our knowledge, this is the first study investigating the relationship between the preoperative hemodynamic status of the ipsilateral STA as a donor artery and the postoperative outcomes of patients with MMD using PC-MR imaging. We found that patients with greater V_{mean} , V_{peak} , and BVF of the ipsilateral STA were more likely to have better postoperative collateral formation. Furthermore, V_{peak} of the ipsilateral STA was associated with improvement of symptoms. Our results suggest that good hemodynamic status of ipsilateral STA may serve as a predictor of favorable outcome in patients with MMD after EDAS surgery.

The PC-MR imaging technique has been widely used in quantitatively analyzing vascular diseases and evaluating hemodynamic status.^{17,18} The hemodynamic characteristics of intracranial vessels in patients with MMD have been evaluated in previous studies using PC-MR imaging, and most of them explored the hemodynamic change of the anterior and posterior circulation before and after the operation.^{10,11,19} However, few studies focused on the hemodynamic status of the STA. EDAS, as one of the most commonly used indirect surgical procedures in MMD, mostly adopted

STA and its branches as donor arteries. Therefore, the hemodynamic features of the STA before the operation may be more significantly associated with the postoperative outcomes compared with those of the ICA and the posterior cerebral artery. In the present study, we used PC-MR imaging to assess the velocity and BVF of the STA and found an excellent reliability in the measurements of these hemodynamic parameters.

EDAS surgery reroutes branches of the external carotid artery such as the STA to the surface of the brain. With the development of collateral circulation, blood flow is diverted from the external carotid artery to the blood supply area of the ICA. Therefore, abundant blood flow in the STA enables the formation of collateral circulation after EDAS surgery. The mechanism by which the good hemodynamic status of the STA may promote the development of collateral circulation may be as follows: 1) The greater blood volume flow of the STA may provide sufficient blood supply for collateral formation, and 2) the higher flow velocity of the STA may indicate better vasoreactivity and function status as a donor artery, which can enable richer neovascularization after EDAS. In this study, we found that there were no significant differences in the morphologic features of the ipsilateral STA, which included caliber, straightness, and high bifurcation position, between patients with good and poor collateral formation. This finding may be because morphologic information about the STA could not directly reflect the hemodynamic status. Therefore, morphologic features of the ipsilateral STA alone could not be used to predict the prognosis of EDAS surgery.

In the present study, we found that the greater V_{mean} , V_{peak} , and BVF of the ipsilateral STA were significantly associated with good collateral formation after EDAS surgery. The cutoff values of V_{mean} , V_{peak} , and BVF were 6.020 cm/s, 18.315 cm/s, and 0.585 mL/s, respectively. Furthermore, no statistically interactive effect was found among clinical factors (age, sex and preoperative rCBV) in predicting collateral formation. A previous study showed that the blood flow velocity of the STA as the bypass artery could be used to predict the postoperative outcomes in the direct revascularization surgery using sonography.²⁰ Similar to the conclusion of the sonographic study, we found that good hemodynamic status was also associated with a favorable outcome after EDAS surgery, which is an indirect revascularization surgery mostly using the STA as a donor artery. Thus, we recommend that for patients with MMD, PC-MR imaging could be regarded as a supplementary examination to predict collateral formation after EDAS surgery.

Our results showed greater V_{peak} of the ipsilateral STA closely related to the improved mRS scores after the operation, suggesting that better hemodynamic status of the ipsilateral STA may serve as a predictor of clinical outcomes in patients with MMD. As discussed above, the ipsilateral STA with better hemodynamic status correlated with more abundant collateral circulation formation, which could provide sufficient blood flow. Therefore, this result ameliorated the ischemic status of the hemispheres, and better mRS scores were obtained. In

Table 3: Association of hemodynamic status of the ipsilateral STA and collateral formation using logistic regression analysis^a

	Univariate Regression			Multivariate Regression		
	OR	95% CI	P	OR	95% CI	P
V_{mean}	1.66	1.08–2.53	.020	2.28	1.23–4.25	.009
V_{peak}	1.16	1.04–1.30	.009	1.18	1.04–1.34	.010
BVF	1.04	1.01–1.07	.024	1.73	1.02–2.94	.043

^a Multivariate regression was adjusted for age, sex, hypertension, hyperlipidemia, diabetes, smoking, interval from the operation to the latest DSA examination, cross-sectional area, straightness and high bifurcation position of the STA, preoperative rCBV, and the diameter of the MMA after EDAS.

Table 4: Comparison of PC-MR imaging of STA between participants with improved mRS and those with poor response

	Patients with MMD, Mean (SD) or No. (%)		P
	Improved mRS (n = 24)	Poor Response mRS (n = 21)	
PC-MR imaging of ipsilateral STA			
V_{mean} (cm/s)	6.43 (SD, 1.91)	5.53 (SD, 1.73)	.106
V_{peak} (cm/s)	22.13 (SD, 6.59)	17.30 (SD, 6.13)	.015
BVF (mL/s)	0.65 (SD, 0.30)	0.55 (SD, 0.24)	.268
PC-MR imaging of contralateral STA			
V_{mean} (cm/s)	6.92 (SD, 2.37)	6.15 (SD, 2.50)	.295
V_{peak} (cm/s)	21.97 (SD, 6.60)	19.79 (SD, 6.22)	.263
BVF (mL/s)	0.71 (SD, 0.28)	0.64 (SD, 0.34)	.453

Table 5: Interactive effects of age, sex, and rCBV on collateral formation

	F	P
Age	1.829	.186
Sex	1.773	.193
rCBV	1.839	.185
Age × sex	1.781	.192
Age × rCBV	1.832	.186
Sex × rCBV	1.756	.195
Age × sex × rCBV	1.77	.193

addition, Gao et al¹² found that patients with poor hemodynamic status of the ipsilateral STA were more likely to develop cerebral hyperfusion syndrome, which could result in lower mRS scores.

This study had several limitations. First, the sample size of the study is limited, and further investigations with larger sample sizes are warranted. Second, in the present study, 2D-PC-MR imaging was used to assess the hemodynamic features. Recently, 3D-PC-MR imaging has been increasingly used in the evaluation of vascular diseases, which could be more time-saving and provide more information. Third, the present study included only patients with MMD who had undergone unilateral EDAS surgery; therefore, the prognosis of those who underwent bilateral surgery should be further investigated using PC-MR imaging. Fourth, the hemodynamic status of the MMA and the accessory meningeal artery before and after EDAS surgery was not included.

CONCLUSIONS

The good hemodynamic status of the ipsilateral STA as a donor artery evaluated by PC-MR imaging was significantly associated with better collateral formation and improved mRS after EDAS surgery in patients with MMD. Our results suggest that PC-MR imaging could provide valuable information on the prediction of clinical outcomes in patients with MMD after EDAS surgery.

Disclosure forms provided by the authors are available with the full text and PDF of this article at www.ajnr.org.

REFERENCES

1. Suzuki J, Takaku A. Cerebrovascular “Moyamoya” disease: disease showing abnormal net-like vessels in base of brain. *Arch Neurol* 1969;20:288–99 CrossRef Medline
2. Research Committee on the Pathology and Treatment of Spontaneous Occlusion of the Circle of Willis; Health Labour Sciences Research Grant for Research on Measures for Intractable Diseases. Guidelines for diagnosis and treatment of Moyamoya disease (spontaneous occlusion of the circle of Willis). *Neurol Med Chir* 2012;52:245–66 CrossRef Medline
3. Acker G, Fekonja L, Vajkoczy P. Surgical management of Moyamoya disease. *Stroke* 2018;49:476–82 CrossRef Medline
4. Park SE, Kim JS, Park EK, et al. Direct versus indirect revascularization in the treatment of Moyamoya disease. *J Neurosurg* 2018;129:480–89 CrossRef Medline

5. Nakashima H, Meguro T, Kawada S, et al. Long-term results of surgically treated Moyamoya disease. *Clin Neurol Neurosurg* 1997;99 (Suppl 2):S156–61 CrossRef Medline
6. Ishii D, Okazaki T, Matsushige T, et al. Chronic dilatation of superficial temporal artery and middle meningeal artery associated with development of collateral circulation after bypass surgery for Moyamoya angiopathy. *World Neurosurg* 2018;119:e864–73 CrossRef Medline
7. Zhao J, Liu H, Zou Y, et al. Clinical and angiographic outcomes after combined direct and indirect bypass in adult patients with Moyamoya disease: a retrospective study of 76 procedures. *Exp Ther Med* 2018;15:3570–76 CrossRef Medline
8. Spilt A, Box FM, van der Geest RJ, et al. Reproducibility of total cerebral blood flow measurements using phase-contrast magnetic resonance imaging. *J Magn Reson Imaging* 2002;16:1–5 CrossRef Medline
9. Henriksen OM, Larsson HBW, Hansen AE, et al. Estimation of intersubject variability of cerebral blood flow measurements using MRI and positron emission tomography. *J Magn Reson Imaging* 2012;35:1290–99 CrossRef Medline
10. Neff KW, Horn P, Schmiedek P, et al. 2D cine phase-contrast MRI for volume flow evaluation of the brain-supplying circulation in Moyamoya disease. *AJR Am J Roentgenol* 2006;187:W107–15 CrossRef Medline
11. Khan N, Lober RM, Ostergren L, et al. Measuring cerebral blood flow in Moyamoya angiopathy by quantitative magnetic resonance angiography noninvasive optimal vessel analysis. *Neurosurgery* 2017;81:921–27 CrossRef Medline
12. Gao F, Zhao W, Zheng Y, et al. Phase-contrast magnetic resonance imaging analysis of cerebral hyperperfusion syndrome after surgery in adult patients with Moyamoya disease. *World Neurosurg* 2019;129:e48–55 CrossRef Medline
13. Dusick JR, Gonzalez NR, Martin NA. Clinical and angiographic outcomes from indirect revascularization surgery for Moyamoya disease in adults and children: a review of 63 procedures. *Neurosurgery* 2011;68:34–43; discussion 43 CrossRef Medline
14. Houkin K, Nakayama N, Kuroda S, et al. How does angiogenesis develop in pediatric Moyamoya disease after surgery? A prospective study with MR angiography. *Childs Nerv Syst* 2004;20:734–41 CrossRef Medline
15. Nael C, Kronsteiner N, Schindler E, et al. Standardized time to peak in ischemic and regular cerebral tissue measured with perfusion MR imaging. *AJNR Am J Neuroradiol* 2004;25:945 Medline
16. Matsushima T, Inoue T, Suzuki SO, et al. Surgical treatment of Moyamoya disease in pediatric patients: comparison between the results of indirect and direct revascularization procedures. *Neurosurgery* 1992;31:401–05 CrossRef Medline
17. Zarrinkoob L, Wählin A, Ambarki K, et al. Blood flow lateralization and collateral compensatory mechanisms in patients with carotid artery stenosis. *Stroke* 2019;50:1081–88 CrossRef Medline
18. Ando T, Sekine T, Murai Y, et al. Multiparametric flow analysis using four-dimensional flow magnetic resonance imaging can detect cerebral hemodynamic impairment in patients with internal carotid artery stenosis. *Neuroradiology* 2020;62:1421–31 CrossRef Medline
19. Zhu F, Qian Y, Xu B, et al. Quantitative assessment of changes in hemodynamics of the internal carotid artery after bypass surgery for Moyamoya disease. *J Neurosurg* 2018;129:677–83 CrossRef Medline
20. Arakawa S, Kamouchi M, Okada Y, et al. Ultrasonographically predicting the extent of collateral flow through superficial temporal artery-to-middle cerebral artery anastomosis. *AJNR Am J Neuroradiol* 2003;24:886–91 Medline

Quantitative Intracerebral Iodine Extravasation in Risk Stratification for Intracranial Hemorrhage in Patients with Acute Ischemic Stroke

C. Ma, D. Xu, Q. Hui, X. Gao, and M. Peng



ABSTRACT

BACKGROUND AND PURPOSE: Intracerebral hemorrhage poses a severe threat to the outcomes in patients with postthrombectomy acute stroke. We aimed to compare the absolute intracerebral iodine concentration and normalized iodine concentration ratio in predicting intracerebral hemorrhage in patients postthrombectomy.

MATERIALS AND METHODS: Patients with acute anterior circulation large-vessel occlusion who underwent mechanical thrombectomy and had successful recanalization were retrospectively included in the study. Dual-energy CT was performed within 1 hour after mechanical thrombectomy. Postprocessing was performed to measure the absolute intracerebral iodine concentration and the normalized iodine concentration ratio. The correlation between the absolute intracerebral iodine concentration and the normalized iodine concentration ratio was analyzed using the Spearman rank correlation coefficient. We compared the area under the receiver operating characteristic curve of the absolute intracerebral iodine concentration and the normalized iodine concentration ratio using the DeLong test.

RESULTS: We included 138 patients with successful recanalization. Of 43 patients who did not have parenchymal contrast staining on postthrombectomy dual-energy CT, 5 (11.6%) developed intracerebral hemorrhage. Among patients (95/138, 68.8%) with parenchymal contrast staining, 37 (38.9%, 37/95) developed intracerebral hemorrhage. The absolute intracerebral iodine concentration was significantly correlated with the normalized iodine concentration ratio ($\rho = 0.807$; 95% CI, 0.718–0.867; $P < .001$). The cutoffs of the normalized iodine concentration ratio and absolute intracerebral iodine concentration for identifying patients with intracerebral hemorrhage development were 222.8%, with a sensitivity of 67.6% and specificity of 76.4%, and 2.7 mg I/mL, with a sensitivity of 75.7% and specificity of 65.5%, respectively. No significant difference was found between the areas under the receiver operating characteristic curve for the absolute intracerebral iodine concentration and the normalized iodine concentration ratio (0.753 versus 0.738) ($P = .694$).

CONCLUSIONS: The hemorrhagic transformation predictive power of the normalized iodine concentration ratio is similar to that of the absolute intracerebral iodine concentration in patients with successful recanalization.

ABBREVIATIONS: AIIC = absolute intracerebral iodine concentration; AUC = area under the receiver operating characteristic curve; DECT = dual-energy CT; ICH = intracerebral hemorrhage; IQR = interquartile range; MT = mechanical thrombectomy; NICR = normalized iodine concentration ratio; SSS = superior sagittal sinus

Endovascular mechanical thrombectomy (MT) has become the management choice for acute ischemic anterior circulation large-vessel stroke and is implemented within up to 24 hours after stroke onset.^{1,2} Although advances have been made in patient

selection for endovascular recanalization, clinical outcomes vary after thrombectomy.³ Intracerebral hemorrhage (ICH) poses a severe potential threat to outcomes in patients postthrombectomy.⁴

Hyperattenuation commonly appears on NCCT after the MT procedure.^{5–7} Both iodine contrast agent extravasation and hemorrhage can be seen as high attenuation on NCCT. Differentiating contrast staining from hemorrhage is challenging in conventional single-energy CT.⁵ In dual-energy CT (DECT), remarkable progress has been made in material separation through the use of material-specific methods; consequently, it is easy to identify whether such high attenuation is due to hemorrhage or iodine contrast staining.^{8–11} At the same time, DECT parameters can be used to quantify iodine contrast staining. A recent study by Bonatti et al¹²


Received June 3, 2022; accepted after revision September 7.

From the Departments of Radiology (C.M., Q.H., X.G.), Laboratory (D.X.), and Neurology (M.P.), Deyang People's Hospital, Deyang, Sichuan, China.

Dan Xu made an equal contribution to this study.

This work was funded by the Deyang City Science and Technology Research Foundation Grant No. 2022SCZ116.

Please address correspondence to Chun Ma, MD, Department of Radiology, Deyang People's Hospital, Deyang, 61800, Sichuan, China; e-mail: windeyesword@163.com

 Indicates article with online supplemental data.

<http://dx.doi.org/10.3174/ajnr.A7671>

suggested that quantitative iodine contrast staining plays an essential role in predicting hemorrhagic transformation in patients after MT. Byrne et al¹³ hypothesized that systematic differences, namely the timing/volume of contrast agent administration, procedural technique, and patient-related factors, might lead to variability in iodine quantification. They used the relative ratio of the maximum iodine concentration in the brain parenchyma to the iodine concentration in the superior sagittal sinus (SSS) on DECT after

MT to reduce the variability and improve the prediction of hemorrhagic transformation on follow-up CT.

This study included patients with small infarct cores and good recanalization. It was concluded that compared with the absolute intracerebral iodine concentration (AIIC) measured in the parenchymal hyperattenuating area, the relative ratio of the maximum iodine concentration to the iodine concentration in the SSS (normalized iodine concentration ratio [NICR]) was a better predictor of ICH development than the absolute values.

In our clinical practice, we had observed that a higher AIIC was strongly correlated with late development of ICH in patients postthrombectomy with good reperfusion. Therefore, we aimed to investigate a homogeneous cohort of patients, similar to the study by Byrne et al,¹³ with ASPECTS of ≥ 7 and good endovascular reperfusion, to compare the capability of the AIIC and NICR in predicting ICH development in patients postthrombectomy.

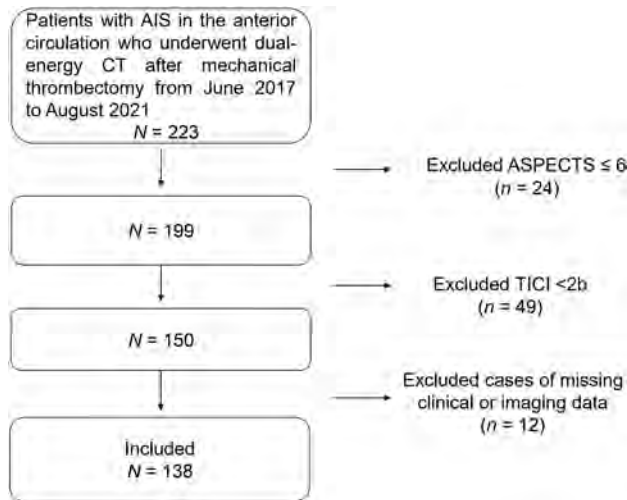


FIG 1. Flow chart of the steps involved in patient inclusion and exclusion.

MATERIALS AND METHODS

Study Population

The local institutional research ethics review board approved this retrospective study and waived the need for written consent from patients. From June 2017 to August 2021, consecutive patients who underwent MT for acute anterior circulation large-vessel ischemic stroke were enrolled in this study. The inclusion criteria were as follows: MT performed for anterior circulation large-vessel occlusion with an onset time within 6 hours. The exclusion criteria included no imaging data or missing imaging data, ASPECTS ≤ 6 , unsuccessful endovascular recanalization (TICI score, $< 2b$), proximal ICA occlusion, and nonqualified CT image quality (Fig 1).

Table 1: Scanning parameters of the noncontrast CT and noncontrast DECT

	Single-Source CT	Dual-Energy CT
Scanner	Somatom Emotion 16	Somatom FORCE
Manufacturer	Siemens	Siemens
Scanning mode	Spiral	Spiral
Scanning direction	Caudal-cranial	Caudal-cranial
kV(p) (kV)	110	80/Sn 150
Reference mAs	240	310/207
Collimation (mm)	16 × 0.6	192 × 0.6
Section thickness (mm)	5	1
Rotation time (sec)	0.6	1
Pitch	0.65	0.7
CARE Dose 4D ^a	On	On
Reconstruction (A + B)		
Kernel	H41s medium+	Hr40
Iterative algorithm	NA	ADMIRE 2

Note:—ADMIRE indicates advanced modeled iterative reconstruction; NA, not applicable.

^aSiemens.

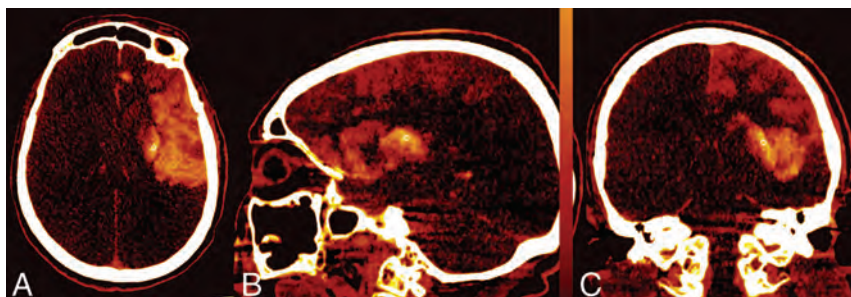


FIG 2. Examples of ROIs drawn on axial, coronal, and sagittal iodine overlay maps.

Imaging Protocol

NCCT scans were performed at admission and at the 24- to 8-hour follow-up time point using a single-source CT scanner (Somatom Emotion 16; Siemens). Noncontrast DECT was performed to assess patients within 1 hour after MT in the dual-energy mode (Somatom Definition Force; Siemens). The scanning parameters used in NCCT and noncontrast DECT are shown in Table 1.

Clinical-Radiologic Data Collection

We collected the following patient data from our medical database: sex, age, ASPECTS, NIHSS score at admission, site of occlusion, thrombectomy devices, history of hypertension, history of diabetes mellitus, history of atrial fibrillation, number of attempts at aspiration or stent retriever placement, procedural duration, onset time to puncture, thrombolytic therapy, and other treatments during hospitalization. The mRS scores were used to quantify the clinical outcomes 90 days after onset.

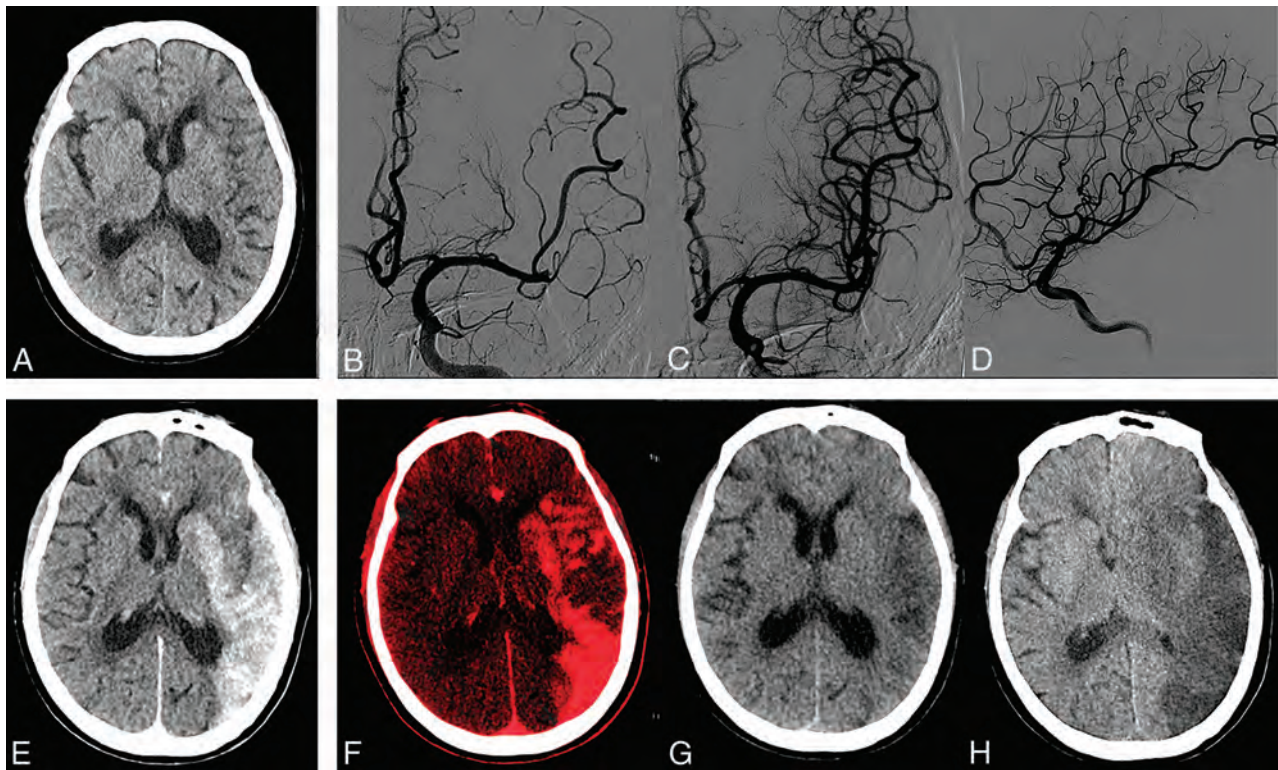


FIG 3. A 75-year-old woman with an ASPECTS of 7 on preprocedural CT (A). B, C, and D, Left M2 middle trunk occlusion with modified TIC1 3 recanalization. E, Simulated conventional 120 kV(peak) images show hyperattenuation involving the left basal ganglia and temporal, frontal, and parietal lobes. F, Iodine overlay maps show contrast staining, with the AIIc (2.4 mg I/mL) and NICR (151.9%), respectively. G, Virtual noncontrast CT reveals no hemorrhage signs. H, Contrast staining resolved on 36-hour follow-up CT. Her 90-day mRS score was 4.

Image Analysis

Two neuroradiologists (X.G. and C.M., with >5 years of neuro-radiology experience) jointly evaluated the head NCCT and CTA images and recorded ASPECTS and regional leptomeningeal collateral scores at admission.¹⁴ Two interventional neuroradiologists (M.P. and H.C., with ≥ 16 years of interventional neuroradiology experience) performed the thrombectomy procedure and recorded the modified TIC1 score in each case.

X.G. and C.M. evaluated the DECT images using a commercially available software application (syngo.via, DECT brain hemorrhage application, Version VA30A; Siemens). Simulated 120-kV images (nonlinear blending images), virtual noncontrast images, and iodine overlay maps were generated using a 3-material decomposition algorithm.

Three mutually perpendicular ROIs (0.1–0.3 cm²) were subjectively placed at the site of maximum apparent contrast staining in the axial, coronal, and sagittal images (Fig 2). The iodine concentration was obtained by averaging these 3 values. To normalize the contrast concentration, we placed an ROI on the SSS while the NICR mode was selected. The NICR was calculated as follows: $NICR = I_{\text{staining}}/I_{\text{SS}} \times 100\%$, where I_{staining} and I_{SS} represent the absolute iodine concentrations of the contrast staining and SSS, respectively.¹³ We used the average of the values recorded by the 2 neuroradiologists in the statistical analysis. Two reviewers analyzed the virtual noncontrast images and iodine overlay maps to distinguish hemorrhage from iodinated contrast extravasation and reached an agreement. High attenuation present on the iodine overlay

map that was not present on the virtual noncontrast map was classified as contrast staining. High attenuation on the virtual noncontrast map was classified as hemorrhage. The 2 radiologists jointly analyzed the follow-up CT images, and a consensus was reached on the diagnosis of hemorrhagic transformation. The locations of the contrast staining and hemorrhage were recorded (parenchymal, subarachnoid, or intraventricular). The occurrence of fresh high-attenuation or high-attenuation incongruous with that of postoperative DECT was classified as hemorrhage on the basis of the neurologic status of the patients. According to the European Cooperative Acute Stroke Study classification, the development of hemorrhagic transformation was evaluated in follow-up NCCT images.¹⁵ We divided these patients into subgroups on the basis of DECT and follow-up examinations. The present study focused only on the 2 groups with iodine staining with and without ICH. We divided the 2 groups into subgroups (groups with ASPECTS of ≤ 8 and > 8).

Statistics Analysis

Continuous variables were summarized using mean (SD) and median and interquartile range (IQR) as appropriate, after assessing normality using the Shapiro-Wilk test. To compare subgroups, we used a Student *t* test for continuous variables with normal distribution, the Mann-Whitney *U* test for continuous variables with non-normal distribution, or the Pearson χ^2 /Fisher exact test for categorical data. The intraclass correlation coefficient was calculated to determine the interrater reliability: <0.50, poor; 0.5–0.75, moderate; 0.75–0.90, good; and >0.90, excellent. The Spearman rank

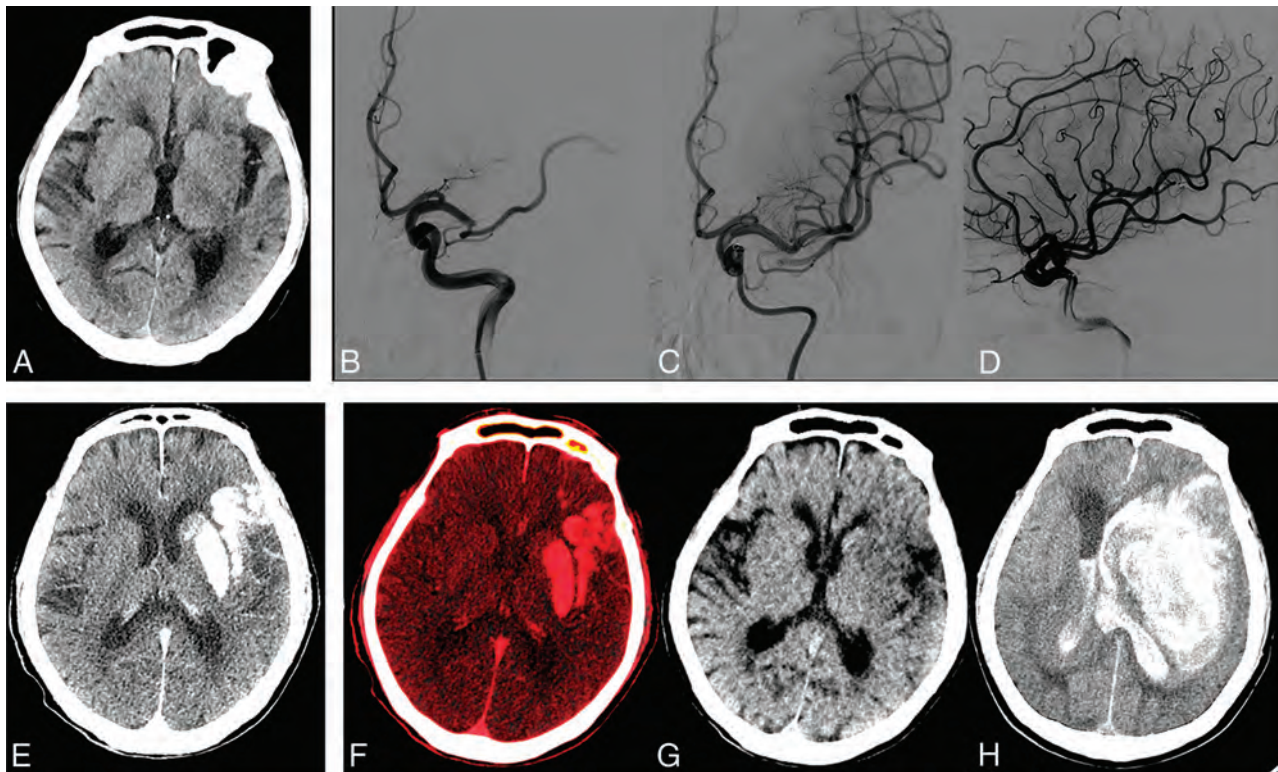


FIG 4. An 80-year-old man with an ASPECTS of 7 on admission CT (A). B, C, and D, Left M1 occlusion with modified TIMI 3 recanalization. E, Simulated conventional 120 kV(p) images show contrast staining involving the left basal ganglia and temporal lobe. F, Iodine overlay maps show contrast staining, with the AIC (4.9 mg I/mL) and the NICR (317.3%), respectively. G, Virtual noncontrast CT shows no hemorrhage signs in the area with hyperattenuation in simulated conventional 120 kV(p) images. H, Parenchymal hematoma type 2 develops with a marked midline shift on 24-hour follow-up CT. The patient died 6 days after recanalization (mRS score of 6).

correlation coefficient was used to analyze the correlation between the AIC and NICR. We compared the AIC and NICR parameters in terms of ICH development on follow-up CT. We compared the area under the receiver operating characteristic curve (AUC) of the AIC and NICR using the DeLong test. Statistical analyses were performed using SPSS 22.0 (Version 22.0; IBM), GraphPad Prism (GraphPad Software), and MedCalc (MedCalc Software). A 2-sided $P < .05$ was considered a significant difference.

RESULTS

Patient Population

Among 223 consecutive patients with acute anterior circulation stroke who underwent thrombectomy, 138 were included in our study. The median age was 69 years (IQR, 62–77 years), and 72 patients were male (52.2%).

The mean baseline NIHSS score was 16.8 (SD, 6.8) in patients who met the inclusion criteria. The mean ASPECTS at admission was 9 (IQR, 8–9). Aspiration was performed in 27 patients, and 88 patients were treated with only a stent retriever. Twenty-three patients underwent aspiration followed by stent retriever placement during the thrombectomy procedure. The median number of attempts at aspiration or stent retriever placement was 1 (IQR, 1–2).

Quantitative Analyses

ICH Development. No contrast staining was seen in the initial DECT scan after thrombectomy in 43 of 138 patients (43/138,

31.2%); among these patients, 2 (2/43, 4.7%) developed parenchymal hematoma type 1, as seen on follow-up NCCT at 48 hours. Three patients (3/43, 7.0%) developed hemorrhagic infarction type 1. In all patients (95/138, 68.8%) with intracranial contrast staining, contrast staining was observed only at the brain parenchyma. On the basis of virtual noncontrast images and iodine overlay maps, contrast staining combined with hemorrhage was seen in only 2 patients (2/138, 1.4%). Follow-up NCCT revealed that 2 patients developed parenchymal hematoma type 2. Of the remaining 93 patients with contrast staining, follow-up NCCT showed that 35 patients (35/93, 37.6%) had hemorrhagic transformation (Online Supplemental Data). Figures 3 and 4 illustrate the development of varied outcomes in patients with contrast staining.

Among the 95 patients with contrast staining, patients (37/95, 38.9%) with ICH development had no significant difference in baseline ASPECTS compared with those (58/95, 61.1%) without ICH development ($P = .348$). Patients with ICH development had lower regional leptomeningeal collateral scores (9.4 ± 4.6) than those without ICH development (11.8 [SD, 4.3]; $P = .01$). Apart from the difference in the presence of diabetes mellitus, no significant differences were found in the other clinical characteristics of the cohorts, including sex, age, hypertension, atrial fibrillation, baseline NIHSS score, MT duration, time of symptom onset to puncture, platelet count, hypersensitive C-reactive protein level, occlusion site, thrombectomy devices, attempts at aspiration or stent retriever placement, and treatment during

Table 2: Univariate analysis of patients' baseline characteristics in cohorts with iodine staining without and with ICH (n = 95)

Patient Characteristics	No Hemorrhage (n = 58)		P Value
	Hemorrhage (n = 37)		
Age (mean) (SD) (yr)	68 (12.1)	67.7 (11.6)	.897 ^a
Male sex (No.) (%)	28 (48.3%)	19 (51.3%)	.770 ^b
History of hypertension (No.) (%)	28 (48.3%)	18 (48.6%)	.972 ^b
History of diabetes mellitus (No.) (%)	13 (22.4%)	17 (45.9%)	.016 ^b
History of atrial fibrillation (No.) (%)	28 (48.3%)	12 (32.4%)	.105 ^b
MT duration (median) (IQR) (min)	70 (55–95)	60 (46–90)	.310 ^c
Time of symptom onset to puncture (median) (IQR) (min)	200 (144–313)	230 (178–343)	.169 ^c
ASPECTS (median) (IQR)	8 (7–9)	8 (7–9)	.348 ^c
Baseline NIHSS (mean) (SD)	16 (6)	19 (7)	.067 ^a
rLMC (mean) (SD)	11.8 (4.3)	9.4 (4.6)	.01 ^a
Platelet count (median) (IQR) (10 ⁹ /L)	133.8 (96.7–175.4)	130 (100.3–167.9)	.694 ^c
hs-CRP (median) (IQR) (mg l/L)	8.4 (1.2–45.3)	6.9 (0.5–41.2)	.904 ^c
Occlusion site			
ICA occlusion (No.) (%)	15 (25%)	13 (31.5%)	.334 ^b
M1 trunk occlusion (No.) (%)	30 (51.7%)	18 (48.6%)	.770 ^b
M2 trunk occlusion (No.) (%)	13 (22.4%)	6 (16.2%)	.461 ^b
Thrombectomy devices			
Solitaire ^d	13 (22.4%)	8 (21.6%)	.983 ^b
Sofia ^e + Aperio ^f	13 (22.4%)	10 (27%)	.609 ^b
Aperio	20 (34.5%)	14 (37.8%)	.739 ^b
Sofia	12 (20.7%)	5 (13.5%)	.374 ^b
Attempts of aspiration or stent retriever (median) (IQR)	1 (1–1)	1 (1–1)	.840 ^c
Antiplatelet therapy (No.) (%)	39 (67.2)	25 (67.6)	.974 ^b
Thrombolytic therapy (No.) (%)	12 (20.7)	7 (18.9)	.833 ^b
Anticoagulant therapy (No.) (%)	12 (20.7)	6 (16.2)	.587 ^b
Statin treatment (No.) (%)	29 (50)	24 (64.9)	.155 ^b

Note.—rLMC indicates regional leptomeningeal collateral score; hs-CRP, hypersensitive c-reactive protein.

^a One-way ANOVA.

^b Pearson χ^2 test.

^c Mann-Whitney test.

^d Covidien.

^e Microvention.

^f Acandis.

Table 3: DECT parameters in groups without and with subsequent ICH

DECT Parameters	Follow-up CT		P Value
	No ICH	ICH	
AIIC (median) (IQR) (mg I/mL)	2.0 (1.7–4.5)	5.9 (2.7–11.4)	<.001
NICR (median) (IQR) (%),	144.5 (105.8–221.0)	330.6 (181.8–703.3)	<.001
90-Day mRS (4–6) (%)	30.2 (29/96)	57.1 (24/42)	.003

hospitalization ($P = .016$). Table 2 presents the baseline clinical data of the cohorts with iodine staining with and without ICH. Patients with diabetes mellitus had a higher incidence of ICH (17/30, 56.7%) than those without diabetes mellitus (20/65, 30.8%) ($P = .016$).

Imaging Analyses. The median AIIC was 2.0 mg I/mL (IQR, 1.7–4.5 mg I/mL; range, 0.4–18.3 mg I/mL) in 58 patients with contrast staining without ICH development and 5.9 mg I/mL (IQR, 2.7–11.4 mg I/mL; range, 1.0–25.2 mg I/mL) in 37 patients who developed ICH, as seen on follow-up images. The 2 groups showed a significant difference ($P < .001$). The median NICR was significantly different between the cohorts: 144.5% (IQR, 105.8%–221.0%) in patients without ICH development versus

330.6% (IQR, 181.8%–703.3%) in patients with ICH development ($P < .001$). Of the 96 patients without ICH development among the total of 138 patients, 30.2% (29/96) had a 90-day mRS score of 4–6, which was significantly different from that in 57.1% of patients (24/42) with ICH development ($P = .003$) (Table 3). The AIIC was significantly correlated with the NICR ($\rho = 0.807$; 95% CI, 0.718–0.867) (Fig 5). The AUCs of the AIIC and NICR were 0.753 (95% CI, 0.652–0.837; $P < .001$) and 0.738 (95% CI, 0.638–0.823; $P < .001$), respectively, in identifying patients with ICH development. The DeLong test for analyzing the AUCs of the AIIC and NICR showed no significant differences between the groups ($Z = 0.394$, 95% CI, –0.006–0.09; $P = .69$). For identifying patients with ICH development, the cutoff NICR was 222.8% with a sensitivity of 67.6% and specificity of 76.4% (likelihood ratio, 2.355), and the cutoff AIIC was 2.7 mg I/mL with a sensitivity of 75.7% and specificity of 65.5% (likelihood ratio, 2.693). There was excellent agreement between the iodine concentrations obtained by the 2 readers. The intraclass correlation coefficient of the AIIC was 0.932 ($P < .001$) and that of the NICR was 0.942 ($P < .001$).

Subgroups Analyses. Of the 95 patients with contrast staining, there were 52 (52/95, 54.7%) patients with ASPECTS of ≤ 8 and 43 (43/95, 45.3%) patients with ASPECTS of > 8 . Among patients with ASPECTS of ≤ 8 , twenty-two patients (22/52, 42.3%) developed ICH. No ICH transformation was observed in the remaining 30 patients (30/52, 57.7%). In

patients with ASPECTS > 8 , there were 15 (15/43, 34.9%) patients with ICH development and 28 (28/43, 65.1%) patients without ICH development.

AIIC and NICR were significantly different in patients (ASPECTS ≤ 8) without ICH and in those (ASPECTS ≤ 8) with ICH ($P = .008$ and $P = .018$, respectively). AIIC and NICR were lower in patients (ASPECTS > 8) without ICH than that in patients (ASPECTS > 8) with ICH ($P = .005$ and $P = .002$, respectively). No significant differences were found in AIIC and NICR between the subgroups (ASPECTS > 8 and ASPECTS ≤ 8) without ICH ($P = .17$ and $P = .134$, respectively). The same results were found in AIIC and NICR between the subgroups (ASPECTS > 8 and ASPECTS ≤ 8) with ICH ($P = .225$ and $P = .28$, respectively) (Online Supplemental Data).

No significant differences were seen in the AIIC and NICR between patients with hemorrhagic infarction type 1 and parenchymal hematoma. The AIIC was higher in patients with parenchymal hematoma type 2 development than in those with hemorrhagic infarction type 1 and parenchymal hematoma type 1 development (Table 4).

DISCUSSION

In this study, we examined patients with small infarct areas at admission who underwent successful MT. Our findings suggest that the AIIC can be used to identify patients with ICH development. Similarly, the NICR could be used to reliably identify patients with hemorrhagic transformation in the same cohort. A significant correlation was observed between the AIIC and NICR ($\rho = 0.807$; 95% CI, 0.718–0.867; $P < .001$) without a significant difference in the AUCs in identifying patients with ICH development ($P = .69$). Patients who developed ICH, as seen on follow-up CT, had worse long-term outcomes than those without hemorrhagic transformation.

Our study demonstrates the capability of the AIIC in predicting ICH development. In vitro experiments have demonstrated that DECT could be used to quantify the iodine concentration through the iodine-based material decomposition algorithm.¹⁶ Quantitative iodine parameters, including stroke, trauma, metastases, tumors, and perfusion, have been widely used in clinical practice.^{12,17–22} Bonatti et al¹² examined patients with acute ischemic stroke undergoing MT with DECT and reported an absolute iodine concentration of >1.35 mg I/mL in the maximum apparent attenuation area, thereby achieving a sensitivity of 100% and specificity of 67.5% in

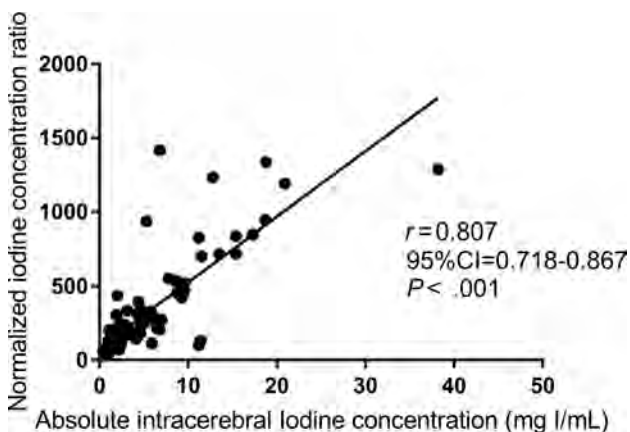


FIG 5. The NICR shows a strong correlation with the absolute intracerebral iodine concentration.

Table 4: AIIC and NICR parameters in terms of the hemorrhage classification on the follow-up CT

	AIIC (Median) (IQR) (mg I/mL)	P Value	NICR (Median) (IQR) (%)	P Value
HI (HI1+HI2)	4.2 (2.3–9.9)	.258	252.8 (186.8–611.2)	.465
PH (PH1+PH2)	8.3 (2.8–11.4)		429.8 (182.1–716.9)	
HI +PH1	3.7 (2.1–8.9)	.024	248.2 (164.6–468.7)	.08
PH2	9.3 (4.9–13.3)		455.3 (218.4–801.3)	

Note:—HI indicates hemorrhagic infarction; PH, parenchymal hematoma.

predicting ICH development. Our study also showed a significant difference in iodine concentration in postprocedural DECT between the 2 groups with and without ICH development, with a cutoff value of 2.7 mg I/mL. There was only a difference in the cutoff values for the two studies, which could be attributed to the different inclusion criteria between the 2 study samples. Our study included only patients with anterior circulation acute ischemic stroke with smaller infarct cores (ASPECTS ≥ 7) as well as patients with good recanalization. By contrast, the study by Bonatti et al included all patients with anterior and posterior circulation stroke without the ASPECTS criteria, and 18.8% (16/85) of the patients were unsuccessfully recanalized. These inclusion criteria might result in a difference in the cutoff value for predicting ICH development. Furthermore, the differences in the spectral separation in the scanners potentially played a role in the differences in cutoff values.

According to our study, both the AIIC and NICR could aid in postthrombectomy risk stratification in the case of hemorrhage, differing from the findings of the study by Byrne et al.¹³ To minimize the variability related to systematic differences in patients, we introduced the NICR to improve the sensitivity of quantifying the iodine contrast of lesions.^{16,20} Patel et al²³ reported that normalized iodine quantification of the aorta was more helpful in differentiating renal vascular lesions from nonvascular lesions. Byrne et al¹³ investigated postprocedural patients with acute ischemic stroke using DECT. They reported that the NICR could be a reliable predictor of hemorrhagic transformation. This study suggested that an NICR cutoff value of $>100\%$ might be a better predictor of ICH development than the AIIC. According to our study results, patients with ICH had a higher NICR than those without hemorrhagic transformation. This result was consistent with that of the study by Byrne et al.¹³ However, regarding the difference in the AIIC among the cohorts, our conclusion was completely different from that of the previous study.¹³ Our findings indicated a notable difference in the AIIC between the cohorts with and without ICH development. The AIIC calculated in our study had a significant positive correlation with the NICR ($\rho = 0.807$). This result indicated that both the AIIC and NICR could be used to predict ICH development in risk stratification for postthrombectomy management. Furthermore, patients with parenchymal hematoma type 2 development had a higher AIIC than those with parenchymal hematoma type 1 and hemorrhagic infarction type 1 development, whereas no significant difference was observed in the NICR between the 2 groups.

The DECT examination performed within 1 hour after the procedure made the results relevant to neurologic outcomes. Endovascularly administered iodine contrast media circulated within the body and reached a balanced state of distribution throughout the body before the DECT examination. Ischemic and reperfusion injuries lead to endothelial dysfunction, resulting in iodine extravasation in the tissues of acute ischemic stroke after successful recanalization. This time interval between the iodine contrast injection and DECT examination may make iodine extravasation directly proportional to the severity of the BBB disruption, and

iodine extravasation is not predominantly affected by systemic factors. This hypothesis sheds light on our findings, indicating that both the NICR and AIIC are related to the severity of BBB disruption, which results in ICH development after successful reperfusion.

According to the subgroup analyses of this study, the AIIC differed significantly between the groups (with the same ASPECTS) with and without ICH but did not differ between subgroups (ASPECTS of ≤ 8 and > 8). Thus, the AIIC had a great impact on the development of ICH. The median AIIC in patients who did and did not develop ICH in this study (5.9 mg I/mL and 2.0 mg I/mL) was higher than that in the study by Byrne et al¹³ (1.2 mg/mL and 0.9 mg/mL), though similar patient inclusion criteria were applied (patients with baseline ASPECTS ≥ 7 and modified TIC1 scores of 2b or 3 after the procedure). Potential reasons may be the larger patient cohort examined in this study, different populations, and differences in spectral separation in the scanners. The use of 3 mutually perpendicular plane images to measure the AIIC in this study may have had the advantage of reducing the measurement bias.

The 90-day mRS scores of 4–6 were observed to be significantly different between patients with and without ICH development. This result was consistent with those of previous studies,^{24,25} indicating that hemorrhagic transformation seriously threatens the patients' neurologic outcomes. Therefore, early identification of patients with a high risk of hemorrhagic transformation is essential for improving the prognosis of patients undergoing successful thrombectomy. Our study also found that the collateral status was significantly worse in patients with ICH than in those without ICH, similar to the results of previous studies.²⁶

Our study has a few limitations. First, the sample size was small owing to the strict inclusion and exclusion criteria, leading to a potential source of bias. A multicenter study with a large sample size is needed to improve the level and quality of evidence. Additionally, ROIs were drawn subjectively within the areas of maximum apparent contrast staining, which might have resulted in measurement errors. However, averaging the values calculated from the 3 planes can resolve this issue. A high concordance was achieved among the readers. Finally, a follow-up examination was performed using NCCT within 48 hours. Contrast staining usually resolves within 24 hours after endovascular therapy.²⁷ Unfortunately, persistent contrast staining may be seen beyond 48 hours in some cases.²⁸ Follow-up DECT should be performed to avoid classifying persistent contrast staining as hemorrhagic transformation.

CONCLUSIONS

We examined DECT quantitative parameters as imaging markers for identifying patients with acute ischemic stroke with hemorrhagic transformation after successful recanalization. The power of the NICR in predicting hemorrhagic transformation was similar to that of the AIIC. Quantitative DECT parameters within 1 hour after successful MT may also help predict poor outcomes in patients. After successful MT, early risk stratification for ICH development can facilitate informed clinical decision-making and aid in predicting prognosis.


Disclosure forms provided by the authors are available with the full text and PDF of this article at www.ajnr.org.

REFERENCES

1. Powers WJ, Rabinstein AA, Ackerson T, et al; American Heart Association Stroke Council. **2018 guidelines for the early management of patients with acute ischemic stroke: a guideline for health-care professionals from the American Heart Association/American Stroke Association.** *Stroke* 2018;49:e46–110 CrossRef Medline
2. Jadhav AP, Desai SM, Jovin TG. **Indications for mechanical thrombectomy for acute ischemic stroke: current guidelines and beyond.** *Neurology* 2021;97:S126–36 CrossRef Medline
3. Khatri P, Wechsler LR, Broderick JP. **Intracranial hemorrhage associated with revascularization therapies.** *Stroke* 2007;38:431–40 CrossRef Medline
4. Desai SM, Tonetti DA, Morrison AA, et al. **Relationship between reperfusion and intracranial hemorrhage after thrombectomy.** *J Neurointerv Surg* 2020;12:448–53 CrossRef Medline
5. Dekeyser S, Nikoubashman O, Lutin B, et al. **Distinction between contrast staining and hemorrhage after endovascular stroke treatment: one CT is not enough.** *J Neurointerv Surg* 2017;9:394–98 CrossRef Medline
6. Cai J, Zhou Y, Zhao Y, et al. **Comparison of various reconstructions derived from dual-energy CT immediately after endovascular treatment of acute ischemic stroke in predicting hemorrhage.** *Eur Radiol* 2021;31:4419–27 CrossRef Medline
7. Shi ZS, Duckwiler GR, Jahan R, et al. **Early blood-brain barrier disruption after mechanical thrombectomy in acute ischemic stroke.** *J Neuroimaging* 2018;28:283–88 CrossRef Medline
8. Ma C, Hui Q, Gao X, et al. **The feasibility of dual-energy CT to predict the probability of symptomatic intracerebral haemorrhage after successful mechanical thrombectomy.** *Clin Radiol* 2021;76:316.e9–316.e18 CrossRef Medline
9. Tijssen MP, Hofman PA, Stadler AA, et al. **The role of dual energy CT in differentiating between brain haemorrhage and contrast medium after mechanical revascularisation in acute ischaemic stroke.** *Eur Radiol* 2014;24:834–40 CrossRef Medline
10. Gupta R, Phan CM, Leidecker C, et al. **Evaluation of dual-energy CT for differentiating intracerebral hemorrhage from iodinated contrast material staining.** *Radiology* 2010;257:205–11 CrossRef Medline
11. Almqvist H, Holmin S, Mazya MV. **Dual energy CT after stroke thrombectomy alters assessment of hemorrhagic complications.** *Neurology* 2019;93:e1068–75 CrossRef Medline
12. Bonatti M, Lombardo F, Zamboni GA, et al. **Iodine extravasation quantification on dual-energy CT of the brain performed after mechanical thrombectomy for acute ischemic stroke can predict hemorrhagic complications.** *AJNR Am J Neuroradiol* 2018;39:441–47 CrossRef Medline
13. Byrne D, Walsh JP, Schmiedeskamp H, et al. **Prediction of hemorrhage after successful recanalization in patients with acute ischemic stroke: improved risk stratification using dual-energy CT parenchymal iodine concentration ratio relative to the superior sagittal sinus.** *AJNR Am J Neuroradiol* 2020;41:64–70 CrossRef Medline
14. Menon BK, Smith EE, Modi J, et al. **Regional leptomeningeal score on CT angiography predicts clinical and imaging outcomes in patients with acute anterior circulation occlusions.** *AJNR Am J Neuroradiol* 2011;32:1640–45 CrossRef Medline
15. Hacke W, Kaste M, Fieschi C, et al. **Randomised double-blind placebo-controlled trial of thrombolytic therapy with intravenous alteplase in acute ischaemic stroke (ECASS II).** *Lancet* 1998;352:1245–51 CrossRef Medline
16. Lv P, Lin XZ, Li J, et al. **Differentiation of small hepatic hemangioma from small hepatocellular carcinoma: recently introduced spectral CT method.** *Radiology* 2011;259:720–29 CrossRef Medline
17. Liu X, Ouyang D, Li H, et al. **Papillary thyroid cancer: dual-energy spectral CT quantitative parameters for preoperative diagnosis of metastasis to the cervical lymph nodes.** *Radiology* 2015;275:167–76 CrossRef Medline
18. Lv Y, Zhou J, Lv X, et al. **Dual-energy spectral CT quantitative parameters for the differentiation of glioma recurrence from treatment-related changes: a preliminary study.** *BMC Med Imaging* 2020;20:5 CrossRef Medline

19. Xu X, Sui X, Zhong W, et al. **Clinical utility of quantitative dual-energy CT iodine maps and CT morphological features in distinguishing small-cell from non-small-cell lung cancer.** *Clin Radiol* 2019;74:268–77 CrossRef Medline
20. Ge X, Yu J, Wang Z, et al. **Comparative study of dual energy CT iodine imaging and standardized concentrations before and after chemoradiotherapy for esophageal cancer.** *BMC Cancer* 2018;18:1120 CrossRef Medline
21. Bodanapally UK, Shanmuganathan K, Gunjan YP, et al. **Quantification of iodine leakage on dual-energy CT as a marker of blood-brain barrier permeability in traumatic hemorrhagic contusions: prediction of surgical intervention for intracranial pressure management.** *AJNR Am J Neuroradiol* 2019;40:2059–65 CrossRef Medline
22. Kay FU, Beraldo MA, Nakamura MAM, et al. **Quantitative dual-energy computed tomography predicts regional perfusion heterogeneity in a model of acute lung injury.** *J Comput Assist Tomogr* 2018;42:866–72 CrossRef Medline
23. Patel BN, Vernuccio F, Meyer M, et al. **Dual-energy CT material density iodine quantification for distinguishing vascular from nonvascular renal lesions: normalization reduces intermanufacturer threshold variability.** *AJR Am J Roentgenol* 2019;212:366–76 CrossRef Medline
24. Boisseau W, Fahed R, Lapergue B, et al; ETIS Investigators. **Predictors of parenchymal hematoma after mechanical thrombectomy: a multicenter study.** *Stroke* 2019;50:2364–70 CrossRef Medline
25. Paciaroni M, Agnelli G, Corea F, et al. **Early hemorrhagic transformation of brain infarction: rate, predictive factors, and influence on clinical outcome: results of a prospective multicenter study.** *Stroke* 2008;39:2249–56 CrossRef Medline
26. Bang OY, Saver JL, Kim SJ, et al; UCLA-Samsung Stroke Collaborators. **Collateral flow averts hemorrhagic transformation after endovascular therapy for acute ischemic stroke.** *Stroke* 2011;42:2235–39 CrossRef Medline
27. Nikoubashman O, Reich A, Gindullis M, et al. **Clinical significance of post-interventional cerebral hyperdensities after endovascular mechanical thrombectomy in acute ischaemic stroke.** *Neuroradiology* 2014;56:41–50 CrossRef Medline
28. Amans MR, Cooke DL, Vella M, et al. **Contrast staining on CT after DSA in ischemic stroke patients progresses to infarction and rarely hemorrhages.** *Interv Neuroradiol* 2014;20:106–15 CrossRef Medline

Diagnostic Performance of Whole-Body Ultra-Low-Dose CT for Detection of Mechanical Ventriculoperitoneal Shunt Complications: A Retrospective Analysis

 S. Afat,  R. Pjontek,  O. Nikoubashman,  W.G. Kunz, M.A. Brockmann,  H. Ridwan,  M. Wiesmann,  H. Clusmann,  A.E. Othman, and  H.A. Hamou



ABSTRACT

BACKGROUND AND PURPOSE: Radiographic shunt series are still the imaging technique of choice for radiologic evaluation of VP-shunt complications. Radiographic shunt series are associated with high radiation exposure and have a low diagnostic performance. Our aim was to investigate the diagnostic performance of whole-body ultra-low-dose CT for detecting mechanical ventriculoperitoneal shunt complications.

MATERIALS AND METHODS: This retrospective study included 186 patients (mean age, 54.8 years) who underwent whole-body ultra-low-dose CT (100 kV[peak]; reference, 10 mAs). Two radiologists reviewed the images for the presence of ventriculoperitoneal shunt complications, image quality, and diagnostic confidence. On a 5-point Likert scale, readers scored image quality and diagnostic confidence (1 = very low, 5 = very high). Sensitivity, specificity, positive predictive value, and negative predictive value were calculated. Radiation dose estimation of whole-body ultra-low-dose CT was calculated and compared with the radiation dose of a radiographic shunt series.

RESULTS: 34 patients positive for VP-shunt complications were correctly identified on whole-body ultra-low-dose CT by both readers. No false-positive or -negative cases were recorded by any of the readers, yielding a sensitivity of 100% (95% CI, 87.3%–100%), a specificity of 100% (95% CI, 96.9%–100%), and perfect agreement ($\kappa = 1$). Positive and negative predictive values were high at 100%. Shunt-specific image quality and diagnostic confidence were very high (median score, 5; range, 5–5). Interobserver agreement was substantial for image quality ($\kappa = 0.73$) and diagnostic confidence ($\kappa = 0.78$). The mean radiation dose of whole-body ultra-low-dose CT was significantly lower than the radiation dose of a conventional radiographic shunt series (0.67 [SD, 0.4] mSv versus 1.57 [SD, 0.6] mSv; 95% CI, 0.79–1.0 mSv; $P < .001$).

CONCLUSIONS: Whole-body ultra-low-dose CT allows detection of ventriculoperitoneal shunt complications with excellent diagnostic accuracy and diagnostic confidence. With concomitant radiation dose reduction on contemporary CT scanners, whole-body ultra-low-dose CT should be considered an alternative to the radiographic shunt series.

ABBREVIATIONS: IQR = interquartile range; VP-shunt = ventriculoperitoneal shunt; WB-ULD-CT = whole-body ultra-low-dose CT

Hydrocephalus is a common, surgically treatable disorder, defined as a pathologic accumulation of CSF resulting in a serious expansion of the brain ventricles. Ventriculoperitoneal

shunt (VP-shunt) is an effective treatment for hydrocephalus. VP-shunts drain the excess CSF into the peritoneum, where it can be absorbed.^{1–3} However, VP-shunts have a high complication rate of 20%–40% within the first year of placement.^{4–8} The clinical symptoms of VP-shunt complications can vary and are often not specific. Errors in diagnosis can have serious consequences for patients. Thus, imaging is the primary method to detect VP-shunt complications.⁹

Radiographic shunt series are still the imaging technique of choice for radiologic evaluation of VP-shunt complications.¹⁰ Shunt series cover the whole course of VP-shunts from the head to abdomen and usually consist of frontal skull, lateral skull, frontal chest, frontal abdomen, and lateral abdomen radiographs. However, recent studies on the diagnostic performance of radiographic shunt series reported remarkably low sensitivities (between 8.3% and 31%)

Received June 21, 2022; accepted after revision September 7.

From the Department for Diagnostic and Interventional Radiology (S.A., A.E.O.), University Hospital Tuebingen, Tuebingen, Germany; Departments of Neurosurgery (R.P., H.C., H.A.H.) and Diagnostic and Interventional Neuroradiology (O.N., H.R., M.W.), University Hospital RWTH Aachen, Aachen, Germany; Department of Radiology (W.G.K.), University Hospital Ludwig-Maximilians-University, Munich, Germany; and Department of Neuroradiology (M.A.B., A.E.O.), University Medical Center of the Johannes Gutenberg University Mainz, Mainz, Germany.

Please address correspondence to Ahmed Othman, MD, University Medical Center Mainz, Department of Neuroradiology, Langenbeckstr 1, 55131 Mainz, Germany; e-mail: ahmed.e.othman@googlemail.com; @Afatdr

<http://dx.doi.org/10.3174/ajnr.A7672>

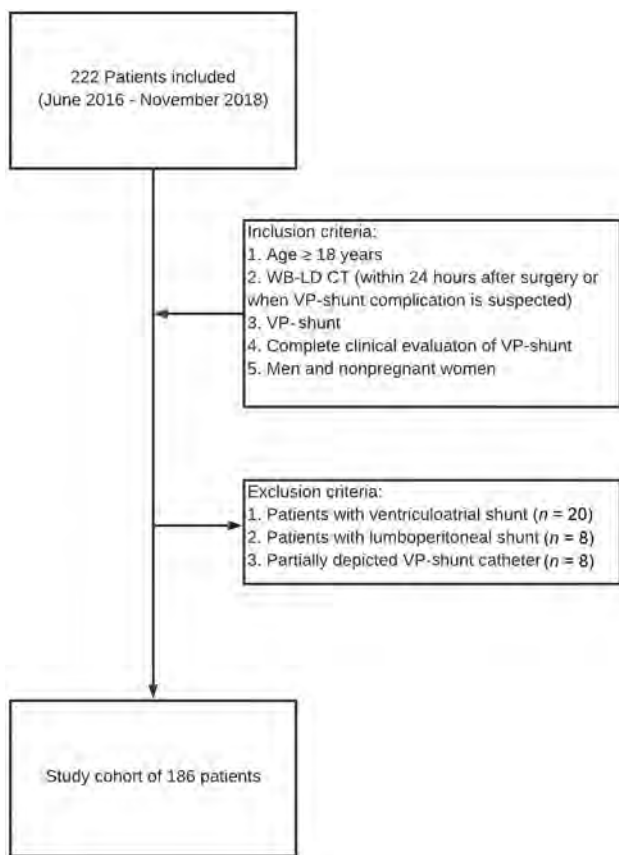


FIG 1. Standards for Reporting of Diagnostic Accuracy flow chart of patient inclusion.

to detect mechanical VP-shunt complications.¹¹⁻¹⁵ Radiographic shunt series often do not provide precise information about the abdominal catheter position. This leads to repeat x-ray examinations or even an additional (full-dose) CT.

Furthermore, radiographic shunt series are associated with high radiation exposure.¹⁴ Due to the low sensitivity and high radiation exposure, better imaging alternatives are necessary. CT is usually associated with considerably higher radiation doses than radiographs. However, the radiation dose of CT protocols can be adapted to the clinical question. For example, in case of VP-shunts, the radiation dose can be remarkably reduced while the hyperdense shunt catheters can easily be visualized despite high image noise. Recent animal studies have shown that whole-body ultra-low-dose CT (WB-ULD-CT) with radiation doses lower than those in the radiographic shunt series visualizes the VP-shunt properly and enables detection of VP-shunt complications with higher accuracy than radiographic images.^{16,17}

Nonetheless, human studies are necessary to evaluate these promising findings. On the basis of experimental findings, ULD-CT protocols for VP-shunt imaging have been implemented into the clinical routine at various centers. Pala et al¹⁸ compared WB-ULD-CT with radiography and showed that ULD-CT allows significantly better visualization of the distal catheter using a lower radiation dose than a radiographic shunt series. We hypothesize that WB-ULD-CT for assessment of VP-shunt complications in humans is feasible and can be

attained with high diagnostic accuracy and lower radiation doses than a radiographic shunt series. In the present study, we aimed to evaluate the diagnostic accuracy of WB-ULD-CT, focusing on the detection of mechanical VP-shunt malfunctions with an even lower radiation dose.

MATERIALS AND METHODS

Our local institutional ethics committee of the University of Aachen, Germany, approved this retrospective study and waived informed patient consent (registration number: EK 219/19).

Study Population

As a consequence of encouraging animal model results, we replaced the conventional radiographic shunt series with WB-ULD-CT for VP-shunt imaging in our institution by June 2016. As in many neurosurgical departments, VP-shunt imaging is performed routinely within 24 hours after implantation to ensure and precisely document the correct placement and verify the postprocedural course of the VP-shunt catheter. VP-shunt imaging is also performed when complications are suspected.

The inclusion period of this retrospective analysis was between June 2016 and November 2018. A total of 222 patients with VP-shunts underwent WB-ULD-CT during the inclusion period. The inclusion criteria for our study were the following: 1) 18 years of age or older, 2) WB-ULD-CT (within 24 hours after implantation of a VP-shunt or when VP-shunt failure was suspected), 3) VP-shunt, 4) complete clinical evaluation of the VP-shunt (including operative assessment if necessary), and 5) men and nonpregnant women. Patients with incomplete imaging of the course of the VP-shunt were excluded. The final sample size consisted of 186 patients; a Standards for Reporting of Diagnostic Accuracy flow chart of patient inclusion is shown in Fig 1.

Age, sex, etiology of hydrocephalus, history of a previous VP-shunt complication, the presence of symptoms, and operative/clinical results were recorded.

Imaging Technique and CT Image Reconstruction

All patients underwent WB-ULD-CT on a 40-section CT scanner (Somatom Definition AS; Siemens). The x-ray tube was operated at a tube voltage of 100 kV(peak) and a reference tube current of 10 mAs (collimation = 40 × 0.6 mm, pitch = 1.5). Automatic attenuation-based tube-current modulation (CARE Dose4D; Siemens) was activated. All reconstructions were acquired using a kernel (B45) with 5-mm (3-mm increment) section thickness and 1 mm (1-mm increment) in the axial, coronal, and sagittal planes. Images were generated using iterative reconstruction (Sinogram Affirmed Iterative Reconstruction Strength 3).

Moreover, 3D reconstructions using a volume-rendering technique were created.

Reference Standard

A neurosurgeon (H.A.H.) with 10 years of experience evaluated all patients' clinical data, including symptoms, clinical examinations, intraoperative findings, and recorded readmissions and VP-shunt revisions for a 3-month period after WB-ULD-CT imaging. Patients were classified as negative when clinical and operative work-up revealed no VP-shunt complications and

Table 1: Patient characteristics

Characteristic	Value
Sex	
Male	85/186 (45%)
Female	101/186 (54%)
Overall age (range) (yr)	54.8 (18–88)
Underlying etiology	
Tumor	12/186 (6%)
Posthemorrhagic hydrocephalus	59/186 (31%)
Congenital hydrocephalus	16/186 (8%)
Postinfectious hydrocephalus	5/186 (2%)
Posttraumatic hydrocephalus	12/186 (6%)
Posterior fossa cyst	2/186 (1%)
Idiopathic intracranial hypertension	23/186 (12%)
Normal-pressure hydrocephalus	40/186 (46%)
Aqueduct stenosis	17/186 (9%)
Symptoms	
Yes	
Headache	33/186 (17%)
Nausea and vomiting	9/186 (4%)
Fatigue	19/186 (10%)
Gait disturbance	34/186 (18%)
Others	36/186 (19%)
Multiple	5/186 (2%)
No	50/186 (26%)
Clinical indication	
24 Hours after implantation	102/186 (54%)
Complication suspected	84/186 (45%)
Secondary findings	
Dyselectasis	7/186 (3%)
Pneumonia	2/186 (1%)
Pleural effusion	6/186 (3%)
Nephrolithiasis	1/186 (0,5%)
Incidental tumor findings	1/186 (0,5%)
Abdominal aortic aneurysm	1/186 (0,5%)

when no VP-shunt-related readmissions were recorded within the 3-month period after imaging. Patients were classified as positive when mechanical VP-shunt complications were identified in the clinical examination and intraoperatively.

Image Evaluation

Image evaluation was performed on a standard PACS workstation. After the definition of the reference standard, 2 radiologists (A.E.O. with 8 years of experience; S.A. with 6 years of experience) who were blinded to all clinical data, independently evaluated WB-ULD-CT reconstructions regarding shunt-specific overall image quality and diagnostic confidence using 5-point Likert scales (1, very low; 5, excellent).¹⁹ The same readers assessed the WB-ULD-CT images regarding the presence/absence and type of mechanical shunt complication.

Radiation Dose Estimation

The dose-length product was obtained and used to estimate the effective radiation dose for all patients. The effective dose was estimated by multiplying the dose-length product by $0.015 \text{ mSv} \times \text{mGy}^{-1} \times \text{cm}^{-1}$ (conversion factor).^{20,21}

Statistical Analysis

Statistical analyses were performed using SPSS Statistics for Windows 25 (IBM). The mean accounted effective dose for WB-ULD-CT was then compared with the reported cumulative

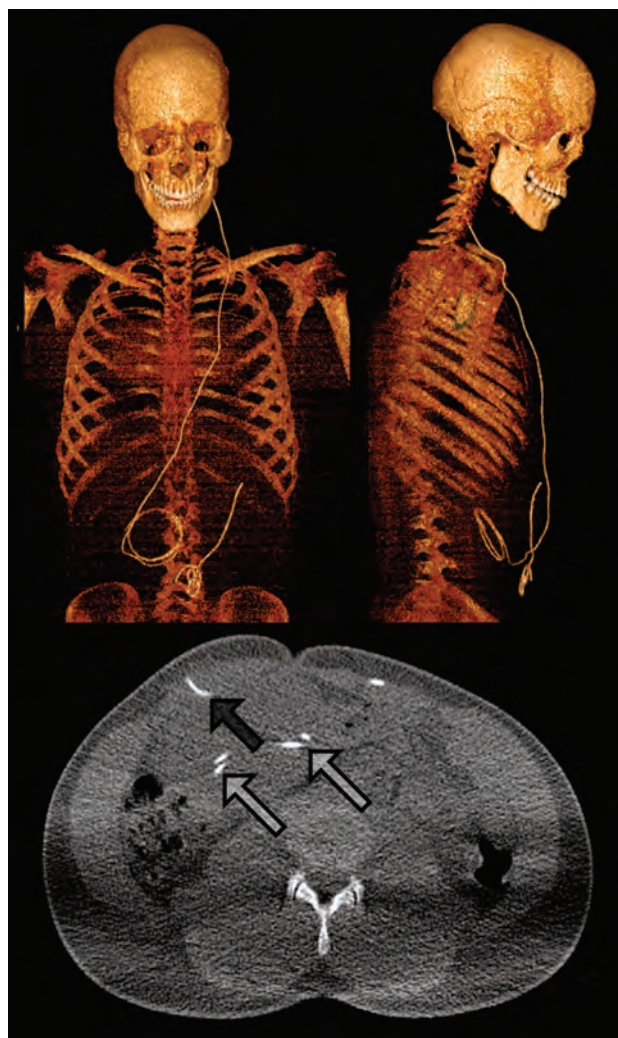


FIG 2. As a premature infant, a 19-year-old man developed intraventricular hemorrhage grade IV with consecutive posthemorrhagic hydrocephalus and formation of a left frontal intracranial cyst. A cysto-ventriculoperitoneal shunt was implanted during the first months of life. At 19 years of age, the patient was referred to our center because of abdominal pain and local induration around the right abdominal scar. WB-ULD-CT revealed an intraperitoneal position of the distal catheter, however with an intraperitoneal cyst or pseudocyst formation. Front (upper left) and lateral (upper right) views of the 3D reconstruction show looping of the peritoneal catheter. On the axial conformation with 5-mm section thickness, intraperitoneal insertion of the catheter (full arrow) as well as intraperitoneal pseudocyst with incorporated catheter loops (transparent arrows) can be detected.

radiation exposure by Shuaib et al¹⁴ of 1.57 (SD, 0.6) mSv per shunt series by calculating the difference between the 2 means, the significance value (*P* value), and the 95% CI. Overall image quality and diagnostic confidence were expressed as median and interquartile range (IQR) of both readers. Sensitivity, specificity, positive predictive value, negative predictive value, and diagnostic accuracy of WB-ULD-CT with 95% CIs were calculated for the detection of mechanical VP-shunt complications on WB-ULD-CT using the above-mentioned reference standard. The Cohen κ coefficient was calculated for interrater agreement. A *P* value was considered significant at *P* < .05.

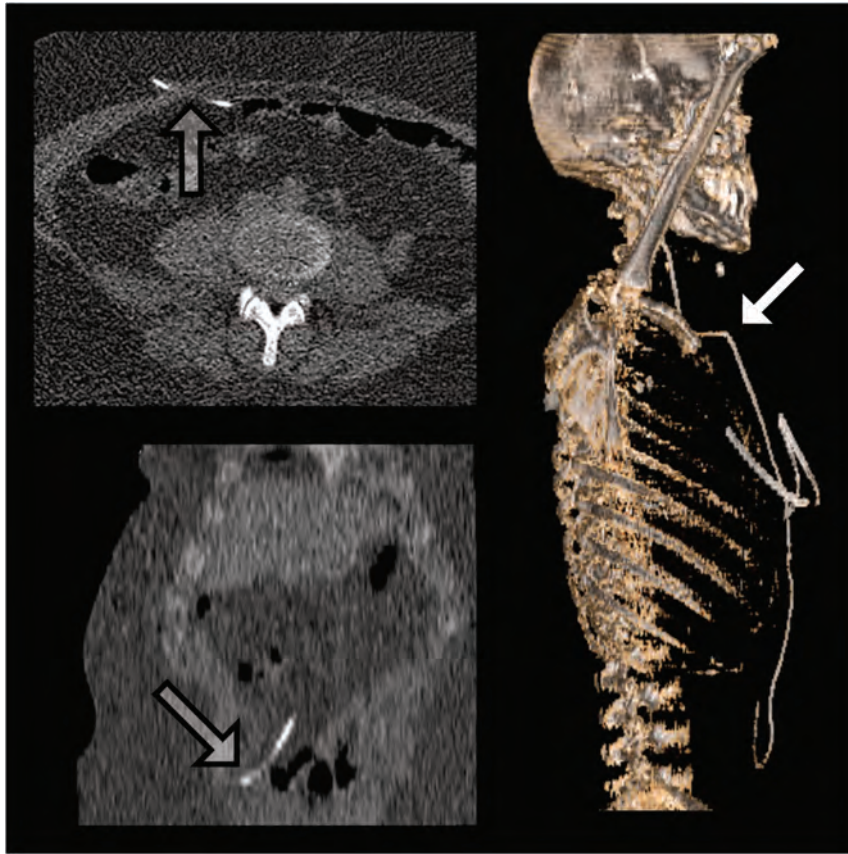


FIG 3. A 33-year-old woman presented with progressive headache, nausea, and vomiting, indicating a shunt dysfunction. Several shunt revisions were needed during infancy. The 3D reconstruction of the current WD-ULD-CT (right) depicts kinking of the shunt tube at the right clavicle (white arrow) as well as a short distal catheter in relation to an adult body size. However, the distal catheter passed through the peritoneum (transparent arrows on axial and coronal reconstructions on the left) and ends intraperitoneally.

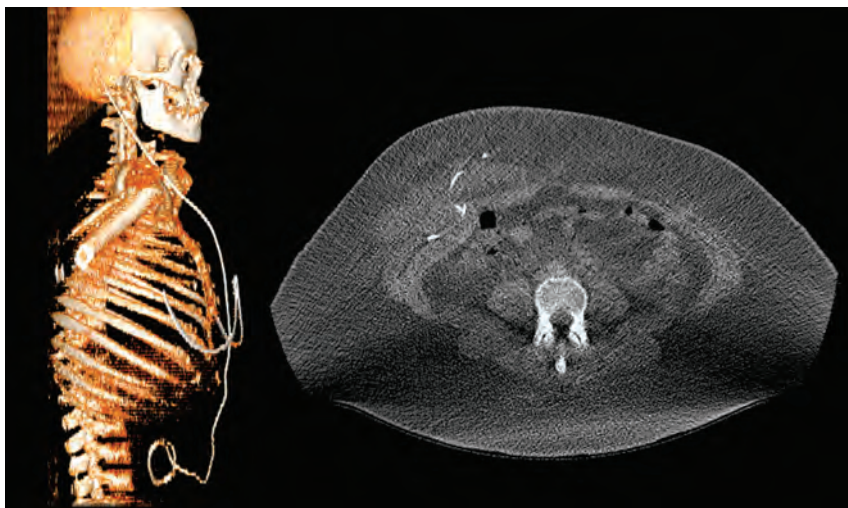


FIG 4. A 26-year-old woman with obesity (body mass index, 35.3 kg/m²) with idiopathic intracranial hypertension received a VP-shunt after the failure of conservative therapy. After the implantation of a VP-shunt, the correct intraperitoneal position of the distal catheter was verified by WB-ULD-CT. Two weeks later she was admitted due to progressive abdominal pain. WB-ULD-CT (lateral view on 3D reconstruction on the left and axial reconstruction on the right) shows an extraperitoneal shunt dislocation.

RESULTS

Patient Characteristics

The study cohort consisted of 186 patients (mean age, 54.8 years; range, 18–88 years), including 85 men (45.7%; mean age, 58.5 years; range, 19–87 years) and 101 women (54.3%; mean age, 51.6 years; range, 18–88 years); 54.8% of the WB-ULD-CT studies were within 24 hours after implantation of a new VP-shunt; and 45.2% of the WB-ULD-CT studies were performed when shunt failure was suspected. Further patient characteristics are given in Table 1.

Diagnostic Evaluation

Of the 186 patients, 152 patients (81.7%) were negative for mechanical complications. Thirty-four patients (18.3%) had VP-shunt complications. Seven patients (3.8%) had a breakage/disconnection of the subcutaneous shunt catheter, 1 patient had an abdominal pseudocyst (0.5%) (Fig 2) at the tip of the catheter, 2 patients (1.1%) had kinking of the catheter (Fig 3), and 24 patients (12.9%) (Fig 4) had a dislocation of the distal/peritoneal VP-shunt catheter (Table 2).

Both readers detected all 34 complications (18.3%) of 186 patients with a perfect agreement ($\kappa = 1$). There were no patients with false-negative or false-positive findings, resulting in a sensitivity of 100% (95% CI, 87.3%–100%) and a specificity of 100% (95% CI, 96.9%–100%). WB-ULD-CT showed a high positive predictive value of 100% (95% CI, 87.3%–100%) and a high negative predictive value of 100% (95% CI, 96.9%–100%).

Overall Image Quality and Diagnostic Confidence

The overall shunt-specific image quality was rated very high by both readers, with a mean score of 5 (IQR, 25%–75%; range, 5–5) and substantial interrater agreement ($\kappa \geq 0.73$). The diagnostic confidence of both readers was rated very high with a median score of 5 (IQR, 25%–75%; range, 5–5), and a substantial interrater agreement ($\kappa \geq 0.78$).

Radiation Dose Estimation

The mean dose-length product of WB-ULD-CTs was 45.04 (SD, 26.91) mGy ×

Table 2: Overview of detected shunt complications in WB-LD-CT by 2 readers (A.E.O. and S.A.)

Complication Type	Reader A	Reader B
Disconnection	7/7 (100%)	7/7 (100%)
Dislocation	24/24 (100%)	24/24 (100%)
Kinking	2/2 (100%)	2/2 (100%)
Pseudocyst	1/1 (100%)	1/1 (100%)
Total	34/34 (100%)	34/34 (100%)

cm (minimum, 12 mGy × cm; maximum, 225 mGy × cm), resulting in a mean estimated effective radiation dose of 0.67 (SD, 0.4) mSv (minimum, 0.18 mSv; maximum, 3.37 mSv). The mean radiation dose of WB-ULD-CT was significantly lower than the radiation dose of the radiographic shunt series as reported by Shuaib et al¹⁴ (0.67 [SD, 0.4] mSv versus 1.57 [SD, 0.6] mSv; 95% CI, 0.79–1.0 mSv; $P < .001$).

DISCUSSION

Imaging plays an essential role in the clinical work-up of adult patients with suspected VP-shunt complications or in postprocedural diagnostics. In daily practice, suspicion of VP-shunt complications is mostly confirmed on the basis of the combination of imaging findings and clinical work-up. In the present work, we evaluated radiation exposure and diagnostic performance of WB-ULD-CT for the detection of mechanical VP-shunt complications, and this study is currently the largest cohort of patients with VP-shunts who underwent WB-ULD-CT.

Our findings indicate that WB-ULD-CT has a high diagnostic accuracy for the detection of mechanical VP-shunt complications with a lower radiation dose than in radiographic shunt series.

Despite the restricted radiation dose of WB-ULD-CT, VP-shunt catheters could be appropriately visualized with sufficient image quality and diagnostic confidence. The readers were able to detect all 34 VP-shunt complications correctly without producing false-positive or false-negative findings.

Other studies, such as the one by Lehnert et al,¹² showed a poor sensitivity of a radiographic shunt series for the detection of mechanical complications (sensitivity = 4%), which resulted in no significant impact on patient outcome regarding surgical shunt revision (OR, 0.9; 95% CI, 0.7–1.2; $P = .74$). A further study also reported the poor sensitivity of a radiographic shunt series for the detection of VP-shunt complications (sensitivity = 31%).¹¹

On the other hand, animal studies have shown that WB-ULD-CT is remarkably superior to a radiographic shunt series for the detection of mechanical VP-shunt complications.^{16,17,22} Especially, extraperitoneal dislocation, which can easily be missed on a radiographic shunt series, is easy to detect on CT images.

Our results have the potential to make WB-ULD-CT the criterion standard of diagnostic imaging of VP-shunts because many neurosurgical centers perform radiographic shunt series and non-contrast-enhanced CT of the head in the early postoperative phase as a routine procedure after implanting new hardware in the body of the patient and to detect postoperative complications if suspected.¹⁰

In addition, our study supports previous studies showing a significantly lower radiation dose compared with a radiologic

shunt series, even though in our study, the comparison was not intraindividual.^{11,12,16,17,22}

The observed high diagnostic accuracy of WB-ULD-CT for the detection of VP-shunt complications in our study emphasizes the potential role of WB-ULD-CT as an alternative to plain radiographs for VP-shunt imaging.

In a retrospective study by Pala et al,¹⁸ the low-dose CT had a lower radiation exposure than the x-ray series. However, the mean radiation exposure was higher than in our study (0.67 mSv versus 1.9 mSv). Also, another strength of our study is the size of the cohort, which is larger than the cohort of Pala et al.

We believe that WB-ULD-CT is more applicable for routine clinical practice because it is a time-saving, one-stop-shop method with high diagnostic accuracy and a reduced radiation dose compared with a radiographic series.¹⁴ Patients are not repositioned several times as is the case with x-ray examinations when several regions of the body must be examined. Instead, they are placed on the CT table only once, and the examination is performed from the entire shunt course. This approach is of great importance, especially postoperatively or in patients requiring intensive care.

We believe that the radiation dose could even be further reduced and image quality improved by using new technologies like advanced new iterative reconstruction, new filtering techniques, dual-energy CT, modern radiography hardware, and artificial intelligence-based reconstruction techniques.^{23,24}

The retrospective single-center design of this study is a limitation. A multicenter approach with a larger cohort is required to reconfirm the results of our study. Due to the retrospective nature of the study, it was not possible to perform an interpatient comparison of performance and radiation dose between WB-ULD-CT and a conventional radiographic shunt series.

CONCLUSIONS

Our retrospective study indicates that WB-ULD-CT yields a high diagnostic accuracy for the detection of VP-shunt complications. Therefore, we believe that WB-ULD-CT is the first stage in the further development of the WB-ULD-CT protocol to replace radiologic shunt series as the new criterion standard.

Ethics Approval

Institutional Review Board approval was obtained from the University of Aachen before the initiation of this study.

Disclosure forms provided by the authors are available with the full text and PDF of this article at www.ajnr.org.

REFERENCES

- Little AS, Zabramski JM, Peterson M, et al. **Ventriculoperitoneal shunting after aneurysmal subarachnoid hemorrhage: analysis of the indications, complications, and outcome with a focus on patients with borderline ventriculomegaly.** *Neurosurgery* 2008;62:618–27; discussion 618–27 CrossRef Medline
- Hoh BL, Kleinhenz DT, Chi YY, et al. **Incidence of ventricular shunt placement for hydrocephalus with clipping versus coiling for ruptured and unruptured cerebral aneurysms in the Nationwide Inpatient Sample database: 2002 to 2007.** *World Neurosurg* 2011;76:548–54 CrossRef Medline

3. Brean A, Eide PK. **Prevalence of probable idiopathic normal pressure hydrocephalus in a Norwegian population.** *Acta Neurol Scand* 2008;118:48–53 CrossRef Medline
4. Al-Tamimi YZ, Sinha P, Chumas PD, et al; British Pediatric Neurosurgery Group Audit Committee. **Ventriculoperitoneal shunt 30-day failure rate: a retrospective international cohort study.** *Neurosurgery* 2014;74:29–34 CrossRef Medline
5. Farahmand D, Hilmarsen H, Hogfeldt M, et al. **Perioperative risk factors for short term shunt revisions in adult hydrocephalus patients.** *J Neurol Neurosurg Psychiatry* 2009;80:1248–53 CrossRef Medline
6. Park MK, Kim M, Park KS, et al. **A retrospective analysis of ventriculoperitoneal shunt revision cases of a single institute.** *J Korean Neurosurg Soc* 2015;57:359–63 CrossRef Medline
7. Reddy GK, Bollam P, Caldito G. **Long-term outcomes of ventriculoperitoneal shunt surgery in patients with hydrocephalus.** *World Neurosurg* 2014;81:404–10 CrossRef Medline
8. Barton SE, Campbell JW, Piatt JH. **Quality measures for the management of hydrocephalus: concepts, simulations, and preliminary field-testing.** *J Neurosurg Pediatr* 2013;11:392–97 CrossRef Medline
9. Lee MJ, Streicher DA, Howard BM, et al. **Ventricular shunt radiographs: still relevant in the cross-sectional era? Pictorial review of the radiographic appearance of ventricular shunts and approach to interpreting shunt series radiographs.** *Neurographics* 2016;6:202–12 CrossRef
10. Kamenova M, Rychen J, Guzman R, et al. **Yield of early postoperative computed tomography after frontal ventriculoperitoneal shunt placement.** *PLoS One* 2018;13:e0198752 CrossRef Medline
11. Desai KR, Babb JS, Amodio JB. **The utility of the plain radiograph “shunt series” in the evaluation of suspected ventriculoperitoneal shunt failure in pediatric patients.** *Pediatr Radiol* 2007;37:452–56 CrossRef Medline
12. Lehnert BE, Rahbar H, Relyea-Chew A, et al. **Detection of ventricular shunt malfunction in the ED: relative utility of radiography, CT, and nuclear imaging.** *Emerg Radiol* 2011;18:299–305 CrossRef Medline
13. Griffey RT, Ledbetter S, Khorasani R. **Yield and utility of radiographic “shunt series” in the evaluation of ventriculo-peritoneal shunt malfunction in adult emergency patients.** *Emerg Radiol* 2007;13:307–11 CrossRef Medline
14. Shuaib W, Johnson JO, Pande V, et al. **Ventriculoperitoneal shunt malfunction: cumulative effect of cost, radiation, and turnaround time on the patient and the health care system.** *AJR Am J Roentgenol* 2014;202:13–17 CrossRef Medline
15. Pujara S, Natalwala A, Robertson I. **Referrals for suspected ventriculo-peritoneal shunt dysfunction and necessity for further imaging.** *Br J Neurosurg* 2017;31:320–21 CrossRef Medline
16. Afat S, Pjontek R, Hamou HA, et al. **Imaging of ventriculoperitoneal shunt complications: comparison of whole-body low-dose computed tomography and radiographic shunt series.** *J Comput Assist Tomogr* 2016;40:991–96 CrossRef Medline
17. Othman A, Hamou HA, Pjontek R, et al. **Evaluation of whole body ultralow-dose CT for the assessment of ventriculoperitoneal shunt complications: an experimental ex-vivo study in a swine model.** *Eur Radiol* 2015;25:2199–2204 CrossRef Medline
18. Pala A, Awad F, Braun M, et al. **Value of whole-body low-dose computed tomography in patients with ventriculoperitoneal shunts: a retrospective study.** *J Neurosurg* 2018;129:1598–1603 CrossRef Medline
19. Notohamiprodjo S, Stahl R, Braunagel M, et al. **Diagnostic accuracy of contemporary multidetector computed tomography (MDCT) for the detection of lumbar disc herniation.** *Eur Radiol* 2017;27:3443–51 CrossRef Medline
20. Christner JA, Kofler JM, McCollough CH. **Estimating effective dose for CT using dose-length product compared with using organ doses: consequences of adopting International Commission on Radiological Protection publication 103 or dual-energy scanning.** *AJR Am J Roentgenol* 2010;194:881–89 CrossRef Medline
21. American Association of Physicists in Medicine Task Group 23. **The Measurement, Reporting, and Management of Radiation Dose in CT.** American Association of Physicists in Medicine; 2008 CrossRef
22. Othman AE, Afat S, Hamou HA, et al. **High-pitch low-dose whole-body computed tomography for the assessment of ventriculoperitoneal shunts in a pediatric patient model: an experimental ex vivo study in rabbits.** *Invest Radiol* 2015;50:858–62 CrossRef Medline
23. Abdi AJ, Mussmann B, Mackenzie A, et al. **Visual evaluation of image quality of a low dose 2D/3D slot scanner imaging system compared to two conventional digital radiography x-ray imaging systems.** *Diagnostics (Basel)* 2021;11:1932 CrossRef Medline
24. Monuszko K, Malinzak M, Yang LZ, et al. **Image quality of EOS low-dose radiography in comparison with conventional radiography for assessment of ventriculoperitoneal shunt integrity.** *J Neurosurg Pediatr* 2021;27:375–81 CrossRef Medline

Schizencephaly in Hereditary Hemorrhagic Telangiectasia

JJ. Gaines, B.C. Gilbert, J.R. Gossage, W. Parker, A. Reddy, and S.E. Forseen



ABSTRACT

BACKGROUND AND PURPOSE: The presence of malformations of cortical development in patients with hereditary hemorrhagic telangiectasia has been reported on previous occasions. We evaluated a sample of adults with hereditary hemorrhagic telangiectasia for the presence of malformations of cortical development, spatial coincidence of malformations of cortical development and AVMs, and the coincidence of brain and pulmonary AVMs.

MATERIALS AND METHODS: A total of 141 patients 18 years of age or older who were referred to the Augusta University hereditary hemorrhagic telangiectasia clinic and underwent brain MR imaging between January 19, 2018, and December 3, 2020, were identified. MR imaging examinations were reviewed retrospectively by 2 experienced neuroradiologists, and the presence of malformations of cortical development and AVMs was confirmed by consensus. Demographic and clinical information was collected for each case, including age, sex, hereditary hemorrhagic telangiectasia status by the Curacao Criteria, mutation type, presence of malformations of cortical development, presence of brain AVMs, presence of pulmonary AVMs, and a history of seizures or learning disabilities.

RESULTS: Five of 141 (3.5%) patients with hereditary hemorrhagic telangiectasia had malformations of cortical development. Two of the 5 patients with polymicrogyria also had closed-lip schizencephaly. One of the patients had a porencephalic cavity partially lined with heterotopic GM. The incidence of spatially coincident polymicrogyria and brain AVMs was 40% (2/5 cases). Of the patients with hereditary hemorrhagic telangiectasia and malformations of cortical development, 4/5 (80%) had pulmonary AVMs and 2/5 (40%) had brain AVMs.

CONCLUSIONS: To our knowledge, we are the first group to report the presence of schizencephaly in patients with hereditary hemorrhagic telangiectasia. The presence of schizencephaly and porencephaly lends support to the hypothesis of regional in utero cerebral hypoxic events as the etiology of malformations of cortical development in hereditary hemorrhagic telangiectasia.

ABBREVIATIONS: HHT = hereditary hemorrhagic telangiectasia; MCD = malformation of cortical development

Hereditary hemorrhagic telangiectasia (HHT), also known as Osler-Weber-Rendu syndrome, is an autosomal dominant disorder that results from mutations in genes related to blood vessel formation. The 2 primary forms of HHT, HHT1 and HHT2, account for up to 85% of HHT diagnoses. HHT1 is caused by mutations of the *ENG* gene (coding for endoglin); and mutations in the *ACVRL1* gene (coding for *ALK1*) result in HHT2. The products of these genes are receptor proteins involved in the

transforming growth factor β signaling pathway. This pathway regulates normal endothelial cell growth, migration, and proliferation. Without functioning endoglin and *ALK1*, vessels form abnormal connections and exhibit a tortuous and leaky endothelium that has a tendency to rupture.¹

Common clinical symptoms of HHT include recurrent nosebleeds and telangiectasias of the hands, face, and oral cavities. HHT exhibits age-related penetrance with more severe symptoms seen later in life. AVMs can be found in pulmonary (40%–60%), hepatic (50%–75%), gastrointestinal (50%–78%), cerebral (10%), and spinal (1%) circulations. Complications related to CNS AVMs can present as headache, seizure, intracranial hemorrhage, or stroke.

Malformations of cortical development (MCDs) are a diverse group of neurodevelopmental disorders. Cortical development is a highly structured process that involves a complex set of precisely timed events. Disruptions in cell proliferation, neuronal

Received May 23, 2022; accepted after revision September 12.

From the Neuroradiology Section (B.C.G., W.P., A.R., S.E.F.), Department of Radiology and Imaging; and Department of Hereditary Hemorrhagic Telangiectasia (J.R.G.), Section of Pulmonary Diseases, Department of Medicine, Medical College of Georgia (J.J.G.) at Augusta University, Augusta, Georgia.

Please address correspondence to Scott E. Forseen, MD, Neuroradiology Section, Department of Radiology and Imaging, Medical College of Georgia at Augusta University, 1120 15th St, Augusta, GA 30912; e-mail: sforseen@augusta.edu

Indicates article with online supplemental data.

<http://dx.doi.org/10.3174/ajnr.A7677>

migration, and postmigrational cortical organization, caused by environmental or genetic factors, can result in MCDs.² The exact mechanisms of MCD formation are largely unknown. The clinical presentation of MCDs is highly variable and ranges from asymptomatic to intellectual disabilities and epilepsy.³ Pathologic findings are equally heterogeneous and may include excessive cortical folding, abnormal cell arrangement, and fusion of gyral surfaces.⁴

Summary of 141 patients

Demographics	Summary
Sex	
Male	36.9%
Female	63.1%
Age (mean) (yr)	45.3
MCD	
Yes	5
No	136
HHT mutation	
Endoglin	35.4%
ALK1 ^a	27.7%
SMAD4 ^a	2.8%
RASA1	0.7%
Negative × 5	15.6%
Unknown/not tested	17.7%
AVMs	
Brain AVM	12.0%
Brain AVM (possible)	2.8%
Pulmonary AVM (macroscopic) ^b	43.3%
Pulmonary AVM (microscopic) ^b	32.6%
Spinal AVM	0.7%
Brain vascular malformations	
Developmental venous anomaly	14.9%
Capillary vascular malformation, definite	1.4%
Capillary vascular malformation, possible	4.3%
Curacao category	
Definite HHT	79.4%
Possible or suspected HHT	12.1%
Probable	4.3%
Unlikely	4.3%

^aALK1 includes 2 variants of unknown significance; SMAD4 includes 1 variant of unknown significance.

^bPulmonary AVMs were defined as macroscopic if they were definitely visible on a CT scan and microscopic if contrast echocardiography showed a Grade 1 or greater delayed shunt and the CT findings were negative.

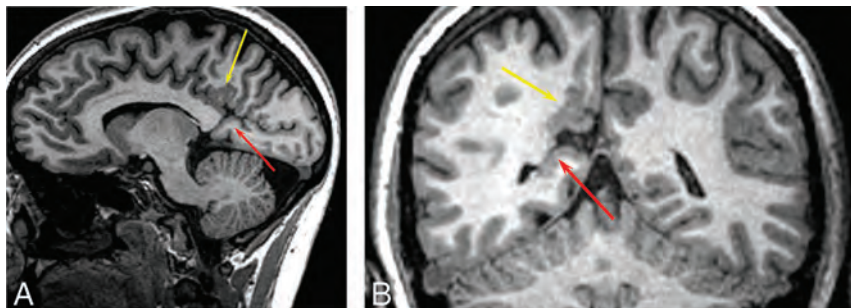


FIG 1. A 26-year-old woman with HHT. Sagittal 3D fast-spoiled gradient recalled imaging demonstrates polymicrogyria involving the right posterior cingulate gyrus (A, yellow arrow). There is an abnormal GM-lined cleft between the calcarine sulcus and the occipital horn of the right lateral ventricle consistent with schizencephaly (A, red arrow). Coronal T1 image shows polymicrogyria (B, yellow arrow) and schizencephaly (B, red arrow).

The presence of MCDs in patients with HHT has been reported on 3 previous occasions, once in a pediatric sample⁵ and twice in adult samples.^{6,7} The prevalence of MCDs in HHT in these studies ranged between 5% and 12%. To date, nearly all of the MCDs reported in patients with HHT have been polymicrogyrias. Unlike polymicrogyrias in general, polymicrogyrias in patients with HHT are largely unilateral, more focal, and rarely associated with symptoms.

Klostranec et al⁷ reported a sample of patients with HHT with MCDs that were spatially coincident with AVMs and proposed a mechanism by which endoglin impairment leads to regional hypoperfusion which, in turn, leads to impairment in neuronal migration and cortical organization. Palagallo et al⁵ reported spatially coincident MCDs and AVMs in one-quarter of their sample. They also found that patients with HHT and MCDs were statistically more likely to have pulmonary and brain AVMs than patients with HHT without MCDs.

In the current study, we evaluated a sample of adults with HHT for the presence of MCDs, spatial coincidence of MCDs and AVMs, and the coincidence of brain and pulmonary AVMs.

MATERIALS AND METHODS

Consent requirements were waived by the internal review board for this retrospective chart review study. A total of 141 patients 18 years of age or older who were referred to the Augusta University HHT clinic and who underwent brain MR imaging between January 19, 2018, and December 3, 2020, were identified. All MR imaging examinations were performed using a 3T field strength and included pre- and postcontrast 3D T1-weighted FSPGR images. MR imaging examinations were reviewed retrospectively by 2 board-certified radiologists who hold Certificates of Added Qualification in Neuroradiology (B.C.G. and S.E.F.) with 7 and 10 years of experience, respectively.

The presence of MCDs and AVMs was confirmed by consensus. MCDs were defined in accordance with Severino et al.⁸ AVMs were defined as a network of dilated vessels (ie, nidus) with dilated feeding arteries and dilated draining veins. The Curacao Criteria were used to diagnose HHT and included the following: 1) spontaneous and recurrent epistaxis, 2) mucocutaneous telangiectasias, 3) visceral AVMs, and 4) HHT diagnosis in a first-degree relative. The diagnosis of HHT was considered “definite” if 3 or 4 of these criteria were met, “possible” if 2 criteria were met, and “unlikely” if <2 criteria were met.⁹

Demographic and clinical information was collected from the medical record for each case, including age, sex, HHT status by the Curacao Criteria, mutation type, presence of MCDs, presence of brain AVMs, presence of pulmonary AVMs (including the presence of macroscopic pulmonary AVMs or a delayed right-to-left shunt on contrast echocardiography), and a history of seizures or learning disabilities. Descriptive

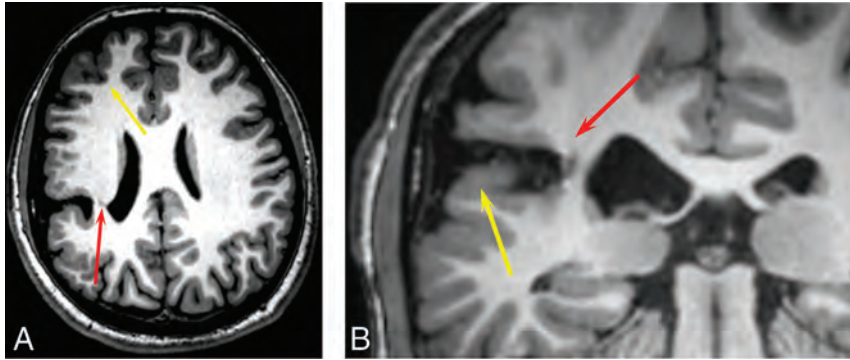


FIG 2. A 20-year-old man with HHT. 3D volume T1 images demonstrate a closed-lip schizencephaly projecting through the right inferior parietal lobe that extends to the lateral margin of the right lateral ventricle at the junction of the posterior body and atrium (A, red arrow). There is polymicrogyria involving the adjacent frontal and parietal cortex (A, yellow arrow). Coronal T1 image shows polymicrogyria (B, yellow arrow) and schizencephaly (B, red arrow).

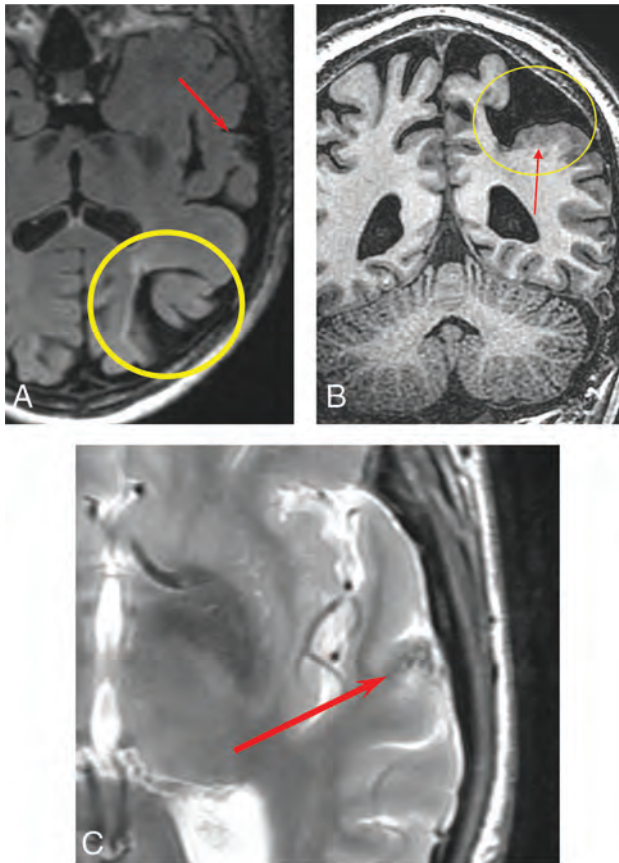


FIG 3. An 80-year-old man with HHT. Axial T2 FLAIR image shows porencephaly with surrounding gliosis (A, yellow circle) and an AVM in the left superior temporal gyrus (A, red arrow). Coronal volume T1 image shows porencephaly (B, yellow circle) partially lined by polymicrogyria (B, red arrow). Axial T2 FSE image shows flow voids associated with a small AVM (C, red arrow).

and inferential statistics were calculated with StatPlus software (<https://statplus.io/>). The Fisher exact test was performed with a threshold of $P < .05$ established for statistical significance.

RESULTS

Patient demographic data are summarized in the Table. Five of 141 (3.5%) patients with HHT had MCDs. Of the 5 patients with HHT with MCDs, all 5 had polymicrogyria. All 4 patients with HHTs with polymicrogyria in whom testing was performed had endoglin mutations. Two of the 5 patients with polymicrogyria also had CSF-containing clefts lined with polymicrogyria (ie, schizencephaly), both of which were of the closed-lip variety (Figs 1 and 2). One of the patients had a porencephalic cavity partially lined with heterotopic GM (Fig 3). The other 2 cases of polymicrogyria included an 18-year-old man (Fig 4) and a 28-year-old man (Fig 5).

The incidence of spatially coincident polymicrogyria and brain AVMs in this sample was 40% (2/5 cases; Figs 3 and 4). Neither of the patients with schizencephaly had a spatially coincident brain AVM. Of the patients with HHT and MCDs, 4/5 (80%) had pulmonary AVMs and 2/5 (40%) had brain AVMs. Summary data for patients with HHT and polymicrogyria are seen in the Online Supplemental Data.

Patients with MCDs were not more likely to have coincident brain AVMs than patients without MCDs. Two of 5 (40%) patients with MCDs had brain AVMs, compared with 17/136 (13%) patients without MCDs ($P = .11$). Patients with MCDs were not more likely to have coincident pulmonary AVMs than patients without MCDs. Four of 5 (80%) patients with MCDs had pulmonary AVMs versus 103/136 (76%) patients without MCDs ($P = 1.0$).

Three of the patients with MCDs reported a history of migraine headaches. Two of the patients with MCDs were asymptomatic. One of the patients with polymicrogyria reported right-handed contracture and weakness. Both patients with schizencephaly reported a history of migraine headaches. None of the patients with MCDs had a history of seizures or learning disabilities.

DISCUSSION

Five of 141 (3.5%) patients in our sample of patients with HHT had MCDs, in the general range of prevalence observed by other authors examining adult patients with HHT.^{6,7} Polymicrogyria was present in all 5 of these patients. A novel finding in our sample was the presence of 2 patients with schizencephaly. To our knowledge, we are the first group to report the presence of schizencephaly in patients with HHT. The clefts were unilateral, lined with polymicrogyria, and closed-lip in morphology. Both patients with schizencephaly had a history of migraine headaches. Neither of these patients had a history of seizures or cognitive disabilities. Schizencephaly is now added to the growing list of MCDs reported in HHT, including polymicrogyria,^{5-7,10-12} nodular GM heterotopia,⁵ and focal cortical dysplasia.⁶

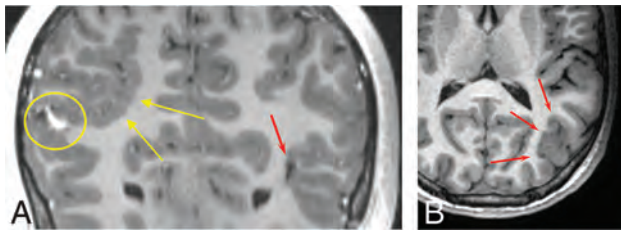


FIG 4. An 18-year-old man with HHT. Coronal 3D T1 postcontrast imaging shows right parietal polymicrogyria (A, yellow arrows), an AVM (A, yellow circle), and a small AVM (A, red arrow). Axial T1 image shows left parietal occipital polymicrogyria (B, red arrows).

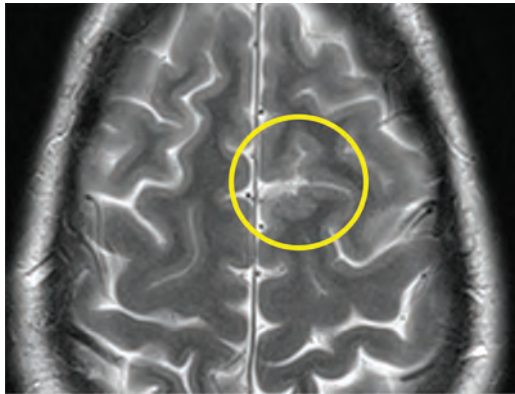


FIG 5. A 28-year-old man with HHT. Axial T2 FSE image shows polymicrogyria in the left superior frontal gyrus (yellow circle).

Polymicrogyria is thought to arise from a brain insult occurring in the late migration to early cortical organizational stages of corticogenesis.^{2,4} All patients with HHT with polymicrogyria reported to date, including our sample, have shown focal polymicrogyria, the pattern most commonly associated with hypoxic events and infections. Generalized polymicrogyria is most commonly associated with congenital cytomegalovirus infection and peroxisomal disorders.¹³ Overall, polymicrogyria is most commonly perisylvian in location and bilateral.⁴ All reported cases of polymicrogyria in HHT to date, including our cases, are unilateral and not strictly perisylvian in location.

Schizencephaly is widely believed to be the result of a destructive lesion, particularly prenatal ischemic injuries.^{4,14-17} Porencephaly and schizencephaly are both considered to result from destructive lesions that occur within different developmental timeframes. If the destructive lesion occurs within 4–6 months' gestation, neuroglial migration is possible and polymicrogyria or GM heterotopia along the margins of the cavity will result. After 6 months' gestation, the involved brain parenchyma is resorbed. Because neuroglial migration is no longer possible, the cavity is not lined with polymicrogyria or GM heterotopia.^{3,16} The presence of patients with MCDs partially outlining porencephalic cavities in the current sample and in a previous report⁵ may indicate that the ischemic events in these patients occurred at the transition between the late migrational and early cortical organizational stages of corticogenesis.

We were not able to replicate an earlier finding of the high rate of spatially coincident MCDs and brain AVMs.⁷ Spatial

coincidence of brain AVMs and MCDs has been described by multiple groups.^{5,10-12} Only 2 of our patients had an AVM spatially related to an MCD. Palagallo et al⁵ reported spatial coincidence of MCDs and AVMs in only 3 of 12 patients. There are many possible explanations for these discrepant findings. First, it is possible that MCDs or AVMs were present but below current MR imaging resolution. Second, although suggestive imaging findings were not present, it is possible that spatially coincident AVMs were present and had spontaneously resolved. Third, spatially coincident AVMs may have not yet developed at the time of imaging. Finally, it is possible that spatial coincidence is an inconstant finding.

Patients with HHT with MCDs in our sample were not more likely to have pulmonary AVMs than patients with HHT without MCDs. As in previous studies, all patients with HHT with MCDs in our sample who were tested had HHT1 and did not have clinically evident seizures or developmental or cognitive disabilities.

Our study has a number of limitations, first and foremost being the retrospective nature of this study. Another limitation is the small sample of patients obtained with this rare disease. Although up-to-date MR imaging protocols for HHT were used throughout the study period, it is possible that additional MCDs and AVMs may not have been detected due to limitations in current MR imaging protocols.

CONCLUSIONS

Our study replicates many of the findings of previous studies showing an association between HHT and MCDs. To our knowledge, we are the first group to report the presence of schizencephaly in patients with HHT. The presence of schizencephaly and porencephaly lends support to the hypothesis of regional in utero cerebral hypoxic events as the etiology of MCDs in HHT.

Disclosure forms provided by the authors are available with the full text and PDF of this article at www.ajnr.org.

REFERENCES

- McDonald J, Woolderchak-Donahue W, VanSant Webb C, et al. **Hereditary hemorrhagic telangiectasia: genetics and molecular diagnostics in a new era.** *Front Genet* 2015;6:1–8 CrossRef Medline
- Barkovich AJ, Guerrini R, Kuzniecky RI, et al. **A developmental and genetic classification for malformations of cortical development: update 2012.** *Brain* 2012;135:1348–69 CrossRef Medline
- Raybaud C, Widjaja E. **Development and dysgenesis of the cerebral cortex: malformations of cortical development.** *Neuroimaging Clin N Am* 2011;21:483–543, vii CrossRef Medline
- Squier W, Jansen A. **Polymicrogyria: pathology, fetal origins and mechanisms.** *Acta Neuropathol Commun* 2014;2:80 CrossRef Medline
- Palagallo GJ, McWilliams SR, Sekarski LA, et al. **The prevalence of malformations of cortical development in a pediatric hereditary hemorrhagic telangiectasia population.** *AJNR Am J Neuroradiol* 2017;38:383–86 CrossRef Medline
- Bergerot JF, Dupuis-Girod S, Berthezene Y, et al. **Malformations of cortical development and brain vessels in patients with hereditary haemorrhagic telangiectasia.** In: *Proceedings of the International Hereditary Hemorrhagic Telangiectasia Scientific Conference*, Cork, Ireland; June 12–15, 2013

7. Klostranec JM, Chen L, Mathur S, et al. **A theory for polymicrogyria and brain arteriovenous malformations in HHT.** *Neurology* 2019;92:34–42 CrossRef Medline
8. Severino M, Geraldo AF, Utz N, et al. **Definitions and classification of malformations of cortical development: practical guidelines.** *Brain* 2020;143:2874–94 CrossRef Medline
9. Faughnan ME, Mager JJ, Hetts SW, et al. **Second International Guidelines for the Diagnosis and Management of Hereditary Hemorrhagic Telangiectasia.** *Ann Intern Med* 2020;173:989–1001 CrossRef Medline
10. Abe T, Singer RJ, Marks MP, et al. **Arterial vascular abnormality accompanying cerebral cortical dysplasia.** *AJNR Am J Neuroradiol* 1997;18:144–46 Medline
11. Shankar JJ, Banerjee ST, Hogan M, et al. **A rare case of cerebral cortical dysplasia with arterial vascular dysplasia.** *Can J Neurol Sci* 2009;36:757–60 CrossRef Medline
12. Villa D, Cinnante C, Valcamonica G, et al. **Hereditary hemorrhagic telangiectasia associated with cortical development malformation due to a start loss mutation in ENG.** *BMC Neurol* 2020;20:316 CrossRef Medline
13. Leventer RJ, Jansen A, Pilz DT, et al. **Clinical and imaging heterogeneity of polymicrogyria: a study of 328 patients.** *Brain* 2010;133:1415–27 CrossRef Medline
14. Curry CJ, Lammer EJ, Nelson V, et al. **Schizencephaly: heterogeneous etiologies in a population of 4 million California births.** *Am J Med Genet A* 2005;137:181–89 CrossRef Medline
15. Barkovich AJ, Rowley H, Bollen A. **Correlation of prenatal events with the development of polymicrogyria.** *AJNR Am J Neuroradiol* 1995;16:822–27 Medline
16. Griffiths PD. **Schizencephaly revisited.** *Neuroradiology* 2018;60:945–60 CrossRef Medline
17. Yakovlev PI, Wadsworth RC. **Schizencephalies; a study of the congenital clefts in the cerebral mantle; clefts with hydrocephalus and lips separated.** *J Neuropathol Exp Neurol* 1946;5:169–206 CrossRef Medline

Delayed CTP-Derived Deep Venous Outflow: A Novel Predictor of Striatocapsular Infarction after M1 Thrombectomy

S. Peretz, K. Pardo, J. Naftali, M. Findler, G. Raphaeli, R. Barnea, V. Khasminsky, and E. Auriel



ABSTRACT

BACKGROUND AND PURPOSE: Isolated striatocapsular infarction occurs commonly in patients with ischemic stroke following M1 thrombectomy. We aimed to explore the correlation between CTP-derived parameters of deep venous outflow at presentation and subsequent striatocapsular infarction in a retrospective cohort of such patients.

MATERIALS AND METHODS: TTP and peak enhancement were measured on CTP-derived time-attenuation curves of the internal cerebral and thalamostriate veins bilaterally. The difference in TTP (Δ TTP) and the relative decrease in venous enhancement between the ischemic and normal sides were calculated. NCCT performed 24 (SD, 12) hours postthrombectomy was used to determine tissue fate in the caudate head, caudate body, lentiform nucleus, and internal capsule. Striatocapsular ischemia (striatocapsular infarction–positive) was defined as infarction and striatocapsular injury as either infarction, contrast enhancement, or hemorrhagic transformation in ≥ 1 of these regions. A striatocapsular ischemia score was calculated (0 = no ischemic region, 1 = 1 ischemic region, 2 = ≥ 2 ischemic regions).

RESULTS: One hundred sixteen patients were included in the analysis. Sixty-one patients had striatocapsular infarction (striatocapsular infarction–positive). The mean thalamostriate Δ TTP was 1.95 (SD, 1.9) seconds for patients positive for striatocapsular infarction and 0.79 (SD, 2.1) for patients negative for it ($P = .010$). Results were similar for striatocapsular injury. The mean thalamostriate Δ TTP was 0.79 (SD, 2.1), 1.68 (SD, 1.4), and 2.05 (SD, 2) for striatocapsular infarction scores of 0, 1, and 2, respectively ($P = .030$).

CONCLUSIONS: CTP-derived thalamostriate Δ TTP is an excellent surrogate marker for striatocapsular infarction in patients post-M1 thrombectomy. The novel approach of extracting venous outflow parameters from CTP has numerous potential applications and should be further explored.

ABBREVIATIONS: DT = distance from the carotid T to the thrombus; ICC = intraclass correlation coefficient; IVT = intravenous thrombolytic; LSAs = lenticulostrate arteries; SCAs+ = ASPECTS-based striatocapsular involvement; SCI = striatocapsular infarction; SCInj = striatocapsular injury; SCIs = striatocapsular ischemia score

The lenticulostrate arteries (LSAs) are a collection of small, deep perforating arteries arising most commonly from the M1 and supplying the basal ganglia and superior part of the internal capsule. They are commonly considered as end arteries without reliable anastomoses or collateral supply.¹⁻³

Isolated striatocapsular infarction (SCI), resulting from simultaneous occlusion of the ostia of multiple LSAs, is a common

occurrence in patients who have had successful endovascular reperfusion of the target M1 segment occlusion.⁴⁻⁶ In these patients, a rich leptomeningeal collateral supply maintains cortical and subcortical WM viability, while the deeper striatocapsular territory has infarction. Postulated mechanisms are the lack of striatocapsular collateral supply, lack of reperfusion to occluded perforators during clot retrieval, and a low ischemic threshold of basal ganglionic gray matter. Individual vascular anatomic variants have also been shown to determine the fate of striatocapsular tissue.⁷ The exact site of M1 occlusion as measured by the distance from the carotid T to the thrombus (DT) independently predicts the involvement of the LSAs and subsequent SCI as recently reported.⁸

Venous outflow of the striatocapsular region relies mainly on paired thalamostriate veins, which drain into the straight sinus through paired internal cerebral veins and the great cerebral vein

Received July 12, 2022; accepted after revision September 8.

From the Departments of Neurology (S.P., K.P., J.N., M.F., G.R., R.B., E.A.) and Radiology (V.K.), Rabin Medical Center, Beilinson Hospital, Petach Tikva, Israel; and Sackler School of Medicine (S.P., K.P., J.N., M.F., G.R., R.B., V.K., E.A.), Tel-Aviv University, Tel-Aviv, Israel. S. Peretz and K. Pardo contributed equally to this work.

Please address correspondence to Eitan Auriel, MD, Department of Neurology, Rabin Medical Center, Beilinson Hospital, 39 Jabotinsky St, Petach Tikva 49100, Israel; e-mail: Eitanman1@gmail.com

Indicates article with online supplemental data.

<http://dx.doi.org/10.3174/ajnr.A7670>

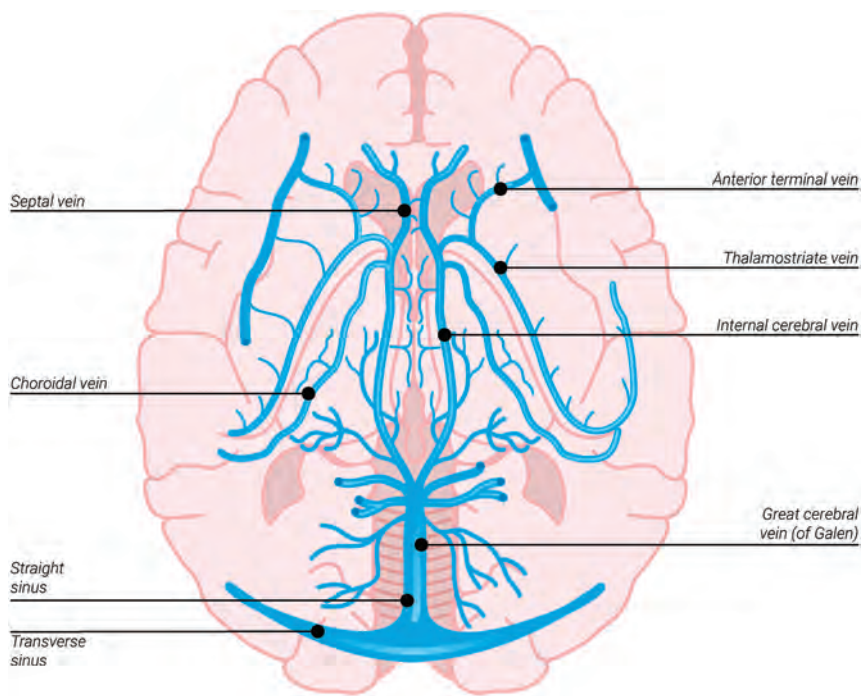


FIG 1. Illustration of deep cerebral venous drainage. The thalamostriate and septal veins drain into paired internal cerebral veins, which, in turn, drain into the great cerebral vein of Galen, the straight sinus, and the transverse sinuses. Also noted are the anterior terminal veins that drain into the thalamostriate veins.

of Galen (Fig 1). Measuring flow parameters within these deep venous channels may be useful for tissue prognostication in patients with stroke and an M1 occlusion.

CTP is used extensively to determine the eligibility of patients with anterior circulation acute ischemic stroke for mechanical thrombectomy worldwide. Currently, CTP postprocessing algorithms focus on the voxel-based analysis of cerebral parenchymal perfusion data to produce maps of the infarct core and penumbra. However, data on flow within the cerebral veins may also be extracted from the CTP images. Analysis of these widely available data enables direct, dynamic assessment of cerebral venous flow.

In this study, we aimed to explore the correlation between CTP-derived parameters of venous outflow in the deep cerebral veins and SCI in a cohort of patients with stroke following acute M1 thrombectomy.

MATERIALS AND METHODS

Study Subjects

We retrospectively reviewed all patients who had undergone mechanical thrombectomy for acute ischemic stroke with M1 occlusion and had CTP performed in the acute phase from January 2018 to December 2021 in the Rabin Medical Center. We retrieved demographics and relevant clinical data including age, sex, vascular risk factors, NIHSS at admission, intravenous thrombolytic (IVT) treatment, procedural complications, mRS score, and mortality at 90 days.

Imaging data included NCCT, CTA, and CTP from admission and NCCT that was performed 24 (SD, 12) hours postthrombectomy.

Imaging Acquisition

All study images were acquired using the same multidetector row scanner (Brilliance iCT 256 Slice CT Scanner; Philips Healthcare) including NCCT, CTA, and CTP. CTP was acquired as a 60-second cine series beginning immediately after a power injection of 40 mL of contrast at 5.2 mL/s. The scan was performed in non-Jog mode with a scan slab of 8 cm. The lower edge of the FOV was positioned at the sella turcica. The scan consisted of 30 cycles with an intercycle delay of 2 seconds. Imaging parameters included 80 kV(peak), 100 mAs, and an 0.4-second rotation time.

Imaging Analysis

Admission NCCT images were reviewed by an experienced stroke neurologist (S.P.) who determined the ASPECTS for each patient. Involvement of at least 1 striatocapsular region (caudate head, lentiform nucleus, or internal capsule) on the ASPECTS score (SCAs+) was recorded.

CTA images were reviewed by a trained neuroradiologist (M.F.) who verified M1 occlusion and assessed the cerebral collateral status using the Tan collateral score.⁹ He additionally reviewed postthrombectomy DSA images and recorded the modified TIC1 score. Successful reperfusion was defined as a modified TIC1 score of $\geq 2b$. The DT on the coronal MIP (section thickness, 10 mm) was also measured for each patient.

CTP data were postprocessed with the Brain Perfusion application of the IntelliSpace Portal (Philips Healthcare). All CTP scans underwent automated 3D correction for head movement during the CTP acquisition before they were analyzed. Suboptimal scans due to either excessive motion or inadequate contrast injection were excluded. Total penumbra and core volumes were automatically calculated by the application. Mean relative CBF and relative CBV of the lentiform nucleus and caudate head were measured using a manually drawn ROI. Venous outflow parameters were extracted from the CTP data by a trained neurologist (K.P.), blinded to postadmission imaging. After the bilateral internal cerebral and thalamostriate veins were visually identified on axial images of the time MIP CTP images, a circular ROI was manually placed over these veins. The software automatically detects the voxel with highest peak enhancement within this user-defined ROI and presents the time-attenuation curve and other parameters for the voxel. Measurements of TTP in seconds and peak enhancement in Hounsfield units were recorded (Fig 2). For each patient, the difference in TTP ($\Delta TTP = TTP$ ischemic hemisphere $- TTP$ normal hemisphere) and the relative decrease in venous enhancement (enhancement ischemic hemisphere $-$ enhancement normal hemisphere / enhancement normal hemisphere) were calculated for both internal cerebral and thalamostriate veins.

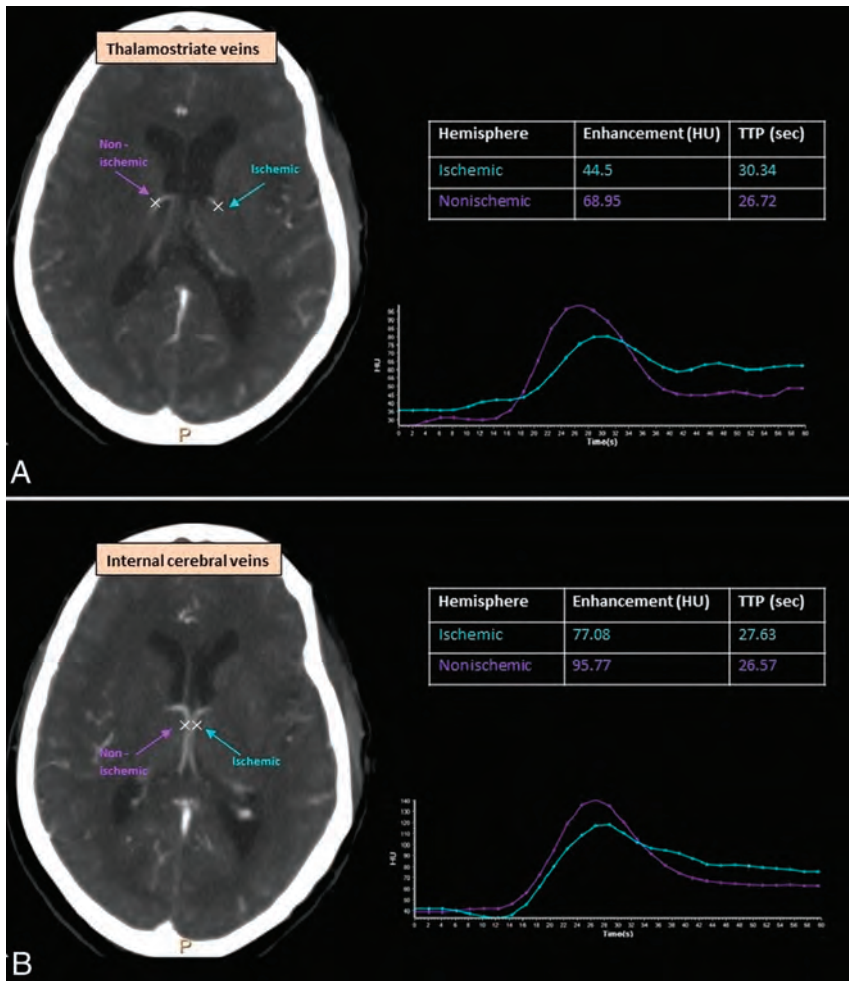


FIG 2. Measurement of venous flow parameters on CTP: vein selection and time-attenuation curves. A, Thalamostriate veins. B, Internal cerebral veins.

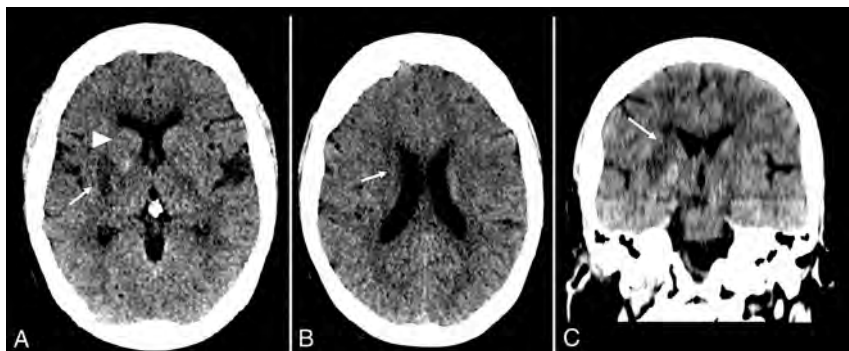


FIG 3. NCCT of a patient after right M1 thrombectomy. Infarcts involving the putamen (A, arrow), caudate body (B, arrow), and internal capsule (C, arrow) with no involvement of caudate head (A, arrowhead). SCIs of 2.

Images of NCCT performed 24 (SD, 12) hours postthrombectomy were reviewed by a second trained neurologist (J.N.) at a window width of W:40; L:40 to determine tissue fate within the 4 striatocapsular regions drained by the internal cerebral and thalamostriate veins, including the caudate head, caudate body,

lentiform nucleus, and internal capsule. Caudate and lentiform nuclei infarction was evaluated on axial NCCT images. The internal capsule was evaluated shortly before the fiber tracts passed through the GM bridges between the caudate and the lentiform nucleus on coronal-reformatted NCCT images.¹⁰ Each of these regions was classified as normal, infarcted, contrast-enhanced, or with hemorrhagic transformation. A region was labeled as infarcted or contrast-enhanced when >10% of that region was involved; otherwise, it was labeled as normal (Fig 3). When available, a repeat NCCT performed from 48 hours to 7 days postthrombectomy was additionally reviewed to better define the tissue status on the 24-hour NCCT. Hemorrhagic transformation was defined as an enhanced lesion with significant mass effect, a rim of hypoattenuation, and/or when significant hyperattenuation was still evident on a repeat NCCT performed 48–72 hours postthrombectomy.¹¹

Ischemic damage was recorded separately for each of the above 4 striatocapsular regions (0 = normal, 1 = ischemic). Striatocapsular infarction-positive (SCI+) was defined as isolated infarction in at least 1 of these regions. Striatocapsular injury-positive (SCInj+) was defined more broadly as either infarction, contrast enhancement, or hemorrhagic transformation in at least 1 of these regions. A striatocapsular ischemia score (SCIs) was also calculated for each patient (0 = no ischemic region, 1 = 1 ischemic region, 2 = ≥ 2 ischemic regions).

Thirty CTP scans and 50 NCCT scans were independently reviewed by a third experienced neurologist (S.P.) to assess interrater reliability.

Statistical Analysis

Statistical analyses were performed using SPSS Statistics for Windows, Version 25.0 (IBM). Qualitative data were represented as frequencies and percentages; the Pearson χ^2 test was used for comparison of baseline characteristics, treatment

(IVT), and clinical outcomes (mortality, intracerebral hemorrhage); the *t* test was used for comparison of treatment (arrival times) and clinical outcomes (mRS); 1-way ANOVA analysis was used for comparing intergroup differences of CTP parameters; and ORs were calculated by binary univariate logistic regression analysis to

quantify the association between CTP-derived venous outflow parameters and SCI as well as between DT and SCI. Normality distribution of CTP parameters was assessed using the Kolmogorov-Smirnov test. A secondary multivariable logistic regression analysis for SCI was performed to adjust for confounders. Results were considered significant at a level of $P < .05$. Interrater reliability was calculated with intraclass correlation coefficients (ICCs) from 2-way ANOVA analyses that were derived to compare readers.

RESULTS

A total of 123 patients were reviewed. Two patients were excluded from the analysis due to simultaneous acute ischemia involving the contralateral hemisphere, and 1 patient was excluded due to lack of 24-hour postthrombectomy NCCT. Four additional patients were excluded due to excessive motion or inadequate contrast injection. A total of 116 patients were included in the analysis. A repeat NCCT from 48 hours to 7 days postthrombectomy was available in 43/116 (37%) patients. The internal cerebral veins were clearly demonstrated bilaterally on CTP images in all study patients. In 7/116 (6%) patients, the thalamostriate veins were not demonstrated in a sufficient quality to extract venous flow data due to variant anatomy and gross section thickness of the time MIP CTP images; for those patients, only the internal cerebral vein data were analyzed.

Demographic, clinical, and procedural data of the 116 patients included in the analysis are presented in the Online Supplemental Data. The median age was 79 years (interquartile range, 68–86 years); 49 patients were women (54.4%). There was no significant difference between patients with SCI and those without in either age, sex, vascular risk factors, NIHSS, IVT treatment, procedural complications, mRS score, or mortality at 90 days.

Baseline imaging characteristics at admission are presented in the Online Supplemental Data. The total ASPECTS was not significantly different among groups, but a higher proportion of SCAs+ was found in the SCI+ and SCIInj+ groups, 24 (39.3%) and 37 (43%), respectively, compared with 4 (13.8%) in the SCI-negative (SCI-) group ($P = .014$). The CTA Tan collateral score was similar among the groups.

Additional CTP parameters are presented in the Online Supplemental Data. The CTP-derived core volume was higher in the SCI+ group (18.8 [SD, 24] cm^3) compared with the SCI- group (7.3 [SD, 8.2] cm^3 , $P = .018$). Relative CBF in the lentiform nucleus and caudate head was decreased in the SCI+ group compared with SCI- group; relative CBV was significantly decreased in the lentiform nucleus of the SCI+ group compared with SCI- group, but not in the caudate head nucleus.

Correlation between Venous Outflow Parameters and SCI

Of 116 patients included in the analysis, 61 patients were found to have isolated striatocapsular ischemia in ≥ 1 of the striatocapsular regions (SCI+), and 29 patients had no SCI at all (SCI-). Patients from these 2 groups were included in the main SCI analysis.

Twenty-six additional patients had striatocapsular regions with either contrast enhancement or hemorrhagic transformation. These patients together with the patients with SCI+ were defined as the SCIInj+ group and analyzed separately.

The delay in venous outflow in the thalamostriate vein, ipsilateral to the occluded MCA, was significantly higher in patients with SCI+ than in patients in the SCI- group. The mean $\Delta\text{TTP}_{\text{SCI}+}$ was 1.95 (SD, 1.9) seconds compared with $\Delta\text{TTP}_{\text{SCI}-}$ of 0.79 [SD, 2.1] seconds ($P = .01$). A trend toward higher mean ΔTTP in the internal cerebral vein in the SCI+ compared with SCI- group could also be seen, but statistical significance was not reached. No significant difference was found between the groups in relative enhancement (relative peak enhancement in the ischemic hemisphere) of either the thalamostriate or internal cerebral veins.

Analysis of patients with SCIInj+ showed similar results with a mean ΔTTP in the thalamostriate vein of 1.95 (SD, 2.2) seconds compared with 0.79 (SD, 2.1) seconds in patients without any SCIInj ($P = .014$).

A higher ΔTTP in the thalamostriate vein was significantly correlated with SCI (OR, 1.412; 95% CI, 1.072–1.86; $P = .014$) and SCIInj (OR, 1.345; 95% CI, 1.052–1.719; $P = .018$). These results are presented in Tables 1 and 2. As previously reported,⁸ the DT was significantly correlated with SCI+ in our cohort (OR, 1.138; 95% CI, 1.058–1.223; $P = .001$), but the OR was lower than for ΔTTP .

Analysis of the SCIs as an ordinal score between 0 and 2, presented in Table 3, showed a direct correlation between ΔTTP and the SCIs, with mean ΔTTP s of 0.79 (SD, 2.1) seconds, 1.68 (SD, 1.4) seconds, and 2.05 (SD, 2) seconds for a SCIs of 0, 1, and 2, respectively ($P = .030$).

We also analyzed the correlation between venous outflow parameters and infarction of each of the 4 striatocapsular regions separately. The correlation between higher ΔTTP and infarction was statistically significant for the caudate body and lentiform nucleus, whereas the caudate head and internal capsule showed only a trend. Results are presented in the Online Supplemental Data.

Interrater Reliability

The ICCs for the reviewed imaging parameters were 0.81 (95% CI, 0.57–0.92) for SCI on NCCT, 0.95 (95% CI, 0.91–0.98) for internal cerebral TTP, 0.95 (95% CI, 0.90–0.98) for thalamostriate TTP, 0.90 (95% CI, 0.82–0.95) for internal cerebral enhancement, and 0.93 (95% CI, 0.85–0.97) for DT on CTA. These high values represent either good (≥ 0.75) or excellent (≥ 0.9) agreement between readers for these parameters.¹² The ICC was only 0.39 (95% CI, 0.05–0.65) for thalamostriate enhancement, indicating a low reliability for this parameter in our analysis.

Control of Potential Confounding Factors

Results of multivariable logistic regression analysis for SCI adjusted for age, sex, admission ASPECTS-based striatocapsular involvement, successful reperfusion, collateral score, and IVT are presented in the Online Supplementary Data. Higher thalamostriate ΔTTP remained significantly correlated with SCI (OR, 1.511; 95% CI, 1.102–2.072; $P = .01$). SCAs+ was a potential confounding factor and correlated with SCI (OR, 2.895; 95% CI 0.97–8.644; $P = .057$). However, in a secondary univariate analysis including only patients without striatocapsular involvement (SCAs-, $n = 62$), ΔTTP remained significantly correlated with

Table 1: CTP-derived venous outflow parameters in SCI and injury^a

		Striatocapsular Fate	Mean (SD)	P Value	
SCI (n = 90)	ΔTTP (sec)	Thalamostriate vein	Viable	0.786 (2.1)	.010
			Infarcted	1.954 (1.8)	
	Relative enhancement	Internal cerebral vein	Viable	0.853 (1.5)	.327
			Infarcted	1.12 (1.1)	
		Thalamostriate vein	Viable	-0.1 (0.5)	.643
			Infarcted	-0.04 (0.5)	
SCIinj (n = 116)	ΔTTP (sec)	Thalamostriate vein	Viable	0.786 (2.1)	.014
			Injured	1.953 (2.2)	
	Relative enhancement	Internal cerebral vein	Viable	0.853 (1.5)	.315
			Injured	1.101 (1)	
		Thalamostriate vein	Viable	-0.1 (0.5)	.479
			Injured	-0.5 (0.13)	
Internal cerebral vein	Viable	0.13 (0.3)	.620		
	Injured	0.17 (0.3)			

^a SCI indicates infarction in either the caudate head, caudate body, lentiform nucleus, or internal capsule. All CTP-derived venous outflow parameters were normally distributed using the Kolmogorov-Smirnov test, with the exception of thalamostriate vein relative enhancement.

Table 2: Correlation between delayed TTP and SCI or injury

		OR (95% CI) Infarct	P Value	
SCI	Delayed TTP	Thalamostriate vein	1.412 (1.072–1.86)	.014
		Internal cerebral vein	1.212 (0.827–1.776)	.325
	Delayed TTP	Thalamostriate vein	1.345 (1.052–1.719)	.018
Internal cerebral vein	1.217 (0.831–1.783)	.314		

Table 3: Thalamostriate ΔTTP and SCIs

SCIs	Mean (SD)	P Value
0	0.786 (2.1)	.030
1	1.676 (1.4)	
2	2.053 (2.0)	

SCI, with a mean $\Delta\text{TTP}_{\text{SCI}+}$ of 1.91 (SD, 2.07) seconds compared with $\Delta\text{TTP}_{\text{SCI}-}$ of 0.89 (SD, 1.86) seconds ($P = .048$).

DISCUSSION

Our study establishes a significant association between delay in deep venous outflow in the acute phase of MCA ischemic stroke and subsequent SCI after M1 thrombectomy. Accumulating evidence suggests that venous outflow may be an independent modulator of stroke evolution and clinical outcomes. Formation of microthrombi in venules distal to a cerebral arterial occlusion and a “venous steal” phenomenon possibly modulate ischemic cerebral tissue fate and may explain the failure of reperfusion despite successful recanalization.^{13–16} Incorporating venous outflow into collateral status assessment in patients having undergone thrombectomy has recently been shown to improve the prediction of clinical and radiologic outcomes.¹⁷

The evaluation of cortical venous outflow patterns in acute ischemic stroke through neuroimaging surrogate markers such as opacification of cortical veins on monophasic or multiphase

CTA^{18,19} or delayed cortical vein filling on dynamic CTA²⁰ has been recently reported. Favorable cortical venous outflow patterns have been associated with distal vessel occlusion, good baseline collaterals, successful reperfusion, decreased infarct edema, and good clinical outcome.^{18–23} Administration of IVT was strongly associated with the presence of favorable venous outflow profiles in patients before endovascular thrombectomy.²⁴ However, these neuroimaging markers have focused on the superficial cerebral venous system, which drains only cortical and juxtacortical structures. The impact of deep venous outflow on striatocapsular tissue survival has not yet been explored.

Here we present a novel approach that uses widely available CTP data to quantitate deep venous outflow as a surrogate marker for SCI. In our cohort of patients having undergone M1 thrombectomy, a higher delay in the TTP of the time-attenuation curve in the thalamostriate vein ipsilateral to an M1 occlusion (thalamostriate ΔTTP) was significantly correlated with infarction of the caudate body and lentiform nucleus separately and the striatocapsular region as a whole. Moreover, a

higher thalamostriate ΔTTP was directly correlated with a larger extent of striatocapsular ischemia represented by the striatocapsular ischemia score. These results indicate that delayed thalamostriate venous flow is an excellent surrogate marker for striatocapsular ischemia. The ORs for the correlation of thalamostriate ΔTTP with SCI was higher than that of the recently reported DT⁸ in our cohort of patients, indicating that thalamostriate ΔTTP may be more accurate than DT as a surrogate marker for SCI.

Sparing of the lateral LSAs according to preprocedural digital DSA and asymmetric dilation of LSAs following successful thrombectomy on MRA have also been shown to predict favorable outcome following M1 thrombectomy.^{25,26} However, thalamostriate ΔTTP derived from CTP may be a superior surrogate marker for SCI because it provides equivalent information in a noninvasive manner and at an earlier preprocedural stage.

In our study, 2 independent raters visually identified and manually marked the bilateral internal cerebral and thalamostriate veins on axial images of the CTP scan to produce measurements of TTP and peak enhancement. These veins were easily detectable on CTP images of most of our patients. Interrater agreement was excellent for both thalamostriate and internal cerebral TTP (ICC = 0.95) and for internal cerebral enhancement (ICC = 0.899). This finding supports the strength and reliability of our novel approach to extract venous outflow parameters from CTP raw data. Indeed, interrater agreement for thalamostriate enhancement was poor, making this

parameter unreliable for the analysis of deep venous outflow. This issue is probably due to the smaller diameter and high tortuosity of this vein combined with measurement of absolute peak enhancement on CTP images being highly angle-dependent. Subsequently, patient positioning may also affect this parameter.

Our results indicate that internal cerebral venous outflow is less accurate than thalamostriate outflow as a surrogate marker for SCI. While the thalamostriate veins drain the striatocapsular region exclusively, the internal cerebral veins receive several other major tributaries including the anterior septal veins, lateral direct veins, medial atrial veins,²⁷ and choroidal veins, which drain extra-striatocapsular cerebral tissue. This process probably dampens the effect of striatocapsular ischemia on the time-attenuation curve of the internal cerebral veins. Most interesting, thalamostriate Δ TTP was highly associated with infarction of the caudate body and lentiform nucleus but less associated with caudate head infarction. This association is probably because the caudate head is drained separately by the anterior caudate vein, which enters the thalamostriate vein beyond the point where the time-attenuation curve was measured (Figs 1 and 2). Association of internal capsule infarction with thalamostriate Δ TTP also did not reach statistical significance. We hypothesize that this finding may be due to the challenge in assessing internal capsule infarction using NCCT, resulting in limited reliability. Of note, despite high anatomic variance of the thalamostriate vein tributaries, the thalamostriate vein itself is reportedly present bilaterally in >92% of patients and consistently drains most of the striatocapsular territory.²⁸ This finding further supports the role of the thalamostriate vein as a robust imaging marker of striatocapsular drainage.

These intriguing interactions point to the enormous potential of this novel approach to extract dynamic cerebral venous outflow data with high temporal resolution from CTP images. Using the same technique, one may explore venous outflow parameters not only in acute ischemic stroke but also in healthy subjects and in patients with other acute or chronic cerebrovascular disease states. Further research may allow semi- or even fully-automatic analysis of deep venous outflow patterns in these situations.

Currently used multiphase CTA provides dynamic, high-spatial-resolution images of the cerebral vasculature. However, imaging acquisition is performed at only 3 different time points after contrast injection, and time-resolved assessment of cerebral blood flow is limited. In contrast, CTP raw data provide low spatial resolution but contain multiple time points (usually >15) and allow thorough analysis of flow parameters from the time-enhancement curve. Because our study was primarily a proof-of-concept study, we measured only TTP and peak enhancement. These parameters were the most intuitive, reproducible, and simple to extract. Additional parameters such as arrival time, wash-in time, or ascending slope may add more information and should be the subject of future analyses.

The clinical impact of SCI in the setting of successful M1 thrombectomy is uncertain. While previous studies reported pretreatment SCI to be associated with higher rates of hemorrhagic transformation, worse dysfunction and disability at discharge, and longer hospitalization,²⁹ more recent studies have reported that it does not have a significant impact on clinical outcome.^{30,31} In our cohort, functional status indices at 90 days including mean

mRS and the proportion of patients with good functional outcome ($mRS \leq 2$) were not significantly different between patients with SCI+ and SCI- (Online Supplemental Data). This result possibly indicates that isolated SCI is not an important determinant of clinical long-term prognosis and should not directly affect the decision on thrombectomy in such patients. Nevertheless, our results are highly relevant as a proof-of-concept for the use of CTP-derived venous outflow parameters for tissue prognostication. Further studies using the same concept to explore both superficial and deep venous drainage in larger-territory MCA infarctions would most likely lead to a more significant clinical correlation.

Our study has several limitations. The patient cohort was relatively small, including only 116 patients. Data were collected retrospectively, which may introduce bias. The use of a single CT scanner type and postprocessing software may limit the generalizability of our findings. Deep cerebral veins were visually identified and manually rather than automatically marked on CTP images. Tissue fate in the striatocapsular region was determined by NCCT rather than MR imaging, due to low availability of this technique in our institution. SCAs+ on admission NCCT was common in our study and correlated with eventual SCI, raising the possibility that delayed venous outflow on CTP represents the result of early infarction rather than the cause of it. However, in a multivariable analysis that controlled for admission SCAs+ and in a secondary analysis that excluded patients with SCAs+ altogether, the correlation between thalamostriate Δ TTP and SCI+ remained significant, excluding this possibility. Finally, the use of Δ TTP as a single tissue-prognostication tool is limited by a significant overlap in Δ TTP distributions between the SCI- and SCI+ groups. However, we present a simple technique with excellent interrater reliability, and the statistical power of our findings is high. These support the high reproducibility and generalizability of our results.

CONCLUSIONS

CTP-derived thalamostriate Δ TTP is an excellent surrogate marker for SCI in patients post-M1 thrombectomy. The novel approach of extracting venous outflow parameters from CTP has numerous potential applications and should be further explored.

Disclosure forms provided by the authors are available with the full text and PDF of this article at www.ajnr.org.

REFERENCES

1. Marinkovic SV, Kovacevic MS, Marinkovic JM. **Perforating branches of the middle cerebral artery: microsurgical anatomy of their extra-cerebral segments.** *J Neurosurg* 1985;63:266–71 CrossRef Medline
2. Rosner SS, Rhoton AL, Ono M, et al. **Microsurgical anatomy of the anterior perforating arteries.** *J Neurosurg* 1984;61:468–85 CrossRef Medline
3. Marinkovic SV, Milisavljevic MM, Kovacevic MS, et al. **Perforating branches of the middle cerebral artery: microanatomy and clinical significance of their intracerebral segments.** *Stroke* 1985;16:1022–29 CrossRef Medline
4. Kaesmacher J, Huber T, Lehm M, et al. **Isolated striatocapsular infarcts after endovascular treatment of acute proximal middle cerebral artery occlusions: prevalence, enabling factors, and clinical outcome.** *Front Neurol* 2017;8:272 CrossRef Medline

5. Sancho Saldaña A, Tejada Meza H, Serrano Ponz M, et al. **Incidence, outcomes, and associated factors of isolated striatocapsular infarct after mechanical thrombectomy.** *Neurologia (Engl Ed)* 2022;37:250–56 CrossRef Medline
6. Sancho-Saldana A, Tejada-Meza H, Serrano-Ponz M, et al. **Influence of mechanical thrombectomy on the incidence of isolated striatocapsular infarction and a description of its clinical characteristics** [in Spanish]. *Rev Neurol* 2019;68:236–40 CrossRef Medline
7. Kleine JF, Beller E, Zimmer C, et al. **Lenticulostriate infarctions after successful mechanical thrombectomy in middle cerebral artery occlusion.** *J Neurointerv Surg* 2017;9:234–39 CrossRef Medline
8. Friedrich B, Lobsien D, Maegerlein C, et al. **Distance to thrombus in acute middle cerebral artery stroke predicts basal ganglia infarction after mechanical thrombectomy.** *Oncotarget* 2016;7:85813–18 CrossRef Medline
9. Tan IY, Demchuk AM, Hopyan J, et al. **CT angiography clot burden score and collateral score: correlation with clinical and radiologic outcomes in acute middle cerebral artery infarct.** *AJNR Am J Neuroradiol* 2009;30:525–31 CrossRef Medline
10. Kaesmacher J, Kaesmacher M, Berndt M, et al. **Early thrombectomy protects the internal capsule in patients with proximal middle cerebral artery occlusion.** *Stroke* 2021;52:1570–79 CrossRef Medline
11. Whitney E, Khan YR, Alastra A, et al. **Contrast extravasation post thrombectomy in patients with acute cerebral stroke: a review and recommendations for future studies.** *Cureus* 2020;12:e10606 CrossRef Medline
12. Koo TK, Li MY. **A guideline of selecting and reporting intraclass correlation coefficients for reliability research.** *J Chiropr Med* 2016;15:155–63 CrossRef Medline
13. Liebeskind DS. **Imaging the collaterome: a stroke renaissance.** *Curr Opin Neurol* 2015;28:1–3 CrossRef Medline
14. Tong L, Guo Z, Ou Y, et al. **Cerebral venous collaterals: a new fort for fighting ischemic stroke?** *Prog Neurobiol* 2018;163-164:172–93 CrossRef Medline
15. Del Zoppo GJ, Mabuchi T. **Cerebral microvessel responses to focal ischemia.** *J Cereb Blood Flow Metab* 2003;23:879–94 CrossRef Medline
16. Pranevicius O, Pranevicius M, Pranevicius H, et al. **Transition to collateral flow after arterial occlusion predisposes to cerebral venous steal.** *Stroke* 2012;43:575–79 CrossRef Medline
17. Faizy TD, Mlynash M, Kabiri R, et al. **The cerebral collateral cascade: comprehensive blood flow in ischemic stroke.** *Neurology* 2022 April 18. [Epub ahead of print] CrossRef Medline
18. Jansen IG, Van Vuuren AB, Van Zwam WH, et al; MR CLEAN Trial Investigators. **Absence of cortical vein opacification is associated with lack of intra-arterial therapy benefit in stroke.** *Radiology* 2018;286:643–50 CrossRef Medline
19. Singh N, Bala F, Kim BJ, et al. **Time-resolved assessment of cortical venous drainage on multiphase CT angiography in patients with acute ischemic stroke.** *Neuroradiology* 2022;64:897–903 CrossRef Medline
20. Bhaskar S, Bivard A, Parsons M, et al. **Delay of late-venous phase cortical vein filling in acute ischemic stroke patients: associations with collateral status.** *J Cereb Blood Flow Metab* 2017;37:671–82 CrossRef Medline
21. Faizy TD, Kabiri R, Christensen S, et al. **Association of venous outflow profiles and successful vessel reperfusion after thrombectomy.** *Neurology* 2021 May 5. [Epub ahead of print] CrossRef Medline
22. Faizy TD, Kabiri R, Christensen S, et al. **Venous outflow profiles are linked to cerebral edema formation at noncontrast head CT after treatment in acute ischemic stroke regardless of collateral vessel status at CT angiography.** *Radiology* 2021;299:682–90 CrossRef Medline
23. Faizy TD, Kabiri R, Christensen S, et al. **Distinct intra-arterial clot localization affects tissue-level collaterals and venous outflow profiles.** *Eur J Neurol* 2021;28:4109–16 CrossRef Medline
24. Faizy TD, Mlynash M, Marks MP, et al. **Intravenous tPA (tissue-type plasminogen activator) correlates with favorable venous outflow profiles in acute ischemic stroke.** *Stroke* 2022 June 30. [Epub ahead of print] CrossRef Medline
25. Liu F, Chen C, Hong L, et al. **Lenticulostriate arteries appearance before thrombectomy predicts good outcome in acute middle cerebral artery occlusion.** *BMC Neurol* 2020;20:139 CrossRef Medline
26. Kaesmacher J, Kreiser K, Manning NW, et al. **Clinical outcome prediction after thrombectomy of proximal middle cerebral artery occlusions by the appearance of lenticulostriate arteries on magnetic resonance angiography: a retrospective analysis.** *J Cereb Blood Flow Metab* 2018;38:1911–23 CrossRef Medline
27. Brzegowy K, Zarzecki MP, Musiał A, et al. **The internal cerebral vein: new classification of branching patterns based on CTA.** *AJNR Am J Neuroradiol* 2019;40:1719–24 CrossRef Medline
28. Zhang X, Li J, Wen X, et al. **Susceptibility-weighted imaging of the anatomic variation of thalamostriate vein and its tributaries.** *PLoS One* 2015;10:e0141513 CrossRef Medline
29. Loh Y, Towfighi A, Liebeskind DS, et al. **Basal ganglionic infarction before mechanical thrombectomy predicts poor outcome.** *Stroke* 2009;40:3315–20 CrossRef Medline
30. Baek BH, Yoon W, Lee YY, et al. **Impact of isolated basal ganglia infarction at pretreatment DWI on outcomes after endovascular thrombectomy in acute anterior circulation stroke.** *Neuroradiology* 2019;61:89–96 CrossRef Medline
31. Horie N, Morofuji Y, Iki Y, et al. **Impact of basal ganglia damage after successful endovascular recanalization for acute ischemic stroke involving lenticulostriate arteries.** *J Neurosurg* 2020;132:1880–88 CrossRef Medline

Learning Curve for Flow Diversion of Posterior Circulation Aneurysms: A Long-Term International Multicenter Cohort Study

N. Adeeb, M. Dibas, C.J. Griessenauer, H.H. Cuellar, M.M. Salem, S. Xiang, A. Enriquez-Marulanda, T. Hong, H. Zhang, P. Taussky, R. Grandhi, M. Waqas, A.S. Aldine, V.M. Tutino, A. Aslan, A.H. Siddiqui, E.I. Levy, C.S. Ogilvy, A.J. Thomas, C. Ulfert, M.A. Möhlenbruch, L. Renieri, J.D. Bengzon Diestro, G. Lanzino, W. Brinjikji, J. Spears, J.E. Vranic, R.W. Regenhardt, J.D. Rabinov, P. Harker, E. Müller-Thies-Broussalis, M. Killer-Oberpfalzer, C. Islak, N. Kocer, M. Sonnberger, T. Engelhorn, A. Kapadia, V.X.D. Yang, A. Salehani, M.R. Harrigan, T. Krings, C.C. Matouk, S. Mirshahi, K.S. Chen, M.A. Aziz-Sultan, M. Ghorbani, C.M. Schirmer, O. Goren, S.S. Dalal, T. Finkenzeller, M. Holtmannspötter, J.-H. Buhk, P.M. Foreman, M.C. Cress, R.A. Hirschl, W. Reith, A. Simgen, H. Janssen, T.R. Marotta, C.J. Stapleton, A.B. Patel, and A.A. Dmytriv

ABSTRACT

BACKGROUND AND PURPOSE: Flow diversion has gradually become a standard treatment for intracranial aneurysms of the anterior circulation. Recently, the off-label use of the flow diverters to treat posterior circulation aneurysms has also increased despite initial concerns of rupture and the suboptimal results. This study aimed to explore the change in complication rates and treatment outcomes across time for posterior circulation aneurysms treated using flow diversion and to further evaluate the mechanisms and variables that could potentially explain the change and outcomes.

MATERIALS AND METHODS: A retrospective review using a standardized data set at multiple international academic institutions was performed to identify patients with ruptured and unruptured posterior circulation aneurysms treated with flow diversion during a decade spanning January 2011 to January 2020. This period was then categorized into 4 intervals.

RESULTS: A total of 378 procedures were performed during the study period. Across time, there was an increasing tendency to treat more vertebral artery and fewer large vertebrobasilar aneurysms ($P = .05$). Moreover, interventionalists have been increasingly using fewer overlapping flow diverters per aneurysm ($P = .07$). There was a trend toward a decrease in the rate of thromboembolic complications from 15.8% in 2011–13 to 8.9% in 2018–19 ($P = .34$).

CONCLUSIONS: This multicenter experience revealed a trend toward treating fewer basilar aneurysms, smaller aneurysms, and increased usage of a single flow diverter, leading to a decrease in the rate of thromboembolic and hemorrhagic complications.

Flow diversion has become an established treatment for intracranial aneurysms. The initial FDA approval for the Pipeline Embolization Device (PED; Covidien) was to treat large and giant

wide-neck intracranial aneurysms in the ICA, from the petrous to the superior hypophyseal segments.¹ This indication was expanded to include wide-neck ICA aneurysms up to the carotid

Received February 6, 2022; accepted after revision June 28.

From the Departments of Neurosurgery and Interventional Neuroradiology (N.A., M.D., H.H.C., A.S.A., A.A.), Louisiana State University Hospital, Shreveport, Louisiana; Departments of Neurosurgery and Radiology (C.J.G., C.M.S., O.G., S.S.D.), Geisinger, Danville, Pennsylvania; Department of Neurology/Institut of Neurointervention (C.J.G., E.M.-T.-B., M.K.-O.), University Hospital Salzburg, Paracelsus Medical University, Salzburg, Austria; Neurosurgical Service (M.M.S., A.E.-M., P.T., C.S.O.), Beth Israel Deaconess Medical Center, Harvard Medical School, Boston, Massachusetts; Department of Neurological Surgery (A.J.T.), Cooper University Health Care, Cooper Medical School of Rowan University, Camden, New Jersey; Department of Neurosurgery (S.X., H.Z., T.H.), Xuanwu Hospital, Capital Medical University, Beijing, China; Department of Neurosurgery (P.T., R.G.), University of Utah, Salt Lake City, Utah; Department of Neurosurgery (M.W., V.M.T., A.H.S., E.I.L.), State University of New York at Buffalo, Buffalo, New York; Department of Neuroradiology (C.U., M.A.M.), Universitätsklinikum Heidelberg, Heidelberg, Germany; Department of Interventional Neuroradiology (L.R.), University of Florence, Florence, Italy; Division of Diagnostic and Therapeutic Neuroradiology (J.D.B.D., J.S., T.R.M.), St. Michael's Hospital, Toronto, Ontario, Canada; Department

of Neurological Surgery (G.L., W.B.), Mayo Clinic, Rochester, Minnesota; Department of Neuroradiology (C.I., N.K.), Cerrahpasa Medical School, Istanbul University, Istanbul, Turkey; Department of Neuroradiology (M.S.), Kepler Universitätsklinikum Linz, Linz, Austria; Department of Neuroradiology (T.E.), University Hospital Erlangen, Erlangen, Germany; Departments of Medical Imaging and Neurosurgery (A.K.), Sunnybrook Health Sciences Centre, University of Toronto, Toronto, Ontario, Canada; Neurointerventional Program (V.X.D.Y., A.A.D.), Departments of Medical Imaging & Clinical Neurological Sciences, London Health Sciences Centre, Western University, Ontario, Canada; Department of Neurosurgery (A. Salehani, M.R.H.), University of Alabama at Birmingham, Birmingham, Alabama; Division of Interventional Neuroradiology (T.K.), Toronto Western Hospital, University Health Network, Toronto, Ontario, Canada; Department of Neurosurgery (C.C.M.), Yale School of Medicine, New Haven, Connecticut; Neuroendovascular Program (J.E.V., R.W.R., J.D.R., P.H., S.M., K.S.C., M.A.A.-S., C.J.S., A.B.P., A.A.D.), Massachusetts General Hospital & Brigham and Women's Hospital, Harvard Medical School, Boston, Massachusetts; Division of Vascular and Endovascular Neurosurgery (M.G.), Firoozgar Hospital, Iran University of Medical Sciences, Tehran, Iran; Institute of Radiology and Neuroradiology (T.F., M.H.), Klinikum Nuernberg Sued, Paracelsus Medical University

terminus of all sizes in February 2019.² In December 2019, the Flow Redirection Endoluminal Device (FRED; MicroVention) was approved by the FDA with indications similar to those of the PED.

Despite the remarkable advancements in technology, flow diverters were being used reluctantly to treat posterior circulation aneurysms. However, due to the challenging nature of posterior circulation aneurysms, including their high risk of rupture and the suboptimal results associated with the use of standard techniques, the off-label use of flow diverters in the treatment of these aneurysms has gradually increased, with several studies attempting to evaluate the risks and benefits.^{3–14} In a propensity-matched comparison between the PED and FRED for the treatment of posterior circulation aneurysms, Griessenauer et al¹⁵ reported no significant differences in aneurysm occlusion or neurologic complications between the devices.

A recent multicenter study investigated the change in complication rates across time for anterior circulation aneurysms treated by the PED.¹⁶ A significant decline in complications was noted, which was attributed to the continuous improvement in clinical practice and experience with the PED, including the increased use of platelet function testing before the procedures.¹⁷ In this study, we aimed to examine changes in complication rates and outcomes with time for posterior circulation aneurysms treated by the PED and FRED, given that both devices had no significant difference in treatment outcomes.¹⁵ We further sought to evaluate the mechanisms and covariates that could explain these changes.

MATERIALS AND METHODS

Patient Population

A retrospective review of prospectively maintained databases at multiple academic institutions in the United States, Canada, Europe, and Asia was performed to identify patients with posterior circulation aneurysms treated with flow diversion using the PED or FRED during a decade spanning January 2011 to January 2020. Inclusion criteria consisted of adult patients (18 years of age or older) with the pathology and treatment mentioned above. Both ruptured and unruptured aneurysms with all morphologies (ie, saccular and fusiform) were included. All consecutive patients who fit the inclusion criteria at the participating center were included. Then, these patients were categorized on the basis of the treatment year to four 2-year intervals, except for the first 3 years due to low case numbers: 2011–2013, 2014–2015, 2016–2017, and 2018–2019. We collected the following information retrospectively: patient demographics, aneurysm characteristics, antiplatelet regimen,

Nuernberg, Nuernberg, Germany; Department of Neuroradiology (M.H.), Klinikum Weiden, Weiden, Germany; Department of Neuroradiology (J.-H.B.), University Hospital Hamburg Eppendorf, Hamburg, Germany; Neuroscience and Rehabilitation Institute (P.M.F., M.C.C., R.A.H.), Orlando Health, Orlando, Florida; Clinic for Diagnostic and Interventional Neuroradiology (W.R., A. Simgen), Universitätsklinikum des Saarlandes, Homburg/Saar, Germany; and Institute for Neuroradiology (H.J.), Klinikum Ingolstadt, Ingolstadt, Germany.

Please address correspondence to Nimer Adeeb, MD, Departments of Neurosurgery and Interventional Neuroradiology, Louisiana State University, 1501 Kings Highway, Shreveport, LA 71104; e-mail: nimer_adeeb@hotmail.com; @Nimeradeeb; @adamdmytriv

 Indicates article with online supplemental data.

<http://dx.doi.org/10.3174/ajnr.A7679>

procedural details, complications, and angiographic and functional outcomes. Institutional review board approval was obtained at all centers. Patient consent was not required for this study, given that it was a retrospective analysis of de-identified data.

Complications and Outcomes

Thromboembolic complications occurring from the date of the procedure to the last follow-up were included. Intraprocedural thromboembolic complications were identified on DSA as either thrombus formation, slow filling of a previously normal-filling vessel, or complete vessel occlusion. Intraprocedural thromboembolism was treated at the discretion of the interventionalist performing the procedure. Postprocedural thromboembolic complications were identified using a combination of clinical and radiographic findings. Postprocedural imaging was performed at the discretion of the individual institutions. Routine screening for clinically silent ischemic stroke was not performed in all centers. Postprocedural imaging performed to detect an ischemic stroke could include any combination of a noncontrast CT, CTA, or MR imaging. Only ischemic strokes in the territory of the treated vessel were included. An ischemic complication was considered symptomatic if the patient reported symptoms attributable to thromboembolism or demonstrated signs attributable to thromboembolism, including both transient and permanent signs and symptoms. Hemorrhagic complications were identified intraoperatively as contrast extravasation on DSA or on postprocedural imaging. Hemorrhagic complications occurring from the time of the procedure until the last follow-up were included. Hemorrhages were counted as symptomatic if the patient reported symptoms or demonstrated signs attributable to hemorrhage. In contrast to ischemic complications, all vascular territories were included. Minor complications were defined as intraprocedural technical complications and vascular-access complications, which did not result in permanent deficits.

The angiographic outcome was assessed using DSA, MRA, or CTA. Aneurysm occlusion was categorized as complete occlusion (100%), near-complete occlusion (90%–100%), and partial occlusion (< 90%). Functional outcome was assessed using the mRS at the last follow-up. An mRS of 0–2 was considered a favorable outcome.

Statistical Analysis

Statistical analysis was conducted using R statistical and computing software (Version 4.0.2; <http://www.r-project.org/>). Numeric variables were compared using the Mann-Whitney *U* test or the Kruskal-Wallis test, depending on the number of groups, while categorical variables were compared using the χ^2 test. Univariable and multivariable logistic regression analyses were performed to identify predictors of good outcome (mRS 0–2) and thromboembolic and hemorrhagic complications. The examined covariates included age, sex, smoking, pretreatment mRS, multiple aneurysms, aneurysm location, aneurysm shape, aneurysm size, previous SAH, prior treatment, number of devices, antiplatelet regimen changed, and adjunctive coiling. Covariates that had a *P* value ≤ 0.1 in the univariable analysis were included in the multivariable analysis. A *P* value $< .05$ was considered statistically significant.

Table 1: Change in treatment outcome with time^a

	2011–2013 (n = 76)	2014–2015 (n = 118)	2016–2017 (n = 94)	2018–2019 (n = 90)	P Value	Total (n = 378)
Last follow-up imaging lapsed time (months) ^b	14.0 [28.8]	24.0 [24.0]	14.0 [16.5]	6.80 [5.00]	<.001	13.0 [20.6]
Last follow-up clinical time from treatment (months) ^c	22.5 [40.5]	29.0 [29.0]	17.0 [17.3]	6.50 [6.00]	<.001	13.0 [24.0]
Follow-up occlusion rate ^d						
Complete occlusion (100%)	47 (66.2%)	75 (68.9%)	69 (77.5%)	46 (67.7%)	.273	237 (70.3%)
Incomplete occlusion (<90%)	15 (21.1%)	14 (12.8%)	7 (7.9%)	12 (17.6%)		48 (14.2%)
Near-complete occlusion (90%–99%)	9 (12.7%)	20 (18.3%)	13 (14.6%)	10 (14.7%)		52 (15.4%)
Retreatment ^e	9 (12.2%)	13 (11.2%)	5 (5.4%)	3 (3.5%)	.092	30 (8.2%)
mRS on last follow-up ^f						
0–2	66 (88.0%)	96 (84.2%)	82 (87.2%)	78 (88.6%)	.793	322 (86.8%)
3–6	9 (12.0%)	18 (15.8%)	12 (12.8%)	10 (11.4%)		49 (13.2%)
Follow-up mRS ^f						
Improved	23 (30.7%)	28 (24.6%)	21 (22.3%)	10 (11.4%)	.034	82 (22.1%)
No change	40 (53.3%)	65 (57.0%)	58 (61.7%)	68 (77.2%)		231 (62.3%)
Worsened	12 (16.0%)	21 (18.4%)	15 (16.0%)	10 (11.4%)		58 (15.6%)
Neurologic complications						
Thromboembolic	12 (15.8%)	19 (16.1%)	10 (10.6%)	8 (8.9%)	.342	49 (13.0%)
Thromboembolic (symptomatic)	9 (11.8%)	14 (11.9%)	3 (3.2%)	7 (7.8%)	.107	33 (8.7%)
Hemorrhagic	5 (6.6%)	5 (4.2%)	4 (4.3%)	3 (3.3%)	.781	17 (4.5%)
Hemorrhagic (symptomatic)	3 (3.9%)	4 (3.4%)	3 (3.2%)	3 (3.3%)	.994	13 (3.4%)
Other procedural related complications	7 (9.2%)	9 (7.6%)	4 (4.3%)	5 (5.6%)	.57	25 (6.6%)
Mortality ^f	6 (8.0%)	9 (7.9%)	5 (5.3%)	6 (6.8%)	.881	26 (7.0%)

^a Continuous variables are presented as median [IQR]. Otherwise, data are No. (%).

^b Data missing for 46 patients.

^c Data missing for 56 patients.

^d Data missing for 41 patients.

^e Data missing for 10 patients.

^f Data missing for 7 patients.

RESULTS

Patient and Aneurysm Characteristics

A total of 378 procedures using either the PED or FRED were performed to treat posterior circulation aneurysms during the study period. The median age of the patients was 57 years, with an observed female/male ratio of 1:1. There was no significant difference in patient characteristics among the different periods as seen in the Online Supplemental Data.

Across time, there was an increasing tendency to treat vertebral artery, posterior cerebral artery, and PICA aneurysms, with a lower rate of treating large vertebrobasilar fusiform aneurysms and superior cerebellar artery aneurysms ($P = .05$). Also, there was a tendency to treat smaller aneurysms across time, but this tendency was not found to be statistically significant ($P = .27$) (Online Supplemental Data).

Treatment Outcome

There was an increasing rate of using a single device for aneurysm treatment across time, from 72.4% in 2011–13 to 87.8% in 2018–19 ($P = .07$). At a mean follow-up of 13 months, complete or near-complete occlusion (>90%) was achieved in 84.5% of aneurysms. There was no significant change in the occlusion rate during 9 years of flow-diversion experience. However, the rate of retreatment decreased with time from 12.2% in 2011–13 to 3.5% in 2018–19 ($P = .09$). Similarly, the percentage of patients with reported worsening of their clinical outcome had declined across the years, from 16% in 2011–13 to 11.4% in 2018–19 ($P = .03$).

Thromboembolic complications occurred in 13% of procedures, of which 8.7% were symptomatic. There was a trend toward a decrease in the rate of thromboembolic complications

from 15.8% in 2011–13 to 8.9% in 2018–19 ($P = .3$). There was also a nonsignificant decline in the rate of hemorrhagic complications ($P = .78$) and mortality ($P = .88$) (Table 1 and Figure).

Factors Associated with Complication Rates

Univariable analyses for determinants of thromboembolic complications are shown in Table 2. In a multivariable analysis, having a pretreatment mRS of 3–5 (adjusted OR, 3.00; 95% CI, 1.30–6.68; $P = .008$) and multiple aneurysms (adjusted OR, 2.55; 95% CI, 1.16–5.42; $P = .017$) was significantly associated with a higher risk of thromboembolic complications. On the other hand, vertebral artery aneurysms (as opposed to the basilar artery) (OR, 0.41; 95% CI, 0.18–0.90; $P = .025$) and saccular shape (as opposed to fusiform aneurysms) (OR, 0.43; 95% CI, 0.18–0.95; $P = .045$) were significantly associated with a lower risk of thromboembolic complications.

Univariable and multivariable logistic regression analyses for predictors of hemorrhagic complications are shown in the Online Supplemental Data. In a multivariable analysis, only a pretreatment mRS of 3–5 (OR, 10.15; 95% CI, 3.51–30.71; $P < .001$) was found to be associated with a higher risk of hemorrhagic complications (Online Supplemental Data).

DISCUSSION

This study reports a multicenter experience with flow diversion of posterior circulation aneurysms and the learning curve built on that experience. During the study period, there was a significant increase in the tendency to treat vertebral artery, posterior cerebral artery, and PICA aneurysms. Conversely, there was a lower tendency to treat large vertebrobasilar aneurysms. Moreover, interventionalists

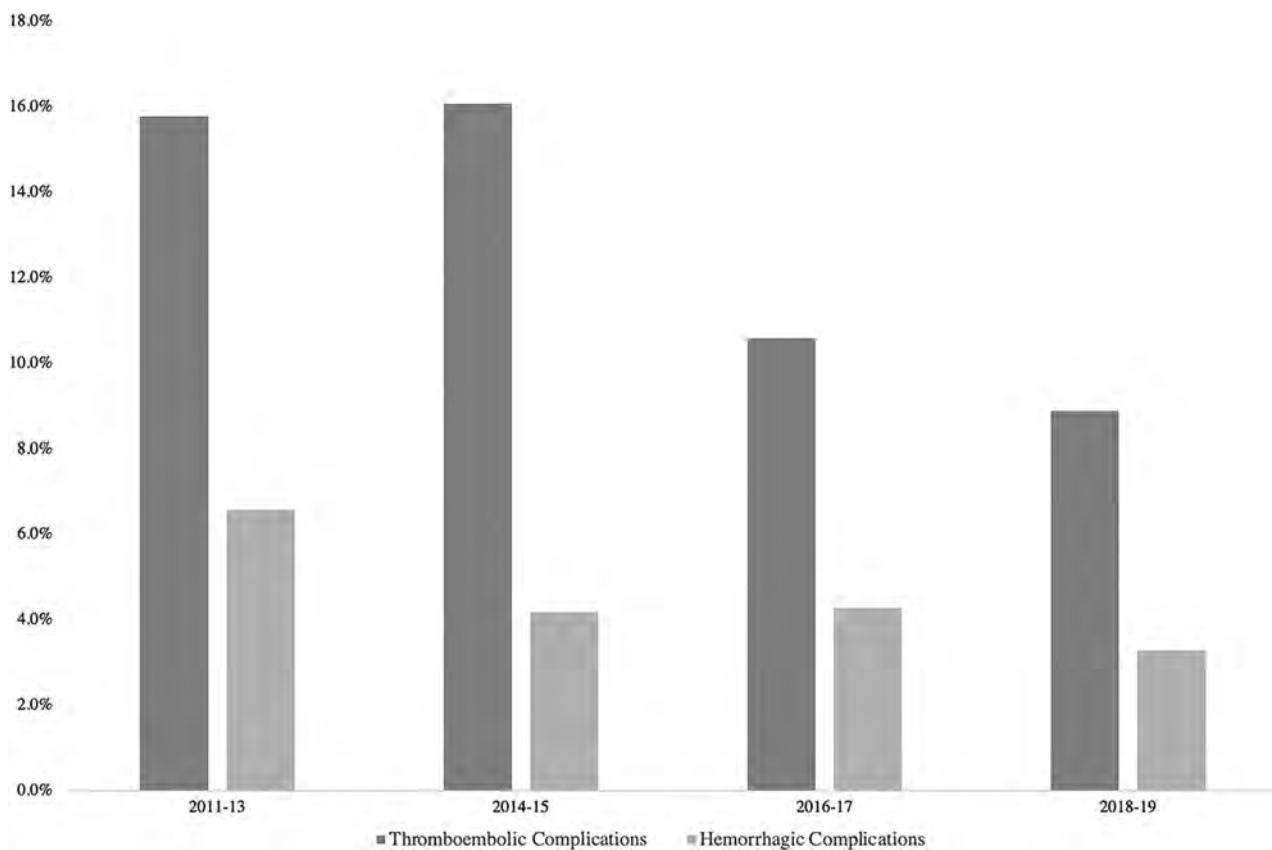


FIGURE. The rates of thromboembolic and hemorrhagic complications during the study years.

have increasingly used fewer overlapping flow diverters per aneurysm, which could also be related to treating smaller aneurysms. There was also a decline in the rate of symptomatic thromboembolic complications and retreatment rates across time. This was significantly correlated with treating saccular aneurysms and smaller aneurysms and the increased use of a single flow diverter.

To evaluate the performance of flow diversion for the treatment of posterior circulation aneurysms, Griessenauer et al¹⁸ reported the largest cohort of posterior circulation aneurysms treated with the PED. A total of 129 consecutive patients (median age, 58 years; male/female ratio of 1:1.7) underwent 129 procedures to treat 131 aneurysms. Complete or near-complete occlusion (>90%) was achieved in 79% of cases. Major (≥ 2 points of mRS change) and minor complications (<2 of mRS change), including thromboembolic and hemorrhagic strokes, occurred in 8.5% and 16.3% of patients, respectively.¹⁸ The same group also performed a propensity-matched comparison between the PED and FRED for the treatment of posterior circulation aneurysms and reported no significant differences in aneurysm occlusion or neurologic complications.¹⁵

As for the concern about the fate of posterior circulation branches following flow diversion, Adeeb et al¹⁹ found that major branching arteries in the posterior circulation including the PICA, anterior inferior cerebellar artery, and superior cerebellar artery had a low incidence of branch occlusion after coverage with flow diverters. However, occlusion of these terminal branches may carry a risk of ischemic complications, particularly when the anterior

inferior cerebellar artery is affected. On the other hand, the vertebral and the posterior cerebral arteries had relatively higher incidences of occlusions, 35% and 24%, respectively, which were attributed to the rich collateral supply. Neither branch occlusion nor ischemic complications were associated with aneurysm morphology. There was also no significant effect of the number of flow-diverting devices on branch occlusion.¹⁹

Changes in Practice to Reduce Complications

Flow diverters are designed to divert the blood flow away from the aneurysm, therefore allowing intra-aneurysmal thrombus formation followed by neointimal growth across the neck of the aneurysm. This mechanism theoretically presents an ideal treatment for large, partially thrombosed fusiform vertebrobasilar aneurysms.²⁰ In the multicenter study by Griessenauer et al,¹⁷ the rate of major complications (≥ 2 points in mRS score change) in fusiform aneurysms was 11.5%. However, a study by Natarajan et al¹⁰ showed decreased morbidity (14%–8.3%) and mortality rates (57%–0%) following treatment of those subtypes of aneurysms in their practice across time. One of the proposed reasons behind this decline in complication rates is related to moving away from the treatment of holobasilar aneurysms that are partially thrombosed because these aneurysms have a higher risk of occluding critical perforators that may only be supplied through tenuous channels crossing the thrombus. Other proposed reasons included careful attention to antiplatelet therapy, limiting the number of PEDs, and use of adjunctive coiling.¹⁰

Table 2: Predictors of thromboembolic complications^a

	Thromboembolic Complications	
	Univariable	Multivariable
Age (yr)	1.00 (0.98–1.03, <i>P</i> = .811)	
Sex		
Female	Ref	
Male	0.97 (0.53–1.76, <i>P</i> = .910)	
Smoking	1.39 (0.64–2.87, <i>P</i> = .381)	
Pretreatment mRS		
0–2	Ref	Ref
3–5	3.13 (1.48–6.38, <i>P</i> = .002)	3.00 (1.30–6.68, <i>P</i> = .008)
Multiple aneurysms	2.52 (1.23–4.98, <i>P</i> = .009)	2.55 (1.16–5.42, <i>P</i> = .017)
Aneurysm location		
Basilar artery	Ref	Ref
Posterior cerebral artery	1.00 (0.33–2.66, <i>P</i> = .997)	1.20 (0.38–3.42, <i>P</i> = .747)
Posterior inferior cerebellar artery	0.40 (0.06–1.54, <i>P</i> = .244)	0.52 (0.08–2.17, <i>P</i> = .421)
Superior cerebellar artery	0.69 (0.04–4.24, <i>P</i> = .735)	0.75 (0.04–5.50, <i>P</i> = .806)
Vertebral artery	0.45 (0.21–0.94, <i>P</i> = .032)	0.41 (0.18–0.90, <i>P</i> = .025)
Vertebrobasilar junction	2.25 (0.76–6.25, <i>P</i> = .126)	1.56 (0.46–5.03, <i>P</i> = .461)
Aneurysm shape		
Fusiform/dolichoectatic/dissecting	Ref	Ref
Saccular	0.40 (0.18–0.81, <i>P</i> = .017)	0.43 (0.18–0.95, <i>P</i> = .045)
Size of aneurysm (mm)	1.04 (1.00–1.07, <i>P</i> = .021)	1.01 (0.97–1.05, <i>P</i> = .612)
Previous SAH		
None	Ref	
<2 weeks	1.50 (0.61–3.33, <i>P</i> = .348)	
>2 weeks	0.69 (0.11–2.51, <i>P</i> = .633)	
Prior treatment		
None	Ref	
Endovascular	0.71 (0.16–2.11, <i>P</i> = .585)	
Operation	6.62 (0.26–169.46, <i>P</i> = .184)	
Both	NA	
Number of devices		
1	Ref	Ref
≥2	3.51 (1.84–6.64, <i>P</i> < .001)	1.79 (0.82–3.82, <i>P</i> = .136)
Antiplatelet regimen changed	0.72 (0.04–4.00, <i>P</i> = .759)	
Adjunctive coiling	0.76 (0.30–1.68, <i>P</i> = .531)	

Note:—NA indicates not applicable; Ref, reference variable for comparison.

^a Covariates that have *P* < .1 in the univariable analysis were included in the multivariable analysis. Data are OR (95% CI, *P* Value).

In a meta-analysis of posterior nonsaccular aneurysms treated with flow diversion, Kiyofuji et al¹¹ added that treatment of aneurysms of <10 mm was associated with fewer complications compared with those larger than 10 mm (18% versus 29%). They also found that aneurysms located within the vertebral artery (83%) had a better outcome compared with the vertebrobasilar junction and proximal basilar artery (33%), mid-/distal basilar artery, and holobasilar artery (18%).¹¹ This finding is potentially related to the abundance of perforators along the basilar artery compared with the vertebral artery. Additionally, the holobasilar fusiform dolichoectatic aneurysm is the product of the unique and poorly understood pathophysiology distinct from other aneurysms. In our study, we have noticed significant changes across the years that align with these recommendations. Additionally, basilar artery aneurysms and fusiform shape were independent predictors of thromboembolic complications compared with their vertebral artery aneurysms and saccular counterparts. Thus, interventionalists transitioned to treating more vertebral artery aneurysms and fewer large vertebrobasilar aneurysms across the years, particularly asymptomatic ones. Also, the median size of aneurysms treated declined from 9 mm in 2011–13 to 7.7 mm in 2018–19. Despite the significant change in the size and location of aneurysms treated,

there was no significant change in the rate of fusiform aneurysms treated, per se, across time.

One of the other factors suggested by Natarajan et al¹⁰ to reduce complications was limiting the number of overlapping flow diverters, because more devices were associated with an increased risk of perforator occlusion due to greater metal coverage. In our study, there was a significant shift to using only 1 device across time, from 72.4% of procedures in 2011–13 to 87.8% in 2018–19.

Moreover, as implied in the previous study on anterior circulation aneurysms, careful monitoring of platelet testing before procedures and switching to appropriate antiplatelet regimens in cases of clopidogrel nonresponders may have played a role in the drop of thromboembolic complications.^{16,17} The rate of platelet function testing in this study (72.9%) was lower than the ones reported by previous PED studies (96.1% and 88.5%).^{16,21}

Poor clinical status (mRS 3–5) at presentation was an independent predictor of treatment complications. These patients were more likely to present with a ruptured aneurysm (70.2%) compared with patients with an mRS of 0–2 (19.3%, *P* < .001). Patients with poor clinical status and ruptured aneurysms were more prone to complications related to brain injury and delayed cerebral ischemia.²² Those patients were also more likely to

present with fusiform aneurysms (76.6%) than patients with an mRS of 0–2 (64.5%, $P = .07$). Moreover, 17% of these patients had large or giant aneurysms (>20 mm) compared with 11.7% of patients with an mRS of 0–2 ($P = .2$). All these factors might have contributed to the increased rate of complications in this subgroup of patients.

Limitations

The primary limitations of the current study include its retrospective design and variability in the management of patients across centers. Retrospective studies are subject to incomplete data sets, selection bias, and unidentified confounders. The inclusion of multiple institutions improves the generalizability of the findings but introduces variability in patient management. This also introduces variation in aneurysm measurement and the device compaction rate. However, the use of a standardized datasheet among all centers and the large number of cases included should improve the generalization of the results. Although the study addresses improvement in patient and aneurysm selection, it does not account for improvement in the catheters and implants across the years. Screening of silent ischemic complications postoperatively was not routinely performed, which might underestimate the true thromboembolic rate. Moreover, the variability in the follow-up imaging protocol, especially with the use of noninvasive modalities (ie, CTA and MRA), introduces another bias, given that those modalities are less reliable in assessing endoleaks in fusiform aneurysms.

CONCLUSIONS

This is the largest study that evaluates the real-world practice trends in the treatment of posterior circulation aneurysms using flow diversion. Across the years, fewer basilar and vertebrobasilar junction aneurysms were treated, but more aneurysms of the vertebral artery. The average diameter of treated aneurysms has also decreased. These practice changes align with prior studies that showed a dire outcome from treatment of large and partially thrombosed fusiform basilar aneurysms. This led to a gradual decline in the rate of thromboembolic and hemorrhagic complications.

Disclosure forms provided by the authors are available with the full text and PDF of this article at www.ajnr.org.

REFERENCES

1. Nelson PK, Lylyk P, Szikora I, et al. **The Pipeline Embolization Device for the intracranial treatment of aneurysms trial.** *AJNR Am J Neuroradiol* 2011;32:34–40 CrossRef Medline
2. **Prospective Study on Embolization of Intracranial Aneurysms With Pipeline™ Embolization Device.** Full Text View. ClinicalTrials.gov. <https://clinicaltrials.gov/ct2/show/NCT02186561>. Accessed October 1, 2022
3. Griessenauer CJ, Ogilvy CS, Adeeb N, et al. **Pipeline embolization of posterior circulation aneurysms: a multicenter study of 131 aneurysms.** *J Neurosurg* 2019;130:923–35 CrossRef Medline
4. Chalouhi N, Tjoumakaris S, Dumont AS, et al. **Treatment of posterior circulation aneurysms with the Pipeline Embolization Device.** *Neurosurgery* 2013;72:883–89 CrossRef Medline
5. Albuquerque FC, Park MS, Abla AA, et al. **A reappraisal of the Pipeline Embolization Device for the treatment of posterior circulation aneurysms.** *J Neurointerv Surg* 2015;7:641–45 CrossRef Medline
6. Ducruet AF, Crowley RW, Albuquerque FC, et al. **Reconstructive endovascular treatment of a ruptured vertebral artery dissecting aneurysm using the Pipeline Embolization Device.** *J Neurointerv Surg* 2013;5:e20 CrossRef Medline
7. Mazur MD, Kilburg C, Wang V, et al. **Pipeline Embolization Device for the treatment of vertebral artery aneurysms: the fate of covered branch vessels.** *J Neurointerv Surg* 2016;8:1041–47 CrossRef Medline
8. Phillips TJ, Wenderoth JD, Phatouros CC, et al. **Safety of the Pipeline Embolization Device in treatment of posterior circulation aneurysms.** *AJNR Am J Neuroradiol* 2012;33:1225–31 CrossRef Medline
9. Siddiqui AH, Abla AA, Kan P, et al. **Panacea or problem: flow diverters in the treatment of symptomatic large or giant fusiform vertebrobasilar aneurysms.** *J Neurosurg* 2012;116:1258–66 CrossRef Medline
10. Natarajan SK, Lin N, Sonig A, et al. **The safety of Pipeline flow diversion in fusiform vertebrobasilar aneurysms: a consecutive case series with longer-term follow-up from a single US center.** *J Neurosurg* 2016;125:111–19 CrossRef Medline
11. Kiyofuji S, Graffeo CS, Perry A, et al. **Meta-analysis of treatment outcomes of posterior circulation non-saccular aneurysms by flow diverters.** *J Neurointerv Surg* 2018;10:493–99 CrossRef Medline
12. Bhogal P, Pérez MA, Ganslandt O, et al. **Treatment of posterior circulation non-saccular aneurysms with flow diverters: a single-center experience and review of 56 patients.** *J Neurointerv Surg* 2017;9:471–81 CrossRef Medline
13. Bender MT, Colby GP, Jiang B, et al. **Flow diversion of posterior circulation cerebral aneurysms: a single-institution series of 59 cases.** *Neurosurgery* 2019;84:206–16 CrossRef Medline
14. Adeeb N, Ogilvy CS, Griessenauer CJ, et al. **Expanding the indications for flow diversion: treatment of posterior circulation aneurysms.** *Neurosurgery* 2020;86:S76–84 CrossRef Medline
15. Griessenauer CJ, Enriquez-Marulanda A, Xiang S, et al. **Comparison of PED and FRED flow diverters for posterior circulation aneurysms: a propensity score matched cohort study.** *J Neurointerv Surg* 2021;13:153–58 CrossRef Medline
16. Dmytriw AA, Phan K, Salem MM, et al. **The Pipeline Embolization Device: changes in practice and reduction of complications in the treatment of anterior circulation aneurysms in a multicenter cohort.** *Clin Neurosurg* 2020;86:266–71 CrossRef Medline
17. Adeeb N, Griessenauer CJ, Foreman PM, et al. **Use of platelet function testing before Pipeline Embolization Device placement: a multicenter cohort study.** *Stroke* 2017;48:1322–30 CrossRef Medline
18. Griessenauer CJ, Ogilvy CS, Adeeb N, et al. **Pipeline embolization of posterior circulation aneurysms: a multicenter study of 131 aneurysms.** *J Neurosurg* 2018;130:923–35 CrossRef Medline
19. Adeeb N, Griessenauer CJ, Dmytriw AA, et al. **Risk of branch occlusion and ischemic complications with the Pipeline Embolization Device in the treatment of posterior circulation aneurysms.** *AJNR Am J Neuroradiol* 2018;39:1303–09 CrossRef Medline
20. Szikora I, Turányi E, Marosfoi M. **Evolution of flow-diverter endothelialization and thrombus organization in giant fusiform aneurysms after flow diversion: a histopathologic study.** *AJNR Am J Neuroradiol* 2015;36:1716–20 CrossRef Medline
21. Gupta R, Moore JM, Griessenauer CJ, et al. **Assessment of dual-antiplatelet regimen for Pipeline Embolization Device placement: a survey of major academic neurovascular centers in the United States.** *World Neurosurg* 2016;96:285–92 CrossRef Medline
22. de Oliveira Manoel AL, Goffi A, Marotta TR, et al. **The critical care management of poor-grade subarachnoid haemorrhage.** *Crit Care* 2016;20:21 CrossRef Medline

Effective Dose Measurements of the Latest-Generation Angiographic System in Patients with Acute Stroke: A Comparison with the Newest Multidetector CT Generation

A. Brehm, K.A.T. Nguyen, K.A. Blackham, and M.-N. Psychogios

ABSTRACT

BACKGROUND AND PURPOSE: Patients with acute ischemic stroke are increasingly triaged with one-stop management approaches, resulting in baseline imaging with a flat detector CT scanner. This study aimed to estimate the effective dose to a patient of a novel cervical and intracranial flat detector CT angiography and a flat detector CT perfusion protocol and to compare it with the effective dose of analogous multidetector row CT protocols.

MATERIALS AND METHODS: We estimated the effective dose to the patient according to the International Commission on Radiological Protection 103 using an anthropomorphic phantom with metal oxide semiconductor field effect transistor dosimeters. Placement was according to the organ map provided by the phantom manufacturer. We used 100 measurement points within the phantom, and 18 metal oxide semiconductor field effect transistor dosimeters were placed on the surface of the phantom. All protocols followed the manufacturer's specifications, and patient positioning and collimation were performed as in routine clinical practice. Measurements were obtained on the latest-generation angiography and multidetector row CT systems with identical placement of the metal oxide semiconductor field effect transistor dosimeters.

RESULTS: The estimated effective doses of the investigated perfusion protocols were 4.52 mSv (flat detector CT perfusion without collimation), 2.88 mSv (flat detector CT perfusion with collimation), and 2.17 mSv (multidetector row CT perfusion). A novel protocol called portrait flat detector CT angiography that has a z-axis coverage area comparable with that of multidetector row CT angiography had an estimated effective dose of 0.91 mSv, while the dose from multidetector row CT was 1.35 mSv.

CONCLUSIONS: The estimated effective dose to the patient for flat detector CT perfusion and angiography on a modern biplane angiography system does not deviate substantially from that of analogous multidetector row CT protocols.

ABBREVIATIONS: AIS = acute ischemic stroke; FDCT = flat detector CT; FDCT-A = flat detector CT angiography; FDCT-P = flat detector CT perfusion; ICRP = International Commission on Radiologic Protection; MDCT = multidetector CT; MDCT-A = multidetector CT angiography; MDCT-P = multidetector CT perfusion; MOSFET = metal oxide semiconductor field effect transistor

Implementing a one-stop management workflow can substantially shorten door-to-groin and door-to-reperfusion times.^{1,2} It can, furthermore, lead to improved patient outcomes according to a recently published randomized controlled trial.³ The one-stop management workflow combines diagnostic imaging and interventional therapy of patients with acute ischemic stroke (AIS) in 1 room—the angiography suite. Flat detector CT (FDCT) is used for the initial diagnostic imaging rather than the traditional approach in which the patient must first be transported to the multidetector CT (MDCT) room for diagnostic imaging and then

subsequently to the angiography suite for treatment.¹ One possible disadvantage of FDCT compared with MDCT is the limited coverage of FDCT angiography (FDCT-A), because it is impossible to simultaneously visualize the intracranial vessels, the extracranial vessels, and the aortic arch. This limitation was recently partially resolved by the introduction of a new portrait FDCT-A prototype in which the detector is rotated by 90° for an increased FOV. Furthermore, a recent publication showed a strong correlation between FDCT-perfusion (FDCT-P) and multidetector row perfusion (MDCT-P) for the automated measurements of ischemic core and ischemic penumbra volumes in patients with AIS, suggesting that FDCT-P can be used as effectively and reliably as MDCT-P.⁴ Despite the growing use of these protocols, the effective dose to the patient and, more specifically, the dose to the lens of the eye were not systematically compared with analogous MDCT protocols.

Received March 22, 2022; accepted after revision August 6.

From the Department of Neuroradiology, Clinic of Radiology and Nuclear Medicine, University Hospital Basel, Basel, Switzerland.

Please address correspondence to Alex Brehm, PhD, Department of Neuroradiology, Clinic of Radiology and Nuclear Medicine, University Hospital Basel, Petersgraben 4, 4031 Basel, Switzerland; e-mail: alex.brehm@usb.ch

<http://dx.doi.org/10.3174/ajnr.A7658>

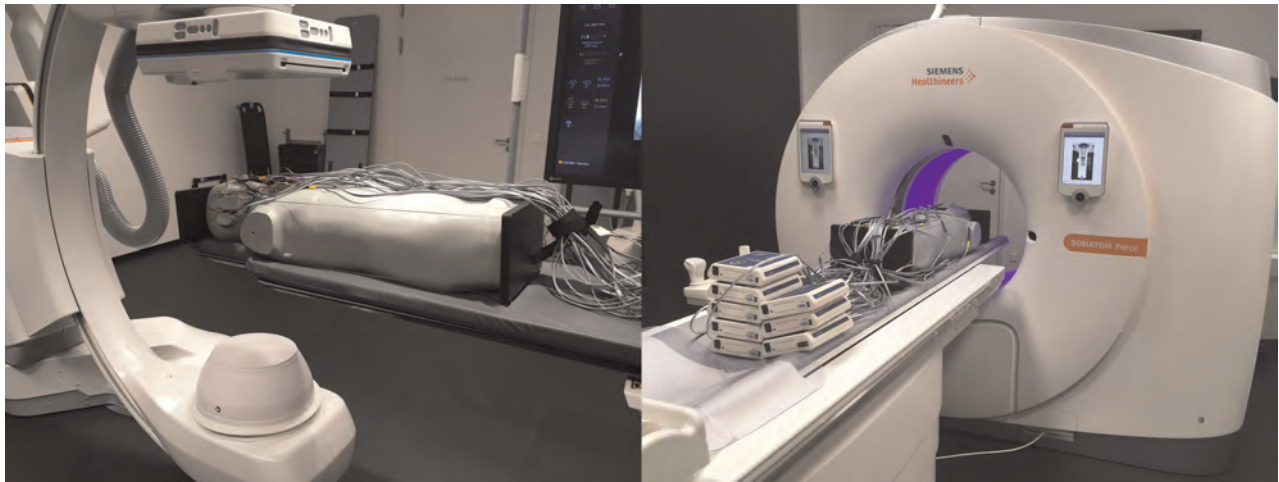


FIG 1. The anthropomorphic ATOM phantom used for effective dose measurement. The phantom in an experimental setup for 3D acquisition is equipped with MOSFET dosimeters on an Artis icono biplane angiography system (*left*) and on the Somatom Force CT scanner (*right*).

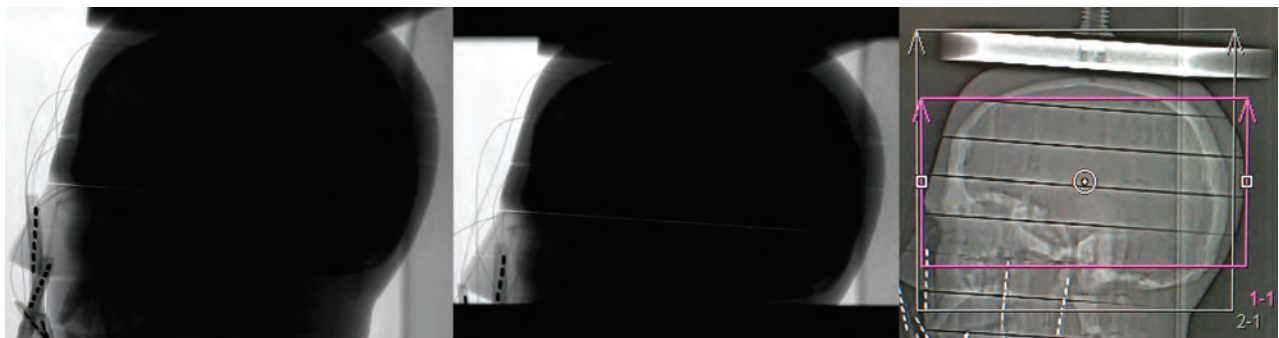


FIG 2. Lateral view of the investigated head area of the phantom for uncollimated measurement (*left*) and collimated measurement (*middle*) of the 60s DCT head perfusion protocol on the Artis icono and for perfusion measurement on the Somatom Force (*right*).

In the present study, we used a phantom to measure the effective dose to the patient and the eye lens dose of FDCT-P and portrait FDCT-A and to compare the results obtained with those obtained from analogous MDCT protocols.

MATERIALS AND METHODS

Phantom

We used an adult male ATOM phantom 701-C (Computerized Imaging Reference Systems) to measure the effective dose (Fig 1); the phantom represents the body of a male human with a height of 173 cm and a body weight of 73 kg. The phantom consists of averaged materials for soft, bone, lung, and brain tissues. The phantom is equipped with 39 slices of 2.5-cm thickness, all of them having cavities for detector placement in a 1.5×1.5 cm grid with a 0.5-cm diameter.

Dosimeters

For assessing the organ dose, we used metal oxide semiconductor field effect transistor (MOSFET) TN 1002RD-H dosimeters used with the MobileMOSFET system, model TN-RD-70-W (Best Medical Canada). The MobileMOSFET system consists of a remote monitoring dose-verification software, a Bluetooth wireless

transceiver, and a reader module that acts as a channel between the MOSFET dosimeters and software. Up to 5 MOSFET dosimeters can be connected to 1 reader. In this study, 8 readers and 40 MOSFET dosimeters were used for simultaneous measurements. Before the measurements, all MOSFET dosimeters were calibrated. For calibration purposes, each of the MOSFET dosimeters was irradiated with a specified dose. The dose was then measured with an ionization chamber (PM500-CII 52.8210; Capintec) connected to the Unidos dosimeter (PTW Friburg) as described before.⁵

C-Arm Angiography and CT Systems

We performed the measurements on an Artis icono biplane angiography system (Siemens Healthineers AG) with a Neuro Tabletop and Mattress (<https://www.sg mattress.sg/>) and on a Somatom Force CT scanner (Siemens Healthineers AG) with syngo CT VB20 software. For measurements on the Artis icono system, the A-plane C-arm was placed in the anterior-posterior position and the FOV for 3D imaging was set in the head region of the phantom. The perfusion measurements on the Artis icono system were performed with and without collimation of the x-ray field (Fig 2). The craniocaudal collimation and positioning of the phantom was applied according to the procedure-specific settings used in the clinical workflow at

the University Hospital Basel. The scan z-coverage in the collimated setup was 15 cm, derived from averaging the scan z-coverage of all scans obtained at the University Hospital Basel. The protocol is described in detail elsewhere.⁶ For perfusion measurements on the Somatom Force CT scanner, we used the standard acquisition protocol from the manufacturer. The scan z-coverage for perfusion measurements on the Somatom Force system is 11.4 cm.

In addition, we investigated the 3D imaging protocols for visualization of the carotid and intracranial arteries. The acquisition protocols for both systems were used as in clinical practice. For measurements on the Artis icono system, the detector was used in portrait mode without collimation (Fig 3). The imaging protocol

with the detector in portrait mode (ie, rotated by 90°) is the latest 3D imaging prototype on the Artis icono. For 3D imaging of the carotid arteries on the Somatom Force CT scanner, the CARE Dose 4D and CARE kV technologies (Siemens) were applied. To ensure comparable results, we used the same z-coverage area for the FDCT-A and MDCT angiography (MDCT-A), excluding the aortic arch. We summarized the technical parameters of the 3D acquisition protocols for both systems in Tables 1 and 2.

Estimation of Effective Dose

To estimate the organ dose, we placed the MOSFET dosimeters in 118 measurement points in the ATOM phantom and on the phantom surface.

The locations of the measurement points within the phantom were defined according to the organ map provided by the phantom manufacturer. These locations represent the anatomic positions of different organs (brain, eye lenses, salivary glands, thyroid, esophagus, bone surface, lung, liver, stomach, pancreas, adrenal gland, small intestine, spleen, kidney, red bone marrow, bladder, gonads, and so forth). To fit the MOSFET dosimeters within the phantom holes, we placed each dosimeter into the tissue-equivalent holder. The skin dose was measured by 18 dosimeters positioned on the surface of the phantom at slices 4, 10, 17, 28, and 38. We used

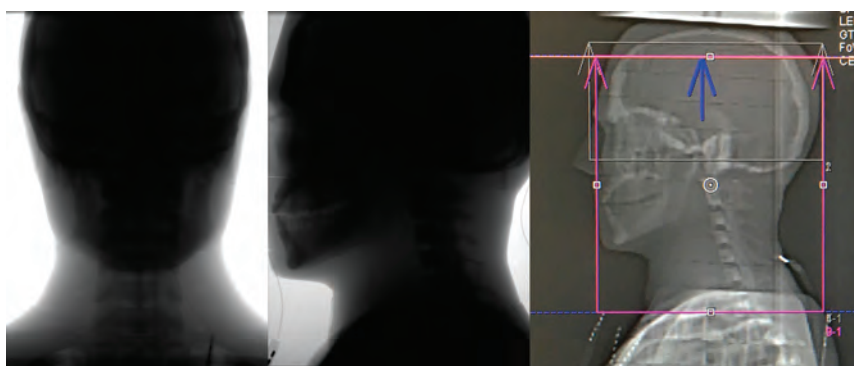


FIG 3. The position of the investigated head area of the phantom for carotid measurement on the Artis icono in frontal (*left*) and lateral (*middle*) views and on the Somatom Force in the lateral view (*right*).

Table 1: Technical parameters of investigated 3D imaging protocols (brain perfusion, portrait angiography with head and neck angiography), measured eye lens dose (for left, right eye and mean), and effective dose for the anthropomorphic ATOM male phantom on Artis icono

3D Imaging Protocol Parameters	60s DCT Head Perfusion (10 Rotations)		4s DCT Head Portrait (1 Rotation)
Reconstructed volume size (diameter × height) (cm)	24 × 18.5 (uncollimated)	24 × 15 ^a	18.5 × 24 (uncollimated)
Tube voltage (nominal) (kV)	70	70	90
Dose/frame (nominal) (nGy/f)	360	360	1200
Rotation range	200°	200°	200°
Angulation step (<i>df</i>)	0.8	0.8	0.8
Eye lens dose (mean) (mGy)	65 and 69 (SD, 67)	54 and 58 (SD, 56)	7.7 and 8.3 (SD, 8)
Estimated effective dose (mSv)	4.52	2.88	0.91

Note:—60s DCT indicates 60s Dyna-CT; 4s DCT, 4s Dyna CT.

^a Collimation was defined on the basis of usual clinical workflow at the University Hospital Basel.

Table 2: Technical parameters of investigated protocols (brain perfusion and head and neck angiography), measured eye lens dose (for left, right eye and mean), and effective dose for the anthropomorphic ATOM male phantom on Somatom Force

3D Imaging Protocol Parameters	NeuroVPCT_Prolonged, DynMulti4D	NeuroVPCT_Prolonged, Head Angio
Scan coverage (cm)	11.4	24
Tube voltage (kV)	70	90
Scan duration (sec)	60	NA
Number of cycles @ 1.5 seconds cycle time	30	NA
CTDIvol (mGy)	144.2	19.9
DLP (mGy × cm)	2169.5	550
Eye lens dose (mean) (mGy)	119 and 125 (SD, 122)	11.8 and 11.7 (SD, 11.8)
Estimated effective dose (mSv)	2.17	1.35

Note:—CTDIvol indicates volume CT dose index; DLP, dose-length product; NA, not applicable.

Table 3: Organ dose in milligrays for selected organs and tissues of investigated 3D imaging protocols on the Artis icono

Organ	60s DCT Head Perfusion (10 Rotations, Uncollimated)	60s DCT Head Perfusion (10 Rotations, Collimated)	4s DCT Head Portrait (1 Rotation)
Brain	100.8	84.7	11.8
Salivary glands	56.2	7.4	11.4
Thyroid	3.5	1.8	6.1
Lung	1.3	0.8	0.2
Red bone marrow	17.4	12.1	2.4
Esophagus	1.1	0.7	0.8

Table 4: Organ dose in milligrays for selected organs and tissues of investigated 3D imaging protocols on the Somatom force

Organ	NeuroVPCT_Prolonged, DynMulti4D	NeuroVPCT_Prolonged, Head Angio
Brain	71.6	7.8
Salivary glands	6.4	8
Thyroid	1.3	17.2
Lung	0.4	1.3
Red bone marrow	9.2	1.3
Esophagus	0.4	2.0

the same distribution and positioning of the dosimeters in all measurements.

With the identical setup of dosimeters, we repeated all 3D imaging protocols 3 times to ensure adequate radiation of the dosimeters outside the direct radiation field. The organ dose was calculated as the mean value of the measured data from all dosimeters placed into the respective organ sites. For organs such as skin, red bone marrow, esophagus, and lungs that, depending on the applied 3D imaging protocol and the scanned area, were exposed to both direct and scattered radiation, the fraction of directly irradiated organ volume in the head and neck region was considered for calculation of the organ dose. The fraction of the directly irradiated skin area was estimated according to the so-called “rule of nines” used in trauma and emergency medicine to assess the total body surface area involved in patients with burns.⁷ We estimated it to be 8% for the whole-head region and 10% for the head and neck region. The red bone marrow in the whole-head region was considered to be roughly 10%, and in the head and neck region, it was roughly 15% of total body red marrow.⁸ These data were used to calculate the effective dose according to the guidelines of the International Commission on Radiologic Protection (ICRP) 103.⁹ The radiation-weighting factor for x-ray was assumed to be 1 in concordance with the ICRP 103.⁹

The accuracy of our measurements was estimated to be $\pm 20\%$. This estimation considers all possible sources of errors, such as uncertainty of the reference dosimeter, uncertainty of estimation of calibration factors, and the uncertainty of calculation of the dose for each organ location.

RESULTS

We summarized the estimated effective dose to the patient values for the investigated FDCT protocols in Table 1 and the investigated MDCT protocols in Table 2.

The estimated effective dose to a patient of the FDCT-P protocol was 4.52 mSv without collimation and 2.88 mSv with collimation. The collimated dose of FDCT-P was 33% higher than the measured dose on MDCT (2.17 mSv). Eye lens doses of the perfusion protocols were 2-fold higher on MDCT (122 mGy) compared with uncollimated FDCT (67 mGy) and collimated FDCT (56 mGy).

The estimated effective dose to a patient of the portrait FDCT-A (0.91 mSv) was 48% lower than the effective dose of the corresponding MDCT-A protocol (1.35 mSv). The eye lens dose was also lower at 8 mGy compared with 11.8 mGy.

In all measurements, at least 95% of the radiation was recorded in the brain, red bone marrow, salivary glands, lung, esophagus, and thyroid. The remaining organs received <5% of the radiation, rendering them relatively clinically unimportant. A detailed overview of the dose distribution can be found in the Tables 3 and 4.

DISCUSSION

Our study has the following main findings: 1) Collimation has a powerful impact on the estimated effective dose to the patient because it can reduce the dose by almost 50%, 2) the estimated effective dose to the patient of the collimated FDCT-P and of the portrait FDCT-A does not deviate substantially from analogous MDCT protocols, and 3) the eye lens dose appears to be similar on FDCT and MDCT.

Two prior publications estimating the effective dose to a patient of FDCT-P on predecessor systems (Artis Q and Artis Axiom; Siemens Healthineers AG) reported higher doses with 5.9 and 5.1 mSv, respectively.^{6,10} However, these measurements must be compared with our uncollimated dose results (4.52 mSv) because no use of collimation was reported in either publication. In this case, a 12% difference in the measurements of Struffert et al¹³ is well within the margin of error; however, the 30% difference compared with our prior publication⁶ is outside this margin. This difference could partly be explained by a different phantom and fewer measurement points. Furthermore, the directly and indirectly irradiated tissues were not analyzed separately in our previous publication, possibly leading to an overestimation of the organ doses, especially red bone marrow.⁸ From a clinical standpoint, the collimated dose of FDCT-P is more important because the z-coverage can easily be reduced to parallel the parameters of MDCT-P.

Even more relevant is our result that the effective dose estimated for the collimated FDCT-P is only slightly higher than that with MDCT-P (33%), despite the considerably larger z-axis coverage area of 15 cm compared with the MDCT-P coverage of 11.4 cm (Fig 2 for reference). Nevertheless, MDCT-P for the triage

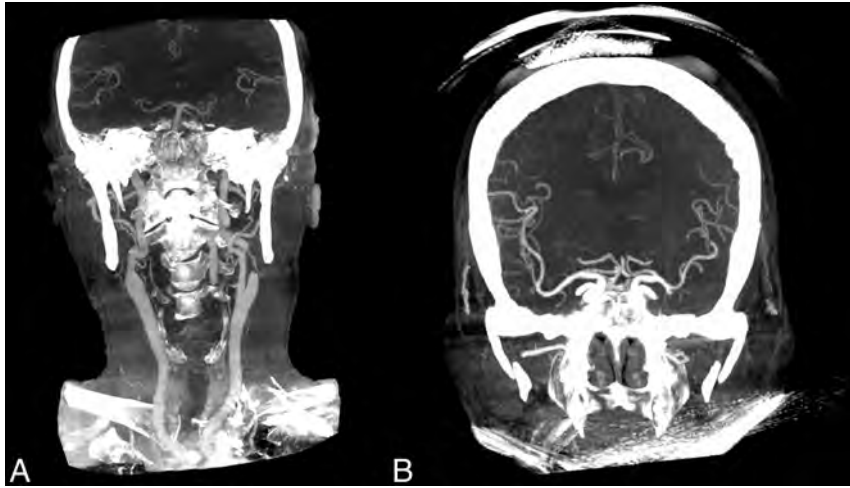


FIG 4. Comparison of the coverage area of portrait FDCT-A (A) and landscape FDCT-A (B) (based on reconstructed coronal MIPs).

of patients with late-window stroke has been validated in 2 randomized controlled trials,^{11,12} while the technical equivalence of FDCT perfusion has yet to be established. A recent pilot trial of 13 patients showed promising results with high correlation for both ischemic core volume measurements on FDCT-P and MDCT-P and for follow-up infarct volumes.⁴ We presuppose that our current results will contribute to the effort to reproduce such clinically meaningful results in larger patient collectives.

While it is widely accepted that FDCT offers higher spatial resolution for high-contrast structures (eg, vessels and bones), an essential shortcoming of FDCT-A is the limited z-coverage area.¹³ This problem is largely solved by the development of a portrait FDCT-A protocol, which has a z-coverage area large enough to simultaneously visualize the circle of Willis and the intra- and extracranial carotid arteries down to their origins (Fig 4). This information is vital for planning interventions because the aortic arch configuration can influence the optimal vascular access site (eg, radial versus femoral) and for determining which catheters should be used for navigation to the intracranial vessels.^{14,15} Another difference between FDCT-A and MDCT-A is that the timing of the acquisition after the injection of the contrast media bolus is operator-dependent. In contrast to MDCT-A, in which an automated Hounsfield unit threshold trigger is typically used for the start of the scan (by placing an ROI in the ascending aorta), the scan start has to be executed manually in FDCT-A.¹⁶ To address this difference, we developed a “bolus-watching” protocol in which DSA is used to monitor the visible influx of contrast media into the common carotid arteries (following a 10-second delay after intravenous contrast injection) to manually initiate the 3D angiography.¹⁶ According to previous measurements, this protocol adds only a minor radiation dose.⁶

The overall dose for perfusion and angiography on FDCT is, at 3.79 mSv, only slightly higher (8%) compared with MDCT. This difference is well below the accuracy threshold for the effective dose for patient measurements and, therefore, could be neglected. Both protocols (perfusion and angiography) are often used, even in the early time window of thrombolysis because it is more commonly recognized that perfusion plays an important role in the

detection of medium and distal vessel occlusions,^{17,18} ie, as potential targets for mechanical thrombectomy.¹⁹ Recent measurements have shown an effective dose of 2 mSv for noncontrast FDCT parenchymal imaging, which is comparable with that of MDCT.^{20,21} Because the cumulative dose of commonly used protocols in one-stop management of acute ischemic stroke does not differ substantially from routine MDCT, we anticipate that our findings will mitigate dose considerations in the triage decisions of patients with AIS.

The lower dose to the lens of the eye from FDCT-P compared with MDCT-P is explained by the reduced range of rotation of the flat detector, which is between 200° and 220° for most protocols with the radiation source being, importantly,

below the patient.²² However, the eye lens doses for the perfusion protocols have to be interpreted with caution because we were not able to incline the head of the phantom. Flexing the head toward the chin, as is performed for MDCT-P at our institution, might reduce the direct irradiation of the lens and, therefore, might reduce the dose substantially.²³ With regard to the standard MDCT-A protocol, the effect of inclining the head should not have a relevant proportional impact due to the large z-coverage area. However, there is an alternative protocol (HeadAngio_Xcare; Siemens Healthineers AG) using an organ-based tube-current modulation, which can reduce the eye lens dose. In this protocol, the direct x-ray exposure to the eye lens is reduced by lowering the x-ray tube current for a certain range of projection angles when the eye lenses are facing toward the x-ray tube. This protocol was not evaluated in this article. Overall, the certainty for the magnitude of the reduction of the lens dose is low because we were not able to incorporate all influencing factors.

One major strength of our study is that we used an anthropomorphic phantom with an identical measurement setup for both systems. This feature allows a reproducible comparison between different x-ray imaging modalities, acquisition protocols, and studies. This approach is superior to other measurement approaches, such as simulations or CT dose index–based approaches because the modern C-arm devices typically use a 210° rotation compared with MDCT, which has a 360° rotation. In the case of FDCT, this difference leads to a nonuniform dose distribution with the peak dose occurring in the central plane, on the side of the phantom closest to the radiation source.²⁴ Furthermore, the larger z-coverage of FDCT compared with MDCT renders the traditional, weighted CT dose index approaches impractical.²² Another strength of our study is that we measured analogous protocols on both systems, enabling us to directly compare the effective dose to the patient from modern stroke imaging protocols.

However, our study has some limitations as well. The ATOM phantom is constructed to represent a broad cohort of different patients. Therefore, the actual dose to a patient might differ from the dose measured with the ATOM phantom. Because the ICRP

103 does not define the distribution and number of measurement points within the phantom, the investigator typically chooses these parameters.⁹ This situation can lead to differences in the estimated effective dose, depending on the number and position of measurement points within an anthropomorphic phantom. In addition, Roser et al²⁵ showed that the organ-equivalent dose values calculated from discrete measurements might underestimate the simulated organ dose that was calculated on the basis of a continuous dose distribution by up to 50%. In the clinical routine, variance to our phantom study could occur not only with the collimation of the x-ray field but also with the ROI, through normal practitioner and patient differences. However, because these parameters can be largely standardized in stroke protocols and because the coverage areas of the FDCT were at least as large as on the MDCT, our collimated results should be generalizable to clinical routine.

CONCLUSIONS

The estimated effective dose to the patient for FDCT-P and FDCT-A protocols on a modern biplane angiography system does not deviate substantially from analogous MDCT protocols.

ACKNOWLEDGMENTS

The authors gratefully acknowledge the technical support and assistance with phantom experiments from Stepina Elizaveta, PhD, and Brehm Marcus, PhD, from Siemens Healthineers, Forchheim, Germany.

Disclosure forms provided by the authors are available with the full text and PDF of this article at www.ajnr.org.

REFERENCES

- Psychogios MN, Maier IL, Tsogkas I, et al. **One-stop management of 230 consecutive acute stroke patients: report of procedural times and clinical outcome.** *J Clin Med* 2019;8:2185 CrossRef Medline
- Brehm A, Tsogkas I, Ospel JM, et al. **Direct to angiography suite approaches for the triage of suspected acute stroke patients: a systematic review and meta-analysis.** *Ther Adv Neurol Disord* 2022;15:17562864221078177 CrossRef Medline
- Requena M, Olivé-Gadea M, Muchada M, et al. **Direct to angiography suite without stopping for computed tomography imaging for patients with acute stroke: a randomized clinical trial.** *JAMA Neurol* 2021;78:1099–1107 CrossRef Medline
- Quispe-Orozco D, Farooqui M, Zevallos C, et al. **Angiography suite cone-beam computed tomography perfusion imaging in large-vessel occlusion patients using RAPID software: a pilot study.** *Stroke* 2021;52:e542–44 CrossRef Medline
- Roser P, Birkhold A, Zhong X, et al. **Pitfalls in interventional x-ray organ dose assessment-combined experimental and computational phantom study: application to prostatic artery embolization.** *Int J Comput Assist Radiol Surg* 2019;14:1859–69 CrossRef Medline
- Brehm A, Stamm G, Lüpke M, et al. **Effective dose to patient measurements for flat-detector computed tomography protocols in acute stroke care.** *Eur Radiol* 2020;30:5082–88 CrossRef Medline
- Moore R, Waheed A, Burns B. *Rule of Nines.* StatPearls Publishing; 2021
- Basic anatomical and physiological data for use in radiological protection: reference values: a report of age- and gender-related differences in the anatomical and physiological characteristics of reference individuals—ICRP publication 89.** *Ann ICRP* 2002;32:5–265 Medline
- The 2007 Recommendations of the International Commission on Radiological Protection. ICRP Publication 103.** *Ann ICRP* 2007;37:1–332 CrossRef Medline
- Struffert T, Deuerling-Zheng Y, Kloska S, et al. **Dynamic angiography and perfusion imaging using flat detector CT in the angiography suite: a pilot study in patients with acute middle cerebral artery occlusions.** *AJNR Am J Neuroradiol* 2015;36:1964–70 CrossRef Medline
- Nogueira RG, Jadhav AP, Haussen DC, et al. **Thrombectomy 6 to 24 hours after stroke with a mismatch between deficit and infarct.** *N Engl J Med* 2018;378:11–21 CrossRef Medline
- Albers GW, Marks MP, Kemp S, et al. **Thrombectomy for stroke at 6 to 16 hours with selection by perfusion imaging.** *N Engl J Med* 2018;378:708–18 CrossRef Medline
- Struffert T, Hauer M, Banckwitz R, et al. **Effective dose to patient measurements in flat-detector and multislice computed tomography: a comparison of applications in neuroradiology.** *Eur Radiol* 2014;24:1257–65 CrossRef Medline
- Chen SH, Snelling BM, Sur S, et al. **Transradial versus transfemoral access for anterior circulation mechanical thrombectomy: comparison of technical and clinical outcomes.** *J Neurointerv Surg* 2019;11:874–78 CrossRef Medline
- McTaggart RA, Ospel JM, Psychogios MN, et al. **Optimization of endovascular therapy in the neuroangiography suite to achieve fast and complete (Expanded Treatment in Cerebral Ischemia 2c-3) reperfusion.** *Stroke* 2020;51:1961–68 CrossRef Medline
- Psychogios MN, Behme D, Schregel K, et al. **One-stop management of acute stroke patients: minimizing door-to-reperfusion times.** *Stroke* 2017;48:3152–55 CrossRef Medline
- Amukotuwa SA, Wu A, Zhou K, et al. **Time-to-maximum of the tissue residue function improves diagnostic performance for detecting distal vessel occlusions on CT angiography.** *AJNR Am J Neuroradiol* 2021;42:65–72 CrossRef Medline
- Amukotuwa SA, Wu A, Zhou K, et al. **Distal medium vessel occlusions can be accurately and rapidly detected using Tmax maps.** *Stroke* 2021;52:3308–17 CrossRef Medline
- Saver JL, Chapot R, Agid R, et al; Distal Thrombectomy Summit Group. **Thrombectomy for distal, medium vessel occlusions: a consensus statement on present knowledge and promising directions.** *Stroke* 2020;51:2872–84 CrossRef Medline
- Lin HC, Lai TJ, Tseng HC, et al. **Radiation doses with various body weights of phantoms in brain 128-slice MDCT examination.** *J Radiat Res* 2019;60:466–75 CrossRef Medline
- Petroulia VD, Kaesmacher J, Piechowiak EI, et al. **Evaluation of Sine Spin flat detector CT imaging compared with multidetector CT.** *J Neurointerv Surg* 2022 Mar 22 [Epub ahead of print] CrossRef Medline
- Kalender WA, Kyriakou Y. **Flat-detector computed tomography (FD-CT).** *Eur Radiol* 2007;17:2767–79 CrossRef Medline
- Nikupaavo U, Kaasalainen T, Reijonen V, et al. **Lens dose in routine head CT: comparison of different optimization methods with anthropomorphic phantoms.** *AJR Am J Roentgenol* 2015;204:117–23 CrossRef Medline
- Fahrig R, Dixon R, Payne T, et al. **Dose and image quality for a cone-beam C-arm CT system.** *Med Phys* 2006;33:4541–50 CrossRef Medline
- Roser P, Birkhold A, Preuhs A, et al. **XDose: toward online cross-validation of experimental and computational X-ray dose estimation.** *Int J Comput Assist Radiology Surg* 2021;16:1–10 CrossRef Medline

Correlation of Collateral Scores Derived from Whole-Brain Time-Resolved Flat Panel Detector Imaging in Acute Ischemic Stroke

C.C. Kurmann, J. Kaesmacher, S. Pilgram-Pastor, E.I. Piechowiak, A. Scutelnic, M.R. Heldner, T. Dobrocky, J. Gralla, and P. Mordasini



ABSTRACT

BACKGROUND AND PURPOSE: Flat panel detector CT imaging allows simultaneous acquisition of multiphase flat panel CTA and flat panel CTP imaging directly in the angio suite. We compared collateral assessment derived from multiphase flat panel CTA and flat panel CTP with collateral assessment derived from DSA as the gold-standard.

MATERIALS AND METHODS: We performed a retrospective analysis of patients with occlusion of the first or second segment of the MCA who underwent pre-interventional flat panel detector CT. The hypoperfusion intensity ratio as a correlate of collateral status was calculated from flat panel CTP (time-to-maximum > 10 seconds volume/time-to-maximum > 6 seconds volume). Intraclass correlation coefficients were calculated for interrater reliability for the Calgary/Menon score for multiphase flat panel CTA and for the American Society of Interventional and Therapeutic Neuroradiology/Society of Interventional Radiology (ASITN/SIR) score for DSA collateral scores. Correlations of the hypoperfusion intensity ratio, multiphase flat panel CTA score, and the ASITN/SIR score were calculated using the Spearman correlation.

RESULTS: From November 2019 to February 2020, thirty patients were included. Moderate interrater reliability was achieved for the ASITN/SIR DSA score (0.68; 95% CI, 0.50–0.82) as well as for the Calgary/Menon multiphase flat panel CTA score (0.53; 95% CI, 0.29–0.72). We found a strong correlation between the ASITN/SIR DSA and Calgary/Menon multiphase flat panel CTA score ($\rho = 0.54$, $P = .002$) and between the hypoperfusion intensity ratio and the Calgary/Menon multiphase flat panel CTA score ($\rho = -0.57$, $P < .001$). The correlation was moderate between the hypoperfusion intensity ratio and the ASITN/SIR DSA score ($\rho = -0.49$, $P = .006$). The infarct core volume correlated strongly with the Calgary/Menon multiphase flat panel CTA score ($\rho = -0.66$, $P < .001$) and the hypoperfusion intensity ratio ($\rho = 0.76$, $P < .001$) and correlated moderately with the ASITN/SIR DSA score ($\rho = -0.46$, $P = .01$).

CONCLUSIONS: The Calgary/Menon multiphase flat panel CTA score and the hypoperfusion intensity ratio correlated with each other and with the ASITN/SIR DSA score as the gold-standard. In our cohort, the collateral scoring derived from flat panel detector CT was clinically reliable.

ABBREVIATIONS: ASITN/SIR = American Society of Interventional and Therapeutic Neuroradiology/Society of Interventional Radiology; FDCT = flat panel detector CT; FDCTP = flat panel detector CTP; HIR = hypoperfusion intensity ratio; ICC = intraclass correlation coefficient; mCTA = multiphase CTA; mFDCTA = multiphase flat panel detector CTA; rCBF = relative CBF; Tmax = time to maximum

In acute ischemic stroke, sufficient and effective collaterals are important, correlate with favorable outcome, and may be used for patient selection.¹⁻³ The gold-standard American Society

of Interventional and Therapeutic Neuroradiology/Society of Interventional Radiology (ASITN/SIR) score for DSA⁴ is the most commonly used scale for visual collateral scoring.⁵ Two alternative collateral scores are the Calgary/Menon score for multiphase CTA (based on visual inspection)⁶ and the hypoperfusion intensity ratio (HIR) as a quantitative and thus objective estimation of the collateral supply. The HIR can be derived from perfusion imaging and is defined as the ratio of the volume of tissue with time to maximum (Tmax) > 10 seconds to the volume of tissue with Tmax > 6 seconds.⁷

The recently introduced whole-brain multiphase flat panel detector CT (FDCT) imaging allows acquisition of time-resolved whole-brain perfusion imaging directly in the angio suite by 10

Received June 17, 2022; accepted after revision August 25.

From the University Institute of Diagnostic and Interventional Neuroradiology (C.C.K., J.K., S.P.-P., E.I.P., T.D., J.G., P.M.), University Institute of Diagnostic and Interventional and Pediatric Radiology (C.C.K.), and Department of Neurology (A.S., M.R.H.), University Hospital Bern, Inselspital, University of Bern, Bern, Switzerland.

Please address correspondence to Pasquale Mordasini, MD, MSc, University Institute of Diagnostic and Interventional Neuroradiology, University Hospital Bern, Inselspital, University of Bern, Freiburgstrasse 10, CH 3010, Bern, Switzerland; e-mail: Pasquale.mordasini@insel.ch; @chris_kurmann; @CheesemakerMD

Indicates open access to non-subscribers at www.ajnr.org

Indicates article with online supplemental data.

<http://dx.doi.org/10.3174/ajnr.A7657>

rotational sweeps. On the basis of flat panel detector CTP (FDCTP) source images, multiphase flat panel detector CTA (mFDCTA) and perfusion maps can be reconstructed.⁸⁻¹⁰ This technology enables direct transport of patients to the angio suite (“direct-to-the angio” approach), which, in turn, can improve in-hospital workflows, reduce the time to treatment, and may ultimately increase the chances of good clinical outcome.¹¹⁻¹⁶

While collateral scores are well-validated in conventional multiphase CTA (mCTA)/CTP, data on the evaluation of the collateral status derived from FDCTP imaging is scarce. FDCTP offers the unique possibility of validating and comparing cross-sectional collateral surrogates with the conventional DSA gold-standard, acquired at almost the same time.

The purpose of this study was to evaluate collateral imaging derived from FDCT as a cornerstone in its possible future use as a first-line stroke imaging technique (direct-to-the angio approach). We assessed interrater reliability and correlation of collateral scores derived from FDCTP (Calgary/Menon mFDCTA score, HIR) and from DSA (ASITN/SIR DSA score). Furthermore, we assessed the correlation of collateral scores with the size of infarct cores.

MATERIALS AND METHODS

The study protocol was approved by the Kantonale Ethikkommission Bern (reference ID 2018-02023). Informed consent was waived owing to the retrospective nature of the study. The data that support the findings of this study are available from the corresponding author on reasonable request.

Population

We included patients from November 2019 to February 2021 with M1 and M2 occlusions who underwent mechanical thrombectomy at our institution and pre-interventional FDCTP. Exclusion criteria were low-quality (qualitative and quantitative features not interpretable, eg, due to delayed contrast bolus arrival) FDCTP scans. Clinical data were extracted from the institutional stroke database or from the Clinical Information System.

Imaging Protocol

After neurologic examination on arrival at the emergency department, patients underwent either CT imaging (noncontrast CT, CTA, CTP) or MR imaging (DWI, FLAIR, SWI, MRA, MR Perfusion) and were subsequently transferred to the angio suite if the eligibility criteria for mechanical thrombectomy were fulfilled. The decision as to whether to perform pre-interventional FDCT imaging was at the discretion of the treating physician based on clinical reasoning. FDCT imaging provided additional information about the penumbra and infarct core volumes and collateral status, which allowed adjusting the treatment strategy accordingly.

FDCT imaging was performed with the patient under general anesthesia. Whole-brain imaging data were acquired using a biplane flat panel detector angiographic system (Artis icono; Siemens) by 10 rotational sweeps (each during 5 seconds) of the angiographic C-arm system around the patient. The first 2 sweeps served as mask runs, and the following 8 rotations recorded in-/outflow of contrast agent (60 mL, Iopamiro 400; Bracco), which was started at the same time as the mask run via an 18G left or right cubital venous line.

Finally, a 40-mL saline flush was administered (power injector injection rate, 5 mL/s).

Postprocessing of the raw perfusion imaging was conducted using a dedicated software (Rapid ANGIO; iSchemaView), and mFDCTA as well as several perfusion maps were reconstructed (relative CBF [rCBF], relative CBV [rCBV], MTT, and Tmax). On the basis of these maps, volumes of tissue with Tmax > 6 seconds, Tmax > 10 seconds, and rCBF < 45% were calculated. Rapid ANGIO is the first and currently only clinically available postprocessing software for multiphase FDCTP acquisitions based on the Rapid software.¹¹

Thick-section axial MIPs at 4-mm thickness and 1-mm intervals of the mFDCTA were reconstructed. Because 10 phases were available for each mFDCTA, 3 phases were defined to mimic a conventional mCTA (to apply the Calgary/Menon mCTA score, see the “Imaging Analysis” section). The arterial phase was defined as the phase in which the arterial vessels were best depicted due to signal increase caused by inflow of contrast agent. The second phase was defined as 6 seconds after the arterial phase, and the third phase, as 12 seconds after the arterial phase.

Infarct core was defined as tissue with rCBF of <45% because phantom data showed that FDCTP is less sensitive than conventional CTP for detecting CBF values of <30 mL/100 g/min. Furthermore, a pilot study in patients with acute stroke demonstrated a strong correlation with conventional CTP (Pearson = 0.91, Spearman = 0.87) with an intraclass correlation coefficient (ICC) of 0.89 (95% CI, 0.67–0.96) using the <45% threshold for FDCTP.¹⁷ The HIR was defined as the ratio of the Tmax > 10-second volume divided by the Tmax > 6-second volume.¹⁸

Imaging Analysis

Two experienced interventional neuroradiologists (E.I.P., S.P.P.) and 1 neuroradiology resident (C.C.K.), who were blinded to other clinical data performed ratings of the collaterals on DSA (biplane flat panel detector angiographic system) and mFDCTA. After the initial rating, a consensus rating was determined for all cases with discrepant ratings in a joint session. Images were not anonymized, but initial and consensus ratings were performed separately for DSA and mFDCTA with 1 month of washout between them.

For the DSA, we used the 5-point ASITN/SIR collateral flow grading system:⁴ grade 0, no collaterals visible to the ischemic region; grade 1, slow collaterals to the periphery with persisting defect; grade 2, rapid collaterals to the periphery with persisting defect; grade 3, slow-but-complete collateral flow to the ischemic territory; and grade 4, rapid and complete collateral flow to the ischemic territory.

For the mFDCTA, we used the 6-point Calgary/Menon score:⁶ 0, no filling in any phase within the ischemic territory; 1, just a few vessels visible in any phase in the affected territory; 2, delay of 2 phases in the filling of peripheral vessels and decreased extent or a 1-phase delay and some ischemic regions without vessels; 3, delay of 2 phases in the filling of peripheral vessels or a 1-phase delay and reduced number of vessels in the ischemic territory; 4, delay of 1 phase in filling of peripheral vessels, with prominence and extent the same; and 5, no delay and normal or increased prominence of pial vessels.

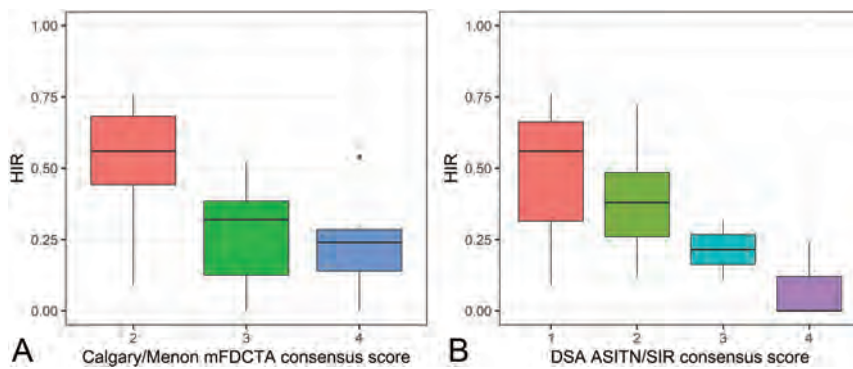


FIG 1. Boxplots showing HIR versus Calgary/Menon mFDCTA consensus scores (A) and HIR versus ASITN/SIR DSA consensus scores (B).

Statistical Analysis

Normal distribution was tested using graphic distribution and the Shapiro-Wilk test. Data are displayed as number (percentage) and median (interquartile range) if not otherwise specified. No data of the examined variables were missing.

The ICC was used to calculate interrater reliability because it is fit to handle ordinal data.¹⁹ ICC estimates and their 95% confidence intervals were calculated on the basis of a single rating, absolute agreement, and the 2-way random effects model. Interpretation was as follows: <0.5, poor; 0.5–0.75, moderate; 0.75–0.9, good; and >0.9, excellent reliability.¹⁹ As proposed by Koo et al,¹⁹ categories of agreement were determined on the basis of 95% confidence intervals, and if confidence intervals included 2 categories, agreement was described as transition (eg, moderate-to-good).

For correlation analysis, the consensus ratings for ASITN/SIR DSA scores and Calgary/Menon mFDCTA scores were used. Correlations were calculated using the Spearman correlation because the Spearman correlation can handle ordinal and non-normally distributed data. Spearman correlation coefficients were interpreted as follows: $\rho < 0.3$, weak relationship; $0.3 \leq \rho \leq 0.5$, moderate relationship; $\rho > 0.5$, strong relationship.²⁰

In boxplot analyses, overall differences were compared using the Kruskal-Wallis test.

All statistical analyses were conducted using R (Version 4.0.2; <http://www.r-project.org/>).²¹ A 2-tailed P value < .05 was considered statistically significant.

RESULTS

Population

Of 36 patients, we excluded 6 patients due to bad FDCTP quality caused by delayed bolus arrival ($n = 5$) or a dispersed bolus ($n = 1$), leaving a final population of 30 patients for the final analysis (Online Supplemental Data). The median age was 76.5 years, 40% were women, and 21 patients presented with M1 occlusions. Baseline characteristics and distribution of patients according to the ASITN/SIR DSA score and the Calgary/Menon mFDCTA score are shown in the Online Supplemental Data.

Interrater Reliability

Interrater reliability was moderate-to-good for the ASITN/SIR DSA score (ICC estimate, 0.68; 95% CI, 0.50–0.82) and poor-to-moderate

for the Calgary/Menon mFDCTA score (ICC estimate, 0.53; 95% CI, 0.29–0.72). When considering only M1 occlusions, interrater reliability improved for the ASITN/SIR DSA score (ICC estimate, 0.75; 95% CI, 0.56–0.88) and for the Calgary/Menon mFDCTA score (ICC estimate, 0.66; 95% CI, 0.43–0.83).

Correlation of Collateral Scores

The Online Supplemental Data show the distribution of ASITN/SIR DSA versus Calgary/Menon mFDCTA consensus scores for each case.

We found strong correlations between ASITN/SIR DSA score and Calgary/Menon mFDCTA score ($\rho = 0.54$, $P = .002$) and between the HIR and the Calgary/Menon mFDCTA score ($\rho = -0.57$, $P < .001$), and moderate correlation between the HIR and ASITN/SIR DSA score ($\rho = -0.49$, $P = .006$). Again, when we considered only M1 occlusions, correlations among all scores were strong: between the ASITN/SIR DSA score and Calgary/Menon mFDCTA score ($\rho = 0.65$, $P = .001$), between the HIR and Calgary/Menon mFDCTA score ($\rho = -0.56$, $P = .008$), and between HIR and ASITN/SIR DSA score ($\rho = -0.62$, $P = .003$).

Comparing the HIR for distinct Calgary/Menon mFDCTA degrees revealed a trend for lower HIR values in increasing Calgary/Menon mFDCTA scores (overall difference, $P = .006$; Fig 1A). The same trend was present for the different ASITN/SIR DSA scores (overall difference, $P = .035$; Fig 1B).

Illustrative cases are shown in Fig 2.

Correlation of Collateral Scores and Infarct Core

We also found a trend of decreasing infarct volumes with better collateral scores (Fig 3). This trend was present for the Calgary/Menon mFDCTA score (overall difference, $P = .002$; Fig 3A) as well as for the ASITN/SIR DSA score (overall difference, $P = .03$; Fig 3B). Correlation with rCBF of <45% was moderate for the ASITN/SIR ($\rho = -0.46$, $P = .01$), strong for the Calgary/Menon ($\rho = -0.66$, $P < .001$), and strong for the HIR ($\rho = 0.76$, $P < .001$; Fig 3C).

DISCUSSION

This exploratory study has the following main findings: 1) Interrater reliability was moderate for the ASITN/SIR DSA score and the Calgary/Menon mFDCTA score, 2) collateral grading derived from FDCTP (mFDCTA, HIR) correlated with collateral grading derived from DSA as the gold-standard, and 3) collateral scores correlated with the size of infarct core.

Similar to previous studies, interrater reliability was only moderate for the ASITN/SIR DSA collateral score and the Calgary/Menon score for mFDCTA. Interrater reliability for the Calgary/Menon score of conventionally acquired mCTA was also moderate in the study of Kauw et al²² but excellent in other studies.^{6,23} A reason for our lower interrater reliability could be the inclusion of M2 occlusions in our study because it was not the case in the study of Lyndon et al²³ and was not clear in the study of Menon et al.⁶ Additionally, our interrater reliability improved in both modalities

when only considering M1 occlusions. Interrater reliability for the ASITN/SIR DSA collateral score for 19 readers was only poor in another study (generalized $\kappa = 0.16$).²⁴

In a study including 24 patients, Maier et al⁹ found a strong correlation between the Calgary/Menon mFDCTA collateral score and the ASITN/SIR DSA collateral score (Pearson correlation coefficient, 0.86). However, collaterals were not graded by consensus but by a single rater. For trichotomized (poor, intermediate, excellent) mCTA and DSA scores, a Spearman correlation coefficient of 0.827 was reported.²⁵

One explanation for our lower correlation of the Calgary/Menon mFDCTA score and the ASITN/SIR DSA score could be that we included a considerably higher proportion of M2 occlusions (30% in our study versus 18.5%²⁵ and 4.2%,⁹ respectively). Another reason could be some incomplete pre-interventional DSA runs in which the selected DSA of the nonoccluded cervical and intracranial vessels were not performed, and consequently, the examination of collaterals and cross-flow was limited. This point, on the other hand, highlights an important advantage of mFDCTA, in which imaging of collaterals can be performed immediately pre-intervention with a single injection of contrast agent instead of selective angiographies of different vessels with the potential to cause complications as for example dissections or emboli.

Guenego et al²⁶ found a significant correlation of the HIR derived from conventional CTP maps and DSA collaterals (Pearson correlation coefficient, -0.327 ; $P = .01$). Our correlation was substantially better, likely because we calculated the HIR from FDCTP in the angio suite, which was performed only a few minutes before the pre-interventional DSA. The correlation of the HIR and mFDCTA

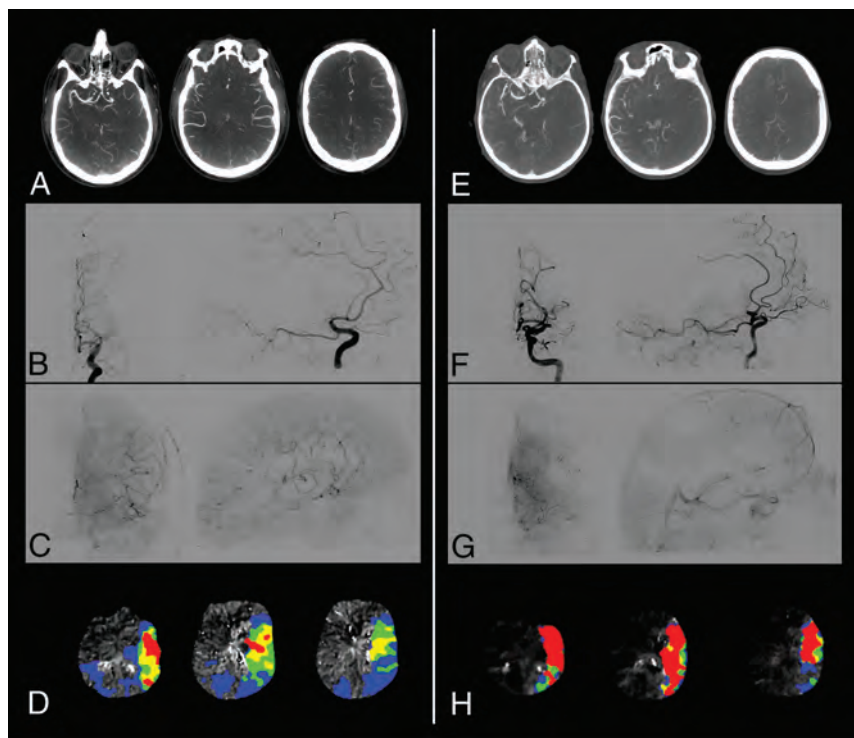


FIG 2. A–D, Patient with M1 occlusion (*left*) and good collaterals visualized (A) on pre-interventional mFDCTA (arterial phase, Calgary/Menon grade 4). Pre-interventional DSA (*left*: anterior-posterior view; *right*: lateral view) in the early arterial phase (B) and in a later venous phase (C) shows good leptomeningeal retrograde filling of the initial antegrade capillary blush deficit (target downstream territory, ASITN/SIR grade 4). D, Tmax perfusion maps on different levels that depict the low ratio of tissue with Tmax > 10 seconds (red) to Tmax > 6 seconds (green) (HIR = 0.2). E–H, Patient with M1 occlusion (*left*) and bad collaterals depicted (E) on pre-interventional mFDCTA (arterial phase, Calgary/Menon grade 2). Pre-interventional DSA (*left*: anterior-posterior view; *right*: lateral view) in the early arterial phase (F) and in a later venous phase (G) shows poor leptomeningeal retrograde filling of the initial antegrade capillary blush deficit (target downstream territory, ASITN/SIR grade 1). H, Tmax perfusion maps show the high ratio of tissue with Tmax > 10 seconds (red) to Tmax > 6 seconds (green) (HIR = 0.7).

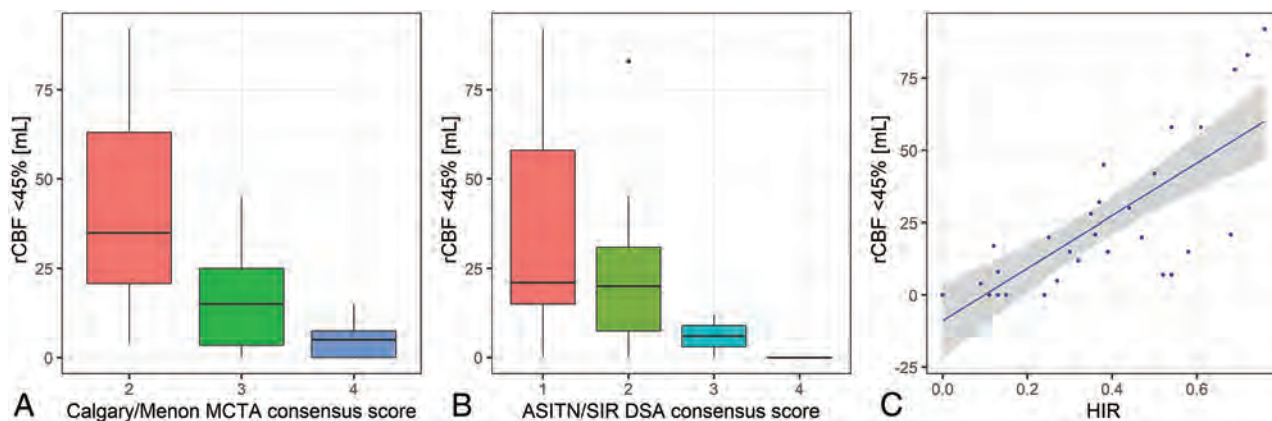


FIG 3. Boxplots showing rCBF < 45% versus Calgary/Menon mFDCTA consensus scores (A) and rCBF < 45% versus ASITN/SIR DSA consensus scores (B). C, Scatterplot with HIR versus rCBF < 45%.

reached similar correlation as HIR and mCTA derived from CT (Pearson correlation coefficient, -0.55 ; $P < .001$),²³ highlighting again the clinical comparability of FDCT and CT. Imperfect inter-rater reliability is certainly a limitation of visual collateral assessment, and the particular strength of the HIR derived from FDCTP is that it provides an objective surrogate of collateral status that is also relatively easy to interpret.

The association of good collaterals and small infarct core is well-known.²⁷ We could confirm these findings because the Calgary/Menon mFDCTA collateral score showed a strong correlation with the infarct core (rCBF $<45\%$), similar to previous findings examining conventional CTP.²⁸ Corroborating these results, we also found a strong correlation between the HIR and infarct core. Last, correlation of the ASITN/SIR DSA score and infarct core was moderate but nonetheless significant.

Our results show that measures of collateral status derived from FDCTP, namely mFDCTA and HIR, are clinically reliable and reached similar results compared with collateral scoring derived from CT in other studies. FDCTP collateral imaging provides some advantages over conventional CT/MR collateral imaging. First, it is acquired in the angio suite and, therefore, omits the delay between imaging and intervention caused by transfer of the patient. Second, mFDCTA makes selective DSA of nonoccluded vessels dispensable, potentially reducing the amount of contrast agent required and reducing the time to recanalization. Third, it allows the acquisition of 8 angiographic phases instead of 3 phases in the mCTA, providing more detailed information with better resolution in time of collateral flows.

Another important advantage of FDCTP is that it allows acquisition of nonenhanced brain CT, mFDCTA, and qualitative and quantitative perfusion maps simultaneously instead of the separately acquired sequences of CT/MR imaging.

Motion artifacts can have a severe negative impact on FDCTP imaging. Because it is our institutional guideline to perform all mechanical thrombectomies with the patient under general anesthesia, we were able to prevent the occurrence of motion artifacts and case exclusion was restricted to problems with the application of the contrast agent. Performing FDCTP without general anesthesia could compromise image quality and is a problem that remains to be resolved.

However, if technically adequate, pre-interventional FDCTP allows ruling out intracranial hemorrhage, determination of vessel occlusions, and, as we showed, assessing the collateral situation and estimating infarct core size. Our findings encourage the direct-to-the-angio approach, in which the patient is transported directly to the angio suite bypassing conventional CT or MR imaging. This approach can optimize in-hospital workflows, reduce time to treatment, and may ultimately improve clinical outcome.¹¹⁻¹⁶ Furthermore, FDCTP imaging after incomplete recanalization could add significant value, for example, in deciding whether to extend thrombectomy or to stop.

Limitations

This study is limited by its retrospective and single-center study design. Furthermore, we did not include patients consecutively and present results of a relatively small and highly selected sample size. Due to our small sample size, we also did not cover all degrees

of the ASITN/SIR DSA and Calgary/Menon mFDCTA collateral scores. However, other studies also reported only very few patients with either very high or very low collateral scores, representing a regular distribution with most patients with moderate-to-good collaterals. Last, we included only patients with large-vessel occlusions of the anterior circulation, and validation of FDCTP-derived collateral assessment in vessel occlusions of the posterior circulation is still needed. In summary, larger and prospective studies would be needed to overcome these limitations.

CONCLUSIONS

In our cohort, the Calgary/Menon mFDCTA collateral score and the HIR derived from FDCTP have good correlation with the ASITN/SIR DSA collateral score as gold-standard and with each other. Collateral scoring derived from FDCTP, especially the HIR as an objective measurement, is a promising tool to evaluate collateral status, but larger studies are needed to confirm our findings. In addition, our results support the implementation of the direct-to-the-angio approach, potentially reducing time to recanalization.

Disclosure forms provided by the authors are available with the full text and PDF of this article at www.ajnr.org.

REFERENCES

1. Fanou EM, Knight J, Aviv RI, et al. **Effect of collaterals on clinical presentation, baseline imaging, complications, and outcome in acute stroke.** *AJNR Am J Neuroradiol* 2015;36:2285-91 CrossRef Medline
2. Liebeskind DS, Tomsick TA, Foster LD, et al; IMS III Investigators. **Collaterals at angiography and outcomes in the Interventional Management of Stroke (IMS) III Trial.** *Stroke* 2013;44:759-64 CrossRef Medline
3. Vagal A, Aviv R, Sucharew H, et al. **Collateral clock is more important than time clock for tissue fate a natural history study of acute ischemic strokes.** *Stroke* 2018;49:2102-07 CrossRef Medline
4. Higashida RT, Furlan AJ, Roberts H, et al; Technology Assessment Committee of the American Society of Interventional and Therapeutic Neuroradiology; Technology Assessment Committee of the Society of Interventional Radiology. **Trial design and reporting standards for intra-arterial cerebral thrombolysis for acute ischemic stroke.** *Stroke* 2003;34:109-37 CrossRef Medline
5. Zaidat OO, Yoo AJ, Khatri P, et al; Cerebral Angiographic Revascularization Grading (CARG) Collaborators; STIR Revascularization Working Group; STIR Thrombolysis in Cerebral Infarction (TICI) Task Force. **Recommendations on angiographic revascularization grading standards for acute ischemic stroke.** *Stroke* 2013;44:2650-63 CrossRef Medline
6. Menon BK, D'Este CD, Qazi EM, et al. **Multiphase CTA: a new tool for the imaging triage of patients with acute ischemic stroke.** *Radiology* 2015;275:510-20 CrossRef Medline
7. Bang OY, Saver JL, Alger JR, et al; UCLA Collateral Investigators. **Determinants of the distribution and severity of hypoperfusion in patients with ischemic stroke.** *Neurology* 2008;71:1804-11 CrossRef Medline
8. Kurmann C, Kaesmacher J, Cooke DL, et al. **Evaluation of time-resolved whole brain flat panel detector perfusion imaging using RAPID ANGIO in patients with acute stroke: comparison with CT perfusion imaging.** *J Neurointerv Surg* 2022 April 2 [Epub ahead of print] CrossRef Medline
9. Maier IL, Scalzo F, Leyhe JR, et al. **Validation of collateral scoring on flat-detector multiphase CTA in patients with acute ischemic stroke.** *PLoS One* 2018;13:e0202592 CrossRef Medline

10. Struffert T, Deuerling-Zheng Y, Engelhorn T, et al. **Feasibility of cerebral blood volume mapping by flat panel detector CT in the angiography suite: first experience in patients with acute middle cerebral artery occlusions.** *AJNR Am J Neuroradiol* 2012;33:618–25 CrossRef Medline
11. Brehm A, Tsogkas I, Maier IL, et al. **One-stop management with perfusion for transfer patients with stroke due to a large-vessel occlusion: feasibility and effects on in-hospital times.** *AJNR Am J Neuroradiol* 2019;40:1330–34 CrossRef Medline
12. Psychogios MN, Maier IL, Tsogkas I, et al. **One-stop management of 230 consecutive acute stroke patients: report of procedural times and clinical outcome.** *J Clin Med* 2019;8:2185 CrossRef Medline
13. Mendez B, Requena M, Aires A, et al. **Direct transfer to angio-suite to reduce workflow times and increase favorable clinical outcome a case-control study.** *Stroke* 2018;49:2723–27 CrossRef Medline
14. Ribo M, Boned S, Rubiera M, et al. **Direct transfer to angiosuite to reduce door-to-puncture time in thrombectomy for acute stroke.** *J Neurointerv Surg* 2018;10:221–24 CrossRef Medline
15. Sarraj A, Goyal N, Chen M, et al. **Direct to angiography vs repeated imaging approaches in transferred patients undergoing endovascular thrombectomy.** *JAMA Neurol* 2021;78:916 CrossRef Medline
16. Requena M, Muchada MÁ, Garcia-Tornel Á, et al. **Evaluation of direct transfer to angiography suite vs. computed tomography suite in endovascular treatment of stroke: ANGIO-CAT randomized clinical trial.** Abstract L. *Present Int Stroke Conf* 2021
17. Quispe-Orozco D, Farooqui M, Zevallos C, et al. **Angiography suite cone-beam computed tomography perfusion imaging in large-vessel occlusion patients using RAPID software.** *Stroke* 2021;52:e542–44 CrossRef Medline
18. Olivot JM, Mlynash M, Inoue M, et al; DEFUSE 2 Investigators. **Hypoperfusion intensity ratio predicts infarct progression and functional outcome in the DEFUSE 2 cohort.** *Stroke* 2014;45:1018–23 CrossRef Medline
19. Koo TK, Li MY. **A guideline of selecting and reporting intraclass correlation coefficients for reliability research.** *J Chiropr Med* 2016;15:155–63 CrossRef Medline
20. Khamis H. **Measures of association: how to choose?** *J Diagnostic Med Sonogr* 2008;24:155–62 CrossRef
21. R Core Team. **R: A Language and Environment for Statistical Computing.** R Foundation for Statistical Computing; 2019
22. Kauw F, Dankbaar JW, Martin BW, et al. **Collateral status in ischemic stroke: a comparison of computed tomography angiography, computed tomography perfusion, and digital subtraction angiography.** *J Comput Assist Tomogr* 2020;44:984–92 CrossRef Medline
23. Lyndon D, van den Broek M, Niu B, et al. **Hypoperfusion intensity ratio correlates with CTA collateral status in large-vessel occlusion acute ischemic stroke.** *AJNR Am J Neuroradiol* 2021;42:1380–86 CrossRef Medline
24. Ben Hassen W, Malley C, Boulouis G, et al. **Inter- and intraobserver reliability for angiographic leptomeningeal collateral flow assessment by the American Society of Interventional and Therapeutic Neuroradiology/Society of Interventional Radiology (ASITN/SIR) scale.** *J Neurointerv Surg* 2019;11:338–41 CrossRef Medline
25. Kim SJ, Noh HJ, Yoon CW, et al. **Multiphase perfusion computed tomography as a predictor of collateral flow in acute ischemic stroke: comparison with digital subtraction angiography.** *Eur Neurol* 2012;67:252–55 CrossRef Medline
26. Guenego A, Fahed R, Albers GW, et al. **Hypoperfusion intensity ratio correlates with angiographic collaterals in acute ischaemic stroke with M1 occlusion.** *Eur J Neurol* 2020;27:864–70 CrossRef Medline
27. Vagal A, Menon BK, Foster LD, et al. **Association between CT angiogram collaterals and CT perfusion in the Interventional Management of Stroke III Trial.** *Stroke* 2016;47:535–38 CrossRef Medline
28. Seker F, Potreck A, Möhlenbruch M, et al. **Comparison of four different collateral scores in acute ischemic stroke by CTA.** *J Neurointerv Surg* 2016;8:1116–18 CrossRef Medline

Successful Reperfusion is Associated with Favorable Functional Outcome despite Vessel Perforation during Thrombectomy: A Case Series and Systematic Review

C. Ducroux, W. Boisseau, A.Y. Poppe, N. Daneault, Y. Deschaintre, J.D.B. Diestro, J. Eneling, L.C. Gioia, D. Iancu, B. Maier, B. Nauche, L. Nico, C. Odier, J. Raymond, D. Roy, C. Stapf, A. Weill, and G. Jacquin



ABSTRACT

BACKGROUND: Arterial perforation is a potentially serious complication during endovascular thrombectomy.

PURPOSE: Our aim was to describe interventional approaches after arterial perforation during endovascular thrombectomy and to determine whether reperfusion remains associated with favorable outcome despite this complication.

DATA SOURCES: Data from consecutive patients with acute stroke undergoing endovascular thrombectomy were retrospectively collected between 2015 to 2020 from a single-center cohort, and a systematic review was performed using PubMed, EMBASE, and Ovid MEDLINE up to June 2020.

STUDY SELECTION: Articles reporting functional outcome after arterial perforation during endovascular thrombectomy were selected.

DATA ANALYSIS: Functional outcomes of patients achieving successful reperfusion (TICI 2b/3) were compared with outcomes of those with unsuccessful reperfusion in our single-center cohort. We then summarized the literature review to describe interventional approaches and outcomes after arterial perforation during endovascular thrombectomy.

DATA SYNTHESIS: In our single-center cohort, 1419 patients underwent endovascular thrombectomy, among whom 32 (2.3%) had vessel perforation and were included in the analysis. The most common hemostatic strategy was watchful waiting (71% of cases). Patients with successful reperfusion had a higher proportion of favorable 90-day mRS scores (60% versus 12.5%; $P = .006$) and a lower mortality rate (13.3% versus 56.3%, $P = .01$) than patients without successful reperfusion. Thirteen articles were included in the systematic review. Successful reperfusion also appeared to be associated with better outcomes.

LIMITATIONS: Given the low number of published reports, we performed only a descriptive analysis.

CONCLUSIONS: Arterial perforation during endovascular thrombectomy is rare but is associated with high mortality rates and poor outcome. However, successful reperfusion remains correlated with favorable outcome in these patients.

ABBREVIATIONS: EVT = endovascular thrombectomy; IQR = interquartile range; mTICI = modified TICI; sICH = symptomatic intracerebral hemorrhage

Endovascular therapy (EVT) is the standard of care for the treatment of patients with acute ischemic stroke due to large-vessel occlusion.¹ Technologic advances have allowed development of new devices that have greatly improved the efficacy and safety of EVT compared with older-generation tools.² Despite

these improvements, as well as greater comfort and expertise among interventionalists across time, the procedure is still not exempt from severe complications.^{3,4} Arterial perforation, defined as contrast extravasation noticed during a procedural angiographic run, is one of the most serious and feared complications during EVT because it has been associated with poor functional outcomes and death.⁵ In large EVT trials, the rate of procedural arterial perforations varied between 0.6% and 4.9%.¹

Received February 17, 2022; accepted after revision July 17.

From the Department of Neurosciences (C.D., A.Y.P., N.D., Y.D., L.C.G., C.O., C.S., G.J.), Faculté de Médecine, Université de Montréal, Montréal, Quebec, Canada; Departments of Medicine (Neurology) (C.D., A.Y.P., N.D., Y.D., L.C.G., C.O., C.S., G.J.), and Radiology (W.B., J.D.B.D., J.E., D.I., B.M., L.N., J.R., D.R., A.W.), and Neurovascular Group (A.Y.P., N.D., Y.D., L.C.G., C.O., C.S., G.J.), Neurosciences Axis, Centre de Recherche, Centre Hospitalier de l'Université de Montréal, Montréal, Quebec, Canada; Division of Neurology (C.D.), Department of Medicine, The Ottawa Hospital, Ottawa, Ontario, Canada; Bibliothèque du Centre Hospitalier de l'Université de Montréal (B.N.), Montreal, Quebec, Canada; Department of Interventional Neuroradiology (W.B., B.M.), Hôpital Fondation A. De Rothschild, Paris, France; and Université Paris-Cité (B.M.), Paris, France.

Please address correspondence to Grégory Jacquin, MD, Centre Hospitalier de l'Université de Montréal, 1051 Rue Sanguinet, Montréal, QC H2X 3E4 Canada; e-mail: gregory.jacquin.med@ssss.gouv.qc.ca

Indicates article with online supplemental data.

<http://dx.doi.org/10.3174/ajnr.A7650>

When a vessel perforation occurs, some operators might be tempted to abort the procedure, with the risk of leaving the culprit occlusion untreated. Others may decide to pursue EVT once hemostasis is achieved, risking further arterial wall damage. However, little is known regarding the best approach when facing an arterial perforation during EVT and whether reperfusion still represents a reasonable goal in the context of such a complication.⁵

Therefore, we aimed to describe rescue therapies, management, and clinical outcomes after intraprocedural arterial perforation during EVT, and we sought to determine whether reperfusion is still associated with favorable outcome in this setting.

MATERIALS AND METHODS

This single-center observational study retrospectively analyzed clinical and imaging data prospectively gathered from a quality-improvement database: the Montreal Neurovascular and STroke Repository (MONSTER), maintained by a high-volume comprehensive stroke center in Montreal, Canada (Center Hospitalier de l'Université de Montréal).

Patient Population

All consecutive adult patients (18 years of age or older) treated with EVT for a large-vessel occlusion between March 1, 2015, and December 31, 2020, in whom arterial perforation occurred during EVT were included. Patients were included when an arterial perforation, defined as contrast extravasation noticed during a procedural angiographic run, was reported in radiology reports or clinical notes. Baseline demographics, stroke characteristics, and procedural details were collected, including information regarding the procedural technique, location of arterial occlusion, type of devices used (stent retriever, contact aspiration, and combined technique), number of passes, procedural duration, and the adopted rescue therapy after vessel perforation. All angiograms were reviewed by 2 interventional neuroradiologists (D.R. and B.M.). We then performed a descriptive analysis of the main steps undertaken after arterial perforation was observed.

Outcomes

Patients were divided in 2 groups with either successful reperfusion or unsuccessful reperfusion to correlate the angiographic results with functional outcomes. Successful reperfusion was defined as a modified TICI (mTICI) \geq 2b on the final intracranial run. Favorable functional outcome was defined as an mRS score of 0–2, as determined by a certified assessor at 90-day telephone or in-person follow-up. Proportions of hemorrhagic transformation, symptomatic intracerebral hemorrhage (sICH, defined as any hemorrhagic transformation associated with a 4-point increase in the baseline NIHSS score⁶), and death at 90 days were also collected. All patients had immediate brain imaging following the end of their procedure (plain CT or DynaCT [Siemens] in the angio suite) and a 24-hour follow-up CT. The 24-hour CT was used to identify hemorrhagic transformation to better distinguish true hemorrhagic transformation from contrast staining.

Systematic Review of the Literature

We also performed a systematic review to identify articles reporting on outcomes of patients with acute ischemic stroke with

arterial perforation during EVT. With the help of a medical librarian having expertise in systematic reviews (B.N.), we searched the PubMed database, EMBASE database, and Ovid MEDLINE with search terms including “perforation,” “complication,” “stent retriever,” “contact aspiration,” “thrombectomy,” and “stroke” (see the Online Supplemental Data for the full search strategy). We included any study published between January 1, 2015, and June 30, 2020, specifically describing functional outcomes of patients who had arterial perforation observed during EVT. This date range was used to capture studies primarily completed in the modern EVT era. We selected only the references that met all of the following criteria: full-text articles in French or English, studies reporting 3-month clinical outcomes using the mRS score, and studies of patients with stroke undergoing EVT with a procedural arterial perforation. Using a free Web-based application,⁷ two reviewers (C.D., G.J.) independently screened all titles and abstracts. Full texts were obtained for any article considered relevant for the research question. Disagreements about eligibility were resolved by consensus. Data collection was completed by one author (C.D.) and reviewed by a second (G.J.). Collected data for each study included, when available, the following: baseline NIHSS score, thrombus location, ASPECTS, intravenous thrombolysis, type of anesthesia, EVT technique (stent retriever, contact aspiration, and a combined technique), mTICI score, causes of perforation, sICH, mRS score, and death at 90-day follow-up. The review was performed according to the Preferred Reporting Items for Systematic Reviews and Meta-Analysis (PRISMA) guidelines.⁸

Statistics

Differences between groups were tested using the χ^2 test of independence or the Fisher exact test for categorical variables and the Mann-Whitney *U* test for continuous variables. We described the population according to reperfusion status. Reperfusion status was dichotomized as either successful reperfusion (mTICI \geq 2b) or unsuccessful reperfusion (mTICI < 2b). The statistical level of significance was set at $P < .05$. Data were analyzed using SPSS (Version 26.0.0.1; IBM). Given the expected low number of previously published reports, we did not plan to perform a statistical meta-analysis of the systematic review results and only performed a descriptive analysis.

The study was approved by our local institutional ethics board for retrospective data collection and review (project No. 20.028). The data supporting the findings of this study are available on reasonable request by a qualified investigator to the corresponding author.

RESULTS

From March 1, 2015, to December 31, 2020, a total of 1419 patients underwent EVT for acute ischemic stroke in our comprehensive stroke center, among whom 32 (2.3%) experienced a vessel perforation during EVT and were included in the study. The annual proportion of EVT procedures complicated by a perforation appeared to decrease during the study period (Online Supplemental Data). Follow-up at 90 days was unavailable for 1 (3%) patient. Baseline demographics and stroke characteristics are shown in the Online Supplemental Data.

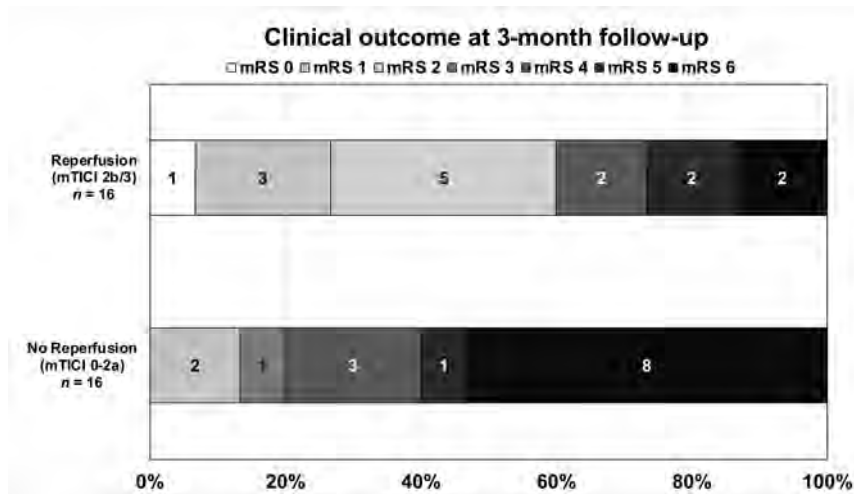


FIG 1. The mRS score distribution at 90 days for patients with successful reperfusion (TICI 2b/3) and no reperfusion (TICI 0-2a), despite vessel perforation during endovascular thrombectomy.

Procedural Details

We extracted data from radiology reports and review of source angiographic images, though only 29 complete angiographic studies were available for analysis.

Endovascular thrombectomy was performed with the patient under general anesthesia in 5 patients (15.6%) (including 2 cases with conversion to general anesthesia after arterial perforation), under conscious sedation in 12 patients (37.5%), and under local anesthesia only in the remaining 15 patients (46.9%). The median number of device passes was 1 (interquartile range [IQR], 0–1.75). Vessel perforation occurred more often with the use of a microwire ($n = 14$, 43.8%) than with a microcatheter ($n = 9$, 28.1%). The cause of vessel perforation was unknown in the remaining 9 patients (28.1%) (Online Supplemental Data). Patients with perforation due to a microwire had numerically better 3-month outcomes than patients with microcatheter perforation (6/14 patients, 46.2%, versus 3/9 patients, 33.3%, respectively).

After review of available angiograms, we found that 16 patients had a perforation identified only on microcatheter injection (16/29; 55.2%), 13 patients (44.8%) had a perforation noticed after ICA injection, and 13 patients (44.8%) had a perforation viewed on multiple runs. Outcomes of these patients were similar regardless of how perforation was identified or the number of runs on which the perforation was viewed (Online Supplemental Data).

Most intraprocedural vessel perforations occurred at a distal location: the MCA M2 in 18 patients (56.3%) and the anterior cerebral artery in 3 patients (9.4%). The remainder occurred proximally: the MCA M1 in 7 patients (21.9%) and the ICA in 2 patients (6.3%). Among patients with proximal perforation (ICA and M1), rescue therapy was performed in 4/9 patients (intermittent balloon inflation in 2 patients and parent vessel occlusion in 1 patient). In the last case, the microcatheter was left in place and cut and sewn at the groin in an attempt to seal the intracranial arterial perforation point. Contrast extravasation stopped spontaneously in the 5 remaining cases (Fig 2). Among patients with distal perforation, contrast extravasation was self-resolving in

most (17/22 patients), parent vessel occlusion was performed in 4 cases, and intermittent balloon inflation was performed in the last case. “Self-resolving” is defined as contrast extravasation stopping without a specific intervention. The median number of runs before concluding that a bleed was self-resolving was 1 (IQR, 1–2).

Outcomes and Association with Reperfusion

Of 31 patients with an available 90-day mRS, 11 (34.4%) patients had favorable outcomes and 11 (34.4%) patients died (5 sICH, 3 cases of malignant edema, 2 cases of aspiration pneumonia, and 1 from multiple causes).

Reperfusion (mTICI 2b/3) was successful in 16 (50%) patients and unsuccessful in 16 (50%) others, with baseline

characteristics being similar in these 2 groups (Online Supplemental Data).

As shown in Fig 1, patients with successful reperfusion had a higher proportion of favorable functional outcomes at 90 days than patients without successful reperfusion (60% versus 12.5%, $P = .006$) as well significantly lower mortality rates (13.3% versus 56.3%, $P = .01$) (Table).

Among patients with successful reperfusion, vessel perforation occurred before achieving reperfusion in 13 cases (13/16, 81.3%) and after achieving reperfusion in 3 cases (18.7%). In these last 3 cases, a secondary medium vessel occlusion (A2 and M3) was targeted and recanalized, despite a reperfusion status of \geq TICI 2b.

Among patients with unsuccessful reperfusion, the procedure was aborted after vessel perforation in 5 patients, while in the remaining 11 cases, the procedure was stopped because of failure to achieve successful recanalization. Among these patients, 9 had unsuccessful thrombectomy despite several passes and 2 patients had persistent distal emboli.

Patients with self-resolving bleeding did not have a greater proportion of favorable outcomes than patients needing hemostatic intervention (14/23 patients [60.9%] versus 6/9 patients [66.7%]).

Intracerebral Hemorrhage

The median delay between the groin puncture and control imaging was 18 hours (IQR, 13–24 hours). One patient died within 24 hours before any follow-up imaging was performed. All patients had an SAH on their 24-hour CT. Intraparenchymal hemorrhage of any type occurred in 14 patients (37.5%), of whom 6 (18.8%) had sICH (Table). Among patients with sICH, 4 patients had a distal perforation (distal M2, M3, or A2) and 2 patients had a proximal perforation (M1 segment).

Systematic Review

The initial literature search yielded 6052 articles. After all titles and abstracts were screened by C.D. and G.J., 5969 articles were considered irrelevant. Of the remaining 83 articles, 70 were excluded for

Outcomes of patients with procedural perforation with successful reperfusion (mTICI $\geq 2b/3$) and with unsuccessful reperfusion (mTICI $< 2b/3$)^a

Follow-up	All Patients (n = 32)	mTICI $< 2b$ (n = 16)	mTICI $\geq 2b$ (n = 16)	P Values
Efficacy outcomes				
NIHSS day 1	18 (9–24)	22 (219–24)	13 (59–21)	.04
mRS at 3 months ^b	4 (29–6)	6 (49–6)	2 (1.59–5)	.01
Favorable outcome (mRS, 0–2)	11 (34.4)	2 (12.5)	9 (60.0)	.006
Death at 3 mo	11 (34.4)	9 (56.3)	2 (13.3)	.01
Safety outcomes				
Any hemorrhagic transformation	15 (46.9)	6 (40.0)	9 (56.3)	.4
sICH	6 (18.8)	3 (20.0)	3 (18.8)	.7
SAH	28 (87.5)	14 (93)	14 (87.5)	.6

^a Values are presented as No. (%), mean (SD), or median (IQR).

^b Follow-up at 3 months was unavailable for 1 patient in the unsuccessful reperfusion group.

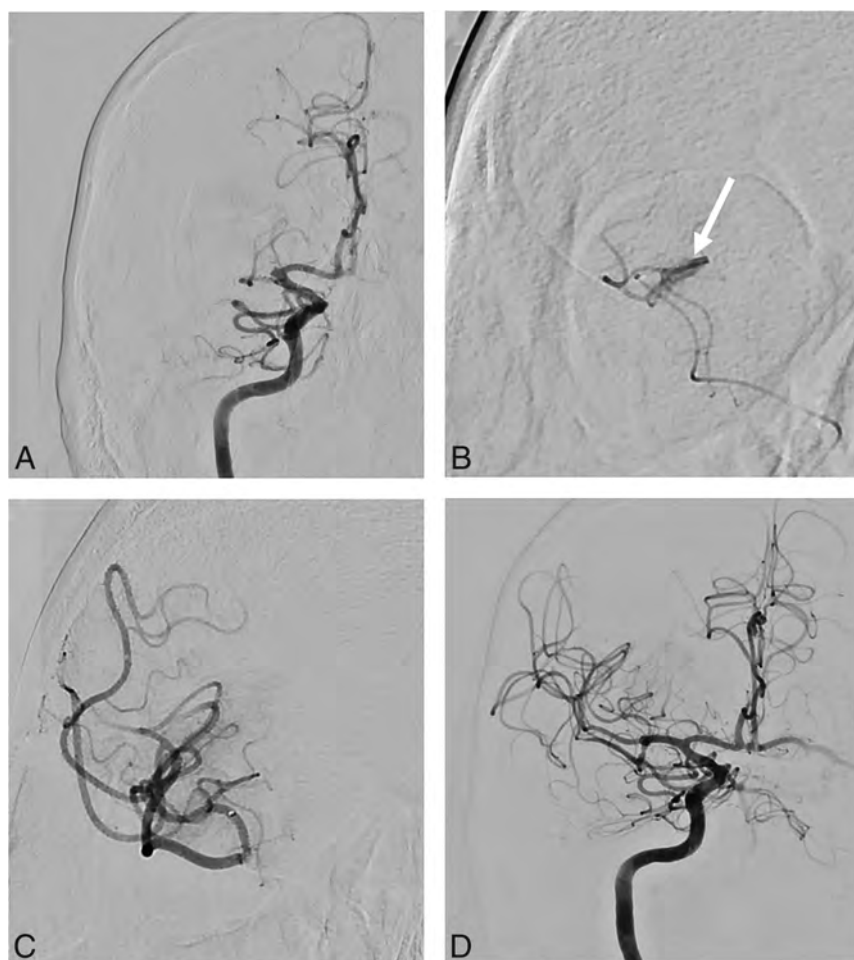


FIG 2. Illustrative case. A 69-year-old man with a proximal right MCA occlusion (A). B, After catheterization of M1, contrast extravasation (white arrow) was identified on microcatheter injection. C, After 10 minutes, contrast extravasation stopped spontaneously. D, Thrombectomy was pursued without further complications, and successful reperfusion was achieved. The patient had a favorable outcome at 3 months (mRS 1).

incorrect outcome assessments, wrong population, wrong study design, and wrong publication type (abstract only, language other than French or English), leaving a total of 13 studies eligible for analysis (n = 37 patients; Online Supplemental Data: PRISMA diagram). Eight studies were cohort studies, and 5 were case reports (Online Supplemental Data). The median baseline NIHSS score

was 14.5 (IQR, 11.75–19). A stent retriever was used in most cases (28/37 cases); contact aspiration, in 13/37 cases; and combined therapy, in 1 case. Nine patients had multiples passes using different techniques. Vessel perforation occurred more often in distal branches (16/37 cases; 43%), while 14 patients (38%) had proximal vessel perforation, and the exact location was not detailed in the remainder.

In most cases (23/37, 62%), the cause of vessel perforation was not described. For those in whom the cause was mentioned, 9 patients (24%) had vessel perforation due to a microwire; 4 patients (11%), due to a microcatheter; and 1 patient (0.03%), due to a strong contrast injection. Different hemostatic strategies were described for 26 patients: 1) procedural abandonment without any additional maneuver despite a persistent intracranial occlusion (7 cases); 2) inflation of an intracranial balloon (8 cases); 3) parent vessel occlusion using coils or glue (6 cases); or 4) watchful waiting (no intervention performed because of spontaneous regression of bleeding) in 2 cases. In 1 case, despite inflation of an intracranial balloon catheter, bleeding persisted, and therapeutic occlusion using coils was performed.

In all studies included in this literature review, the functional outcome at 3 months was available for 35 of 37 patients. The outcomes were poor (median mRS, 6 [IQR, 2.5–6]): Only 9 patients (9/35, 26%) had a favorable outcome (mRS, 0–2) at 3 months, and mortality was high (20/35 cases, 57%). Both reperfusion status and outcome at 3 months were available for 34 patients. Although formal statistical analysis was not possible due to an overall paucity of data in the published reports, the median mRS appeared slightly better in patients with successful reperfusion

(median mRS, 5; IQR, 2–6, versus 6; IQR, 4–6) as did mortality, which was numerically lower in these patients (7/14, 50%, versus 13/20, 65%).

DISCUSSION

Our findings demonstrate that vessel perforation in the context of EVT for acute stroke is infrequent but may result in a high rate of mortality and poor functional outcome. In our series, the proportion of patients having this complication was similar to that reported in recent EVT randomized trials (0.6%–4%), registries,^{1,4} and a previous cohort study by Mokin et al⁵ (1%). However, our results suggest that patients might, nevertheless, do better despite perforation if successful reperfusion is achieved.

Vessel perforation is arguably one of the most serious and feared complications during EVT and is associated with high rates of mortality.^{3–5,9,10} The risk of vessel perforation is increased during “blind maneuvering” while trying to gain access to occluded intracranial vessels with a microwire or microcatheter^{11–17} and while withdrawing a stent retriever.^{5,18,19}

Vessel perforation tends to involve more distal vessel segments: 65% of cases in our study and 61% in our literature review. This finding is particularly relevant because the field is moving toward more aggressive recanalization of distal vessel occlusions,²⁰ with upcoming trials evaluating the role of EVT in such patients (NCT05029414). However, the clinical impact of distal perforation might be less severe than that of proximal perforation (ICA or M1). In our cohort, rescue therapy was performed more often in patients with proximal perforation, but outcomes were similar regardless of perforation site.

It is usually thought that intraprocedural vessel perforation requires immediate action to achieve hemostatic control, such as blood pressure reduction and/or the interruption or reversal of any ongoing thrombolytic agent or blood thinners,¹⁰ temporary intracranial balloon occlusion,^{5,16} or parent vessel occlusion by injection of either liquid embolic agents^{16,21} or detachable coils.^{10,22} These maneuvers were used in most patients found in our systematic review, other than cases in which the procedure was simply aborted prematurely. However, in our cohort, most cases of contrast extravasation resolved spontaneously (71.9%) after the device or microcatheter was withdrawn. In some cases, the offending thrombus itself may provide effective hemostasis when a perforation occurs in the vasculature distal to the occlusion. On the other hand, parent vessel occlusion may potentially result in major stroke with severe disability and could increase the risk of poor clinical outcome and mortality.^{3,22,23}

In our series, as well as in previously published reports, procedural perforations during EVT were associated with overall high mortality rates and low rates of good clinical outcome.^{5,24} Compared with outcomes found in the major EVT trials¹ and in most large EVT registries,²⁵ functional outcomes of patients with vessel perforation remain relatively poor. However, such poor clinical outcomes might be due to the absence of reperfusion²⁶ rather than cerebral hemorrhage. The decision to resume or abort EVT should be based on stroke severity, hemostatic control, technical difficulty, and the safety of pursuing thrombectomy, while always being aware that successful reperfusion appears to be associated with better outcomes and lower mortality in this population.^{5,27}

There are several suspected risk factors for vessel perforation, notably a distal occlusion, the presence of arterial tortuosity, and intracranial atherosclerosis.¹⁸ Moreover, some clot types can be more difficult to cross with a microcatheter and microwire, thus increasing the risk of traumatic vessel injury and perforation.^{5,23} Contact aspiration does not always require crossing the clot with a microcatheter and might intuitively seem safer than stent retrievers in this regard. However, a randomized trial comparing both techniques did not show a significant difference in vessel perforation.²⁸ Some authors have suggested that crossing the clot with a wireless microcatheter may reduce the risk of vessel perforation.²⁹

In our cohort, functional outcome and mortality at 3 months were better than in the literature review. Most studies reporting procedural complications, including vessel perforation, described only severe cases with poor outcomes. Conversely, in our study, we reported all cases of perforation, which could be more representative of real life than smaller series or case reports. Since the widespread adoption of EVT following the major randomized trials,¹ the tools and techniques available have continuously improved,² and in our center, the rate of vessel perforation decreased from 3% in 2015 to 1.6% in 2020.

Despite being a larger cohort than those in previously published reports, our study has several limitations, including its single-center, retrospective design, a relatively small sample size, and the heterogeneity in the management of complications. This last limitation reflects the known variety of practices among neurointerventionalists and stroke physicians regarding the management of vessel perforation during EVT.^{3,5} Because this complication is, fortunately, rare, the limited number of cases precluded the use of statistical analysis to reliably determine which clinical or technical variables were associated with favorable outcome. We did not assign degrees of severity to the perforations, given the lack of a standardized angiographic definition and because procedural imaging of the perforation varied widely among cases. Finally, the 90-day mRS was assessed by raters who were not necessarily blinded to perforation status, and although performed by certified assessors, the mRS is known to have only fair-to-moderate interobserver reliability.³⁰

CONCLUSIONS

Procedural vessel perforation during EVT is a rare-but-serious complication, associated with high mortality and poor clinical outcome. However, successful reperfusion remains correlated with favorable outcome in these patients and can be pursued when technically safe and feasible.











Disclosure forms provided by the authors are available with the full text and PDF of this article at www.ajnr.org.

REFERENCES

1. Goyal M, Menon BK, van Zwam WH, et al. **Endovascular thrombectomy after large-vessel ischaemic stroke: a meta-analysis of individual patient data from five randomised trials.** *Lancet* 2016;387:1723–31 CrossRef Medline
2. Yoo AJ, Andersson T. **Thrombectomy in acute ischemic stroke: challenges to procedural success.** *J Stroke* 2017;19:121–30 CrossRef Medline

3. Balami JS, White PM, McMeekin PJ, et al. **Complications of endovascular treatment for acute ischemic stroke: prevention and management.** *Int J Stroke* 2018;13:348–61 CrossRef Medline
4. Happi Ngankou E, Gory B, Marnat G, et al. **Thrombectomy complications in large vessel occlusions: incidence, predictors, and clinical impact in the ETIS Registry.** *Stroke* 2021;52:e764–68 CrossRef Medline
5. Mokin M, Fargen KM, Primiani CT, et al. **Vessel perforation during stent retriever thrombectomy for acute ischemic stroke: technical details and clinical outcomes.** *J Neurointerv Surg* 2017;9:922–28 CrossRef Medline
6. von Kummer R, Broderick JP, Campbell BC, et al. **The Heidelberg Bleeding Classification: classification of bleeding events after ischemic stroke and reperfusion therapy.** *Stroke* 2015;46:2981–86 CrossRef Medline
7. Ouzzani M, Hammady H, Fedorowicz Z, et al. **Rayyan: a web and mobile app for systematic reviews.** *Syst Rev* 2016;5:210 CrossRef Medline
8. Moher D, Liberati A, Tetzlaff J, et al; PRISMA Group. **Preferred reporting items for systematic reviews and meta-analyses: the PRISMA statement.** *Int J Surg* 2010;8:336–41 CrossRef Medline
9. Nguyen TN, Lanthier S, Roy D. **Iatrogenic arterial perforation during acute stroke interventions.** *AJNR Am J Neuroradiol* 2008;29:974–75 CrossRef Medline
10. Akpınar SH, Yılmaz G. **Periprocedural complications in endovascular stroke treatment.** *Br J Radiol* 2016;89:20150267 CrossRef Medline
11. Frahm D, Wunderlich S, Schubert MI, et al. **Mechanical thrombectomy in acute occlusion of the carotid-T: a retrospective single centre study in 51 patients.** *Clin Neuroradiol* 2016;26:23–99 CrossRef Medline
12. Matsumoto H, Nishiyama H, Tetsuo Y, et al. **Initial clinical experience using the two-stage aspiration technique (TSAT) with proximal flow arrest by a balloon guiding catheter for acute ischemic stroke of the anterior circulation.** *J Neurointerv Surg* 2017;9:1160–65 CrossRef Medline
13. Raz E, Dehkharghani S, Shapiro M, et al. **Possible empirical evidence of glymphatic system on computed tomography after endovascular perforations.** *World Neurosurg* 2020;134:e400–04 CrossRef Medline
14. Seo JH, Jeong HW, Kim ST, et al. **Adjuvant tirofiban injection through deployed Solitaire stent as a rescue technique after failed mechanical thrombectomy in acute stroke.** *Neurointervention* 2015;10:22–27 CrossRef Medline
15. Wong JH, Do HM, Telischak NA, et al. **Initial experience with SOFIA as an intermediate catheter in mechanical thrombectomy for acute ischemic stroke.** *J Neurointerv Surg* 2017;9:1103–06 CrossRef Medline
16. Xu H, Guan S, Liu C, et al. **Rescue glue embolization of vessel perforation during mechanical thrombectomy for acute ischemic stroke: technical note.** *World Neurosurg* 2019;121:19–23 CrossRef Medline
17. Balkan B, Gezmiş A, Erol AT, et al. **Cushing reflex: a sign of vessel perforation during mechanical thrombectomy performed under general anesthesia.** *Turkish Journal of Cerebrovascular Diseases* 2018;24:82–86 CrossRef
18. Leishangthem L, Satti SR. **Vessel perforation during withdrawal of Trevo ProVue stent retriever during mechanical thrombectomy for acute ischemic stroke.** *J Neurosurg* 2014;121:995–98 CrossRef Medline
19. Kallenberg K, Solymosi L, Taschner CA, et al. **Endovascular stroke therapy with the Aperio thrombectomy device.** *J Neurointerv Surg* 2016;8:834–89 CrossRef Medline
20. Ospel JM, Goyal M. **A review of endovascular treatment for medium vessel occlusion stroke.** *J Neurointerv Surg* 2021;13:623–30 CrossRef Medline
21. Davis MC, Deveikis JP, Harrigan MR. **Clinical presentation, imaging, and management of complications due to neurointerventional procedures.** *Semin Intervent Radiol* 2015;32:98–107 CrossRef Medline
22. Watanabe S, Oda J, Nakahara I, et al. **Experimental analysis of intraluminal pressure by contrast injection during mechanical thrombectomy: simulation of rupture risk of hidden cerebral aneurysm in tandem occlusion with blind alley.** *Neurol Med Chir (Tokyo)* 2020;60:286–92 CrossRef Medline
23. Dobrocky T, Piechowiak E, Cianfoni A, et al. **Thrombectomy of calcified emboli in stroke. Does histology of thrombi influence the effectiveness of thrombectomy?** *J Neurointerv Surg* 2018;10:345–50 CrossRef Medline
24. Haussen DC, Ferreira IM, Barreira C, et al. **Active reperfusion hemorrhage during thrombectomy: angiographic findings and real-time correlation with the CT “spot sign.”** *Interv Neurol* 2018;7:370–77 CrossRef Medline
25. Jansen IG, Mulder M, Goldhoorn RB; MR CLEAN Registry Investigators. **Endovascular treatment for acute ischaemic stroke in routine clinical practice: prospective, observational cohort study (MR CLEAN Registry).** *BMJ* 2018;360:k949 CrossRef Medline
26. Dargazanli C, Fahed R, Blanc R, et al; ASTER Trial Investigators. **Modified thrombolysis in cerebral infarction 2c/thrombolysis in cerebral infarction 3 reperfusion should be the aim of mechanical thrombectomy: insights from the ASTER trial (Contact Aspiration Versus Stent Retriever for Successful Revascularization).** *Stroke* 2018;49:1189–96 CrossRef Medline
27. Massari F, Henninger N, Lozano JD, et al. **ARTS (Aspiration-Retriever Technique for Stroke): Initial clinical experience.** *Interv Neuroradiol* 2016;22:325–32 CrossRef Medline
28. Lapergue B, Blanc R, Gory B, et al; ASTER Trial Investigators. **Effect of endovascular contact aspiration vs stent retriever on revascularization in patients with acute ischemic stroke and large vessel occlusion: the ASTER randomized clinical trial.** *JAMA* 2017;318:443–52 CrossRef Medline
29. Keulers A, Nikoubashman O, Mpotsaris A, et al. **Preventing vessel perforations in endovascular thrombectomy: feasibility and safety of passing the clot with a microcatheter without microwire: the wireless microcatheter technique.** *J Neurointerv Surg* 2019;11:653–58 CrossRef Medline
30. Quinn TJ, Dawson J, Walters MR, et al. **Exploring the reliability of the modified Rankin scale.** *Stroke* 2009;40:762–66 CrossRef Medline

MR Imaging Findings of Carcinoma Ex Pleomorphic Adenoma Related to Extracapsular Invasion and Prognosis

 A. Akutsu,  T. Horikoshi,  H. Yokota,  T. Wada,  K. Motoori,  K. Nasu,  K. Yamasaki,  T. Hanazawa,  J.-I. Ikeda, and  T. Uno



ABSTRACT

BACKGROUND AND PURPOSE: MR imaging can reflect the pathologic progression of carcinoma ex pleomorphic adenoma (CXPA). This study aimed to identify the imaging findings related to extracapsular invasion of CXPA. Additionally, the pathologic background of these findings was investigated.

MATERIALS AND METHODS: This retrospective study included 37 patients with histologically confirmed CXPA. Three radiologists independently evaluated whether the CXPA showed the following characteristic MR imaging findings: border, capsule, the corona sign on fat-saturated T2WI and contrast-enhanced fat-saturated T1WI, and the black ring sign. The corona sign appeared larger on fat-saturated and/or contrast-enhanced fat-saturated T1WI than on T1WI. The black ring sign was defined as an intratumoral nodule with a thick low-intensity rim on T2WI. Interreader agreement of the visual assessment was performed using κ analysis, and MR imaging and histopathologic findings were also correlated. Kaplan-Meier survival and the log-rank test were used to estimate the 3-year disease-free survival.

RESULTS: MR imaging findings, especially peritumoral findings, showed a significant difference between invasive and noninvasive CXPA. The reliability was poor for the border and capsule. In contrast, it was good for the corona sign on fat-saturated and contrast-enhanced fat-saturated T1WI and the black ring sign. Pathologically, the corona sign reflected the invasiveness of the tumor and inflammatory cells, while the black ring sign reflected hyalinization or fibrosis. The corona sign also showed a significant difference in the 3-year disease-free survival.

CONCLUSIONS: MR imaging findings, including the corona and black ring signs, reliably differentiated invasive and noninvasive CXPA. The corona sign can be used as a prognostic factor for CXPA.

ABBREVIATIONS: CE = contrast-enhanced; CXPA = carcinoma ex pleomorphic adenoma; FS = fat-saturated; PA = pleomorphic adenoma

Carcinoma ex pleomorphic adenoma (CXPA) arises from a pre-existing pleomorphic adenoma (PA). It is more likely to occur in cases of PA with multiple recurrences or requiring long-term follow-ups. CXPA comprises 3.6% and 11.6% of all salivary gland tumors and malignancies, respectively, and is most often found in the parotid gland.^{1,2}

Carcinoma in PA develops in the luminal cells of the tubular structures, and the malignant cells then destroy the pre-existing PA


structure.³⁻⁵ CXPA is classified by the World Health Organization as noninvasive, minimally invasive, or frankly invasive.⁶ In CXPA, the carcinoma is considered noninvasive if the malignant cells are confined within the pre-existing PA capsule and invasive if the malignant cells cross over the capsule.^{6,7} Noninvasive and minimally invasive CXPAs have a better prognoses and can be treated with localized resection. In contrast, frankly invasive CXPAs have a poor prognosis and require widespread resection, including the margins around the tumor.⁶⁻⁸

We hypothesized that MR imaging findings could reflect this pathologic spectrum of CXPA. CXPA may initially resemble PA, and the imaging findings are likely to change according to the pathologic changes that occur with carcinomatous invasion. The internal components of CXPA can show various imaging findings, depending on the proportions of the mucinous stroma and hyalinization/fibrosis proportions in the pre-existing PA and the histologic diversity of the carcinoma component.^{9,10} Hence, we predicted that the imaging features of CXPA could be captured by focusing on the tumor margins rather than on its internal morphology.

Received March 11, 2022; accepted after revision August 19.

From the Department of Radiology (A.A., T.H., T.W., K.N.), Chiba University Hospital, Chiba, Japan; Diagnostic Radiology and Radiation Oncology (H.Y., T.U.) and Departments of Diagnostic Pathology (J.-I.I.) and Otorhinolaryngology, Head and Neck Surgery (K.Y., T.H.), Chiba University Graduate School of Medicine, Chiba, Japan; and Department of Radiology (K.M.), Tsudanuma Central General Hospital, Chiba Narashino-shi Yatsu, Japan.

Please address correspondence to Takuro Horikoshi, MD, Department of Radiology, Chiba University Hospital, 1-8-1, Inohana, Chuo-ku, Chiba, Chiba, 260-8677, Japan; e-mail: horikoshi@chiba-u.jp

 Indicates article with online supplemental data.

<http://dx.doi.org/10.3174/ajnr.A7656>

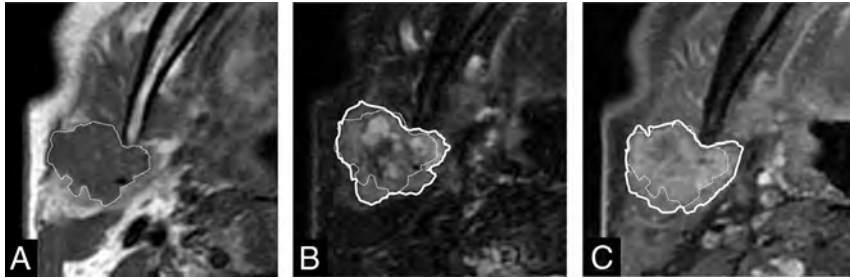


FIG 1. Corona sign on FS-T2WI and CE-FS-T1WI. Invasive CXPA (salivary duct carcinoma) of the right parotid gland in a 77-year-old man. MRI shows a homogeneous low-intensity tumor on axial T1WI (A), mixed high- and low-intensity signals on axial FS-T2WI (B), and irregularly enhanced signal on axial CE-FS-T1WI (C). The tumor size on FS-T2WI and CE-FS-T1WI (solid line) was larger than that on T1WI (dotted line). We defined these MRI findings as corona signs on FS-T2WI and CE-FS-T1WI.

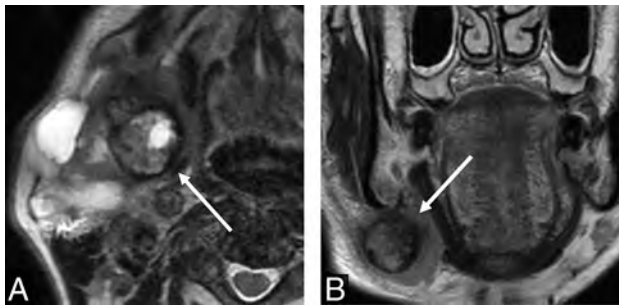


FIG 2. Black ring sign. Invasive CXPA (high-grade mucoepidermoid carcinoma) of the right submandibular gland in a 76-year-old man. MRI shows a nodule with a thick low-intensity rim (A and B, arrows) and an intra-ring component with mixed high- and low-intensity signals on axial and coronal T2WI (A and B). We defined this MRI finding as the black ring sign.

Only a few case reports describing the radiologic features of CXPA have been published. A previous review showed encapsulated components with a hypointense rim on T2WI and fat-saturated (FS) T2WI in some CXPA cases, which may be a characteristic finding.³ However, the clinical significance of this finding has not been fully investigated.

Thus, we aimed to reveal the imaging spectrum of CXPA, specifically focusing on the imaging findings reflecting invasion beyond the PA capsule. In addition, we correlated the imaging findings with the pathologic background and subsequently evaluated the contribution of the imaging findings to prognosis.

MATERIALS AND METHODS

Study Participants

This retrospective study was approved by Chiba University Hospital review board, and the need for written informed consent was waived.

We found 41 potentially relevant cases via a computer search of the pathologic records between August 2007 and April 2020 at Chiba University Hospital. The following keyword phrase was used during the search: “carcinoma ex pleomorphic adenoma.”

Patients were excluded for the following reasons: 1) absent or inaccessible MR images because the MR imaging was performed about 15 years ago ($n = 1$), 2) no head and neck MR imaging

because of CXPA metastasis to the vertebral body ($n = 1$), 3) nonstandard MR imaging protocol (only intracranial MR imaging) ($n = 1$), and 4) lack of surgical-pathologic confirmation ($n = 1$). Of the 41 potential cases that were reviewed, only 37 patients who underwent an operation and had histopathologically proved CXPA were included. Five patients were aware of the mass for about 10 years but had neglected it. Six were under observation because of benign or suspected PA on fine-needle aspiration and imaging tests, and in 1 patient the tumor was surgically removed in the past. The patients underwent multiple

preoperative imaging studies at various time points as part of their standard care.

In our institution, all patients underwent an initial CT examination approximately 3 months after the operation, followed by CT evaluations every 6 months. If recurrence was suspected, additional imaging studies, such as MR imaging and FDG-PET/CT or biopsies were performed. Patients who were pathologically positive or those with close surgical margins and who were histologically identified as having a high-grade malignancy also underwent postoperative radiation (60 Gy/30 fractions).

MR Imaging Protocol

MR images were obtained using a 1.5T scanner (Signa HDxt; GE Healthcare). The imaging protocol included axial T1WI, T2WI, FS-T2WI, and coronal T2WI sequences. Dynamic MR imaging, contrast-enhanced (CE)-FS-T1WI, and DWI/ADC mapping were also performed.

Image and Data Analysis

Clinical and prognostic data were extracted from the medical records, and MR imaging findings were independently evaluated by 3 radiologists with 6, 10, and 18 years of imaging experience, respectively. In cases involving initial disagreement, the final evaluation was decided by consensus among the 3 raters. Visual assessment of the tumor margins included the border and capsule. The border was evaluated using only conventional T1WI and T2WI, and the capsule was defined as the low-signal area and/or the contrast-effect area of the margin, in consideration of the chemical shift artifacts. The border was evaluated first, followed by the capsule. The border was assessed as well-defined, partially ill-defined, or totally ill-defined, and the capsule was assessed as complete, incomplete, or absent on a 3-point scale.

In addition, the corona signs on FS-T2WI and CE-FS-T1WI and the black ring sign were evaluated. The corona sign was considered if the tumor size on FS-T2WI or CE-FS-T1WI was larger than that on T1WI (Fig 1 and Online Supplemental Data). We defined the presence of a component encapsulated with a hypointense rim on T2WI or FS-T2WI as the black ring sign, as reported by Kashiwagi et al³ (Fig 2). In this study, a lesion with a hypointense rim, which was noticeably thicker than the pre-existing PA capsule, was defined as the black ring sign. Intra-ring signals were not

Table 1: Clinical characteristics of CXPA

	Total	Invasive	Noninvasive	P Value
Age (mean) (yr)	64.7 (SD, 13.4)	65.7 (SD, 12.4)	62.7 (SD, 15.3)	.30
Sex				
Male	26	19	7	.44
Female	11	6	5	
Location				
Parotid gland	25	16	9	.68
Submandibular	7	6	1	
Minor salivary	5	3	2	
Laterality				
Left	17	9	8	.16
Right	20	16	4	
Swelling				
Yes	32	20	12	.15
No	5	5	0	
Pain				
Yes	13	10	3	.48
No	24	15	9	
Infection				
Yes	2	2	0	1
No	35	23	12	
Immobility				
Yes	12	10	2	.26
No	25	15	10	
Nerve palsy				
Yes	6	6	0	.15
No	31	19	12	
Skin infiltration				
Yes	1	1	0	1
No	36	24	12	

Table 2: Pathologic characteristics of CXPA

Pathology	Total	Invasive	Noninvasive	P Value
Salivary duct	18	11	7	.53
Myoepithelial	6	5	1	
Adenocarcinoma	3	3	0	
Squamous	3	1	2	
Mucoepidermoid	2	2	0	
Undifferentiated	1	1	0	
Unknown	4	2	2	

considered. Because the thickness of the PA capsule ranged from 15 to 1750 μm , we defined lesions with >2 mm thickness as having the black ring sign.⁸

Radiology-Pathology Correlation

Radiology-pathology correlation was assessed by 2 of the 3 radiologists who performed the imaging evaluations and a pathologist. The review was done with a consensus among these 3 individuals. In particular, we focused on peritumoral findings and the region corresponding to the black ring sign.

Statistical Analyses

We sorted the raters' findings into 2 groups for statistical analyses. Specifically, noninvasive and minimally invasive CXPAs were categorized into the noninvasive group, and frankly invasive CXPAs were categorized into the invasive group. For each imaging assessment, the Fisher exact probability test was performed in both the invasive and noninvasive groups. Interreader agreement of the visual assessment was performed using κ analysis. κ values were interpreted as follows: <0.40 , poor to fair agreement; 0.41 –

0.60 , moderate agreement; 0.61 – 0.80 , substantial agreement; and 0.81 – 1.00 , almost perfect agreement.¹¹ Kaplan-Meier survival and the log-rank test were used to estimate the 3-year disease-free survival. All statistical analyses were performed using R (Version 3.6.3; <http://www.r-project.org/>), and statistical significance was set at $P < .05$.

RESULTS

Clinical Findings

Two of the 37 patients were excluded from the CE image analysis because they had not undergone CE MR imaging. Twelve patients had noninvasive tumors, 25 with frankly invasive and 0 with minimally invasive tumors. The clinical characteristics of the patients are summarized in Table 1. Clinical information, such as age, sex, location, laterality, swelling, pain, infection, immobility, nerve palsy, and skin infiltration, showed no significant difference in relation to extracapsular invasion.

Pathologic Findings

The pathologic characteristics of the patients are summarized in Table 2. No

significant difference was observed in the extracapsular invasion based on the histologic subtypes of the carcinoma.

MR Imaging Findings

The MR imaging findings of the border, capsule, corona sign on FS-T2WI and CE-FS-T1WI, and the black ring sign were significantly different in the 2 groups (Table 3). In the noninvasive group, the black ring sign was not observed in 11 of the 12 patients (91.7%). The black ring sign was observed with massive calcification of the left buccal region on CT in 1 case of maxillary CXPA; the calcification showed no signal on MR imaging and was mistakenly judged as the black ring sign.

Interrater Reliability

The κ values among the 3 raters are summarized in Table 4 and Online Supplemental Data. The border and capsule assessments showed poor agreement; in contrast, assessments of the corona signs on FS-T2WI and CE-FS-T1WI showed substantial agreement. Assessments of the black ring sign showed near-perfect agreement.

Radiology-Pathology Correlation

In the noninvasive group, the malignant component was completely surrounded by the fibrous capsule of the PA. Additionally, there was no infiltrating tumor or inflammatory cell infiltration into the normal salivary gland tissue beyond the lesion margins in this group (Fig 3).

In the invasive group, the corona signs on FS-T2WI and CE-FS-T1WI reflected tumor and/or inflammatory cells. The tumor

Table 3: Imaging findings of CXPA

	Total	Invasive	Noninvasive	P Value	OR 95% CI
Border					
Totally ill-defined	2	2	0	.002	14.41 (2.23–171.2) ^a
Partially ill-defined	19	17	2		
Well-defined	16	6	10		
Capsule					
None	9	9	0	<.001	38.18 (4.06–1956.7) ^b
Partial	12	11	1		
Total	16	5	11		
Corona sign on FS-T2WI					
Present	21	19	2	.001	14.40 (2.23–171.2)
Absent	16	6	10		
Corona sign on CE-FS-T1WI ^c					
Present	22	19	3	.007	9.31 (1.55–76.4)
Absent	13	5	8		
Black ring sign					
Present	15	14	1	.011	13.11 (1.49–642.2)
Absent	22	11	11		

^a These ORs and 95% CIs were calculated between the 2 groups as well-defined versus totally ill-defined and partially ill-defined.

^b These ORs and 95% CIs were calculated between the 2 groups as none and partial versus total.

^c Two cases lacked contrast-enhanced images.

Table 4: Interrater reliability of visual assessment (κ value)^a

	Rater 1 vs 2	Rater 1 vs 3	Rater 2 vs 3
Border	0.12	0.10	0.45
Capsule	0.19	0.38	0.16
Corona sign on FS-T2WI	0.78	0.79	0.67
Corona sign on CE-FS-T1WI	0.65	0.78	0.65
Black ring sign	0.89	0.84	0.84

^a Raters 1, 2, and 3 had 6, 10, and 18 years of experience, respectively.

or inflammatory cells or both showed infiltration into the surrounding fatty tissue or salivary gland tissue. The black ring sign reflected hyalinization/fibrosis. Intra-ring components showed various cells and tissues (eg, carcinoma cells; hyalinization/fibrosis; comedonecrosis; and epithelial, myoepithelial, and mesenchymal components) containing mucoid, myxoid, and chondroid areas. These intra-ring components had diverse ratios of mucoid, myxoid, and chondroid stroma, depending on the individual case (Fig 4). Additionally, some PA components were present outside the black ring sign.

Prognosis

Significant differences were observed in the disease-free survival for invasiveness (Fig 5A, $P = .002$). Imaging findings showed significant differences in the corona signs on FS-T2WI and CE-T1WI. However, no difference was observed in the black ring sign (Fig 5B, -D, corona signs on FS-T2WI and CE-FS-T1WI [$P < .001$ and $P = .001$, respectively] and black ring sign [$P = .31$]).

DISCUSSION

The current study yielded 3 main findings: First, the imaging findings (the border, capsule, corona signs on FS-T2WI and CE-FS-T1WI, and black ring sign) were significantly different between

the invasive and noninvasive groups. These differences were useful for distinguishing invasiveness beyond the ex-PA capsule. Second, the corona signs on FS-T2WI and CE-FS-T1WI reflected the presence of an extracapsular tumor and/or inflammatory cells. For the black ring sign, the hypointense rim on T2WI or FS-T2WI indicated hyalinization/fibrosis, and the intra-ring components reflected various cells and tissues pathologically. Third, a significant difference in disease-free survival was observed between the invasive and noninvasive groups, and pathologic extracapsular invasion was confirmed to be a prognostic factor. In addition, the imaging findings of the corona signs on FS-T2WI and CE-FS-T1WI were also prognostic factors.

To the best of our knowledge, this study included the largest number of

CXPAs and is the first to compare the imaging findings of CXPA based on the World Health Organization's classification of invasiveness. Surgical resection is the first choice of treatment for CXPA. Partial lobectomy is indicated for noninvasive or minimally invasive CXPAs localized in the superficial lobe of the parotid gland, and total parotidectomy is indicated for frankly invasive CXPA.¹² Preoperative MR imaging may facilitate surgical planning and prognosis when one is seeking to manage CXPA.

Marginal information could be used to differentiate invasive and noninvasive CXPAs. We considered that a fibrous capsule usually surrounds a PA and that the appearance of invasion beyond the capsule affects the morphology of the capsule and border. However, the interrater reliability was poor for border and capsule findings. This poor reliability might be due to variations in the pre-existing PA. PA can present with a lobulated morphology, and even a normal PA can have an incomplete capsule or no capsule. In PA of minor salivary glands, the capsule surrounding the lobules could be unclear or missing.^{13,14} In addition, chemical shift artifacts make it difficult to assess thin capsules. Conversely, the corona signs on FS-T2WI and CE-FS-T1WI and the black ring sign showed good interrater reliability (Table 4). These findings may be useful for assessing marginal findings.

The corona signs on FS-T2WI and CE-FS-T1WI reflected pathologically extracapsular tumor and/or inflammatory cells, which could indicate invasion. The black ring sign was a highly specific finding (Table 3; specificity, 91.7% [11 of 12 patients]) for invasive CXPA, with 1 case in which massive calcification was mistaken for a black ring sign. Calcification can be easily recognized on CT images, and its specificity may increase further. In the pathologic evaluation, severe hyalinization and fibrosis were observed, which manifested as a hypointense rim of the black ring sign on T2WI or FS-T2WI. On MR imaging, the intra-ring components of the black ring sign showed various signals.

Pathologically, various components, such as hyaline, mucoid, myxoid, and chondroid stroma, were present, and the proportions of these components varied in each case. The organization of PA shows various patterns and a wide range of morphologic and structural diversity.^{13,14} The black ring sign is suggested to reflect a pre-existing PA or a part of the existing PA. Extensive hyalinization or fibrosis has been identified as an important predictor of malignant transformation in PAs in several pathologic studies. This finding supports our hypothesis,¹⁵⁻¹⁷ and we observed that the black ring sign effectively assessed invasiveness. If the black ring sign reflects a pre-existing PA, it could be a sign of invasive CXPA.

In the survival curve, pathologic invasion beyond the pre-existing PA capsule was associated with recurrence. This result was consistent with previous reports, and CXPA without extracapsular infiltration showed benign behavior.^{15,18-21} Our results

showing no recurrence in noninvasive cases were similar to those reported by Mariano et al¹⁸ and Zhao et al.¹⁹ Therefore, noninvasive CXPA may be managed surgically, similar to benign PAs.

Information on the tumor margins, such as the corona signs on FS-T2WI and CE-FS-T1WI, was a prognostic finding. The black ring sign did not show a significant difference in prognosis. This finding is because the black ring sign had high specificity but low sensitivity to extracapsular infiltration of the CXPA (Table 3; sensitivity, 56% [14 of 25 patients]).

This study had some limitations. First, the histologic types of the carcinomas in the CXPA varied in our study, and this variation may have affected the imaging findings. Second, only CXPA—and no other type of salivary gland tumor—was studied. Third, although CXPA has been classified into 3 types based on the degree of invasiveness, this study did not include cases of minimally invasive CXPA. Minimally invasive CXPA may be overlooked because it requires pathologic evaluation of all tumor margins. However, none of the cases that were actually considered noninvasive showed recurrence, and the prognosis was clearly divided between invasive and noninvasive cases. These findings indicate that a proper pathologic classification was performed.

CONCLUSIONS

MR imaging is useful for differentiating invasive and noninvasive CXPAs. The corona signs on FS-T2WI and CE-FS-T1WI were reliable predictors of the invasiveness of CXPA and overall prognosis. The black ring sign was also a characteristic feature of invasive CXPA. Distinction between invasive

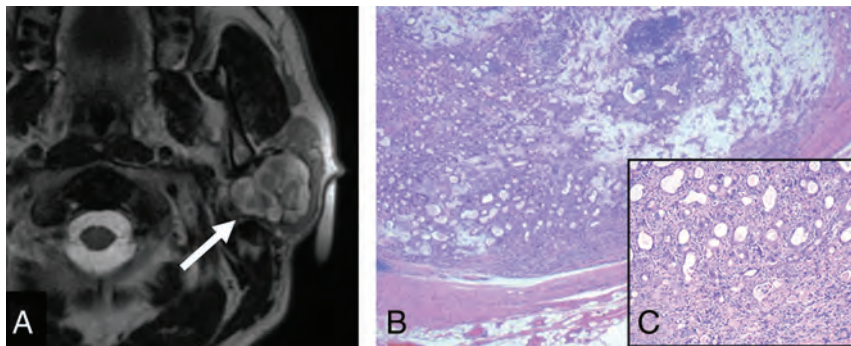


FIG 3. MR imaging–pathology correlation: noninvasive type. Noninvasive CXPA (salivary duct carcinoma) of the left parotid gland in a 56-year-old man. MRI showed a heterogeneous high-intensity tumor on axial T2WI (A, arrow). The corona signs on FS-T2WI and CE-FS-T1WI and the black ring sign were absent. Photomicrograph shows ductal and myoepithelial cells in the chondromyxoid stroma. A part of the tumor contained ductal and myoepithelial cells with atypical hyperchromatic nuclei. The malignant component was completely surrounded by the fibrous capsule of the pre-existing pleomorphic adenoma (B, H&E, original magnification $\times 20$). Note higher magnification of the malignant component (C, H&E, original magnification $\times 100$).

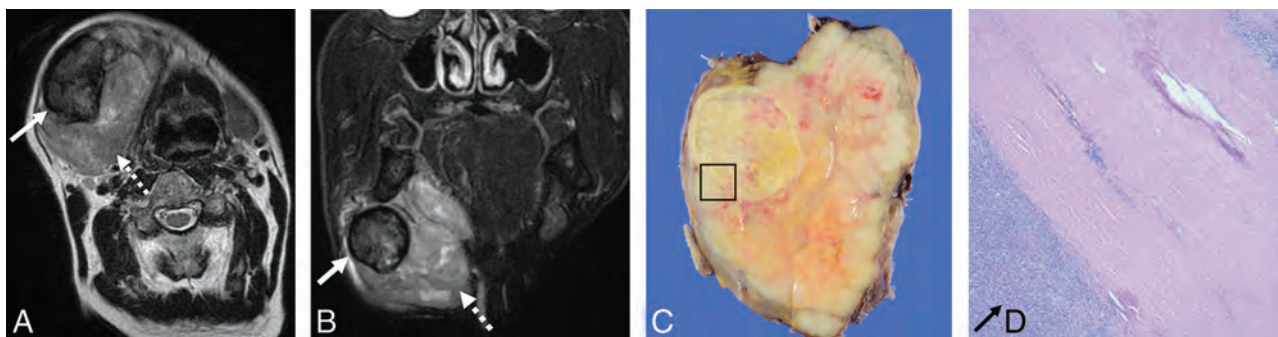


FIG 4. MR imaging–pathology correlation: invasive type. Invasive CXPA (undifferentiated carcinoma, large-cell type) of the right submandibular gland in a 72-year-old man. A huge mass replaced the right submandibular gland. MRI shows heterogeneous high intensity on T2WI and FS-T2WI (A and B, dotted arrows). Encapsulated nodules with thick low-intensity rims are present inside the tumor on axial T2WI and FS-T2WI (A and B, solid arrows). Macroscopic findings show a solid and white-yellow tumor with nodules in the nodule pattern. The nodule within the tumor corresponds to a black ring sign on MRI (C). Photomicrograph shows ductal and myoepithelial cells with atypical hyperchromatic nuclei (D, H&E, original magnification $\times 20$). The malignant component invaded beyond the capsule (D, arrows) and infiltrated the surrounding fatty tissue. Most nodules within the tumor showed extensive hyalinization/fibrosis with myxoid stroma (D), and the black ring sign matched the hyalinization/fibrosis. The corona sign on FS-T2WI and CE-FS-T1WI reflects pathologically extracapsular tumor cells and/or inflammatory cells.

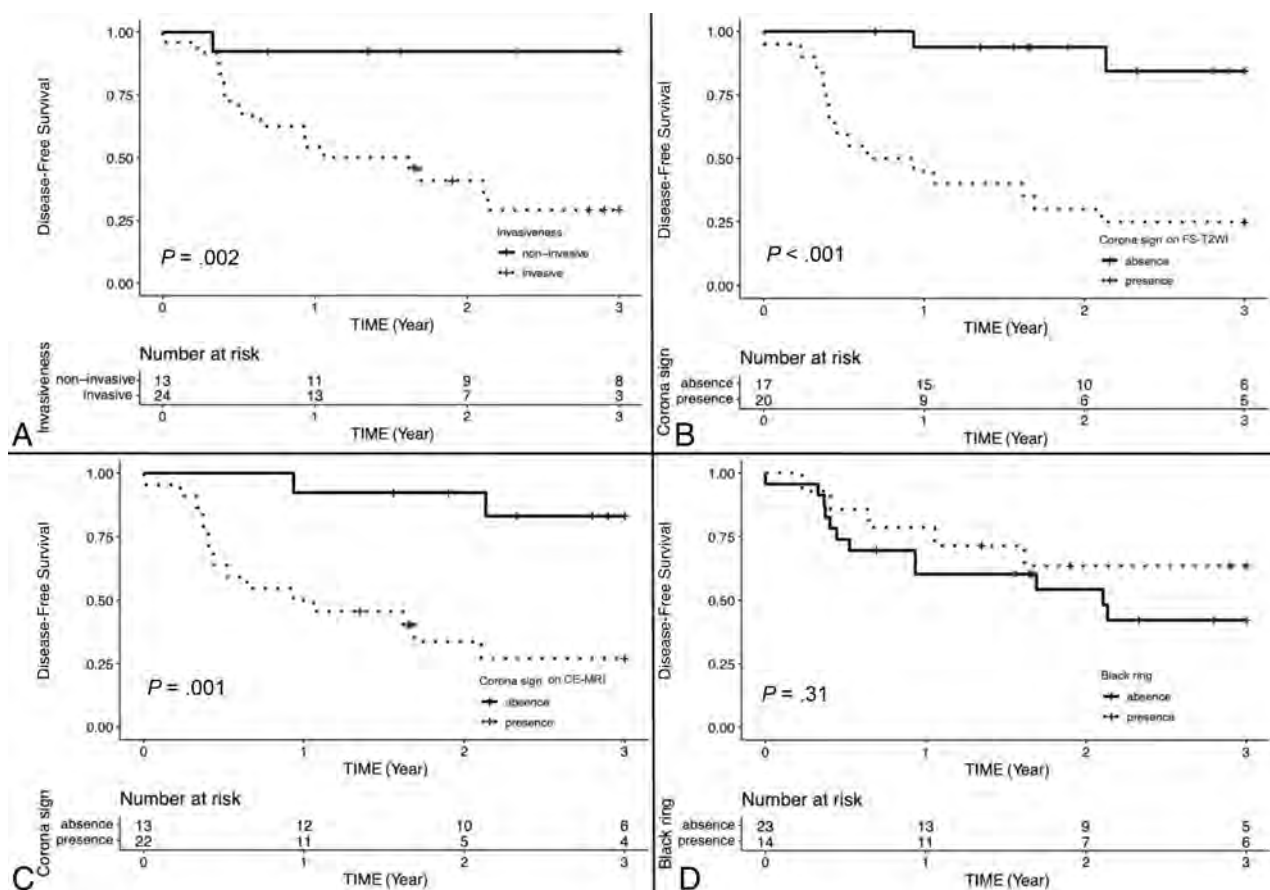


FIG 5. Kaplan-Meier disease-free survival curves and number-at-risk table of invasiveness (A), corona signs on FS-T2WI and CE-FS-T1WI (B and C), and the black ring sign (D).

and noninvasive CXPA using preoperative MR imaging may contribute to surgical planning and prediction of the prognosis of CXPA.

Disclosure forms provided by the authors are available with the full text and PDF of this article at www.ajnr.org.

REFERENCES

- Gnepp DR. Malignant mixed tumours of the salivary glands: a review. *Pathol Annu* 1993;28:279–328 Medline
- Olsen KD, Lewis JE. Carcinoma ex pleomorphic adenoma: a clinicopathologic review. *Head Neck* 2001;23:705–12 CrossRef Medline
- Kashiwagi N, Murakami T, Chikugo T, et al. Carcinoma ex pleomorphic adenoma of the parotid gland. *Acta Radiol* 2012;53:303–06 CrossRef Medline
- Kato H, Kanematsu M, Mizuta K, et al. Carcinoma ex pleomorphic adenoma of the parotid gland; radiopathologic correlation with MR imaging including diffusion-weighted imaging. *AJNR Am J Neuroradiol* 2008;29:865–67 CrossRef Medline
- Weiler C, Zengel P, van der Wal JE, et al. Carcinoma ex pleomorphic adenoma with special reference to the prognostic significance of histological progression: a clinicopathological investigation of 41 cases. *Histopathology* 2011;59:741–50 CrossRef Medline
- El-Naggar AK, Chan JK, Grandis JR, et al. *World Health Organization Classification of Tumours: Pathology and Genetics of Head and Neck Tumours*. 4th ed. International Agency for Research on Cancer; 2017
- Guzzo M, Locati LD, Prott FJ, et al. Major and minor salivary gland tumors. *Crit Rev Oncol Hematol* 2010;74:134–48 CrossRef Medline
- Webb AJ, Eveson JW. Pleomorphic adenomas of the major salivary glands: a study of the capsular form in relation to surgical management. *Clin Otolaryngol Allied Sci* 2001;26:134–42 CrossRef Medline
- Klijanienko J, El-Naggar AK, Vielh P. Fine-needle sampling findings in 26 carcinoma ex pleomorphic adenomas: diagnostic pitfalls and clinical considerations. *Diagn Cytopathol* 1999;21:163–66 CrossRef Medline
- Wada T, Yokota H, Horikoshi T, et al. Diagnostic performance and inter-operator variability of apparent diffusion coefficient analysis for differentiating pleomorphic adenoma and carcinoma ex pleomorphic adenoma: comparing one-point measurement and whole-tumor measurement including radiomics approach. *Jpn J Radiol* 2020;38:207–14 CrossRef Medline
- Landis JR, Koch GG. The measurement of observer agreement for categorical data. *Biometrics* 1977;33:159–74 CrossRef Medline
- Antony J, Gopalan V, Smith RA, et al. Carcinoma ex pleomorphic adenoma: a comprehensive review of clinical, pathological and molecular data. *Head Neck Pathol* 2012;6:1–9 CrossRef Medline
- Mărgăritescu C, Raica M, Simionescu C, et al. Tumoral stroma of salivary pleomorphic adenoma-histopathological, histochemical and immunohistochemical study. *Rom J Morphol Embryol* 2005;46:211–23 Medline
- de Sousa Lopes ML, Barroso KM, Henriques AC, et al. Pleomorphic adenomas of the salivary glands: retrospective multicentric study of 130 cases with emphasis on histopathological features. *Eur Arch Otorhinolaryngol* 2017;274:543–51 CrossRef Medline
- Lewis JE, Olsen KD, Sebo TJ. Carcinoma ex pleomorphic adenoma: pathologic analysis of 73 cases. *Hum Pathol* 2001;32:596–604 CrossRef Medline

16. Auclair PL, Ellis GL. **Atypical features in salivary gland mixed tumors: their relationship to malignant transformation.** *Mod Pathol* 1996;9:652–67 [Database] Medline
17. Ethunandan M, Witton R, Hoffman G, et al. **Atypical features in pleomorphic adenoma—a clinico-pathologic study and implications for management.** *Int J Oral Maxillofac Surg* 2006;35:608–12 CrossRef Medline
18. Mariano FV, Noronha AL, Gondak RO, et al. **Carcinoma ex pleomorphic adenoma in a Brazilian population: clinico-pathological analysis of 38 cases.** *Int J Oral Maxillofac Surg* 2013;42:685–92 CrossRef Medline
19. Zhao J, Wang J, Yu C, et al. **Prognostic factors affecting the clinical outcome of carcinoma ex pleomorphic adenoma in the major salivary gland.** *World J Surg Onc* 2013;11:180 CrossRef Medline
20. Masahiro S, Takashi M, Satoshi S, et al. **Carcinoma ex pleomorphic adenoma of the parotid gland: a multi-institutional retrospective analysis in the Northern Japan Head and Neck Cancer Society.** *Acta Otolaryngol* 2016;136:1154–58 CrossRef Medline
21. Katabi N, Gomez D, Klimstra DS, et al. **Prognostic factors of recurrence in salivary carcinoma ex pleomorphic adenoma, with emphasis on the carcinoma histologic subtype: a clinicopathologic study of 43 cases.** *Hum Pathol* 2010;41:927–34 CrossRef Medline

The Cochlea in Branchio-Oto-Renal Syndrome: An Objective Method for the Diagnosis of Offset Cochlear Turns

 A.F. Juliano,  F. D'Arco,  J. Pao,  S. Picariello,  E. Clement,  G. Moonis, and  C.D. Robson

ABSTRACT

BACKGROUND AND PURPOSE: An “unwound” or “offset” cochlea has been described as a characteristic imaging feature in patients with branchio-oto-renal syndrome, and recently recognized to be associated in particular to those with *EYAI* gene mutations. Determination of this feature has traditionally relied on subjective visual assessment. Our aim was to establish an objective assessment method for cochlear offset (the cochlear turn alignment ratio) and determine an optimal cutoff turn alignment ratio value that separates individuals with *EYAI*-branchio-oto-renal syndrome from those with *SIX1*-branchio-oto-renal syndrome and healthy controls.

MATERIALS AND METHODS: Temporal bone CT or MR imaging from 40 individuals with branchio-oto-renal syndrome and 40 controls was retrospectively reviewed. Cochlear offset was determined visually by 2 independent blinded readers and then quantitatively via a standardized technique yielding the cochlear turn alignment ratio. The turn alignment ratio values were compared between cochleae qualitatively assessed as “not offset” and “offset.” Receiver operating characteristic analysis was used to determine the ability of the turn alignment ratio to differentiate between these populations and an optimal cutoff turn alignment ratio value. Cochlear offset and turn alignment ratio values were analyzed for each branchio-oto-renal syndrome genotype subpopulation and for controls.

RESULTS: The turn alignment ratio can accurately differentiate between cochleae with and without an offset ($P < .001$). The optimal cutoff value separating these populations was 0.476 (sensitivity = 1, specificity = 0.986, $J = 0.986$). All except 1 cochlea among the *EYAI*-branchio-oto-renal syndrome subset and all with unknown genotype branchio-oto-renal syndrome had a cochlear offset and a turn alignment ratio of <0.476 . All except 1 cochlea among the *SIX1*-branchio-oto-renal syndrome subset and all controls had no offset and a turn alignment ratio of >0.476 .

CONCLUSIONS: There is a statistically significant difference in turn alignment ratios between offset and nonoffset cochleae, with an optimal cutoff of 0.476. This cutoff value allows excellent separation of *EYAI*-branchio-oto-renal syndrome from *SIX1*-branchio-oto-renal syndrome and from individuals without branchio-oto-renal syndrome or sensorineural hearing loss. The turn alignment ratio is a reliable and objective metric that can aid in the imaging evaluation of branchio-oto-renal syndrome.

ABBREVIATIONS: BOR = branchio-oto-renal syndrome; ROC = receiver operating characteristic; TAR = turn alignment ratio

Branchio-oto-renal syndrome (BOR) is a cause of hearing loss with autosomal dominant inheritance, first described in 1975 in a family with hearing loss, cup-shaped anteverted pinnae, pre-auricular pits, branchial fistulas, and renal dysplasia.¹ Cochlear

hypoplasia was later noted on tomography.² Since then, with the advent of CT and MR imaging, much more has been described in the literature of characteristic features of the temporal bone among patients with BOR, most notably an “unwound” or “offset” appearance of the cochleae,^{3,4} in which small middle and apical turns are anteriorly offset and appear separated from the basal turn. Most recently, it was shown that the offset appearance of cochlear middle and apical turns is indeed a distinctive finding among patients with BOR, but only among those with *EYAI* gene mutations having the *EYAI* genotype-phenotype; patients with *SIX1* mutations have different phenotypes without cochlear offset,

Received May 2, 2022; accepted after revision August 19.

From the Department of Radiology (A.F.J.), Massachusetts Eye and Ear, Harvard Medical School, Boston, Massachusetts; Department of Radiology (F.D.), Great Ormond Street Hospital for Children, London, UK; Department of Radiology (J.P.), Orlando Health, Orlando Regional Medical Center, Orlando, Florida; Department of General and Specialized Surgery for Women and Children (S.P.), University of Campania “Luigi Vanvitelli,” Naples, Italy; Neuro-Oncology Unit (S.P.), Department of Paediatric Oncology, Santobono-Pausilipon Children's Hospital, Naples, Italy; Department of Clinical Genetics (E.C.), Great Ormond Street Hospital for Children National Health Service Foundation Trust, London, UK; Department of Radiology (G.M.), NYU Langone Medical Center, New York, New York; and Department of Radiology (C.D.R.), Boston Children's Hospital, Harvard Medical School, Boston, Massachusetts.

A.F. Juliano and F. D'Arco are co-first authors.

Please address correspondence to Amy F. Juliano, MD, Department of Radiology, Massachusetts Eye and Ear, 243 Charles St, Boston, MA 02114; e-mail: amy_juliano@meei.harvard.edu; @amyfjuliano
<http://dx.doi.org/10.3174/ajnr.A7653>

but the apical turns have a protuberant “thorny” appearance.⁵ The differing genotype-phenotype correlation could be related to different functions of the *SIX1* and *EYAI* genes, and the different sites of expression and roles of the resultant proteins in the cochlea during the embryologic development of the inner ear. Recognition of these distinct phenotypes on imaging and knowledge of the respective genotype-phenotype correlation offers a powerful tool to radiologists, who can then suggest a genetic diagnosis in the context of a potential syndromic presentation compatible with BOR.⁵

With regard to the offset cochleae seen among patients with *EYAI*-BOR, prior description and determination of this feature in the literature has been based on visual assessment.^{3,4,6} This presumes familiarity with normal cochlear morphology, in order to recognize when the middle and upper turns of the cochleae are anteromedially displaced by a degree that is more than expected for the typical normal cochlea. However, this recognition may be challenging for radiologists who do not regularly interpret temporal bone imaging, and there may be other conditions in which the cochlear turns are not aligned normally or where the turns may not be sufficiently offset to raise the suspicion for *EYAI*-BOR syndrome or another anomaly.

The aim of this study was to define and quantify the cochlear turn alignment ratio (TAR), to analyze the TAR among both cochleae with offset and cochleae without offset as visually assessed by expert head and neck radiologists (the traditional/usual method of assessment), and to determine whether there is a distinct TAR cutoff value that distinguishes the 2 groups. We then examined the cochleae of patients with *EYAI*-BOR, those with *SIX1*-BOR, patients with BOR of unknown genetic association, and controls without evidence of sensorineural hearing loss to determine whether there are quantitative TAR cutoff values that can distinguish patients with BOR from healthy controls and patients with *EYAI*-BOR from those with *SIX1*-BOR. The goal was to establish objective metrics that can separate these populations from each other. The resultant TAR measurement method and criteria can aid any radiologist in the determination of “how offset is too offset” with objectivity and establish normative TAR values for the normal cochlea.

MATERIALS AND METHODS

Participants

This was a multicenter retrospective review of temporal bone imaging studies among individuals with clinically diagnosed BOR (from the same database we previously used for qualitative comparison of BOR cochlear phenotypes) and controls without BOR or sensorineural hearing loss. For the BOR group, 40 individuals from 4 participating institutions were included; inclusion criteria were a clinical diagnosis of BOR syndrome⁷ and diagnostic temporal bone CT and/or MR imaging available for review. Among these 40 patients, 16 had known underlying causative *EYAI* genetic mutations, 4 had known *SIX1* genetic mutations, and 20 had not undergone genetic testing. For the control group, consecutive multidetector row CT scans of 40 patients without clinical or audiometric evidence of sensorineural hearing loss who underwent temporal bone CT for symptoms unrelated to hearing loss (eg, otalgia, otitis media, dizziness, facial palsy) were included. Imaging among the BOR group occurred between April 2001 and April

2021. Imaging among the control group occurred between January 2019 and December 2020. This study was approved by the institutional review board/ethics committee of each institution.

Image Acquisition

BOR Group. Of the 40 patients, 33 had undergone CT, 6 had undergone MR imaging, and 1 had undergone both CT and MR imaging. All CT scanners across the participating institutions were helical multidetector row scanners (Discovery 750 HD, LightSpeed Pro 16 SYS, HiSpeed CT/i SYS, or HiSpeed RP SYS; GE Healthcare; SOMATOM Sensation 40 or SOMATOM Force SYS; Siemens) with parameters ranging as follows: 120 kV (peak), 100–200 mA, section thickness = 0.6–0.625 mm, some with an overlap of 0.2 mm. All MR imaging scanners across the participating institutions were 3T units, with assessment conducted on the heavily T2-weighted sequence such as 3D driven equilibrium radiofrequency reset pulse (DRIVE; Philips Healthcare), constructive interference in steady state (CISS; Siemens), and T2 sampling perfection with application-optimized contrasts by using different flip angle evolution (T2 SPACE; Siemens). All temporal bone images were uploaded onto the PACS, with axial reformats created in a plane parallel to the plane of the lateral semicircular canal (or estimated to be so in cases when the lateral semicircular canal was anomalous), and coronals perpendicular to these reformatted axials, before image analyses.

Control Group. Multidetector row CT scanning (Discovery 750 HD) of the temporal bone was performed with 120 kV(p), 240 mA, 0.6-mm section thickness, and 0.2-mm overlap. Axial reformats of the temporal bones were created in a plane parallel to the lateral semicircular canal, and coronals perpendicular to these reformatted axials before image analyses.

Image Review

Two neuroradiologists with 5 (J.P.) and 15 (A.F.J.) years of experience with subspecialty head and neck expertise reviewed all cases and controls. The reviewers were blinded to the original reports, patient demographics, clinical diagnoses including whether there was BOR syndrome, underlying genetic abnormality, and the other reviewer’s findings.

Qualitative Assessment. The cochleae of all enrolled individuals (patients with BOR and controls) were assessed qualitatively on standardized reformatted axial images in the plane of the lateral semicircular canal. Each cochlea was designated as “with offset” or “without offset” by consensus. Any thorny appearance of the apical turn of the cochlea was also noted as present or absent.⁵

Quantitative Assessment. For each ear, the TAR of the cochlea was assessed quantitatively on standardized reformatted axial images in the plane of the lateral semicircular canal, with the following methodology (Fig 1):

- A line was drawn parallel to the long axis of the basal turn, extending from the round window to the medial bend (line *a*).
- The midpoint of the last complete uppermost turn/apex was identified (point *b*).

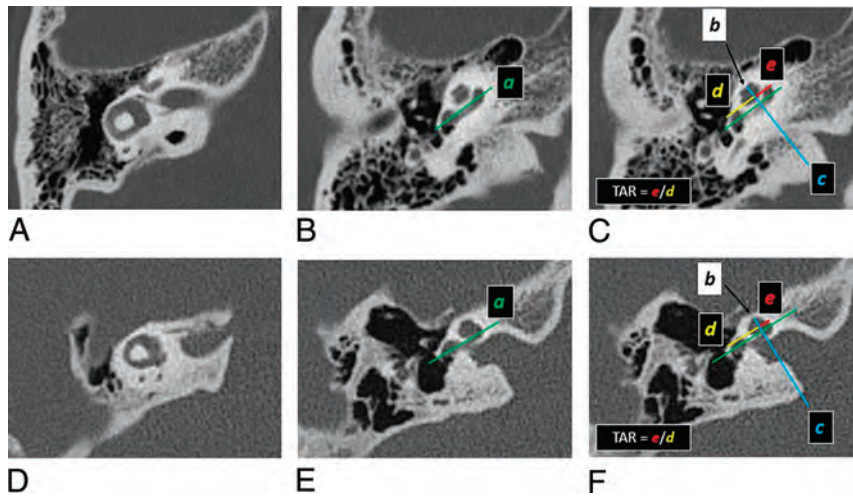


FIG 1. Assessment of TAR of the cochlea on a patient without BOR (A–C) and a patient with *EYAI*-BOR (D–F). Standardized reformatted axial images are utilized, in which the planes are parallel to the plane of the lateral semicircular canal (A and D). Line *a* (green) is drawn parallel to the long axis of the basal turn (B and E), which is propagated across all axial images, including those where the apical or uppermost developed turn is visible (C and F). The midpoint of the uppermost turn is identified on the image that best displays it (black arrows in C and F); this point (point *b*) can also be propagated across all axial images. Line *c* (blue) is then drawn through point *b* (black arrow), perpendicular to line *a* (green). Distance *d* (between the anterior round window and the point of intersection, in yellow) and distance *e* (between medial bend of basal turn and the point of intersection, in red) are measured. TAR is e/d . As can be seen on these images, TAR in the patient with *EYAI*-BOR (F) is smaller than in the patient without BOR (C).

- A perpendicular line was drawn from point *b* to intersect line *a* at a right angle (line *c*), using the “angle” function on PACS to ensure that the angle of intersection measured 90°.
- The distance from the anterior border of the round window to the point of intersection was recorded (distance *d*).
- The distance from the point of intersection to the medial bend of the basal turn was recorded (distance *e*).
- TAR is defined as e/d .

These lines and points were usually not all appreciated on 1 single axial plane; thus, care was taken to scroll through consecutive images while keeping the electronic caliper fixed at 1 point from the initial index image before reaching the end point on another image, or lines were propagated across images with identical orientation. When there was need for confirmation, minimum-intensity projections were made to view structures in a stack.

To accurately and reproducibly quantify the cochlear offset, we carefully determined cochlear turns by considering the cochlea in fifths as mentioned by Fitch et al.⁸ and Chen et al.⁹ The basal turn constitutes the first and second fifths (from the round window to the medial bend, then the medial bend back to the lateral edge), the middle turn constitutes the third and fourth fifths (from the lateral edge to the medial bend, then the medial bend back to the lateral edge), and the apical turn is the last fifth (from the lateral edge at the end of the middle turn going medially toward the end of the tip) (Fig 2). The very short segment of the cochlea that is relatively linear, extending from the round window to the point when the cochlea begins to coil, has been referred to as the “hook region” of the cochlea.^{10,11} For this study, we followed the methodology of a previously published article,⁵ in which the hook region of the cochlea is

grouped with the spiraling main portion of the basal turn to be collectively considered as the first fifth, ensuring a standardized lateral boundary of the basal turn at the round window membrane and thus ensuring measurement consistency.

Statistical Analysis

On the basis of qualitative assessment, the cochleae of all enrolled individuals were divided into 2 groups: with offset and without offset. The number of individuals with *EYAI*-BOR, *SIX1*-BOR and unknown-mutation BOR and healthy controls (non-BOR and without hearing loss) in each group was noted.

On the basis of quantitative assessment that yielded TAR numeric values, interrater reliability was evaluated by the intraclass correlation coefficient. Due to excellent agreement, the average of the 2 readers was used for further analysis.^{12,13}

Continuous parametric variables are presented as mean (SD), whereas categorical data are presented as number and percentage. Normal distribution was determined using the Shapiro-Wilk test ($P > .05$) and histogram plots. A

Student *t* test was performed to explore whether the offset ratio was different between cochleae qualitatively deemed to be with and without offset. Receiver operating characteristic (ROC) curve analysis was used to determine the diagnostic accuracy of the offset ratio. The optimal cutoff point was determined by the Youden index *J*. *P* values $< .05$ were considered statistically significant.

SPSS Statistics 22 software (IBM) was used to perform the analyses. GraphPad Prism 7 (GraphPad Software) was used for graphing.

RESULTS

Eighty participants with a total of 160 cochleae were included in this study: 16 participants (32 cochleae) with *EYAI* mutations, 4 (8 cochleae) with *SIX1* mutations, 20 (40 cochleae) with BOR of unknown genotype, and 40 (80 cochleae) controls (Table 1).

There was excellent interrater reliability in the TAR measurements obtained by the 2 independent reviewers, with an intraclass correlation coefficient of 0.976. The values within each of the 2 groups (offset and not offset) followed normal distributions.

The cochleae deemed “not offset” by visual assessment had TAR values ranging from 0.492 to 0.741; the cochleae deemed “offset” by visual assessment had TAR values ranging from 0.189 to 0.460 with 1 outlier at 0.556 (Fig 3). The mean TAR value was significantly lower in cochleae with offset (0.338 [SD, 0.063]) compared with those without offset (0.599 [SD, 0.050]) ($P < .001$).

ROC curve analysis showed that TAR can accurately distinguish between cochleae with anterior offset and those without, with an area under the curve (AUC) value of 0.997 (95% CI, 0.992–1) ($P < .001$) (Fig 4). Based on Youden index *J*, the optimal cutoff value was 0.476 (sensitivity = 1, specificity = 0.986, $J = 0.986$). TAR

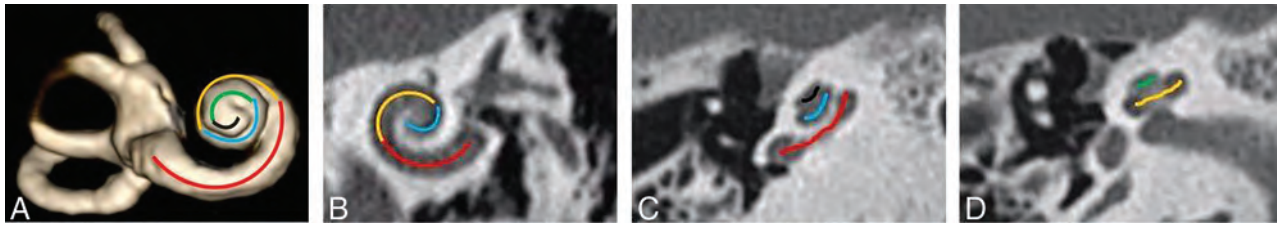


FIG 2. A, Fifths of a cochlea, as demonstrated on a 3D reconstruction of the inner ear from a heavily T2-weighted sequence (3D DRIVE). The first fifth is in red (including the hook region), the second fifth in orange, the third fifth in blue, the fourth fifth in green, and the fifth fifth in black. (B, C, and D). CT of the temporal bone in a bone algorithm in the Stenvers view (B) and axial (C and D) planes shows the fifths of the cochlea in the same color scheme as depicted on the 3D model in A.

Table 1: Qualitative (columns 3 and 4) and quantitative assessment (TAR, column 5) of cochlear offset

	Total No. of Cochleae	No. of Cochleae with Offset	No. of Cochleae without Offset	Mean TAR
<i>EYAI</i> -BOR	32	32	0	0.338 (SD, 0.071)
<i>SIXI</i> -BOR	8	1	7	0.577 (SD, 0.107)
Unknown genotype BOR	40	40	0	0.339 (SD, 0.057)
Controls	80	0	80	0.598 (SD, 0.051)

SIXI-BOR, and 40 were among patients with BOR of unknown genotype. Eighty-seven cochleae showed no offset. Of these, 7 were among patients with *SIXI*-BOR, and the remaining 80 were controls. Of note, all 80 controls showed no offset.

The mean TAR among patients with *SIXI*-BOR (0.577 [SD, 0.107]) was similar to that among controls (0.598 [SD, 0.051]), with none <0.476. The mean TAR among patients with *EYAI*-BOR (0.338 [SD, 0.071]) was much lower. The mean TAR among patients with BOR of unknown genotype (0.339 [SD, 0.057]) was similar to that among patients with *EYAI*-BOR, and all were <0.476. These are listed in Table 1 and depicted in Fig 5.

On qualitative assessment, all individuals with *EYAI*-BOR (32 cochleae of a total of 32) and BOR of unknown genotype (40 cochleae of a total of 40) had bilateral offset cochleae (Fig 6). None had a thorny apical turn (Table 2). On the contrary, cochlear offset was not seen in individuals with *SIXI*-BOR except in 1 cochlea; that cochlea appeared different from the typical unwound, offset cochlea but instead fit the description of cochlear hypoplasia type 4 (Fig 7)^{14,15} and lacked a thorny apical turn. The remainder of the *SIXI*-BOR cochleae had thorny tips (7 cochleae of 8). None of the controls had cochlear offset or a thorny apical turn.

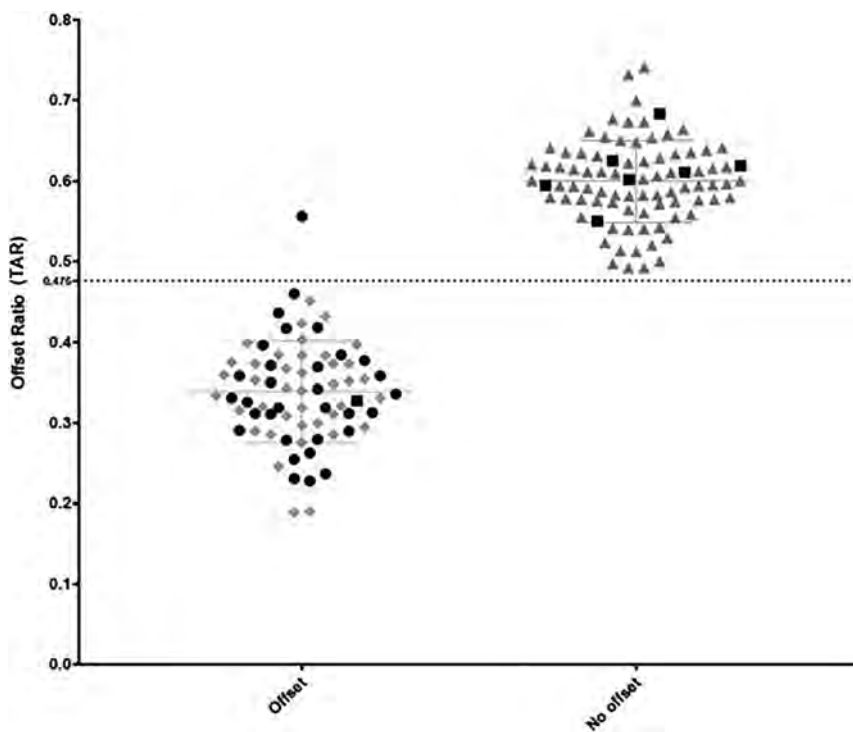


FIG 3. Cochlear TAR among cochleae-deemed offset and not offset on visual assessment. *EYAI*-BOR: black round dots; *SIXI*-BOR: black square dots; unknown genotype: gray rhomboid dots; controls: gray triangle dots. The dashed line indicates the TAR cutoff (0.476) as determined by ROC curve analysis.

values above the cutoff were predictive of a lack of cochlear offset, whereas values below 0.476 were associated with cochlear offset.

Seventy-three cochleae showed anterior offset. Of these, 32 were among patients with *EYAI*-BOR, 1 was among patients with

been determined qualitatively, whereby the radiologist visually estimates whether the alignment of the cochlear turns appears to be anomalous, with the upper turns anteriorly displaced and slightly tipped away relative to the basilar turn, outside the range of normal.

DISCUSSION

The presence of a cochlear offset associated with *EYAI*-BOR has traditionally

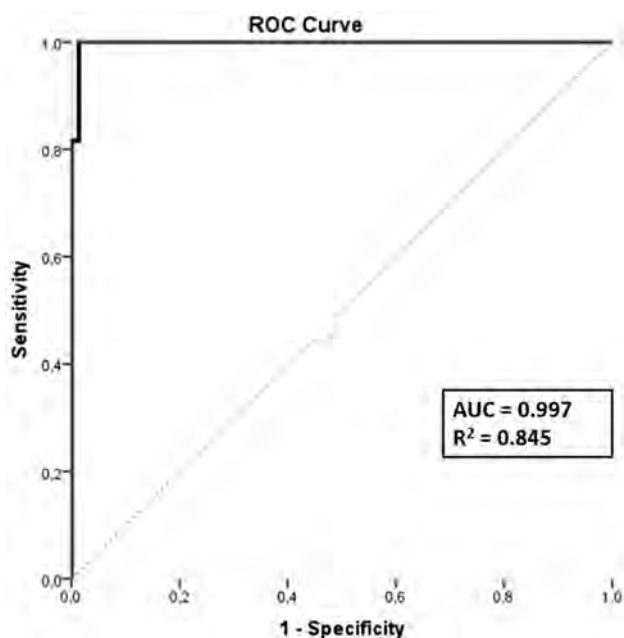


FIG 4. ROC curve.

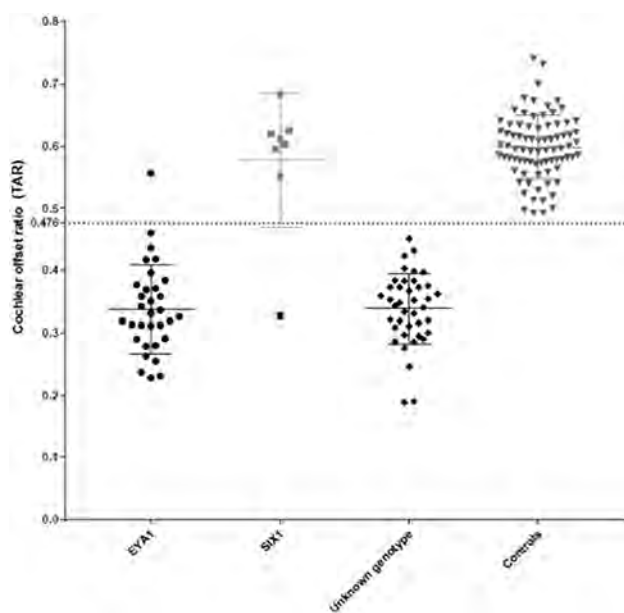


FIG 5. Cochlear TAR among individuals with *EYAI*-BOR, *SIX1*-BOR, BOR of unknown genotype, and controls without BOR or sensorineural hearing loss. The TAR cutoff of 0.476 was determined by ROC curve analysis. All except one of the *EYAI*-BOR cochleae have TAR below the cutoff value. All except one of the *SIX1*-BOR cochleae have TAR above the cutoff value. All individuals with BOR of unknown genotype have TAR below the cutoff value. None of the controls have TAR below the cutoff value.

However, this estimation may be challenging for radiologists who do not routinely interpret temporal bone imaging studies. In this study, we explored an objective method to evaluate and quantify the presence of an anteriorly offset or unwound cochlea in patients with *EYAI*-BOR, to provide a reproducible and reliable diagnostic tool for all radiologists.

All of our patients with a clinical diagnosis of BOR and confirmed *EYAI* mutations (16 patients, 32 cochleae) had anteriorly offset cochleae on subjective visual analysis. We found that there was a statistically significant difference in TAR between individuals with *EYAI*-BOR and controls without a diagnosis of BOR or sensorineural hearing loss. The optimal cutoff value for the upper limit of TAR that produced the greatest sensitivity and specificity for the detection of cochlear offset suggestive of *EYAI*-BOR was 0.476. This implies that this TAR measurement method and cutoff value can be used to suggest *EYAI* mutations in patients with a clinical diagnosis of BOR.

Furthermore, except for 1 outlier, all cochleae among the patients with *SIX1*-BOR in our cohort did not have anterior offset, with a TAR of >0.476 . In the 1 outlier that did demonstrate misaligned cochlear turns, it appeared to be due to an underlying cochlear hypoplasia (type 4) (Figs 7), distinct in morphology from the typical *EYAI*-BOR offset cochlea (Fig 1E, -F). Thus, there is a good degree of quantitative difference in cochlear turn alignment between individuals with *EYAI*-BOR and those with *SIX1*-BOR. This is in addition to morphologic differences in the apical turn of the cochlea previously demonstrated, whereby the *EYAI*-BOR cochlea appears unwound with an anterior offset, while the *SIX1*-BOR cochlea has a thorny apical turn without the characteristic anterior offset (Fig 8).⁵

Notably, in our cohort, all the individuals with BOR of an unknown underlying causative genotype had offset cochleae, with a TAR of <0.476 . In addition, they did not have thorny apical turns. On the basis of the strong phenotype-genotype correlation in patients with BOR and our current results, we speculate that all the patients with BOR in our cohort of an unknown genetic diagnosis may have *EYAI* mutations, given their anteriorly offset cochleae and lack of a thorny apical turn. This finding would be in keeping with the estimated substantially higher prevalence of *EYAI* compared with *SIX1* mutations among patients with BOR reported in the literature.¹⁶⁻¹⁹

Interestingly, all our patients with *EYAI*-BOR (TAR <0.476) had moderate-to-severe conductive hearing loss and mild-to-moderate sensorineural hearing loss. All our patients with *SIX1*-BOR without obvious cochlear dysmorphology (TAR >0.476) had mild conductive hearing loss (35–40 dB) and mild sensorineural hearing loss (25–35 dB). The 1 patient with *SIX1*-BOR with a hypoplastic cochlea had severe conductive hearing loss and profound sensorineural hearing loss. All except one of the patients with BOR of unknown genotype had moderate-to-severe conductive hearing loss and mild-to-moderate sensorineural hearing loss, showing that most of them had hearing ability similar to that of those with the *EYAI* mutation rather than the *SIX1* mutation; this finding would be in

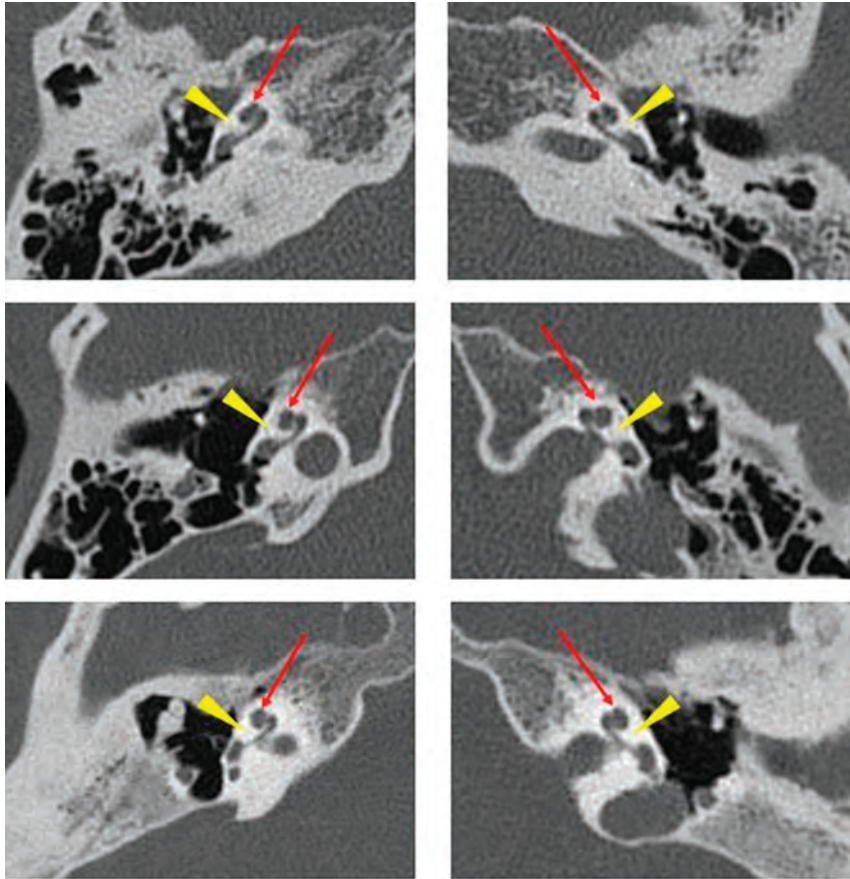


FIG 6. Axial CT images of 3 different patients with *EYA1*-BOR showing the anteriorly offset unwound cochlea, an imaging feature characteristic of *EYA1*-BOR. Notice that the middle and apical turns are anteriorly located relative to the basal turn (red arrows) and slightly tilted away and separated from the basal turn (yellow arrowheads).

Table 2: The presence/absence of thorny tips among the 3 BOR populations and in controls

	Total No. of Cochleae	No. of Cochleae with Thorny Tips
<i>EYA1</i> -BOR	32	0
<i>SIX1</i> -BOR	8	7
Unknown genotype BOR	40	0
Controls	80	0

keeping with the known estimated prevalence of these 2 genotypes among the overall BOR population.

The interactions between *SIX1* and *EYA1* protein expression during cochlear development are complex; however, we know from murine models that while *SIX1* expression is dependent on *EYA1*, *EYA1* expression is not impacted by *SIX1*. Moreover, *SIX1* is mainly expressed in the apical part of the cochlea.²⁰ This location may explain the milder alteration in cochlear phenotype associated with *SIX1* mutations compared with *EYA1* mutations. It is unclear why one of our patients with a *SIX1* mutation had the characteristic thorny cochlea on only 1 side and an anterior offset and hypoplastic cochlea on the other; it is possible that this feature is due to the particular locus of the mutated base pairs in the gene leading to different resultant disturbances in the complex *SIX1/EYA1*

interactions.²¹ Furthermore, the *SIX1* variant in this case (Cys16Tyr) is located closer toward the N-terminal (SD domain) within an α -helix critical for *EYA1* interaction. More studies with larger cohorts of patients with *SIX1*-mutated BOR would be helpful to clarify whether specific mutations within the same gene can create varying and potentially characteristic phenotypes.

As expected, none of the control patients had anteriorly offset cochleae, corroborating the high sensitivity of this radiologic sign. However, there are other genetic causes of malformed cochleae with hypoplastic middle and apical turns reported in literature, such as Walker-Warburg syndrome, where the “hook” of the basal turn is the only well-preserved portion of the cochlea and the upper parts are anteriorly placed and markedly hypoplastic, resembling an extreme anteriorly offset cochlea.²² This appearance may relate to an arrest in embryonic development before the end of the seventh week of gestation, when only the first half of the basal turn is formed and the second half of the basal turn and the middle/upper turns have yet to develop and fold on themselves to create the final cochlear structure. To the best of our knowledge, at the current time, the anterior offset unwound cochlea fitting the original radiologic description^{3,5} has

been described only in *EYA1*-BOR and Walker-Warburg syndrome. However, as knowledge in genetics increases with time, it might be discovered that this offset appearance of the cochlea may be a part of the phenotypic constellation in other, rare causes and genotypes related to cochlear dysplasia.²³

Some limitations of this study are its retrospective design, different CT and MR imaging protocols among the participating institutions, and its relatively small sample size. In the future, we would benefit by prospective enrollment of patients with BOR to achieve a larger population size, preferably with known underlying genotypes, and to perform qualitative and quantitative TAR assessment in a large BOR population.

CONCLUSIONS

This study shows that there is a statistically significant difference in TAR between offset and nonoffset cochleae, with an optimal cutoff at 0.476. This is also the optimal TAR threshold value that allows excellent separation of the *EYA1*-BOR population from the *SIX1*-BOR population, and separation of patients with *EYA1*-BOR from individuals without sensorineural hearing loss. The proposed TAR measurement method and threshold value can aid any radiologist in the determination of “how offset is too

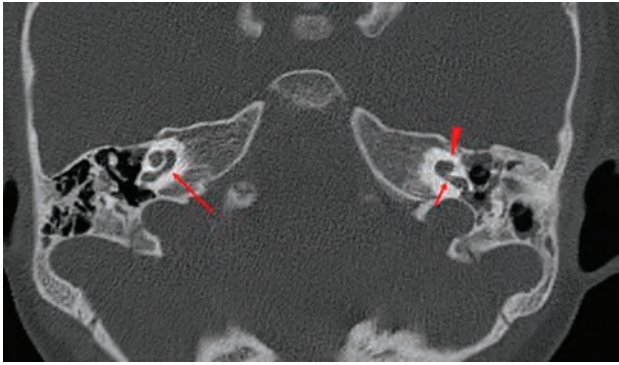


FIG 7. CT image of the patient with *SIX1*-BOR in whom the right cochlea does not demonstrate any offset (*long arrow*), while the left cochlea has an offset but with an appearance akin to cochlear hypoplasia type 4 rather than the typical unwound and offset cochlea of *EYA1*-BOR. Notice the normal size and morphology of the basal turn first half (*short arrow*), while the distal basal, middle, and apical turns are hypoplastic (*arrowhead*).

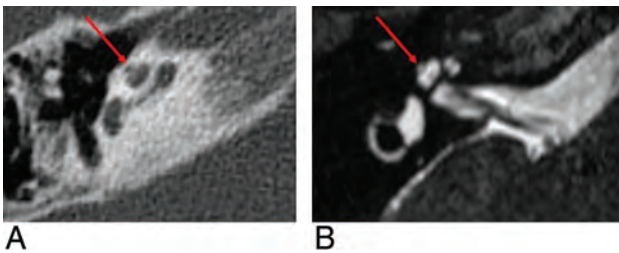


FIG 8. A thorny apical turn in a patient with *SIX1*-BOR. The apical turn of the cochlea appears as a short, protuberant, thorny tip, as seen on CT (A) and MR imaging (B).

offset”, to decide objectively whether there are anomalous offset cochleae compatible with the *EYA1*-BOR genotype-phenotype.

Disclosure forms provided by the authors are available with the full text and PDF of this article at www.ajnr.org.

REFERENCES

- Melnick M, Bixler D, Nance WE, et al. **Familial branchio-oto-renal dysplasia: a new addition to the branchial arch syndromes.** *Clin Genet* 1976;9:25–34 CrossRef Medline
- Ostri B, Johnsen T, Bergmann I. **Temporal bone findings in a family with branchio-oto-renal syndrome (BOR).** *Clin Otolaryngol Allied Sci* 1991;16:163–67 CrossRef Medline
- Robson CD. **Congenital hearing impairment.** *Pediatr Radiol* 2006;36:309–24 CrossRef Medline
- Hsu A, Desai N, Paldino MJ. **The unwound cochlea: a specific imaging marker of branchio-oto-renal syndrome.** *AJNR Am J Neuroradiol* 2018;39:2345–49 CrossRef Medline
- Pao J, D’Arco F, Clement E, et al. **Re-examining the cochlea in branchio-oto-renal syndrome: genotype-phenotype correlation.** *AJNR Am J Neuroradiol* 2022;43:309–14 CrossRef Medline

- Propst EJ, Blaser S, Gordon KA, et al. **Temporal bone findings on computed tomography imaging in branchio-oto-renal syndrome.** *Laryngoscope* 2005;11510:1855–62 CrossRef Medline
- Smith RJ. **Branchiootorenal spectrum disorder.** In: Adam MP, Ardinger HH, Pagon RA eds. *GeneReviews*. University of Washington, Seattle; 1993
- Fitch N, Lindsay JR, Srolovitz H. **The temporal bone in the preauricular pit, cervical fistula, hearing loss syndrome.** *Ann Otol Rhinol Laryngol* 1976;85:268–75 CrossRef Medline
- Chen A, Francis M, Ni L, et al. **Phenotypic manifestations of branchio-oto-renal syndrome.** *Am J Med Genet* 1995;58:365–70 CrossRef Medline
- Kim N, Steele CR, Puria S. **The importance of the hook region of the cochlea for bone-conduction hearing.** *Biophys J* 2014;107:233–41 CrossRef Medline
- Atturo F, Barbara M, Rask-Andersen H. **On the anatomy of the “hook” region of the human cochlea and how it relates to cochlear implantation.** *Audiol Neurootol* 2014;19:378–85 CrossRef Medline
- Lange RT. **Inter-rater reliability.** In: Kreutzer JS, DeLuca J, Caplan B, eds. *Encyclopedia of Clinical Neuropsychology*. Springer; 2011:1348
- Kreutzer JS, DeLuca J, Caplan B, eds. **Inter-rater agreement.** In: Kreutzer JS, DeLuca J, Caplan B, eds. *Encyclopedia of Clinical Neuropsychology*. Springer; 2011:1348
- Sennaroglu L. **Histopathology of inner ear malformations: do we have enough evidence to explain pathophysiology?** *Cochlear Implants Int* 2016;171:3–20 CrossRef Medline
- Talenti G, Manara R, Brotto D, et al. **High-resolution 3 T magnetic resonance findings in cochlear hypoplasias and incomplete partition anomalies: a pictorial essay.** *Br J Radiol* 2018;91:20180120 CrossRef Medline
- Kochhar A, Orten DJ, Sorensen JL, et al. ***SIX1* mutation screening in 247 branchio-oto-renal syndrome families: a recurrent missense mutation associated with BOR.** *Hum Mutat* 2008;29:4:565 CrossRef Medline
- Sanggaard KM, Rendtorff ND, Kjaer KW, et al. **Branchio-oto-renal syndrome: detection of *EYA1* and *SIX1* mutations in five out of six Danish families by combining linkage, MLPA and sequencing analyses.** *Eur J Hum Genet* 2007;15:1121–31 CrossRef Medline
- Krug P, Morinière V, Marlin S, et al. **Mutation screening of the *EYA1*, *SIX1*, and *SIX5* genes in a large cohort of patients harboring branchio-oto-renal syndrome calls into question the pathogenic role of *SIX5* mutations.** *Hum Mutat* 2011;32:183–90 CrossRef Medline
- Unzaki A, Morisada N, Nozu K, et al. **Clinically diverse phenotypes and genotypes of patients with branchio-oto-renal syndrome.** *J Hum Genet* 2018;63:647–56 CrossRef Medline
- Zheng W, Huang L, Wei Z-B, et al. **The role of *SIX1* in mammalian auditory system development.** *Development* 2003;130:3989–4000 CrossRef Medline
- Chatterjee S, Kraus P, Lufkin T. **A symphony of inner ear developmental control genes.** *BMC Genet* 2010;11:68 CrossRef Medline
- Talenti G, Robson C, Severino MS, et al. **Characteristic cochlear hypoplasia in patients with Walker-Warburg syndrome: a radiologic study of the inner ear in α -Dystroglycan-related muscular disorders.** *AJNR Am J Neuroradiol* 2021;42:167–72 CrossRef Medline
- Som PM, Curtin HD, Liu K, et al. **Current embryology of the temporal bone, part I: the inner ear.** *Neurographic* 2016;6:250–65 CrossRef

Accelerated Synthetic MRI with Deep Learning–Based Reconstruction for Pediatric Neuroimaging

 E. Kim,  H.-H. Cho,  S.H. Cho,  B. Park,  J. Hong,  K.M. Shin,  M.J. Hwang,  S.K. You, and  S.M. Lee



ABSTRACT

BACKGROUND AND PURPOSE: Synthetic MR imaging is a time-efficient technique. However, its rather long scan time can be challenging for children. This study aimed to evaluate the clinical feasibility of accelerated synthetic MR imaging with deep learning–based reconstruction in pediatric neuroimaging and to investigate the impact of deep learning–based reconstruction on image quality and quantitative values in synthetic MR imaging.

MATERIALS AND METHODS: This study included 47 children 2.3–14.7 years of age who underwent both standard and accelerated synthetic MR imaging at 3T. The accelerated synthetic MR imaging was reconstructed using a deep learning pipeline. The image quality, lesion detectability, tissue values, and brain volumetry were compared among accelerated deep learning and accelerated and standard synthetic data sets.

RESULTS: The use of deep learning–based reconstruction in the accelerated synthetic scans significantly improved image quality for all contrast weightings ($P < .001$), resulting in image quality comparable with or superior to that of standard scans. There was no significant difference in lesion detectability between the accelerated deep learning and standard scans ($P > .05$). The tissue values and brain tissue volumes obtained with accelerated deep learning and the other 2 scans showed excellent agreement and a strong linear relationship (all, $R^2 > 0.9$). The difference in quantitative values of accelerated scans versus accelerated deep learning scans was very small (tissue values, $< 0.5\%$; volumetry, -1.46% – 0.83%).

CONCLUSIONS: The use of deep learning–based reconstruction in synthetic MR imaging can reduce scan time by 42% while maintaining image quality and lesion detectability and providing consistent quantitative values. The accelerated deep learning synthetic MR imaging can replace standard synthetic MR imaging in both contrast-weighted and quantitative imaging.

ABBREVIATIONS: DIFF = percentage difference; DLR = deep learning–based reconstruction; FAST-SyMRI = accelerated synthetic MRI without DLR; FAST-SyMRI+DLR = accelerated synthetic MRI with DLR; ICC = intraclass correlation coefficient; PD = proton density; PSIR = phase-sensitive inversion recovery; ST-SyMRI = standard synthetic MRI

Synthetic MR imaging using a multidynamic, multiecho sequence is a well-known time-efficient technique that simultaneously provides quantitative MR imaging and multiple contrast-weighted images in a single scan. Therefore, the availability of synthetic MR imaging for clinical practice and

research purposes has increased, and this technique has been extensively validated for diagnostic value in neuroimaging in both children and adults.^{1–8} However, its rather long single-scan time of 6–7 minutes, despite being clinically acceptable, can be a practical challenge for pediatric neuroimaging because of the possibility of motion increase; therefore, the application of acceleration techniques to synthetic MR imaging is essential to overcome this limitation. Established methods for reducing the scan time include parallel imaging, compressed sensing, and adjusting MR imaging acquisition


Received May 11, 2022; accepted after revision August 31.


From the Departments of Medical and Biological Engineering (E.K.) and Radiology (S.H.C., B.P., J.H., K.M.S., S.M.L.), School of Medicine, Kyungpook National University, Daegu, South Korea; Korea Radioisotope Center for Pharmaceuticals (E.K.), Korea Institute of Radiological and Medical Sciences, Seoul, South Korea; Department of Radiology and Medical Research Institute (H.-H.C.), College of Medicine, Ewha Womans University, Seoul, South Korea; Department of Radiology (S.H.C., B.P., J.H., K.M.S., S.M.L.), Kyungpook National University Chilgok Hospital, Daegu, South Korea; GE Healthcare Korea (M.J.H.), Seoul, South Korea; and Department of Radiology (S.K.Y.), Chungnam National University Hospital, Chungnam National University College of Medicine, Daejeon, South Korea.

E. Kim and H.H. Cho contributed equally to this work.

This work was supported by the National Research Foundation of Korea (grant No. 2017RIC1B5075974).

Please address correspondence to So Mi Lee, MD, Department of Radiology, Kyungpook National University Chilgok Hospital, 807 Hoguk-ro, Buk-gu, Daegu 41404, South Korea; e-mail: amour7230@knu.ac.kr

 Indicates open access to non-subscribers at www.ajnr.org

 Indicates article with online supplemental data.

<http://dx.doi.org/10.3174/ajnr.A7664>

Synthetic MR imaging–acquisition parameters

	ST-SyMRI	FAST-SyMRI with/without DLR ^a
TR (ms)	4000–4743	4000
TE (ms)	21.2/84.8	17.5/87.4
TI (ms)	4 Automatically calculated saturation delays	
Echo-train length ^b		12
Bandwidth (kHz)	22.73	31.25
Acceleration factor (ASSET)	2	3
Section thickness (mm) ^b		4
Spacing (mm) ^b		1
FOV (cm) ^b		23
Phase FOV ^b		0.8
Frequency matrix (m × n) ^b		308
No of sections ^b		24–32
NEX ^b		1
Scan time (min:sec)	5:04–6:01	3:28

Note:—m × n indicates slices of m by n dimensions; ASSET, array spatial sensitivity encoding technique; NEX, number of excitations.

^a All MR imaging acquisition parameters and scan times were identical for FAST-SyMRI and FAST-SyMRI+DLR.

^b The same parameters were used in all 3 MR imaging protocols.

parameters such as the receiver bandwidth, number of excitations, and in-plane/through-plane resolution.^{9–11} However, accelerated techniques generally reduce the SNR and/or spatial resolution, resulting in degradation of image quality. Recently, deep learning–based reconstruction (DLR) techniques have been proposed to address the trade-off between the image quality and scan time. DLR techniques can mitigate image noise induced by acceleration techniques and improve SNR/spatial resolution, enabling a previously unattainable level of fast imaging.^{12,13}

We hypothesized that the application of DLR to an accelerated synthetic MR imaging protocol can reduce the scan time while maintaining image quality, facilitating the use of synthetic MR imaging in pediatric neuroimaging.^{12,13} For this study, we created an accelerated synthetic MR imaging protocol by increasing both the bandwidth and parallel imaging acceleration factor and then applied a vendor-supplied DLR (AIR Recon DL; GE Healthcare) to the accelerated synthetic protocol. Although several previous studies have investigated the impact of this DLR technique on the image quality and diagnostic performance of conventional MR imaging,^{13–15} no study has investigated the impact of DLR on synthetic MR imaging in terms of the image quality and quantitative value measurements. When one applies the synthetic MR imaging protocol with DLR in clinical practice, in addition to validating its image quality, it is important to determine whether this MR imaging protocol provides less biased and consistent quantitative data.

This study aimed to evaluate the clinical feasibility of accelerated synthetic MR imaging with DLR in pediatric neuroimaging and to investigate the impact of DLR on image quality and quantitative values (tissue values and brain tissue volume measurements) in synthetic MR imaging. To achieve our goals, we compared the accelerated synthetic MR imaging with DLR with the accelerated synthetic MR imaging without DLR and the standard synthetic MR imaging (ST-SyMRI) protocol previously validated in a large prospective study.⁶

MATERIALS AND METHODS

Subjects

This study was approved by the institutional review board of Kyungpook National University Chilgok Hospital. The requirement for informed consent was waived due to the retrospective nature of the study. We retrospectively reviewed the database of our institution. The inclusion criteria for this study were as follows: 1) younger than 19 years of age, and 2) patients who underwent brain MR imaging, including both standard and accelerated (with and without DLR) synthetic MR imaging protocols between October 2021 and December 2021. A total of 52 consecutive patients were identified, and we excluded 5 subjects after reviewing for quality control (the details are provided in Online Supplemental Data). Finally, 47 patients (male/female ratio, 30:17; mean age, 7.2 [SD, 3.7] years; age range, 2.3–14.7 years) were included in this study.

Image Acquisition and Technical Details

All 2D synthetic MR images were acquired using a 3T scanner (Signa Architect; GE Healthcare) with a 48-channel head coil at a single institution. The synthetic MR images were acquired using a multidynamic, multiecho sequence.^{1,16,17} All included patients underwent 2 sets of synthetic MRIs as follows: 1) a standard protocol (manufacturer's suggested protocol, ST-SyMRI),⁶ and 2) an accelerated protocol without DLR (FAST-SyMRI). After acquiring 2 sets of synthetic MR images, a prototype version of DLR (AIR Recon DL) was used to reconstruct the FAST-SyMRI (accelerated synthetic MRI with DLR [FAST-SyMRI+DLR]). The DLR accepts a user-specified denoising level between 0 and 1, and we chose a denoising level of 0.5 when applying the DLR to balance noise reduction with minimizing artificial image textures. Detailed methods for DLR have been described previously.^{13–15,18} Thus, 3 sets of synthetic MR images were acquired for each patient. The detailed imaging parameters are listed in the Table. All MR imaging acquisition parameters and scan times were identical for FAST-SyMRI and FAST-SyMRI+DLR.

Image Quality and Lesion Detectability

Synthetic T1WIs and T2WIs, T2 FLAIR, and phase-sensitive inversion recovery (PSIR) images were automatically generated using synthetic MR imaging software (Version 11.3.3; SyntheticMR; <https://www.syntheticmr.com/>). We used the default settings of TR, TE, and TI to create synthetic contrast-weighted images, except for T1WI (Online Supplemental Data).¹⁹ All anonymized images were independently reviewed on the PACS workstation by 2 radiologists (S.M.L. and H.H.C.) with 10 years of pediatric radiology experience. Both readers were blinded to the type of MR imaging protocol, clinical information, and the results of the available conventional MR imaging examinations. All MR imaging protocol data sets were

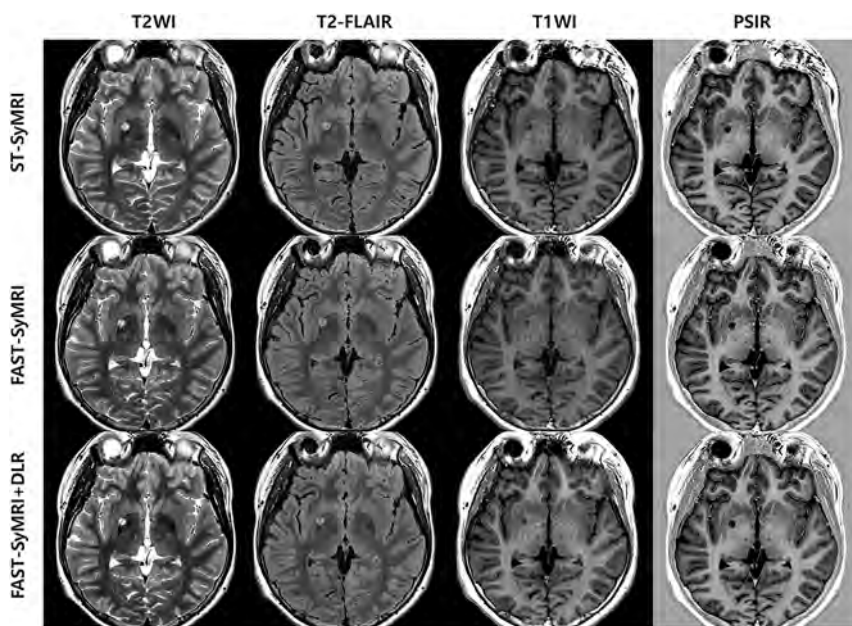


FIG 1. Axial contrast-weighted images of a 14-year-old boy who underwent brain MR imaging due to abnormal movement. By applying DLR, the overall image quality and image artifacts of the FAST-SyMRI appear significantly improved for all contrast-weighted images. FAST-SyMRI+DLR images show comparable or superior overall image quality relative to ST-SyMRI images. No significant difference is noted in lesion detectability between the FAST-SyMRI+DLR and the other 2 MR imaging protocols.

randomly ordered, and image analysis was performed in 3 sessions, with a memory-washout period of at least 2 weeks.

The overall image quality, gray-white matter differentiation (GM-WM), and visibility of anatomic structures were assessed on a 5-point Likert scale (1 = nondiagnostic, 2 = poor, 3 = sufficient, 4 = good, and 5 = excellent). The anatomic structures included the central sulcus, head of the caudate nucleus, lentiform nucleus, posterior limb of the internal capsule, cerebral peduncle, and middle cerebellar peduncle.^{6,9} The severity of artifacts was rated on a similar 5-point Likert scale (1 = severe, 2 = moderate to severe, 3 = moderate, 4 = mild, and 5 = none), and we evaluated the following artifacts: motion artifacts, low SNR, truncation artifacts, blurring, regional low-SNR artifacts, aliasing artifacts, parenchymal-CSF interface hyperintensities, and pulsation artifacts.^{3,6,20} The confidence in the presence of brain lesions was rated on a 5-point scale. The detailed criteria for image assessment are presented in the Online Supplemental Data. After completing the qualitative image analysis, an experienced pediatric radiologist (S.M.L.) confirmed the presence of lesions based on the available conventional MR images, original radiology reports, and clinical diagnoses.

Tissue Value Measurement and Brain Volume Estimation

Quantitative tissue maps (T1, T2, and proton density [PD] maps) and tissue fraction maps were generated using the synthetic MR imaging software (Version 11.3.3). Tissue values of aggregate GM and WM and the brain tissue volumes were automatically obtained using the latest version of the synthetic MR imaging software.^{16,17} To determine the topologic differences in tissue values between the FAST-SyMRI+DLR and the other 2 MR imaging protocols, we

first spatially normalized quantitative tissue maps on the basis of the synthetic T1WIs using SPM 12 (<https://www.fil.ion.ucl.ac.uk/spm/software/spm12/>). Next, the voxelwise differences in tissue values were analyzed by calculating the percentage difference at the group level.^{5,9}

Statistical Analysis

To compare the overall image quality, GM-WM, visibility of anatomic structures, and artifacts between FAST-SyMRI+DLR and the other 2 synthetic protocols, we performed the Wilcoxon signed-rank test and the McNemar test. Because MR images classified as having “good/excellent” image quality and “mild/none” artifacts are generally preferred in routine clinical practice, we dichotomized the readers’ ratings before performing the McNemar test (4 or 5 versus ≤ 3 on a 5-point Likert scale). For lesion detectability, readers’ ratings of 4 and 5 were assigned for the presence of brain lesions, and the McNemar test was also used.

The quantitative values were compared using the paired *t* test. The percentage difference (DIFF) was calculated.⁵ The intraclass correlation coefficient (ICC) and Pearson correlation coefficient (*r*) were computed to assess the agreement and correlation among quantitative data.⁵ Linear regression analysis and Bland-Altman analysis were performed. SPSS software, Version 28.0 (IBM) and MedCalc, Version 19.2 (MedCalc software) were used for analysis. A *P* value < .05 was considered statistically significant.

RESULTS

Scan Time

The scan times for ST-SyMRI and FAST-SyMRI with and without DLR were 5 minutes 4 seconds - 6 minutes 1 second and 3 minutes 28 seconds, respectively (the details are provided in the Online Supplemental Data).

Image Quality and Lesion Conspicuity

The results of the 2 readers’ ratings were pooled for analysis because there were no significant differences in the overall image-quality scores between the 2 readers (*P* > .05, 2-tailed *t* test). The results of the qualitative image analysis performed by the 2 radiologists and pair-wise comparison results between FAST-SyMRI+DLR and the other 2 MR imaging protocols are summarized in the Online Supplemental Data. Representative examples of contrast-weighted images acquired using 3 synthetic MR imaging protocols are shown in Fig 1 and the Online Supplemental Data.

For FAST-SyMRI+DLR versus ST-SyMRI, PSIR derived from FAST-SyMRI+DLR showed superior overall image quality compared with the corresponding sequence of ST-SyMRI (*P* < .001),

Overall Image Quality

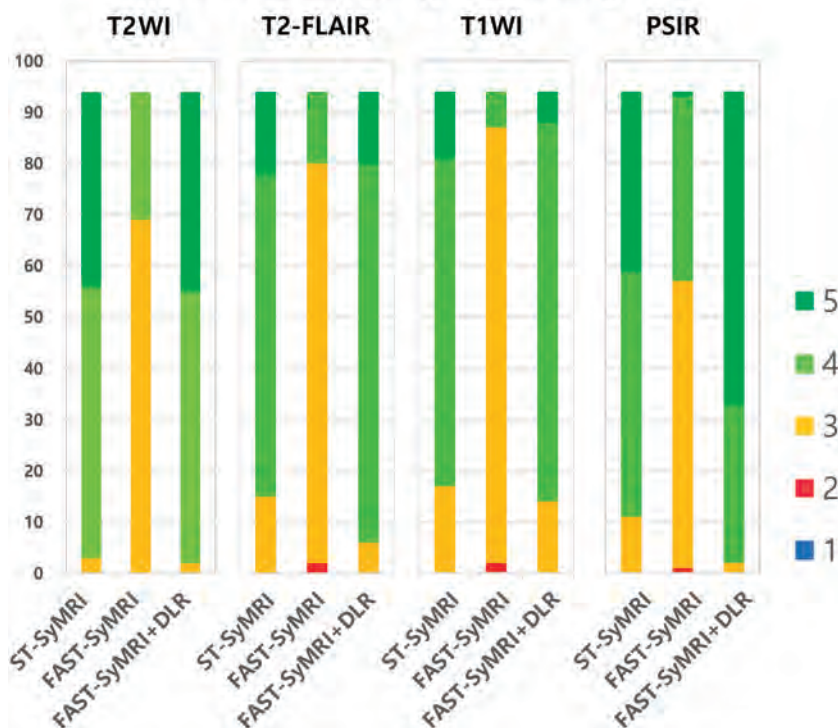


FIG 2. Comparison of the overall image quality among contrast-weighted images obtained with 3 synthetic MR imaging protocols. Each contrast-weighted image in 47 patients was rated on a 5-point Likert scale by 2 readers.

and there was no significant difference in overall image quality for other sequences (P values for T2WI, T2-FLAIR, and T1WI were .56, .22, and .47, respectively). When we considered all contrast-weighted images, 93.6% (352/376) of FAST-SyMRI+DLR images and 87.8% (330/376) of ST-SyMRI images were rated as good or excellent for overall image quality (Fig 2). Although visibility of some anatomic structures was inferior on FAST-SyMRI+DLR images compared with that on ST-SyMRI images ($P < .05$), when we applied a dichotomous classification, only the visibility of the cerebral peduncle on T1WI ($P = .02$) showed a statistical difference (Online Supplemental Data). No significant difference was found in the GM-WM between the 2 MR imaging protocols for all contrast weightings ($P > .05$). Scores for low SNR, truncation artifacts, and pulsation artifacts were higher on FAST-SyMRI+DLR than in ST-SyMRI for all contrast weightings ($P < .05$), suggesting a lesser degree of artifacts on FAST-SyMRI+DLR than on ST-SyMRI.

Meanwhile, the overall image quality of FAST-SyMRI+DLR was significantly superior to that of FAST-SyMRI for all contrast weightings ($P < .001$). The visibility of anatomic structures (eg, the lentiform nucleus, posterior limb of the internal capsule, cerebral peduncle, and middle cerebellar peduncle) was mostly more superior on FAST-SyMRI+DLR than on FAST-SyMRI ($P < .05$) (Online Supplemental Data). The low SNR and truncation artifacts were significantly reduced after the application of DLR for all contrast weightings ($P < .001$). The pulsation artifact was not significantly different (T2 FLAIR, $P = .41$; PSIR, $P = .59$) or was

slightly emphasized after DLR application (T1WI, $P = .046$; T2WI, $P < .001$).

This study included 7 cases of abnormal findings on MR imaging based on radiology reports, available conventional MR images, and clinical diagnoses: neoplasm ($n = 3$), cerebellar heterotopia ($n = 1$), brain abscess ($n = 1$), and chemotherapy-induced leukoencephalopathy ($n = 2$) (Online Supplemental Data). All pathologies were rated 4 or 5 on synthetic contrast-weighted images acquired using 3 MR imaging protocols by 2 radiologists, and there were no false-positive cases. Therefore, there was no significant difference in lesion detectability between FAST-SyMRI+DLR and the other 2 MR imaging protocols ($P > .05$).

Tissue-Value Measurement

The Online Supplemental Data summarize the comparison of tissue values of the GM and WM between FAST-SyMRI+DLR and the other 2 MR imaging protocols. The tissue values of GM and WM were significantly different between FAST-SyMRI+DLR and ST-SyMRI (WM-PD, $P = .02$; others,

$P < .001$). GM T1 showed the highest values of DIFF (−4.76%) across all tissue values of GM and WM in FAST-SyMRI+DLR versus ST-SyMRI (Fig 3). In the WM, the mean DIFF of T2 values was the highest (3.6%), but this finding may be attributable to the relatively low T2 values rather than the absolutely large differences between the 2 protocols (81.0 [SD, 4.0] ms [FAST-SyMRI+DLR] versus 78.2 [SD, 3.7] ms [ST-SyMRI]). Except for GM T1 and WM T2, the mean DIFFs were small, ranging from −1.5% to 1.86%. Regarding topologic differences, higher DIFFs were noted in the cerebral/cerebellar cortices for T1 values and in the CSF space for T2 values. The interface between different tissue types, such as ventricle walls and brain surfaces, showed a higher DIFF for both T1 and T2 values (Online Supplemental Data). Despite these differences in tissue value measurements between FAST-SyMRI+DLR and ST-SyMRI, the agreement and correlation between the tissue values were excellent (ICC = 0.94–0.99) and strong ($r = 0.89$ –0.98) for all tissue values of GM and WM. Linear regression analysis also showed a strong linear relationship with a robust fit ($R^2 = 0.96$ –0.998), indicating good consistency between the tissue values derived from the 2 MR imaging protocols (Fig 3).

For FAST-SyMRI+DLR versus FAST-SyMRI, there were no significant differences in the tissue values, except for GM T1 (GM T1, $P < .001$; others, $P > .05$). Additionally, the differences in tissue values between the 2 MR imaging protocols were very small or negligible (mean DIFFs = −0.34%–0.09%). Regarding the topologic differences in tissue values, all tissue values showed little difference in the brain parenchyma; only small differences at the brain surface and ventricle walls were observed in the T2

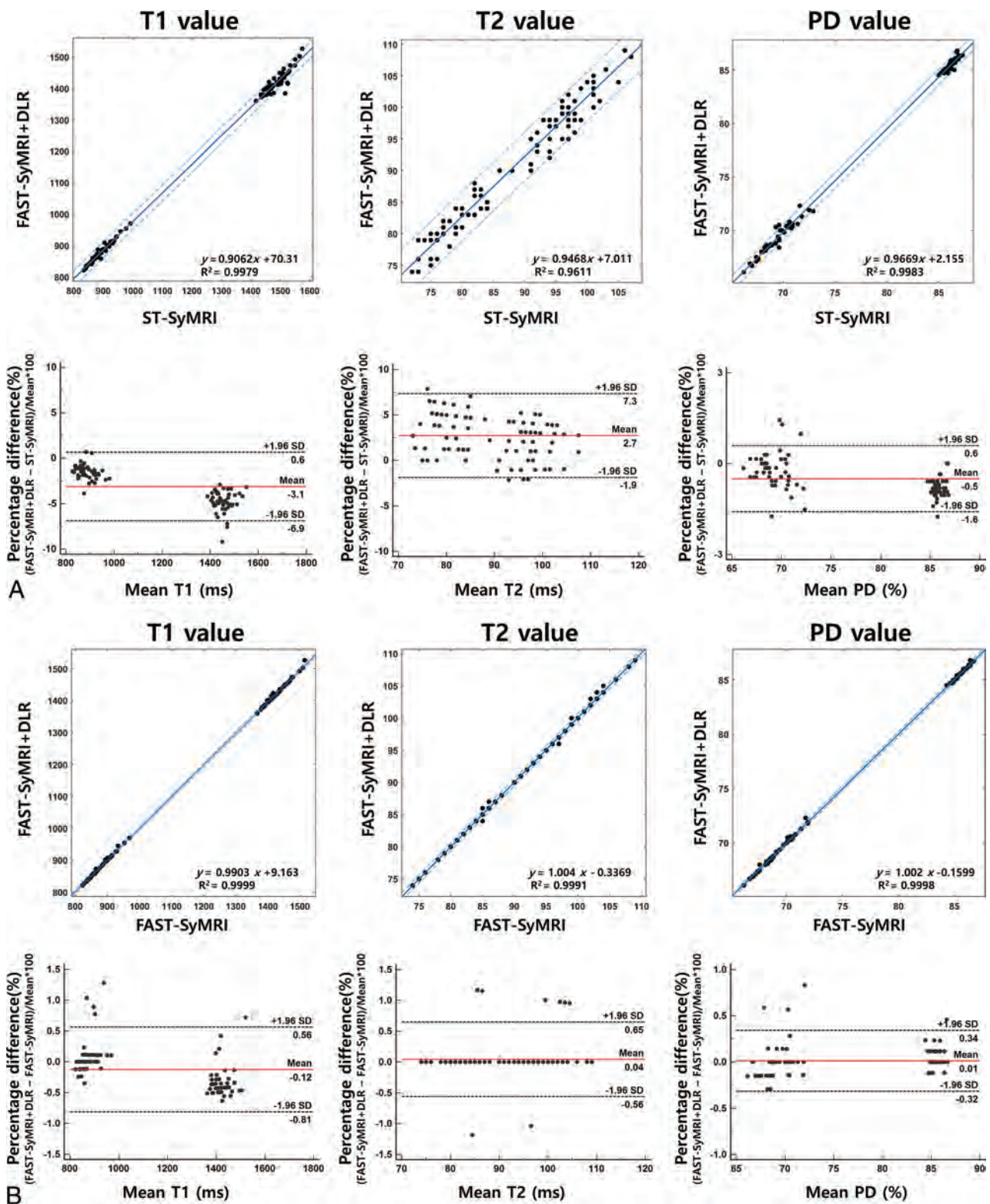


FIG 3. Scatterplots and Bland-Altman plot results for FAST-SyMRI+DLR versus ST-SyMRI (A) and FAST-SyMRI+DLR versus FAST-SyMRI (B). The linear regression lines fit to the data of 47 patients (solid blue line), which are shown along with 95% confidence intervals (dotted blue lines), represent a strong linear relationship with a robust fit between the tissue value measurements of GM and WM obtained from the 2 MR imaging protocols. Bland-Altman plots show mean differences (solid red line) and the mean difference (SD, 1.96) of the differences (dotted black line).

values. The tissue values derived from FAST-SyMRI+DLR and FAST-SyMRI yielded excellent agreement (ICC = 0.993–0.999), strong correlations ($r = 0.987$ – 0.998), and strong linear relationships in the linear regression analysis ($R^2 > 0.999$ for all) (Fig 3).

Brain Volume Estimation

A comparison of the brain tissue volume estimates between FAST-SyMRI+DLR and the other 2 MR imaging protocols is summarized in the Online Supplemental Data. In FAST-SyMRI+DLR versus ST-SyMRI, all brain-tissue volumes were significantly different between the 2 MR imaging protocols (CSF volume, $P = .02$; others, $P < .001$). All volume measurements of GM and voxels not classified as GM/WM/CSF (hereafter referred to as “non-WM/GM/CSF”) obtained with FAST-SyMRI+DLR were smaller (mean DIFF = -8.46%) and larger (mean DIFF = 50.73%) compared with ST-SyMRI-derived volume estimates, respectively (Online Supplemental Data). However, the mean DIFFs for brain parenchymal volume and intracranial volume between the 2 MR imaging protocols were minimal (-0.59% , -0.77% , respectively), and the Bland–Altman plot also showed minimal spread. Despite this systematic bias, excellent agreement and strong correlation between volume measurements derived from the 2 MR imaging protocols were found for all brain tissues (ICC = 0.98 – 1.0 , $r = 0.96$ – 0.999). Linear regression analysis also demonstrated a strong linear relationship with a robust fit ($R^2 = 0.92$ – 0.998) (Online Supplemental Data).

For FAST-SyMRI+DLR versus FAST-SyMRI, the differences in the brain tissue volumes between the 2 MR imaging protocols were very small (mean DIFFs = -1.46% – 0.83%). Additionally, the agreement (ICC = 0.98 – 1.0) and correlation ($r = 0.97$ – 1.0) between the brain tissue volumes derived from the 2 MR imaging protocols were very high, and the linear regression analysis exhibited a strong linear relationship ($R^2 = 0.99$ – 1.0).

DISCUSSION

In this study, we applied DLR to a FAST-SyMRI protocol that reduced the scan time by up to 42% by adjusting both the receiver bandwidth and the parallel imaging acceleration factor. We found that the use of DLR in the FAST-SyMRI protocol improved image quality by effectively mitigating the noise generated using accelerated techniques. After applying DLR to FAST-SyMRI, the low SNR and truncation artifacts, which were the main image-quality issues in FAST-SyMRI, were noticeably improved for all contrast weightings, and the visibility of anatomic structures was mostly enhanced. This result was consistent with the findings of previous studies in which DLR reduced image noise and truncation artifacts while increasing image sharpness.^{13–15,18} This is possibly because DLR provides effective interpolation by estimating the high-frequency k -space information needed to support the acquired data, thus improving image sharpness while suppressing noise.¹⁸ Consequently, FAST-SyMRI+DLR-derived images showed significantly higher perceived SNR and less pronounced truncation artifacts without noticeable loss of anatomic structure visibility compared with ST-SyMRI images for all contrast weightings; thus, in this study, FAST-SyMRI+DLR yielded image quality comparable with or superior to that in ST-SyMRI, validated in a large prospective study. Additionally, pulsation artifacts were less

pronounced on FAST-SyMRI+DLR than on ST-SyMRI for all contrast weightings. However, this finding is likely attributed to the use of different MR imaging acquisition parameters rather than the artifact-reduction effect of DLR; indeed, when we compared FAST-SyMRI+DLR and FAST-SyMRI, the pulsation artifact was not significantly different or was slightly emphasized after DLR application. Our findings are in line with those reported by van der Velde et al,¹⁵ who demonstrated that ghosting artifacts became more pronounced when late gadolinium-enhancement images of the myocardium were reconstructed with DLR.

When one applies DLR in conjunction with accelerated techniques, there is a concern about whether the pathology is less visible.²¹ A previous study reported that accelerated conventional shoulder MR imaging using this DLR pipeline showed diagnostic performance comparable with that of standard conventional MR imaging.¹³ Our study also showed no significant difference in lesion detectability between FAST-SyMRI+DLR and ST-SyMRI. This result shows the potential of FAST-SyMRI+DLR for application in clinical practice. However, because only a small number of lesions were analyzed and subjects with very small lesions such as intracranial metastases and multiple sclerosis were not included in our study, its diagnostic value should be validated in future studies with large cohorts. We expect that further research on the impact of postcontrast FAST-SyMRI+DLR on lesion diagnosis may reveal additional clinical utility of this protocol.²²

Tissue values obtained from FAST-SyMRI+DLR and ST-SyMRI showed excellent agreement and strong correlation, indicating good consistency between the MR imaging protocols, thus supporting the clinical use of FAST-SyMRI+DLR in synthetic MR imaging-based quantitative imaging. In addition, there was a small systematic bias between FAST-SyMRI+DLR and ST-SyMRI (mean DIFFs = -4.76% – 3.6%). We speculated that the main source of the systematic bias is different MR imaging acquisition parameters between the MR imaging protocols, because there was no significant difference in tissue values between FAST-SyMRI+DLR and FAST-SyMRI, indicating that the impact of DLR on quantitative tissue values was negligible (mean DIFF, -0.34% – 0.09%). It is important to preserve quantitative tissue values when DLR is applied in identical synthetic MR imaging protocols. These results allow DLR to be used for the optimization of synthetic MR imaging protocols without concern about whether quantitative tissue values change remarkably after DLR application.

The brain tissue volumes obtained with FAST-SyMRI+DLR and ST-SyMRI also showed excellent agreement and a strong correlation for all brain-tissue volumes, suggesting the applicability of FAST-SyMRI+DLR in brain volumetry. However, in FAST-SyMRI+DLR versus ST-SyMRI, systematic over- and underestimations were observed. In particular, the difference in GM volume was relatively larger than that in the other brain-tissue volumes; our finding that differences in GM T1 between these 2 MR imaging protocols were noticeable supports this volumetric result because tissue values deviating from the narrow range of the predefined tissue cluster in the R1–R2–PD space can affect the segmentation and volume measurements. More specifically, differences in T1 values occurred mainly in the cerebral/cerebellar cortices, and higher differences in both T1 and T2 values were found in the brain surfaces.

These brain regions are mostly partial volume voxels containing a mixture of GM and CSF. In these brain regions, the substantial deviations of tissue values from a predefined tissue cluster in the R1-R2-PD space can lead to misclassification of the GM volume fraction within partial volume voxels as non-WM/GM/CSF volume (Online Supplemental Data);¹⁶ thus, these potential misclassifications of GM volume in FAST-SyMRI+DLR, in addition to the systematic bias, may result in a relatively large GM volume difference between the 2 MR imaging protocols. Notably, differences in brain parenchymal volume (mean DIFF, -0.59%) and intracranial volume (mean DIFF, -0.77%) between the FAST-SyMRI+DLR and ST-SyMRI were sufficiently small, and the Bland-Altman plot also showed minimal spread. For FAST-SyMRI+DLR versus FAST-SyMRI, the brain-tissue volumes were generally preserved and showed good consistency between the 2 protocols.

This study had some limitations. First, we did not compare synthetic contrast-weighted images with conventional MR images. However, previous studies have suggested that synthetic MR imaging has the potential to be used as an alternative to conventional MR imaging.^{4,6} Therefore, we used a synthetic MR imaging protocol validated in a large prospective study as a reference standard.⁶ Second, each subject was scanned only once in a single session; therefore, we could not evaluate the intraprotocol repeatability. However, quantitative data obtained from the multidynamic, multiecho sequence at 3T exhibited robust repeatability and reproducibility.¹ Third, the sample size was small, and only a small number of lesions with heterogeneous disease were included in our study. In this pilot study, we did not investigate the impact of adjusting MR imaging acquisition parameters and applying DLR on lesion count, size, and quantitative values. Therefore, future studies focusing on the diagnostic performance and quantitative assessment of the lesion would be helpful in confirming the effectiveness of the accelerated synthetic protocol with DLR.

CONCLUSIONS

The use of DLR in synthetic MR imaging can reduce scan time by 42% while maintaining image quality. The quantitative values obtained with FAST-SyMRI+DLR and ST-SyMRI were consistent. Therefore, FAST-SyMRI+DLR can be an alternative to ST-SyMRI in both contrast-weighted and quantitative imaging, which will facilitate the clinical application of synthetic MR imaging in pediatric neuroimaging. Furthermore, the quantitative values were generally preserved after DLR application, supporting the clinical application of DLR in synthetic MR imaging-based quantitative imaging.

Disclosure forms provided by the authors are available with the full text and PDF of this article at www.ajnr.org.

REFERENCES

- Hagiwara A, Hori M, Cohen-Adad J, et al. **Linearity, bias, intrascanner repeatability, and interscanner reproducibility of quantitative multidynamic multiecho sequence for rapid simultaneous relaxation at 3 T: a validation study with a standardized phantom and healthy controls.** *Invest Radiol* 2019;54:39–47 CrossRef Medline
- Kim HG, Moon WJ, Han J, et al. **Quantification of myelin in children using multiparametric quantitative MRI: a pilot study.** *Neuroradiology* 2017;59:1043–51 CrossRef Medline
- Lee SM, Choi YH, Cheon JE, et al. **Image quality at synthetic brain magnetic resonance imaging in children.** *Pediatr Radiol* 2017;47:1638–47 CrossRef Medline
- Granberg T, Uppman M, Hashim F, et al. **Clinical feasibility of synthetic MRI in multiple sclerosis: a diagnostic and volumetric validation study.** *AJNR Am J Neuroradiol* 2016;37:1023–29 CrossRef Medline
- Lee SM, Kim E, You SK, et al. **Clinical adaptation of synthetic MRI-based whole brain volume segmentation in children at 3 T: comparison with modified SPM segmentation methods.** *Neuroradiology* 2022;64:381–92 CrossRef Medline
- Tanenbaum LN, Tsiouris AJ, Johnson AN, et al. **Synthetic MRI for clinical neuroimaging: results of the Magnetic Resonance Image Compilation (MAGiC) prospective, multicenter, multireader trial.** *AJNR Am J Neuroradiol* 2017;38:1103–10 CrossRef Medline
- Ambarki K, Lindqvist T, Wahlin A, et al. **Evaluation of automatic measurement of the intracranial volume based on quantitative MR imaging.** *AJNR Am J Neuroradiol* 2012;33:1951–56 CrossRef Medline
- McAllister A, Leach J, West H, et al. **Quantitative synthetic MRI in children: normative intracranial tissue segmentation values during development.** *AJNR Am J Neuroradiol* 2017;38:2364–72 CrossRef Medline
- Fujita S, Hagiwara A, Takei N, et al. **Accelerated isotropic multiparametric imaging by high spatial resolution 3D-QALAS with compressed sensing: a phantom, volunteer, and patient study.** *Invest Radiol* 2021;56:292–300 CrossRef Medline
- Saccetti L, Andica C, Hagiwara A, et al. **Brain tissue and myelin volumetric analysis in multiple sclerosis at 3T MRI with various in-plane resolutions using synthetic MRI.** *Neuroradiology* 2019;61:1219–27 CrossRef Medline
- Bauer S, Markl M, Honal M, et al. **The effect of reconstruction and acquisition parameters for GRAPPA-based parallel imaging on the image quality.** *Magn Reson Med* 2011;66:402–09 CrossRef Medline
- Bash S, Wang L, Airriess C, et al. **Deep learning enables 60% accelerated volumetric brain MRI while preserving quantitative performance: a prospective, multicenter, multireader trial.** *AJNR Am J Neuroradiol* 2021;42:2130–37 CrossRef Medline
- Hahn S, Yi J, Lee HJ, et al. **Image quality and diagnostic performance of accelerated shoulder MRI with deep learning-based reconstruction.** *AJR Am J Roentgenol* 2022;218:506–16 CrossRef Medline
- Kim M, Kim HS, Kim HJ, et al. **Thin-slice pituitary MRI with deep learning-based reconstruction: diagnostic performance in a postoperative setting.** *Radiology* 2021;298:114–22 CrossRef Medline
- van der Velde N, Hassing HC, Bakker BJ, et al. **Improvement of late gadolinium enhancement image quality using a deep learning-based reconstruction algorithm and its influence on myocardial scar quantification.** *Eur Radiol* 2021;31:3846–55 CrossRef Medline
- Wartjes JB, Leinhard OD, West J, et al. **Rapid magnetic resonance quantification on the brain: optimization for clinical usage.** *Magn Reson Med* 2008;60:320–29 CrossRef Medline
- West J, Wartjes JB, Lundberg P. **Novel whole brain segmentation and volume estimation using quantitative MRI.** *Eur Radiol* 2012;22:998–1007 CrossRef Medline
- Lebel RM. **Performance characterization of a novel deep learning-based MR image reconstruction pipeline.** *ArXiv* 2020. <https://arxiv.org/abs/2008.06559>
- Vanderhasselt T, Naeyaert M, Watte N, et al. **Synthetic MRI of preterm infants at term-equivalent age: evaluation of diagnostic image quality and automated brain volume segmentation.** *AJNR Am J Neuroradiol* 2020;41:882–88 CrossRef Medline
- Deshmane A, Gulani V, Griswold MA, et al. **Parallel MR imaging.** *J Magn Reson Imaging* 2012;36:55–72 CrossRef Medline
- Recht MP, Zbontar J, Sodickson DK, et al. **Using deep learning to accelerate knee MRI at 3 T: results of an interchangeability study.** *AJR Am J Roentgenol* 2020;215:1421–29 CrossRef Medline
- Hagiwara A, Hori M, Suzuki M, et al. **Contrast-enhanced synthetic MRI for the detection of brain metastases.** *Acta Radiol Open* 2016; 5:2058460115626757 CrossRef Medline

Distinctive Brain Malformations in Zhu-Tokita-Takenouchi-Kim Syndrome

 B.J. Halliday, G. Baynam, L. Ewans, L. Greenhalgh,  R.J. Leventer, D.T. Pilz, R. Sachdev,  I.E. Scheffer,  D.M. Markie,  G. McGillivray,  S.P. Robertson, and  S. Mandelstam



ABSTRACT

BACKGROUND AND PURPOSE: Zhu-Tokita-Takenouchi-Kim syndrome is a severe multisystem malformation disorder characterized by developmental delay and a diverse array of congenital abnormalities. However, these currently identified phenotypic components provide limited guidance in diagnostic situations, due to both the nonspecificity and variability of these features. Here we report a case series of 7 individuals with a molecular diagnosis of Zhu-Tokita-Takenouchi-Kim syndrome, 5 ascertained by their presentation with the neuronal migration disorder, periventricular nodular heterotopia.

MATERIALS AND METHODS: Individuals with a molecular diagnosis of Zhu-Tokita-Takenouchi-Kim syndrome were recruited from 2 sources, a high-throughput sequencing study of individuals with periventricular nodular heterotopia or from clinical diagnostic sequencing studies. We analyzed available brain MR images of recruited individuals to characterize periventricular nodular heterotopia distribution and to identify the presence of any additional brain abnormalities.

RESULTS: Pathogenic variants in *SON*, causative of Zhu-Tokita-Takenouchi-Kim syndrome, were identified in 7 individuals. Brain MR images from these individuals were re-analyzed. A characteristic set of imaging anomalies in addition to periventricular nodular heterotopia was identified, including the elongation of the pituitary stalk, cerebellar enlargement with an abnormally shaped posterior fossa, rounding of the caudate nuclei, hippocampal malformations, and cortical anomalies including polymicrogyria or dysgyria.

CONCLUSIONS: The recurrent neuroradiologic changes identified here represent an opportunity to guide diagnostic formulation of Zhu-Tokita-Takenouchi-Kim syndrome on the basis of brain MR imaging evaluation.

ABBREVIATIONS: PVNH = periventricular nodular heterotopia; VUS = variant of uncertain significance; WES = whole-exome sequencing; WGS = whole-genome sequencing; ZTTK syndrome = Zhu-Tokita-Takenouchi-Kim syndrome

Understanding of the distinctive phenotypic features of a rare syndromic disorder facilitates earlier diagnosis. This is particularly evident when genomic sequencing studies yield ambiguous

findings, such as variants of uncertain significance (VUSs) in syndromic genes.¹ Moreover, characteristic phenotypic features, or “phenotypic handles,” often guide focused investigations. Rare phenotypically heterogeneous disorders present a considerable challenge in this respect due to prior ascertainment biases and limited cohort sizes.


Zhu-Tokita-Takenouchi-Kim (ZTTK) syndrome (OMIM #617140) is a rare phenotypically heterogeneous disorder characterized by developmental delay and a wide array of congenital multisystem anomalies. Haploinsufficiency of *SON*, mediated by either truncating variants or whole-gene deletions, has been identified as the underlying cause of ZTTK syndrome.²⁻⁵ *SON* encodes the RNA-binding protein *SON* and is constitutively expressed, though expression is enriched during early brain

Received February 24, 2022; accepted after revision August 8.

From the Departments of Women's and Children's Health (B.J.H., S.P.R.) and Pathology (D.M.M.), Otago Medical School, University of Otago, Dunedin, New Zealand; Western Australian Register of Developmental Anomalies and Genetic Services of Western Australia (G.B.), Undiagnosed Diseases Program, King Edward Memorial Hospital, Perth, Australia; Centre for Population Genomics (L.E.), Garvan Institute of Medical Research, Sydney, Australia; Centre for Clinical Genetics (L.E., R.S.), Sydney Children's Hospital, Sydney, Australia; Liverpool Centre for Genomic Medicine (L.G.), Liverpool Women's Hospital, Liverpool, England; Murdoch Children's Research Institute (R.J.L., I.E.S., G.M., S.M.), Melbourne, Australia; Department of Paediatrics (R.J.L., I.E.S., S.M.), Epilepsy Research Centre, Austin Health (I.E.S.), and Florey Institute (I.E.S.), University of Melbourne, Melbourne, Australia; Departments of Neurology (R.J.L., I.E.S.) and Radiology (S.M.), Royal Children's Hospital, Melbourne, Australia; West of Scotland Genetics Service (D.T.P.), Queen Elizabeth University Hospital, Glasgow, UK; and Victorian Clinical Genetics Services (G.M.), Murdoch Children's Research Institute, Melbourne, Australia.

S.P. Robertson is supported by the Health Research Council and Cure Kids. B.J. Halliday is supported by a University of Otago Doctoral Scholarship. R.J. Leventer is supported by a Melbourne Children's Clinician Scientist Fellowship. I.E. Scheffer is supported by the Australian National Health and Medical Research Council, the Australian Medical Research Future Fund, and the Australian Epilepsy Research Fund.

Please address correspondence to Benjamin J. Halliday, MD, 60 Hanover St, Department of Pathology, Otago Medical School, University of Otago, Dunedin 9016, New Zealand; e-mail: benjamin.halliday@otago.ac.nz

 Indicates open access to non-subscribers at www.ajnr.org

<http://dx.doi.org/10.3174/ajnr.A7663>

Table 1: Molecular findings identified in a cohort of 7 unrelated individuals with ZTTK syndrome

	Individuals						
	1	2	3	4	5	6	7
cDNA (NM_138927.2)	c.5753_57 56del	c.2357_23 58dup	c.457del	c.1881_18 82del	c.5753_57 56del	c.3852_38 56del	WGD
Protein (NP_620305.2)	p.Val1918 Glufs*87	p.Ala787*	p.Asp1531 lefs*4	p.Val629 Alafs*56	p.Val1918 Glufs*87	p.Met1284I lefs*2	WGD
Inheritance	<i>De novo</i>	<i>De novo</i>	<i>De novo</i>	<i>De novo</i>	Unknown	Unknown	<i>De novo</i>
Sequencing method	WES	WES	WES	WGS	WGS	WES	CMA
Capture platform	SureSelect V5 (Agilent)	SeqCap EZ V2 (Roche)	SureSelect V5+UTRs (Agilent)	No capture	No capture	SureSelect QXT CRE V2 (Agilent)	SurePrint G3 CGH ISCA V2 (Agilent)

Note:—WGD indicates whole-genome deletion; CMA, chromosomal microarray.

development.³ *SON* has been implicated in the splicing of pre-mRNA and has been shown to have a pivotal role in the regulation of pluripotency, cell-cycle progression, neurogenesis, and transcriptional regulation through its DNA-binding activity.⁶⁻¹⁰

The phenotypic spectrum of ZTTK syndrome has been highlighted in descriptions of >60 individuals.^{2-5,11-14} The core neurologic phenotypes identified include moderate-to-severe intellectual disability, hypotonia, and epilepsy. Brain MR imaging, available for 41 published patients, typically demonstrate a range of nonspecific structural abnormalities.¹² Ventriculomegaly (24/41) is most frequently observed, with cortical dysplasia (7/41) and abnormalities of the corpus callosum (18/41), cerebellum (6/41), and cerebral WM (6/41) also being noted.¹² Growth retardation and neonatal feeding difficulties are frequently reported. Dysmorphic facial features are observed in all cases; however, these features are variable, with no consistent pattern observed.¹² Hearing and visual impairments as well as a range of cardiac, gastrointestinal, musculoskeletal, and renal abnormalities are common. The phenotypic features associated with ZTTK syndrome are both nonspecific and highly variable, presenting a diagnostic challenge.

Here we report 7 unrelated individuals with a confirmed molecular diagnosis of ZTTK syndrome. All individuals have periventricular nodular heterotopia (PVNH), a distinctive phenotypic feature on brain MR imaging, which we propose is an underappreciated element of ZTTK syndrome. PVNH is a neuronal migration disorder characterized by heterotopic GM nodules abutting the margins of the lateral ventricles. PVNH is an infrequent feature of many rare genetic disorders, with a small number manifesting it as a consistent association, as summarized by Vriend and Oegema.¹⁵ The major genetic locus for PVNH is *FLNA*, with pathogenic variants estimated to account for one-quarter of cases.¹⁶

In addition to PVNH, we observed a previously unrecognized characteristic pattern of additional structural brain anomalies in ZTTK syndrome. These include abnormalities of the pituitary gland, caudate nuclei, and hippocampi and cerebral sulcation and gyration. Our characterization of brain imaging findings in ZTTK syndrome will improve diagnostic formulation, particularly in circumstances in which genetic sequencing studies are not possible or identify a VUS in *SON*.

MATERIALS AND METHODS

Cohort Recruitment and Ethics

A cohort of 7 unrelated individuals with pathogenic variants in *SON* was assembled by 2 approaches. Individuals 1–5 were ascertained through a physician-initiated referral into a high-throughput sequencing study of individuals with PVNH. This cohort was pre-emptively screened for pathogenic variants in *FLNA*. Individuals 6 and 7 were identified through diagnostic sequencing studies and were included after demonstration of a pathogenic *SON* variant. Individuals 1–3 were previously analyzed by Heinzen et al,¹⁷ however, the pathogenic *SON* variants described here failed validation but are now confirmed as true-positives. Individuals 3 and 4 were reported in brief by Dingemans et al.¹² This study was approved by the Health and Disability Ethics Committee of New Zealand (13-STH/56).

Sequence Analysis

Genomic DNA from probands and parents was extracted from peripheral blood for either whole-exome sequencing (WES) or whole-genome sequencing (WGS), summarized in Table 1. WES libraries were constructed for individuals 1–3 by Otogenetics (Atlanta) and sequenced using a HiSeq 2500. WGS libraries were prepared for individuals 4 and 5 using a TruSeq DNA Nano v2.5 kit and sequenced using a HiSeq X Ten at the Kinghorn Center for Clinical Genomics (Sydney). Paired-end FASTQ reads were aligned to the human reference GRCh37 using BWA MEM (Version 0.7.17; <https://github.com/bwa-mem2/bwa-mem2>) and outputted in BAM format.

Single sample variant calls were produced using GATK HaplotypeCaller (Version 3.8; <https://github.com/broadinstitute/gatk>), in genomic VCF format. Genomic VCFs were then jointly genotyped using GATK GenotypeGVCFs producing a multisample VCF. Annotation with gene context information was performed using SnpEff (Version 4.3S; <https://github.com/pcingola/SnpEff>), and additional information from the gnomAD project (Version 2.1.1; <https://gnomad.broadinstitute.org/>)¹⁸ was added using BCFtools annotate (Version 1.9; <https://github.com/samtools/bcftools>).

Variant Prioritization

Sequence data from individuals 1–5 were filtered under a monogenic disease model. Variants were required to have a read depth of >7 and an alternative allele percentage of >20%. Missense and

predicted loss-of-function variants were selected. Common variants with a gnomAD allele frequency of >0.001 were removed.

For individuals 1–4, parental sequence data were available, permitting identification of *de novo* variants. For individual 5, parental data were unavailable, so a restrictive disease-gene filtering model was implemented. Variants in genes with a dominant disease phenotype were retained based on data from the Developmental Disorder Genotype-Phenotype database.¹⁹ Remaining variants for all 5 individuals were interpreted on the basis of the American College of Medical Genetics and Genomics guidelines.¹

Neuroradiologic Evaluation

Brain MR images were systematically reviewed by a pediatric neuroradiologist (S.M.) with >20 years of experience in the imaging of brain dysmorphology. Normative data for the corpus callosum²⁰ and cerebellum²¹ were used to assess abnormalities of these structures.

Data Availability

Individual genomic data sets are not freely available due to restrictions imposed by the consenting process and privacy concerns.

RESULTS

Molecular Findings

De novo loss-of-function *SON* variants were identified for individuals 1–4, consistent with pathogenic class 5 variants causative of ZTTK syndrome.³ For individual 5, a heterozygous *SON* frameshift variant (NM_138927.2:c.5753_5756del) of unknown inheritance was identified, which was classified as a class 5 pathogenic variant based on recurrence in other published cases of ZTTK syndrome.^{3,4} Identified *SON* variants for individuals 1–5 were validated using polymerase chain reaction and Sanger sequencing.

Class 5 pathogenic *SON* variants were identified for individuals 6 and 7 before recruitment into this study. A recurrent heterozygous frameshift variant (NM_138927.2:c.3852_3856del)³ of unknown inheritance was identified for individual 6 and a *de novo* heterozygous whole-gene deletion (NC_000021.8:g.(34849772_34911445)_(35109752_35171289del) was identified for individual 7. Sequencing results are summarized in Table 1.

Clinical Descriptions

Individual 1. Individual 1 is a female who presented with hypotonia and mild global developmental delay at 10 months of age. Intrauterine growth restriction occurred during pregnancy. Delivery was by cesarean delivery, and her weight and height were both below the 3rd centile. Poor feeding and febrile seizures were noted, with hemiplegic migraine attacks occurring from 6 years of age. She was diagnosed with mild intellectual disability in childhood. She had a ridged, sagittal suture, broad nasal bridge, anteverted nares, a small chin, and cupped posteriorly rotated ears.

Recurrent respiratory and middle ear infections occurred throughout childhood. At 13 years of age, she developed end-stage polyuric renal disease, requiring renal transplantation. When last examined at 17 years of age, her weight and head circumference were in the 50th centile, with height below the 3rd

centile. She had hearing loss, hypermetropia, and convergent strabismus. Echocardiogram findings were normal.

Individual 2. Individual 2 is a female who presented in early childhood with global developmental delay with severe intellectual disability and hypotonia. She had an irregular whole-body tremor from birth. Poor feeding occurred from early infancy, requiring the insertion of a gastrostomy tube at 6 years of age. Myoclonic seizures with fever began at 6 years of age, developing into multifocal myoclonic and clonic seizures by 11 years of age. At 13 years of age, she had an episode of status epilepticus. Dysmorphic features included a flat nasal bridge, broad nose, and anteverted nares. Divergent strabismus and nonsensorineural deafness were also noted.

When last examined at 28 years of age, her height was below the 1st centile, her weight was below the 3rd centile, and her head circumference was between the 2nd and 50th centile. She could walk with assistance but was nonverbal and displayed self-harm behaviors. Partial second- and third-digit syndactyly was noted. She had bilateral hypoplastic kidneys and osteopenia. She developed heart failure after an episode of sepsis.

Individual 3. Individual 3 is a male who presented with global developmental delay with moderate intellectual disability. He had asthma and recurrent respiratory infections throughout infancy. Through childhood, he developed selective mutism and disrupted sleep patterns, as well as epilepsy with mixed seizure types. Major feeding difficulties occurred throughout his life, and he is now predominantly fed by gastrostomy.

During childhood, his height tracked below the 2nd centile, and his weight, between the 9th and 25th centiles. His dysmorphic features included down-slanting palpebral fissures and epicanthal folds. Craniosynostosis of the left coronal suture was observed. Other congenital anomalies included astigmatism, joint hypermobility, and a unilateral multicystic kidney.

Individual 4. Individual 4 is a female who presented with moderate developmental delay and hypotonia. When last examined at 4 years of age, her height and weight were below the 1st and 3rd centiles, respectively. Dysmorphic features included down-slanting palpebral fissures, epicanthal folds, and a flat philtrum. Feeding difficulties were pronounced during infancy. Additional anomalies included fourth and fifth digit camptodactyly, sensorineural hearing loss, hypermetropia and astigmatism, strabismus, and a horseshoe kidney. She developed coronal craniosynostosis, requiring surgical intervention. After the operation, she developed seizures, well-controlled with levetiracetam.

Individual 5. Individual 5 is a female who presented with moderate developmental delay with intellectual disability and hypotonia in early childhood. Notable facial features included frontal bossing and epicanthal folds. Conductive hearing impairment and strabismus were noted. She required surgical intervention for right-hip dysplasia. When last examined at 5 years 8 months of age, her height was at the 25th centile, her weight, in the 3rd centile, and her head circumference, in the 90th centile.

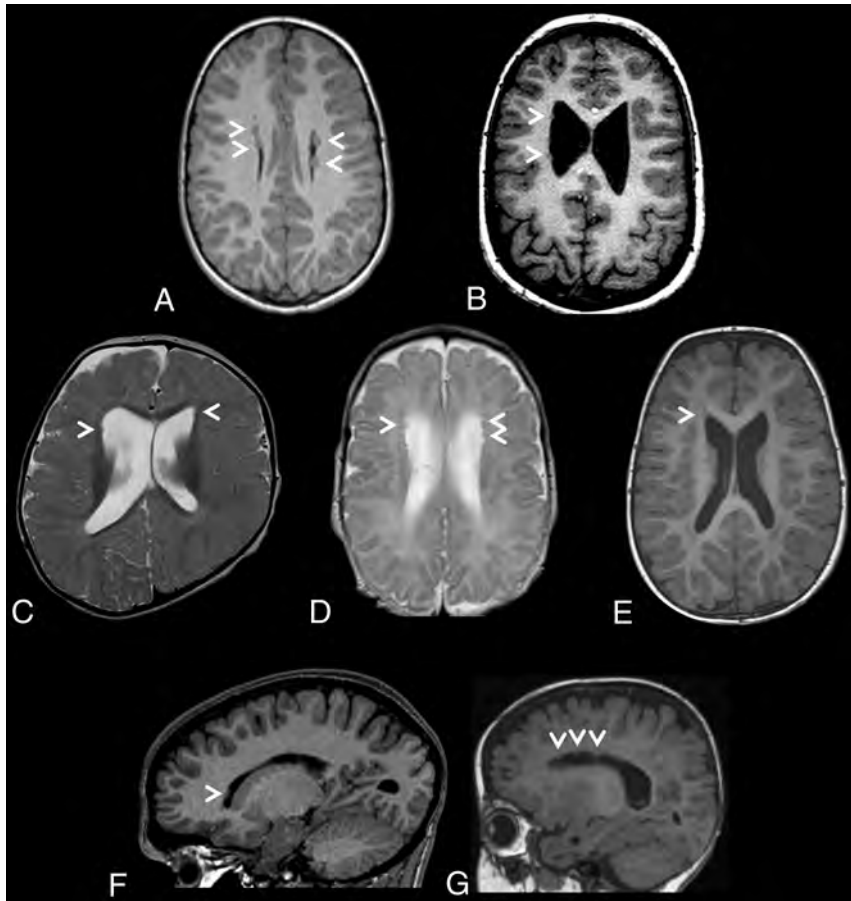


FIG 1. Brain MR images depicting periventricular nodular heterotopia distributions in a cohort of 7 unrelated individuals with ZTTK syndrome. A, Axial T1-weighted MRI of the brain of individual 1 at 7 years 7 months of age revealing sparse bilateral frontal heterotopia (white arrowheads). B, Axial T1-weighted MRI of the brain of individual 2 at 11 years and 6 months of age revealing sparse right unilateral frontal and midbody heterotopia (white arrowheads). C, Axial T2-weighted MRI of the brain of individual 3 at 1 year of age revealing sparse bilateral frontal horn heterotopia (white arrowheads). D, Axial T2-weighted MRI of the brain of individual 4 at 1 year 4 months of age revealing sparse bilateral frontal horn heterotopia (white arrowheads). E, Axial T1-weighted MRI of the brain of individual 5 at 1 year 8 months of age revealing a heterotopion of the right frontal horn (white arrowhead). F, Right parasagittal T1-weighted MRI of the brain of individual 6 at 15 years 2 months of age revealing a heterotopion of the right frontal horn (white arrowhead). G, Left parasagittal T1-weighted MRI of the brain of individual 7 at 1 year 2 months of age revealing sparse left frontal horn heterotopia (white arrowheads).

Individual 6. Individual 6 is a male who presented with suspected seizures after several episodes of confusion, later diagnosed as a concussion. He was delivered at term after an uneventful pregnancy. Early childhood developmental milestones were normal, but he was diagnosed with mild intellectual disability during his early school years. When examined at 14 years of age, his height and weight were between the 10th and 25th centiles. No dysmorphic facial features were noted, but he had fifth finger and toe clinodactyly as well as elbow extension limitation. A ventricular septal defect was noted on an echocardiogram.

Individual 7. Individual 7 is a female who presented prenatally with intrauterine growth restriction, breech presentation, and oligohydramnios. She was delivered at 37 weeks by cesarean delivery, with an 11th centile birth weight. During infancy she had central hypotonia with a peripheral increase in tone. At 4 years of

age, she had onset of seizures, with an episode of status epilepticus. Her development was globally delayed, with suspected moderate intellectual disability and autism spectrum disorder.

During early childhood, her height and weight were between the 10th and 25th centiles, with a head circumference at the 73rd centile. She had down-slanting and short palpebral fissures, epicanthal folds, smooth philtrum, small mouth with thin lips, and low-set ears with diagonally creased earlobes. Additional anomalies included developmental hip dysplasia and a ventricular septal defect.

Neuroradiologic Findings

A prior diagnosis of PVNH was available for individuals 1–5 before recruitment into this study. The initial goal of neuroradiologic re-evaluation was to categorize the PVNH of these individuals and assess whether it demonstrates characteristics distinctive to ZTTK syndrome. However, after re-evaluation of MR images, PVNH was also identified for individuals 6 and 7, who were recruited solely on the basis of their molecular diagnosis of ZTTK syndrome.

Heterotopic nodules were sparse, small, and predominantly frontal in all 7 individuals. They were bilateral in 5 of 7 cases. Similarly, sparse and small nodules were identified in the posterior infrasyllian regions in 3 of 7 cases. MR images depicting the PVNH distribution for each individual are presented in Fig 1. No nodules were observed in the occipital horns.

In addition to PVNH, consistent involvement of abnormalities in specific structures were identified in all 7 individuals, summarized in Table 2. These included malformations of the corpus callosum, cerebellum, pituitary stalk, caudate nuclei, hippocampi, and cortex.

Corpus callosum abnormalities were frequently observed and included short anterior-posterior diameter (<3 centiles, 3 of 7) and thinning of the corpus callosum, particularly at the genu (<3 centiles, 5 of 7).²⁰ Dysmorphic corpora callosa were observed in 2 individuals, depicted in Fig 2C, -F. Abnormalities of the pituitary gland and stalk were also seen, with glands appearing small (5 of 7), with a markedly elongated pituitary stalk (5 of 7). The pituitary stalk elongation observed in individuals may relate to platybasia or a similar anomaly at the base of the skull; however, this was not assessed in the current study. Examples of identified corpus callosum and pituitary abnormalities are depicted in Fig 2A–C.

Table 2: Neuroradiologic findings identified in a cohort of 7 unrelated individuals with ZTTK syndrome

	Individuals						
	1	2	3	4	5	6	7
PVNH	Sparse; bilateral; FH	Sparse; bilateral; FH, midbody, peritrigonal	Sparse; bilateral; FH, TH	Sparse; bilateral; FH, midbody	Sparse; bilateral; FH, TH, peritrigonal	Single; unilateral; right FH	Sparse; unilateral; left FH
Vermis height (centile) ²¹	50–97	>97	>97	>97	>97	50	50
Vermis diameter (centile) ²¹	>97	50–97	>97	>97	>97	>97	>97
Cerebellar tonsils	Normal	Normal	Normal	Herniated	Normal	Herniated	Normal
Posterior fossa	Abnormal shape	Abnormal shape; cyst	Normal	Abnormal shape; cyst	Abnormal shape	Abnormal shape; cyst	Normal
Corpus callosum diameter (centile) ²⁰	<3	50–97	<3	50–97	50–97	<3	50–97
Genu diameter (centile) ²⁰	3–50	<3	<3	<3	50–97	<3	<3
Pituitary gland	Small	Small	Small	Small	Small	Normal	Normal
Pituitary stalk	Normal	Elongated	Elongated	Elongated	Elongated	Normal	Elongated
Caudate nuclei	Dysmorphic	Dysmorphic	Dysmorphic	Dysmorphic	Dysmorphic	Normal	Small
Caudate heads	Malrotated	Malrotated	Malrotated	Malrotated	Malrotated	Large	Normal
Hippocampi	Small and malrotated	Small and malrotated	Small and malrotated	Small and malrotated	Normal sized; LIA	Normal sized; LIA	Small; LIA
Lentiform nucleus	Normal-sized	Small globus pallidus	Normal-sized	Small globus pallidus	Small	Small globus pallidus	Normal-sized
Lateral ventricles	Dysmorphic; large FH; small OH	Dysmorphic; large FH and OH	Dysmorphic; large FH	Dysmorphic; large FH	Dysmorphic; large FH	Dysmorphic; large OH	Large FH
Third ventricle	Small	Dilated	Small	Dilated	Small	Normal	Small
Fourth ventricle	Small	Small	Small	Small	Small	Small	Small
Cortex malformations	Abnormal temporal lobe sulcation	Bilateral PS-PMG; thick PS cortex	Bilateral PS-dysgyria; thick PS cortex	Bilateral PS-PMG	Bilateral PS-PMG	Bilateral PS-dysgyria; thick PS cortex	Thick PS cortex
WM volume	Normal	Decreased	Decreased	Decreased	Normal	Normal	Decreased
Myelination	Normal	Normal	Delayed	Normal	Delayed	Normal	Delayed

Note:—FH indicates frontal horns; TH, temporal horns; OH, occipital horns; PS, perisylvian; PMG, polymicrogyria; LIA, lack of internal architecture.

The cerebellum was large in all individuals, with 4 individuals above the 97th centile for craniocaudal vermis height and 6 individuals above the 97th centile for anterior-posterior vermis diameter.²¹ The cerebellar tonsils were herniated through the foramen magnum in 2 of 7 individuals (>3 mm below the level of the foramen magnum). For individual 4, MR images were available at 2 time points, revealing a normal-sized cerebellum at 16 days of age. However, by 16 months of age, the cerebellum was overgrown with tonsillar herniation. Appearances most consistent with posterior fossa cysts were observed in 3 of 7 individuals. The posterior fossa was “box-shaped” in 5 of 7 individuals due to a steepened tentorial angle and may be related to an apparent increase in cerebellar size in these individuals. Representative MR imaging slices showing posterior fossa abnormalities are presented in Fig 2F–H.

The caudate nuclei were dysmorphic in all individuals, with caudate heads appearing malrotated and globular in 5 individuals, depicted in Fig 2L, –M. Abnormalities in the lentiform nucleus were frequently observed, restricted to the globus pallidus in 3 individuals and generalized in an additional case. Abnormal hippocampi were seen in all individuals, appearing small and malrotated in 4 individuals (Fig 2E). The hippocampi of the remaining 3 individuals showed a lack of internal architecture (Fig 2D). The thalami were normal in all individuals.

The lateral ventricles were dysmorphic and dilated in all individuals, affecting both the frontal (6 of 7) and occipital (3 of 7) horns. Further abnormalities of the ventricular system were also observed, with a small fourth ventricle in all individuals, likely

secondary to enlargement of the cerebellum. A generalized decrease in WM volume was seen in 4 individuals, with delays in age-appropriate myelination in 3 individuals.

Malformations in cerebral cortical gyrification and sulcation were seen in all individuals. Examples are depicted in Fig 2I, –J, –L, –N, –O. These cortical malformations included bilateral perisylvian polymicrogyria (3 of 7), bilateral perisylvian dysgyria or polymicrogyria-like cortical dysplasia (2 of 7), and perisylvian cortex thickening (3 of 7). Disorganized sulcation was also observed in 2 individuals, appearing to be especially localized to the temporal lobe in individual 1.

DISCUSSION

ZTTK syndrome is a rare disorder with a wide phenotypic spectrum, posing diagnostic challenges in the absence of genomic testing. Instead, high-throughput sequence screening of *SON* has been suggested as the only practical way of diagnosing ZTTK syndrome.^{12–14} The cohort described here manifests the core phenotypic features of ZTTK syndrome, including developmental delay, seizures, and dysmorphic features. However, this core presentation remains both nonspecific and highly variable, offering limited utility for recognition in a clinical setting.

We identified PVNH as an imaging feature that may aid clinical recognition of ZTTK syndrome and analyzed a cohort of 7 cases with this phenotypic feature. The distribution of *FLNA*-associated PVNH overlaps that seen with the frontal predominant distribution of ZTTK syndrome. However, *FLNA*-associated nodules are typically larger and more contiguous and do not frequently

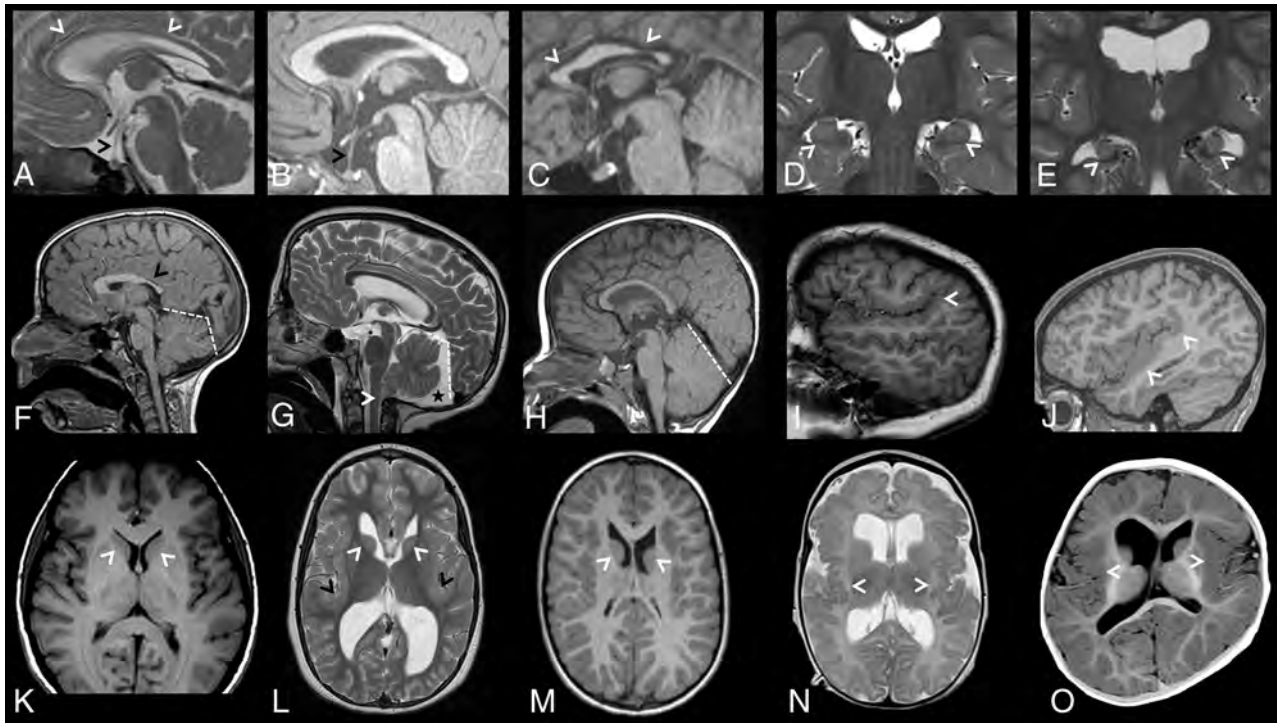


FIG 2. Brain MR images depicting additional brain anomalies in a cohort of 7 unrelated individuals with ZTTK syndrome. *A*, Sagittal midline T2-weighted MRI of the brain of individual 4 at 1 year 4 months of age showing a thin corpus callosum (white arrowheads), an elongated pituitary stalk (black arrowhead), and small pituitary gland. *B*, Sagittal midline T1-weighted MRI of the brain of individual 5 at 1 year 8 months of age showing an elongated pituitary stalk (black arrowhead) and a small pituitary gland. *C*, Sagittal midline T1-weighted MRI of the brain of individual 6 at 15 years 2 months of age showing a shortened corpus callosum with a hypoplastic anterior and posterior body (white arrowheads), a normal-sized pituitary stalk, and a normal-sized pituitary gland. *D*, Coronal T2-weighted MRI of the brain of individual 5 at 1 year 8 months of age revealing normal-sized hippocampi with a lack of internal architecture (white arrowheads). *E*, Coronal T2-weighted MRI of the brain of individual 2 at 11 years 6 months of age revealing small malrotated hippocampi (white arrowheads). *F*, Sagittal midline T1-weighted MRI of the brain of individual 1 at 7 years 7 months of age showing a box-shaped posterior fossa (white dashed lines) and a shortened corpus callosum with a hypoplastic posterior body, isthmus, and splenium (black arrow). *G*, Sagittal midline T2-weighted MRI of the brain of individual 2 at 11 years 6 months of age showing a box-shaped posterior fossa (white dashed lines) with a posterior fossa cyst (black star) and dysmorphic cerebellar tonsils (white arrowhead). *H*, Sagittal midline T1-weighted MRI of the brain of individual 3 at 1 year of age shows a large cerebellum. *I*, Right parasagittal T1-weighted MRI of the brain of individual 2 at 11 years 6 months of age revealing perisylvian polymicrogyria with upswept Sylvian fissures (white arrowhead). *J*, Right parasagittal T1-weighted MRI of the brain of individual 6 at 15 years 2 months of age revealing a thick perisylvian cortex and dysgyria (white arrowheads). *K*, Axial T1-weighted MRI of the brain of a control individual depicting caudate nuclei with caudate heads (white arrowheads) that are less rounded than in *L* and *M*. *L*, Axial T2-weighted MRI of the brain of individual 2 at 11 years 6 months of age revealing a dysmorphic caudate nucleus with rounded and malrotated caudate heads (white arrowheads), large dysmorphic frontal and occipital horns, and a bilaterally thickened perisylvian cortex (black arrowheads). *M*, Axial T1-weighted MRI of the brain of individual 1 at 7 years 7 months of age revealing dysmorphic caudate nuclei with rounded and malrotated caudate heads (white arrowheads) and large dysmorphic frontal horns. *N*, Axial T2-weighted MRI of the brain of individual 4 at 1 year 4 months of age revealing bilateral posterior perisylvian polymicrogyria (white arrowheads). *O*, Axial T1-weighted MRI of the brain of individual 3 at 1 year of age revealing a thick perisylvian cortex and dysgyria (white arrowheads).

extend to the temporal horns.¹⁶ In addition, the co-occurrence of polymicrogyria and other cortical malformations distinguishes the pattern observed in ZTTK syndrome from *FLNA*-associated PVNH. However, these features alone are not pathognomonic of this condition because similar combinations of features have been previously observed, such as in individuals with *MAP1B*- and *NEDD4L*-associated cortical malformations.^{17,22,23}

Three additional instances of PVNH in ZTTK syndrome have been described previously, of a total of >41 individuals with MR imaging screening.^{3,11,12,24} This observation likely represents an underestimate of the true prevalence of PVNH in ZTTK syndrome because previous studies did not report PVNH as a discrete neuro-radiologic entity. Additionally, the subtle nature of the sparse and isolated heterotopia identified here could lead to underreporting, as occurred for individuals 6 and 7.^{25,26}

Neuroradiologic assessment of MR imaging data led to the identification of a set of brain structures with recurrent abnormalities. These features may suggest the diagnosis of ZTTK syndrome in situations in which hypothesis-free high-throughput sequencing is not available. Additionally, these features may support the pathogenic nature of VUS identified in *SON*, such as the multiple missense variants that have now been reported in conjunction with ZTTK syndrome-like features.^{4,11,12} Interestingly, craniosynostosis was also noted in 2 patients, both involving the coronal sutures. Craniosynostosis has been previously reported in individuals with ZTTK syndrome and could represent another phenotypic feature overrepresented in this disorder.^{3,11}

Most individuals reported in this study were recruited based on the presence of PVNH with a subsequent molecular diagnosis, representing a potential recruitment bias. As a consequence, the

neuroradiologic signature identified may be associated with PVNH, with no direct association with ZTTK syndrome. The frequency of these newly identified neuroradiologic features in ZTTK syndrome will be best assessed through studying individuals recruited purely on the basis of a molecular diagnosis. Re-assessing published ZTTK cohorts for these imaging features may validate the clinical utility of the observations made in this cohort.^{3,4,11,12}

CONCLUSIONS

We identify a recurrent set of cortical malformations in a cohort of individuals with ZTTK syndrome. These imaging features have the potential to aid in the diagnosis of ZTTK syndrome in the absence of high-throughput sequencing.

ACKNOWLEDGMENTS













Patients and their families are thanked for their willing participation. The authors wish to acknowledge access to New Zealand eScience Infrastructure high-performance computing facilities for the processing of whole-exome and genome sequence data in this research.

Disclosure forms provided by the authors are available with the full text and PDF of this article at www.ajnr.org.

REFERENCES

- Richards S, Aziz N, Bale S, et al; ACMG Laboratory Quality Assurance Committee. **Standards and Guidelines for the Interpretation of Sequence Variants: A Joint Consensus Recommendation of the American College of Medical Genetics and Genomics and the Association for Molecular Pathology.** *Genet Med* 2015;17:405–24 CrossRef Medline
- Zhu X, Petrovski S, Xie P, et al. **Whole-exome sequencing in undiagnosed genetic diseases: Interpreting 119 trios.** *Genet Med* 2015;17:774–81 CrossRef Medline
- Kim JH, Shinde DN, Reijnders MR, et al; Deciphering Developmental Disorders Study. **De novo mutations in SON disrupt RNA splicing of genes essential for brain development and metabolism, causing an intellectual-disability syndrome.** *Am J Hum Genet* 2016;99:711–19 CrossRef Medline
- Tokita MJ, Braxton AA, Shao Y, et al. **De novo truncating variants in SON cause intellectual disability, congenital malformations, and failure to thrive.** *Am J Hum Genet* 2016;99:720–27 CrossRef Medline
- Takenouchi T, Miura K, Uehara T, et al. **Establishing SON in 21q22.11 as a cause a new syndromic form of intellectual disability: possible contribution to Braddock-Carey syndrome phenotype.** *Am J Med Genet A* 2016;170:2587–90 CrossRef Medline
- Sharma A, Markey M, Torres-Muñoz K, et al. **SON maintains accurate splicing for a subset of human pre-mRNAs.** *J Cell Sci* 2011;124:4286–98 CrossRef Medline
- Ahn EE, DeKolver RC, Lo MC, et al. **SON controls cell-cycle progression by coordinated regulation of RNA splicing.** *Mol Cell* 2011;42:185–98 CrossRef Medline
- Livyatan I, Meshorer E. **SON sheds light on RNA splicing and pluripotency.** *Nat Cell Biol* 2013;15:1139–40 CrossRef Medline
- Ueda M, Matsuki T, Fukada M, et al. **Knockdown of SON, a mouse homologue of the ZTTK syndrome gene, causes neuronal migration defects and dendritic spine abnormalities.** *Mol Brain* 2020;13:1–9 CrossRef Medline
- Kim JH, Baddoo MC, Park EY, et al. **SON and its alternatively spliced isoforms control MLL complex-mediated H3K4me3 and transcription of leukemia-associated genes.** *Mol Cell* 2016;61:859–73 CrossRef Medline
- Kushary ST, Revah-Politi A, Barua S, et al. **ZTTK syndrome: clinical and molecular findings of 15 cases and a review of the literature.** *Am J Med Genet A* 2021;185:3740–53 CrossRef Medline
- Dingemans AJ, Truijien KM, Kim JH, et al. **Establishing the phenotypic spectrum of ZTTK syndrome by analysis of 52 individuals with variants in SON.** *Eur J Hum Genet* 2022;30:271–81 CrossRef Medline
- Kim JH, Park EY, Chitayat D, et al. **SON haploinsufficiency causes impaired pre-mRNA splicing of CAKUT genes and heterogeneous renal phenotypes.** *Kidney Int* 2019;95:1494–1504 CrossRef Medline
- Slezak R, Smigiel R, Rydzanicz M, et al. **Phenotypic expansion in Zhu-Tokita-Takenouchi-Kim syndrome caused by de novo variants in the SON gene.** *Mol Genet Genomic Med* 2020;8:1–7 CrossRef Medline
- Vriend I, Oegema R. **Genetic causes underlying grey matter heterotopia.** *Eur J Paediatr Neurol* 2021;35:82–92 CrossRef Medline
- Parrini E, Ramazzotti A, Dobyns WB, et al. **Periventricular heterotopia: phenotypic heterogeneity and correlation with Filamin A mutations.** *Brain* 2006;129:1892–1906 CrossRef Medline
- Heinzen EL, O'Neill AC, Zhu X, et al; for the Epi4K Consortium. **De novo and inherited private variants in MAP1B in periventricular nodular heterotopia.** *PLoS Genet* 2018;14:e1007281–23 CrossRef Medline
- Karczewski KJ, Francioli LC, MacArthur DG. **The mutational constraint spectrum quantified from variation in 141,456 humans.** *Nature* 2020;581:434–43 CrossRef
- Thormann A, Halachev M, McLaren W, et al. **Flexible and scalable diagnostic filtering of genomic variants using G2P with Ensembl VEP.** *Nat Commun* 2019;10:2373 CrossRef Medline
- Garel C, Cont I, Alberti C, et al. **Biometry of the corpus callosum in children: MR imaging reference data.** *AJNR Am J Neuroradiol* 2011;32:1436–43 CrossRef Medline
- Jandeaux C, Kuchcinski G, Ternynck C, et al. **Biometry of the cerebellar vermis and brain stem in children: MR imaging reference data from measurements in 718 children.** *AJNR Am J Neuroradiol* 2019;40:1835–41 CrossRef Medline
- Broix L, Jagline H, Ivanova E, et al; Deciphering Developmental Disorders Study. **Mutations in the HECT domain of NEDD4L lead to AKT-mTOR pathway deregulation and cause periventricular nodular heterotopia.** *Nat Genet* 2016;48:1349–58 CrossRef Medline
- Wieck G, Leventer RJ, Squier WM, et al. **Periventricular nodular heterotopia with overlying polymicrogyria.** *Brain* 2005;128:2811–21 CrossRef Medline
- Quintana Castanedo L, Sánchez Orta A, Maseda Pedrero R, et al. **Skin and nails abnormalities in a patient with ZTTK syndrome and a de novo mutation in SON.** *Pediatr Dermatol* 2020;37:517–19 CrossRef Medline
- Conti V, Carabalona A, Pallesi-Pocachard E, et al. **Periventricular heterotopia in 6q terminal deletion syndrome: role of the C6orf70 gene.** *Brain* 2013;136:3378–94 CrossRef Medline
- Myers KA, Mandelstam SA, Ramantani G, et al. **The epileptology of Koolen-de Vries syndrome: electro-clinico-radiologic findings in 31 patients.** *Epilepsia* 2017;58:1085–94 CrossRef Medline

Neuroimaging in Pediatric Patients with Juvenile Xanthogranuloma of the CNS

 B.L. Serrallach,  S.F. Kralik,  B.H. Tran,  T.A.G.M. Huisman,  R.P. Patel,  C.E. Allen,  K.L. McClain,  N. Gulati,  C.Q. Dillard-Ilboudo,  M.J. Hicks,  C.A. Mohila, and  N.K. Desai



ABSTRACT

BACKGROUND AND PURPOSE: Juvenile xanthogranuloma is a rare clonal, myeloid, neoplastic disorder. Typically, juvenile xanthogranuloma is a self-limited disorder of infancy, often presenting as a solitary red-brown or yellow skin papule/nodule. A small subset of patients present with extracutaneous, systemic juvenile xanthogranuloma, which may include the CNS. The goal of this retrospective study was to evaluate and categorize the neuroimaging findings in a representative cohort of pediatric patients with CNS juvenile xanthogranuloma.

MATERIALS AND METHODS: The brain and/or spine MR imaging data of 14 pediatric patients with pathology-proven juvenile xanthogranuloma were categorized and evaluated for the location; the signal intensity of xanthogranulomas on T1WI, T2WI, DWI, and a matching ADC map for the pattern and degree of contrast enhancement; and the presence of perilesional edema, cysts, or necrosis.

RESULTS: Fourteen pediatric patients (8 girls, 6 boys; mean age, 84 months) were included in the study. Patients presented with a wide variety of different symptoms, including headache, seizure, ataxia, strabismus, hearing loss, facial paresis, and diabetes insipidus. Juvenile xanthogranuloma lesions were identified in a number of different sites, including supra- and infratentorial as well as intracranial and spinal leptomeningeal. Five patients were categorized into the neuroradiologic pattern unifocal CNS juvenile xanthogranuloma; 8, into multifocal CNS juvenile xanthogranuloma; and 1, into multifocal CNS juvenile xanthogranuloma with intracranial and spinal leptomeningeal disease. In most cases, xanthogranulomas were small-to-medium intra-axial masses with isointense signal on T1WI (compared with cortical GM), iso- or hyperintense signal on T2WI, had restricted diffusion and perilesional edema. Almost all xanthogranulomas showed avid contrast enhancement. However, we also identified less common patterns with large lesions, nonenhancing lesions, or leptomeningeal disease. Four cases had an additional CT available. On CT, all xanthogranulomas were homogeneously hyperdense (solid component) without evident calcifications.

CONCLUSIONS: CNS juvenile xanthogranuloma may demonstrate heterogeneous neuroimaging appearances potentially mimicking other diseases, such as primary brain neoplasms, metastatic disease, lymphoma and leukemia, other histiocytic disorders, infections, or granulomatous diseases.

ABBREVIATIONS: ALK = anaplastic lymphoma kinase; BRAF V600 = B-Raf proto-oncogene, serine/threonine kinase (V600E); CE = contrast-enhanced; ECD = Erdheim-Chester disease; GRE = gradient recalled-echo; HLH = hemophagocytic lymphohistiocytosis; JXG = juvenile xanthogranuloma; LCH = Langerhans cell histiocytosis; MAPK = mitogen-activated protein kinase; RDD = Rosai-Dorfman disease

Juvenile xanthogranuloma (JXG) is a rare, clonal, myeloid, neoplastic disorder traditionally belonging to the group of non-

Langerhans cell histiocytosis.^{1,2} Typically, JXG is a self-limited condition in infancy with skin lesions often presenting as a solitary red-brown or yellow skin papule or nodule on the head, neck, or upper trunk.^{3,4} A small subset present with systemic JXG, which is commonly progressive without therapy and is potentially fatal.^{2,5} Extracutaneous systemic involvement may include the eyes, oral cavity, heart, lung, gastrointestinal tract, liver, spleen, kidneys, lymph nodes, bone marrow, soft tissue, and the CNS.⁵⁻⁷ Characteristic histopathologic features include vacuolated CD163, factor-XIIIa- and fascin-positive histiocytic cells, and multinucleated Touton giant cells (which may not be present in CNS lesions).^{5,8} Involvement of the CNS is seen in only up to 7% of cases with JXG.^{5,9} The clinical

Received May 31, 2022; accepted after revision August 8.

From the Edward B. Singleton Department of Radiology (B.L.S., S.F.K., B.H.T., T.A.G.M.H., R.P.P., N.K.D.), Department of Pediatrics (C.E.A., K.L.M., N.G., C.Q.D.-I), Section of Hematology-Oncology, and Department of Pathology and Immunology (M.J.H., C.A.M.), Texas Children's Hospital and Baylor College of Medicine, Houston, Texas.

B.L. Serrallach was supported by the Edward B. Singleton endowment.

Please address correspondence to Bettina L. Serrallach, MD, Edward B. Singleton Department of Radiology, Texas Children's Hospital and Baylor College of Medicine, 6701 Fannin St, Suite 470, Houston, TX 77030; e-mail: bettinaserallach@icloud.com



Indicates article with online supplemental data.

<http://dx.doi.org/10.3174/ajnr.A7683>

presentation of CNS JXG is nonspecific and includes a wide range of symptoms, such as headache, seizures, ataxia, increased intracranial pressure, macrocrania, developmental delay, weakness, numbness, cranial nerve abnormalities, and diabetes insipidus.^{1,2,5,10} To date, there is no generally accepted consensus or standard-of-care treatment for CNS JXG. Successful outcomes have been reported in individual cases and case series, including chemotherapy (eg, clofarabine), anaplastic lymphoma kinase (*ALK*) inhibition (for *ALK* fusion events), or mitogen-activated protein kinase (*MAPK*) pathway blockade with B-Raf proto-oncogene, serine/threonine kinase (V600E) (*BRAF* V600E) or mitogen-activated protein kinase kinase (*MAP2K*) inhibitors.^{5,11,12} Only scarce literature on imaging in CNS JXG exists, and the imaging spectrum remains incompletely characterized.^{1,6,7,13-15} Accordingly, the goal of this article was to study and categorize the neuroimaging findings in a representative cohort of pediatric patients with confirmed CNS JXG.

MATERIALS AND METHODS

Following institutional review board approval, an electronic search of the pediatric histopathologic and pediatric neuroradiologic database covering January 1, 2010, to August 31, 2021, was performed using the following keywords: juvenile xanthogranuloma (JXG). Inclusion criteria for this retrospective study were the following: 1) pediatric patients (younger than 19 years of age) with pathology-proven JXG (from CNS and/or other lesions), and 2) brain and/or spine MR imaging data (indication: initial diagnostic work-up of newly emerged symptoms).

All MR imaging studies were performed at either 1.5T or 3T magnetic field strength. Images were obtained by different institutions, but protocols mostly included axial and/or sagittal T1WI and axial T2WI, axial FLAIR, axial contrast-enhanced T1-weighted (T1+CE) images, axial SWI or T2*-gradient recalled-echo (T2*-GRE) sequences, and axial DWI or DTI. Isotropic diffusion-weighted images were generated; and matching ADC maps were automatically calculated using vendor-specific software. The relevant clinical and histopathologic data, including the age at diagnosis/biopsy, age at initial imaging, sex, sites of disease involvement, presenting symptoms, histologic diagnosis, and clinical molecular data were extracted from the electronic medical charts.

MR imaging studies were independently reviewed and categorized on the PACS workstation by 2 board-certified pediatric neuroradiologists (N.K.D. and R.P.P.). The readers were not blinded to the patient's medical history. The interrater reliability was assessed by the Cohen κ (for categoric variables) and the intraclass correlation coefficient (for interval and metric variables). The MR imaging studies were evaluated for the exact location (including an intra- versus extra-axial classification), the T1WI and T2WI signal intensity of xanthogranulomas (hypo-, iso-, or hyperintense compared with the cortical GM), the pattern of contrast enhancement (contrast enhancement versus no contrast enhancement; homogeneous contrast enhancement versus heterogeneous contrast enhancement), the degree of contrast enhancement (none, mild, moderate, marked), the percentage (proportion of the mass; visually estimated) of contrast enhancement of the lesion (0%–25%, 26%–50%, 51%–75%, and 76%–100%), the extent of perilesional T2-weighted hyperintensity suggestive of vasogenic

edema (no, mild, moderate, marked), evidence of blood products or calcium on SWI or T2*-GRE (yes/no), the presence of cysts or necrosis (yes/no; "cyst" was defined as a well-defined collection, and "necrosis", as a nonsolid irregular area), and the signal intensity on DWI and the matching ADC map (diffusion restriction or no diffusion restriction with reference to the brain). In addition, quantitative measurements of ADC values were performed. An ROI was manually placed within the xanthogranuloma on the ADC maps as follows: section with the largest expansion of the solid component of the xanthogranuloma using a 5-mm² ROI. The mean ADC value and the standard deviation (SD) were determined.

Statistical analyses were performed using the software package SPSS Statistics, Version 28.0 (IBM).

RESULTS

Fourteen pediatric patients (8 girls, 6 boys; mean age, 84 months at imaging; median age, 65.5 months; age range, 1 month to 18 years 11 months) fulfilled the inclusion criteria. Patients were categorized into 3 primary neuroradiologic patterns: 1) unifocal, 2) multifocal, and 3) multifocal leptomeningeal. Five subjects had unifocal CNS JXG (Fig 1 and Online Supplemental Data), 8 patients had multifocal CNS JXG (Fig 2), and 1 child had multifocal CNS JXG with additional intracranial and spinal leptomeningeal disease (Fig 3).

Isolated CNS involvement was found in all 5 patients categorized into the unifocal neuroradiologic pattern. Of the 8 patients categorized into the multifocal neuroradiologic pattern, 2 had a single-system involvement of the CNS, while 6 patients showed involvement of ≥ 2 organ systems. From the latter, the skin was involved in all 6 patients, followed by bone involvement in 3 patients. Furthermore, 1 patient had, in addition to CNS and skin involvement, lesions in the conjunctiva and eye globe; 1 patient had, in addition to CNS and skin involvement, a lesion in the soft tissue (pharynx); and 1 patient had extensive systemic involvement with lesions in the CNS, skin, bone, lung, kidneys, and lymph nodes. The 1 patient categorized into the multifocal leptomeningeal neuroradiologic pattern had lesions in the CNS and peripheral nervous system. In total, 7 of 14 patients (50%) had isolated CNS involvement, and 7 patients (50%) had involvement of ≥ 2 organ systems. The involved organ systems of all 14 patients are summarized in the Online Supplemental Data.

Xanthogranulomas had an average maximum diameter at presentation of 2.2 (SD, 1.3) cm (range, 0.8–4.8 cm). Lesions were found in a number of different sites, including supra- and infratentorial, intra-axial or extra-axial (in the hypothalamic-pituitary region, the internal auditory canal, or the Meckel cave), as well as in spinal leptomeningeal locations. With the 5 subjects categorized into the neuroradiologic pattern, unifocal CNS JXG, lesions were located in the right frontal lobe (cortical/subcortical WM; Fig 1), in the left parietal lobe (cortical/subcortical WM; Online Supplemental Data), cerebellar vermis, pons, and infundibulum. With patients with multifocal CNS JXG, lesions were scattered supra- and infratentorially (Figs 2 and 3). Supratentorial lesions were mainly found in the cortex, subcortical WM, or central GM, followed by deep WM and periventricular WM. Infratentorial xanthogranulomas were located in the pons in 6 patients; in the

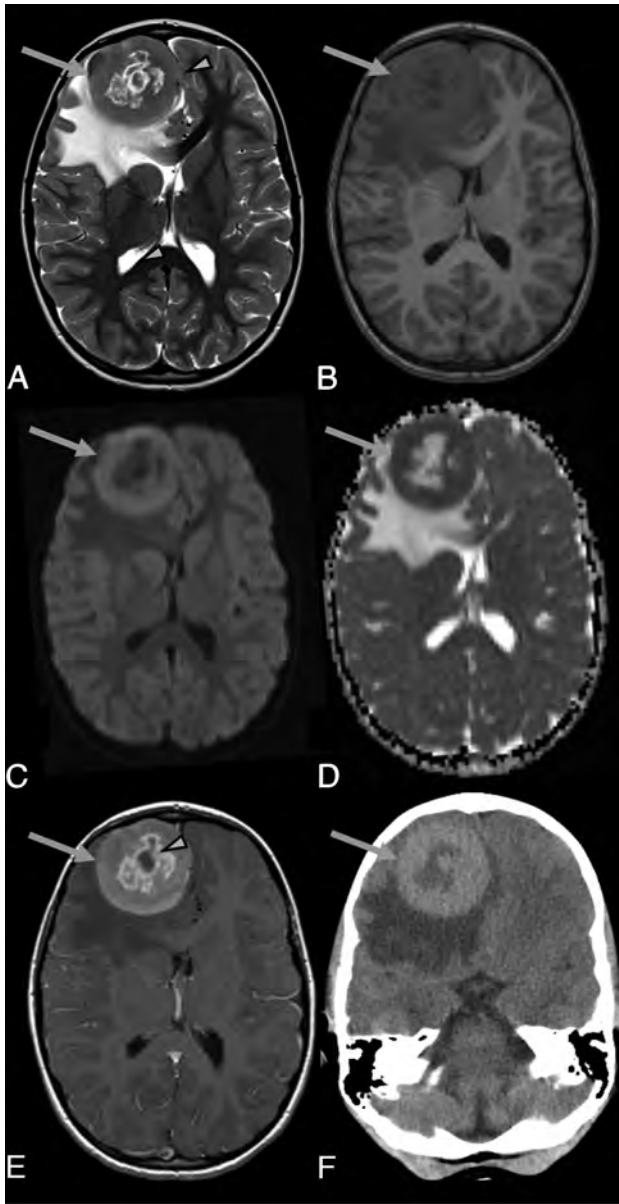


FIG 1. Brain images of a 6-year-old girl with pathology-proven unifocal JXG who presented with increased frequency of headaches, occasionally accompanied by vomiting. Brain MR imaging with an axial T2-weighted image (A), axial T1-weighted image (B), axial DWI (C), axial ADC map (D), axial T1+CE-weighted image (E), and axial noncontrast CT (F) shows a large, round, unifocal mass lesion located in the right frontal lobe (arrows in A–F) with central necrosis (arrowhead in E), perilesional edema, and right-to-left midline shift (arrowhead in A). Compared with cortical GM, the solid non-necrotic peripheral component of the lesion is T2-isointense (A) and T1-isointense (B) and shows contrast enhancement (E) and restricted diffusion (C and D). The axial CT image (F) demonstrates the hyperdense (solid portion), large mass lesion.

cerebellar GM in 5 patients; in the brachium pontis in 3 patients; in the cerebellar WM in 2 patients; in the midbrain in 2 patients; in the vermis in 1 patient; and in the medulla in 1 patient. Lesions were found in the infundibulum in 6 patients; in the corpus callosum, pituitary gland, and hypothalamus in 3 patients each; in the optic chiasm and septum pellucidum in 2 patients each; in

the ventricles in 1 patient; and in the internal auditory canal and the Meckel cave on both sides in 1 patient. In 1 patient, the infundibulum was involved in isolation, and in 5 patients, the infundibulum was part of a multifocal manifestation. Two children were diagnosed with diabetes insipidus. In 1 patient, diabetes insipidus was an initial presenting symptom, and the other patient developed diabetes insipidus later in the disease course.

Images were obtained from different institutions. In 2 patients, no T1WI (12/14 with available T1WI); in 1 child, no T2WI (13/14 with available T2WI); in 4 subjects, no DWI (10/14 with available DWI); and in 3 patients no SWI/T2*-GRE (11/14 with available SWI/T2*-GRE) images were available. On T1WI, xanthogranulomas were isointense compared with cortical GM in 7 patients (7/12), hyperintense in 4 patients (4/12), and hypo- to isointense in 1 patient (1/12). In the 12 patients with available T1WI, the pituitary bright spot was lost in 3 subjects (3/12). The infundibulum was involved in all 3 patients in whom the pituitary bright spot was lost. On T2WI, xanthogranulomas were isointense compared with cortical GM in 5 patients (5/13), hyperintense in 4 patients (4/13), iso- to hyperintense in 3 patients (3/13), and hypo- to isointense in 1 patient (1/13), respectively. In 13 patients with available T2WI, perilesional edema was evident in 11 patients (11/13). The xanthogranulomas of 2 patients had no edema, and 4 patients had mild, 3 patients had moderate, and 4 patients had marked perilesional edema. Necrosis was seen in 6 patients (6/14), and 2 patients (2/14) had cystic components within the lesions. The xanthogranulomas of 13 patients (13/14) showed contrast enhancement on T1+CE-weighted images; the xanthogranulomas of 6 patients had homogeneous and the xanthogranulomas of 5 patients had heterogeneous contrast enhancement. In 2 patients with multifocal JXG, larger xanthogranulomas showed heterogeneous and smaller xanthogranulomas showed homogeneous contrast enhancement. One patient with multifocal xanthogranulomas had lesions with and without contrast enhancement on T1+CE-weighted images. All contrast-enhancing xanthogranulomas were characterized by marked contrast enhancement, comprising >50% of the lesion size, with 13 patients having 76%–100%, and 1 patient having 51%–75% of the lesion enhancing.

Seven of 10 patients with available DWI (7/10) showed restricted diffusion, and 3 had no restricted diffusion (equivalent values compared with normal brain on the ADC map; increased ADC values were not found). The mean ADC values and SD were determined on the available ADC maps. For 1 patient, no measurement could be obtained because the small size of the lesion prevented proper ROI positioning. The overall ($n = 9$) mean ADC value was 868.96 (SD, 179.24); the mean ADC value calculated for lesions with diffusion restriction ($n = 7$) was 823.97 (SD, 175.99); and without diffusion restriction ($n = 2$), it was 1026.42 (SD, 86.15).

Three of 11 patients with available SWI or T2*-GRE images demonstrated hypointense blood products or calcifications.

Due to an obstructive mass effect of the xanthogranulomas, hydrocephalus was found in 2 patients (2/14).

In 9 patients (9/14), additional spine MRIs were available. By means of these spine MRIs, spinal leptomeningeal disease

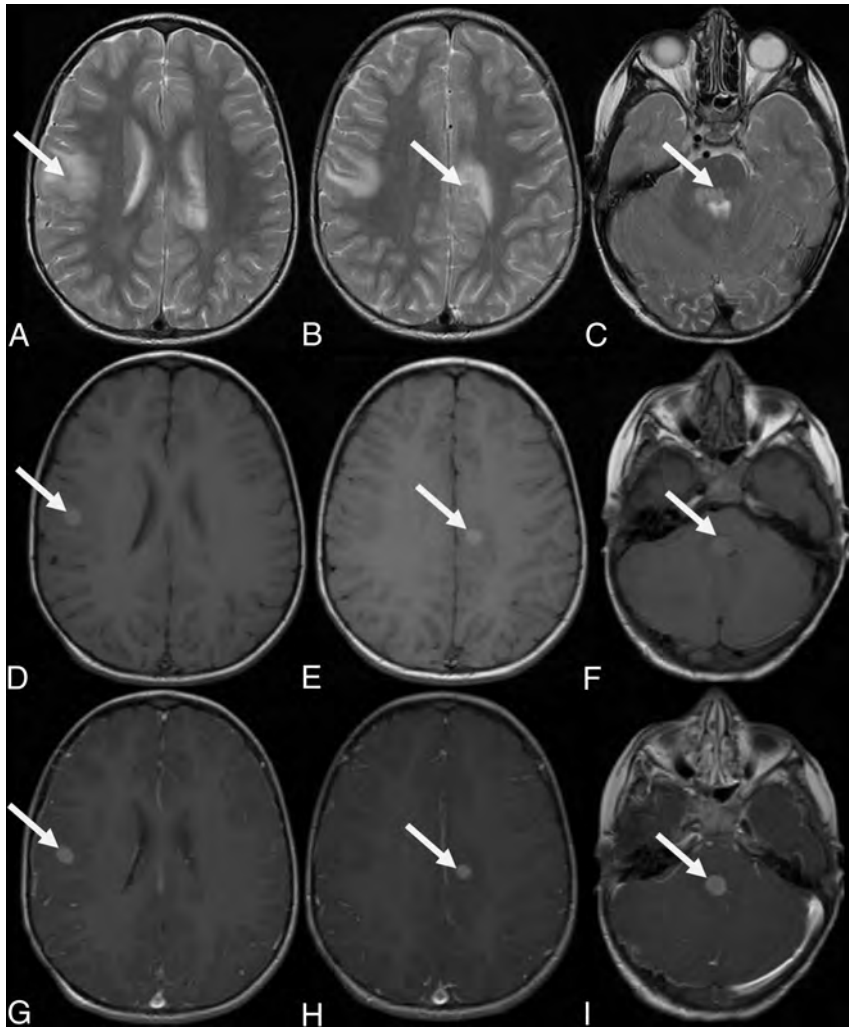


FIG 2. Brain MR images of a 3-year-old boy with pathology-proven multifocal JXG and new-onset strabismus. Axial T2-weighted (A–C), axial T1-weighted (D–F), and axial T1+CE-weighted (G–I) MR imaging sequences show exemplary 3 round-to-oval lesions located in the right (arrows in A, D, and G) and left paracentral (arrows in B, E, and H) regions and the pons (arrows in C, F, and I), respectively. Compared with cortical GM, the lesions are T2-iso- to hyperintense (A–C) and T1-hyperintense (D–F) and show homogeneous contrast enhancement (G–I) and mild perilesional edema.

was found in 1 patient (neuroradiologic pattern: multifocal leptomeningeal).

In addition to MRIs, 4 patients had an additional CT available. Xanthogranulomas were homogeneously hyperdense (solid component) on all 4 CT scans without evident calcifications. Two demonstrated central necrosis; and 1, a marginal cyst.

The interrater reliability was assessed using the Cohen κ (for categorical variables) and by the intraclass correlation coefficient (for interval and metric variables). The Cohen κ and the intraclass correlation coefficient values ranged from 0.71 to 1.00. According to Field,¹⁶ values of >0.7 represent reliable ratings.

Detailed information comprising the demographics, imaging features, and clinical information including the clinical mutational data are shown as Online Supplemental Data. A summary focusing on the signal characteristics of CNS xanthogranulomas is presented in the Table.

DISCUSSION

In this cohort of pediatric patients with biopsy-proven CNS JXG (from the CNS site and/or from other locations), most JXG lesions were typified by small-to-medium masses with iso-intense signal on T1WI, iso- or hyper-intense signal on T2WI, restricted diffusion and perilesional edema. Almost all xanthogranulomas showed marked contrast enhancement. Cases were categorized into 3 primary neuroradiologic patterns: unifocal, multifocal, and multifocal leptomeningeal.

The category of histiocytosis includes Langerhans cell histiocytosis (LCH), Erdheim-Chester disease (ECD), JXG, Rosai-Dorfman disease (RDD), hemophagocytic lymphohistiocytosis (HLH), and malignant histiocytosis. These entities are characterized by pathogenic myeloid cells that share histologic features with macrophages or dendritic cells.^{5,8} The lesional cells may originate from the embryonic yolk sac, fetal liver, or postnatal bone marrow.⁵ The term “histiocytic disorders” for LCH, ECD, JXG, RDD, and HLH has been proposed to differentiate them from hyperproliferative cancer-typical lesions such as Langerhans cell sarcoma and malignant histiocytosis.⁵ While LCH, ECD, JXG, and RDD have somatic mutations in *MAPK* pathway genes and show an accumulation of clonal, mononuclear phagocytes, HLH is a syndrome of immune dysregulation.^{5,8}

The Working Group of the Histiocyte Society published the first classification system of histiocytic diseases in 1987, which consisted of 3 categories, namely,

Langerhans cell histiocytosis, histiocytosis of mononuclear phagocytes other than Langerhans cells, and malignant histiocytic disorders.¹⁷ In the past decades with the incorporation of molecular features, there have been several revisions, with the most recent revision in 2016.^{8,18} This updated contemporary classification consists of 5 groups (the Langerhans-related; cutaneous and mucocutaneous histiocytoses; malignant histiocytoses; RDD; and HLH and macrophage activation syndrome) and is based on histology, phenotype, molecular alterations, and clinical characteristics.⁸ The proposed Langerhans group includes LCH, ECD, and extracutaneous JXG.⁸

Depending on the histiocytic entity, these diseases may be seen in both the pediatric and adult populations in various proportions and may show a broad variety of clinical presentations and outcomes.^{1,5,8,18} The intense inflammatory infiltrates in histiocytic disorders play a key role in the origination and maintenance of

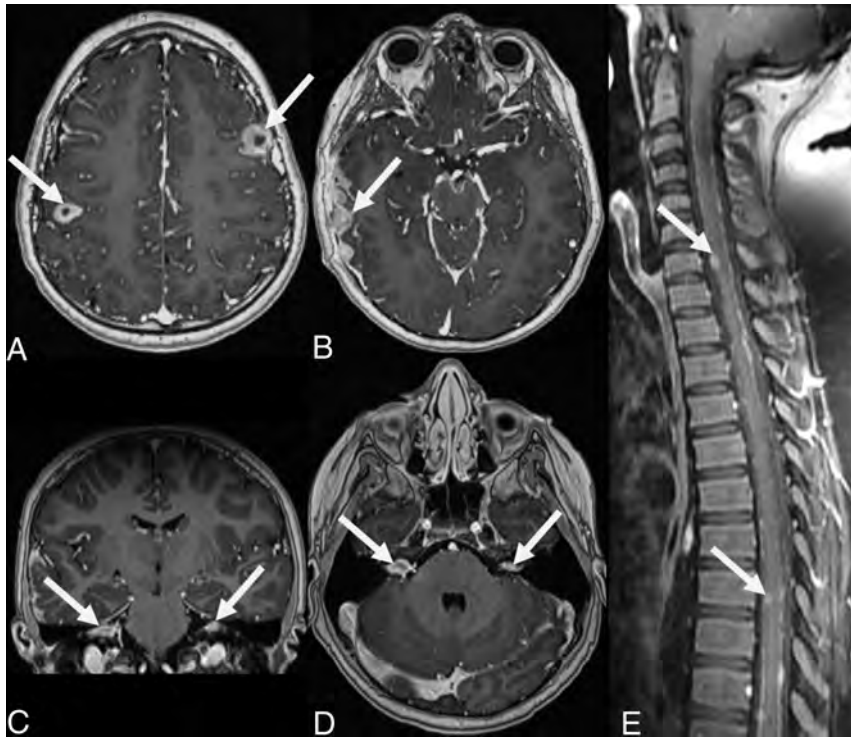


FIG 3. MR images obtained in a 10-year-old boy with pathology-proven multifocal JXG with leptomeningeal brain and spine involvement. The patient presented with progressive right-ear pain and erythema and decreased hearing and right-sided facial nerve palsy along with headaches. Axial (A, B, and D) and coronal T1+CE-weighted (C) MR images of the brain. E, Sagittal T1+CE-weighted fat-suppressed MR image of the spine. For example, 2 centrally necrotic, peripherally contrast-enhancing lesions are noted within both cerebral hemispheres (arrows in A). In addition, nodular contrast enhancement involving the leptomeninges of the right temporal lobe (arrow in B) and contrast enhancement within both internal auditory canals (arrows in C and D) are shown. Sagittal T1+CE-weighted images of the spine depict increased contrast enhancement of the leptomeninges (“sugar coating”), partially with nodular components, most obvious at the C7 and T8 level (arrows in E).

organ-specific lesions and contribute to the clinical symptoms.⁵ To date, very little is known concerning the underlying pathogenetic mechanisms of JXG.⁵ JXG cells share some common features with dermal macrophages, including expression of fascin, factor-XIIIa, CD163, and CD68 (Online Supplemental Data).⁵

JXG is a rare entity; a frequency of approximately 1 per million children and a male/female ratio of 1.4:1 have been described in the Kiel Pediatric Tumor Registry.⁹ In our cohort, there was a 1.33:1 female predominance. With systemic JXG, a predominance of females of up to 3:1 has been reported in the literature.¹⁹ Most often, JXG presents in children (< 4 years) as a solitary red-brown or yellow skin papule or nodule of 0.5–1 cm in diameter and may undergo spontaneous regression.^{2,3,5,8} Most skin lesions involve the head, neck, or upper trunk.^{3,4} Some patients have isolated or very few cutaneous lesions, while others may develop hundreds of lesions.⁵ A small subset present with systemic JXG.² Besides the CNS (7%), extracutaneous JXG may involve the liver (22%), lungs (16%), soft tissue (16%), spleen (11%), eyes (9%), oral cavity (7%), adrenal glands (7%), gastrointestinal tract (7%), lymph nodes (7%), bone marrow (7%), and heart (4%).^{5–7} In this study, 7 of 14 patients (50%) had isolated CNS involvement. Seven patients (50%) had involvement of ≥ 2 organ systems, with involvement of

the skin and/or bones being most common (Online Supplemental Data).

The clinical presentation depends on the involved organ systems.^{5,10} For CNS JXG, clinical presentation is nonspecific and includes headache, seizures, ataxia, increased intracranial pressure, macrocrania, developmental delay, weakness, numbness, cranial nerve abnormalities, and diabetes insipidus.^{1,2,5,10} These findings are in line with the initial presentation of the patients in our study, which included headache, seizure, ataxia, strabismus, hearing loss, facial paresis, and diabetes insipidus, among others (Online Supplemental Data).

In general, JXG is a self-limiting disease.⁴ However, systemic JXG, especially with CNS involvement, may be associated with long-term problems such as structural damage by brain lesions or liver failure by large hepatic tumors or may even be fatal.^{2,5,9,20} Available treatment options for JXG include “wait and see/follow-up,” chemotherapy (eg, clofarabine), targeted therapies such as *ALK* inhibition (for *ALK* fusion events) and *MAPK* pathway blockade with *BRAF* V600E or *MAP2K* inhibitors, surgery, or a combination of these modalities.^{5,9,11,12,14} Most skin-limited JXG lesions show spontaneous involution, but surgical excision may be considered if lesions are cosmetically unacceptable or endanger or impair

functions such as vision or swallowing.⁵ In patients with systemic JXG including CNS lesions, there is evidence of successful treatment using chemotherapy (eg, clofarabine) or targeted therapies such as *MAPK* pathway blockade, or *ALK* inhibition (for *ALK* fusion events).^{5,11,12}

Recurrent activating somatic mutations in *MAPK* genes have been identified in JXG.^{5,8} In our cohort, there were 1 patient with coexisting LCH and JXG and 1 patient with coexisting JXG and RDD. There is evidence of the coexistence of JXG and LCH²¹ and JXG and RDD,²² supporting a potential common cell of origin.⁵ Additionally, JXG has been reported in patients with neurofibromatosis 1 and other “RASopathies”.^{23,24} JXG can be found in up to 29% of patients with neurofibromatosis 1,²⁴ consistent with the known role of *MAPK* pathway activation in the pathogenesis of both diseases.²⁵ The literature concerning a triple association between JXG, neurofibromatosis 1, and juvenile myelomonocytic leukemia is contradictory, with some studies suggesting an association²⁶ and others reporting no increased incidence.²⁴ In addition, there is a rare subtype of histiocytic disorder, the *ALK*-positive histiocytosis, which is mainly associated with *KIF5B-ALK* fusions and shows frequent neurologic involvement and may have a successful outcome with *ALK* inhibition treatment.¹² A subgroup of *ALK*-

Imaging features of CNS JXG^a

No.	T1-Weighted	T2-Weighted	T1+CE	DWI/ADC
4/12	↔	↔	4 Marked contrast enhancement	4 Diffusion restriction
3/12	↔	↔ - ↑ or ↑	3 Marked contrast enhancement	1 Diffusion restriction, 2 no diffusion restriction
2/12	↑	↑	2 Marked contrast enhancement	1 Diffusion restriction, 1NA
2/12	↑	↔ or ↔ - ↑	1 Marked contrast enhancement/1 with lesions with marked and lesions without contrast enhancement	1 No diffusion restriction, 1NA
1/12	↓ - ↔	↓ - ↔	1 Marked contrast enhancement	1 Diffusion restriction

Note:↔ indicates isointense; ↑, hyperintense; ↔ - ↑, iso- to hyperintense; ↓ - ↔, hypo- to isointense; NA, not applicable.

^aCases were included only when both T1WI and T2WI were available.

positive histiocytosis demonstrates histopathologic features of classic JXG.¹² Additionally, recurrent mutations in *CSF1R* have recently been described in JXG.²⁷

To date, data describing imaging features of CNS JXG are largely limited to case studies^{1,6,13-15} and reviews, including clinical and pathological aspects as well as a summary description of the imaging features.² This article aims to present a large case series focusing on neuroimaging features of CNS JXG in children. Intracranial xanthogranulomas have been described variously as T1-/T2-hypo-, iso-, or hyperintense lesions on MR imaging.^{1,2,6,13-15,20} In our cohort, on T1WI, xanthogranulomas were mainly isointense compared with cortical GM (7/12; Online Supplemental Data), several lesions were hyperintense (4/12; Fig 2), and 1 lesion was hypo- to isointense (1/12). On T2WI, xanthogranulomas were mainly isointense (5/13; Fig 1 and Online Supplemental Data) or hyperintense (4/13), followed by an iso- to hyperintense (3/13; Fig 2) or hypo- to isointense (1/13) appearance.

Ginat et al²⁸ characterized the imaging features of head and neck xanthogranulomas of 10 patients, with 6 patients undergoing MR imaging.²⁸ They reported that on T1WI, lesions were characterized by an iso- or hyperintensity, and on T2WI, by an iso- or hypointensity.²⁸ Within our cohort, several lesions showed a high signal on T1WI and T2WI. This could be due to lipid components within these lesions because lipidized or xanthomatous cells may be found within xanthogranulomas.²⁹ In general, CNS JXGs^{1,2} and head and neck JXGs²⁸ are described as showing homogeneous contrast enhancement on T1+CE-weighted images. Marked contrast enhancement seems to be a reliable imaging feature of JXG because almost all xanthogranulomas showed avid contrast enhancement (Fig 1–3 and Online Supplemental Data), and only 1 patient (1/14) who had multifocal xanthogranulomas showed lesions with marked contrast enhancement as well as lesions without contrast enhancement on T1+CE-weighted images. Most lesions (7/10) demonstrated restricted diffusion (Figs 1 and Online Supplemental Data). This finding is in agreement with the literature describing decreased diffusion in such lesions.^{1,28} Ginat et al described decreased diffusivity as likely attributed to hypercellularity and/or a collagenous matrix.

Because there are heterogeneous, non-pathognomonic imaging appearances of CNS JXG with neuroradiologic patterns ranging from unifocal to multifocal leptomeningeal involvement, neuroradiology alone is not able to provide an accurate diagnosis. Accordingly, a wide array of differential diagnoses must be considered, including primary brain neoplasms, lymphoma and leukemia, other histiocytic disorders such as LCH or ECD, and infections. If multifocal lesions with leptomeningeal involvement are evident, metastatic and granulomatous diseases such as sarcoidosis and tuberculosis should be included in the differential diagnosis.

The range of intracranial CNS findings in LCH is better known and comprises a neurodegenerative pattern including infratentorial WM abnormalities more pronounced in the peridentate regions, abnormalities of the dentate nuclei and basal ganglia, and bilateral symmetric leukoencephalopathy-like abnormalities in the supratentorial white matter.³⁰⁻³² In addition, CNS LCH may show mass lesions in the hypothalamic-pituitary region, seen as thickening and enhancement of the pituitary stalk with possibly loss of the posterior bright spot, and it is clinically frequently accompanied by diabetes insipidus.^{31,32} Rare neuroimaging manifestations include enlargement of the pineal gland, thickening and enhancement of the choroid plexus, and intraparenchymal masses.^{31,32} Hence, in contrast to CNS JXG, in CNS LCH, intra-axial parenchymal mass lesions are rather uncommon. However, involvement of the hypothalamic-pituitary region appears to be a common feature of both CNS JXG and LCH. In our cohort, infundibular involvement was seen in 6 patients, and pituitary gland or hypothalamic involvement was noted in 3 patients each. In addition, the posterior pituitary gland T1-hyperintense signal or bright spot was absent in 3 patients. In general, a loss of the posterior bright spot is thought to be a result of a lack of vasopressin-containing granules.³¹ We assume a similar mechanism as seen in LCH, in which an absent pituitary bright spot and involvement of the infundibulum are frequent but do not necessarily occur in all patients. In our cohort, we did not find changes suggestive of posterior fossa neurodegeneration. In addition to CNS LCH, neurodegeneration has also been described in the context of ECD.³³ CNS JXG may not be prone to neurodegeneration, or neurodegeneration could potentially develop later in the course of the disease because neuroimaging in our cohort was performed for the initial diagnostic work-up of new symptoms.

We are aware of several limitations in our study. The imaging findings are based on a retrospective study design with a quite limited number of pediatric patients and MR imaging was performed as a diagnostic work-up of newly emerged symptoms on various scanners with somewhat different protocols. Subsequent studies with larger cohorts and standardized imaging protocols are needed to confirm the proposed imaging patterns presented in our study. In addition, future prospective studies should correlate histologic features to neuroimaging characteristics, and longitudinal follow-up

studies may shed more light on the rate of progression, the response to therapy, and the possible changes in imaging characteristics.

CONCLUSIONS

In this study, pediatric patients with biopsy-proven CNS JXG were categorized into 3 primary neuroradiologic patterns: 1) unifocal, 2) multifocal, and 3) multifocal leptomeningeal. CNS JXG lesions were typified by small-to-medium masses with isointense signal on T1WI, iso- or hyperintense signal on T2WI, restricted diffusion, perilesional edema, and marked contrast enhancement. However, we also identified less common patterns with large lesions, nonenhancing lesions, or leptomeningeal disease. These findings demonstrate the heterogeneous neuroimaging appearances of JXG potentially mimicking other diseases, such as primary brain neoplasms, metastatic disease, lymphoma and leukemia, other histiocytic disorders, and infections or granulomatous diseases. Pediatric neuroradiologists should be familiar with this entity.

ACKNOWLEDGMENT

The authors thank M. Christiner for providing statistical support.

Disclosure forms provided by the authors are available with the full text and PDF of this article at www.ajnr.org.

REFERENCES

1. Deisch JK, Patel R, Koral K, et al. **Juvenile xanthogranulomas of the nervous system: a report of two cases and review of the literature.** *Neuropathology* 2013;33:39–46 CrossRef Medline
2. Wang B, Jin H, Zhao Y, et al. **The clinical diagnosis and management options for intracranial juvenile xanthogranuloma in children: based on four cases and another 39 patients in the literature.** *Acta Neurochir (Wien)* 2016;158:1289–97 CrossRef Medline
3. Hock M, Zelger B, Schweigmann G, et al. **The various clinical spectra of juvenile xanthogranuloma: imaging for two case reports and review of the literature.** *BMC Pediatr* 2019;19:128 CrossRef Medline
4. Szczerkowska-Dobosz A, Kozicka D, Purzycka-Bohdan D, et al. **Juvenile xanthogranuloma: a rare benign histiocytic disorder.** *Postepy Dermatol Alergol* 2014;31:197–200 CrossRef Medline
5. McClain KL, Bigenwald C, Collin M, et al. **Histiocytic disorders.** *Nat Rev Dis Primers* 2021;7:73 CrossRef Medline
6. Meshkini A, Shahzadi S, Zali A, et al. **Systemic juvenile xanthogranuloma with multiple central nervous system lesions.** *J Cancer Res Ther* 2012;8:311–13 CrossRef Medline
7. Rajendra B, Duncan A, Parslew R, et al. **Successful treatment of central nervous system juvenile xanthogranulomatosis with cladribine.** *Pediatr Blood Cancer* 2009;52:413–45 CrossRef Medline
8. Emile JF, Ablu O, Fraitag S, al; Histiocyte Society. **Revised classification of histiocytoses and neoplasms of the macrophage-dendritic cell lineages.** *Blood* 2016;127:2672–81 CrossRef Medline
9. Janssen D, Harms D. **Juvenile xanthogranuloma in childhood and adolescence: a clinicopathologic study of 129 patients from the Kiel Pediatric Tumor Registry.** *Am J Surg Pathol* 2005;29:21–28 CrossRef Medline
10. Freyer DR, Kennedy R, Bostrom BC, et al. **Juvenile xanthogranuloma: forms of systemic disease and their clinical implications.** *J Pediatr* 1996;129:227–37 CrossRef Medline
11. Diamond EL, Durham BH, Ulaner GA, et al. **Efficacy of MEK inhibition in patients with histiocytic neoplasms.** *Nature* 2019;567:521–24 CrossRef Medline
12. Kems PG, Picarsic J, Durham BH, et al. **ALK-positive histiocytosis: a new clinicopathologic spectrum highlighting neurologic involvement and responses to ALK inhibition.** *Blood* 2022;139:256–80 CrossRef Medline
13. Ernemann U, Skalej M, Hermisson M, et al. **Primary cerebral non-Langerhans cell histiocytosis: MRI and differential diagnosis.** *Neuroradiology* 2002;44:759–63 CrossRef Medline
14. Gressot LV, Patel AJ, Bollo RJ, et al. **Disseminated intracranial juvenile xanthogranulomatosis in a neonate without cutaneous lesions.** *J Neurosurg Pediatr* 2013;12:187–91 CrossRef Medline
15. Orsey A, Paessler M, Lange BJ, et al. **Central nervous system juvenile xanthogranuloma with malignant transformation.** *Pediatr Blood Cancer* 2008;50:927–30 CrossRef Medline
16. Field AP. *Discovering Statistics Using SPSS (Introducing Statistical Methods)*. 3rd ed. SAGE Edge; 2009
17. Writing Group of the Histiocyte Society. **Histiocytosis syndromes in children.** *Lancet* 1987;1:208–09 Medline
18. Favara BE, Feller AC, Pauli M, et al. **Contemporary classification of histiocytic disorders: the WHO Committee on Histiocytic/Reticulum Cell Proliferations—Reclassification Working Group of the Histiocyte Society.** *Med Pediatr Oncol* 1997;29:157–66 CrossRef Medline
19. Isaacs H Jr. **Fetal and neonatal histiocytoses.** *Pediatr Blood Cancer* 2006;47:123–29 CrossRef Medline
20. Lalitha P, Reddy M, Reddy KJ. **Extensive intracranial juvenile xanthogranulomas.** *AJNR Am J Neuroradiol* 2011;32:E132–33 CrossRef Medline
21. Patrizi A, Neri I, Bianchi F, et al. **Langerhans cell histiocytosis and juvenile xanthogranuloma: two case reports.** *Dermatology* 2004;209:57–61 CrossRef Medline
22. Picarsic J, Pysner T, Zhou H, et al. **BRAF V600E mutation in juvenile xanthogranuloma family neoplasms of the central nervous system (CNS-JXG): a revised diagnostic algorithm to include pediatric Erdheim-Chester disease.** *Acta Neuropathol Commun* 2019;7:168 CrossRef Medline
23. Ali MM, Gilliam AE, Ruben BS, et al. **Juvenile xanthogranuloma in Noonan syndrome.** *Am J Med Genet A* 2021;185:3048–52 CrossRef Medline
24. Liy-Wong C, Mohammed J, Carleton A, et al. **The relationship between neurofibromatosis type 1, juvenile xanthogranuloma, and malignancy: a retrospective case-control study.** *J Am Acad Dermatol* 2017;76:1084–87 CrossRef Medline
25. Cambiagli S, Restano L, Caputo R. **Juvenile xanthogranuloma associated with neurofibromatosis 1: 14 patients without evidence of hematologic malignancies.** *Pediatr Dermatol* 2004;21:97–101 CrossRef Medline
26. Zvulunov A, Barak Y, Metzker A. **Juvenile xanthogranuloma, neurofibromatosis, and juvenile chronic myelogenous leukemia; world statistical analysis.** *Arch Dermatol* 1995;131:904–08 CrossRef Medline
27. Durham BH, Lopez Rodrigo E, Picarsic J, et al. **Activating mutations in CSF1R and additional receptor tyrosine kinases in histiocytic neoplasms.** *Nat Med* 2019;25:1839–42 CrossRef Medline
28. Ginat DT, Vargas SO, Silvera VM, et al. **Imaging features of juvenile xanthogranuloma of the pediatric head and neck.** *AJNR Am J Neuroradiol* 2016;37:910–16 CrossRef Medline
29. Dehner LP. **Juvenile xanthogranulomas in the first two decades of life: a clinicopathologic study of 174 cases with cutaneous and extracutaneous manifestations.** *Am J Surg Pathol* 2003;27:579–93 CrossRef Medline
30. Prosch H, Grois N, Wnorowski M, et al. **Long-term MR imaging course of neurodegenerative Langerhans cell histiocytosis.** *AJNR Am J Neuroradiol* 2007;28:1022–28 CrossRef Medline
31. Prayer D, Grois N, Prosch H, et al. **MR imaging presentation of intracranial disease associated with Langerhans cell histiocytosis.** *AJNR Am J Neuroradiol* 2004;25:880–91 Medline
32. Yeh EA, Greenberg J, Ablu O, et al; North American Consortium for Histiocytosis. **Evaluation and treatment of Langerhans cell histiocytosis patients with central nervous system abnormalities: current views and new vistas.** *Pediatr Blood Cancer* 2018;65:e26784 CrossRef Medline
33. Boyd LC, O'Brien KJ, Ozkaya N, et al. **Neurological manifestations of Erdheim-Chester Disease.** *Ann Clin Transl Neurol* 2020;7:497–506 CrossRef Medline

Volumetric Brain MRI Study in Fetuses with Intrauterine Growth Restriction Using a Semiautomated Method

R. Peretz, T. Halevy, M. Gafner, S. Fried, Y. Revesz, A. Mayer, and E. Katorza



ABSTRACT

BACKGROUND AND PURPOSE: According to the medical literature, it is known that intrauterine growth restriction is associated with abnormal fetal brain findings. The aim of this study was to assess the volume of fetal brain structures in fetuses with intrauterine growth restriction compared with the control group and to examine the effect of intrauterine growth restriction on birth weight in relation to the effect on the volumes of these structures.

MATERIALS AND METHODS: This historical cohort study included 26 fetuses diagnosed with intrauterine growth restriction due to placental insufficiency. The control group included 66 fetuses with MR imaging scans demonstrating normal brain structures. The volumes of the supratentorial brain, left and right hemispheres, and the cerebellum were measured using a semiautomated method. In addition, the cerebellum and supratentorial brain ratio was calculated. The measurements of each brain structure were then converted to percentiles according to growth curves.

RESULTS: The absolute volumes and percentiles of all brain structures examined were smaller in the intrauterine growth restriction group. All examined brain structures showed results that were statistically significant ($P < .015$). There was no statistically significant difference in the cerebellum/supratentorial brain ratio ($P > .39$). The difference in brain volume percentiles was statistically smaller than the difference in birth weight and birth weight percentiles (Dolberg growth curves) between the groups.

CONCLUSIONS: Intrauterine growth restriction affects the volume of brain structures, as measured by quantitative MR imaging. Compared with healthy controls, the effect on birth weight was more prominent than the effect on brain structures, possibly due to the “brain-preserving” capability.

ABBREVIATIONS: CER = cerebellum; GA = gestational age; ICC = intraclass correlation coefficient; IUGR = intrauterine growth restriction; LH = left hemisphere; RH = right hemisphere; ST = supratentorial brain

Intrauterine growth restriction (IUGR) is a halt in growth or a change in the growth rate of the fetus. The American College of Obstetricians and Gynecologists has defined IUGR as a fetus with a birth weight below the 10th percentile for gestational age (GA).¹ IUGR affects 5%–10% of all pregnancies² and has many etiologies. Some etiologies are related to maternal factors (age, poor diet, hypertension, preeclampsia), some are related to fetal factors (chromosomal abnormalities, genetic syndromes, major

congenital anomalies, multiple gestation, metabolic disorders), and some are related to the placenta.^{3,4} The diagnosis of IUGR is usually made with the help of a sonographic examination during pregnancy.⁵ Studies have shown that early detection of IUGR leads to better management of the pregnancy and thus to a better outcome for the neonate.⁶ Currently, a number of prenatal and long-term effects caused by IUGR are known.² These effects include both prenatal³ and neonatal mortality and morbidity,⁷ growth retardation,³ hypertension, obesity, diabetes,⁸ neurodevelopmental impairment, impaired cognitive and motor function, as well as impaired attention and performance at school.^{3,6} Studies have shown a relationship between IUGR and abnormal findings in fetal brain tissue such as abnormal brain topology,⁹ reduced volume ratio between the cerebellum (CER) and supratentorial areas,¹⁰ metabolic changes,¹¹ decreased size of the intracranial structures,¹² decreased gray⁹ and white matter,^{13–15} and decreased diffusion in certain areas of the brain.^{16,17} Measuring the volume of the brain structures with manual and automatic

Received June 2, 2022; accepted after revision August 31.

From the Sackler School of Medicine (R.P., M.G., S.F., Y.R., A.M., E.K.), Tel Aviv University, Tel Aviv, Israel; Sheba Medical Center (T.H., Y.R.), Tel-Hashomer, Israel; Department of Pediatrics B (M.G.), Schneider Children's Medical Center of Israel, Petach Tikva, Israel; Department of Obstetrics and Gynecology (E.K.), Gertner Institute for Epidemiology and Health Policy Research (E.K.), and Department of Diagnostic Radiology (A.M.), Sheba Medical Center, Tel-Hashomer, Israel.

Please address correspondence to Reut Peretz, BMedSc, Tel Aviv University, Mitzpe 6/3, 6437606 Tel Aviv, Israel; e-mail: reutperetz1@gmail.com

Indicates article with online supplemental data.

<http://dx.doi.org/10.3174/ajnr.A7665>

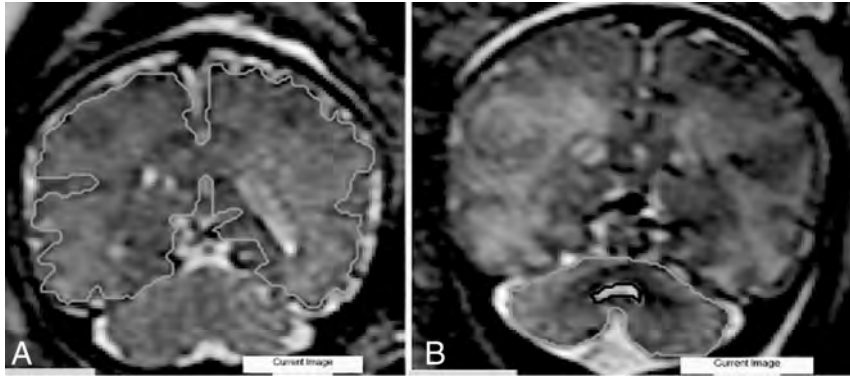


FIG 1. Examples of anatomic boundaries. A, ST. B, CER.

methods presents various difficulties,^{18,19} and as a result, a Matlab-based method (MathWorks) has been developed to measure 3D brain volumes in a semiautomatic fashion.¹⁸ This study used a semiautomatic method to assess volume changes of in utero brain structures in fetuses with IUGR compared with controls and examined the association between IUGR and birth weight in relation to the association between IUGR and the volumes of these structures.

MATERIALS AND METHODS

This is a historical cohort study during which MR imaging scans were obtained between 2011 and 2017 at a tertiary medical center. Data regarding medical history, obstetric history, sonography and MR imaging, perinatal history, and medical follow-up were collected from patients' medical records, and a database was constructed.

Subjects

The study population included 26 fetuses with IUGR due to placental insufficiency who underwent MR imaging. The only indication for fetal MR imaging was IUGR. The MR imaging examination was performed as part of a pilot study at our medical center. This pilot study aimed to assess the contribution of fetal brain MR imaging in the diagnosis and management of IUGR.

Subject selection criteria were as follows:

1. Women who underwent fetal MRI at Sheba Medical Center during 8 years.
2. Age of pregnancy at the time of fetal MRI between 25 and 38 weeks.
3. Pregnancies with IUGR below 10% according to Dolberg growth curves, intrauterine or at birth.
4. Pregnancies of a single fetus.
5. IUGR pregnancies caused by placental insufficiency were selected using an ultrasound examination with abnormal placental findings: notch in the umbilical arteries, high arterial resistance in the umbilical arteries, abnormal systolic-diastolic flow ratio in the umbilical arteries, increased diastolic flow in the umbilical arteries, abnormal MCA pulsatility index/pathologic or thickened placenta/low amniotic fluid.

Fetuses were excluded from the test group on the basis of the following criteria:

1. Clinical or laboratory findings that indicated nonplacental reasons for the presence of IUGR:
 - Fetal causes: intrauterine fetal infection, abnormal anatomic fetal findings, abnormal genetic test results, and pregnancies with multiple fetuses.
 - Maternal causes: uterine malformations, background diseases such as chronic cardiovascular disease and so forth and women with substance abuse disorder (including alcohol and drugs).
2. Significant imaging findings according to MRI or previous ultrasound examination; mild findings without prognostic significance were included (Online Supplemental Data).
3. Lack of sufficient data on the case.
4. Poor MRI scan quality, preventing the production of essential information.

The control group included 66 fetuses who underwent MR imaging examinations between 2011 and 2017, and their examination revealed no abnormal findings. The indications for fetal MR imaging in these women included a previous child with prenatal neurologic findings, a previous abnormal pregnancy, fetal ultrasound examination with abnormal findings that were later ruled out with an MR imaging examination, and suspicion of cytomegalovirus infection without confirmation by amnio-polymerase chain reaction.

Measurements

MR Imaging and Semiautomated Algorithm. Fetal MR imaging was performed in a 1.5T MR imaging system in T1 and T2 sequences. The performed protocol is consistent with the one described in Katorza et al.²⁰

Measurements were obtained using a semiautomated algorithm previously described by Ber et al.¹⁸ To evaluate the consistency of the semiautomated method, we examined interobserver reliability by comparing measurements of 20 fetuses (10 fetuses from the study group and 10 fetuses from the control group) made by 2 independent observers. Intraobserver reliability was assessed by 1 observer who measured a sample of 20 different fetuses twice.

Anatomic Boundaries

Supratentorial Brain Volume. External boundaries were determined by the parenchyma of the frontal, parietal, occipital, and temporal lobes. The measurement did not include the brainstem, supratentorial ventricular system, and CER. The lateral ventricles were measured separately and then reduced (Fig 1A).

Left Hemisphere Volume and Right Hemisphere Volume. The hemispheres were measured independently with a lateral boundary identical to the boundary set in the cerebral measurement. The medial border is determined by the longitudinal groove

separating the hemispheres. The lateral ventricles were measured separately and then reduced.

Cerebellar Volume. External boundaries were determined by the cerebellar hemispheres. The measurement included the peduncles and vermis. The brainstem and the fourth ventricle were not included (Fig 1B).

Comparison among Subjects. To compare the subjects and overcome the differences in GA, we converted our data into percentiles. The measurements for each fetal brain structure were converted according to growth curves previously published by Ber et al,¹⁸ based on data from measurements of 94 healthy fetuses who ranged from 25 + 1 to 39 + 0 GA.

Statistics

The percentile of each brain structure in the study group and in the control group is presented as mean (SD). The quantitative variable between 2 independent groups was compared using an independent *t* test. Categorical variables were compared using the χ^2 test or Fisher exact test. The intraclass correlation coefficient (ICC) was used to evaluate the inter- and intraobserver agreement. All statistical tests were 2-tailed, and *P* < .05 was considered statistically significant, as

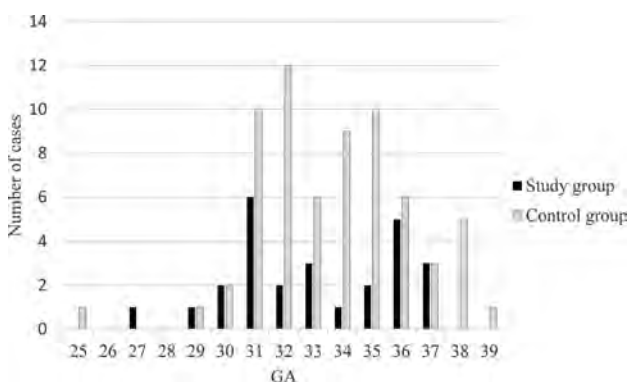


FIG 2. Distribution of MR images according to GA in the study and control groups.

Table 1: Characteristics of the control population alongside the study population expressed as mean (SD) or frequency and percentage and level of significance

	Study Group (n = 26)	Control Group (n = 66)	P Value
Mothers' characteristics			
Maternal age at pregnancy (yr)	32.38 (SD, 5.26)	33.03 (SD, 4.66)	.57
Thyroid disorders	3/26 (11.5%)	4/66 (6%)	.40
Anemia	1/26 (3.8%)	5/66 (7.5%)	.67
Blood clotting disorders	1/26 (3.8%)	7/66 (10.6%)	.43
Hypertension	1/26 (3.8%)	2/66 (3%)	1
Pregestational diabetes	1/26 (3.8%)	0	.28
Pregnancy characteristics			
Spontaneous conception	21/26 (80%)	57/65 ^a (88%)	.51
Fetal sex	Male 15/26 (57%) Female 11/26 (42%)	Male 32/66 (48%) Female 34/66 (52%)	.43
GA at MR imaging examination	33.3 (SD, 2.79)	34.1 (SD, 2.58)	.20
Neonate characteristics			
Type of birth	Vaginal 4/25 ^a (16%) Cesarean 21/25 ^a (84%)	Vaginal 43/64 ^a (67%) Cesarean 21/64 ^a (33%)	<.001 <.001
Week of birth	35.04 (SD, 2.66)	38.52 (SD, 1.27)	<.001

^a There are some cases in which the data are not documented in our records.

is customary in the literature. SPSS Statistical software for Windows, Version 25 (IBM, 2017), was used for all statistical analyses.

Ethics

The study was approved by the local institutional Helsinki Committee, with the following registration number: 0256-13-SMC. The medical information collected will be kept confidential and will not be passed on to those who do not belong to the study. The information is displayed anonymously without revealing the identities of the study participants.

RESULTS

Twenty-six fetuses were included in the study group. The characteristics of the study population are detailed in the Online Supplemental Data.

The mean GA in which the MR imaging was performed in the control group was 34.1 (SD, 2.58) weeks. The distribution of MR images according to GA in the study and control groups is shown in Fig 2.

Additional data relevant for comparison between the study and the control groups are presented in Table 1. No statistically significant difference was found between the study and the control groups in terms of maternal and pregnancy characteristics. In terms of neonatal characteristics, a statistically significant difference was found when comparing the type (*P* < .001) and the week of birth (*P* < .001).

3D MRI Measurements

The mean volume of the structures and the SD in the study and control groups as well as the significance are shown in Table 2. In all structures, the mean volume in the study group was smaller than that of the control group. All the structures had a statistically significant difference. The CER/supratentorial brain (ST) ratio was also smaller in the study group than in the control group, but this result was not statistically significant.

Comparison with Percentiles

The mean percentiles and SD of each brain structure as well as the level of significance difference between the groups are shown in Table 3. In all brain structures examined, the mean percentile in the IUGR group was smaller than the mean percentile in the control group. The difference was statistically significant. The CER/ST ratio was smaller in the study group compared with the control group; this result, however, was not statistically significant.

A comparison of the mean percentile of brain structures of the 2 groups is shown in Fig 3.

Comparison with Birth Weight and Birth Weight Percentile (Dolberg Growth Curves)

The mean birth weight (in grams) and birth weight percentile, SD in both

groups, and level of significance are shown in Table 4. The birth weight and percentile difference were significantly greater than the difference in brain volumes.

Comparison among the Percentiles of Brain Structures within the Different Birth Weight Percentiles of the Study Group

The mean percentile of the brain structures in each subgroup and its level of significance are shown in Table 5. All measured structures were above the 10th percentile. In all structures, excluding the CER, the mean percentile within the birth weight group of $\leq 3\%$, was smaller compared with the birth weight group of 3%–10%. The results were not statistically significant.

Table 2: Mean volume of brain structures (mL), ratio (CER/ST), and SD in the study group compared with the control group and level of significance

Brain Area	Study Group	Control Group	P Value
ST	179.93 (SD, 45.71)	210.66 (SD, 48.99)	.006
RH	88.43 (SD, 22.02)	105.34 (SD, 24.59)	.003
LH	88.76 (SD, 22.68)	105.22 (SD, 24.82)	.004
CER	10.25 (SD, 3.5)	12.16 (SD, 3.27)	.015
CER/ST	0.056 (SD, 0.01)	0.058 (SD, 0.01)	.39

Table 3: Mean percentile of the brain structures or ratio (CER/ST), the SD in the research group compared with the control group, and the level of significance for the difference between them

Brain Area	Study Group	Control Group	P Value
ST	15.57 (SD, 23.4)	40.78 (SD, 37.24)	<.001
RH	15.25 (SD, 23.03)	41.76 (SD, 37.22)	<.001
LH	14.52 (SD, 22.64)	41.86 (SD, 37.7)	<.001
CER	30.82 (SD, 30.24)	46.62 (SD, 34.39)	.04
CER/ST	57.58 (SD, 34.04)	60.17 (SD, 31.72)	.73

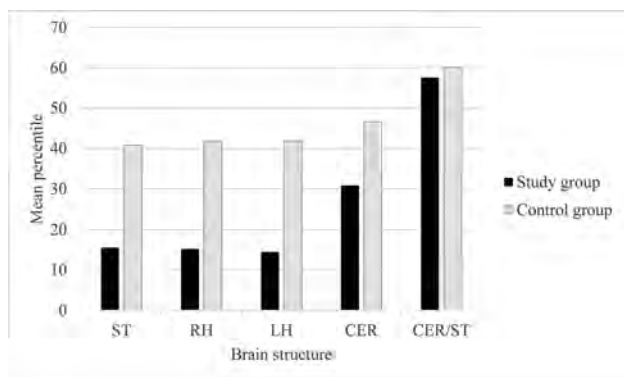


FIG 3. Comparison of the mean percentile of brain structures between the 2 groups.

Table 4: Mean birth weight and birth weight percentile and SD in the study group compared with the control group and level of significance

	Study Group (n = 25) ^a	Control Group (n = 63) ^a	P Value
Birth weight (g)	1639.16 (SD, 543.70)	3209.4286 (SD, 456.93)	<.001
Birth weight percentile	4.04 (SD, 3.29)	54.09 (SD, 26.76)	<.001

^a There are some cases in which the birth weight and birth weight percentile are not documented in our records.

A comparison of the mean percentile between the subgroups is shown in Fig 4.

Inter- and Intraobserver Reliability

The results of the inter- and intraobserver reliability were excellent in all measured structures (ICC > 0.996). The results are shown in Table 6.

DISCUSSION

IUGR affects 5%–10% of all pregnancies.² This pathologic fetal condition has been associated with abnormal findings in the brain. In all examined structures, the mean volume in the study group was smaller compared with the control group. The measurements in our study are consistent with previous studies. In a study by Polat et al,¹⁰ similar values were found when adjusting the measurements by GA. Furthermore, the cerebellar volume in normal-growing fetuses in our study is comparable with that in a study by Clouchoux et al,²¹ who examined fetuses at weeks 25–36 of pregnancy and found that cerebellar volumes ranged between 3.3 and 16 mL, and comparable with a study by Grossman et al,²² which found that the volume of the CER ranged from 5 to 15 mL for the same GA.

To neutralize the effect of the GA for the MR images, we converted the volumes of the structures to percentiles according to the normal curves.¹⁸ That the volumes of structures were significantly smaller in the IUGR group relative to the control group, both in terms of absolute size (milliliters) and percentiles, reinforces our hypothesis that IUGR affects brain volumes.

When comparing birth weight and birth weight percentile between the 2 groups, we found that the difference in these variables was statistically greater than the difference in brain structure percentiles. Furthermore, after creating an additional division within the study group according to the birth weight percentile, we discovered that in all structures, excluding the CER, the mean percentile within the birth weight group of $\leq 3\%$ was smaller compared with the birth weight group of 3%–10%. The results were not statistically significant but suggest a correlation between the birth percentile of the fetus and the brain structure percentile. However, the percentile of the fetus did not represent the percentile of brain structures. Even fetuses with very low birth weight percentiles below 3 maintained brain volume percentiles above 10. The fetuses were not microcephalic, and the CER was only slightly abnormal in volume. These results would support the concept of a brain-preserving effect.

In the past, a number of studies have shown neurologic developmental outcomes in fetuses with IUGR.³ However, in a recent study that examined discordant twins, no statistical difference was found in neurodevelopment outcomes between the appropriate for gestational age twin and the small for gestational age twin.²³ The results of our study may support the hypothesis that some degree of change in brain volume in IUGR might have no or only limited effect on neurologic developmental outcomes, potentially due to the brain-preserving effect. The long-term neurologic outcome seems not to be determined solely by weight assessment, and further research should be performed.

Table 5: Mean percentile of brain structures by birth weight percentiles in the study group and level of significance for the difference between them^a

Brain Area	<3% (n = 16)	3%–10% (n = 9)	P Value
ST	12.84 (SD, 25.27)	22.11 (SD, 20.55)	.36
RH	13.53 (SD, 24.89)	19.89 (SD, 20.98)	.52
LH	12.81 (SD, 25.15)	19.11 (SD, 18.99)	.52
CER	35.68 (SD, 32.56)	25.56 (SD, 25.99)	.43

^a There is 1 case in which the weight percentile is not documented in our records.

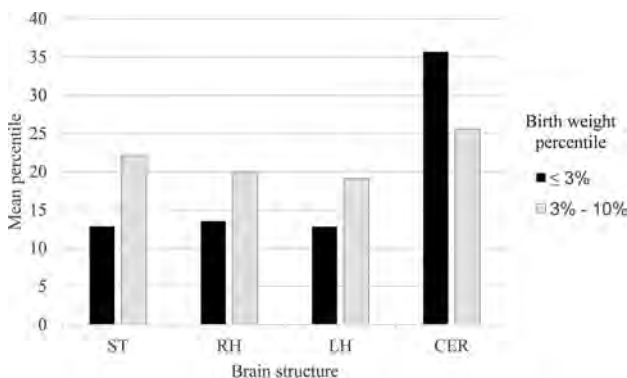


FIG 4. Mean percentile of brain structures by birth weight percentiles in the study group.

Table 6: Intraobserver and interobserver reliability of measurements expressed as ICC and 95% CI

Brain Area	Intraobserver		Interobserver	
	ICC	95% CI	ICC	95% CI
ST	1	0.999–1	0.998	0.992–1
RH	0.999	0.997–1	0.998	0.993–1
LH	0.997	0.988–0.999	0.996	0.985–0.999
CER	0.999	0.995–1	0.998	0.993–1

We acknowledge some limitations of this study. First, despite a relatively high prevalence of IUGR in the population (5%–10%), it was rare to find fetuses diagnosed with IUGR due to placental insufficiency and who, therefore, underwent MR imaging at our institution as well as had their records collected. We were able to assemble a study group of 26 fetuses that met the inclusion criteria. Our study group is larger than groups collected in similar studies in the past,^{19,23} even so, it is still difficult to prove a correlation and reach statistically significant results. Another limitation was due to the control group not being composed of fetuses of random volunteers without any findings, as we would ideally like. Due to ethical limitations in our environment, it is not possible to perform MR imaging scans on healthy fetuses; therefore, research is limited to the use of existing scans that were necessary for the fetal examination. To best simulate the healthy fetus population, only scans without abnormal findings and in which chromosomal abnormalities and intrauterine infections were ruled out were selected for the control group. This limitation is known in studies of this type, and it is likely that random selection of women for future research will reduce this bias.

This study has several strengths. First, the size of the study group, though small relative to the prevalence of IUGR in the

population, is large compared with previous studies that examined similar research questions. Second, it uses a semiautomatic method, which allows us to overcome the existing challenges in measuring fetal brain structure volumes. Another strength is that we analyzed the volume of brain structures both as absolute values and as percentiles. Converting the measurements to percentiles neutralizes the effect of GA, thus allowing more accurate analysis.

CONCLUSIONS

IUGR affects the volume of structures in the brain (ST, right hemisphere [RH], left hemisphere [LH], and CER). However, the effect on the volume of brain structures is smaller than the effect on birth weight. Despite various studies on the subject, it is still unclear whether IUGR by itself has a negative neurologic implication. Our findings support the concept of brain-sparing, but further research is needed to correlate with neurodevelopmental outcomes.

Disclosure forms provided by the authors are available with the full text and PDF of this article at www.ajnr.org.

REFERENCES

- Vayssière C, Sentilhes L, Ego A, et al. **Fetal growth restriction and intra-uterine growth restriction: guidelines for clinical practice from the French College of Gynaecologists and Obstetricians.** *Eur J Obstet Gynecol Reprod Biol* 2015;193:10–18 CrossRef Medline
- Egaña-Ugrinovic G, Sanz-Cortés M, Couve-Pérez C, et al. **Corpus callosum differences assessed by fetal MRI in late-onset intrauterine growth restriction and its association with neurobehavior.** *Prenat Diagn* 2014;34:843–49 CrossRef Medline
- Sharma D, Shastri S, Sharma P. **Intrauterine growth restriction: antenatal and postnatal aspects.** *Clin Med Insights Pediatr* 2016;10:67–83 CrossRef Medline
- Balayla J, Desilets J, Shrem G. **Placenta previa and the risk of intrauterine growth restriction (IUGR): a systematic review and meta-analysis.** *J Perinat Med* 2019;47:577–84 CrossRef Medline
- Giabicani E, Pham A, Brioude F, et al. **Diagnosis and management of postnatal fetal growth restriction.** *Best Pract Res Clin Endocrinol Metab* 2018;32:523–34 CrossRef Medline
- Lausman A, McCarthy FP, Walker M, et al. **Screening, diagnosis, and management of intrauterine growth restriction.** *J Obstet Gynaecol Can* 2012;34:17–28 CrossRef Medline
- Aucott SW, Donohue PK, Northington FJ. **Increased morbidity in severe early intrauterine growth restriction.** *J Perinatol* 2004;24:435–40 CrossRef Medline
- Leitner Y, Fattal-Valevski A, Geva R, et al. **Neurodevelopmental outcome of children with intrauterine growth retardation: a longitudinal, 10-year prospective study.** *J Child Neurol* 2007;22:580–87 CrossRef Medline
- Malhotra A, Allison BJ, Castillo-Melendez M, et al. **Neonatal morbidities of fetal growth restriction: pathophysiology and impact.** *Front Endocrinol (Lausanne)* 2019;10:55 CrossRef Medline
- Polat A, Barlow S, Ber R, et al. **Volumetric MRI study of the intrauterine growth restriction fetal brain.** *Eur Radio* 2017;27:2110–18 CrossRef Medline
- Simões RV, Muñoz-Moreno E, Cruz-Lemini M, et al. **Brain metabolite alterations in infants born preterm with intrauterine growth restriction: association with structural changes and neurodevelopmental outcome.** *Am J Obstet Gynecol* 2017;216:62.e1–62.e14 CrossRef Medline
- Caetano AC, Zamarian AC, Araujo Júnior E, et al. **Assessment of intracranial structure volumes in fetuses with growth restriction by 3-dimensional sonography using the extended imaging virtual organ**

- computer-aided analysis method. *J Ultrasound Med* 2015;34:1397–1405 CrossRef Medline
13. Padilla N, Falcón C, Sanz-Cortés M, et al. **Differential effects of intrauterine growth restriction on brain structure and development in preterm infants: a magnetic resonance imaging study.** *Brain Res* 2011;1382:98–108 CrossRef Medline
 14. Kutuk MS, Sahin M, Gorkem SB, et al. **Relationship between Doppler findings and fetal brain apparent diffusion coefficient in early-onset intra-uterine growth restriction.** *J Matern Fetal Neonatal Med* 2018;31:3201–08 CrossRef Medline
 15. Saunavaara V, Kallankari H, Parkkola R, et al. **Very preterm children with fetal growth restriction demonstrated altered white matter maturation at nine years of age.** *Acta Paediatr* 2017;106:1600–07 CrossRef Medline
 16. Shen JM, Xia XW, Kang WG, et al. **The use of MRI apparent diffusion coefficient (ADC) in monitoring the development of brain infarction.** *BMC Med Imaging* 2011;11:2 CrossRef Medline
 17. Arthurs OJ, Rega A, Guimiot F, et al. **Diffusion-weighted magnetic resonance imaging of the fetal brain in intrauterine growth restriction.** *Ultrasound Obstet Gynecol* 2017;50:79–87 CrossRef Medline
 18. Ber R, Hoffman D, Hoffman C, et al. **Volume of structures in the fetal brain measured with a new semiautomated method.** *AJNR Am J Neuroradiol* 2017;38:2193–98 CrossRef Medline
 19. Damodaram MS, Story L, Eixarch E, et al. **Foetal volumetry using magnetic resonance imaging in intrauterine growth restriction.** *Early Hum Dev* 2012;88(Suppl 1):S35–40 CrossRef Medline
 20. Katorza E, Strauss G, Cohen R, et al. **Apparent diffusion coefficient levels and neurodevelopmental outcome in fetuses with brain MR imaging white matter hyperintense signal.** *AJNR Am J Neuroradiol* 2018;39:1926–31 CrossRef Medline
 21. Clouchoux C, Guizard N, Evans AC, et al. **Normative fetal brain growth by quantitative in vivo magnetic resonance imaging.** *Am J Obstet Gynecol* 2012;206:173.e1–8 CrossRef Medline
 22. Grossman R, Hoffman C, Mardor Y, et al. **Quantitative MRI measurements of human fetal brain development in utero.** *Neuroimage* 2006;33:463–70 CrossRef Medline
 23. Halevy T, Nezer M, Halevy J, et al. **Twin discordance: a study of volumetric fetal brain MRI and neurodevelopmental outcome.** *Eur Radiol* 2021;31:6676–85 CrossRef Medline

Peer Learning Program Metrics: A Pediatric Neuroradiology Example

 N. Kadom, K.M. Reddy,  G. Khanna,  S.F. Simoneaux,  J.W. Allen, and  M.E. Heilbrun



ABSTRACT

BACKGROUND AND PURPOSE: The American College of Radiology is now offering an accreditation pathway for programs that use peer learning. Here, we share feasibility and outcome data from a pilot peer learning program in a pediatric neuroradiology section that, in its design, follows the American College of Radiology peer learning accreditation pathway criteria.

MATERIALS AND METHODS: We retrospectively reviewed metrics from a peer learning program with 5 participating full-time pediatric neuroradiologists during 1 year: 1) number of cases submitted, 2) percentage of radiologists meeting targets, 3) monthly attendance, 4) number of cases reviewed, 5) learning points, and 6) improvement actions. In addition, a faculty survey was conducted and is reported here.

RESULTS: Three hundred twenty-four cases were submitted (mean, 7 cases/faculty/month). The faculty never met the monthly submission target. Peer learning meeting attendance was 100%. One hundred seventy-nine cases were reviewed during the peer learning meetings. There were 22 learning points throughout the year and 30 documented improvement actions. The faculty survey yielded the highest ratings (4.8 of 5) for ease of meeting the 100% attendance requirement and for the learning value of the peer learning sessions. The lowest rating (4.2 of 5) was given for the effectiveness of improvements as a result of peer learning discussions.

CONCLUSIONS: Implementing a peer learning program that follows the American College of Radiology peer learning accreditation pathway criteria is feasible. Program metric documentation can be time-consuming. Participant feedback led to meaningful program improvement, such as improving trust, expanding case submission categories, and delegating tasks to administrative staff. Effort to make peer learning operations more efficient and more effective is underway.

ABBREVIATIONS: ACR = American College of Radiology; CME = Continuing Medical Education; PL = peer learning

The American College of Radiology (ACR) is now offering an accreditation pathway for programs that use peer learning (PL).¹ To qualify, a PL program should have a PL policy, explicit program targets, and annual documentation of program metrics. Specifically, the annual report should include the total number of case submissions to the PL program, the number and percentage of radiologists meeting targets as defined in the facility practice policy, a determination of whether PL activities met the minimum standard as defined by the facility practice

policy, and a summary of related quality-improvement effort and accomplishments.¹

Many radiology practices in the United States are adopting PL in lieu of or in addition to traditional score-based peer review.²⁻⁴ PL is an approach to performance improvement that is based on quality and safety concepts found in high-reliability organizations.⁵ PL builds a safety culture by creating a safe environment for error disclosure, it facilitates joint learning from mistakes, and it creates opportunities for improvement through group discussions that elucidate sources of errors.⁶⁻¹² Higher case submission rates have been observed after switching from score-based peer review to PL, indicating higher engagement of radiologists.^{6,7}

Here, we share feasibility and outcomes data from a pilot PL program in a pediatric neuroradiology section that, in its design, follows the ACR PL accreditation pathway criteria.¹ Our program uses several PL metrics, including radiologist participation rates, number of cases submitted, number of cases reviewed, tangible lessons learned, and improvement projects completed.

Received June 27, 2022; accepted after revision September 12.

From the Department of Radiology and Imaging Sciences (N.K., K.M.R., G.K., S.F.S., J.W.A., M.E.H.), Emory University School of Medicine, Atlanta, Georgia; and Department of Radiology (N.K., K.M.R., G.K., S.F.S.), Children's Healthcare of Atlanta, Atlanta, Georgia.

Please address correspondence to Nadja Kadom, MD, Department of Radiology, 1405 Clifton Rd NE, Atlanta, GA 30322; e-mail: nkadom@emory.edu; @nkpiano

 Indicates article with online supplemental data.

<http://dx.doi.org/10.3174/ajnr.A7673>

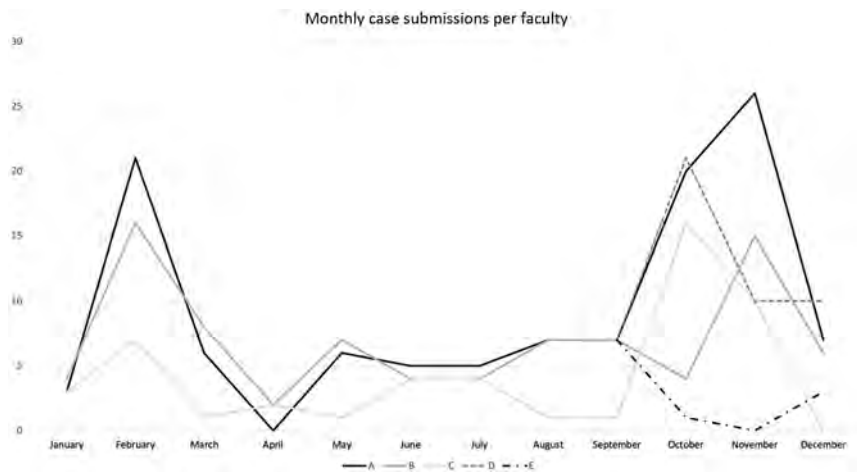


FIG 1. Monthly cases submitted by faculty. Five faculty members (A–E) were observed during this study period; 2 of the faculty joined in August.

MATERIALS AND METHODS

This quality-assurance study was exempt from institutional review board approval. The data were collected at Children’s Healthcare of Atlanta (CHOA), a freestanding academic pediatric hospital with nearly 300,000 examinations annually. Five full-time pediatric neuroradiologists participated in the PL program during the 1-year study period, January 1, 2021, through December 31, 2021. A total of 24,724 neuroradiology examination reports were issued during this time.

PL Program

In December 2020, we incorporated an additional pediatric site into our practice and added substantially to our pediatric neuroradiology faculty, resulting in a separation of pediatric from adult neuroradiology service lines. This created an opportunity for implementing a pilot PL program for the pediatric neuroradiologists who previously participated in score-based peer review.

Our PL program is informed by a written policy that incorporates the elements recommended by the ACR accreditation checklist for PL.¹ Our section chief defined the program targets as follows: PL conferences to occur monthly, 100% faculty attendance, and 5 PL cases submitted each month per pediatric neuroradiologist. The annual documentation of our PL program metrics includes the following: a statement of commitment to sequestering PL from performance evaluations, the total number of case submissions to the PL program, the number and percentage of radiologists meeting targets as defined in the facility practice policy, a determination of whether PL activities met the minimum standard as defined by the facility practice policy, and a summary of related quality-improvement effort and accomplishments.¹

PL conferences occur monthly throughout the calendar year and are recorded for asynchronous viewing. The meetings occur between 12:00 and 1:00 PM, when, in most instances, there is service coverage by a fellow, and they last for 1 hour. There are 2 dedicated faculty members who alternate monthly in selecting and presenting cases. During the study period, we reviewed not only discrepancies of perception, interpretation, or communication,

but also interesting cases. Each month, cases submitted during the previous month were reviewed. Cases were presented as anonymized PowerPoint slides (Microsoft). The case discussion was documented for each case on a case-review form, along with any learning points and improvement actions. Each session was recorded (Teams; Microsoft) and saved in an online location outside the institution’s health records system, where it is protected under peer review state law. Recordings are shared only with faculty and PL staff and can be accessed for remote viewing by those who could not attend the in-person session. During the study period, any improvement actions were immediately assigned to a faculty volunteer who set a

deadline; he or she was followed to the conclusion at the beginning of subsequent PL meetings.

Data Collection

We analyzed the following items that were collected monthly: 1) the number of cases submitted per faculty per month, 2) the percentage of radiologists meeting PL program targets for case submissions (5 per month per faculty), 3) monthly faculty PL attendance (target of 100% live attendance or asynchronous viewing of session recordings), 4) the number of cases reviewed during the PL session, 5) the number and nature of learning points, and 6) the number and nature of improvement actions with assigned faculty volunteer and documented completion.

Faculty Survey

An 11-item survey (Online Supplemental Data) was developed and face-validated by the radiology quality director (N.K.). Responses were collected anonymously in January 2022. There were 2 yes/no questions, 3 open-comment items, and 6 Likert items requesting a Likert star rating with the maximum rating of 5 stars.

Data Analysis

Descriptive statistics were performed in Excel (Microsoft).

RESULTS

PL Program Metrics

The number of monthly case submissions varied widely. During the year, 324 cases were submitted for the PL meetings, with an average of 7 case submissions per faculty per month, and monthly submissions ranging from 0 to 26 cases for a single faculty member (Online Supplemental Data and Fig 1).

There was no month during which >80% of the faculty met the monthly submission target of 5 cases (Fig 2). The low case-submission rate for review in January could be due to the program being new (it was started December 2020), and low submission rates in April correspond to high case volumes and diminished staffing in the same month (data not shown).

PL meeting attendance was 100% for each faculty member.

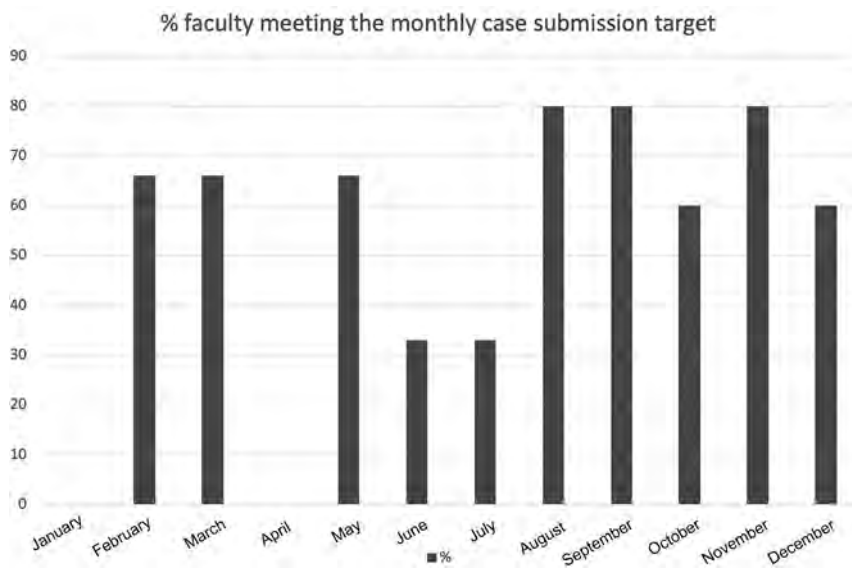


FIG 2. Percentage of faculty meeting the monthly case-submission target. Five faculty members (A–E) were observed during this study period; 2 of the faculty joined in August.

A total of 179 cases were reviewed throughout the year, which is about 50% of all case submissions (179/324). On average, we reviewed 14 cases per PL meeting, ranging from 6–24 case reviews per session.

The session moderator documented any learning points and improvement actions during each PL meeting. There were 22 learning points throughout the year, which averages to 2 learning points per session. Lessons learned included recognizing the importance of accurate use of overnight agree/disagree statements, identifying potential pitfalls in image interpretation, importance of report proofreading, identifying instances when it is appropriate to reference normative values for measurements, and identifying imaging signs of rare diagnoses.

There were 30 documented improvement actions throughout the year, which average to 2.5 improvements identified per session. Improvements that resulted from the PL program thus far included changes to CT and MR imaging protocols, education of radiologists and technologists, changes to reporting templates, changes to EPIC workflows, and modifications of team communications.

PL Faculty Survey

All faculty members responded to the survey (response rate, 100%) (Online Supplemental Data). All section members had previously participated in randomized score-based peer review, and only 2 faculty members had experienced PL previously.

When asked to list any differences between random score-based review and PL that favor random score-based review, respondents listed the following: faster, more objective, simple, easy metric, and mixed agree/disagree (versus only reporting disagreements) as giving a sense of accuracy. Respondents listed differences that favor PL as the following: more fun, learning, discovering improvement opportunities, group discussion, interactive and constructive feedback, and better experience overall.

The highest ratings (4.8 of 5) were given for ease of meeting the 100% attendance requirement and for the learning value of

the PL sessions. A slightly lower rating (4.6 of 5) was given for feeling safe during case discussions, for the ease of submitting cases, and for the ability to gain Continuing Medical Education (CME) credit for session participation. The lowest rating (4.2 of 5) was given for effectiveness of improvements as a result of PL discussions.

Additional general comments included lowering the participation target to 80% to include good calls and not just discrepancies, having too many case-submission tools, and improvement actions being rushed and seeming reactive.

DISCUSSION

We were able to set up a PL program in pediatric neuroradiology that incorporates the checklist items for the new ACR accreditation pathway for PL, demonstrating feasibility in program design and implementation. However,

we have not yet sought ACR accreditation through this pathway.

Most interesting, generating the data required for ACR reporting adds to the overall time commitment for running a PL program. While we did not measure this issue, we estimate that the annual time commitment for the physician leaders is 56 hours, which includes 4 hours/month to collate, select, prepare, and discuss cases for the monthly PL conference, 0.5 hour/month for transcribing PL program data and submitting CME materials, and 2 hours for writing the annual report. We have now trained an administrative assistant who reviews the PL session recording to track attendance, fill out the case-review forms, and handle any activities related to CME credit. While obtaining CME credit for PL was rated less important in our survey, we will continue to offer it because our administrative staff is now managing this aspect of the program. The more time-intensive effort for PL programs compared with score-based peer review has been acknowledged by others.¹³

The monthly PL meeting attendance target was easily met when allowing our faculty who could not attend the live session to attest to viewing session recordings. Faculty rated the ease of compliance with this target very favorably. Similar to others, we used the virtual format due to coronavirus disease 2019 (COVID-19) conditions¹⁴ but realize now that it remains the best option for participating from various sites and practice locations within our system. Most interesting, we are not using any incentives or penalties to drive up our faculty participation rate.¹⁵

There was not a single month when our entire faculty met the target for case submissions. Two faculty members (Fig 1, faculty D and E) disclosed not entirely trusting the separation of learning from performance assessment and, therefore, avoiding case submissions, which was also reflected in the survey by low ratings for the perceived safety during PL meetings. The other faculty member struggled with the multitude of reporting tools to be used, ie, RADPEER (<https://www.acr.org/Clinical-Resources/RADPEER>), EPIC, and e-mails. In response to these concerns, we have

uninvited an external PL session participant who represented the system Peer Practice Evaluation Committee. We also informed our faculty about the educational nature of the PL program and its protection under state peer review legislation, and a reminder slide is now included in the introductory portion of the PL meeting slides. As another change in response to these concerns, we are now keeping case discussions completely anonymous, meaning that we no longer allow faculty to self-identify in any way during a case discussion. Regarding the case submission tools, we are currently still required to use the ACR RADPEER tool for ongoing professional practice evaluation. Unfortunately, our RADPEER is not set up to allow reviews for past faculty readers nor can we submit cases when the current and past reader is the same person. In those instances, we have configured a quality reporting tool in EPIC, but it can only be used as long the report has not been finalized. For all other cases, we notify the PL leaders by e-mail so that cases can be included. We are currently developing an alternate performance review system for ongoing professional practice evaluation^{16,17} so that we can abandon RADPEER and replace all current submission options with a single tool.

At the start of the PL program, we randomly determined the target for monthly case submission per faculty on the basis of what seemed “reasonable.” Because our faculty never met that target, we propose several changes. In our program we reviewed a maximum of 24 cases in a PL conference, which can help determine faculty case submissions per month. For example, for our general pediatric radiology section with currently 18 faculty, it was decided to maintain a minimum submission of 2 cases per month per faculty. This still yields a surplus of cases that allows the PL program leads to select cases with the highest yield for discussion and omit redundant/repetitive cases. If we continually fail to meet our monthly case-submission target in pediatric neuroradiology, we may lower the monthly target below 5 cases or set the target at the section rather than the individual level. Another option to consider, especially for smaller radiology subspecialties, could be to expand PL programs across multiple institutions to spread the shared learning experience and variety of cases.^{18,19}

On the basis of the collected data on learning points and survey responses highly rating the learning value, our program performs similar to those of others who reported higher rates of satisfaction and learning.^{6,20,21} On the basis of the feedback submitted in the survey, we have expanded the submission categories from only discrepancies to also include good calls,²² interesting cases, and cases for any type of group discussion (communication, protocols, imaging technique, and so forth). Sources for PL cases in our program include routine workflow, clinical conferences, consultations, as well as a provider feedback submission system. In the future, we may be able to integrate artificial intelligence applications that can identify cases with radiology-pathology correlations.²³

The lowest survey ratings from our faculty were issued for the improvement effectiveness of the PL program. On further inquiry, faculty members were concerned that improvement actions were decided too quickly without deeper reflection on root causes and balancing measures. We are now documenting any improvement ideas that are mentioned during PL conferences, but we hold off on initiating improvements until a subsequent discussion with the section director has occurred.

Of note, our PL process eliminates faculty “voting” on discrepancies of perception, interpretation, and communication. In our system, the radiologist who identifies a discrepancy is in charge of immediately addressing any patient care issues and notifying the original interpreting radiologist of the discrepancy. He or she can suggest that the original radiologist should act, eg, by issuing an addendum to a report. Whether the recommended action is implemented by the original radiologist, however, is left to that radiologist’s professional decision. Any concerns regarding a radiologist’s clinical practice or behaviors are to be submitted to our system’s Peer Practice Evaluation Committees, which review any physician practice or behavior concerns and determine possible actions.

This study has several limitations. While we assume that PL is more effective than score-based peer review when it comes to improved practice, we do not have any data to show this to be true. Some programs use addendum rates as a proxy for improvement effects and show higher addendum rates with PL compared with score-based peer review.^{8,15} Our survey supports the notion that PL is a valued activity for our faculty, and that at a minimum, it creates opportunities for teambuilding and collaboration.²⁴ Some of the submitted discrepancies may be unproven, disputed, or clinically insignificant. We have not yet needed a system to address disputes. We currently have the person identifying a discrepancy notify the original reader and indicate that either no further action is needed on the basis of an existing follow-up report or an action would be helpful on the basis of a clinician request or patient care impact. It is then up to the radiologist receiving this feedback to act appropriately and responsibly.

CONCLUSIONS

We show the feasibility of a PL program in a pediatric neuroradiology section that follows the ACR PL accreditation pathway criteria. At our academic institution, PL is currently piloted in the pediatric radiology sections. Solicitation of feedback from PL program participants has been helpful in making changes to certain aspects of the program, such as improving trust in the PL program, including meaningful case submission types, and more thoughtful improvement actions. While radiologists favor PL over score-based review, the lack of tools and support to run PL meetings efficiently and effectively may present a barrier to a widespread replacement of score-based review with PL. We are currently developing a submission and data collection tool that supports semiautomated reporting for the ACR accreditation pathway, and we are exploring aspects of the PL process that can be handed off to administrative staff.

ACKNOWLEDGMENTS

Special thanks goes to Jennifer Broder, MD, who provided insight and support throughout the process of designing and implementing our peer learning program.

Disclosure forms provided by the authors are available with the full text and PDF of this article at www.ajnr.org.

REFERENCES

1. American College of Radiology (ACR). **Peer Learning Program Checklist for ACR Accredited Facilities**. <https://www.acr.org/-/>

- media/ACR/Files/Peer-Learning-Summit/Peer-Learning-Program-Checklist-for-ACR-accredited-facilities.pdf. Accessed September 30, 2022
2. Lee CS, Neumann C, Jha P, et al. **Current status and future wish list of peer review: a national questionnaire of U.S. radiologists.** *AJR Am J Roentgenol* 2020;214:493–97 CrossRef Medline
 3. Larson DB, Broder JC, Bhargavan-Chatfield M, et al. **Transitioning from peer review to peer learning: report of the 2020 peer learning summit.** *J Am Coll Radiol* 2020;17:1499–1508 CrossRef Medline
 4. RADPEER. <https://www.acr.org/Clinical-Resources/RADPEER>. Accessed September 30, 2022
 5. Larson DB, Nance JJ. **Rethinking peer review: what aviation can teach radiology about performance improvement.** *Radiology* 2011;259:626–32 CrossRef Medline
 6. Sharpe RE Jr, Huffman RI, Congdon RG, et al. **Implementation of a peer learning program replacing score-based peer review in a multispecialty integrated practice.** *AJR Am J Roentgenol* 2018;211:949–56 CrossRef Medline
 7. Donnelly LF, Dorfman SR, Jones J 3rd, et al. **Transition from peer review to peer learning: experience in a radiology department.** *J Am Coll Radiol* 2018;15:1143–49 CrossRef Medline
 8. Trinh TW, Boland GW, Khorasani R. **Improving radiology peer learning: comparing a novel electronic peer learning tool and a traditional score-based peer review system.** *AJR Am J Roentgenol* 2019;212:135–41 CrossRef Medline
 9. Brook OR, Romero J, Brook A, et al. **The complementary nature of peer review and quality assurance data collection.** *Radiology* 2015;274:221–29 CrossRef Medline
 10. Itri JN, Donithan A, Patel SH. **Random versus nonrandom peer review: a case for more meaningful peer review.** *J Am Coll Radiol* 2018;15:1045–52 CrossRef Medline
 11. Harvey HB, Alkasab TK, Prabhakar AM, et al. **Radiologist peer review by group consensus.** *J Am Coll Radiol* 2016;13:656–62 CrossRef Medline
 12. Alkasab TK, Harvey HB, Gowda V, et al. **Consensus-oriented group peer review: a new process to review radiologist work output.** *J Am Coll Radiol* 2014;11:131–38 CrossRef Medline
 13. Sayyoub MM, Sella EC, Shankar PR, et al. **Lessons learned from peer learning conference in cardiothoracic radiology.** *Radiographics* 2022;42:579–93 CrossRef Medline
 14. Virarkar M, Morani AC, Bhosale P, et al. **Peer learning and operationalizing during COVID-19 pandemic and beyond.** *Cureus* 2021;13:e16568 CrossRef Medline
 15. Zhao AH, Burk KS, Enamandram SS, et al. **Peer learning in radiology: effect of a pay-for-performance initiative on clinical impact and usage.** *AJR Am J Roentgenol* 2021;216:1659–67 CrossRef Medline
 16. Donnelly LF, Larson DB, Heller RE III, et al. **Practical suggestions on how to move from peer review to peer learning.** *AJR Am J Roentgenol* 2018;210:578–82 CrossRef Medline
 17. The Joint Commission. **What are the key elements needed to meet the ongoing professional practice evaluation (OPPE) requirements?** 2021. <https://www.jointcommission.org/standards/standard-faqs/critical-access-hospital/medical-staff-ms/000001500/>. Accessed September 14, 2021
 18. Bowman AW, Tan N, Adamo DA, et al. **Implementation of peer learning conferences throughout a multi-site abdominal radiology practice.** *Abdom Radiol (NY)* 2021;46:5489–99 CrossRef Medline
 19. Chow RA, Tan N, Henry TS, et al. **Peer learning through multi-institutional case conferences: abdominal and cardiothoracic radiology experience.** *Acad Radiol* 2021;28:255–60 CrossRef Medline
 20. Broder JC, Scheirey CD, Wald C. **Step by step: a structured approach for proposing, developing and implementing a radiology peer learning program.** *Curr Probl Diagn Radiol* 2021;50:457–60 CrossRef Medline
 21. Haas BM, Mogel GT, Attaya HN. **Peer learning on a shoe string: success of a distributive model for peer learning in a community radiology practice.** *Clin Imaging* 2020;59:114–18 CrossRef Medline
 22. Lee RK, Cohen M, David N, et al. **Transitioning to peer learning: lessons learned.** *J Am Coll Radiology* 2021;18:499–506 CrossRef Medline
 23. Filice RW. **Radiology-pathology correlation to facilitate peer learning: an overview including recent artificial intelligence methods.** *J Am Coll Radiol* 2019;16:1279–85 CrossRef Medline
 24. Chetlen AL, Petscavage-Thomas J, Cherian RA, et al. **Collaborative learning in radiology: from peer review to peer learning and peer coaching.** *Acad Radiol* 2020;27:1261–67 CrossRef Medline

Celebrating 35 Years of the AJNR

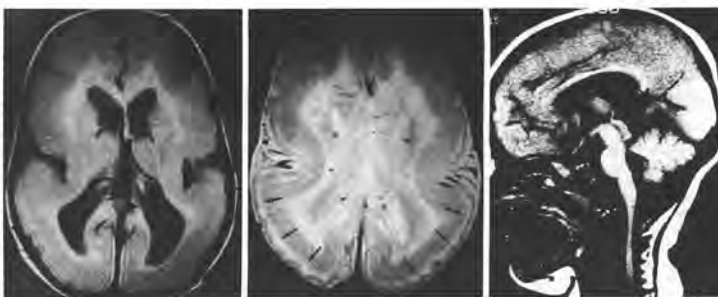
November 1987 edition

MR of Neuronal Migration Anomalies

A. James Barkovich^{1,2}
Sylvester H. Chuang³
David Norman⁴

Migration anomalies are congenital malformations neurogenesis during the third to fifth gestational months. Pachygyria, polymicrogyria, unilateral megalencephaly, heterotopias. Patients who have these conditions present with delay and seizures, and abnormal motor skills are noted in infants. To determine the utility of MR as a method to use MR to evaluate 13 patients who had the full spectrum of these anomalies between gray and white matter. We found that MR is detecting schizencephaly, where recognizing the presence of schizencephaly is critical to distinguishing this disease from polymicrogyria, where critical details of cortical architecture overlying bone. Multiplanar capabilities were also found. MR should be the primary imaging method for infants with mental delay.

Abnormalities of cell migration are characterized in the cerebral cortex. This broad group of anomalies includes polymicrogyria, schizencephaly, unilateral megalencephaly. All these entities have been characterized with CT. MR is an imaging technique that provides anatomic detail and its high-resolution multiplanar display of anatomy. In a review of 537 MR studies in the pediatric patients with migration anomalies. We review the anomalies and their MR appearance. The relationship of theories of pathogenesis is emphasized.



This article appears in the November/December 1987 issue of AJNR and the January 1988 issue of AJNR.

Received March 13, 1987; accepted June 1, 1987.

The views expressed in this article are those of the authors and do not reflect the official policy or position of the Department of the Army, Department of Defense, or the U.S. Government.

Presented in part at the annual meeting of the American Society of Neuroradiology, New York, May 1987.

¹Department of Radiology, Letterman Army Medical Center, Presidio of San Francisco, CA 94124-5120. Address reprint requests to Technical Publications Editor HSNM-2CT.

²Department of Radiology, Neurosurgery Section, University of California School of Medicine, San Francisco, CA 94143.

³Department of Radiology, Neurosurgery Section, Hospital for Sick Children, Toronto, Ontario M5G 1X8, Canada.

AJNR 8:1099-1011, November/December 1987; 0195-9584/87/0609-1009

© American Society of Neuroradiology

Variable Appearances of Subacute Intracranial Hematomas on High-Field Spin-Echo MR

John M. Gomori^{1,2}
Robert I. Grossman¹
David B. Hackney¹
Herbert I. Goldberg¹
Robert A. Zimmerman¹
Larissa T. Bilaniuk¹

Subacute intracranial hematomas have variable appearances on MRI. They are hyperintense on T1-weighted images owing to methemoglobin. Observation of the drift echo MR intensity patterns of five subacute hematomas suggests migration into different methemoglobin states may be possible. Intracranial methemoglobin is hyperintense on T1-weighted images and dilute free methemoglobin is hypointense on T2-weighted images, undiluted free methemoglobin is hyperintense on T1-weighted images and isointense or slightly hypointense on T2-weighted images. However, it appears that certain regions of subacute hematomas to differentiate, by intensity patterns alone, from melanotic melanoma. We believe that, despite some limitations, MR is useful in dividing hematomas into their respective methemoglobin states, and also migration is possible.

Early experience with MR imaging of intracranial hematomas revealed three characteristic signal-intensity patterns (1):

1. Acute hematomas (<1 week old) are isointense to gray matter and markedly hypointense on T2-weighted images. T2-selective T2 proton relaxation enhancement (relaxation time at cellular deoxyhemoglobin).

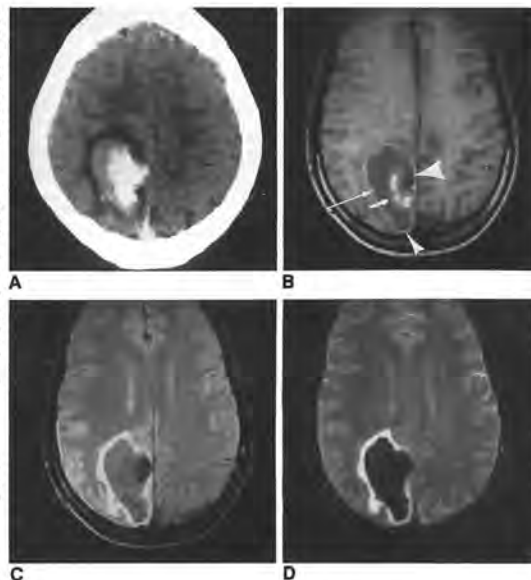
2. Subacute hematomas (about 1 week to <1 month old) are isointense to gray matter on T1-weighted images. The T2-weighted images proceeds to fill the whole hematoma and even becomes observable on T2-weighted images as well. This is formation of intracellular methemoglobin, which is paramagnetic, cell lysis and watery dilution by resorption of the resultant free iron.

3. In subacute and chronic hematomas, the adjacent brain parenchyma is hyperintense on T1-weighted images and markedly hypointense on T2-weighted images and shows a satellite enhancement. This is because hemosiderin deposits produce a satellite enhancement.

We report our observations on the previously unappreciated high-field MR intensities of subacute hematomas and discuss relaxation mechanisms and relevant differential diagnoses.

Subjects and Methods

Over a period of 1 year, we observed five patients with subacute intracranial hematomas. All hematomas were diagnosed and staged by CT. Two were confirmed surgically and pathologically. MR imaging was performed on a 1.5T superconducting unit. Spin-echo pulse sequences were obtained with two excitations, and 256 × 128 acquisition matrices. T1-weighted images



This article appears in the November/December 1987 issue of AJNR and the January 1988 issue of AJNR.

Received October 27, 1986; accepted after revision May 21, 1987.

¹Department of Radiology, Hospital of the University of Pennsylvania, 3420 Spruce St., Philadelphia, PA 19104. Address reprint requests to Dr. I. Grossman.

²Present address: Department of Radiology, Hahnemann Hospital, P.O. Box 12000, Jerusalem, Israel 91120.

AJNR 8:1016-1026, November/December 1987; 0195-9584/87/061016-11

© American Society of Neuroradiology

Recalling the Usefulness of Conebeam CT in Temporal Bone Imaging: Higher Resolution with Lower Radiation Dose

We read with great interest the article by Benson et al¹ on the potential clinical utility of photon-counting detector CT on temporal bone imaging. They prospectively recruited 13 patients who underwent clinically indicated temporal bone imaging on an energy-integrating detector CT (ie, conventional CT) and performed an additional temporal bone scan using an investigational photon-counting detector CT system. Reconstructed images from both examinations were then compared side-by-side by 2 blinded neuroradiologists using a 5-point Likert scale, and 2 important results were obtained: 1) significant preference for images from the photon-counting detector CT scanner; and 2) images obtained with this technique rated superior for the evaluation of all individual anatomic structures, with particularly higher scores on the oval window and incudostapedial joint. These results were mainly due to higher spatial resolution (0.2 mm image thickness versus 0.4 mm for conventional CT), with the additional advantage of performing the examinations with a 31% decrease in the total radiation dose (compared with conventional CT).

After reading these interesting results, we immediately recalled the role of conebeam CT (CBCT) in temporal bone imaging; thus, with the hope of adding to the aforementioned results, we would like to share some thoughts on this topic. CBCT systems operate using an x-ray beam with a conical geometry between the source and the detector; this is in contrast to the fan-beam geometry of conventional CT, in which the collimator restricts the x-ray beam to a 2D geometry.² This difference explains why, in CBCT systems using a 2D flat panel detector, a volumetric data set can be acquired with a single rotation of the gantry,² a fact that enables a spatial resolution of ≤ 0.1 mm with some systems, using low radiation protocols of about 10–100 μSv .³

Although initially used almost exclusively to perform dental radiology, such as implant placement-planning, temporal bone imaging applications became relatively frequent throughout some centers, obtaining a spatial resolution in the order of 0.075–0.15 mm with a much lower radiation dose than conventional CT scanners (in some cases down to 14% of the total dose obtained with a conventional CT³). This high spatial resolution leads to better capability of evaluating chronic otitis media complications (lysis of the long process or lenticular process of the incus, subtle tympanosclerosis, and/or incudostapedial subluxation), discrete fractures of the ossicles, dehiscence of the facial nerve canal or superior semicircular canal, and discrete

foci of otosclerosis. One should remember that the latter can manifest solely as thickening and hypodensity of the stapes footplate (type Ia of the Veillon classification), which is much more easily detected on CBCT due to its higher resolution. However, this technique has a few limitations: 1) the high resolution comes with the expense of a long acquisition time (up to 40 seconds³), a problem for patients who are not able to cooperate enough (ie, pediatric and very elderly patients), leading to motion artifacts that degrade image quality; 2) the need for more powerful x-ray tubes to study the dense temporal bone, which can lead to image degradation by increased scatter, especially in patients with large heads.³ There are, however, multiple approaches to scatter reduction, such as the use of a bowtie filter and an antiscatter grid.²

Nevertheless, many centers still rely on conventional CT for temporal bone imaging, possibly due to the reluctance to invest in a scanner that lacks soft-tissue contrast resolution (limiting its use in general diagnostic imaging⁴), with conventional CT having much broader general application. Due to the apparently similar diagnostic capabilities of CBCT and photon-counting detector CT (eg, higher resolution and lower radiation dose), we wonder if there could be an important difference in the diagnostic capability of the latter that could prevail over the somewhat clinically established CBCT. Moreover, it would be interesting for future studies to compare both of these techniques.

Disclosure forms provided by the authors are available with the full text and PDF of this article at www.ajnr.org.

REFERENCES

1. Benson JC, Rajendran K, Lane JI, et al. **A new frontier in temporal bone imaging: photon-counting detector CT demonstrates superior visualization of critical anatomic structures at reduced radiation dose.** *AJNR Am J Neuroradiol* 2022;43:579–84 CrossRef Medline
2. Miracle AC, Mukherji SK. **Conebeam CT of the head and neck, Part 1: physical principles.** *AJNR Am J Neuroradiol* 2009;30:1088–95 CrossRef Medline
3. Casselman JW, Gieraerts K, Volders D, et al. **Cone beam CT: non-dental applications.** *JBR-BTR* 2013;96:333–53 CrossRef Medline
4. Miracle AC, Mukherji SK. **Conebeam CT of the head and neck, Part 2: clinical applications.** *AJNR Am J Neuroradiol* 2009;30:1285–92 CrossRef Medline

© M. Quintas-Neves

© J. Saraiva

Neuroradiology Department
Hospital de Braga
Braga, Portugal

REPLY:

We thank the authors for their interest and commentary on our study¹ published in *American Journal of Neuroradiology*. We agree with the authors that studies comparing the diagnostic capabilities of conebeam CT (CBCT) and photon-counting detector (PCD) CT are of potential interest. However, there are key advantages of multidetector CT (MDCT) over CBCT that led to its widespread adoption in clinical practice for temporal bone imaging. Here, we will highlight the benefits offered by both MDCT in general and specifically PCDs, which may further enhance the utility of MDCT for temporal bone imaging.

First, modern MDCT systems offer considerable speed benefits. Such systems use conebeam geometry² (versus true fan-beam geometry used in older CT systems), multiple detector rows (eg, 120 detector rows, 0.2 mm/row¹) in a helical configuration, and fast gantry rotation times (0.5–1.0 seconds). These result in a typical temporal bone scan time of ≤ 5 seconds, with little-to-no motion artifacts and minimal patient discomfort. CBCT, in comparison, requires a scan time of up to 40 seconds.³ Second, radiation dose comparisons between CBCT and MDCT have been historically challenging due to the lack of standardized dose metrics and reliable measurement techniques for CBCT. The absorbed doses in CBCT and MDCT are reportedly similar if the scan FOV and image-quality parameters are approximately matched.^{4,5} The radiation dose in MDCT has continued to decrease with technical advancements in detector technology and reconstruction software (eg, iterative reconstruction). For instance, Leng et al⁶ reported a volume CT dose index (CTDI_{vol}) of 82 mGy for ultra-high-resolution temporal bone imaging and a further 50% potential dose reduction using z-deconvolution and iterative reconstruction algorithms in a second-generation MDCT system without sacrificing diagnostic image quality.

A recent MDCT temporal bone imaging study⁷ reported a CTDI_{vol} of 30 mGy and dose-length product (DLP) of 119 mGy \times cm. For CBCT, a DLP of 134 mGy \times cm for unilateral temporal bone imaging with a small in-plane FOV (8 \times 8 cm) has been reported in a cadaveric study.⁸ Our study¹ used a mean CTDI_{vol} of 35 mGy and a DLP of 250 mGy \times cm without a tin filter for bilateral imaging. By means of PCD-CT with a tin filter, the CTDI_{vol} can be further reduced to ≤ 10 mGy,⁹ and the DLP, to ≤ 150 mGy \times cm, without sacrificing diagnostic image quality. Therefore, the substantial improvement in PCD-CT in spatial resolution relative to non-PCD MDCT could be achieved at doses comparable with those of CBCT for bilateral temporal bone imaging.

Next, the utility of spectral images (such as virtual monoenergetic images) that are routinely available on PCD-CT is yet to be fully explored for temporal bone evaluation. Finally, CBCT has poor CT number uniformity and accuracy, poor soft-tissue contrast, and image artifacts compared with MDCT. Scatter-correction techniques such as antiscatter grids could help reduce artifacts at the cost of increased noise, which con-


sequently warrants an increase in the radiation dose or a reduction in spatial resolution.⁵ Unlike MDCT with fixed-source-detector geometry, CBCT uses an open gantry setup with flexible source-to-detector distance configurations, which requires robust and frequent geometric calibrations; residual calibration errors may degrade the spatial resolution in CBCT.

Spatial resolution and radiation dose are 2 of several factors contributing to the diagnostic utility of an x-ray imaging technique, and the limitations of CBCT may hinder its widespread adoption in large medical centers for temporal bone imaging as an alternative to MDCT. Current academic centers using conventional MDCT for temporal bone examinations may find the transition to PCD-based MDCT practical and reliable, with minimal changes to the imaging workflow. As with any technology, CBCT is likely to evolve beyond its current limitations and challenges, and we anticipate that research studies comparing CBCT with PCD-based MDCT for temporal bone imaging may provide insight regarding the strengths and weaknesses of each imaging technique.

REFERENCES


1. Benson JC, Rajendran K, Lane JI, et al. **A new frontier in temporal bone imaging: photon-counting detector CT demonstrates superior visualization of critical anatomic structures at reduced radiation dose.** *AJNR Am J Neuroradiol* 2022;43:579–84 CrossRef Medline
2. Bushberg JT, Seibert JA, Leidholdt EM Jr, et al. *The Essential Physics of Medical Imaging*. Lippincott Williams & Wilkins; 2012
3. Casselman JW, Gieraerts K, Volders D, et al. **Cone beam CT: non-dental applications.** *JBR-BTR* 2013;96:333–53 CrossRef Medline
4. Gupta R, Grasruck M, Suess C, et al. **Ultra-high resolution flat-panel volume CT: fundamental principles, design architecture, and system characterization.** *Eur Radiol* 2006;16:1191–1205 CrossRef Medline
5. Miracle AC, Mukherji SK. **Conebeam CT of the head and neck, Part 1: physical principles.** *AJNR Am J Neuroradiol* 2009;30:1088–95 CrossRef Medline
6. Leng S, Diehn FE, Lane JI, et al. **Temporal bone CT: improved image quality and potential for decreased radiation dose using an ultra-high-resolution scan mode with an iterative reconstruction algorithm.** *AJNR Am J Neuroradiol* 2015;36:1599–1603 CrossRef Medline
7. Heutink F, Klabbers TM, Huinck WJ, et al. **Ultra-high-resolution CT to detect intracochlear new bone formation after cochlear implantation.** *Radiology* 2022;302:605–12 CrossRef Medline
8. Kemp P, Stralen JV, De Graaf P, et al. **Cone-beam CT compared to multi-slice CT for the diagnostic analysis of conductive hearing loss: a feasibility study.** *J Int Adv Otol* 2020;16:222–26 CrossRef Medline
9. Rajendran K, Voss BA, Zhou W, et al. **Dose reduction for sinus and temporal bone imaging using photon-counting detector CT with an additional tin filter.** *Invest Radiol* 2020;55:91–100 CrossRef Medline

 K. Rajendran

 J. Benson

 J. Lane

 F. Diehn

 N. Weber

 J. Thorne

 N. Larson

 J. Fletcher

 C. McCollough

 S. Leng

Department of Radiology
Mayo Clinic
Rochester, Minnesota

Expression of Concern: “MRI-Based Deep-Learning Method for Determining Glioma MGMT Promoter Methylation Status” [Am. J. Neuroradiol. 42 (2021) 845-852]

Editorial expression of concern:

In the May 2021 edition, the *American Journal of Neuroradiology* published the article “MRI-Based Deep-Learning Method for Determining Glioma MGMT Promoter Methylation Status” by Yogananda CGB, et al.¹

On August 22, 2022, the authors self-reported data errors related to the computer code and the training and testing data sets. The authors are now in the process of re-evaluating the accuracies using the correct test set.

This notice of concern is to inform readers about these possible issues related to this articles results. After additional tests from the authors on the correct data set are available, we will determine what additional action is warranted, such as an erratum.

REFERENCE

1. Yogananda CGB, Shah BR, Nalawade SS, et al. **MRI-based deep-learning method for determining glioma MGMT promoter methylation status.** *American Journal of Neuroradiology* 2021;42(5):845-852. doi:10.3174/AJNR.A7029.

http://dx.doi.org/10.3174/ajnr.A7029_ERR

**Statement of Ownership, Management and Circulation
(All Periodicals Publications Except Requester Publications)**

1. Publication Title: American Journal of Neuroradiology
 2. Issue Frequency: Monthly
 3. Publication Number: 012630
 4. Filing Date: 10/13/2022
 5. Annual Subscription Price: \$452.00
 6. Complete Mailing Address of Known Office of Publication (Not printer) (Street, city, county, state, and ZIP+4):
 820 Jorie Boulevard, Suite 300
 Oak Brook, IL 60523
 7. Complete Mailing Address of Headquarters or General Business Office of Publisher (Not Printer):
 820 Jorie Boulevard, Suite 300
 Oak Brook, IL 60523
 8. Complete Mailing Address of Publisher, Editor and Managing Editor (do not leave blank):
 American Society of Neuroradiology
 820 Jorie Boulevard, Suite 300
 Oak Brook, IL 60523
 9. Full Name: American Society of Neuroradiology
 Complete Mailing Address: 820 Jorie Boulevard, Suite 300, Oak Brook, IL 60523
 10. Owner (Do not leave blank. If the publication is owned by a corporation, give the name and address of the corporation immediately followed by the names and addresses of all individual owners. If owned by a partnership or other unincorporated firm, give its name and address as well as those of each individual owner. If the publication is published by a nonprofit organization, give its name and address.)
 11. Known Bondholders, Mortgagees and Other Security Holders Owning or Holding 1 Percent or more of Total Amount of Bonds, Mortgages, or Other Securities. If none, check box None
 12. Tax Status (For completion by nonprofit organizations authorized to mail at nonprofit rates) (Check one)
 Has Not Changed During Preceding 12 Months
 Has Changed During Preceding 12 Months (Publisher must submit explanation of change with this statement below)

13. Publication Title: American Journal of Neuroradiology
 14. Issue Date for Circulation Data Below: 10/13/2022
 15. Extent and Nature of Circulation

Extent and Nature of Circulation		Average No. Copies Each Issue During Preceding 12 Months	No. Copies of Single Issue Published Nearest to Filing Date
a. Total Number of Copies (Net press run)		1,573	1,566
b. Paid and/or Requested Circulation			
(1) Mailed Outside-County Paid Subscriptions Stated on PS Form 3541 (Include paid distribution above nominal rate, advertiser's proof copies, and exchange copies)		1,218	1,213
(2) Mailed In-County Paid Subscriptions Stated on PS Form 3541 (Include paid distribution above nominal rate, advertiser's proof copies, and exchange copies)			
(3) Through Dealers and Carriers, Street Vendors, Counter Sales and Other Paid Distribution Outside USPS		139	137
(4) Paid Distribution by Other Classes of Mail Through the USPS (e.g. First-Class Mail)		86	80
c. Total Paid Distribution (Sum of 15b(1), (2), (3), and (4))		1,443	1,430
d. Free or Nominal Rate Outside-County			
(1) Free or Nominal Rate Copies Excluded on PS Form 3541			
(2) Free or Nominal In-County Copies Included on PS Form 3541			
(3) Free or Nominal Rate Copies Mailed at Other Classes Through the USPS (e.g. First-Class Mail)			
(4) Free or Nominal Rate Distribution Outside the Mail (Carriers or other means)		39	30
e. Total Free or Nominal Rate Distribution (Sum of 15d(1), (2), (3), and (4))		39	30
f. Total Distribution (Sum of 15c and 15e)		1,482	1,460
g. Copies not Distributed (See Instructions to Publishers #4 (page #5))		93	106
h. Total (Sum of 15c and g.)		1,575	1,566
i. Percent Paid (15c, Divided by 15e, Times 100)		97.37%	97.95%

16. Electronic copy Circulation
 If present, check box
 a. Paid Electronic Copies: 1,443 (1,430)
 b. Total Paid Print Copies (Line 15c) + Paid Electronic Copies (Line 16a): 1,482 (1,460)
 c. Total Print Distribution (Line 15f) + Paid Electronic Copies (Line 16a): 1,482 (1,460)
 d. Percentage Paid (Both Print & Electronic Copies (16b divided by 16c x 100): 97.37% (97.95%)
 I certify that 50% of all my distribution copies (electronic and Print) are paid above a nominal price

17. Publication of Statement of Ownership
 Publication required. Will be printed in the 11/01/2022 issue of this publication.
 Publication not required

18. Signature and Title of Editor, Publisher, Business Manager, or Owner
 Signature: [Signature]
 Title: Managing Editor
 Date: 10/13/2022

I certify that all information furnished on this form is true and complete. I understand that anyone who furnishes false or misleading information on this form or who omits material or information requested on the form may be subject to criminal sanctions (including fines and imprisonment) and/or civil sanctions (including civil penalties).

Simplify the MOC Process

Manage your CME Credits Online

CMEgateway.org

It's Easy and Free!

Log on to CME Gateway to:

- View or print reports of your CME credits from multiple societies from a single access point.
- Print an aggregated report or certificate from each participating organization.
- Link to SAMs and other tools to help with maintenance of certification.

American Board of Radiology (ABR) participation!

By activating ABR in your organizational profile, your MOC-fulfilling CME and SAM credits can be transferred to your own personalized database on the ABR Web site.

Sign Up Today!
go to CMEgateway.org

Available to Members of Participating Societies

American Board of Radiology (ABR)	Radiological Society of North America (RSNA)
American College of Radiology (ACR)	Society of Interventional Radiology (SIR)
American Roentgen Ray Society (ARRS)	SNM
American Society of Neuroradiology (ASNR)	The Society for Pediatric Radiology (SPR)
Commission on Accreditation of Medical Physics Educational Programs, Inc. (CAMPEP)	

In Planning for Brain Metastases Treatment, Imaging may be the Missing Link in Cost Containment¹

When faced with a patient presenting with metastatic brain cancer, determining whether to use up-front stereotactic radiosurgery (SRS) vs. first treating with whole brain radiotherapy (WBRT) is a significant clinical decision.

WBRT: The whole story on cognitive impairment

While whole brain radiotherapy (WBRT) has been the main treatment option for many years, experts agree that it often results in cognitive deterioration and a negative impact on quality of life. This mental decline has a devastating impact on patients and their families and adds ongoing costs for the healthcare systems managing these symptoms.

Using WBRT instead of SRS in some patients is estimated to decrease the total costs of brain metastasis management, though with increased toxicity.

SRS: Fewer side effects but greater risk of missed tumors

The cost of upfront SRS is the greatest contributor to cost of brain metastasis management.¹ SRS is often more expensive than WBRT. What's more, multiple applications of SRS can increase the cost of treatment greatly.

Stereotactic radiosurgery (SRS) has far fewer side effects, but upfront use of SRS is expensive and can carry the risk of missed tumors, requiring repeat procedures such as salvage SRS.¹

Number of lesions and lesion size are key factors to be considered when determining the treatment plan for these patients. It follows that increased diagnostic information and accuracy could be beneficial in directing the proper therapy and improving overall long-term patient outcomes and containing costs. Getting the diagnosis right the first time is crucial to ensure proper treatment begins quickly, and high cost/high stakes procedures such as SRS need precise surgical planning.

What does optimal visualization mean for outcomes and cost?

For surgical planning with SRS, radiologists need the best visualization achievable to accurately count the number and size of the lesions. These metrics are the key predictors of the need for SRS,¹ WBRT, or a combination of both.

By selecting the ideal contrast agent and equipment protocols, neuroradiologists can identify the proximate numbers of metastases for upfront treatment and reduced salvage treatment occurrences.

The role of radiology

As medical care for oncology patients continues to evolve, it will be increasingly important to assess the cost of various interventions given the often-limited life expectancy of cancer patients, the rising costs of cancer therapy, and the increasing prevalence of cancer in an aging population.

Through seeing all the tumors and tumor borders as clearly as technology allows, radiology can play a part in ensuring that proper treatment can begin quickly,

while containing costs through optimized patient care. Efforts to carefully manage treatment approaches require improvements in protocol design, contrast administration in imaging, and utilizing multimodal imaging approaches.

In this era of precision medicine, radiology departments' contribution to this improved standard of care will have significant short and long-term implications by reducing cost of care, providing a more proximate diagnosis, and ensuring optimal patient outcomes. ■



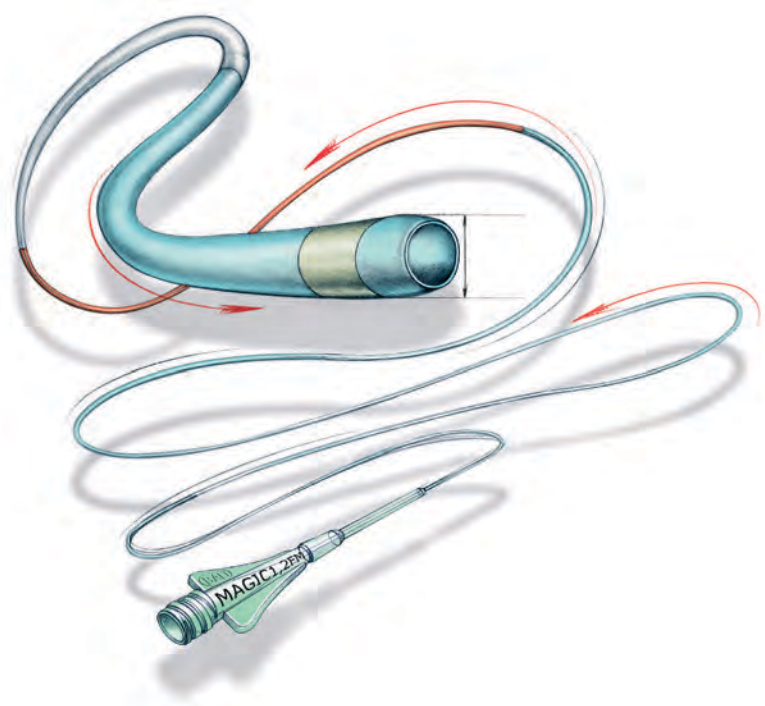
Getting the diagnosis right the first time is crucial to ensure proper treatment begins quickly.

Reference: 1. Shenker, R. F., McTyre, E. R., Taksler, D et al. Analysis of the drivers of cost of management when patients with brain metastases are treated with upfront radiosurgery. *Clin Neurol Neurosurg.* 2019 Jan;176:10-14.

CELEBRATING 45 YEARS
OF PHYSICIAN INSPIRED
INNOVATION



Magic™



THE ONLY FLOW-DEPENDENT MICROCATHETER SERIES



Balt USA
29 Parker, Irvine, CA 92618 • tel 949.788.1443 • fax 949.788.1444
baltgroup.com
©2022 BALT USA MKTG-323 Rev. A

